THE IMPACT OF VISIBILITY RANGE AND ATMOSPHERIC TURBULENCE ON FREE SPACE OPTICAL LINK PERFORMANCE IN SOUTH AFRICA

Okikiade Adewale Layioye

Thesis submitted in fulfilment of the requirements for the Degree of

Doctor of Philosophy in Electronic Engineering,

School of Electrical, Electronic & Computer Engineering,

University of KwaZulu-Natal, South Africa

UNIVERSITY OF
KWAZULU-NATAL

INYUVESI
YAKWAZULU-NATALI

August, 2022

Supervised by

Prof. Thomas J. O. Afullo

&

Co-supervised by

Prof. Pius A. Owolawi

As the candidate's supervisors, we have approved this thesis for submission.

Name of Supervisor: Prof. Thomas J. O. Afullo

Signed…….. Date....26th August 2022...

Name of Co-Supervisor: Prof. Pius A. Owolawi

19/08/2022

Signed…….. Date……..

Declaration 1-Plagiarism

I, **Mr. Okikiade Adewale Layioye**, declare as follows:

1. The research reported in this thesis, except where otherwise indicated, is my original research.
2. This thesis has not been submitted for any degree or examination at any other university.
3. This thesis does not contain other persons' data, pictures, graphs or other information, unless specifically acknowledged as being sourced from other persons.
4. This thesis does not contain other persons' writing, unless specifically acknowledged as being sourced from other researchers. Where other written sources have been quoted, then:
   (a) Their words have been re-written but the general information attributed to them has been referenced,
   (b) Where their exact words have been used, then their writing has been placed in italics and inside quotation marks, and referenced.
5. This thesis does not contain text, graphics or tables copied and pasted from the Internet, unless specifically acknowledged, and the source being detailed in the thesis and in the references sections.

16/08/2022

Signed _____ Date _____

Declaration 2- Publication

List of publications related to this Thesis including their overlapping Chapters:

Publication 1 (Journal): Overlapping Chapter 4

Okikiade A. Layioye, Thomas J. O. Afullo, Pius A. Owolawi, "Performance Analysis of FSO Communication Systems with Higher-Order Spatial Diversity Schemes Using BPSK-SIM over Log-Normal Atmospheric Turbulence Channels," *Journal of Communications*, Vol. 12, No. 6, pp 312-327, June 2017.

Publication 2 (Conference): Overlapping Chapter 5

O. A. Layioye, T. J. O. Afullo and P. A. Owolawi, "Visibility range distribution modeling for free space optical link design in South Africa: Durban as case study," *2017 Progress in Electromagnetics Research Symposium - Fall (PIERS - FALL)*, 2017, pp. 2732-2741, doi: 10.1109/PIERS-FALL.2017.8293601.

Publication 3 (Conference): Overlapping Chapters 4 and 7

O. A. Layioye, T.J.O. Afullo and P. A. Owolawi, "Calculations of the Influence of Diverse Atmospheric Turbulence Conditions on Free Space Optical Communication Systems Using the BPSK-SIM over the Gamma-Gamma Model," In the Proceedings of Southern Africa Telecommunication Networks and Applications Conference, SATNAC 2016, Cape Town, South Africa, September 2016, pp. 362-367.

Publication 4 (Conference): Overlapping Chapter 4

O. A. Layioye, T.J.O. Afullo and P. Owolawi, "Variation of Altitude on the Variance of Angle of Arrival Fluctuations for Beam Propagation in Free Space Optical Communications," 2016 International Conference on Advances in Computing and Communication Engineering (ICACCE), Durban, 28-29 November 2016, pp 117-122.

Publication 5 (Conference): Overlapping Chapters 4 and 5

O. A. Layioye, T. J. O. Afullo, P. A. Owolawi and J. S. Ojo, "Effect of Visibility Variation on Free Space Optical Communication System over the Eastern Coast of South Africa Using Climatic Data," 2022 9th International Conference on Electrical and Electronics Engineering (ICEEE), 2022, pp. 133-140, doi: 10.1109/ICEEE55327.2022.9772582.

16/08/2022

Signed _____ Date _____

Dedication

This thesis is dedicated to my father, the late Engr. G. T. Layioye,

I will not be who I am today without his genuine love and support.

To God be the Glory.

Acknowledgements

Firstly, I will like to express my profound gratitude to Professor Thomas J. O. Afullo and Professor Pius A. Owolawi for their total commitment and consistent guidance support to this research work and their encouragement and inspiration during my doctoral programme. I also thank them for their time, supervision, and motivation. Their invaluable constructive criticisms and suggestions from time to time aided my thorough understanding of the study and enabled me to complete my research work successfully.

I express my appreciation to Prof. J. S. Ojo, Prof. M. O. Ajewole and Prof. K. D. Adedayo for their incessant encouragement and support towards the completion of my programme. I thank my guarantors, Prof. (Mrs.) I. A. Fuwape and Prof. L. Lajide for their trust in me as well as their moral support and encouragement.

My deepest gratitude goes to my mum, Mrs. R. A. Layioye and to my siblings, Mr. B. O. Layioye, Dr. (Mrs.) A. O. Alabi and Miss. M. O. Layioye for their prayers and moral support. None of this would have been possible without the love and patience they showed to me. Also, my heartfelt gratitude goes to my very close friend, Miss. S. C. Malanda, who showed great understanding and consideration towards my work schedule. Likewise, my appreciation goes out to my uncle, Engr. T. F. Oluwafemi for his prayers and support during the course of my studies.

I thank my friends and acquaintances, especially Dr. A. S. Alabi, Mrs. F. M. Layioye, Dr. and Mrs. Ashidi, Mr. Bamidele Kolawole for their encouragement and support.

Finally, but most importantly, I thank God Almighty for His favour and protection over me all through the period of my programme. The wonderful grace he bestowed upon me saw me through the entire period of study.

Abstract

In the recent years, the development of 5G and Massive Internet of Things (MIoT) technologies are fast increasing regularly. The high demand for a back-up and complimentary link to the existing conventional transmission systems (such as RF technology) especially for the "last-mile" phenomenon has increased significantly. Therefore, this has brought about a persistent requirement for a better and free spectrum availability with a higher data transfer rate and larger bandwidth, such as Free Space Optics (FSO) technology using very high frequency ($194\ THz - 545\ THz$) transmission system. There is currently unavailable comprehensive information that would enable the design of FSO networks for various regions of South Africa based on the impact of certain weather parameters such as visibility range (mainly in terms of fog and haze) and atmospheric turbulence (in terms of Refractive Index Structure Parameter (RISP)) on FSO link performance. The components of the first part of this work include Visibility Range Distribution (VRD) modeling using suitable probability density function (PDF) models, and prediction of the expected optical attenuation due to scattering and its cumulative distribution and modeling. The VRD modelling performed in this work, proposed various location-based PDF models, and it was suggested that the Generalized Pareto distribution model best suited the distributions of visibility in all the cities. The result of this work showed that the optical attenuation due to scattering within the coastal and near-coastal areas could reach as high as $169\ dB/km$ or more, while in the non-coastal areas it varies between $34\ dB/km$ and $169\ dB/km$, which suggests significant atmospheric effects on the FSO link, mostly during the winter period. The BER performance analysis was performed and suitable mitigating techniques (such as 4×4 MIMO with BPSK and L-PPM schemes) were suggested in this work. The general two-term exponential distribution model provided a good fit to the cumulative distribution of the atmospheric attenuation due to scattering for all the locations. In order to ascertain how atmospheric variables contribute or affect the visibility range, which in turn determines the level of attenuation due to scattering, a time series prediction of visibility using Artificial Neural Network (ANN) technique was investigated, where an average reliability of about 83 % was achieved for all the stations considered. This suggests that climatic parameters highly correlate to visibility when they are all combined together, and this gave significant predictions which will enable FSO officials to develop and maintain a strategic plan for the future years. The modules of the second part of this work encompass the determination of the Atmospheric Turbulence Level (ATL) for each of the locations in terms of RISP (C_n^2) and its equivalent scintillation index, and then the estimation of the optical attenuation due to scintillation. The cumulative distributions of the optical attenuation due to scintillation and its modeling were also carried out. This research work has been able to achieve the prediction of the ground turbulence strength (through the US-Army Research Laboratory (US-ARL) Model) in terms of RISP using climatic data. In an attempt to provide a more reliable study into the atmospheric turbulence strength within South Africa, this work explores the characteristic behavior of several meteorological variables and other thermodynamic properties such as inner

and outer characteristic scales, Monin-Obhukov length, potential temperature gradient, bulk wind shear and so on. According to the predicted RISP from meteorological variables (such as temperature, relative humidity, pressure, wind speed, water vapour, and altitude), location-based and general attenuation due to scintillation models were developed for South Africa to estimate the optical attenuation. The attenuation due to scintillation results show that the summer and autumn seasons have higher ATL, where January, February and December have the highest mean RISP across all the locations under study. Also, the comparison of the monthly averages of the estimated attenuations revealed that at 850 nm more atmospheric turbulence with specific attenuations between 21.04 dB/km and 24.45 dB/km were observed in the coastal and near-coastal areas than in the non-coastal areas. The study proposes the two-term Sum of Sine distribution model for the cumulative distribution of the optical attenuation based on scintillation, which should be adopted for South Africa. The obtained results in this work for the contributions of scattering and turbulence to the optical link, and the design of the link budget will serve as the major criteria parameters to further compare the outcomes of these results with that of the available terrestrial FSO systems and other conventional transmission systems like RF systems.

LIST OF ABBREVIATIONS AND TERMINOLOGIES (in order of appearance in thesis)

Abbreviations	Definitions
MIoT	Massive Internet of Things
FSO	Free Space Optics
RISP (C_n^2)	Refractive Index Structure Parameter
VRD	Visibility Range Distribution
PDF	Probability Density Function
MIMO	Multiple-Input Multiple-Output
BPSK	Binary Phase Shift Keying
L-PPM	L-ary Pulse Position Modulation
ANN	Artificial Neural Network
ATL	Atmospheric Turbulence Level
US-ARL	United State – Army Research Laboratory
FO	Fibre Optic
MAN	Metropolitan Area Network
RF	Radio Frequency
OWC	Optical Wireless Communication
LOS	Line-of-Sight
EM	Electromagnetic
IR	Infra-Red
BER	Bit Error Rate
SIMO	Single-Input Multiple-Output
MISO	Multiple-Input Single-Output
AA	Aperture Averaging
OOK	On-Off Keying
LN	Log-Normal
GG	Gamma-Gamma
ITU-R	Int. Telecommunication Union-Radio
LWC	Liquid Water Content
GEV	Generalized Extreme Value
SST	Standard Statistical Techniques
SNR	Signal-to-Noise Ratio
CDF	Cumulative Distribution Function
MOST	Monin-Obukhov Similarity Theory
HAP	High Altitude Platforms
UAV	Unmanned Arial Vehicles
ICT	Information Communication Technology
AMS	American Meteorological Society
MVR	Meteorological Visibility Range
WMO	World Meteorological Organization
CIE	International Commission on Illumination
CCN	Cloud Condensation Nuclei
DSD	Drop Size Distribution
CCIR	Int. Radio Consultative Committee
TOWC	Terrestrial Optical Wireless Communication
LED	Light Emitting Diode
FOV	Field of View
QoS	Quality of Service
QAM	Quadrature Amplitude Modulation
OFDM	Orthogonal Frequency Division Multiplexing

Abbreviations	Definitions
PAM	Pulse Amplitude Modulation
SIM	Subcarrier Intensity Modulation
DPSK	Differential Phase Shift Keying
FEC	Forward Error Correction
LDPC	Low Density Parity Check
RS	Reed-Solomon
TCM	Trellis-Coded Modulation
IVC	Int. Visibility Code
LVC/MVC/HVC	Low/Mid/High Visibility Class
MBE	Mean Bias Error
RMSE	Root Mean Square Error
R^2	Coefficient of Determination
SSE	Sum of Squared Errors
TSS	Total Sum of Squares
MSE	Mean Square Error
RVR	Runaway Visibility Range
V	Visibility
SD	Standard Deviation
5G	Fifth-Generation
ACC	Average Channel Capacity
APD	Avalanche Photo-Diode
LM	Link Margin
WP3	Three-parameter Weibull
LP3	Log-Pearson Type-3
ISE	Integral Square Error
GP	Generalized Pareto
T	Temperature
RH	Relative Humidity
WS	Wind Speed
P	Pressure
SMA	Simple Moving Average
MRA	Multi-variant Regression Analysis
ARIMA	Auto-Reg. Int. Moving Average
AI	Artificial Intelligence
PW	Precipitable Water
MLP	Multi-Layer Perceptron
MCF	Mutual Coherence Function
HV	Hufnagel-Valley
HAP	Hufnagel/Andrews/Philips
SI	Scintillation Index
KDE	Kernel Density Estimator
MOM	Method of Moments

TABLE OF CONTENTS

LIST OF TABLES

LIST OF FIGURES

CHAPTER ONE

GENERAL INTRODUCTION

1.1 Introduction

Over the years, there has been an ever-growing interest for high transmission capacity, high data transfer speed, tackling the last mile issue among others. Several communication systems have existed but lack the capacity and potential to successfully handle these issues due to their mode of transmission. The terrestrial wireless transmission system has suffered great power losses and are less efficient due to the conditions of the atmospheric channel, when information is transmitted by the various existing conventional communication means. The development of the Fibre Optics (FO) provided a good resolution to most of these issues due to the nature of its transmission, however it has certain limitations that involve rigorous digging of trenches in order to install its cables for last-mile applications. Therefore, a wireless optical communication system is preferable to handle such situations. The evolution of Free Space Optical (FSO) communication systems are of major significance in order to accomplish the regularly growing demands of high data rates as well as better security network for future terrestrial, ground-to-space and satellite communication applications. According to the ever-growing interests for high transfer speed in terms of bandwidth data rate access as well as reliable connectivity among others, the FSO innovations have advanced with an end goal to take care of the last mile bottleneck issue strongly occurring in Metropolitan Area Networks (MAN) [1] – [4].

Free Space Optical (FSO) communication system is a robust and vastly emerging technology designed to handle and accommodate substantially high data rate due to the fact that its capacity for information handling is very large. This fast-growing Optical Wireless Communication (OWC) technology which is proficient enough to offer full-duplex transmission of multimedia services including voice, data and video in various applications and adequately provide fifth generation (5G) or next generation access network services and Internet of Things (IoT) services, has recently become an obtainable substitute to the Radio Frequency (RF) technology as well as the Fiber Optics (FO) technology. Although, from optics point of view, light wave information can be conveniently routed through the fiber cables by competently inserting the light signals, however, there exist numerous applications whereby the free space between a transmitting laser and receiving photodetector is the only accessible means of creating a communication link. In such cases, the FSO transmission system is a very good alternative. The required transmission path between the transmitting laser and the remote receiving photodetector for FSO system is only a clear Line-of-Sight (LOS) [5] – [9].

As a matter of fact, light beaming has been a very old signaling technique often used for the purpose of communication in the early days. Fire beacons were in existence around 800 BC, and they were

commonly used by the ancient Greeks and Romans for signaling purpose. Around 150 BC, smoke signals was employed by the American Indians for the same purpose. As technology began evolving during 1790 - 1794, optical telegraphs which were designed based on a chain of semaphores were utilized as means of communication between two locations by the French naval navigators. However, around 1880, the evolution of optical wireless connectivity began when Alexandra Graham Bell experimentally tested what was believed to be the first optical wireless communication system [10] – [12]. This renowned scientist had the outright privilege of demonstrating the photo-phone communication system modulated by the energy emanating from sunlight. This optical wireless communication system was designed only to transmit voice signal through a particular range by modulating and adjusting the light reflected from the sun on a foil diaphragm. The photo-phone communication device which transmitted voice signals over a few meters was considered as the world's first wireless telephone technology. Subsequently, the technology supporting the FSO changed in 1960, due to the origination of efficient optical sources like the laser by Hughes Research Laboratory (HRL), Malibu, California [13]. Following this, the FSO was employed in secure military applications. In 1970, a Japan Electrical Company called NIPPON Electric Company (NEC) created what was believed to be the first Full duplex FSO link covering a distance of about 14 km between two cities (Yokohama and Tamagawa) with the aid of the He-Ne laser having a wavelength of 0.6328 micron [14].

1.2 Background Review of the Study

Optical Wireless Communication (OWC) can be described as a promising technology that employs optical carrier to exchange information from a source to a destination by means of an unguided or unbounded channel which can be an atmospheric medium or a free space medium. It is acknowledged as a next generation communication system for very great speed broadband connection, due to the fact that it has the ability to provide tremendously large bandwidth and high transfer speed, unlicensed spectrum allocation, ease of deployment, low consumption of power (which is about half of the power consumption of RF transmission), reduced and compact antenna dimension (approximately one-tenth the diameter size of the RF antenna), optical link availability (of up to 99.99%), link reliability and enhanced channel security [12, 15].

The advancement of complex optical access networks has over the years lead to increase in the demand for higher bandwidths and intensification in the utilization of the EM spectrum. As a result of this, it is important to use the benefits of higher frequencies in the range of Terahertz that are capable of handling these incessant demands. The obvious contenders for the realization of these obligations are the optical wave bands (in terms of near infra-red and visible light spectra). The benefits offered by these EM wave spectra have obviously attracted great attention from the private users, communications industry, researchers and the military. The main characteristics and properties of these optical waves involves frequency re-use, short wavelength (which corresponds to small components) and large bandwidth. The interaction of the propagated optical beam within the free space with the constituents of the atmosphere

(in particular with aerosols or hydrometeors and scintillation), leads into severe impairment of the optical signal at these high frequencies. These impairments include atmospheric scattering, absorption, phase distortion and scintillation resulting to optical attenuation or optical signal fading.
The OWC can be grouped into two general classifications which are indoor and outdoor (open air or outside) OWCs and the detailed classification of the types of OWC system is presented in Figure 1.1.

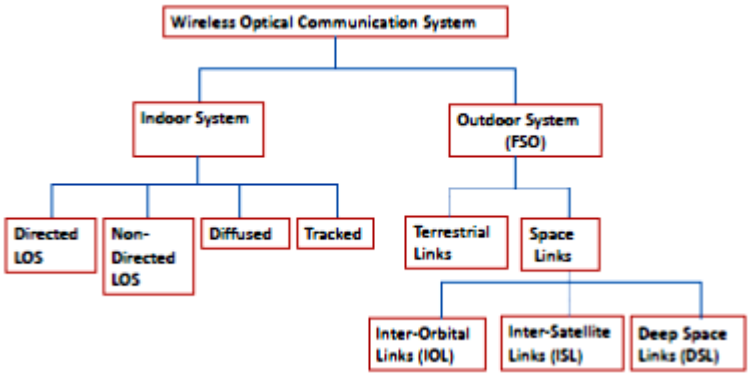

Figure 1.1: Block classification of the OWC system.

FSO systems have so far been considered as a potential leading technology serving as an alternative to the conventional Radio Frequency (RF) transmission system. Amongst several wireless links, it offers an unlicensed spectrum, cost effective network system and secure communication system. But this comes at the expense of various challenges, for example, significant optical signal power loses as a result of atmospheric scattering and absorption, and atmospheric turbulence in form of scintillations that require serious attention and drastic measures.

This research work therefore presents the outcome of the evaluation of the aerosols or hydrometeors (in form of fog, haze and clouds) and scintillation with the light waves propagating in the atmospheric medium consisting of the atmospheric particles, droplets, turbulent eddies and other impairments. It should be noted that the term "aerosols" and "hydrometeors" (are natural phenomena that) denotes the products of fine particles or liquid droplets and condensed water vapour suspended within the air, often observed in form of fog, haze, snow, rain, mist, dust, smoke and clouds. Also, it should be noted that the term "scintillation" is a natural phenomenon which refers to the effects obtained from thermodynamic movement of the irregular three-dimensional turbulent eddies in form of small- and large- characteristic scales of air, resulting into the irregular fluctuations of the atmospheric temperature and pressure. This random phenomenon results into the variation of the refractive index structure parameter (denoted by C_n^2) which is the determinant factor of the turbulence strength. The environment whereby the thermodynamic movements take place is referred to as the inertial subrange, which consists of the two characteristic scales of air creating a form of irregular variation of the refractive index of air (n) . This variation in n, which results into the variation of C_n^2 causes the irradiance and phase distortion of the optical beam propagating through the free space as a function of height. For optical propagation

through the free space, the most significant of these optical attenuation effects is that obtained from the suspended aerosol or hydrometeors, especially fog and haze and then followed by that of the effects of the turbulence, which are as a result of atmospheric scattering and scintillation respectively. Therefore, this research study mainly takes into account the total impacts of fog, haze, clouds and scintillation on the near IR or visible waves at frequencies between 187.5 – 500 THz and optical wavelength between 600 nm – 1600 nm.

In terrestrial and space optical communication links, the light signals transmitted at these high frequency ranges interact with fog or haze particles, small snowballs, rain drops, clouds and turbulence, since they cover a large path of the optical link. An EM wave propagating via a free space consisting of any of these impairments basically suffers three attenuating impacts. These attenuation phenomena are atmospheric absorption by which portion of its energy is absorbed by the existing molecules and then transferred into heat, the second mechanism is atmospheric scattering where most of the optical energy is scattered in all directions, and the last is the atmospheric scintillation resulting into signal power fading and phase distortion as a result of the presence of turbulent eddies. However, various studies have shown that the effects of the atmospheric absorption to the attenuation of optical signals is negligible, and this means the optical energy suffers two main attenuating effects which are atmospheric scattering and scintillation.

The detailed investigation of these two main attenuating mechanisms is due to understanding the characteristics of fog and haze particles, snow falls, rain droplets, clouds and characteristic scales of the turbulent eddies. In this thesis, the various characteristics of the above mentioned impairments are examined in terms of visibility range, worst-month statistics of visibility, probability and cumulative distribution of visibility and its modelling, cumulative distribution of the optical attenuation due to fog and clouds, and its modelling at different categorization classes, while the other aspect examined the impairments in light of C_n^2, worst-month statistics of C_n^2, cumulative distribution of the optical attenuation due to turbulence and its modelling at diverse categorization conditions. All the various afore-mentioned attenuation phenomena are analysed and discussed in this thesis to allow simple determination of the overall optical attenuation of optical frequency signals in the near IR and visible spectra.

1.3 Brief Review of Existing Work

The FSO laser communication system is an optical classification of wireless communication systems which provides an appealing alternative to Radio Frequency (RF) transmission systems, as a result of its bigger data transfer capacity, larger bandwidth, license-free spectrum, improved security and privacy, higher antenna gain, lower components and installation costs, reduced FSO antenna units and component sizes among others, as discussed in [1, 3, 5, 16]. In general, this type of wireless communication system has been extensively utilized as a part of numerous applications, for example,

military applications, terrestrial applications, space communications, last-mile communication solutions, airplane-to-airplane communications, biomedical applications, transient network installations, security add-ons items for important fiber networks [7, 9, 12, 17, 18]. As a result of all its sophisticated features, the FSO has established growing attention with the current commercialization of its applications. Notwithstanding, with all the numerous and sophisticated advantages of the FSO mentioned earlier, it also faces severe challenges because of occurrences and activities within the atmosphere such as absorption, scattering and turbulence as discussed in [19] – [28].

Since the FSO technology-based wireless system like other existing wireless systems have its own challenges which results into a degradation in its optimum performances, therefore errors are introduced into this system as a result of the fact that it is prone to atmospheric conditions, and thus, makes the FSO system to be unworkable or weak for quite a period of time. According to various investigations by [3]; [20] - [22]; [26, 27]; [29] – [31], it can be said that the FSO link signal gets degraded by the atmosphere in numerous ways such as scintillation, scattering and absorption. However, the resultant attenuation obtained over a FSO link is largely as a result of the following atmospheric occurrences: atmospheric turbulence (such as scintillation or beam spreading) and scattering due to water droplets (such as fog, rain, drizzle, snow, mist and so on), while that of absorption as a result of water vapour is negligible. Thus, the negative contributions by these factors adversely affects the Bit Error Rate (BER) performances of the FSO communication link as well as the visibility range.

Several studies provided by [19] – [22]; [32] – [37] have shown the relationship between various atmospheric conditions (such as scattering, absorption, turbulence, etc.) and the terrestrial area, altitude, and meteorological factors like humidity, visibility range, temperature and pressure variations, wind speed, precipitation and so on, for FSO transmission system. In most of these past works, the feasibility studies of FSO implementation in the considered geographical regions were carried out with statistical data of certain atmospheric scattering conditions (in particular, visibility) collected from various weather stations and the turbulence related data were mostly assumed, due to the difficulty in measurement or estimation. To obtain a better feasibility study, this work has been able to achieve the computation of the turbulence associated data (in terms of C_n^2) from collected meteorological variables rather than using an assumed C_n^2 value for the calculation of scintillation.

One of the greatest challenges faced by FSO is the occurrences of fog due to the fact that it is made up of small water drops and aerosols about the magnitude of the wavelengths of near infrared. These water particles resulting into fog, are found to be sufficiently dense enough to cause diffraction of the light pulse as well as result into optical signal extinction along the FSO link. Aerosols such as fog drops have been noted to have the greatest atmospheric effects on FSO links, thereby restricting the range of the optical link to a few hundred meters, especially during the heavy or dense fog events [20]. However, fog has less influence on some Electromagnetic (EM) waves such as RF signals when compared to the

optical beam. Also, rain occurrences have less influence or fading on the optical beam when contrasted with the RF signals [19] – [22]. Consequently, the limitations of atmospheric loss can be overcome by employing the proposed hybrid FSO/RF technique that uses both communication systems as a composed technique [17, 38, 39]. To obtain a better communication network performance, that suits this generation and the future, additional work has been accomplished using various modulation as well as coding techniques over hybrid FSO/RF networks [40] – [43].

Several authors in [3, 29, 31]; [44] - [46] have investigated the atmospheric turbulence effects on FSO, though majority of these investigations are theoretically-based and so few experimental works have been reported. The reason for this is because the measurement of the impacts of the atmospheric turbulence under different conditions is quite difficult to achieve in practice. This is largely as a result of the long-waiting time required to measure as well as experience the reoccurrence of diverse atmospheric conditions. Therefore, the irradiance fluctuations of the received optical beam as a result of atmospheric turbulence introduces a severe issue. The random fluctuations of the atmospheric temperature and pressure induces a reasonable atmospheric turbulence which leads to random variation of the refractive index structure parameter of the atmosphere. This variations in the atmospheric index of refraction along the path of the optical beam results into random fluctuations of the received optical irradiance, thereby leading to a serious degradation in the performance of the system [47] – [50]. However, several methods now exist that can be employed to mitigate the impacts of the induced atmospheric turbulence, like the spatial diversity technique (for instance, the Multiple Input Multiple Output (MIMO) technique) [3, 29, 51, 52] and temporal diversities [44], distinctive modulation techniques, aperture averaging [53], channel coding techniques [54], forward error correction, and so on. It is of great importance to select a suitable modulation format that is highly immune to the impacts of scintillation [3, 31, 52, 55]. Also, most research studies that have examined the impacts of atmospheric fog over the FSO communication system, mostly focused on optical attenuation measurement as well as channel modeling [19] – [22]; [56, 57]. However, not much research work has been reported on the BER performance of FSO communication link during fog, which is one of the objectives of this dissertation.

As a result of the occurrences of scattering and atmospheric turbulence within the air, an excellently fast-tracked and perfectly optimized FSO laser communication system with properly aligned antennas encounters reduction in signal power due to scattering [20] – [22] and random power fading due to turbulence [58] as the case may be. Whereas, the optical link with an imperfect or no fast-tracking may also cause an irregularity in the Probability Density Function (PDF) of the fading power as a result of pointing error which is a resultant of the total displacement between the center of the laser beam and the receiver aperture center. This misalignment phenomenon consists of continuous misalignment as well as random pointing error, and some of its sources are relative movements of the transceivers, optical misalignments, turbulence induced beam wander and mechanical vibrations [58] – [60].

The other important factor that contributes to the attenuation experienced over FSO communication link is loss due to geometric attenuation. Apart from the LOS concept employed by this optical wireless system, it transmits a light beam that is narrow as well as highly directional, which must impinge on the receive aperture of the telescope placed at the receiver side of the communication link. At least one beam of light is transmitted by the optical source, and this spreads naturally as the distance propagated increases as a result of light or laser source divergence. Therefore, the spreading of the transmitted beam of light due to increasing range results into the geometric attenuation [61]. Thus, a portion of the optical signal would be lost, due to the fact that the whole beam of light would not be collected by receiving telescope. In order to take maximum advantage of the applications of the optical wireless link, novel mitigating techniques should be investigated in the near future so as to diminish the FSO limitations. Additionally, the FSO provides an alternate option of ground-to-satellite communication link, inter-satellite communication link alongside the terrestrial (earthly) communication connection. Nevertheless, in order to decrease the occurrences of geometrical attenuation within the FSO communication links which results into increase in optical link distance, the optical beam has to be tracked using highly accurate tracking system. Several procedures are being investigated by many specialists to decrease the problem of tracking. In the cases involving the earth-to-satellite communication links as well as inter-satellite communication links, the tracking problem becomes more severe [58, 60].

The FSO communication link performance can be improved by numerous techniques that have been proposed by different researchers, in terms of BER as well as link availability. Numerous techniques on the reduction of atmospheric turbulence have been studied in [3, 27, 28, 44, 51, 52, 54, 55], in order to provide a mitigating solution to the effects of atmospheric turbulence on the FSO channel, and improve the channel capacity, BER as well as the outage probability of the optical link. The commonly used turbulence mitigation techniques that have been employed in FSO are diversity techniques, distinctive modulation techniques, aperture averaging, channel coding techniques, forward error correction, and so forth.

Diversity technique is one of the most significant mitigating schemes that is capable of diminishing the BER degradation that is generated as a result of atmospheric scattering and turbulence. Diversity, in principle describes the application of multiple copies of the transmitted optical signal from the laser so as to conquer a poor propagation path and then improve the reliability performance, efficiency and degradation of the optical communication systems. Therefore, there will be a reduction in the blockage probability, the optical link reliability will be improved and the requirements for active tracking as a result of the laser misalignment will be restricted. This technique can be employed to alleviate the signal fading in optical wireless transmission system, as well as in other existing transmission systems like RF transmission systems. There are various forms of diversity techniques, which are spatial diversity (such as Single-Input Multiple-Output (SIMO), Multiple-Input Single-Output (MISO) and Multiple-Input

Multiple-Output (MIMO)), time diversity and wavelength diversity. The diversity technique using space mode involves using multiple number of smaller transmit or receive apertures, adequately spaced apart and receiving different optical signals through independent paths in order to reduce the effects of scattering and scintillation. Chen et al., (2009) presented the optical channel model using M number of transmitters and N number of receivers by Monte Carlo method so as to determine the probability of outage of an optical link with spatial diversity under diverse situations of atmospheric turbulence [51]. The error rate capabilities of FSO communication system under strong (K-distributed) turbulence regime were studied by Tsiftsis *et al.* (2009) [62], and the likely benefits of deploying of space diversity techniques at the transceivers were also discussed. Also, for system performance improvement of a FSO link, [54] and [63] discussed the time diversity techniques.

As a result of its simplicity as well as low implementation cost, aperture averaging (AA) technique has also been recommended as one of the approaches to mitigate the effects of atmospheric turbulence and have been discovered to be highly effective particularly for the weak to intermediate atmospheric turbulence regime. The effect of AA on the performance of FSO systems under diverse atmospheric turbulence was reported by [64].

Another significant mitigation technique is the utilization of various signal modulation schemes such as the On-Off Keying (OOK) format, Binary Phase Shift Keying Subcarrier Intensity Modulation scheme (BPSK-SIM), which are probably seen as the simplest forms of modulation schemes, and many others.

In addition, an advance type of modulation scheme which involves a combination of two modulation schemes have been suggested. The effects of atmospheric turbulence can be substantially reduced by the means of this type of mitigation technique. Utilizing OOK and subcarrier BPSK modulation in his work to investigate the BER performance of FSO systems, Barua (2011) detected that the BER performance using subcarrier BPSK modulation is better than that of using OOK modulation format [65]. Also, Faridzadeh *et al.* (2011), performed error probability analysis, by comparing hybrid PPM-BPSK-SIM and PPM modulation schemes and it was observed that the performance of the hybrid PPM-BPSK-SIM was better than BPSK-SIM for all atmospheric scintillation [66].

The overall FSO performance can be dictated by the fading PDF of the beam signal power received at the photo-detector. Since 1970s, several scholars have explained this fading PDF of the received irradiance of the FSO system, and various models that gives the probability distribution have been proposed in this regard. One of the earliest of these models is the Log-Normal (LN) fading PDF, developed in the early 1970s to describe the received irradiance was computed using the first-order of Rytov approximation. Consequently, it was employed to describe the random power fluctuation within the weak atmospheric turbulence regime [23]. In 1979, analysis was carried out on some experimental data, and the K distribution model was found to perfectly fit the probability density trend of the data under a relatively strong atmospheric turbulence regime [67]. The incessant research on the fading PDF of the received optical beam power introduced the Gamma-Gamma (GG) distribution model in 2001,

which was noted to give a good fit to the fading PDF when the aperture of the receiver is significantly lesser than the coherence radius, in the weak to strong turbulence regime [50]

In the first part of this thesis, the effects of aerosol scattering as a result of fog was considered. The empirical results of optical attenuation due to fog on FSO communication links operating between visible to near infra-red wavelengths that ranges from 0.6 micron to 1.6 micron are presented in this research work. Also, the atmospheric conditions related to haze and clear sky conditions were also examined in this work on a FSO link in terms of the corresponding visibility range data. A comparison of the obtained results of the fog attenuation were made with selected experimental fog models such as the Kim, Kruse, Al-Naboulsi (advection and radiation) models, and ITU-R so as to practically validate their performances. The fog occurrence distribution was characterized and modeled for six (6) different provinces within South Africa. This was achieved by obtaining the probability density distribution of fog particles based on the visibility range and then determining the specific optical attenuation for each location. The comparisons of these specific attenuations were made with other models such as the Kim, Kruse, Al-Naboulsi (advection and radiation) models, and the ITU-R models.

In the second part of this thesis, the atmospheric attenuation due to scintillation for the FSO communication system operating through atmospheric turbulence channel were calculated using an analytical method, under the following conditions: diverse turbulence strengths in terms of the refractive index structure parameter, different optical wavelengths, certain size of the receiver aperture, propagation distance, and beam diverging angles and so on.

1.4 Problem Statement

The previous decade up until the present, has experienced immense increase in big data transfer and broadband communication applications, especially for the sustenance of the available generation access networks and the Internet of Things applications. This excessive demand imposed great pressure on the existing link capacity based on bandwidth and high-speed requirements. Therefore, this resulted into the exploitation of higher frequencies (particularly the light wave bands in terms of visible and near infrared bands), which provides a probable answer to the afore-mentioned problems, however it is hindered by the presence of hydrometeors or fog particles and irregular fluctuations in temperature and pressure, causing atmospheric scattering and turbulence. The non-uniformity and randomness of fog, haze, snow, rain, mist and clouds causing degradation in visibility along the optical propagation path is significantly considered through the creation of empirical models, that are dependent on the optical wavelength of the transmitting signals, accuracy of the visibility range, rain-rate, water vapour and Liquid Water Content (LWC) measurements or on the reliability of the collected climatic data, and on the accuracy of the respective measurement devices. Also, the irregular fluctuations of the atmospheric temperature and pressure resulting into variations in the refractive index structure parameter and atmospheric turbulence, is taken into account through various scintillation models which depends on

the optical wavelength of the transmitting signals, altitude, accuracy of the meteorological variable (such as temperature, pressure, wind speed, humidity, water vapour etc.) measurements or on the reliability of the collected climatic data, and on the accuracy of the respective measurement devices.

Based on the many problems facing the employment and commercialization of FSO, this research work has been considered to answer several questions concerning its performance in temperate locations like South Africa. Among several questions to be handled, some have being highlighted as follows: can the reliability of FSO actually reach 99.99 % link availability, how much effect does various atmospheric conditions and impairments (especially fog and scintillation) have on optical transmission through the atmosphere, how best to achieve a sustaining mitigation and what mitigating techniques will be suitable for temperate locations, which probability and cumulative distribution models fits the optical attenuation in this region, how does location and terrain affects the optical link, and can the level of effect of fog and scintillation on FSO in terms of attenuation, received power, SNR, etc., be managed.

Therefore, the evaluation of the extent of optical signal loss due to the interaction between the employed EM wave (i.e., optical wave) with any or all the afore-mentioned impairments or conditions needs to be thoroughly studied and relevant prediction models must be proposed for present use or for future research works. The challenges encountered in optical beam propagation is then divided into two basic sections to proffer a detailed description of the characteristics of fog, haze, clouds (in terms of clear sky) and turbulence that leads to signal impairment or signal power fading: firstly, the statistical characterization of visibility range based on various atmospheric conditions (especially scattering) and determination of the optical attenuation due to fog, haze and clouds, and secondly, the determination of the C_n^2 and investigation of the atmospheric turbulence based on scintillation.

1.5 Research Motivation

FSO problems have persisted for some decades, and this has needed more study to determine suitable techniques to achieve a greater future in the world of communications (specifically optical communications). Also, to meet up with the constant high demands of the future generation access networks and MIoT, certain problems have been raised over the years about the reliability of FSO to achieve 99.99% link availability in particular locations with unfavourable conditions.

Based on the EM band involved in FSO communication system, this research will enable the study of the effects of unpredictability of fog, haze, snow, rain, mist and clouds over the FSO link. Also, it will aid the study of the incidences and effects of various turbulent eddies, and the irregular variations of temperature and pressure resulting into changes in the refractive index structure parameter and turbulence (in terms of scintillation) over the FSO link. Fog, haze, and the turbulent eddies are the distinct constituents, particularly at these Electromagnetic (EM) waves spectrum. Through modelling of the intrinsic meteorological mechanisms, the characteristics of optical wave propagation through the

free space are explained using statistical information of the atmospheric constituents, which serves as the various conditions that restrict the optimal performance of the FSO link. The outcomes of the various empirical fog and turbulence models are integrated into the planning of the optical system software or link power budget, in order to reproduce the optical wireless transmission chain and to determine the performance of the FSO link, before the implementation of the optical wireless communication system.

1.6 Research Aim and Objectives

The aim of this research work is to empirically characterize, investigate and model the effects of atmospheric channel specifically due to atmospheric scattering (i.e., fog, haze and clear air events) and turbulence on the FSO communication link performance.

Since the reoccurrence of these atmospheric events is unpredictable, then to practically measure and verify the effects of atmospheric turbulence (scintillation) as well as atmospheric scattering is very challenging, under diverse conditions such as different combinations of temperature, wind velocity, pressure, relative humidity, altitude, visibility range, light to dense fog conditions, haze and clear sky conditions. Hence, the visibility data collected from the National Oceanic and Atmospheric Administration/National Centers for Environmental Information (NOAA/NCEI) database were used to characterize, analysis and model the atmospheric scattering effects, and then the atmospheric optical attenuation from the FSO channel was determined for each of the locations considered in this study. Also, the obtained atmospheric data from the South African Weather Service (SAWS) consisting of certain atmospheric parameters (such as temperature, pressure, wind speed and relative humidity) were used to simulate, demonstrate, and model the atmospheric scintillation effects on the FSO channel for different selected provinces within South Africa. This empirical study based on the measured atmospheric parameters permits us to investigate the impacts of certain atmospheric impairments such as atmospheric turbulence and fog on the optical signal propagating via the FSO channel for selected locations as well as optical wavelengths.

To accomplish this aim, a list of research objectives has been outlined as follows:

1. To perform a broad visibility range characterization to adequately profile and structure the changes in the atmosphere based on severity and provide analysis on these variations in the atmospheres of various locations in South Africa using climatic data. This analysis is to be achieved in terms of the average atmospheric transmittance and optical depth of the atmosphere for each of the locations under study.
2. To investigate the effects of various classes of atmospheric conditions (such as fog, haze and clear sky) and visibility range on OWC link design in South Africa, by determining the optical attenuation as a result of scattering phenomenon (at different wavelengths characterized by the visibility range).

3. To perform an optical system performance analysis under various atmospheric conditions based on the results obtained from the optical attenuation due to scattering, and the results are used to derive the link budget and BER performance of the FSO system.
4. To perform statistical analyses on the collected visibility data and estimated optical attenuations in terms of synoptic, diurnal, daily and seasonal variations using time and frequency series over the selected locations in South Africa. These analyses provide the visibility and attenuation patterns in terms of various visibility classes.
5. To develop suitable Visibility Range Distribution (VRD) models for South Africa by comparing various PDF models, as well as observing its implication on the link design at various time % exceedance windows. Using the probability distribution models such as Generalized Pareto, Johnson SB, four- and three-parameter Dagum, Generalized Extreme Value (GEV), Four-Parameter Generalized Gamma, Kumaraswamy, among others, the derived results are estimated and compared with the measured PDF.
6. To investigate the time series prediction of visibility in terms of various meteorological variables (in particular, relative humidity, atmospheric temperature, wind speed and pressure) by means of the Standard Statistical Techniques (SST) and Artificial Neural Network (ANN) Technique using climatic data. Using the results obtained from the ANN, a times series prediction model for visibility was developed for South Africa.
7. To determine the refractive index structure parameter (C_n^2) using a selected parametric atmospheric turbulence prediction model (i.e., the US Army Research Laboratory model) in terms of various atmospheric variables and the characteristic properties of the atmospheric channel due to atmospheric turbulence, based on the theories and background literatures of tropospheric scintillation.
8. To investigate the effects of atmospheric scintillation over the FSO link design for South Africa by estimating the scintillation index, Rytov variance and atmospheric optical attenuation due to turbulence at different optical wavelengths, in order to practically validate its performance and to study the implications of channel fading due to atmospheric turbulence.
9. Empirical characterization, verification and modeling of the atmospheric optical turbulence using climatic data for South Africa.
10. To model the cumulative distribution of the optical attenuation due to atmospheric turbulence for South Africa, using curve fitting models such as Fourier, Polynomial, Sum of Sine, etc., to perform a cumulative distribution of the effects of scintillation on the designed FSO link.

1.7 Original Contributions of this Research Work

As a direct outcome of this research work, the original contributions achieved in this research have been outlined as follows:

a. Investigation and comparison of different experimental fog models that calculates the terrestrial optical specific attenuation due to fog, based on the measured visibility range for six different provinces within South Africa at different optical wavelengths in the range of the visible to Near-IR of the Electromagnetic Wave (EM) spectrum.
    - This investigation presented in Chapter 4, involved examining and analyzing the behavior of the obtained optical attenuation due to fog, haze and clear sky which resulted from the application of these fog models for various parameters such as the visibility range in meters, optical wavelength and the transmittance threshold.
    - Therefore, this investigation demonstrates that despite a significant number of studies, these empirical fog models are to be explicitly verified empirically for the whole EM spectrum spanning from visible to Near-IR spectrum, but not just for a specific or selected optical wavelength.

b. In Chapter 4, the estimated optical attenuation results due to scattering were reported in order to test, validate, analyze and mitigate the impacts of atmospheric fog, haze and clouds on FSO link design. The analysis of the effects of scattering was achieved through the investigation of the system performance of the free space optical link under the control of various atmospheric conditions. The following were computed and presented:
    - the received optical power, Signal-to-Noise Ratio (SNR) (also referred to as the Q-factor), outage probability, maximum reachable length, maximum cell size and BER were estimated from the obtained atmospheric attenuation for different atmospheric conditions such as from light to thick/dense fog densities, haze and clear sky.
    - Thus, the outcomes of Chapter 4 determine and validate the influence of fog, haze and clouds on the overall performance of the optical link design for South Africa by observing the optical attenuation, received optical power, SNR, outage probability, transmittance and channel capacity values for a range of visibility values, atmospheric conditions, wavelength, optical link distances and geographical locations.

c. The detailed characterization of various atmospheric conditions based on fog, haze and clear sky in terms of various visibility classes is presented in Chapter 5. Also, at each selected visibility class, the effects of atmospheric particle due to Mie-scattering over the propagating optical beam through the foggy, hazy or clear sky atmospheres can be studied independently.
    - With this method and analyses, the slightest change or effect on the optical link can be noticed and adequately accounted for.
    - Therefore, a total effect of the atmospheric particles or the overall estimated attenuation due to fog, haze and clear sky over the entire visibility range considered, reflects an average accumulation or growth of each stage of the atmospheric conditions occurring at each of the geographical locations.

d. Different PDF models to describe and characterize the measured visibility range for each of the selected geographical locations within South Africa, were compared and analyzed accordingly in Chapter 5. Also in this Chapter, different Cumulative Distribution Function (CDF) models to describe and characterize the estimated optical attenuation based on measured visibility range for each of the selected geographical locations were compared and analyzed. The overall better PDF and CDF models were selected based on their general fitness performance across all the locations within South Africa, and this resulted into:
    - Location-based and general visibility range distribution models,
    - Location-based and general optical attenuation model based on atmospheric scattering and measured visibility range, which can be used to determine optical attenuation values for South Africa at various time exceedance percentages.

e. Proposed visibility prediction model for South Africa using ANN technique based on meteorological variables:
    - The time series prediction model developed in Chapter 6 for visibility range in terms of various meteorological variables using the ANN technique will provide adequate information to the FSO engineers in order to suggest or design good optical links and generate suitable mitigating techniques.
    - Since one of the most important climatic data for FSO is the atmospheric visibility, then visibility prediction improves and refines the learning model in forecasting possible occurrences and effects of fog, haze and clouds in South Africa and surrounding environments.
    - Also, this section shows that ANNs are better suited to solve these kinds of problems, and therefore have a great potential for predicting the occurrence of fog, which then characterises the significance of establishing parameterized models to assist those accountable for strategizing the design of FSO systems and flight instruction activities.

f. The Monin-Obukhov Similarity Theorem (MOST) approach along with the obukhov length were used on the obtained atmospheric data (including temperature, humidity, wind speed pressure and water vapor) to generate the different levels of atmospheric turbulence (in terms of the C_n^2) per hour for the selected provinces in South Africa. The detailed description of this approach and methodology used in obtaining this atmospheric turbulence profile are presented and analyzed in Chapter 7.
    - Here the refractive index structure parameter, C_n^2 (corresponding to the strength of the atmospheric turbulence) due to the dynamic movements of the irregular three dimensional turbulent eddies within the atmosphere were estimated and analyzed in terms of day and night scintillations for South Africa.
    - The Rytov variance and hourly scintillation index were deduced for each of the cities.

- The atmospheric turbulence levels for each of the locations considered are analyzed in terms of the estimated optical attenuation profile due to turbulence, which was obtained from the estimated Rytov Variance and Scintillation index for a range of atmospheric turbulence conditions (i.e., from strong-to-very strong turbulence regimes), optical link distance and operating wavelength.

g. In Chapter 7, the influence of atmospheric turbulence distribution on the terrestrial FSO communication systems based on the measured atmospheric data is investigated.
    - The CDF models of the atmospheric turbulence level for the three-year hourly atmospheric attenuation due to scintillation for various climatic regions in South Africa were developed, based on various meteorological variables and percentages of time.
    - Therefore, the performance evaluation and model validation for each of these distribution models were carried out and the overall best fit (which is 'Sum of Sine' fit) to describe all the considered locations was proposed for South Africa.

h. Additional to the contributions stated above:
    - the design of the link budget and its margin for the contributions of scattering to the optical link were presented in Chapter 4, and this will serve as the major criteria parameters to further compare the outcomes of these results with that of the available terrestrial FSO systems and other conventional transmission systems like RF systems.
    - the BER performance analysis and attenuation mitigation were achieved for the FSO system for each of the locations and presented in Chapter 4. The mitigation techniques such as spatial diversity (4 × 4 MIMO) and modulation schemes (BPSK and L-PPM) were applied to reduce the level of optical attenuation on the FSO link.

CHAPTER TWO

Literature Review

2.1 Introduction

Free Space Optical (FSO) communication system is a wireless transmission system in which the transmitted information signal propagates through the free space in form of light wave which requires no licencing of the spectrum and at the same time transfers big data at a high speed. This fast-growing Optical Wireless Communication (OWC) technology is proficient enough to offer multi-media services for IOT and 5G applications such as video-conferencing facilities, fast speed internet, live streaming services among others, and has recently become a viable alternative to the conventional Radio Frequency (RF) technology and the Fiber Optics (FO) technology. FSO communication system is a laser-based wireless technology that involves transmitting information loaded optical radiations through the atmospheric channel. These optical radiations are electromagnetic emanations having wavelength in the range of the visible and near IR radiations and they serve as the carrier signal. FSO systems makes use of its in-built richness of large capacity of multimedia usage such as voice, video and data, to successfully provide solution to the effects associated with last-mile access network challenges for a foreseeable future [3, 5, 6, 8, 25]. These optical wireless communication systems are to a great extent deployed as the essential (or primary), back-up and disaster recovery links, providing a wide scope of data transmission rate from 10 Mbit/s to 10 Gbit/s [68]. Currently, this optical wireless technology has received great recognition such that majority of the optical links have been deployed on ground stations, satellites, ground-to-satellite, deep space probes, high altitude platforms (HAPs), unmanned aerial vehicles (UAVs) and so on [8, 69].

In the current few years, the Information and Communication Technology (ICT) world has witnessed a tremendous development and progression. The requirements of the demand for more bandwidth as well as transmission capacity are immensely increasing as a result of the increase in the utilization and demand of high-speed internet, audio and video conferencing, bulk multimedia services, live streaming and so forth. Therefore, this forever growing demand of both data (text, voice or video) and multimedia facilities has prompted a clog in conventionally employed RF transmission spectrum and thus emerges a necessity to move from RF carrier on to the prospective optical carrier. In any case, no spectrum licensing is required for the optical carrier, unlike in the case of the RF carrier which needs spectrum licensing and then spectrum usage becomes limited, hence this advantage makes the FSO an attractive prospect for large bandwidth and capacity applications [12, 13, 15]. However, before an overview of the terrestrial FSO system is presented, this Chapter reviewed some past research works on visibility and scintillation.

2.2 Literature Review

2.2.1 Review of Previous Works on Atmospheric Conditions and Visibility

Past research works have examined various atmospheric conditions, their formation, existence and causes in relation to visibility phenomenon. Earlier studies of McKendry (1994), Moulin *et al.* (1998), Shwazhoff and Reid (2000) and Yarnal *et al.* (2001), reported an efficient approach to explain the relationships between the atmospheric circulation classifications and the various environmental variables like the aerosols, gasses or air pollutants [70 – 73]. Also, Lee (1990) and Kulmala *et al.* (2000) reported that the results of the interaction of the regional wind flow pattern and the synoptic atmospheric circulation types is the occurrence of visibility, where the land-sea breeze can be an example of mesoscale meteorological processes that induces the regional wind pattern [74, 75].

An appropriate relationship was defined between visibility and the suspended particulate matter concentration by Sloane (1982), Szymber and Sellers (1985), Vinzani and Lamb (1985) and see also special issue of Journal of Air and Waste Management Association, 2000, vol. 50, No. 5, which suggest that the ambient relative humidity and the physical and chemical properties of the particulate matter (such as chemical composition, particle size and hygroscopicity or amount of water) tends to control the visibility phenomenon [76 – 79]. Therefore, the definition of visibility given by Horvath (1981) is that it is the maximum range where the outline of an object is known against the background (or horizon), which consist of various particulate matter [80].

Also, there have been previous research works that have adopted statistical or numerical modeling techniques to predict atmospheric conditions, especially fog and haze events. For instance, Vislocky and Fritsch (1997) performed an investigation where predictor variables such as sea-level pressure, dewpoint, wind speed and direction, precipitation, opaque cloud amount, and cloud cover were considered in order to predict visibility. This study revealed that the visibility phenomenon can be appropriately predicted by these meteorological parameters [81].

Moreover, Scherrer and Appenzeller (2014) in [82] studied fog climatology and low stratus over the Swiss plateau; it was reported in their work that fog events display a strong seasonality with majority of the fog occurring between the months of October and February and a total of approximately 30 fog days per annum. Giulianelli *et al.* (2014) presented an investigation on the climatology of fog (its occurrence and chemical composition) in Po Valley (North Italy) using 20 years data, over an area where fog occurs frequently, particularly during fall/winter. Moreover, their research showed tendency of heavy fog occurrence during the winter months [83]. Examining the spatial and seasonal variations of fog occurrence within the atmosphere, a number of research works have been carried out and it was reported that the winter periods are often foggier (i.e. consists of mostly dense and thick fogs) than in the summer periods, particularly at the continental environments (inland areas) where radiation fog type

is considered the prevailing type of fog, for instance at Po Valley in Italy [83] and at the Swiss Plateau [82].

2.2.2 Optical Transmission through the Atmosphere

2.2.2.1 Theory of Macroscopical Parameters of the Atmosphere

According to the AMS glossary, visibility phenomena is defined as the greatest distance in a specified direction where it is fairly probable to see as well as to identify with the unassisted eye, a prominent dark object against a white horizon during the daytime and to see an unfocused, fairly intense light source at night [84]. The Koschmieder theory defines the apparent comparison of an object over an ideal distance or against the horizon (which is the background), and as a result of this postulated that the total luminance denoted by L reaching the observer from the object which is located at a certain distance d through a diffusing atmospheric medium with a specific condition (that is, a fog or haze medium) and having an optical extinction coefficient β (expressed in km^{-1}) is given by [85]:

$$L = L_0 e^{-\beta d} + L_f\left(1 - e^{-\beta d}\right) \tag{2.1}$$

where L_0 denotes the luminance of the object at nearby range and L_f represents the luminance of the horizon. The first term $[L_0 e^{-\beta d}]$ of this expression represents the light phenomenon emanating from the object itself, and the second term $[L_f\left(1 - e^{-\beta d}\right)]$ of this expression indicates the diffuse light emanating from the surrounding which has been scattered straight into the observer's vision. Therefore, as the range between the observer and the object steadily increases, the observer will see less and less of the luminance coming from the object, whereas the observer will perceive more and more of the diffused or dim environment light from the environment. Consequently, this results into a reduction in the contrast (C) between the object and its background, which is defined by the law of Duntley as [86]:

$$C = \frac{L - L_f}{L_f} = C_0 e^{-\beta d} \tag{2.2}$$

where C_0 signifies the contrast at nearby range, and it is a quantity that generally depends on both the object and its background. But, in order to describe a standardized visibility, it is preferable to always assume a black object against a white background and also C_0 is taken to be equal to 1. Based on several investigations, certain thresholds of contrast were empirically established to cater for the limit of what the human eye can distinguish. Moreover, a threshold of contrast taken as 0.05 (5 %) is assumed by several researchers to be the limit of what the human eye can differentiate. Therefore, by providing solution to Duntley's equation for the link distance d under these assumptions, then the Koschmieder's formular for visibility is given by [86]:

$$Vis = -\frac{\ln 0.05}{\beta} \approx \frac{3.0}{\beta} \tag{2.3}$$

According to Hautière *et al.* (2006) [86], this visibility equation is known as the "Meteorological Visibility Range" (i.e. MVR). However, Koschmieder initially set this constant to 0.02, which implies that only 2 % contrast is required for an object located at a certain distance for it to be visible to the eye, which then results into the following formulation [87, 88]:

$$Vis = \frac{3.9}{\beta} \tag{2.4}$$

However, at the moment both the World Meteorological Organization (WMO) [89] and the International Commission on Illumination (CIE) [90] applies the 5 % contrast to define the MVR, especially for flight operations. Whereas, the original Kruse model for describing the attenuation due to fog at various optical wavelengths uses 2 % contrast. In addition, the value for the optical extinction coefficient β can be obtained using the various available fog attenuation models such as Kruse, Kim, Al Naboulsi etc.

2.2.2.2 Theory of Microscopical Parameters of the Atmosphere

This section specifically deals with the basic mechanism of the formation of droplets within the atmosphere at different atmospheric conditions. Suspended particles within the atmosphere (referred to as aerosols) tends to grow when the relative humidity of the atmosphere approaches 100 %. This is as a result of the fact that they absorb water (from vapour within the atmosphere) due to their solubility. This growth is quite limited to a dimension of bout 1 μm until these aerosols particles are activated and thereby becomes Cloud Condensation Nuclei (CCN) or commonly called droplets [91]. However, the CCN that could not reach this critical size of activation probably due to the lower relative humidity will definitely not grow proportionally, and will therefore be termed as haze [84]. Therefore, the total number of droplets (N) can be expressed as [91, 92]:

$$N = \int_{D_{min}}^{\infty} n(D) dD \tag{2.5}$$

where D is the diameter of the droplets, D_{min} is the minimum size of the diameter, and $n(D)$ is the Drop Size Distribution (DSD) with units of $cm^{-3}\mu m^{-1}$. This theory can be used to define the dropsize distribution of the fog droplets, but when they are large enough to descend at a substantial speed, then this is called drizzle [84]. Therefore, the total Liquid Water Content (LWC, in g/m^3) of fog is given in in terms of the third moment of the DSD as [84, 91 – 93]:

$$LWC = \int_{D_{min}}^{\infty} \frac{\pi Q_w}{6} n(D) D^3 dD \tag{2.6}$$

where Q_w represents the density of liquid water. Moreover, the size distribution can be related to visibility distance using the expression of the optical extinction coefficient given as [94]:

$$\beta = \int_{D_{min}}^{\infty} \frac{\pi Q_{ext}(D)}{4} n(D) D^2 dD \tag{2.7}$$

where Q_{ext} is the extinction efficiency, and it describes the quantity of radiation that the droplet can scatter or absorb comparative to the radiation that travels through its cross-sectional area (given by $\frac{nD^2}{4}$). It should be noted that these droplets are efficient at scattering the optical radiation within the visible range of the EM spectrum, whereas absorption within this range is very weak.

2.2.2.3 Atmospheric Optical Depth

In recent FSO studies, direct and indirect radiative forcing by water droplets or aerosols and scintillations within the atmosphere has been reported to contribute significantly to the atmospheric attenuation of optical signals. A certain magnitude of the optical radiation from the laser transmitter is absorbed, scattered and reflected by atmospheric air molecules, aerosols, clouds and turbulence before reaching the photodetector, which then directly affects the optical link budget. Therefore, the atmospheric optical depth can be referred to as the coefficient of attenuation of optical radiation by the atmosphere. This phenomenon can be estimated by measuring the intensity or strength of the direct optical radiation reaching the photodetector.

Figure 2.1 shows the summary of the atmospheric optical depth theory, which involves the transmission of an optical signal from the laser source of light through the atmosphere and then received at the photodetector. The atmosphere or free space as shown in the diagram depicts the numerous activities that could occur within its domain, due to the presence of various constituents listed in the illustration. The direct optical radiation reaches the receiver after propagating through an optical link distance (d) and relating with the air constituents such as aerosols, water droplets, gas molecules, turbulent air-masses and air particles such as dust. This reaction yields several atmospheric processes such as absorption, scattering, reflection depending on the type of particle present in its path and scintillation. However, the optical power at the receiver becomes diminished as a result of this atmospheric process and thus hampers the connectivity and link availability of the FSO system. In other words, it is only a fraction of the transmitted optical power that will reach the receiver.

Therefore, according to Beer-Lambert exponential law for transmission of light [95 – 97]:

$$P(\lambda, d) = P(\lambda, 0) \cdot e^{-d\gamma(\lambda)} \tag{2.8}$$

$$P(\lambda, d) = P(\lambda, 0) \cdot \exp\left(-d\gamma(\lambda)\right) \tag{2.9}$$

where $P(\lambda, 0)$ is the transmitted optical power at a certain wavelength (λ) outside the atmosphere, $P(\lambda, d)$ is the received optical power at a given wavelength (λ) and optical link distance (d), and $\gamma(\lambda)$ is the attenuation coefficient of the direct optical radiation for a horizontal column at a specified wavelength (λ) and at a given optical air distance. This attenuation coefficient of the direct optical radiation is also referred to as the total extinction coefficient per unit length and it represents the

attenuation of light, which its origin and determination is as a result of the principles of the atmospheric optical depth.

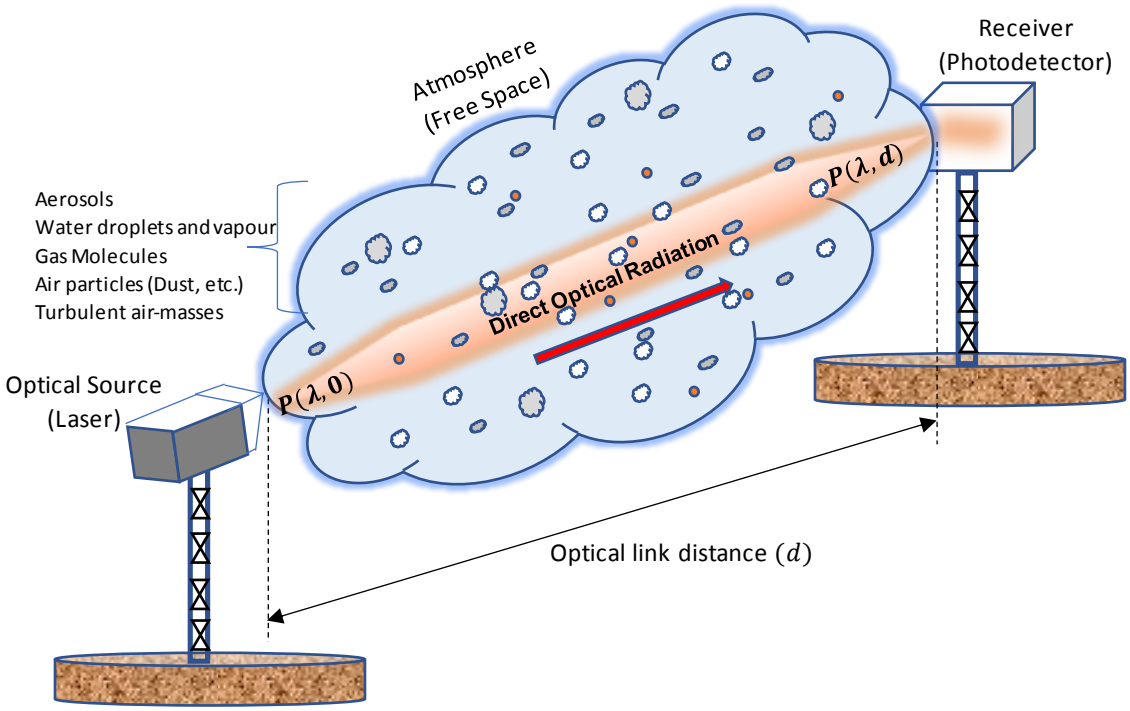

Figure 2.1: Diagram of a typical FSO communication link under diverse atmospheric conditions and showing the atmospheric optical depth.

2.2.2.4 Atmospheric Transmittance

The atmospheric transmittance is a unitless quantity which is described as a fraction of radiated optical power that initially arrives at the receiver, and by definition, it is between zero and one [98]. It can also be defined in terms of percentage of amount of light wave that can travel through a particular free space at a certain time. This quantity can be used to predict the expected behavior or characteristics of the FSO link when an optical signal is transmitted through the free space. However, from Equation (2.9), the ratio of the received optical power at a given wavelength and optical link distance to the transmitted optical power at a certain wavelength outside the atmosphere gives the total transmittance of the atmosphere $\tau(\lambda)$ as [99]:

$$\tau(\lambda) = \frac{P(\lambda, d)}{P(\lambda, 0)} = e^{-d\gamma(\lambda)} \tag{2.10}$$

The transmission of visible light and IR waves through the atmosphere which is described by the Beer-Lambert exponential law shows that the total transmittance of the atmosphere is mainly dependent on the optical wavelength, distance covered and the constituents of the air. This total transmittance of the atmosphere at an optical wavelength and certain distance is a function of the total extinction coefficient per unit length, which characterizes the atmospheric attenuation of light waves. This is made up of the scattering and absorption processes, contributed by the collision of the suspended constituents of the air

such as water droplets, aerosols, dusts, atmospheric gases. The fog, haze and clear air conditions relates to water droplets and dust suspended in the air, which leads to the reduction in visibility or cloudiness of the air and restricts optical transmittance. Therefore, these atmospheric constituents define the main atmospheric transmission window broadly used for FSO communication system (i.e., around 850 nm and 1550 nm). Therefore, the estimation of total transmittance of the atmosphere gives an idea of how much optical power will be absorbed or lost due to directivity drop of the signal. These results allow a rough prediction of the optical attenuation of directed or specular light radiation. However, due to the insignificance of the amount of both molecular and aerosol absorptions of light energy, then this study is solely based on the scattering term.

2.2.3 Review of Previous Works on Atmospheric Scintillation

This review of past research works will focus more on the tropospheric scintillation (particularly the ground level scintillations), since the investigations and analyses in this dissertation are also based on the propagation of terrestrial FSO communication system through atmospheric turbulence (as a result of scintillation) and the study of the effects of the atmospheric activities within the earth surface layer over the optical link. Investigations on atmospheric (especially tropospheric) scintillation have been carried out by different researchers at different frequency bands, wavelengths and in several geographical locations. Earlier research works generally started with the study of the effect of the turbulent atmosphere on wave propagation, reported by Tatarskii (1961) in [100]; it also include the observation of atmospheric turbulence with radio telescope as presented in the work of Hinder (1970) in [101]; the estimation of atmospheric turbulence parameters in an earth-space path using measurement and modelling of scintillation intensity by Vilar and Haddon (1984) [102], and Vilar *et al.* (1985) in [103] carried out measurement and modeling of amplitude and phase scintillations in an earth-space path across different locations in Europe.

Tatarskii (1961) studied the intensity fluctuations in the atmosphere due to scintillations, and then presented a theoretical formulation for the approximation of log-amplitude fluctuations created due to turbulent scattering, which is based on the typical assumptions that the spatial structure of the refractive index of air obeys the Kolmogorov-type spectrum [104]. Based on the report presented by Tatarskii (1961), it was observed that when the atmospheric turbulence lies within the inertial sub-range where a relation comprising the sizes of the irregular slabs of air mass, that is $\frac{l_o^2}{\lambda} < L < \frac{L_o^2}{\lambda}$ is satisfied; the parameters l_o and L_o represents the inner- and outer-scale of the irregularities of the refractive index respectively, L denotes the effective path length between the boundary of turbulence and the reception point, and λ represents the optical wavelength, thus the variance of log-amplitude (σ_χ^2) in decibels is given as [105]:

$$\sigma_{\chi}^{2} = 42.9\, k^{7/6} \int_{0}^{L} C_n^2(r) r^{5/6} dr \tag{2.11}$$

where χ (expressed in dB) indicates the logarithm of the ratio between the mean and fluctuating amplitudes, C_n^2 is the refractive index structure parameter along the earth-space path at position r, which mainly determines the amount of scintillation intensity or index within the atmosphere, and the parameter k represents the wave number, and it is expressed by the relation $2\pi/\lambda$.

Also, the scintillation index which is also known as the normalized variance of the irradiance fluctuations can be defined in terms of the log-amplitude variance when it satisfies $\sigma_{\chi}^{2} \ll 1$ for the weak fluctuation regime as follows [106]:

$$\sigma_I^2 \approx \sigma_{\ln I}^2 = 4\sigma_{\chi}^2 \tag{2.12}$$

In 1986, an organization called the International Radio Consultative Committee (CCIR), which is now renamed as International Telecommunication Union – Radio (ITU-R) stated that C_n^2 is difficult to measure directly [107]. Also, calculating the values of C_n^2 along a slant path using atmospheric variables is not easy to achieve, unlike using the refractive index variance of the atmosphere and outer scale (L_o) [105]. However, the atmospheric variables that can be used for its estimation are temperature, wind speed, relative humidity, pressure, altitude etc. At different heights and locations, the C_n^2 estimate changes from around 10^{-12} to 10^{-19}, relating to strong to weak turbulence conditions [23, 108 – 111]. The variance of the log-amplitude fluctuations was modified by Tatarskii due to the impacts of turbulence scattering on LOS path for a point receiver, and the revision is expressed as [100, 112]:

$$\sigma_{\chi}^{2} = 23.39\overline{C_n^2}\left(\frac{2\pi}{\lambda}\right)^{7/6} L^{11/6} \tag{2.13}$$

where $\overline{C_n^2}$ represents the weighted mean refractive index structure parameter and L denotes the atmospheric path length.

In 1986, the CCIR offered a more real scintillation model known as "CCIR - Rep. 718-2" (based on the Haystack observatory measurements), that can eliminate the involvement of C_n^2 [113]. The complexities in determining C_n^2 (in Equations (2.11) and (2.13) or from meteorological elements) resulted into this development. Using simple parameters, this model produced estimated values of the log-amplitude fluctuations close to the reported measured values. However, the CCIR model was observed to be deficient in some ways, which are lack of ability to appropriately describe regional and seasonal variations, it only provides standard variation rather than time percentages to estimate the fading of the signal and it showed inappropriateness when the most significant φ for satellite communication design is used. These deficiencies were examined by Karasawa *et al.* (1988) in [104], where the authors discovered that there is a high relationship between the characteristics of scintillation and the influence

of various variables like water vapor or the wet-term of refractivity (N_{wet}) gotten from temperature and humidity measurements. However, this model is developed for observing scintillations along the earth-space paths, on the other hand it has proved that there is a strong correlation between atmospheric variables and scintillations, and this has also served as part of the motivation for the Chapter 7 of this research work.

Further investigations presented on tropospheric scintillation and its effects or characteristics by Mayer *et al.* (1997) [114] reported among others, that in hot and moist atmospheric conditions, the magnitude of atmospheric scintillation is observed to be much larger than that of the cold and dry atmospheric conditions, as was observed in this thesis. Using Fairbanks, Alaska (where it is warm and moist in the summer season, and cold and dry in the winter season) as a case study, it was also reported that all the prediction models as well as measured scintillations reveal a sinusoidal seasonal variation. In addition, it was also reported that the hourly standard deviations of the propagation data from the location were observed to be slightly better represented by a Lognormal distribution than a Gamma distribution model. Furthermore, it was reported in Priyadarshi (2015) [115], Ahmed *et al.* (2017) [116] and Sahithi *et al.* (2019) [117] that the magnitude of scintillation during the winter period is higher than that of the summer, because the anomalies in the winter period produces more ionospheric scintillation during the winter season than that of other seasons.

However, in this study, the tropospheric scintillation of great interest is the ground-level scintillation since we are investigating a terrestrial FSO link. Also, the quantification of the scintillation intensity producing atmospheric turbulence over the optical wave propagating through free space is scintillation index and log-amplitude fluctuations.

2.2.4 Characteristics of Atmospheric Scintillation over Electromagnetic Wave Transmission

A summary of the common characteristics of atmospheric (precisely, tropospheric) scintillation, its dependence on certain weather factors, and the factors that are utilized to measure scintillation are provided in this sub-section as follows.

a. The hypothesis that the fluctuations of the atmospheric refractive index follow a Kolmogorov-type spectrum results into a dependence of scintillation intensity on frequency of the form $\sigma \propto f^{7/12}$. In the investigations carried out by Karasawa *et al.* (1988) [104], a net frequency dependence of about $f^{0.45}$ was obtained from a set of experimental data. In addition, measurements by both Thompson *et al.* (1975) [118] and Yokoi *et al.* (1970) [119] delivered results which ranges from f^0 to $f^{0.5}$. The validity of the theoretical frequency dependence of scintillation intensity was also confirmed by the more current measurements carried out by Haidara *et al.* (1994) [120] and Ortgies (1993) [121] using the Olympus satellite.

b. Scintillation with respect to meteorological elements, can be said to be strongly dependent on both temperature, humidity and pressure among others. It can be deduced from several atmospheric studies that warm humid climates are more prone to atmospheric scintillation than the climates that are cold and less humid. Therefore, just like visibility, this dependence shows geographical, seasonal and diurnal variations. Karasawa *et al.* (1988) in [104] detected from their investigations that there exists a high relationship between the monthly mean scintillation intensity (σ) and the wet term of refractivity (N_w) averaged over similar month. As a result, the following expression between the two parameters was then given from their analysis:

$$\sigma\ (dB) = 0.15 + 5.2\ \times\ 10^{-3} N_w \tag{2.14}$$

In sub-section 2.2.3, the theoretical dependence of N_w on temperature, pressure and relative humidity was briefly stated. Also, the ITU-R scintillation model in Thompson *et al.* (1975) predicts that regardless of their atmospheric temperature, totally dry climates may experience similar quantity of atmospheric scintillation [118].

On the other hand, there is also a high correlation between scintillation index in terms of Rytov variance and the refractive index structure parameter C_n^2, which has been described briefly in sub-section 2.2.3 and in detail in Chapter 7. The quantity C_n^2 in turn has a strong dependence with certain meteorological parameters such as temperature, pressure, relative humidity, wind speed and wind shear. This is the approach that was used in this study to obtain the scintillation intensity and then resulting into the optical attenuations at various locations within South Africa. Moreover, at higher latitudes it should be noted that atmospheric scintillation has a tendency to be lower, however for a specified latitude it does not have any considerable longitudinal dependence.

c. Another characteristic of atmospheric scintillation which has been partially discussed earlier is that it has some unique correlation with the wind speed. In connection with this assumption, the correlations of 0.313 and 0.314 between σ and the hourly values of overall and transverse wind speeds respectively, were discovered by Banjo and Vilar (1987) [122]. This shows that wind speed dependence of the scintillation intensity has some credibility and should be taken into consideration.

d. The quantity of scintillation detected in the atmosphere over a particular time is dependent on the scale size of the irregularity (often in form of an air-mass), the magnitude of the distance between the so-called irregularities and the receiver of the transmission system, the size of the antenna and the first Fresnel zone. The relationship between these variables can be illustrated using Figure 2.2, which involves an irregular air-mass of transverse linear dimension signified by d_s, existent between transmitter T_x and receiver R_x, at range d_T and d_R from T_x and R_x respectively. According to this illustration, d_s can be written as [123]:

$$d_s \cong \sqrt{\frac{(n\lambda)d_T d_R}{d_T + d_R}} \tag{2.15}$$

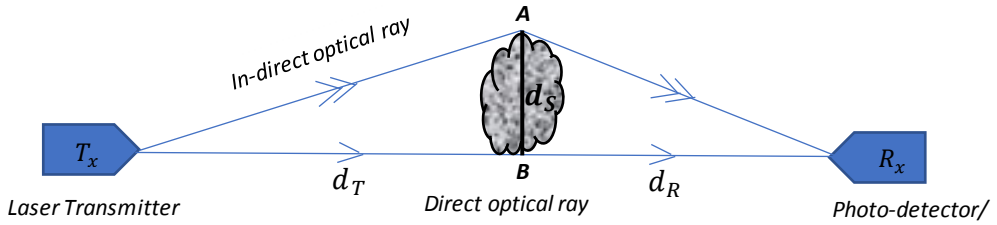

Figure 2.2: Fresnel zone of a free space optical communication link.

2.2.5 Physical Causes of Atmospheric Scintillation

Scintillation phenomenon is one of the numerous random effects the Earth's atmosphere can have on a propagating Electromagnetic wave (EM), especially the optical signal. This random phenomenon usually takes place when the wave travels through the atmospheric regions that exhibits slight spatial and temporal variations in the main weather parameters affecting signal propagation. It is basically as a result of the inhomogeneity in the fluctuations of atmospheric temperature and pressure. These variations are displayed by the turbulent eddies or air-masses within the atmosphere, which then results into rapid temporal fluctuations in the free space. These rapid temporal fluctuations resulting into atmospheric scintillation can affect both the amplitude and phase of an optical signal.

2.3 The Electromagnetic Spectrum

Over the years, the physics of Electromagnetic (EM) radiation and its energy has been very well investigated and the Maxwell equations are generally employed to comprehend the EM waves propagation in diverse environments and media [68]. The spectrum of the EM waves is very broad, having wavelengths that extends from $10^{-14}\ m\ -\ 10^{4}\ m$. Moreover, different frequency bands are related with these sorts of waves, and they are very well-defined and well characterized for the purposes of communication and other uses in industry, health and military applications. For historical reasons, these bands of frequency have diverse and distinctive names while being comparable in nature. This is particularly true and valid in optics, in which frequencies corresponding to visible light is of a great concern, while the EM range largely extends above and beyond this band [68, 124]. The electromagnetic wave spectrum is as well characterized into two in-homogenous regions, that is [68, 125],

(i) The ionizing part of the EM spectrum which consists of gamma rays, x-rays and ultraviolet rays. This region has very short wavelengths and very high optical intensities, and therefore are not possible for wireless communication and,

(ii) The non-ironizing part of the spectrum which involves radio waves, visible and near IR lights are mostly feasible for optical wireless communication systems.

The schematic presented in Figure 2.3 demonstrates the spectrum of the EM wave ranging as a function of the wavelength for different bands of frequency, and each band having typical names. This representation particularly shows an augmented view for wavelengths in the range of the visible light and the region circled is a special range which is considered the generally adopted range for FSO communication systems [68, 126].

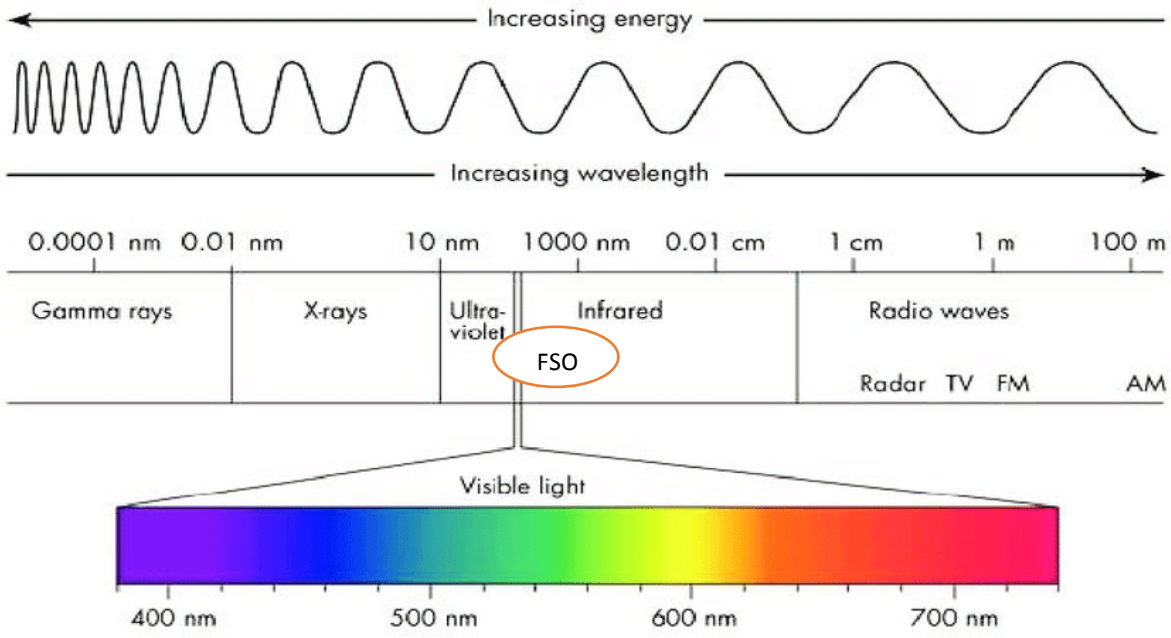

Figure 2.3: The synopsis of the electromagnetic (EM) wave spectrum with its selected wavelength and frequency bands, and the narrow range of visible light is shown enlarged at the right [127].

2.4 Terrestrial FSO Link

Terrestrial Optical Wireless Communication (TOWC) is a communication technology that exist between building-to-building, mountain top-to-mountain top or any other sort of horizontal optical link between two or more ground stations. The FSO communication network could be deployed using different network topology such as ring, mesh, point to point or point to multipoint topologies. As a laser beam propagates through the atmospheric medium, power loss or atmospheric optical attenuation is experienced as a result of the various factors present within the atmosphere. Since the atmospheric medium consist of various conditions, therefore to combat the random changes within this medium, the system designers must perform their role of making sure they examine carefully the design requirements of the system. However, in order to construct a reliable FSO network communication system, the planners must possess an in-depth knowledge of optical beam propagation through a random atmospheric medium as well as its related power losses [8, 12]. As the optical beam propagates through the atmospheric optical channel, it is confronted by various atmospheric losses which will be discussed in detail later in this thesis.

2.5 Advantages and Comparisons of FSO and RF Transmission Systems

FSO communication system has numerous benefits that makes it different from other existing communication systems. The difference in wavelengths is one of the most important differences amongst these communication systems, where the wavelength of FSO is about 0.001 times that of the RF. This huge contrast caused the differences between both communication systems. These two technologies can be combined to give the hybrid FSO/RF communication link, which can give up to 99.999 % link availability even during harsh weather conditions. In addition, FSO has high directivity and narrow beam than the RF, according to $\theta \propto {}^{\lambda}/_{D_R}$, whereby θ, λ and D_R are the divergence angle, wavelength and aperture size respectively [128]. Therefore, the smaller the wavelength, the narrower the beam (as shown in Figure 2.4). The review of the advantages and comparisons between the FSO and RF communication technologies are presented in Table 2.1.

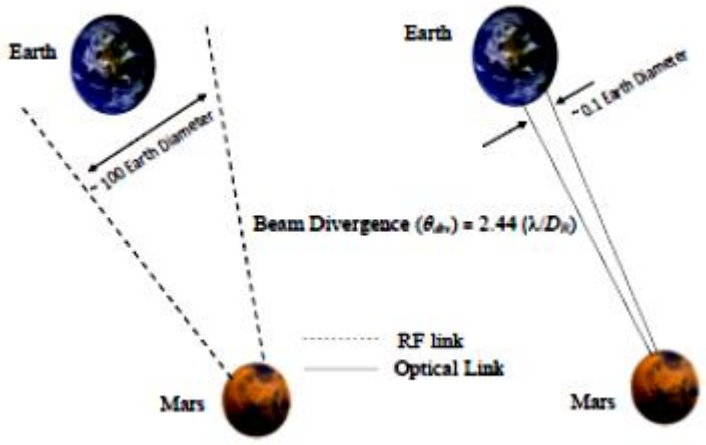

Figure 2.4: Comparison of optical and RF beam divergence from Mars towards the Earth [128].

Table 2.1: Summary of the comparison between FSO and RF communication technologies.

Parameter	***FSO Link***	***RF Link***
Bandwidth regulations and License acquisition	License-free domain	License required
Channel and Link Performance challenges	Fog, Haze, Atmospheric turbulence, Misalignment or obstruction	Rain, Multipath fading, Interferences
Beam Divergence	Very Narrow	Broad
Data Rate (ε)	ε: $10's\ Mbps\ to\ 10's\ Gbps$	$\varepsilon < 100\ Mbps$
Bandwidth Capacity	Large	Narrow
Directivity and Gain	High	Low
Network Security	High	Low
Size of Devices	Small	Large
Power Efficiency	High	Low
Channel Distance	Small	Long
Fog Attenuation (at $V = 200\ m$*)*	$37\ dB/km\ at\ 830\ nm$	$3\ dB/km\ at\ 58\ GHz$
Rain Attenuation (at $R = 40\ mm/hr$*)*	$2\ dB/km\ at\ 830\ nm$	$17\ dB/km\ at\ 58\ GHz$
Noise	Background light	Other sources
Network Architecture	Scalable	Non-scalable

2.6 Overview of the Atmosphere

The earth's atmosphere is basically defined as a set of strata of gases encompassing the earth. This can be further described as a layered medium where EM waves (in particular, optical waves) interact and propagate at very high frequencies in THz range and within the LOS distances. Figure 2.5 shows the stratification of the atmosphere which describes the five different layers starting from the surface level to about an altitude of 800 km, and these are namely the troposphere, stratosphere, mesosphere, thermosphere and the exosphere.

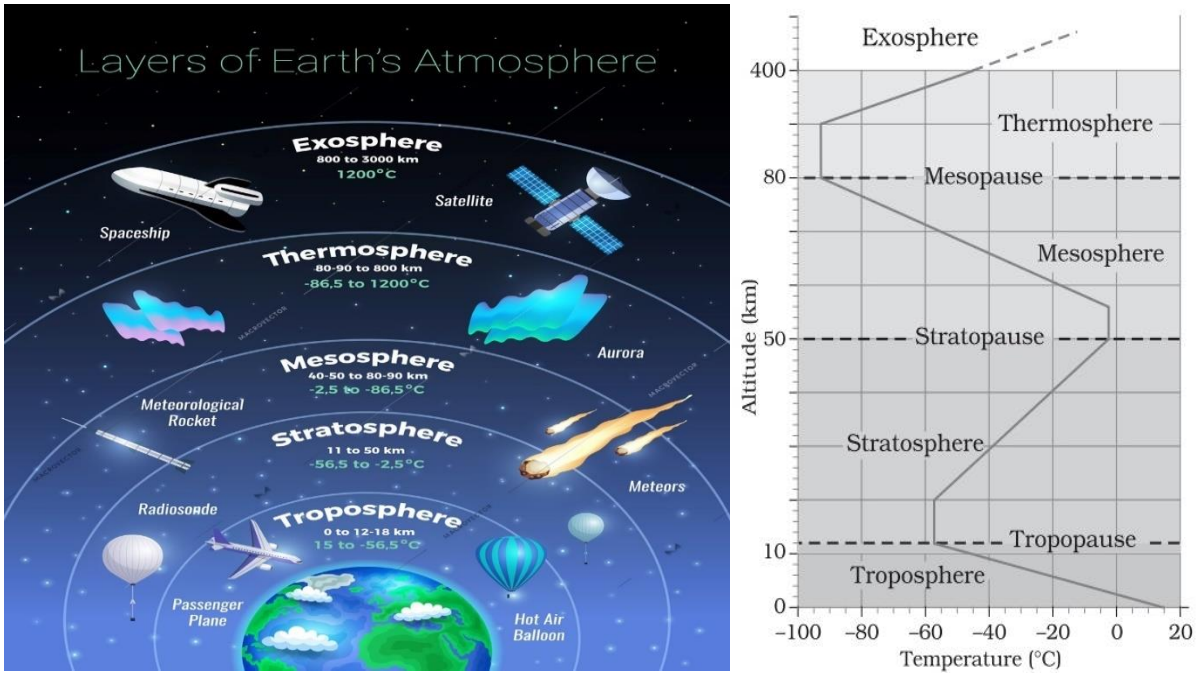

Figure 2.5: Stratification of the atmosphere showing the five different layers along with their altitudes and climatic conditions (*Source:* https://www.dreamstime.com).

The first and lowest of them all is the troposphere (which is the major area of concern of this research work) and its altitude extends from the surface of the earth to between 12 and 17 km. It is an atmospheric space that comprises of 75 % of the total molecular or gaseous mass and 98 % of all the water vapour and aerosols of the atmosphere. As a result of this, the tropospheric layer accounts for the effects of atmospheric turbulence that govern the terrestrial weather. This is the level at which the weather phenomenon as well as atmospheric turbulence are most noticeable [129, 130]. The other layers of the atmosphere are shown in Figure 2.5 along with their altitudes and climatic conditions.

2.7 The Concept of FSO Communication System

There exists a close relationship between the basic concept of the FSO communication system and that of the RF communication system, with regards to some features such as generation of data, signal modulation, signal transmission and reception, signal demodulation and data processing. FSO communication link requires a line of sight (LOS) communication system, which is generally employed

in a point-to-point configuration within any of star, mesh or ring network architectures. Its LOS path must be without any physical obstacles between the transmitter (either laser or LED) and optical receiver. According to the typical structure of the FSO communication technology, it can be said that it comprises of three major functional blocks as illustrated in Figure 2.6, which are an optical transmitter unit, optical receiver unit and an atmospheric channel which forms the link between the transmitter and the receiver units.

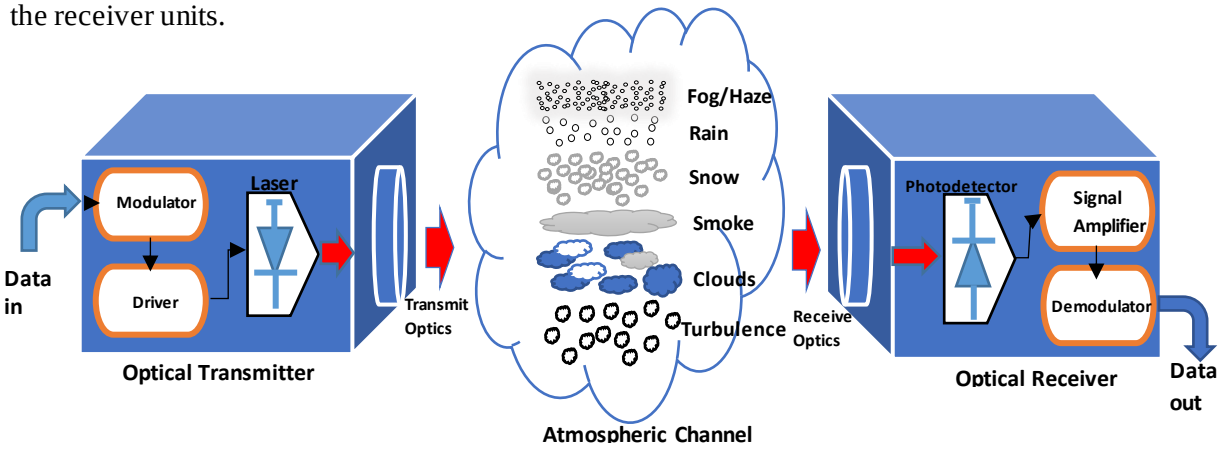

Figure 2.6: The schematic diagram of line-of-sight FSO communication system.

2.8 Atmospheric Channel

Depending on the type of atmospheric conditions (such as turbulence, fog, haze, snow, rain, smoke, dust particles and low clouds) dominating a specific layer or region of the atmosphere at a particular time, the optical beam propagating from the transmitter through the atmosphere will encounter scattering, absorption or irradiance fluctuations. Although, fog and atmospheric turbulence mostly dominates the FSO communication link losses induced as a result of the atmosphere when compared to the others [131, 132]. Atmospheric absorption and scattering of the propagating optical beam as it passes through the atmosphere (in the absence of scintillations) are some of the causes of the main impairments experienced in FSO communication system during the propagation of laser beams. These two processes result from the unavoidable interaction of the travelling optical beam with atmospheric particles (aerosols) of various types as well as shapes existing in the atmosphere at a specific time.

The atmospheric absorption process is described as a quantum effect, and it is highly dependent on the operating wavelength of the transmission. This process takes place due to the annihilation of a transmitted light photon by means of diverse traces of gases existing within the atmosphere [133, 134]. Therefore, the photon energy absorbed by the molecules of the gas during this process rises the kinetic energy. This forms the basis of the random heating of the earth's atmosphere. In certain cases, whereby the effect of absorption is quite minimal, the selection of an appropriate wavelength window, is essential in order to minimize the level of absorption [135]. Thus, the losses due to absorption can be ignored without having any significant effects on the practical results.

Atmospheric scattering can be described as a phenomenon that occurs when the transmitted light photon collides with gas molecules within the atmospheric channel, and therefore causes the light photon to alter its incident direction with or without changing its wavelength. However, during this process, it can be noticed that a portion of the optical beam energy will be scattered by the aerosols. Therefore, it will then be re-radiated into a solid angle away from the PD's Field of View (FoV). There are basically three different types of atmospheric scattering processes that are relevant in wireless transmission, which are the Mie scattering, Rayleigh scattering and Geometric scattering. Mie scattering results when the sizes of the atmospheric particles in terms of particle radius (r) are equal to the operating wavelength. One of the main contributors to Mie scattering is the atmospheric fog. Fog occurrences results into Mie scattering within the atmosphere as the sizes of the fog particles varies between 0.5 μm to 2 μm and then corresponds to optical wavelengths [21, 37, 56]. However, Rayleigh scattering is a phenomenon that takes place when the particle radius $r \ll 0.5\ \mu m$, while the Geometric scattering takes place as the particle radius $r \gg 2\ \mu m$ [24]. Figure 2.7 present schematic diagrams showing the comparison between the three aforementioned types of scattering of the incident light in FSO communication.

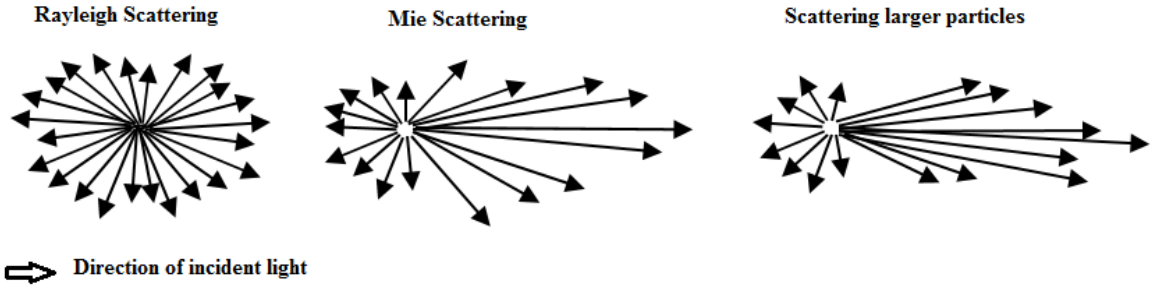

Figure 2.7: Patterns and comparison between Rayleigh, Mie and Geometric (Non-selective) scattering [136].

Atmospheric turbulence is another major source of optical signal fading or degradation within the atmosphere, in the absence of either fog or other aerosols due to inhomogeneity of temperature and pressure. This temperature inhomogeneity within the atmosphere results into corresponding random fluctuations of the refractive index of air (n). These random changes in the index of refraction of the atmosphere creates varying sizes of eddies (or sometimes called cells), which ranges from approximately 0.1 cm to about 10 m with different temperatures [137]. These eddies or mirror-like cells created in the atmosphere due to temperature fluctuations tends to deviate as well as fluctuates the transmitted light beam away from its original direction. Therefore, this results into a significant fading and phase distortion of the optical beam [138].

Some of the major influences of atmospheric turbulence are the 'twinkling of stars' phenomenon which is basically as a result of random variations of the irradiance of the stars, and also the glistening of the horizon on a hot day resulting from the random variations in the optical phase of the optical signal, therefore causing a reduction in the resolution of images [139]. According to several investigations on

atmospheric turbulence, it has been revealed that it depends on some factors such as the altitude, temperature, wind velocity, pressure and the refractive index of air. The most common effects of atmospheric turbulence are scintillation, beam wandering, beam spreading, spatial coherence degradation, image dancing, polarization fluctuation, and beam steering.

2.9 Challenges in FSO Communication System

The FSO communication system is a typical wireless transmission system that employs the atmospheric channel as a propagating medium. This type of medium has certain properties such as random function of space and time, thereby making this communication system a random phenomenon which is a function of weather as well as geographical location. Therefore, the presence of several unpredictable environmental factors in the atmosphere such as fog, clouds, haze, snow, mist, rain and so on, results into a strong attenuation in the optical signal. Thus, leading into a limitation in the optical link range at which the FSO system can be deployed. The numerous challenges encountered by the terrestrial FSO system design engineers are highlighted in this section as follows:

2.9.1 Scattering and Absorption Loss

The attenuation experienced within the atmospheric channel as the optical beam propagates through it, is mostly as a result of scattering and absorption process which is defined by Beer's law. The main atmospheric absorbers inducing power losses at visible as well as IR wavelengths are the molecules of water, carbon dioxide and ozone. Like the scattering phenomenon, this atmospheric absorption mechanism is also classified as a strongly wavelength-dependent phenomenon. A few typical estimates of the coefficients of molecular absorption for clear weather (clear-air) conditions are presented in Table 2.2. The range of the optical wavelengths available to FSO communication technology is selected to possess minimal absorption, and it is denoted as the atmospheric transmission window. Thus, within this transmission window, the power loss as a result of aerosol or molecular absorption is lower than 0.2 dB/km. Numerous transmission windows exist in the wavelength range of 0.7 μm to 1.6 μm. Most of FSO communication technologies are designed to function within the transmission windows of 0.780 μm to 0.850 μm and 1.520 μm to 1.600 μm. These particular sets of operating wavelengths have been selected as a result of the readily availability of the transmitter as well as receiver (photodetector) components at these wavelengths [97, 99, 140, 141].

Table 2.2: Specific molecular absorption (specific attenuation values) at typical wavelengths [36].

Wavelength (nm)	Molecular Absorption (dB/km)
550	0.13
690	0.01
850	0.41
1550	0.01

One of the major factors that are responsible for degrading the FSO communication system's performance when the beam propagates through the free space medium is scattering of light. This process is strongly dependent on the optical wavelength of the traveling light beam through the atmospheric medium. However, if the aerosols within the atmosphere are in small dimensions in comparison with the operating wavelength of the optical beam, therefore Rayleigh scattering is produced. For FSO systems transmitting within the visible and ultra-violet bands (that is, bands having optical wavelengths below 1000 nm), the scattering process becomes quite prominent. But, at longer optical wavelengths around the near-IR (N-IR) range, this can be ignored. Aerosols such as air molecules and haze particles cause Rayleigh scattering. On the other hand, if the sizes of these particles are relatively comparable or equal with the wavelength of the optical signal, thus Mie scattering is produced. This sort of process is quite dominant close to the infra-red wavelength band or longer. However, the main contributors of Mie scattering are certain atmospheric particles like fog and haze. Then if these atmospheric particles present within the path of the optical link are much bigger than wavelength such as in the case of snow, rain and hail, the scattering process is better defined by geometrical optics model [142-144].

The total atmospheric attenuation of FSO system due to atmospheric particles is represented by atmospheric attenuation coefficient, which is expressed as a combination of both scattering of light and absorption. Therefore, it can be defined as the summation of four individual attenuation coefficient parameters given by:

$$\gamma = \alpha_m + \alpha_a + \beta_m + \beta_a \tag{2.16}$$

where α_m and α_a respectively represents the molecular and aerosol absorption coefficients, and β_m and β_a respectively represents the molecular and aerosol scattering coefficients.

Several factors that bring about absorption and scattering of light particles in FSO communication systems are presented as follows:

2.9.1.1 Fog

The most important donor for optical atmospheric attenuation is as a result of fog occurrences, which can lead into both scattering and absorption. These fog incidences which is a function of fog particle size and distribution, can be classified based on their density or intensity of occurrences, or on the atmospheric visibility range. These classes are basically represented by five conditions which are known as: dense, thick, moderate, light and thin fog conditions. Therefore, during the occurrences of dense fog (that is, when the visibility range is even lesser than 50 m), the optical specific attenuation may be higher than 350 dB/km. As a matter of fact, this obviously infer that it has the ability to totally limit the availability of the optical link. Under such situations, the application of a very high-power laser and a unique mitigation scheme assists to provide an improvement on the probability of optical link availability. Normally, during heavy atmospheric attenuation, the lasers operating with optical

wavelength of about 1550 nm are preferred selections due to their high transmitted laser power. However, some literatures on attenuation and wavelength-dependency have suggested that during dense fog conditions, the specific attenuation is independent of the selected optical wavelength [140, 141, 145]. Therefore, Figure 2.8 clearly reveals that during very low visibility weather condition which corresponds to heavy or dense fog, all wavelengths (for instance, specific wavelengths of 650 nm, 850 nm, 950 nm, 1330 nm and 1550 nm) are nearly closely packed following similar pattern indicating that specific attenuation is not dependent on the selected optical wavelength. During moderate fog to thin fog conditions as shown in Figure 2.8, where the range of visibility is from about 0.8 km to about 2.7 km, the fog specific attenuation is quite lower for optical wavelengths of about 1550 nm as compared to the other selected operating wavelengths.

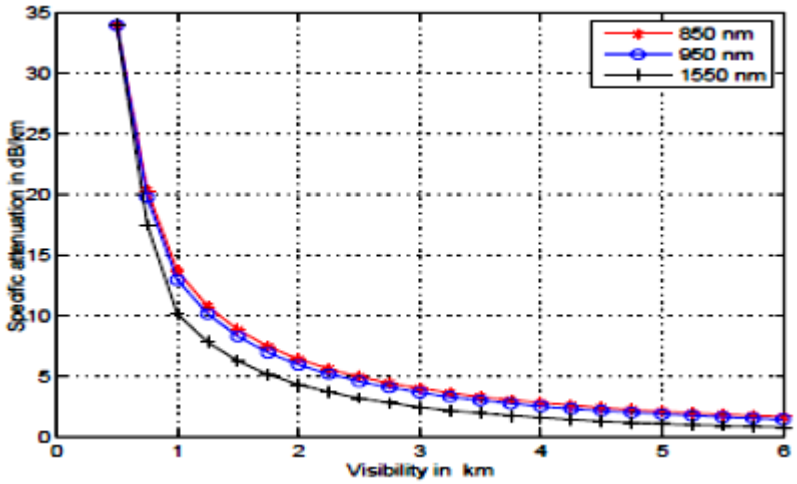

Figure 2.8: Specific attenuation against atmospheric visibility range during various fog conditions [136]

2.9.1.2 Rain

Since the droplets of rain (ranging from 100 μm to 10,000 μm) are significantly larger in dimension than the optical wavelengths utilized in FSO systems, then the effects of rain over the optical beam is not much noticeable like that of fog. The specific attenuation for wavelengths of 0.85 μm and 1.5 μm as a result of light rain of about 2.5 mm/hr to heavy rain of 25 mm/hr ranges from 1 dB/km to 10 dB/km [146, 147]. As a result of this, the choice of employing a hybrid RF/FSO communication technology enhances the optical link availability particularly for transmission systems operating at frequency of about 10 GHz and above.

International Telecommunication Union- Radio-communication sector (ITU-R) suggested Rain attenuation modelling for FSO communication systems. Thus, for optical wireless links, the rain specific attenuation α_{rain} given in dB/km is expressed as follows [148, 149]:

$$\alpha_{rain} = k_1 R^{k_2} \tag{2.17}$$

where R represents the rain rate (in mm/hr) and constants k_1 and k_2 are the model parameters whose values depend on the rain drop size as well as the rain temperature. The estimates of the parameters of the model suggested by the ITU-R are presented in Table 2.3.

Table 2.3: Parameters for rain attenuation model proposed by ITU-R for FSO system [148].

Model	Origin	k_1	k_2
Carbonneau	France	1.076	0.67
Japan	Japan	1.58	0.63

It is important to note that when rain event is accompanied by low clouds, it leads into a very high atmospheric attenuation. During the occurrence of heavy rain accompanied by low clouds, the huge loss of optical power experienced can be mitigated by applying lasers with high-power, as well as adequate link margin which is larger than 30 dB should be attained for maximum optical link availability [40].

2.9.1.3 Snow

The snow particles have sizes that fall between that of the fog and rain particles. Consequently, snow attenuation is reasonably less than that of fog but more than attenuation due to rain. In the course of the occurrences of a heavy snow downpour, the laser beam path becomes blocked as a result of increase in the density or concentration of snowflakes within the path of propagation or as a result of the formation of ice on windowpane. Therefore, in this instance, its power loss is highly comparable to that of fog attenuation ranging between 30 dB/km to 350 dB/km, such that it can significantly cause a reduction in the FSO system's link availability. However, if link margin of about 50 dB is selected, FSO communication system can supply link availability of 99.9% during heavy snow of about 150 dB/km [40]. Snow attenuation can be categorized into wet and dry snow attenuation. For snow rate S given in mm/hr, the specific attenuation due to snow, α_{snow} (in dB/km) is given as [149]:

$$\alpha_{snow} = aS^b \,, \tag{2.18}$$

where the parameter values of constants a and b in wet and dry snow are given in Table 2.4.

Table 2.4: Values of the parameters of the snow attenuation model.

Type of Snow	a	b
Wet Snow	$(5.42 \times 10^{-5}) + 5.49$	1.38
Dry Snow	$(1.02 \times 10^{-4}) + 3.78$	0.72

2.9.2 Atmospheric Turbulence (Over Horizontal Optical Link)

This is described as a random phenomenon which results from the in-homogeneities in the random fluctuations of the atmospheric temperature and pressure within the atmosphere along the optical beam propagation path. Thus, this phenomenon results into the formation of turbulent cells which are also

often known as the three-dimensional eddies or air-masses of various sizes as well as of differing refractive indices. These eddies with diverse sizes act like lenses or a prism and then eventually result into constructive or destructive interference of the propagating optical beam. This results into a form of redistribution of signal energy leading into random intensity and phase fluctuations of the received optical signal. These fluctuations in the intensity of the received optical signal is referred to as scintillation, which is quantified by means of the scintillation index, σ_I^2 (also known as the normalized variance of intensity fluctuations) and it can be expressed in terms of the Rytov variance. The scintillation index can be used to characterize the irradiance fluctuation of the optical beam. It indicates the strength or quality of the irradiance fluctuations. Atmospheric scintillation is a function of the Rytov variance (σ_R^2) and the refractive index structure parameter.

The scintillation levels can be typically categorized into three different regimes based on the Rytov variance which determines the strength of the irradiance fluctuations. These fluctuation regimes are [150]: weak fluctuations or weak atmospheric turbulence regime ($\sigma_R^2 < 1$), moderate fluctuations regime or focusing regime ($1 \leq \sigma_R^2 < 5$), and strong fluctuations regime or saturation regime ($\sigma_R^2 \geq 5$). While for the refractive index structure parameter, in the case of weak atmospheric turbulence it is around $10^{-17}\ m^{-3/2}$ and in the strong atmospheric turbulence case it can be up to $10^{-13}\ m^{-3/2}$ or even much more. The Rytov variance for a plane wave is defined as:

$$\sigma_I^2 = 1.23 C_n^2 k^{7/6} L^{11/6}\,, \tag{2.19}$$

where C_n^2 ($m^{-2/3}$) denotes an atmospheric quantity, which is known as the refractive index structure parameter.

Other important challenges in FSO communication system are beam divergence loss, ambient light, mis-alignment or building sway, physical obstruction of beam paths etc.

2.10 Mitigation Techniques for Minimizing the Atmospheric Channel Effects

As the optical beam propagates through the random atmospheric channel, it brings about degradation in the quality of the received optical signal, which correspondingly leads to deterioration of the BER performance of the FSO system. Several mitigation techniques can be used to enhance the reliability and availability of the FSO communication system in all cases of weather conditions. In wireless communication systems, mitigation technique can be applied either at the physical layer (which is the focus of this research work) or at the network layer. Some of the mitigation techniques that can be employed at the physical layer to improve the performance of the availability of the FSO system are multiple beam transmission (such as using spatial diversity), aperture averaging, adaptive optics, choice of modulation schemes or application of hybrid modulation schemes, background noise rejection methods, increasing the receiver FOV, hybrid RF/FSO, relay transmission and so on. A few of the mitigation techniques that can be applied for the network layer are network re-routing, packet re-transmission (typically in FSO link or network), data re-play, Quality of Service (QoS) control etc. A

variety of the mitigation techniques utilized in FSO communication systems for the physical layer methods are presented in this section as follows:

2.10.1 Diversity Technique

This technique for mitigating the atmospheric turbulence effects can operate on any of space, time, wavelength or frequency. It involves employing an array of smaller-size receiver aperture instead of a single large-size receiver aperture, in order to transmit multiple copies of optical signal that are mutually uncorrelated either in space or time or wavelength or frequency. This technique has the ability to improve the BER performance as well as the optical link availability of the FSO system. Moreover, it limits the necessity of active tracking which is as a result of laser mis-alignment [3, 18, 143]. In 1998, GOLD investigation (which was an explicit example of the spatial diversity technique) demonstrated that by employing four units of $514.5\ nm$ multiple laser beams for uplink transmission, this results into a drastic improvement in the scintillation index. Reports from the research showed that the scintillation index value was 0.12 when only two beams were used, but, when four beams were used the value of the scintillation reduced to 0.045 [151]. To reach the complete advantage of the spatial diversity technique, the separation of the antennas at both or at any of the transmitter or receiver must be at least or larger than the atmosphere's coherence length in order to make the multiple beams independent or at least uncorrelated. Also, investigated in Acampora (2002) [18], is the correlation effect between multiple laser beams, whereby the results of this presentation revealed that a correlation of 0.25 between three transmit apertures could reduce the order of diversity by one. Moreover, with the higher-order correlation, the condition gets worse. Unlike in Radio Frequency (RF) communication system, whereby only full spatial correlation causes diversity loss. In addition, at high level of atmospheric turbulence, the diversity gain is more noticeable than that obtained at lower values turbulence level [3, 152, 153].

There exist various forms of spatial diversity depending on the configuration or arrangement of the antenna array. These configurations can be defined in terms of having multiple and equal number of antennas at both sides of the optical link (often referred to as Multiple-input Multiple-output (MIMO) system), or multiple antennas at the transmitter end (transmit diversity or Multiple-input Single-output (MISO) system) or at the receiver end (Single-input Multiple-output (SIMO) system) of the optical link. Other common types of diversity techniques are time diversity, cooperative diversity and so on.

2.10.2 Modulation Schemes

The choice of optical modulation as well as channel coding schemes in FSO communication systems is mostly dependent on two key criteria which are bandwidth efficiency and optical power efficiency. In the case of a certain optical link length with a specific modulation scheme, the maximum data transfer can be determined by the bandwidth efficiency. Optical power efficiency on the other hand, can be determined by calculating the optical power gain over On-Off Keying (OOK) modulation scheme, as

long as the two schemes to be compared have equal euclidean distance. It was observed that power efficient modulation schemes are quite easier to implement and are relatively effective in reducing the atmospheric turbulence effect for low data rates. However, before applying these schemes to FSO systems, they must obey the eye safety regulations, which may cause a limitation to the propagation distance, especially during strong atmospheric turbulent conditions.

Optical wireless communication system in general supports various binary and multi-level modulation formats. Based on high optical power efficiency as well as simplicity in derivation and implementation, among these two arrangements, the binary level modulation format is the most commonly employed. The most recognized binary level formats are the OOK and PPM modulation schemes. But for best results in atmospheric turbulence conditions, the OOK modulation format needs certain adaptive thresholds [65, 135, 154]. The OOK modulation scheme is seen as the simplest modulation format, and due to its high level of simplicity, it is well known and widely acceptable in FSO communication systems.

Another modulation scheme that can be used for FSO is the *M-ary* Pulse-Position Modulation (M-PPM) scheme which can be used for long-distance communications, as a result of its power efficiency. This modulation scheme does not require an adaptive threshold like OOK modulation scheme [52, 155, 156].

It should be noted that modulation schemes that are power efficient may not necessarily be bandwidth efficient and vice versa. Thus, multi-level modulation schemes are employed in cases whereby the communication system have a limited bandwidth. One of the uniqueness of the multi-level modulation formats is that the transmitted data can take multiple amplitude levels. The most generally employed modulation scheme under the multi-level intensity modulation format are the Quadrature Amplitude Modulation (QAM) and Pulse Amplitude Modulation (PAM) schemes [157]. Nevertheless, reduction in power level is the price paid for bandwidth efficiency. Thus, in the case of high atmospheric turbulence conditions, these modulation schemes are not good choice. According to several literatures on applications of multi-level modulation schemes, the M-PPM scheme is considered as an optimal modulation scheme on Poisson counting channel, particularly in the case of high background noise [52, 155, 156].

Apart from the binary and the multi-level modulation format, there also exist an alternative modulation format which is known as Optical Sub-carrier Intensity Modulation (SIM). In the Optical SIM format, the base-band signal modulates the electrical RF sub-carrier (which is either an analog or digital component) which is then intensity modulated by the optical carrier. Because the sub-carrier signal is typically presented as a sinusoidal signal, then a DC bias is added to the system in order to ignore negative amplitude of the transmitted optical signal. The most common Optical SIM format is the Binary Phase Shift Keying SIM (BPSK-SIM). This modulation scheme does not need an adaptive threshold and it has more bandwidth efficiency than the OOK, but its power efficiency is lower [31].

In addition, the Differential Phase Shift Keying (DPSK) modulation scheme is an alternative for FSO systems, with reasonable power efficiency than OOK modulation scheme. It has only linear effects which improves the DPSK's spectral efficiency over the OOK. Although, based on its high complications, it has high cost of implementation [137, 158].

2.10.2.1 Hybrid Modulation Scheme

It is reported in some literatures, that an optimum performance can be achieved from all of these modulation schemes by combining them to form a hybrid modulation scheme. Also, investigations have shown that for all atmospheric turbulence levels, hybrid PPM-BPSK-SIM yields improved results than the ordinary or common BPSK-SIM scheme [43, 156].

2.10.2.2 Modulation with Spatial Diversity

Another technique that can also produce optimum turbulence mitigating performance is the conjunction of modulation scheme with the diversity techniques such as spatial diversity. Therefore, it has well been proven that in the presence of a turbulent atmosphere, the combination of SIM with diversity technique can provide adequate improvement in the BER performance of the FSO system. For all turbulent atmospheric conditions, the 4x4 MIMO system or higher-order diversity systems are considered as the best choice with BPSK-SIM [31].

2.10.2.3 Orthogonal Frequency Division Multiplexing

Another very good modulation scheme also considered for FSO systems is the Orthogonal Frequency Division Multiplexing (OFDM) combined with any suitable error control coding, in order to improve the BER performance of FSO IM/DD systems [159, 160].

2.10.3 Channel Coding Techniques

Also, error control coding is another technique that can be used to improve the FSO link performance or mitigate the effects of atmospheric turbulence on the propagating optical signal. This approach makes use of various Forward Error Control (FEC) schemes such as convolutional codes, Turbo codes, Low Density Parity Check (LDPC), Reed-Solomon (RS) codes and trellis-coded modulation (TCM). However, investigations concerning error performance using different error correction codes in fading channel has been under study for several years. This technique which is also known as the channel coding technique adds redundant information to the transmitted data in order to detect as well as correct at the receiver any form of error which is as a result of channel fading [28, 42, 46, 54].

2.10.4 Hybrid FSO/RF

Atmospheric turbulence and weather conditions are major factors that severely influences the performance of FSO communication system. These effects can result into poor BER performance of

the FSO system as well as failure in the optical link. To adequately improve the availability and reliability of the optical link, it is reasonable to combine FSO system with another reliable transmission system such as the RF transmission system, which is observed to be more reliable in some weather conditions such as in the atmospheric fog conditions. Therefore, this type of combinational system is referred to as hybrid FSO/RF, and even in drastic weather conditions it has the ability of providing good BER performance and high optical link availability [38, 41-43]. Thus, when the optical link is down, a low data rate RF link can be employed in order to provide improvement to the total system availability. The major cause of signal degradation in the FSO system is due to fog and in RF system is as a result of rain, which occurs as the carrier wavelength becomes comparable to the rain drop-size [161, 162].

2.11 Choice of Optical Wavelength for FSO Communication systems

One of the most important design parameters required in FSO communication system is the wavelength selection, which affects the performance of the optical link as well as the sensitivity of the detector. It is highly advantageous to transmit at lower operating wavelengths because the gain of the antenna is inversely proportional to the system's operating wavelength. But higher operating wavelengths of about 1330 to 1500 nm results into a lesser pointing induced signal fade, thereby providing an improved optical link quality [2, 16, 68]. Thus, in order to obtain a good system performance, it is necessary to cautiously optimize the wavelength of the FSO link design. The atmospheric effects as well as attenuation and the background noise power strongly influence the selection of wavelength. Moreover, in FSO system design procedure, the eye safety regulations, transmitter and receiver components availability as well as optical unit cost are among the several factors that influences the choice of wavelength. Optical radiations have been classified by the International Commission on Illumination into three distinct groups which are: IR-A (with wavelength ranging from 700 nm to 1400 nm), IR-B (from 1400 nm to 3000 nm) and IR-C (ranging from 3000 nm to 1 mm). It can further be sub-classified based on type of electromagnetic waves and its corresponding spectrum band as follows [2, 68]:

a. Near-Infrared (NIR) spectrum band extending from 0.750 μm to 1.450 μm is mostly utilized for fiber optics applications,
b. Short-Infrared (SIR) extending from 1.4 μm to 3 μm, and within this range the dominant spectral band for long range communication is from 1.530 μm to 1.560 μm,
c. Mid-Infrared (MIR) range extending from 3 μm to 8 μm for military applications,
d. Long-Infrared (LIR) extending from 8 μm to 15 μm is applied in thermal imaging,
e. Far-Infrared (FIR) extends from 15 μm to 1000 μm.

The NIR and SIR are mostly used since their components are easily accessible as well as not dangerous to the eyes and skin, as a result of the fact that energy of the light signal at 1.5 μm are absorbed by the cornea and then focusing of light does not happen on the retina [2, 8, 68].

2.12 Summary

In this chapter, the following were comprehensively discussed:

a. The significant contributions of direct and indirect radiative forcing by water droplets or aerosols and scintillations within the atmosphere to the atmospheric attenuation of optical signals, and the findings suggested in several past research works were adequately reported in this chapter, with relevance to FSO communication system and its challenges.
b. The optical transmission through the atmosphere was discussed in terms of the macroscopic and microscopic parameters of the atmosphere. This section was able to describe that the various atmospheric impairments in form of droplets or tiny particles are efficient at scattering the optical radiation within the visible range of the EM spectrum, whereas absorption within this range is very weak. Several empirical and statistical models that specifically deals with the basic mechanism of the formation and distribution of droplets and aerosols within the atmosphere at different atmospheric conditions, as well as their effects on optical signals were discussed.
c. The coefficient of attenuation of optical radiation by the atmosphere were explained by the atmospheric optical depth and transmittance using the Beer-Lambert exponential law for transmission of light in terms of the transmitted and received optical powers at certain wavelength, and optical link distance. Therefore, it was ascertained from this section that the estimation of total transmittance of the atmosphere gives an idea of how much optical power will be absorbed or lost due to directivity drop of the signal. This theoretical analysis allows a rough prediction of the optical attenuation of directed or specular light radiation. However, due to the insignificance of the amount of both molecular and aerosol absorptions of light energy, then this study is solely based on the scattering term.
d. The common characteristics of atmospheric (precisely, tropospheric) scintillation, its dependence on certain weather factors, and the factors that are utilized to measure scintillation are provided in this chapter. Several theories and models based on earlier works such as the Tatarskii model, described the effect of atmospheric scintillation over the EM wave transmission. Also, it was acquired from this chapter that the quantification of the scintillation intensity producing atmospheric turbulence over the optical wave propagating through free space is scintillation index and log-amplitude fluctuations.
e. The concluding part of this chapter gave an overview of the electromagnetic spectrum, the atmospheric channel of an FSO communication system, the challenges of FSO systems such as scattering and absorption loss (which includes fog, rain, snow), mitigation techniques for minimizing the atmospheric channel effects and the choice of optical wavelength for FSO communication systems.

CHAPTER THREE

Research Methodology

3.1 Introduction

In this thesis, various investigations and statistical analyses have been achieved for FSO systems under diverse atmospheric effects and conditions (such as atmospheric scattering and turbulence) for six different locations within South Africa covering a period of three years from 2011 – 2013. The six locations cover two major environmental or regional classifications which are the maritime (coastal) and continental (non-coastal) environments within South Africa, but it should be noted that the non-coastal locations involved in this work are not core continental regions. The sites referred to as the coastal areas in this work are namely Durban and Cape Town, and Umtata (or Mthatha) is a near-coastal region, while the non-coastal environments are namely Bloemfontein, Johannesburg and Mafikeng (or Mahikeng). The choice of sites to be investigated was due to the decision to cover a larger part of the country by spreading the selection across six provinces, and to ensure that this research work covers most types of atmospheric conditions and environments (such as fog, haze and clouds caused by both maritime and continental environments) within South Africa. Therefore, this work will show the effects of various atmospheric conditions including the most severe conditions (such as fog and atmospheric turbulence) on FSO systems under the climatic conditions of the selected locations. It will also show the implication of transmitting optical signals through the atmosphere of these locations under various conditions in terms of the visibility classes and turbulence regimes, using climatic data. The pattern and effects of the atmospheric instability will be determined and analysed in detail with the changes that takes place in the optical attenuation. The frequency of occurrence and probability distribution of the resultants of these atmospheric conditions over the FSO channel are also studied and various models were introduced in the process.

In this section, the geographical representation and setting, and the collection of the local climatic data for Durban, Cape Town, Umtata, Bloemfontein, Johannesburg and Mafikeng all within South Africa (SA) are described.

3.2 Description of Study Site

The six study sites in this work are all situated in South Africa (officially referred to as the Republic of South Africa, RSA), which is a country located on the southern-most region of the African continent (as shown in Figure 3.1), surrounded and marked by several distinct climate and ecosystem which makes it uniquely associated with a long coastal (ocean) line and a moderate semi-arid zone sectioned in the north-west. It is situated within the latitudinal coordinates $22° - 35°$ and longitudinal coordinates $17° - 33°$, and it is bordered in the west and southwest by the Atlantic Ocean, and by the Indian Ocean in the south and southeast [163-166]. South Africa which consists of nine geographical provinces (as

shown in Figure 3.1), has a human population of over 51 million people as at 2011, and it covers an area of about 1.23 million km^2 [167, 168]. In terms of its enormous coastline, South Africa is bounded to the south and east by $2{,}798\ km$ of coastline of Southern Africa, which stretches along the South Atlantic and Indian ocean, and to the east and northeast (by Mozambique and Eswatini), and towards the north by the neighboring countries (of Namibia, Botswana and Zimbabwe) [163-165].

The interior region of SA (as shown in Figure 3.2) consists majorly of an enormous but almost flat (in most places) plateau, which has an altitude that ranges between $1\ km$ to $2.1\ km$. Towards the south and southwest, the trend of the plateau becomes slightly less noticeable, but it is highest in the east and sloping slightly downwards towards the western and northern parts of the country [169]. Due to the central location of this plateau, it is referred to as the central plateau and it is surrounded or edged by the Great Escarpment (i.e., simply referred to as a cliff), where its eastern section as well as highest part is called the Drakensberg, reaching an altitude of over $3\ km$ [169, 170]. The majority of the exterior part of SA consist of the coastal belt, which are also commonly low-lands and rarely mid-lands with altitudes less than $100\ m$ and about $0.7\ km$ respectively.

The climate of SA is generally a temperate climate based on the Köppen-Geiger climate classification [171], since [163-165, 169]:

(a) it is surrounded on three sides by the Atlantic and Indian oceans,
(b) its mean altitude rises gradually towards the equator (which is towards the north) and further inland, and
(c) it is situated within the climatically milder Southern Hemisphere.

Therefore, the great variety of climatic zones observed in SA which is described in Figure 3.3 [171] by the Köppen-Geiger climate types, is as a result of the varied oceanic influence and topography. The weather periods of SA are divided into four climate seasons, which are the autumn (or fall), winter, spring and summer seasons. In SA, the autumn months are between March and May, the winter periods occur between June and August, the spring period is between September to November, and lastly the summers occurs between December and February [172-174].

The local climatic data which includes the temperature, pressure, wind speed, relative humidity and visibility range measurement campaigns conducted by various weather agencies approved by the South Africa Weather Service (SAWS) and National Oceanic and Atmospheric Administration/National Centers for Environmental Information (NOAA/NCEI) for all the six cities considered within South Africa took place at; King Shaka International Airport (KSIA) in Durban (located in a Humid Subtropical area at -29° 36' 25.42" S and 31° 11' 2.12" E), Cape Town International Airport (CTIA) in Cape town (located in a Mediterranean climate or dry summer climate at 33° 58' 21" S and 18° 36' 15" E), Umtata Airport (UTT) in Umtata (located in a Temperate climate at 31° 32' 52" S and 28° 40' 27" E), Bram Fischer International Airport (BFIA) in Bloemfontein (located in the Semi-arid or Steppe

climate at 29° 05' 34" S and 26° 18' 48.05" E), O.R. Tambo International Airport (ORTIA) in Johannesburg (located in an Oceanic climate or Marine climate, also known as Temperate Oceanic climate at 26° 8' 5.2404" S and 28° 14' 25.9008" E) and Mafikeng International Airport (MIA) in Mafikeng (located in a Semi-arid or Steppe climate at 25° 48' 27" S and 25° 32' 40" E). The climatic conditions of each of these cities differ considerably, even though they are all situated within South Africa. The KSIA in Durban which is situated in a Humid Subtropical climate is characterized by cold to mild winters as well as hot and humid summers, while the climate of the location of the CTIA in Cape Town is a Mediterranean or dry summer climate which is characterized by mild and wet winters as well as dry summers. In Umtata, the winters are short, cool, and dry, and the summers are warm and wet and it is mostly clear year-round, while the climate of the BFIA in Bloemfontein has a Semi-arid or "Steppe" climate which is characterized by areas that collects precipitation or rain below potential evapo-transpiration with hot summer days and cooler, dry winters, often with frosts. The ORTIA in Johannesburg which has an Oceanic or Marine climate features cool but cold winters and cool summers, and lastly is the MIA in Mafikeng which is a Semi-desert or "Steppe" climate characterized by long warm and partly cloudy winters, and short cold, dry and clear summers [163-166, 169, 171].

The Geographical map of South Africa showing each of the cities and weather stations under consideration is presented in Figure 3.4. From this figure, the environmental location and topology of each of the selected cities in terms of altitude, maritime or continental environment can be vividly identified. Table 3.1 shows a brief description of the climatic conditions (based on the Köppen-Geiger climate classification) and various features of the study sites.

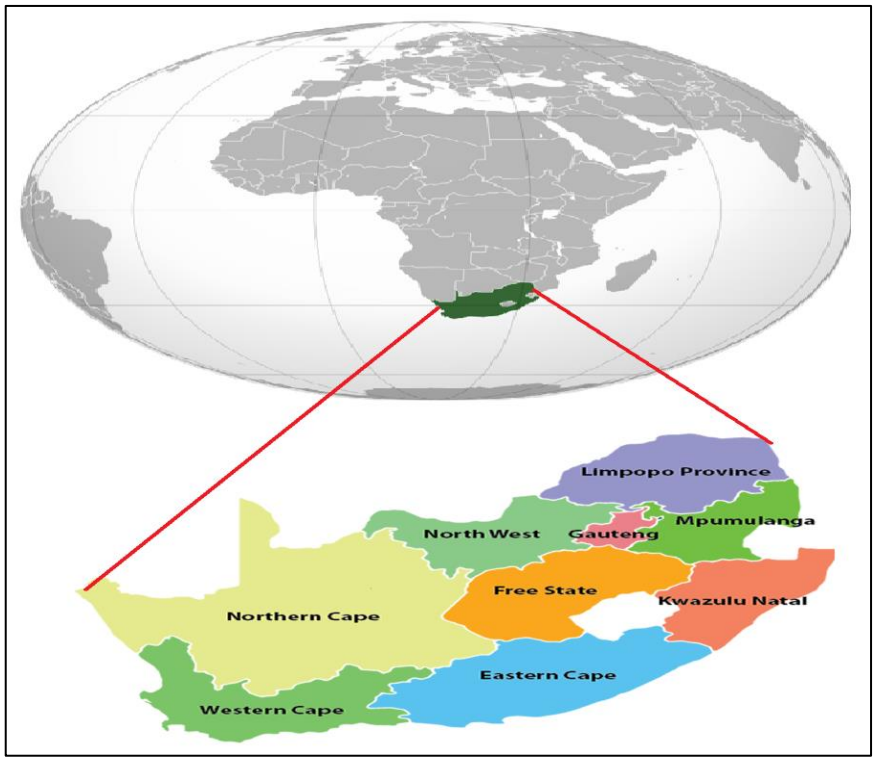

Figure 3.1: Global map showing the African continent and indicating South Africa (orthographic projection), and the extracted map of South Africa showing all the nine provinces.

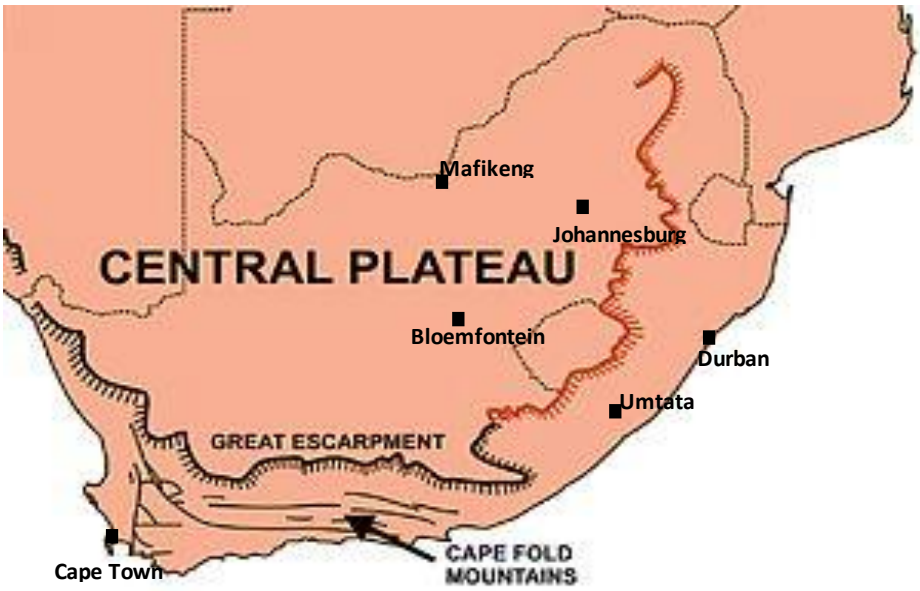

Figure 3.2: The map of SA showing the main topological features such as the central plateau edged by the Great Escarpment. The portion of the Great Escarpment shown in red is officially known as the Drakensberg, although the Drakensberg has always been thought of as only that portion of the escarpment that forms the border between KwaZulu-Natal and Lesotho. Here, the escarpment rises to its greatest height of more than 3,000 metres (9,800 ft) (Image adapted from https://en.wikipedia.org/wiki/Great_Escarpment,_Southern_Africa).

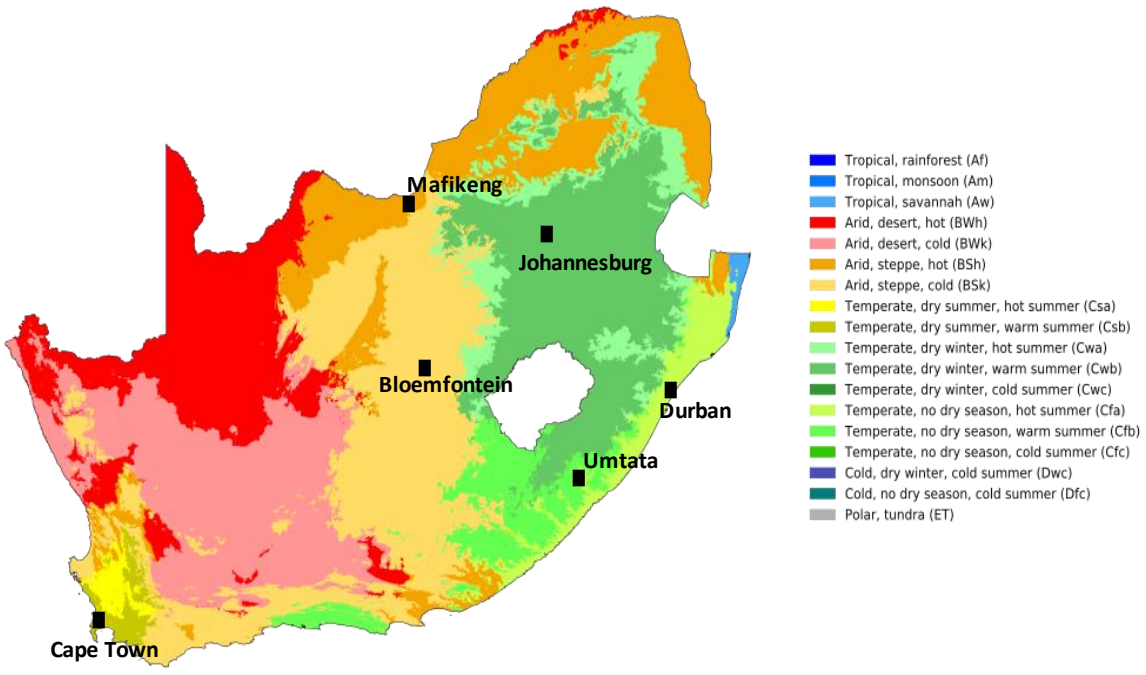

Figure 3.3: Köppen-Geiger climate classification map for South Africa (1980-2016) [*Source: Beck et al., (2018)*, Present and future Köppen-Geiger climate classification maps at 1-km resolution, *Nature Scientific Data*, doi: https://10.1038/sdata.2018.214, retrieved from: https://commons.wikimedia.org/w/index.php?curid=74674206].

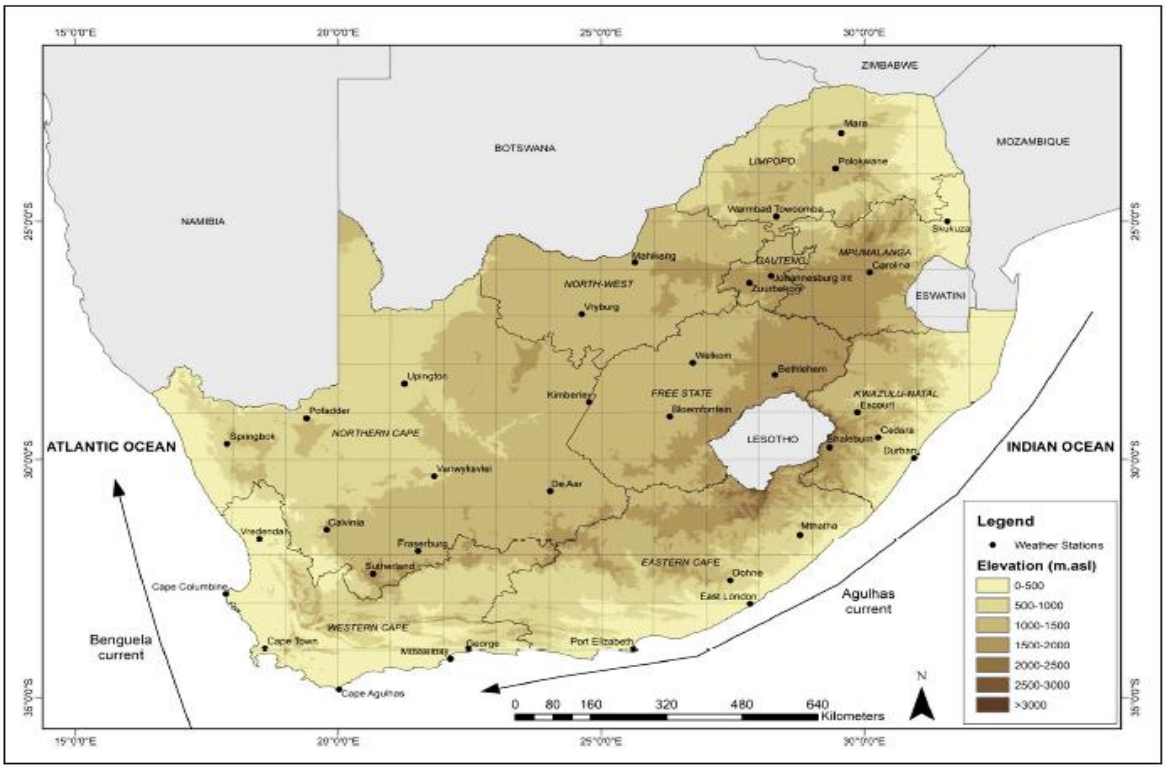

Figure 3.4: Map of SA showing the study sites and indicating all the SA weather stations (SAWS), the surrounding oceans and their respective ocean currents, and the topology (including elevation) [175].

Table 3.1: Brief description of the selected study sites.

Study Site	Province	Latitude	Longitude	Climatic Condition (Based on Köppen Classification)	Elevation (m.asl) (m)	Area (km^2)	Population Size (as at 2019)
Durban (Coastal Area)	KwaZulu-Natal (East)	-29° 36' 25.42" S	31° 11' 2.12" E	Humid Subtropical	106	225.91	3,442,361
Cape Town (Coastal Area)	Western Cape	33° 58' 21" S	18° 36' 15" E	Mediterranean climate or dry summer climate	45	2,461	3,740,025
Umtata (Near-Coastal Area)	Eastern Cape	31° 32' 52" S	28° 40' 27" E	Temperate climate	732	54.97	96,114
Bloemfontein (Continental Area)	Free State	29° 05' 32.08" S	26° 18' 48.05" E	Semi-arid or Steppe climate	1359	236.17	556,000
Johannesburg (Continental Area)	Gauteng	26° 8' 5.24" S	28° 14' 25.90" E	Oceanic climate or Marine climate	1694	1,644.98	4,434,827
Mafikeng (Continental Area)	North-West	25° 48' 27" S	25° 32' 40" E	Semi-arid or Steppe Climate	1290	24.57	291 527

3.3 Data Collection and Processing

The main reason for collecting the local climatic data for Durban, Cape Town, Umtata, Bloemfontein, Johannesburg and Mafikeng was to investigate and estimate the transmitted light signal attenuations

during different atmospheric conditions, and then further study the optical link availability at each of those cities. These atmospheric conditions are classified into various visibility ranges (as shown in Section 3.5) as well as scintillation levels corresponding to various optical attenuation levels, where the atmospheric fog conditions and atmospheric turbulence are the primary focus because of their adverse effects on the atmospheric channel. Therefore, these data collection and analyses are carried out, especially to predict or estimate the effects of optical attenuations in different classes of the atmospheric conditions. The hourly measurements of various atmospheric parameters (such as temperature, pressure, wind speed, relative humidity and visibility range) for all the above-mentioned cities for the entire period of three years (2011-2013) were collected from the database of the SAWS at www.saws.za and NOAA/NCIE at www.noaa.org. In particular, the meteorological parameters such as temperature, pressure, wind speed and relative humidity were collected from the database of SAWS, while the hourly measurements of visibility were obtained from the NOAA database.

The climatic data of the chosen locations, collected from the various archived databases were subjected to quality control. The first step involves checking all the data and time, and in order to maintain consistency all through the analysis, two decimal point rounding was used. Also, if possible, missing data from each of the stations were replaced with those of the surrounding sites (found within a 10 km to 20 km radius). Alternatively, in a situation where the previous option is not possible as a result of technical issues, then they can be replaced with a one-day running average data. Another probable option was to find the average of the immediate past and next data to fill up the present empty data point. However, if the climatic data were not available for over 10 consecutive days within a month, thus those periods were omitted from the study.

In this research work, the hourly visibility range measurements extracted from these measured local climatic data were processed into a three hours (synoptic hours) interval data and were used to estimate the optical attenuations as well as power link margin at a particular optical wavelength. The estimated optical attenuation effects and the power link margin were calculated using the optical link specifications of the installed FSO link at the University of KwaZulu-Natal (UKZN), Durban, South Africa, which is summarized in Table 3.2. The received optical power estimated from these measured data is sampled once every three hours. These measured visibility range data collected from the NOAA/NCEI data source contains some dense/thick fog events at around mostly the autumn and spring, and winter which is unique for all the cities considered.

Before performing any statistical analysis and statistical techniques over the archived data, data processing in terms of data treatment and smoothing were applied, in order to remove all forms of irregularities or randomness in the data. This further data processing which is carried out immediately after processing into synoptic hours interval, involves checking for visible outliers within the data series, by comparing the obtained datasets with other data from the adjacent stations spanning the time of interest as well as physical inspection of anomalous weather reports. After this stage, then the detailed

exploratory data analyses were performed to estimate the optical attenuations as well as power link margin at a particular optical wavelength, as well as other relevant objectives.

3.4 Optical Link Specification

For the purpose of determining the impacts of diverse atmospheric conditions on FSO applications within South Africa, the specifications of the optical unit at UKZN (as presented in Table 3.2) were selected to calculate the expected atmospheric attenuations, received optical power and optical link budget, based on its parameters. The results of the influence of different conditions on FSO system at the selected locations can be used to generate a general model for South Africa.

The FSO link set-up for experimental purposes by the Electronic Department of the University of KwaZulu-Natal, Durban, South Africa has a range of about 25 m, and it is installed on the roof top of the School of Electrical, Electronic and Computer Engineering building within the campus premises. The computer system, electrical to optical (E/O) signal converter and other accessories connected to this outdoor optical unit are located in the Electronic research laboratory. This FSO device is an Optelix Nano1000 optical unit consisting of four identical transceivers, which can transfer data at a rate of about *155 Mbps* and transmit a single carrier at a wavelength of about 850 nm. The semiconductor laser diodes of this optical system have nominal output power of *16 mW* as well as a beam divergence of *2.8 mrad*.

3.5 Visibility Classification and Methodology based on Atmospheric Condition

Since the availability of the optical link should be strongly considered for the worst cases, therefore the collected climatic data for the visibility range were basically classified into low visibilities (that is, the various fog conditions), medium visibilities (mostly the haze conditions) and the high visibilities (which includes the clear sky conditions). The classification of the collected visibility into various ranges due to various weather conditions is based on the International Visibility Code (IVC) adopted by the ITU-R [176], and this is given in Table 3.3. In this work, a further classification was made to divide the various weather conditions based on different visibility ranges into different visibility classes by giving them different class codes (that is from Class-0 to Class-8), as well as into groups (which includes Low Visibility Class (LVC) range, Middle Visibility Class (MVC) range and High Visibility Class (HVC) range).

The classification of the atmospheric conditions into various visibility ranges corresponding to various optical attenuation levels is analyzed in this work, especially to predict or estimate the effects of optical attenuations due to fog and clouds in different classes of the atmospheric conditions. However, this resulting classification which is more elaborate, is a slight modification to the visibility range of each weather conditions. This slight modification allows the total visibility range to cover all the visibility values between $0\ km$ and $> 50\ km$. The modifications to the initial IVC are designed for this research work and for other research works in this field so as to cover for some visibility gaps and also to determine the occurrences and the magnitude of attenuations for each feasible weather condition.

Table 3.2: Optical link specification values of the installed optical link device at the University of KwaZulu-Natal, Durban.

	Operating Parameter		Value	Symbol
Transmitter	Transmitter Power		40 mW (+16 dBm)	P_t
	Transmitter aperture diameter		8 cm	D_t
	Transmitter (Laser) beam divergence angle		2.8 mrad/ $1 \leq \theta(mrad) \leq 3$	θ
	Optical efficiency of transmitter		0.75 or 0.9	τ_t
	Laser Source		4xVCSEL	
	Wavelength		650 – 1550 nm/850 nm	λ
Receiver	Receiver aperture diameter		15.24 cm	D_r
	Optical efficiency of receiver		0.75	τ_r
	Responsivity		0.7 A/W	R
	Receiver Sensitivity		$-38\ dBm@\ BER = 10^{-10}$	P_S
	APD gain		100	
	Field of View		10 $mrad$	
other relevant Receiver Parameters...	**Noise Parameters**	APD Average Output Photocurrent	$RP_r\ (nA)$	I_P
		APD Bulk dark current	10 nA	I_D
		Electron charge	$1.6 \times 10^{-19}\ C$	q
		Electrical bandwidth	2.1 GHz/or 25 MHz	B
		Avalanche Multiplication factor	40	M
		Excess Avalanche Noise factor	$40^{0.7}\ or$ 0.5	M^X
		Boltzmann constant	$1.38 \times 10^{-23} J.K$	K
		System temperature	298 K	T_{APD}
		Noise figure	1	F_n
		Load resistance	1 $k\Omega$	R_L
		Surface leakage current	0.001 A	I_{sl}
Optical Link Performance	**Range**	@ < 3 dB/km	1.5 $km \leq L_{opt}(m) \leq\ last\ mile$	L_{opt}
		@ 3 dB/km	@ 1500 m	
		@ 10 dB/km	@ 1200 m	
		@ 17 dB/km	@ 700 m	
		@ > 17 dB/km	< 700 m	
	Data rate (Max Throughput)		2.5 $Gbps$/ 1.25 $Gbps$	
	BER		Less than $1e-12$ (unfaded)	
Weather Condition	Clear sky to Extremely Clear Sky		$\ll$ 3 dB/km	
	Light Rain (5-10 mm/hour)		@ 3 dB/km	
	Light to medium Rain (15-20 mm/hour)		@ 10 dB/km	
	Cloudburst (100 mm/hour) or medium snow or light fog		@ 17 dB/km	
	Thin fog to Dense fog		$\gg$ 17 dB/km	

Therefore, in this work the analysis of the visibility range characterization and its influence on the optimal performance of the FSO communication system is described based on each of the visibility classes and the sub-groups.

Table 3.3: Modified International Visibility Code for weather conditions and their corresponding visibility range values, along with the class codes and classification.

Weather Condition	*Visibility Range (km)*	*Class*	*Group*
Dense fog	*0 – 0.05*	Class 0	Low Visibility Class (LVC) Range
Thick fog	*0.05 – 0.2*		
Moderate fog	*0.2 – 0.5*	Class 1	
Light fog	*0.5 – 1*	Class 2	
Thin fog	*1 – 2*	Class 3	Middle Visibility Class (MVC) Range
Haze	*2 – 4*	Class 4	
Light Haze	*4 – 10*	Class 5	
Clear sky	*10 – 20*	Class 6	High Visibility Class (HVC) Range
Very Clear Sky	*20 – 50*	Class 7	
Extremely Clear Sky	➢ *50*	Class 8	

3.6 Performance Evaluation Techniques and Accuracy Measures

To perform an error analysis, certain measures such as the coefficient of determination (R^2), Mean Bias Error (MBE, or simply known as 'Bias') and Root Mean Square Error (RMSE) were calculated over a specified period using datasets with synoptic hours interval for all the six locations considered. These accuracy measures indicate how close the derived and measured values will be. The MBE and $RMSE$ are both related to one another by the inequalities given as [177]:

$$MBE \leq RMSE. \tag{3.1}$$

3.6.1 Coefficient of Determination

The coefficient of determination can be described as an error metric which defines the percentage of the variance of one variable (i.e., a dependent factor) produced by its functional relationship to another variable (i.e., an independent factor). Also, the coefficient of determination can be described as a statistical measurement that evaluates how variations in one factor can be described by the variability in a second factor, when the result of a particular event is predicted. In other words, this phenomenon describes how well the data generated from the model fits the measured data. A higher R^2 value shows a better fit or relationship to the model, though its interpretation often depends on the research work. Therefore, it indicates how much (in terms of percentage) of the data of the independent variable fits the regression model. The R^2 estimate is a measure of the amount of functional dependence between the dependent and independent variables, which also suggests the amount of variation described by the generated model. The R^2 estimate can be derived using the following equation [178, 179]:

$$R^2 = 1 - \frac{SSE}{TSS} \tag{3.2}$$

where SSE is the sum of squared errors (which is known as the variation described by the developed model) and it is given as:

$$SSE = \sum_{i=1}^{N} \left(Y_{m,i} - Y_{f,i}\right)^2 \tag{3.3}$$

and TSS is the total sum of squares, which is given as:

$$TSS = \sum_{i=1}^{N} \left(Y_{m,i} - \overline{Y_{m,i}}\right)^2 \tag{3.4}$$

where N denotes the number of samples, $Y_{f,i}$ is the ith predicted value of output Y, $Y_{m,i}$ is the ith actual value of output Y and $\overline{Y_{m,i}}$ is the mean of the measured value.

In statistical analysis of models for data, R^2 values typically range from 0 to 1, which are often stated in percentages from 0 % to 100 % respectively. This statistical range can be used to explain the error associated with the estimated data when compared to the observed data, by interpreting its statistical value. Therefore, the R^2 value can be generally considered as a "none or very weak" effect size, if the $R^2 < 0.3$. However, if $0.3 < R^2 < 0.5$, then this estimate can be typically considered as a "low or weak" effect size. If the R^2 value falls within the range of $0.5 < R^2 < 0.7$, then this value can be termed as a "moderate or average" effect size. Finally, If the $R^2 > 0.7$, then this value can be generally considered as a "strong" effect size [178, 179].

3.6.2 Mean Bias Error

The MBE (or bias) is defined as the average forecast error that represents the Systematic Error (SE, or also known as Systematic Deviation) of a prediction model describing the over-forecast or under-forecast. In other words, the bias can indicate when the prediction model (such as the statistical or ANN model) overestimate or underestimate the output [177]. However, to significantly minimize the obtained MBE, a post-processing of model output is necessary [180]. This quantity is to be used as an average bias of the predicted model and not to be used as an amount of the model error [200]. The expression for the MBE in terms of the measured and estimated data is given as follows [177, 178, 180]:

$$MBE = \frac{1}{N}\sum_{i=1}^{N} \left(Y_{f,i} - Y_{m,i}\right) \tag{3.5}$$

where N, $Y_{f,i}$ and $Y_{m,i}$ are the same as before. The negative estimates of the MBE imply that there exist little or high underestimation (depending on the magnitude), while the positive estimates of the MBE indicate an overestimation in the model used to achieve the prediction. In addition, it should be noted that when a nearly zero MBE is obtained, it is an indication that the model neither overestimates nor underestimates the prediction of the variable examined.

3.6.3 Mean Square Error

The Mean Square Error (MSE) is an error metric that represents the ratio of the sum of the square of the two norms (i.e., $V_{m,i}$ and $V_{f,i}$) of the error vector to the number of samples of the data, and this is mathematically given as [177, 178]:

$$MSE = \frac{1}{N}\sum_{i=1}^{N}\left(Y_{f,i} - Y_{m,i}\right)^2 \tag{3.6}$$

3.6.4 Root Mean Square Error

The RMSE (which is derived from the square root of the MSE) just like the MSE tends to give more weight or focus to the obtained largest errors. The RMSE can be derived using the following equation [178, 180]:

$$RMSE = \sqrt{\frac{1}{N}\sum_{i=1}^{N}\left(Y_{f,i} - Y_{m,i}\right)^2} \tag{3.7}$$

The RMSE is an error metric that can be used to evaluate the degree of accuracy of a model, and it is a good indicator representing the quality of the proposed model. As a result of this, it has the ability to describe the behaviour of the examined system.

The normalization of the RMSE of the data is defined as the ratio of the RMSE of the predicted data to that of mean of the measured data, and this is given as follows [177]:

$$NRMSE = \sqrt{\frac{\sum_{i=1}^{N}\left(Y_{f,i} - Y_{m,i}\right)^2}{\sum_{i=1}^{N}\left(Y_{f,i} - \bar{Y}\right)^2}} \tag{3.8}$$

where $\bar{Y}$ is the mean of the measured data.

3.7 Visibility Range Data Processing and Characterization

The local climate visibility data (such as the Meteorological Visibility Range (MVR) obtained at weather stations or the Runway Visibility Range (thereafter, RVR) obtained at airports) of a particular location is usually available averaged over a longer period (for instance in half-hour, hourly or sometimes in three-hour intervals).

The measured visibility range data was subjected to quality control before the raw data was analysed. Some of the two methods used to achieve the quality control and data treatments are visual inspection and smoothing. These methods were used to fine tune the measured visibility range data, and the statistical tool used for the smoothing of the data is the box plot. Box plots were used after the data processing and data treatments to show that the processed data does not consists of outliers. Typical Box plots of the visibility data after sorting and filtering, for all of the stations over the period of years considered in this work are shown in Figure 3.5.

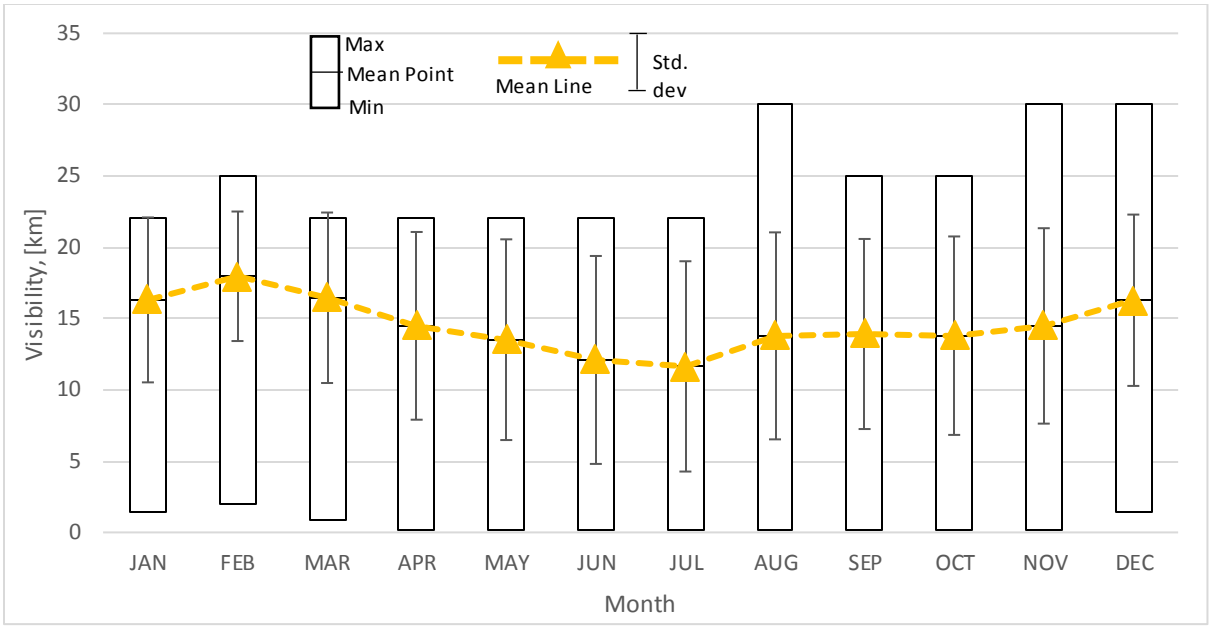
Max
Mean Point
Min
Mean Line
Std. dev
Visibility, [km]
0
5
10
15
20
25
30
35
JAN
FEB
MAR
APR
MAY
JUN
JUL
AUG
SEP
OCT
NOV
DEC
Month

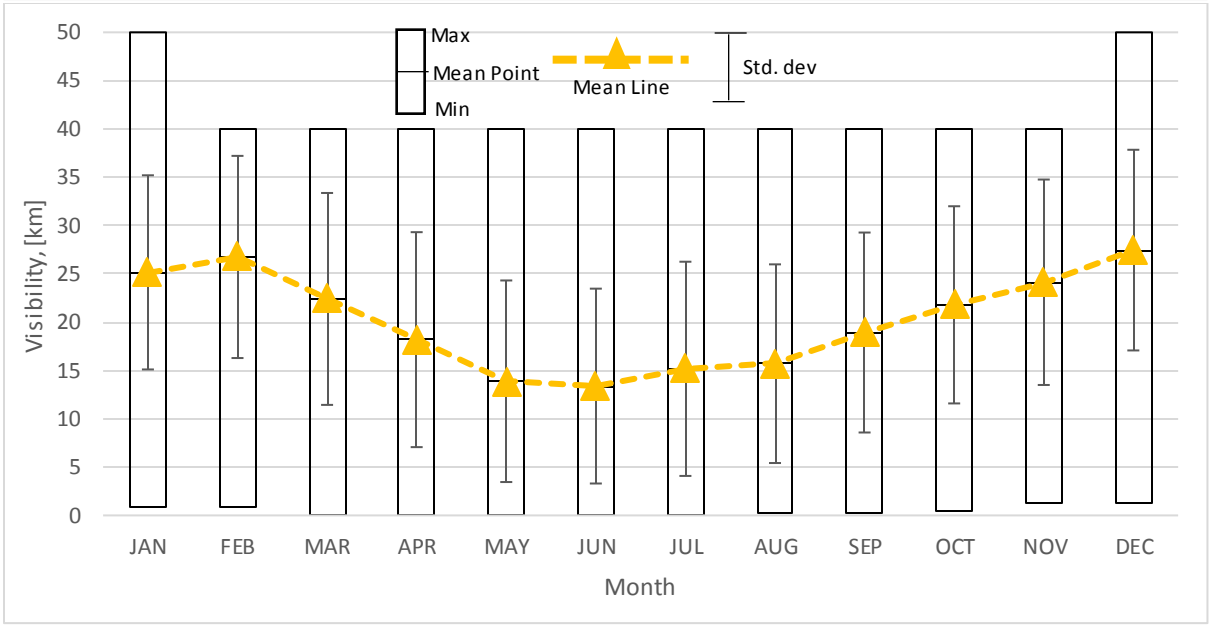
Max
Mean Point
Min
Mean Line
Std. dev
Visibility, [km]
0
5
10
15
20
25
30
35
40
45
50
JAN
FEB
MAR
APR
MAY
JUN
JUL
AUG
SEP
OCT
NOV
DEC
Month

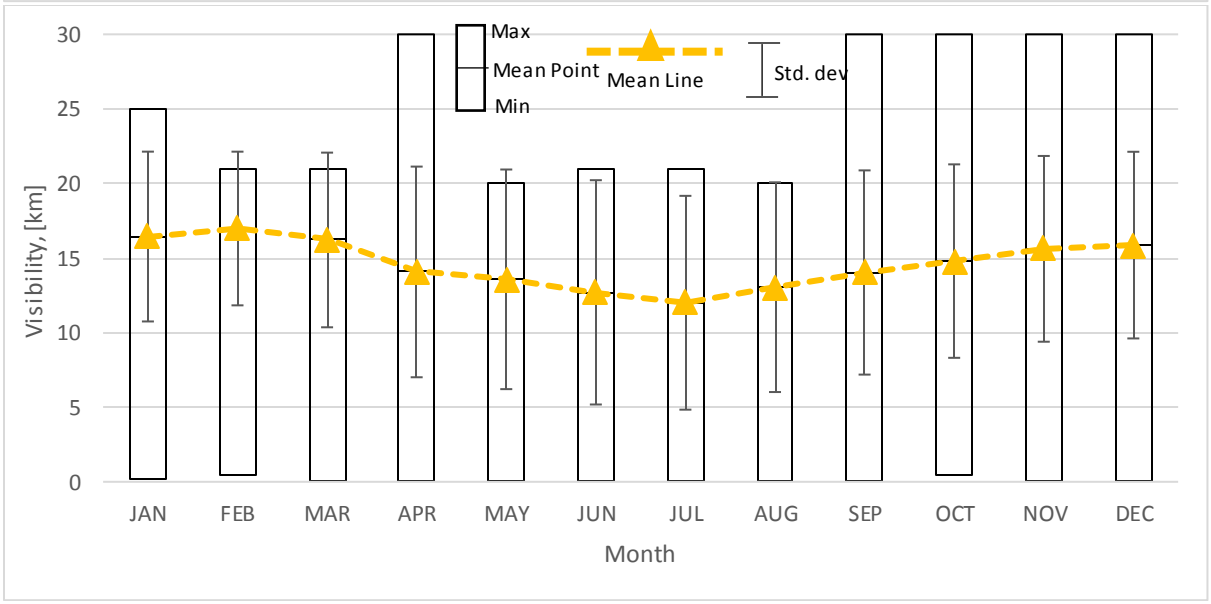
Max
Mean Point
Min
Mean Line
Std. dev
Visibility, [km]
0
5
10
15
20
25
30
JAN
FEB
MAR
APR
MAY
JUN
JUL
AUG
SEP
OCT
NOV
DEC
Month

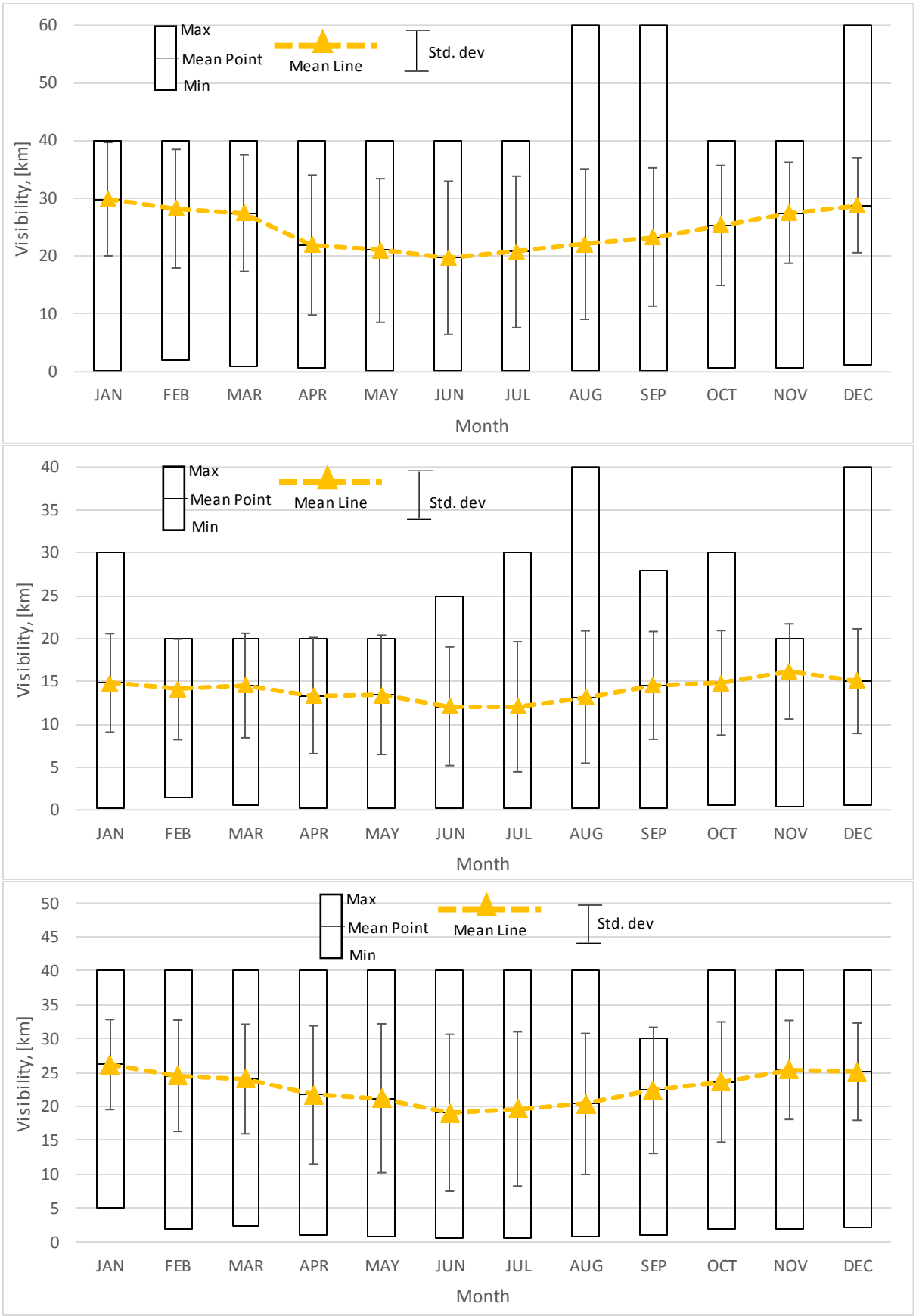

Figure 3.5: Typical box plots of the characterization of the monthly mean visibility range data over the years 2011-2013 for (a) Durban; (b) Cape Town; (c) Umtata; (d) Bloemfontein; (e) Johannesburg and (f) Mafikeng.

The smoothing achieved in this section allows significant patterns to vividly stand out, and thus the patterns of visibility across each location can be predicted even before analysing it. It can be observed from the results in Figure 3.5 that the one-time outliers have been ignored and the impacts of seasonality can clearly be analysed without any difficulties. Also, it can be observed that the variabilities in the visibility data have been reduced or normalized, and now it can be observed that monthly mean of the data has a more pronounced trend. In general, this trend shows that there is a usual dip in the middle of the year, which suggests lower visibility values within these periods.

3.8 Brief Step by Step Processing and analysis of Raw Data for Estimating the Optical Attenuations

The obtained visibility range data were characterized and used to determine the optical attenuations due to scattering under various atmospheric conditions, and other atmospheric parameters such as temperature, pressure, wind speed and relative humidity were processed and analysed to compute the scintillation index and Rytov variance to determine the optical attenuations due to atmospheric turbulence. Attenuation from visibility range and attenuation from atmospheric turbulence or scintillation were computed independently. The total attenuation due to concurrent effects of both the visibility and scintillation can be observed using this work.

3.9 Statistical and Computational Analysis Methods

3.9.1 Probability Density Function

The Probability Density Function (PDF) of a typical random variable (x) is defined as a continuous and smooth data that provides a description of the relative distribution of x, and its product is a positive function. One of the properties of the PDF is that, if the PDF of a given population is described as $p(x)$, then the portion of the population for which $a < x \leq b$ is satisfied is given as $\int_a^b p(x)\ dx$. Also, it can be said that the expression $p(x)dx$ determines the probability that x lies within the interval $x_i \pm \frac{1}{2}dx$, for an infinitesimal range of width dx. In other words, the function $p(x)$ can be mathematically defined as follows [181 - 183]:

$$p(x) = \frac{P\left(x_i - \frac{dx}{2} < x \leq x_i + \frac{dx}{2}\right)}{dx} \tag{3.9}$$

where $P\left(x_i - \frac{dx}{2} < x \leq x_i + \frac{dx}{2}\right)$ is the probability that the variable x lies within the specified range and dx is the width of the bin.

One other significant property of this phenomenon is that its integral sum over all possible values of the random variable must be unity. Therefore, it is also known that for any density function (x), we have [182]:

$$P(-\infty < x < \infty) = C \int_{-\infty}^{+\infty} p(x)dx = 1 \tag{3.10}$$

where the parameter C is a constant that makes the equation true and must be determined before the probability function $p(x)$ can be converted into a PDF through normalization. To determine the PDF of the visibility range and RISP (atmospheric turbulence factor) distributions over the entire period (2011-2013) and for all the locations in this analysis, a three-stage process which is described below were used through various mathematical based application softwares such as *Mathworks (MATLAB) and Mathwave (Easyfit)* applications.

3.9.1.1 Smoothing

This process involves a systematic arrangement of the visibility data sets in terms of bins or intervals, where the procedure is a form of merging of various visibility occurrences into various sets referred to as bins in order to achieve a smooth PDF curve. This phenomenon is required to provide a smooth PDF curve with continuous data which does not change its slope in a sudden or erratic way. This process starts by considering the largest observed visibility bin and then working downwards to the smallest detected visibility bin, such that each empty lower visibility bin was merged with its nonempty upper neighbour. The merging process involves finding a suitable way of sharing the number of occurrences obtained in the nonempty bin uniformly among all the empty bins immediately beneath it. Therefore, if there were k contiguous empty visibility bins beneath a bin with n occurrences, thus after this process the $k+1$ bins will respectively contain $n/(k+1)$ occurrences, which will not certainly be an integer

3.9.1.2 Likelihood Estimation

Here, the probability of the event or variable for each visibility bin (m) is obtained as a function of the ratio of the number of occurrences (n) observed for each visibility bin to the total number of occurrences (N) observed from the whole visibility data set or from the summation of all the bin occurrences, that is $\sum_{m=1}^{q} n_m$, where q is the number of visibility bins. Therefore, the likelihood estimation is given as [181, 184]:

$$p_{r\,m}\big|_{m=1}^{q} = \frac{n_m}{\sum_{m=1}^{q} n_m}. \tag{3.11}$$

This process also involves the determination of the PDF by estimating the ratio of the probability $(p_{r\,m})$ to the respective bin width (w) of all the visibility bins, that is:

$$p(x) = \frac{p_{r\,m}}{w_m}. \tag{3.12}$$

Hence, a smoothed plot $p(x)$ versus the variable x is known as the smoothed PDF curve.

3.9.1.3 Normalization

This mathematical operation is defined when the sum of all the possible values of the function is equal to unity, that is, the PDF $p(x)$ of the random variable (x) is determined as a scaled frequency curve with unit area in the form of [184]:

$$\int_{x_{min}}^{x_{max}} p(x)dx = 1\,. \tag{3.13}$$

Here, the random values x and PDF $p(x)$ are normalized into non-dimensional z values and $p(z)$ values respectively. This can be accomplished by converting each mid value of x into z and $p(x)$ into $p(z)$ using $z = (x - \mu_x)/\sigma$ and $p(z) = \sigma \cdot p(x)$ respectively. Thus, a plot of $p(x)$ against z can be generated, and a smooth curve through these data points is the normalized PDF.

3.9.2 Cumulative Distribution Function

The Cumulative Distribution Function (CDF) of a random quantity (X) whose density function $P_r(x)$ is defined as the fraction of the density that falls below some certain value x, and it is mathematically expressed as [182, 185]:

$$P_r(X < x) = C \int_{-\infty}^{x} p(y)dy\,. \tag{3.14}$$

The computation of the CDF gives the following:

a. The proportion or amount of the population with value less than x,

b. The probability of having a value less than x.

3.9.3 Complementary Cumulative Distribution Function

The Complementary Cumulative Distribution Function (commonly referred to as CCDF) is another important distribution tool which is statistically derived from [182, 185]:

$$1 - CDF = 1 - P_r(X < x) = P_r(X \geq x)\,. \tag{3.15}$$

Therefore, it is mathematically defined as:

$$P_r(X \geq x) = C \int_{x}^{\infty} P(y)dy\,. \tag{3.16}$$

3.10 Summary

The methodology of this work has provided the study site description, data collection procedures, mathematical analysis, statistical analysis tools and various models to compute the influence of the

various atmospheric impairments described in the literature review over the optical link as well as the relevant error measurements methods, and this is summarized as follows:

a. Six locations consisting of both coastal and non-coastal sites were selected in South Africa due to the decision to cover a larger part of the country by spreading the selection across six provinces, and to ensure that this research work covers most types of atmospheric conditions and environments (such as fog, haze and clouds caused by both maritime and continental environments) within South Africa. The detailed description of the geographical and climatic features of each of the selected locations within South Africa were provided.
b. The meteorological data for each station for a duration of five years (2011-2015) were collected from two database sources which are SAWS and NOAA.
c. A further classification based on the IVC was made in this work to divide the various weather conditions based on different visibility ranges into different visibility classes (that is from Class-0 to Class-8), as well as into groups (which includes Low Visibility Class (LVC) range, Middle Visibility Class (MVC) range and High Visibility Class (HVC) range).
d. The performance evaluation techniques and accuracy measures to be used in this work have been discussed in this chapter. The error estimation techniques such as coefficient of determination, Mean Bias Error, Mean Square Error and Root mean Square Error are the selected techniques to be used to compare the measured values to the estimated values.
e. The collected data were processed using Excel and MATLAB softwares, which involved quality control and data treatments. The Box plots provided in this chapter were used after the data processing and data treatments to show that the processed data does not consists of outliers. The results of this fine tuning showed that the one-time outliers have been ignored and the impacts of seasonality can clearly be analysed without any difficulties. Also, it can be observed that the variabilities in the visibility data have been reduced or normalized, and now it can be observed that monthly mean of the data has a more pronounced trend.
f. Since the attenuations from visibility range and atmospheric turbulence are considered to be undeterministic and can be represented by a random variable, therefore the distribution of the attenuation can be investigated using different statistical distribution models such as the pdf, cdf and ccdf models.

CHAPTER FOUR

Estimation of Fog and Cloud Attenuations from Visibility Range Characterization for FSO Link Design Using Climatic Data for South Africa

4.1 Introduction

As earlier discussed, certain atmospheric attenuators altogether constantly and significantly debase the optimum performance of the optical link, which results into the key reasons for the slow acceptability of the FSO system as an ideal access technology [16]. So far, most researchers have suggested improved changes in the design of the FSO system by just focusing on the atmospheric turbulence induced fading problems, and thus have broadly used the distribution models established for atmospheric turbulences of weak and strong regimes within the optical channel to obtain knowledge into the several aspects of the FSO system design [3, 31, 49, 186]. However, significantly less consideration has been given to the additional optical link atmospheric attenuators such as fog (special case), haze, snow and clouds (mists). For dense maritime fog as well as moderate maritime fog conditions, current investigations established that the optical power attenuations respectively approach 480 dB/km and 120 dB/km [19-21, 187-189]. Also, the optical signal power losses for intense shower and heavy snowfall conditions are respectively up to 30 dB/km and 70 dB/km. As a matter of fact, for rain and snow attenuations, certain empirical models have been recommended in literature (for instance, the Crane and ITU-R models) [22, 30, 33, 190], whereas for the empirical modeling and observational displaying of the fog conditions in terms of visibility range, the notable Kruse and Kim models are broadly used [95, 191].

The efforts in modeling fog related events have remained focused up until now on the development as well as the enhancement of empirical models in order to obtain estimates of the fog attenuations resulting from various atmospheric fog conditions [20-22, 95, 188, 191], while atmospheric turbulence modeling efforts are continuously focused on or worked towards accomplishing and developing upon controllable PDFs for the fluctuations observed in the irradiance of the optical signal [49, 50, 186]. Though, for the case of fog, very few endeavours in this direction have been established. The main causes for this are due to the undeterministic and random behaviour of the atmospheric fog formation, the long persistence of the nature of fog within the atmosphere as well as the fact that in multiple occasions the occurrence of fog results into such high magnitudes of atmospheric attenuations that can render the FSO link to be inaccessible for a period of time or permanently in severe cases [19-22, 189]. Thus far, these existing empirical models all have the ability to give good estimates and assessments of atmospheric attenuations resulting from atmospheric optical link impairments, though, they give no knowledge about the variations of the Received Signal Strength (RSS). In order to obtain facts and insights on the variations observed in the optical RSS under the effects of the atmospheric attenuators,

FSO system engineers have remained in need of stochastic models which might provide them with this insight. These stochastic models may well give the needed foundation and principle for suitable FSO system design improvements such as appropriate modulation scheme, optical channel codes, estimators as well as equalizers for the optical link. In short, it is not enough to recommend FSO system design improvements which enhances the optical link performance of the FSO system only under the atmospheric turbulent conditions [21, 22, 189].

At a specific location, the visibility range as well as the LWC resulting from the occurrences of the atmospheric aerosol, both varies significantly and depend upon the type of fog or cloud existing within the atmosphere. The classification of these weather conditions is greatly interrelated to their origin, the magnitude of the visibility and the amount of the LWC. The combination of the visibility range, LWC and the source permits to readily forecast the sorts of weather conditions that may be most possibly present within the region of the FSO link. Therefore, fog or clouds with extremely low densities, results into lower estimations of LWC values of about $0.05\ g/m^3$ for a moderate fog (having visibility range of around $300\ m$), because it contains very little amount of water. But significantly higher estimations of LWC of around $0.5\ g/m^3$, typically indicates the formation of thick fog (or dense fog) with a visibility range of about 50 m [96, 192]. Likewise, when measured in a similar amount of space, clouds such as the Cirrus and Cumulonimbus clouds can respectively have LWC value of about $0.06405\ g/m^3$ and $1-3\ g/m^3$ [193]. The fog or cloud drops of the maritime (oceanic) source have a tendency to possess lesser amount of droplets of water with relatively bigger drop-size radius when compared to the size of the continental (mainland) droplets [19, 21, 22, 189, 193, 194]. The water droplets of the maritime origin can be said to have a concentration that ranges between $100\ drops/cm^3$ to around $200\ drops/cm^3$, while that of the continental origin is around $900\ drops/cm^3$ [195].

The focus of this section of this thesis dwells on atmospheric fog modeling and the presentation of the specific fog attenuation for the selected cities in South Africa, under various weather conditions and visibility range characterization.

4.2 Visibility Range Characterization

Visibility is defined as an optical parameter that can be used to characterize the degree of opacity of the atmosphere in meters. In other words, it can be described as the distance to an object at which the observed image contrasts reduces to a particular percentage of the original contrast of the object, equal to a specific transmission threshold (τ_{TH}) over the atmospheric path. However, there exist two definitions for the transmission threshold, that is the 2 % threshold as well as the 5 % threshold. The former is employed in the original Kruse formula to be used in this chapter to determine the optical attenuation and received signal power, while the latter is typically employed at the airports in order to signify the RVR [21, 22, 97, 196-200].

Visibility range which is occasionally referred to as see-ability can be measured technically at the center of sensitivity of the human eye, at a certain optical wavelength of about $0.550\ \mu m$ with a typical spectral bandwidth of $0.250\ \mu m$. Thus, the Koschmieder law defines the visibility range as follows [97, 197]:

$$V = \frac{\ln(\tau_{TH})}{\gamma(550\ nm)}. \tag{4.1}$$

Equation (4.1) which shows the relationship between visibility (V) and the extinction coefficient (γ), can provide the characterization of visibility in terms of the optical extinction caused by various atmospheric conditions (such as fog, haze and clouds events) relating to different scattering components. This characterization provides a form of relationship between the visibility range, optical attenuation, scattering components, density of the atmospheric particles and types of atmospheric conditions (such as fog, haze, clear air etc.). The visibility range characterization is quite important in FSO communications, and it is a function of particle size or concentration characterization. A typical range of specific optical attenuation estimates for FSO can be obtained based on the characterization and distribution of visibility range for different atmospheric conditions. The occurrences and variations of the atmospheric aerosol (in terms of the fog, haze or mist particles etc.) within the atmosphere at each of these locations results into a significant variation of the LWC and then the visibility range. The amount of the LWC in the atmosphere which results into the magnitude of the visibility range provides a classification of the various weather conditions, based on Table 3.3. It is highly possible to readily predict the type of atmospheric condition that may be most likely present at a particular location where the FSO link is situated based on the type of environment of the condition (such as either maritime or continental environs), LWC and visibility range. Therefore, the magnitude of the observed visibility range is an indication of the contributions and density of the optical link atmospheric attenuators such as fog (special case), haze, snow and clouds (mists) events within the atmosphere [21, 22, 97, 196-200]. To characterize the properties of the visibility parameter into different ranges of the optical specific attenuation, several statistical and modeling (such as ANN) techniques needs to be used to investigate the visibility range.

4.3 Descriptive Statistics of Visibility Events

The statistical description for the synoptic interval scale data of the obtained visibility range covering the cumulative period in this study and for all the six cities are provided in Table 4.1. The range of visibility (in terms of minimum and maximum values) obtained across the entire period under study for the city of Durban is from $0.1\ km$ to $30\ km$, which suggests that the atmospheric conditions due to visibility range over Durban within this period spans from dense/thick fog (i.e. very severe or worst atmospheric condition) to very clear air conditions, with the modal visibility obtained as $20\ km$ corresponding to very clear air. For Cape Town, the range of visibility obtained across the same period is from $0.1\ km$ to $50\ km$, which suggests that the atmospheric conditions due to visibility range over

Cape Town spans from dense/thick fog to Extremely clear air conditions with the most occurring visibility obtained as 20 km corresponding to very clear air. Though, during the data processing and treatment in the previous chapter of this thesis, it was ascertained that there were only very few or inconsiderable number of situations where the visibility range of Cape Town extended to about 50 km, which was only overlooked during data processing in order to determine how extreme the weather of this location can be, and at the same time they could have been considered as outliers. Also, minimum value of visibility obtained for the city of Umtata over the considered period is 0.1 km which corresponds to the dense/thick fog condition, while the maximum value of visibility is 30 km which relates to very clear air condition, and the modal visibility is 20 km corresponding to very clear air. The range of visibility obtained for the city of Bloemfontein over the whole period considered ranges from 0.1 km to 60 km, which indicates that atmospheric conditions due to visibility range over Bloemfontein spans from dense/thick fog to Extremely clear air situations, with the most occurring visibility obtained as 30 km corresponding to very clear air. The minimum and maximum values of visibility obtained for the city of Johannesburg are 0.2 km and 40 km, which corresponds to moderate fog and very clear air conditions respectively and the most occurring visibility obtained is 20 km corresponding to very clear air. Lastly, for Mafikeng, the minimum visibility over the studied period is 0.5 km which represents light fog condition, whereas the maximum visibility recorded is 40 km which corresponds to the very clear air condition and the most occurring visibility obtained is 30 km (i.e. very clear air condition).

The statistical description for the daily data of the obtained visibility range covering the three successive years and for all the six cities considered in this study are provided in Table 4.2. In other words, this table shows the descriptive statistics of all the fog and cloud events within the atmosphere at each of the locations for the specified period. These statistics showed that Cape Town had the lowest daily mean visibility value of about 1.75 km in the year 2011, while the highest of about 13.93 km was observed in Mafikeng in the year 2012. This statistical table also shows that the standard deviation (SD) for Cape Town is the highest (with SD of 7.02 km, 6.84 km and 8.02 km) across all the three years under study, while Bloemfontein has the next highest SD, except in year 2013. This observation may probably be due to their wide range of visibility values exhibited by the two stations. Therefore, this may likely indicate a temporal instability in the weather condition or an extreme climate condition (where a particular location often exhibit extreme weather parameters or characteristics). In overall, it was also revealed that Bloemfontein and Mafikeng had the highest median values all through the period under study.

Table 4.1: Descriptive statistics for the visibility range data in synoptic interval scale over the entire period for all locations.

Summary Stat-2011-2013		***Durban***	***Cape Town***	***Umtata***	***Bloemfontein***	***Johannesburg***	***Mafikeng***
Descriptive Statistics							
Minimum	*Value (km)*	0.1	0.1	0.1	0.1	0.2	0.5
	Atmospheric Condition	Dense/Thick fog	Dense/Thick fog	Dense/Thick fog	Dense/Thick fog	Moderate fog	Light fog
Maximum	*Value (km)*	30	50	30	60	40	40
	Atmospheric Condition	Very clear sky	Extremely clear sky	Very clear sky	Extremely clear sky	Very clear sky	Very clear sky
Mode	*Value (km)*	20	20	20	30	20	30
	Atmospheric Condition	Very clear sky	Very clear sky	Very clear sky	Very clear sky	Very clear sky	Very clear sky
Other Descriptive Statistics							
Mean		14.54	20.22	14.60	24.68	14.00	22.74
Range		29.90	49.90	29.90	59.90	39.80	39.50
Median		20	20	20	30	15	30
Standard Error		0.07	0.12	0.07	0.13	0.07	0.10
Standard Deviation		6.82	11.56	6.77	11.75	6.62	9.60
Sample Variance		46.47	133.64	45.86	138.14	43.84	92.17
Kurtosis		-0.99	-0.72	-0.88	-0.70	-0.83	-0.60
Skewness		-0.69	0.11	-0.77	-0.53	-0.34	-0.76
Sum		127515.05	177252.75	128019.10	216368.50	122791.35	199386.40
Count		8768	8768	8768	8768	8768	8768

Table 4.2: Descriptive statistics for the daily visibility range (km) data for each of the locations.

Summary Stat-2011	**DBN**	**CPT**	**UMT**	**BLFT**	**JHB**	**MFK**
Mean	14.219	18.740	15.146	26.058	14.190	26.121
Standard Error	0.207	0.367	0.192	0.317	0.173	0.195
Median	14.458	17.875	15.375	26.375	14.375	26.875
Mode	19.000	22.500	20.000	30.000	20.000	27.500
Standard Deviation	3.956	7.017	3.671	6.061	3.302	3.735
Sample Variance	15.648	49.237	13.479	36.735	10.906	13.950
Kurtosis	-0.429	0.424	-0.561	0.619	-0.530	1.723
Skewness	-0.303	0.644	-0.438	-0.697	-0.216	-0.787
Range	21.121	38.250	17.688	34.038	15.275	26.125
Minimum	2.754	1.750	4.813	3.463	4.725	8.875
Maximum	23.875	40.000	22.500	37.500	20.000	35.000
Sum	5189.825	6839.994	5528.325	9511.025	5179.388	9534.025
Count	365	365	365	365	365	365
Summary Stat-2012	**DBN**	**CPT**	**UMT**	**BLFT**	**JHB**	**MFK**
Mean	16.071	24.663	16.364	28.881	15.119	25.492
Standard Error	0.166	0.358	0.167	0.262	0.148	0.169
Median	16.500	23.750	17.250	29.438	15.438	26.250
Mode	20.000	23.750	19.375	31.250	18.125	27.500
Standard Deviation	3.181	6.844	3.200	5.014	2.827	3.235
Sample Variance	10.120	46.838	10.242	25.139	7.991	10.466
Kurtosis	0.740	-0.662	1.645	1.841	-0.446	0.279
Skewness	-0.886	0.209	-1.303	-0.932	-0.412	-0.653
Range	15.250	30.563	16.938	33.175	12.563	19.200
Minimum	5.250	9.438	4.313	5.575	7.438	13.925
Maximum	20.500	40.000	21.250	38.750	20.000	33.125
Sum	5881.950	9026.825	5989.400	10570.590	5533.550	9329.888
Count	366	366	366	366	366	366
Summary Stat-2013	**DBN**	**CPT**	**UMT**	**BLFT**	**JHB**	**MFK**
Mean	16.161	24.908	16.148	26.673	15.361	25.505
Standard Error	0.176	0.420	0.180	0.167	0.224	0.164
Median	16.500	24.375	16.750	27.250	15.500	26.250
Mode	20.000	36.250	18.750	28.125	17.500	28.750
Standard Deviation	3.354	8.018	3.437	3.197	4.282	3.130
Sample Variance	11.253	64.289	11.815	10.219	18.338	9.798
Kurtosis	0.394	-0.893	1.864	0.563	7.714	1.399
Skewness	-0.871	0.096	-1.274	-0.544	1.259	-1.055
Range	15.813	36.600	18.163	17.150	39.338	18.350
Minimum	4.688	3.400	3.713	16.600	4.725	11.650
Maximum	20.500	40.000	21.875	33.750	44.063	30.000
Sum	5898.813	9091.563	5894.025	9735.588	5606.694	9309.313
Count	365	365	365	365	365	365

4.4 Time Series Analysis of Visibility Range

In this work, the visibility data used were processed over three hours interval time scale covering a period of three successive years from 2011 to 2013, and was obtained for the six different locations in

South Africa (as described in Table 3.1). Since the visibility data are known, then the time series analysis of the visibility range for the six cities can be shown over all the years in this study. Figures 4.1 to 4.6 show the typical hourly time series profile of the visibility range for each of the locations over the three years considered in this study. The general observation from these figures is that they all have unique trend which shows that their climatic conditions are quite similar or have some close characteristics, even if their atmospheric parameters (such as temperature, humidity, pressure and wind speed) are not in the same range. One of the common features among these graphs for each of the locations and for all the years is that there is a dip towards the middle of the year, showing that there is a climate change taking place across the whole country at those periods, resulting into lower visibility values. This is expected to be an interesting and important feature or factor in the FSO analysis to be carried out in this work. It will be interesting to investigate what effects this pattern and lower visibility values will have on the transmission of optical signals through the free space medium.

4.5 Atmospheric Optical Depth and Transmittance Estimation

The atmospheric transmittance of each of the stations in this study can be obtained using the optical depth phenomenon. This optical signal transmission via the atmosphere can be analyzed by the Beer-lambert exponential law, which provides the connection between distance covered, wavelength and the air constituents. The connection between this phenomenon and air components also shows that visibility change must be appropriately taken into account for FSO system. Since a high link availability is needed for FSO, then this study is important to give knowledge about the transmittance phenomenon within the atmosphere, which states the performance of the FSO link. Using the expressions in Equations (2.10) and (4.1), the transmittance of the atmosphere can be calculated by inserting the visibility data. The daily average of the visibility range data for the six cities have been used for the estimation of the daily mean transmittance. Figure 4.7 presents the time series analysis of the mean optical signal transmittance at a link distance of 1.5 km and wavelength of 850 nm for each of the considered cities and for the entire period under study. It can be observed from these results that during the year 2011, the range of the atmospheric transmittance for Durban is from 0.18 to 0.86, and 0.08 to 0.92 for Cape Town, 0.47 to 0.86 for Umtata, 0.31 to 0.92 for Bloemfontein, 0.37 to 0.85 for Johannesburg and 0.69 to 0.90 for Mafikeng. This shows that the minimum atmospheric transmittances of Durban and Cape Town are relatively very low in some periods of 2011, and the other stations also showed considerable low transmittances on some occasions, unlike that of Mafikeng that has most periods with steady transmittances. These low transmittances equivalent to high attenuations has resulted into the need of studying the performance of FSO system. Therefore, similar results were observed for the years 2012 and 2013, where the coastal and near-coastal areas (such as Durban, Cape Town and Umtata) and also Johannesburg (which is a non-coastal city) seem to pose the greatest concern with higher coefficient of attenuation compared to the non-coastal areas (such as Mafikeng and Bloemfontein), as revealed in [96, 189, 195, 197].

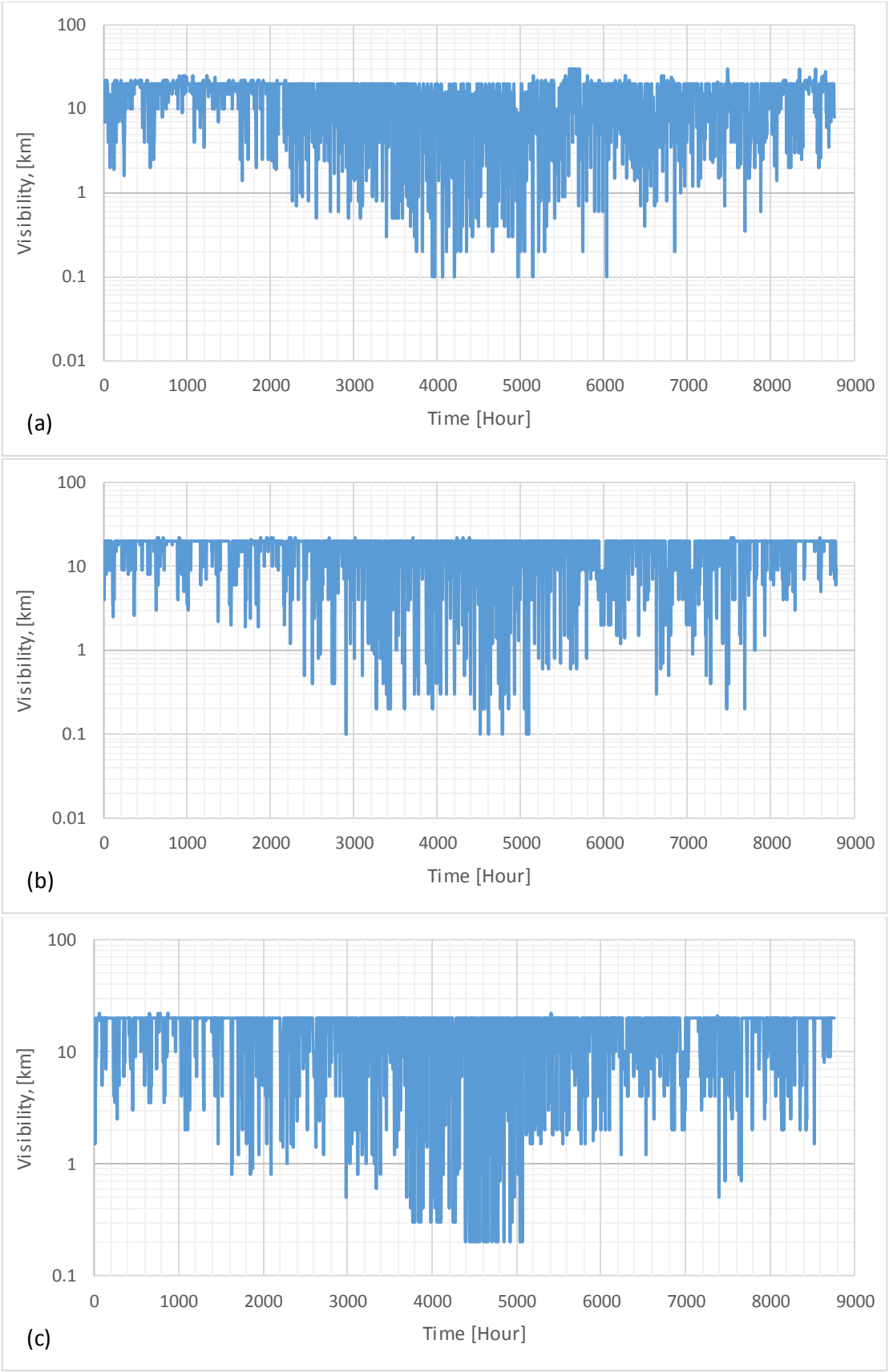

Figure 4.1: Typical hourly time series display of visibility range for Durban over the years (a) 2011; (b) 2012 and (c) 2013.

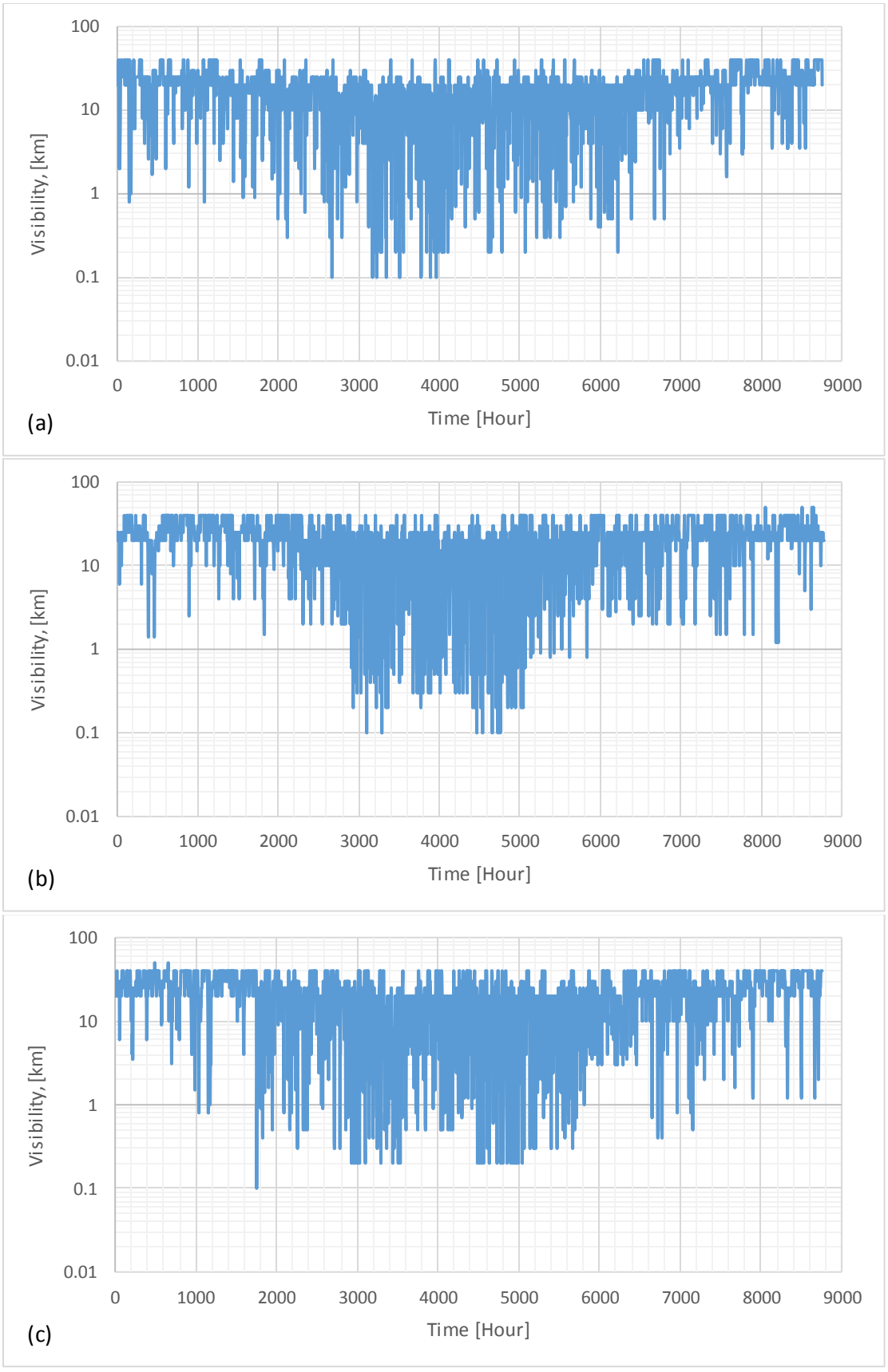

Figure 4.2: Typical hourly time series display of visibility range for Cape Town over the years (a) 2011; (b) 2012 and (c) 2013.

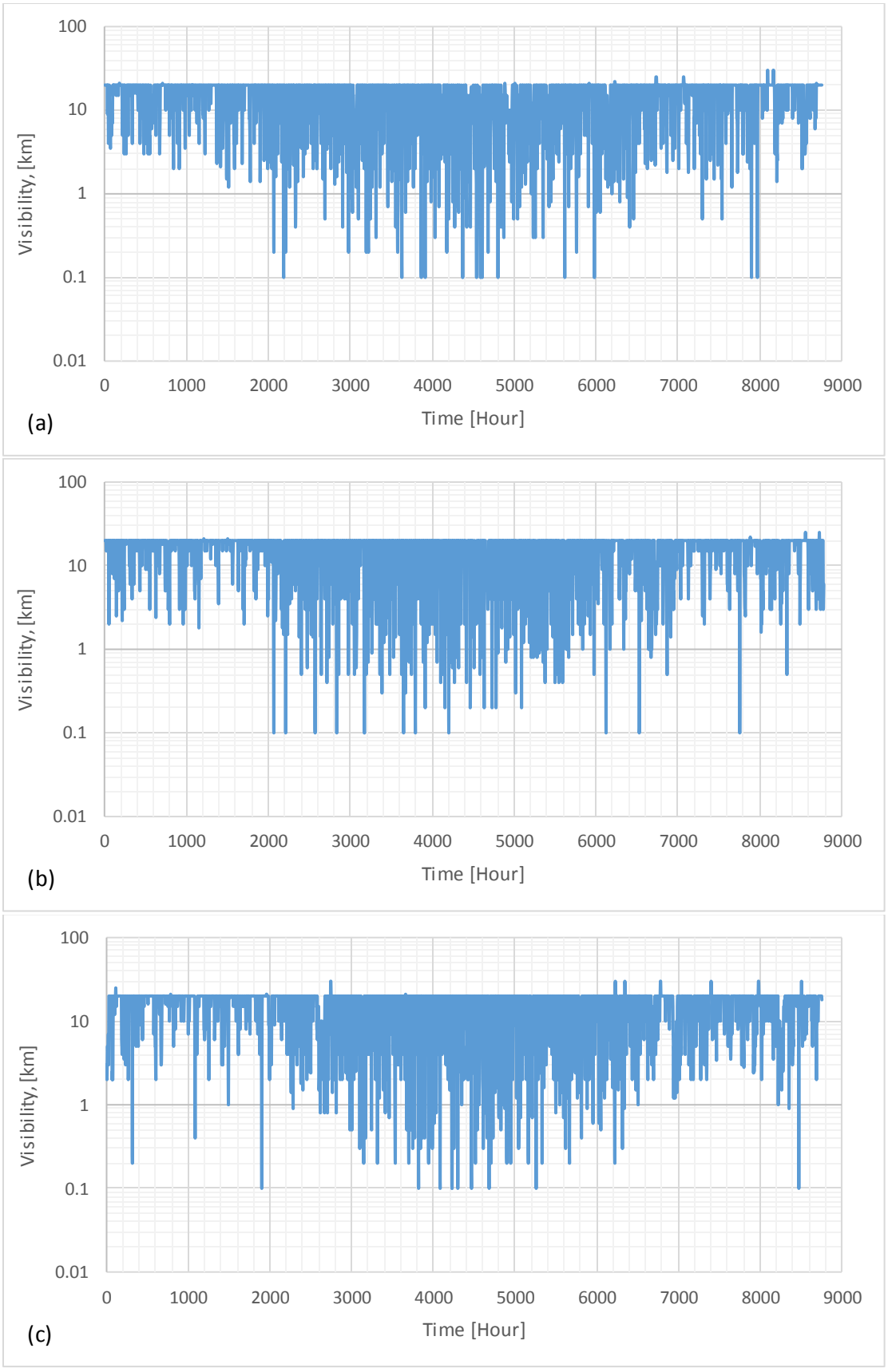

Figure 4.3: Typical hourly time series display of visibility range for Umtata over the years (a) 2011; (b) 2012 and (c) 2013.

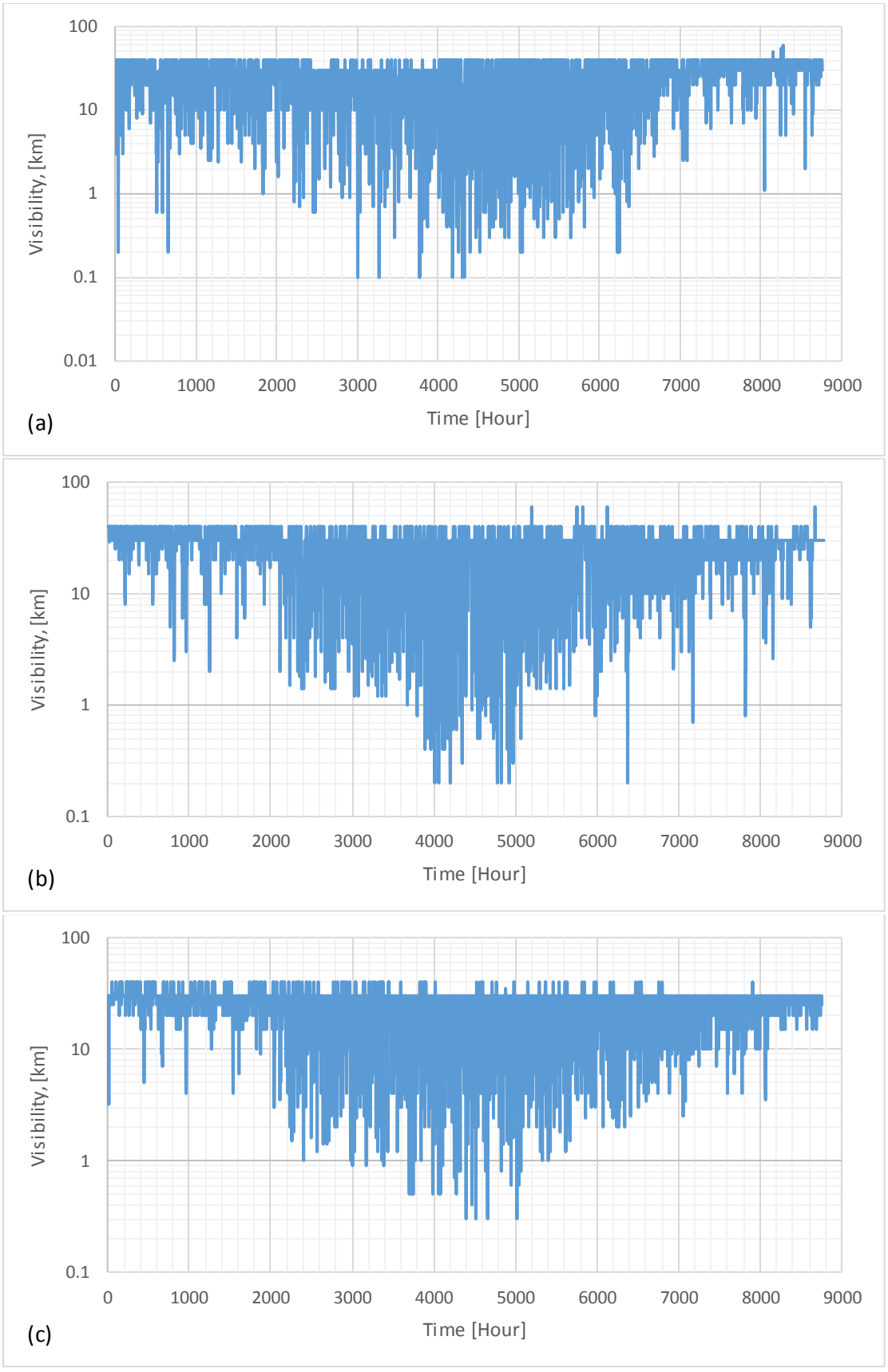

Figure 4.4: Typical hourly time series display of visibility range for Bloemfontein over the years (a) 2011; (b) 2012 and (c) 2013.

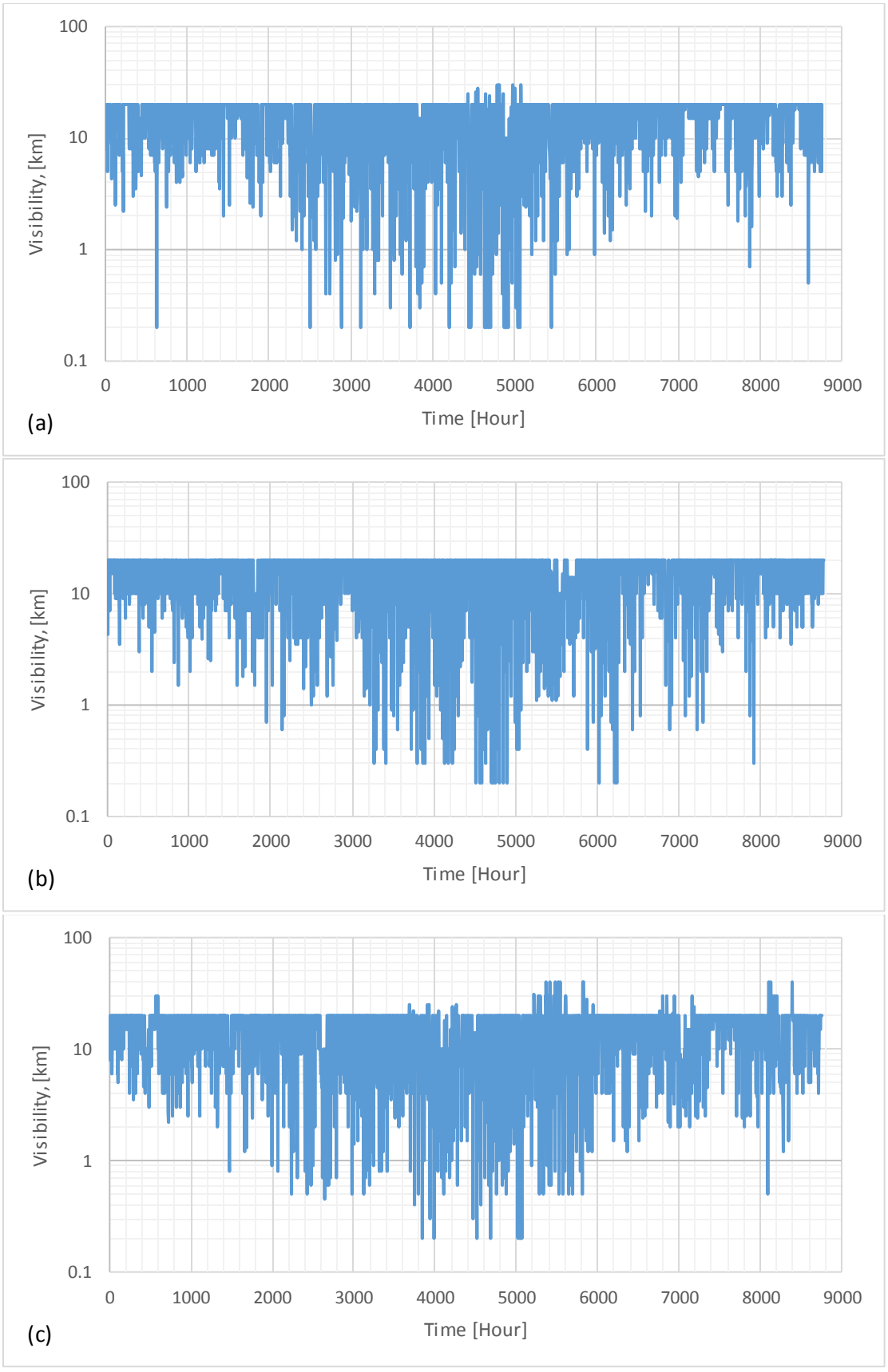

Figure 4.5: Typical hourly time series display of visibility range for Johannesburg over the years (a) 2011; (b) 2012 and (c) 2013.

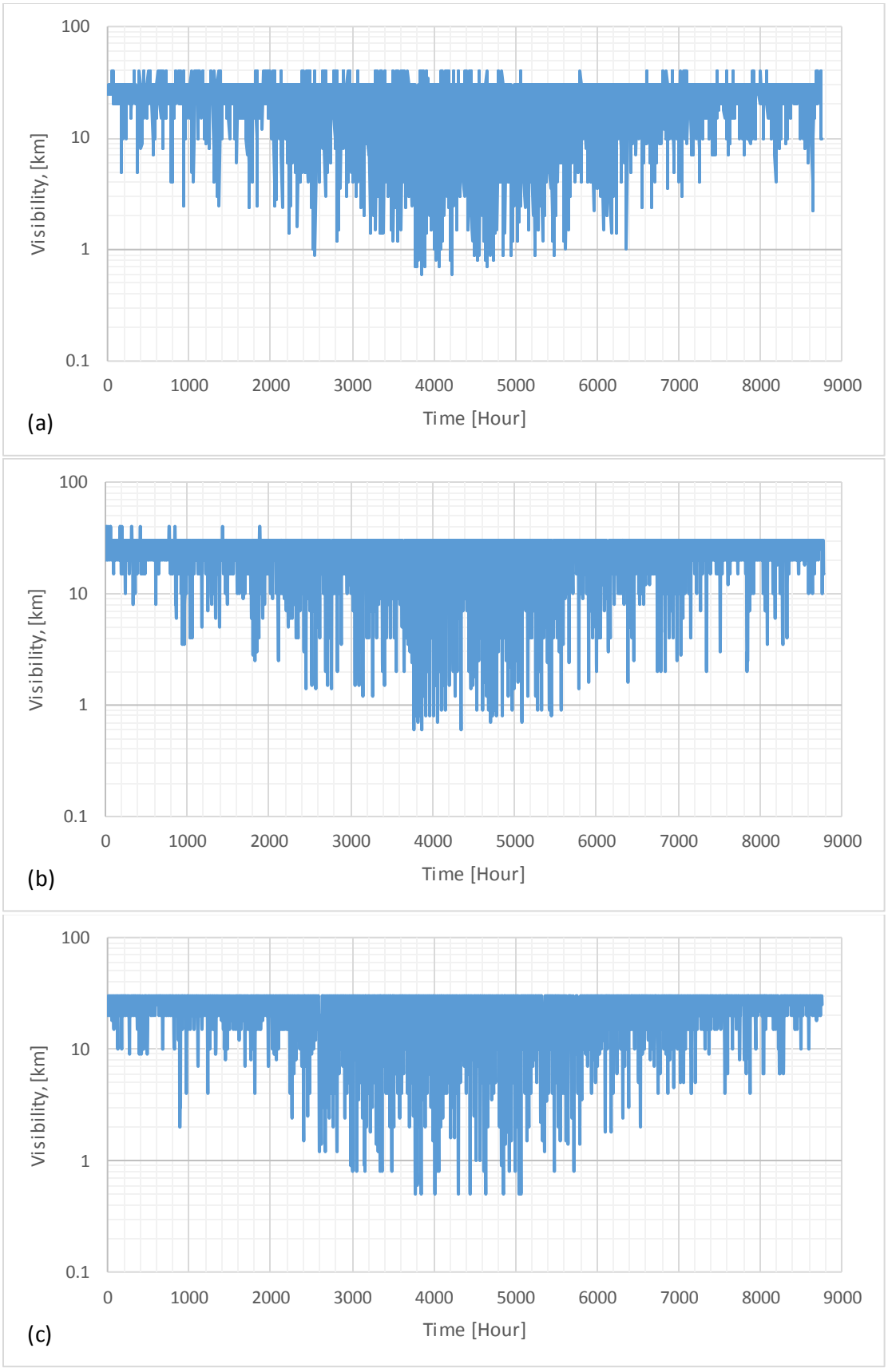

Figure 4.6: Typical hourly time series display of visibility range for Mafikeng over the years (a) 2011; (b) 2012 and (c) 2013.

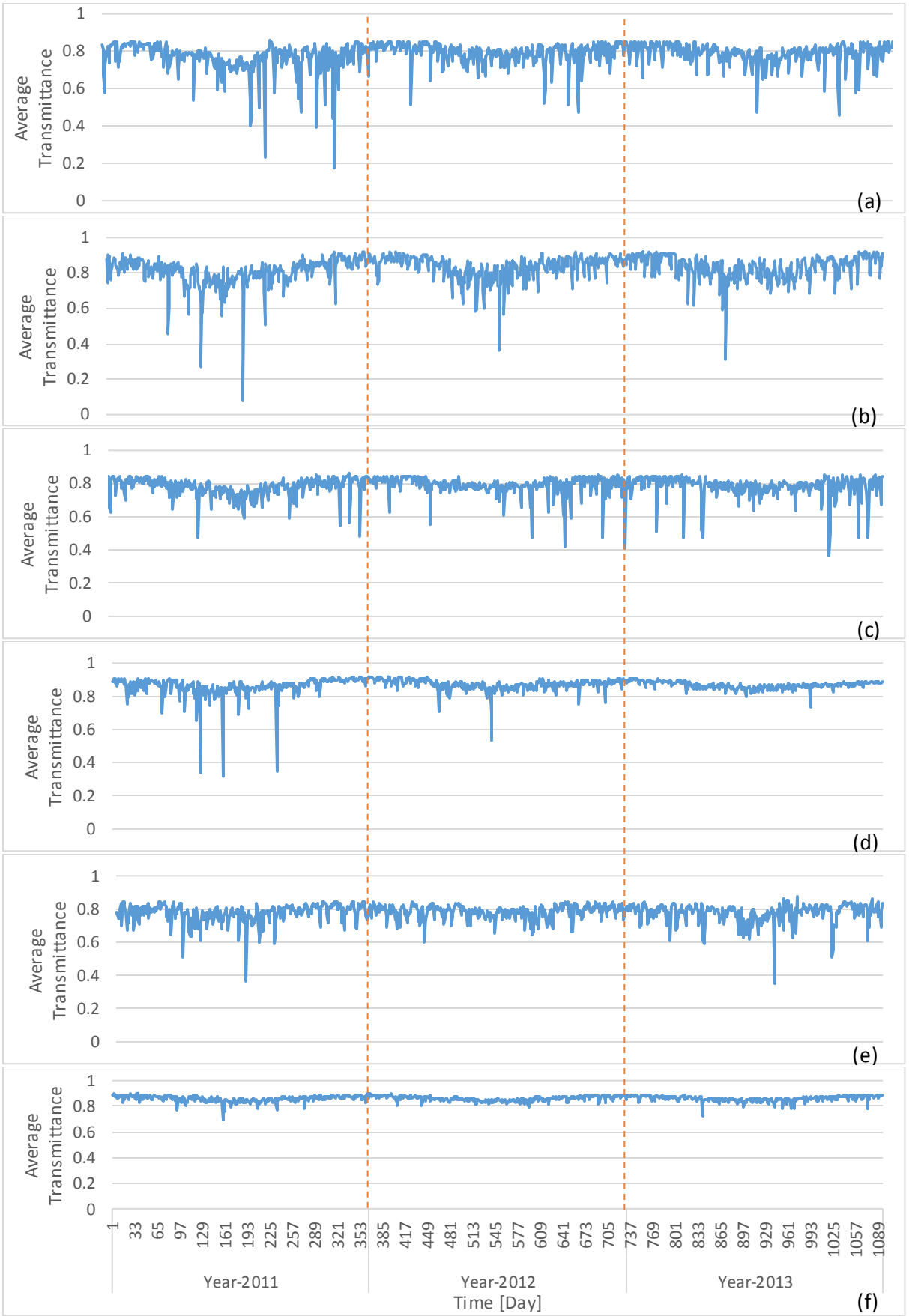

Figure 4.7: Typical time series display of the average transmittance at optical link distance of 1.5 km and wavelength of 850 nm over the years 2011-2013 for (a) Durban; (b) Cape Town; (c) Umtata; (d) Bloemfontein; (e) Johannesburg; (f) Mafikeng.

4.6 Specific Optical Attenuation Estimation

4.6.1 Overview of Various Atmospheric Attenuation Models

An alternative way to predict the atmospheric attenuation apart from computing the attenuation in case of particle droplets based on Mie-scattering theory, is to use the visibility data of a particular location. The Mie-scattering approach is the most accurate way to compute the atmospheric attenuation, but it involves complex calculation and the detailed information of the particle parameters such as particle size, particle mass concentration, particle size distribution, refractive index, liquid water content, etc., are often not readily available at a specific site of installation. As earlier discussed, the Kruse, Kim, ITU-R and Al Naboulsi (either Advection fog or Radiation fog) models are among the several empirical models used for empirically predicting the specific attenuation using visibility range estimate. The lower visibility range conditions primarily as a result of fog, haze, snow, rain and clouds are quite present in the troposphere and they are the predominant weather phenomena that contributes immensely to optical attenuation in FSO communication system. The effects of the optical attenuations due to fog and haze, snow and rain can be estimated using various empirical models. The visibility range estimate of a location can be used to predict the fog, haze or cloud attenuations by considering either a 2 % or 5 % transmission threshold (τ_{TH}) over the free space atmospheric path. The Kim's model approximations of the q parameter can be used in the case of foggy or clear weather with no snow or rain [21, 22, 97, 196-200].

Atmospheric attenuation can be described as the process that occurs within the free space medium whereby some or all the energy of a propagating Electromagnetic (EM) wave is lost in the atmosphere. Therefore, in FSO link the transmitted optical signal attenuates or deteriorates through several ways, such as absorption, scattering and scintillation. The Beer's law given in Equation (2.10) typically defines the atmospheric attenuation (τ) as follows [95-97]:

$$\tau(\lambda, L) = \exp(-\beta(\lambda)L), \tag{4.2}$$

where L denotes the optical link distance (in km) between the telescope and photodetector and β represents the total extinction coefficient per unit length. This total extinction coefficient which basically denotes the attenuation of the light waves, consists of both scattering and absorption terms and it is given as:

$$\beta(\lambda) = \beta_{abs}(\lambda) + \beta_{scat}(\lambda), \tag{4.3}$$

where β_{abs} denotes the total absorption coefficient which represents both the molecular and aerosol absorption at a specific wavelength (λ) and β_{scat} denotes the total scattering coefficient which represents both the molecular and aerosol scattering at a specific wavelength (λ). However, the value of the parameter β_{abs} is considered as insignificant and thus it is negligible. Therefore, the total

attenuation coefficient or total extinction coefficient mainly depends on the scattering loss which is the predominant process for optical attenuation, since the molecular and aerosol absorption coefficients are small.

4.6.2 Fog Attenuation Prediction Models

The various optical attenuation models predicting specific attenuations in terms of visibility, were developed as a result of the complexity involved in Mie-scattering theory and the lack of sufficiently comprehensive information at every installation site. These models are experimentally derived and can estimate to a great extent or minimum error the specific attenuation in terms of the visibility. According to the Beer-Lambert theory, a few models have been suggested for fog attenuation prediction for any optical wavelength. A summary of the some of the most common fog empirical models are presented in Table 4.3. The key reported fog attenuation prediction models in the literature are outlined as follows:

4.6.2.1 Kruse Model

From the Koschmeider law, Kruse proposed a slight variation which resulted into the inclusion of the effect of particles at optical wavelengths other than 550 nm. It estimates the specific attenuation within the visible and N-IR spectrum. Therefore, the modified attenuation model according to Kruse which is the original empirical model that estimates attenuation due to fog is given as [96, 97, 191, 195-200]:

$$A = \frac{17}{V}\left(\frac{\lambda}{0.55}\right)^{-q}, dB/km \tag{4.4}$$

where V stands as earlier discussed and λ represents the light wavelength measured in μm. The coefficient q in the altered expression was estimated from experimented data [191] and given by:

$$q(V) = \begin{cases} 1.6, & V > 50\ km \\ 1.3, & 6\ km < V < 50\ km \\ 0.585V^{1/3}, & V < 6\ km. \end{cases} \tag{4.5}$$

Since this model was originally proposed for haze particles with particle structure quite different from that of fog and the wavelengths of the visible and IR bands, therefore the validity of this model for visibilities lower than 1 km was in doubt.

4.6.2.2 Kim Model

An investigation into the validity of the Kruse model brought about a proposed adjustment by Kim for visibilities lower than 500 m [95]. In 2001, according to the calculations of the Mie scattering theory, the proposed specific fog attenuation prediction model by Kim considered the losses due to fog for visibilities less than 500 m as wavelength independent. Therefore, based on this investigation, Kim modified the original coefficient q given in the Kruse model as follows [95-97, 191, 195-200]:

$$q(V) = \begin{cases} 1.6, & V > 50\ km \\ 1.3, & 6\ km < V < 50\ km \\ 0.16V + 0.34 & 1\ km < V < 6\ km \\ V - 0.5, & 0.5\ km < V < 1\ km \\ 0, & V < 0.5\ km. \end{cases} \quad (4.6)$$

It was proposed in this model that the 550 nm and the 1550 nm will be attenuated at the same level for less than 0.5 km visibility range.

Table 4.3: Summary of the common fog attenuation empirical models.

Model	Formula
Kruse [191]	$A = \frac{17}{V}\left(\frac{\lambda}{0.55}\right)^{-q}$, $q(V) = \begin{cases} 1.6, & V > 50\ km \\ 1.3, & 6\ km < V < 50\ km \\ 0.585V^{1/3}, & V < 6\ km. \end{cases}$
Kim [95]	$A = \frac{17}{V}\left(\frac{\lambda}{0.55}\right)^{-q}$, $q(V) = \begin{cases} 1.6, & V > 50\ km \\ 1.3, & 6\ km < V < 50\ km \\ 0.16V + 0.34 & 1\ km < V < 6\ km \\ V - 0.5, & 0.5\ km < V < 1\ km \\ 0, & V < 0.5\ km. \end{cases}$
Al-Naboulsi (Advection) [201, 198]	$A_{adv} = 4.343\left(\frac{0.11478\lambda + 3.8367}{V}\right)$
Al-Naboulsi (Convection/Radiation) [201, 198]	$A_{conv} = 4.343\left(\frac{0.18126\lambda^2 + 0.13709\lambda + 3.7502}{V}\right)$
ITU-R [202]	$A = \frac{10\ln(e)}{V} = \frac{17}{V}$, where $e = 0.02$
Ijaz [97]	$A = \frac{17}{V}\left(\frac{\lambda}{0.55}\right)^{-q(\lambda)}$, $q(\lambda) = 0.1428\lambda - 0.0947$

4.6.3 Optical Attenuation Estimation and Comparison of Various Optical Attenuation Models

The specific attenuation of an optical signal propagating through the atmosphere can be estimated for the design of an optical link, if the visibility data for the given location is available. The daily mean of the visibility range data for the six cities in this study across the three successive years have been used for the estimation of the daily mean atmospheric attenuation by substituting the visibility data into the attenuation models listed above. The statistical description for the daily data of the mean attenuation covering the three successive years and for all the six cities considered in this study are provided in Appendix I. In this work, the Kruse, Kim, ITU-R and Al Naboulsi (Advection fog and Radiation fog) models have been briefly compared and analysed for a better understanding. These atmospheric attenuation models are mostly wavelength dependent.

Figures 4.8 (a-f) show the comparison of different attenuation models from the visibility data for each of the locations for the entire period (2011-2013) under study. The daily mean specific attenuation was estimated at both 850 nm and 1550 nm optical wavelengths under different atmospheric conditions and geographical locations (which consist of the coastal, near-coastal and non-coastal environments). These estimated daily values of the specific attenuation were used to show the comparison between the various attenuation models earlier mentioned, and at the same time to show the differences in the optical

attenuation obtained at different cities considered in this work. The plots of the specific attenuation against the visibility have the same pattern across all the locations. It can also be confirmed that transmitting at a higher optical wavelength such as $1550\ nm$ is quite advantageous to FSO than using the lower wavelengths like $850\ nm$, because its attenuation is lesser than that of the shorter wavelength as expected. For instance, Figure 4.8b shows that at $V = 1.75\ km$, the mean specific attenuation using $1550\ nm$ is $2.3\ dB$ better than using $850\ nm$ transmitter. It can as well be noticed that as the atmosphere gets clearer (i.e., from 'clear' to 'very clear' air conditions), the performance of both types of transmitters gets closer. The results obtained in Figure 4.8 reveals that the optical signals with longer wavelength are less attenuated by atmospheric conditions. Thus, in order to compensate for the high-power loss during FSO transmission, the optical wavelength with $1550\ nm$ is preferred for FSO systems. Also, it was observed as expected that the Kruse and Kim models have the same estimated extinction coefficient for visibility greater than $6\ km$, and different extinction coefficient for visibility lower than $6\ km$, which is as a result of the modification of q parameter made by Kim. Across all the regions (either coastal or non-coastal), the ITU-R model is observed to be quite close to both the Al Naboulsi advection model and Al Naboulsi radiation model. It can also be observed from the results that maximum daily mean specific attenuation is highest in Cape Town and lowest in Mafikeng.

To avoid bulky discussions, the following analysis and observations are based on the findings of only the Kim model at optical wavelength of 850 nm. Figure 4.8a shows the plot of the estimated daily mean specific attenuation over the daily visibility for the city of Durban for the entire period. Based on these results, it was observed that the lowest and highest estimated daily mean specific attenuation at this coastal location is approximately $0.44\ dB/km$ and $5.04\ dB/km$ respectively (corresponding to the daily visibility of about $21.88\ km$ and $2.45\ km$). This location did not have several daily mean visibility values in the range of Class 7 (that is, the 'very clear' air condition), but it has more within the Class 4 to Class 6 range (that is, within the 'haze' and the 'clear' air conditions). However, its maximum daily mean visibility slightly passes the boundary of the 'very clear' air visibility class. Another maritime environment that exhibits much higher daily mean specific attenuations than Durban is the city of Cape Town (as shown in Figure 4.8b). The estimated daily mean specific attenuation for Cape Town ranges from $0.24\ dB/km$ to as high as $7.41\ dB/km$ over the entire period of study, when an optical signal with operating optical wavelength of 850 nm is transmitted through its atmosphere. The results from Figure 4.8b shows that some days within the entire period have daily mean visibility values as low as $1.75\ km$ and reaches as high as $40\ km$, which are classified as 'Thin fog' and 'very clear sky' respectively. Also, it can be said that this region has occurrences of atmospheric fog conditions and it consists of several periods of very clear sky conditions. This shows that on the average there is dominance of fog events at certain periods and also dominance of very clear air conditions at other periods. These results therefore suggest that the weather condition (in terms of visibility) of Cape Town can be described as an extreme condition due to the fact that the obtained minimum and maximum daily

mean specific attenuations are respectively the lowest and highest attenuation values among all the cities considered in this study. Another reason among others, why this region display so much extreme values in its daily mean visibility is as result of the fact that in the 3-hour measurement interval data collected, the visibility estimates have several events of lower visibility values within the Lower Visibility Class (LVC) and several events in the Higher Visibility Class (HVC). Thus, these effects contribute mainly to the extreme pattern that it exhibits, which is also believed to be as a result of its very cold winter and mildly hot summer periods. The city of Umtata, which is classified as a near-coastal environment, have most of its lower and higher daily visibility values (as shown in Figure 4.8c) within the upper boundary of the mid-class visibility range (MVC) and lower boundary of the HVC, that is majority of the values fall between Class 5 and Class 6. Its lowest and highest daily mean specific attenuation values were observed to be approximately 0.43 dB/km and 2.92 dB/km respectively, obtained from corresponding visibility values of 22.5 km and 3.84 km. This shows that within this period, it did not have low visibility values like that of the other coastal regions and high visibility values like that of the non-coastal regions, especially like that of Bloemfontein and Mafikeng. While the atmosphere of the non-coastal areas such as Bloemfontein and Mafikeng (as shown in Figures 4.8d and 4.8f respectively) exhibit high daily average visibility values resulting into very low daily mean specific attenuation values of about 0.25 dB/km and 0.30 dB/km (corresponding to visibility of 38.8 km and 31.9 km) respectively, when an optical signal of 850 nm is transmitted through them. On the other hand, their peak daily mean specific attenuation values could be as low as 3.32 dB/km and 1.06 dB/km respectively, due to more occurrences of 'very clear air' conditions than any other visibility class. Whereas, Johannesburg (as shown in Figure 4.8e) which is also a non-coastal area, had its lowest and peak daily visibility values within the boundary of the mid-class visibility range. At an operating wavelength of 850 nm, its lowest and highest daily mean specific attenuation values were observed to be approximately 0.39 dB/km and 3.03 dB/km respectively, obtained from corresponding visibility values of 24.94 km and 3.73 km. The results show that most of its daily mean values fall between Class 4 and Class 6, unlike the other non-coastal areas that covers deep into the higher class of visibility range.

In general, based on the daily mean specific attenuation and visibility values, the maritime locations (especially Cape Town and Durban) show characteristics of an atmosphere with higher risk to transmission of optical signals than the non-coastal environs during the entire period under study. Also, Umtata, Bloemfontein and Johannesburg showed considerable qualities of an atmosphere that can cause moderately high risk to FSO in the same period. However, the lowest risk to FSO transmission system within this period was observed in Mafikeng.

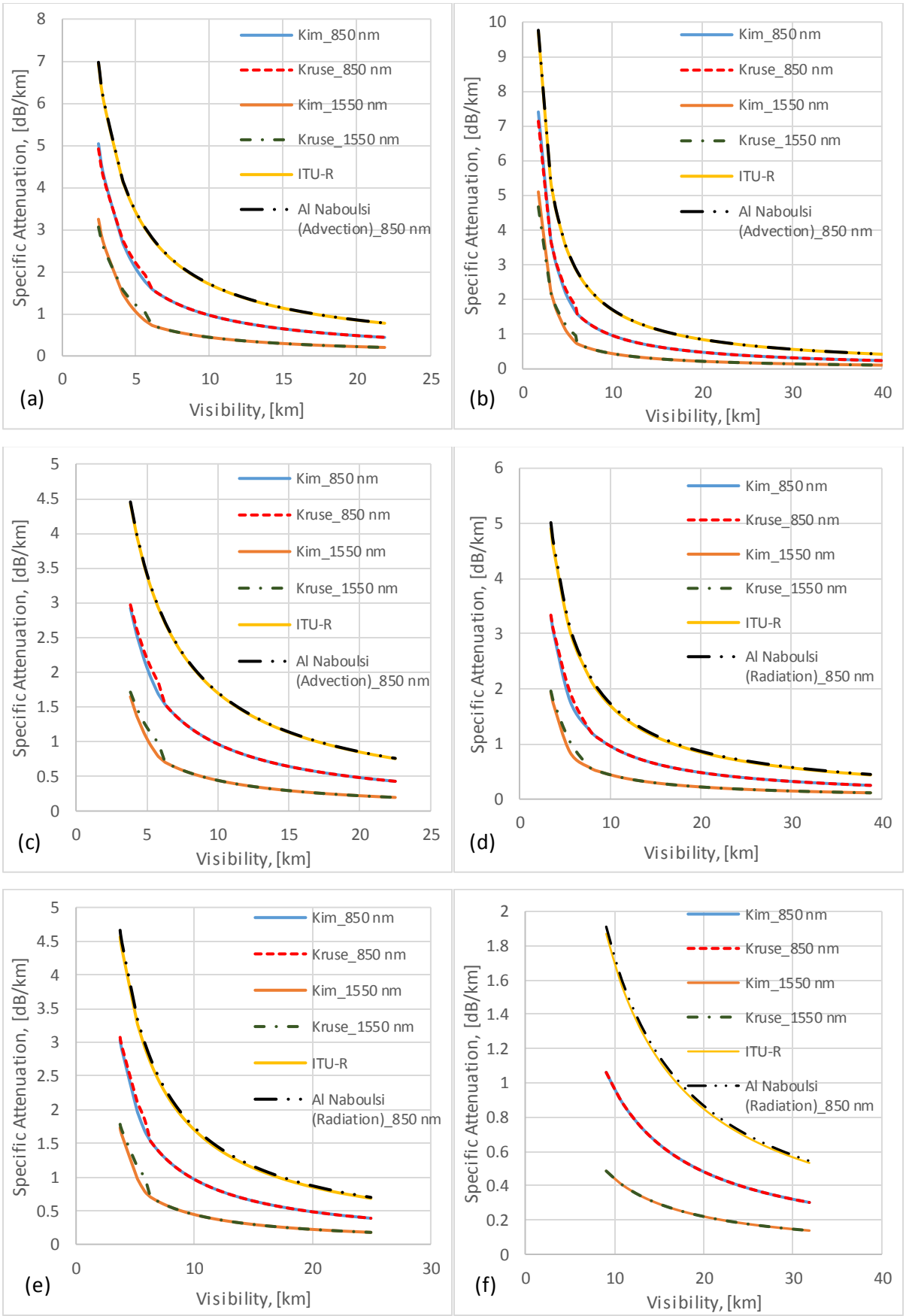

Figure 4.8: Comparison of various models using the estimated daily mean specific attenuation over visibility for the entire period (2011-2013) under study for (a) Durban; (b) Cape Town; (c) Umtata; (d) Bloemfontein; (e) Johannesburg; (f) Mafikeng.

4.6.4 Time Series Analysis of Specific Attenuation

4.6.4.1 Daily Mean Specific Attenuation

The effects of the daily mean visibility on FSO system over time was computed using the Kim model at 2 % transmittance threshold to obtain the time series profile of the predicted daily mean specific attenuation. The daily mean visibility data used is based on the average of the three-hour interval resolution of the collected visibility data. This estimated daily mean specific attenuation at wavelength of 850 nm for each of the six locations for three successive years were obtained as a function of the various daily mean visibility impairments, which is due to the particle mass concentration and different atmospheric conditions. The time series profile of this predicted daily mean specific attenuation for all the locations and for the three years (2011 – 2013) are presented in Figures 4.9 to 4.14. The statistical description of the daily mean specific attenuation provided in Appendix I gives an overview of the average, deviation and distribution of the estimated specific attenuation.

The results in Figure 4.9 for Durban shows that the highest mean specific attenuations expected in a day are 5.04 dB/km, 2.18 dB/km and 2.25 dB/km for 2011, 2012 and 2013 respectively. For Cape Town, Figure 4.10 reveals that the highest mean specific attenuations expected in a day can be as high as 7.41 dB/km, 2.97 dB/km and 3.40 dB/km for 2011, 2012 and 2013 respectively. Figure 4.11 provides the results for Umtata, where the maximum expected daily mean specific attenuations are 2.18 dB/km, 2.52 dB/km and 2.92 dB/km for 2011, 2012 and 2013 respectively. For the non-coastal cities such as Bloemfontein, the results from Figure 4.12 shows that the estimated daily maximum specific attenuations are 3.32 dB/km, 1.78 dB/km and 0.90 dB/km for 2011, 2012 and 2013 respectively. Also, the results presented in Figure 4.13 for Johannesburg reveals that maximum mean specific attenuations expected in a day are 2.89 dB/km, 1.48 dB/km and 3.03 dB/km for 2011, 2012 and 2013 respectively. For Mafikeng, Figure 4.14 reveals that the peak mean specific attenuations expected in a day can be as low as 1.06 dB/km, 0.69 dB/km and 0.91 dB/km for 2011, 2012 and 2013 respectively.

It was observed across the three years that there were certain instances (or years) where the estimated peak daily mean specific attenuations for some of the non-coastal areas (especially Bloemfontein and Johannesburg) were about as high or close to the attenuations obtained within the coastal areas. However, in general most of the daily values of the mean specific attenuation across the three years period for both Bloemfontein and Johannesburg were found to be quite low, with just few daily occasions having an attenuation value in the range of that of the coastal areas. This can be noticed in the case of Bloemfontein in 2011, and Johannesburg in 2011 and 2013, where only very few days or data points had specific attenuations higher than 1.50 dB/km, while majority of the data points were below 1.00 dB/km. Whereas, all through the period under study, the daily mean specific attenuations observed in Mafikeng were far lower than those obtained in the coastal areas and even to the other non-

coastal areas, they were in the range of $\approx 1.00\, dB/km$ or lower. This shows how mild the effects of the atmosphere within this non-coastal location(s) can be over transmission of light signals for communication. That is, the frequency of very high daily specific attenuations experienced or expected over the optical link within the non-coastal areas is much less than that obtained at the maritime areas. Secondly, in general, the values of the daily mean specific attenuation are relatively higher for the maritime locations than that estimated at non-coastal environments (except for very few cases of uniqueness which may be as a result of abnormality or outliers within the obtained visibility data).

Also, from these results, it can be said that the atmospheric conditions of the maritime environments contain lots of LC visibilities (that is, thick, moderate, light and thin fog conditions) more than those of the non-coastal areas. This variation in the frequencies of each visibility class for each location, can help to give adequate information about the rate of occurrence or density of each class within the atmosphere. Therefore, this can be used to decide on the implication of each location over the transmission of optical signal through the free space.

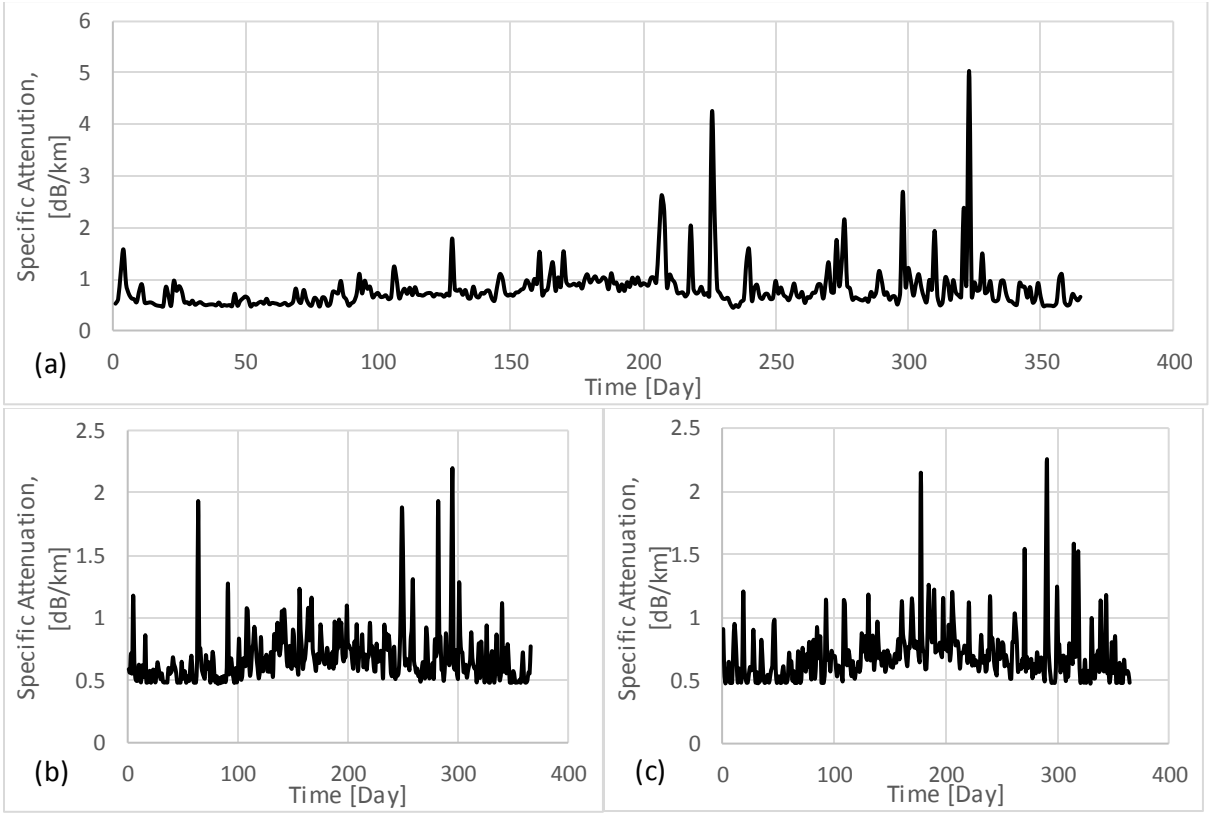

Figure 4.9: Typical time series display of the estimated daily average specific attenuation at 850 nm using Kim model at 2 % transmittance threshold for Durban over the years (a) 2011; (b) 2012 and (c) 2013.

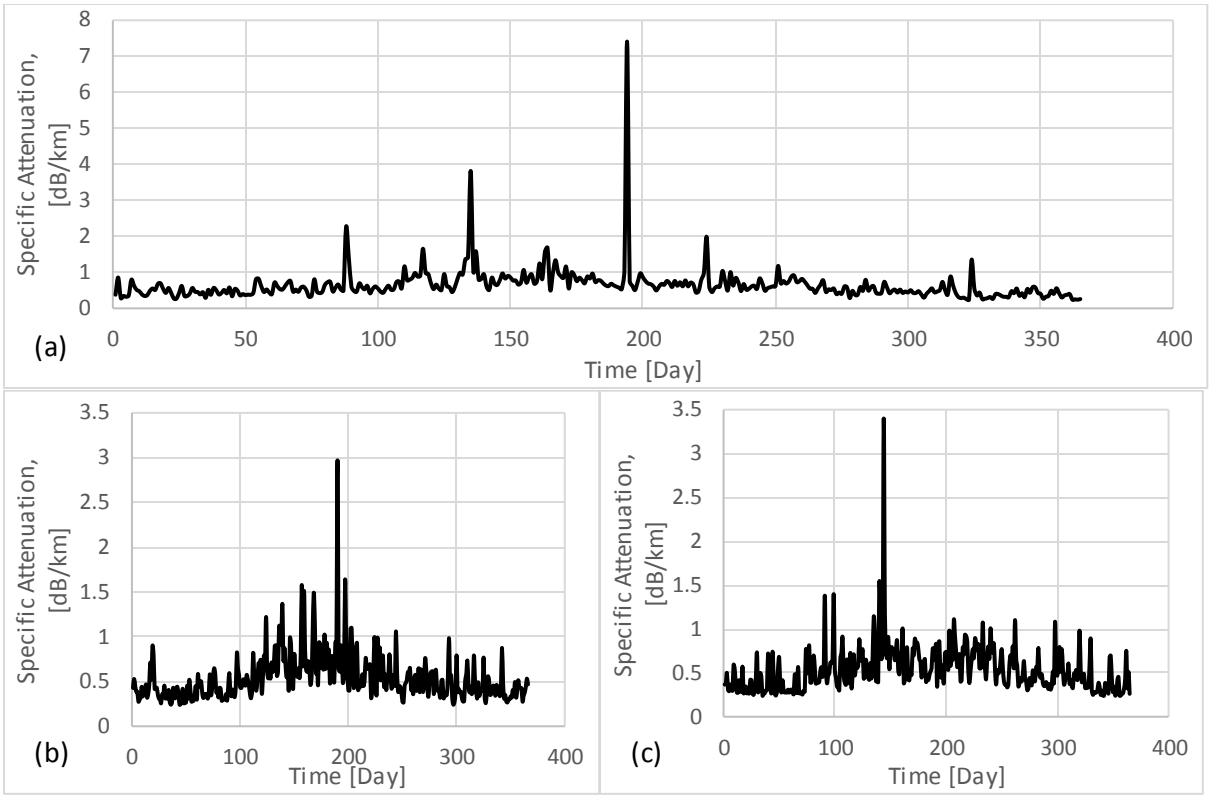

Figure 4.10: Typical time series display of the estimated daily average specific attenuation at 850 nm using Kim model at 2 % transmittance threshold for Cape Town over the years (a) 2011; (b) 2012 and (c) 2013.

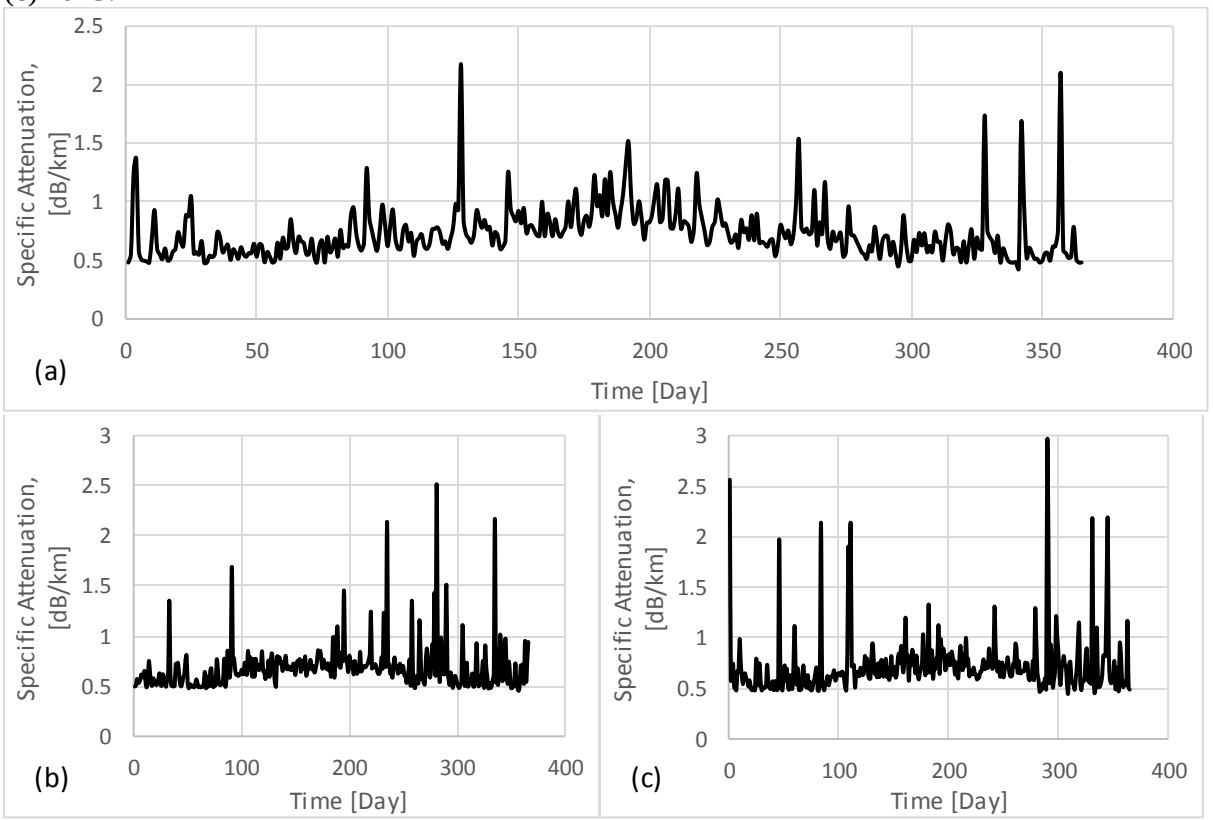

Figure 4.11: Typical time series display of the estimated daily average specific attenuation at 850 nm using Kim model at 2 % transmittance threshold for Umtata over the years (a) 2011; (b) 2012 and (c) 2013.

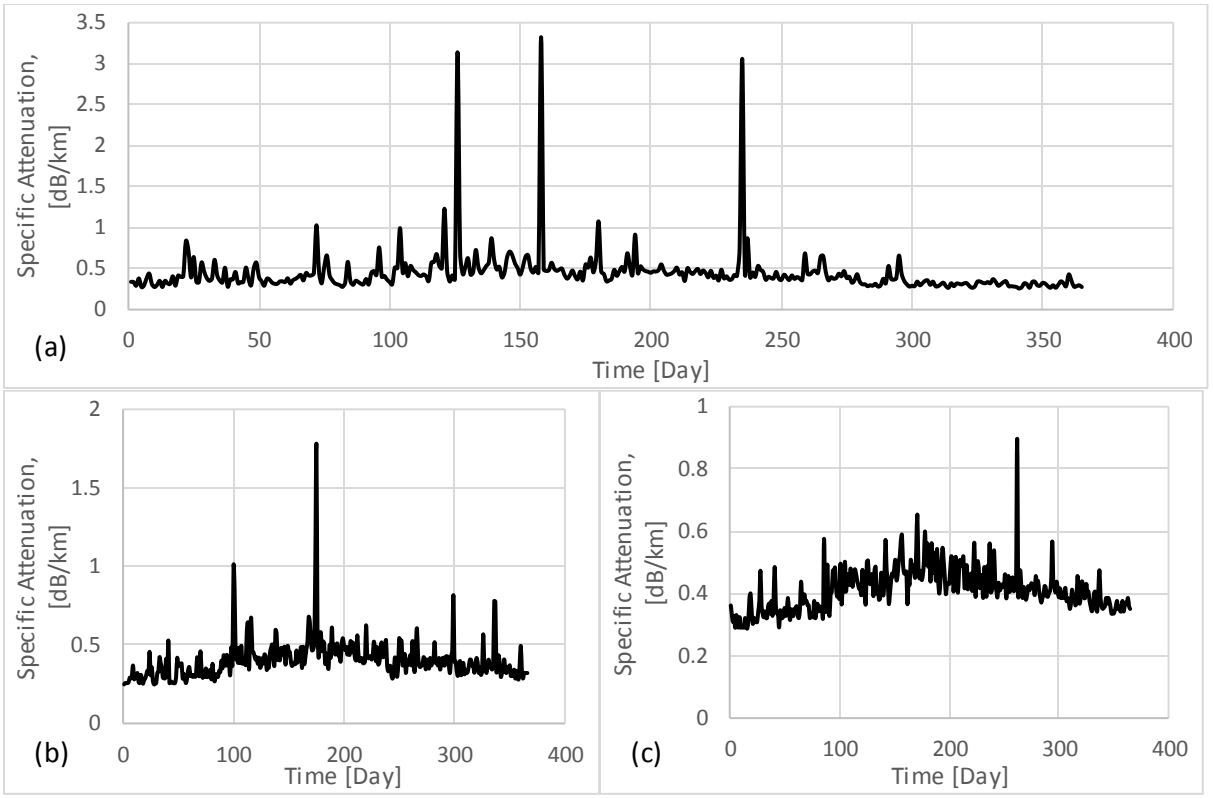

Figure 4.12: Typical time series display of the estimated daily average specific attenuation at 850 nm using Kim model at 2 % transmittance threshold for Bloemfontein over the years (a) 2011; (b) 2012 and (c) 2013.

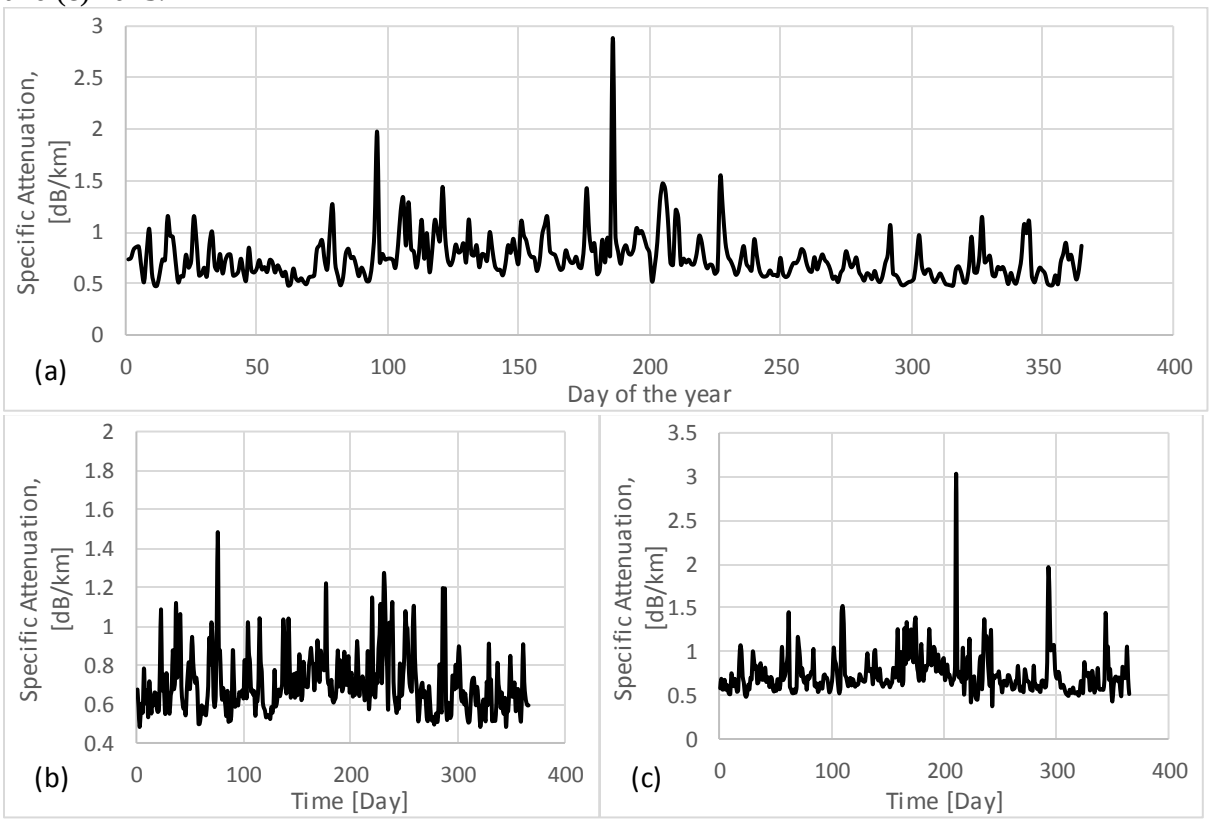

Figure 4.13: Typical time series display of the estimated daily average specific attenuation at 850 nm using Kim model at 2 % transmittance threshold for Johannesburg over the years (a) 2011; (b) 2012 and (c) 2013.

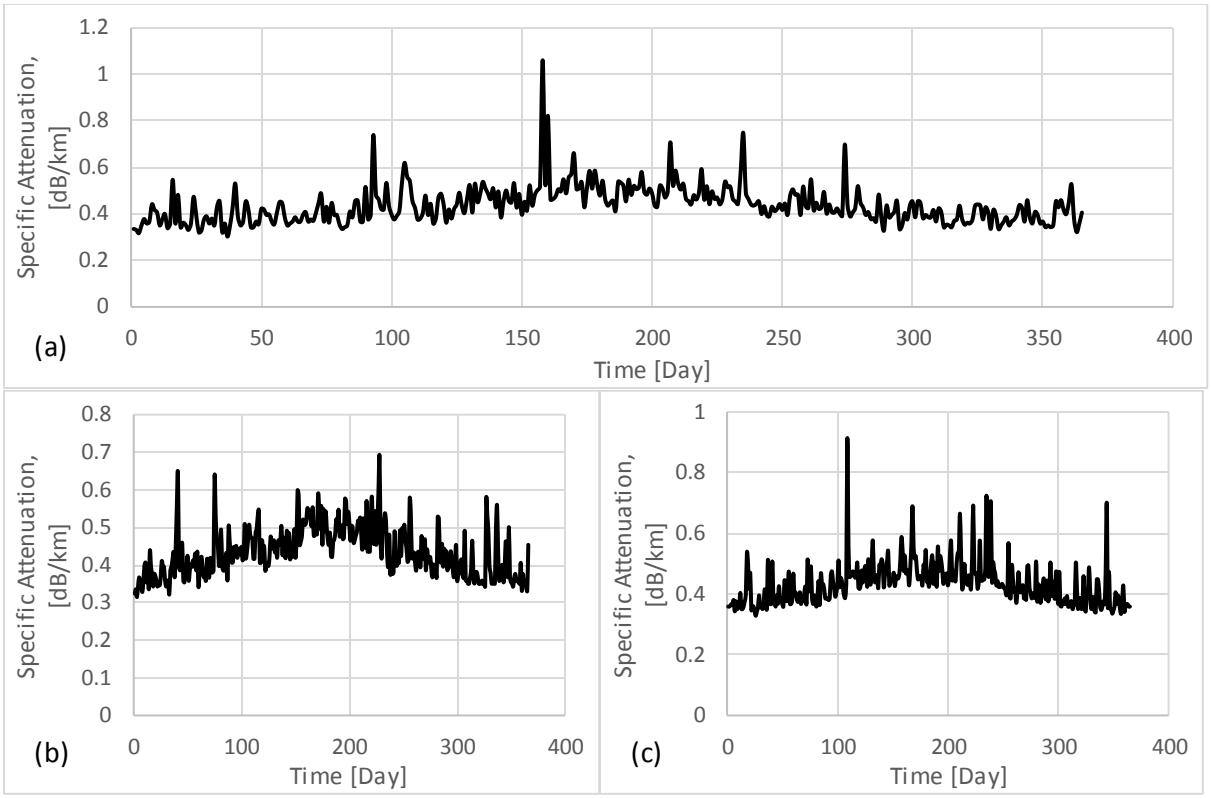

Figure 4.14: Typical time series display of the estimated daily average specific attenuation at 850 nm using Kim model at 2 % transmittance threshold for Mafikeng over the years (a) 2011; (b) 2012 and (c) 2013.

4.6.4.2 Influence of Low Visibility (Worst Case Conditions) over the FSO Link Design

The predicted specific attenuation obtained for the worst-case conditions has really shown how much effects should be expected on a regular basis and the extent at which the optical signals can be attenuated within each of the locations considered. This study can enable an adequate mitigation technique to be chosen for each location based on their environmental factors and optical attenuation trend. The descriptive statistics for the estimated specific attenuation (dB/km) data in synoptic interval scale over the entire period for all locations are presented in Table 4.4. This table gives a clear view of the worst case and mean attenuation of each location.

The time series profile of the predicted daily specific attenuations at worst case conditions (i.e., at the lowest daily visibility values) covering the three years (2011 – 2013) for all the locations in this study are presented in Figures 4.15 to 4.20. Figures 4.15 to 4.17 show the specific attenuation results over time for the maritime environments for the period of three years, and it can be established that within this period their maximum expected specific attenuation within a day reached as high as 169.81 dB/km (corresponding to 0.1 km visibility) at several occasions, except only at Durban in the year 2013 (shown in Figure 4.15c) where the maximum specific attenuation was 84.90 dB/km (corresponding to 0.2 km visibility). For the non-coastal regions (as shown in Figures 4.18 to 4.20), their maximum expected

specific attenuations within a day are quite lower than those of the coastal areas, except for Bloemfontein in the year 2011 (shown in Figure 4.18a) which had few days with 169.81 dB/km. Whereas, the maximum expected specific attenuations obtained at the worst cases of each day for Bloemfontein are 84.90 dB/km and 56.60 dB/km (corresponding to 0.2 km and 0.3 km visibility) in the years 2012 and 2013 respectively. Also, the results presented in Figure 4.19 for Johannesburg reveals that the maximum specific attenuations expected in a day corresponding to the lowest daily visibility values is 84.90 dB/km for all the three years. While, for Mafikeng, Figure 4.20 reveals that the peak specific attenuation expected in a day was as low as 27.10 dB/km for both 2011 and 2012, and 33.96 dB/km for 2013.

4.7 Estimation and Time Series Analysis of the Received Optical Power

4.7.1 Daily Mean Received Optical Power

The estimated daily mean received optical power was calculated from the daily mean optical attenuation obtained at wavelength of 850 nm and optical link distance of 1.5 km, for each of the six locations over the period under study. This received power is obtained indirectly as a function of the various daily mean visibility impairments, which is due to the particle mass concentration and different atmospheric conditions. The time series profile of this predicted daily mean received optical power for all the locations and for the three years (2011 – 2013) are presented in Figures 4.21 to 4.26. The estimated daily mean received optical power gives an overview of the average and distribution of the estimated power received at the photodetector.

The results in Figures 4.21 to 4.26 for Durban, Cape Town, Umtata, Bloemfontein, Johannesburg and Mafikeng show that the expected limits (in terms of minimum and maximum) of the daily mean received optical power ranges from approximately $-16.72\ dBm$ to $-23.01\ dBm$, $-16.51\ dBm$ to $-26.56\ dBm$, $-16.32\ dBm$ to $-19.83\ dBm$, $-16.15\ dBm$ to $-20.43\ dBm$, $-16.42\ dBm$ to $-20.00\ dBm$ and $-15.96\ dBm$ to $-17.04\ dBm$, corresponding to optical attenuations of approximately 0.75 dB to 7.56 dB, 0.54 dB to 11.11 dB, 0.68 dB to 4.38 dB, 0.44 dB to 4.98 dB, 0.69 dB to 4.55 dB and 0.51 dB to 1.59 dB respectively, across all the three years under study. It was observed from the time series analysis of the daily mean received optical power over the specified period of time that there are no instances of received optical power falling below the receiver sensitivity of $-38\ dB$ across all the locations. Based on the daily mean data and using the limit of the receiver sensitivity, this implies that there may not be optical link failures throughout the period of study. Also, it can be inferred that even at the coastal regions, there is no day that the transmission of optical signals through the atmosphere at wavelength of 850 nm and optical link distance of 1.5 km is under threat. However, it is believed that the conditions of the optical link will get worse as the distance increases (i.e., as $L \rightarrow \infty$), and therefore the received optical power will continue to drop and then the link may fail at some saturated point.

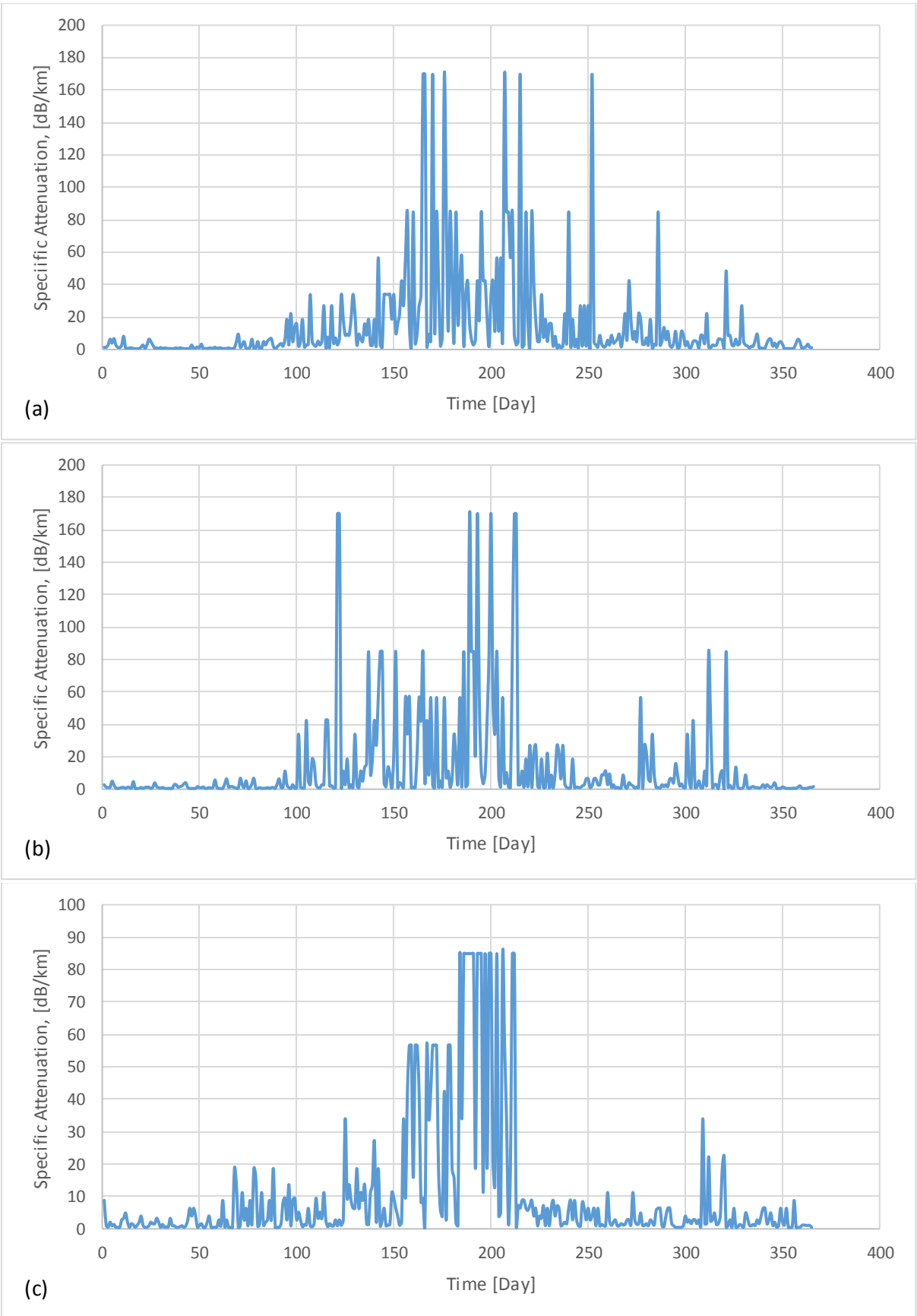

Figure 4.15: Typical time series display of the estimated specific attenuation at 850 nm using Kim model at 2 % transmittance threshold, at worst case conditions for Durban over the years (a) 2011; (b) 2012 and (c) 2013.

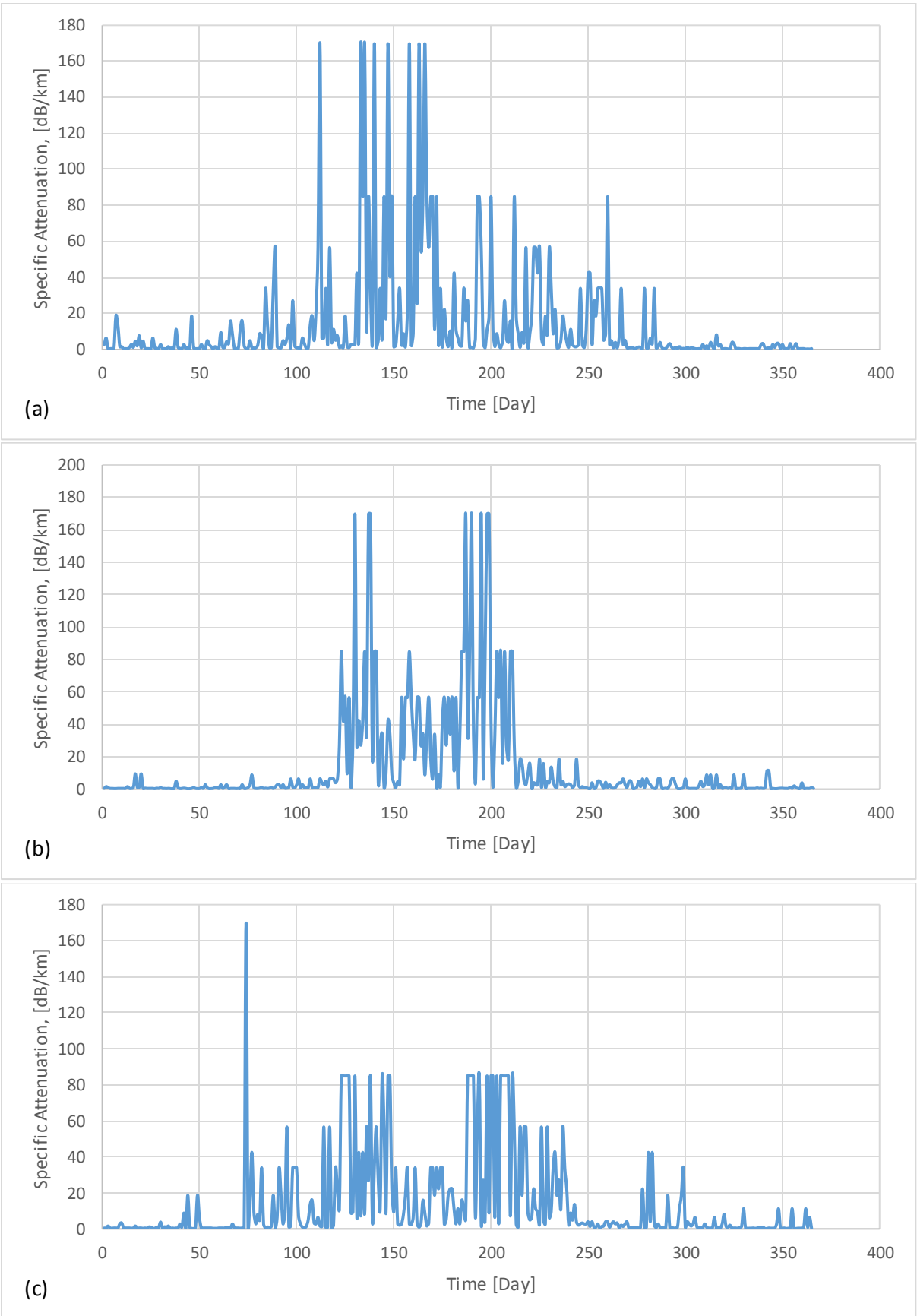

Figure 4.16: Typical time series display of the estimated specific attenuation at 850 nm using Kim model at 2 % transmittance threshold, at worst case conditions for Cape Town over the years (a) 2011; (b) 2012 and (c) 2013.

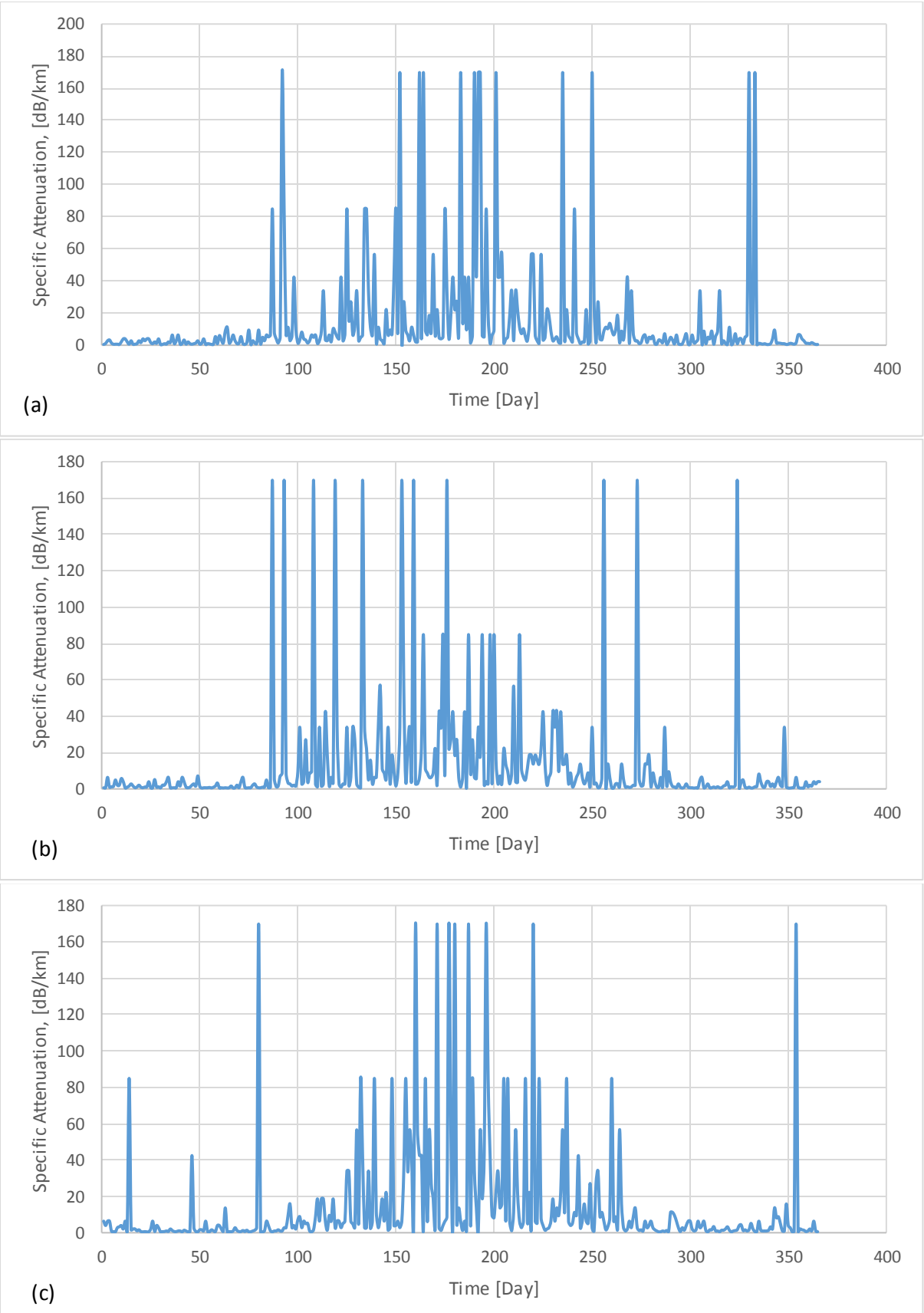

Figure 4.17: Typical time series display of the estimated specific attenuation at 850 nm using Kim model at 2 % transmittance threshold, at worst case conditions for Umtata over the years (a) 2011; (b) 2012 and (c) 2013.

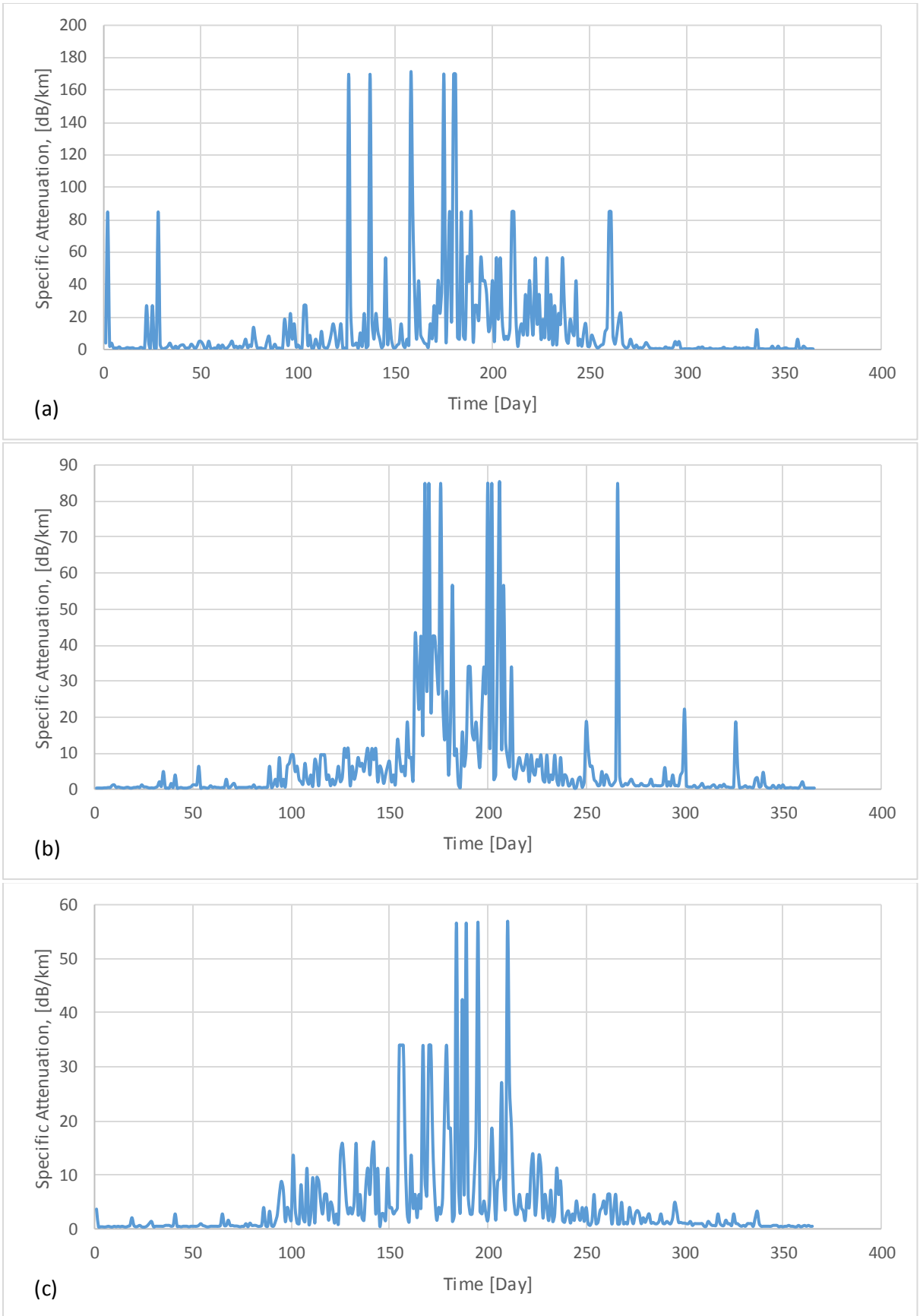

Figure 4.18: Typical time series display of the estimated specific attenuation at 850 nm using Kim model at 2 % transmittance threshold, at worst case conditions for Bloemfontein over the years (a) 2011; (b) 2012 and (c) 2013.

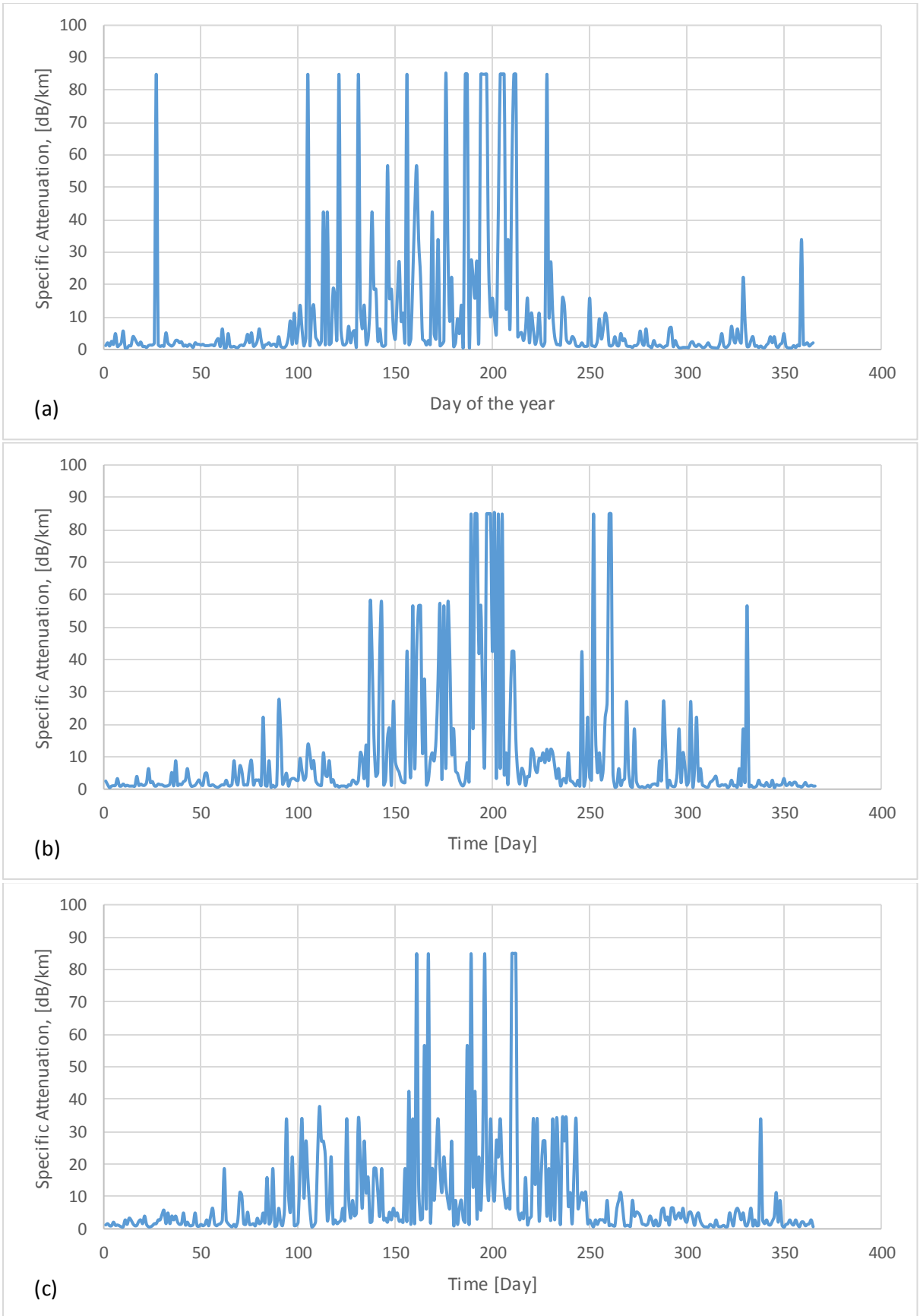

Figure 4.19: Typical time series display of the estimated specific attenuation at 850 nm using Kim model at 2 % transmittance threshold, at worst case conditions for Johannesburg over the years (a) 2011; (b) 2012 and (c) 2013.

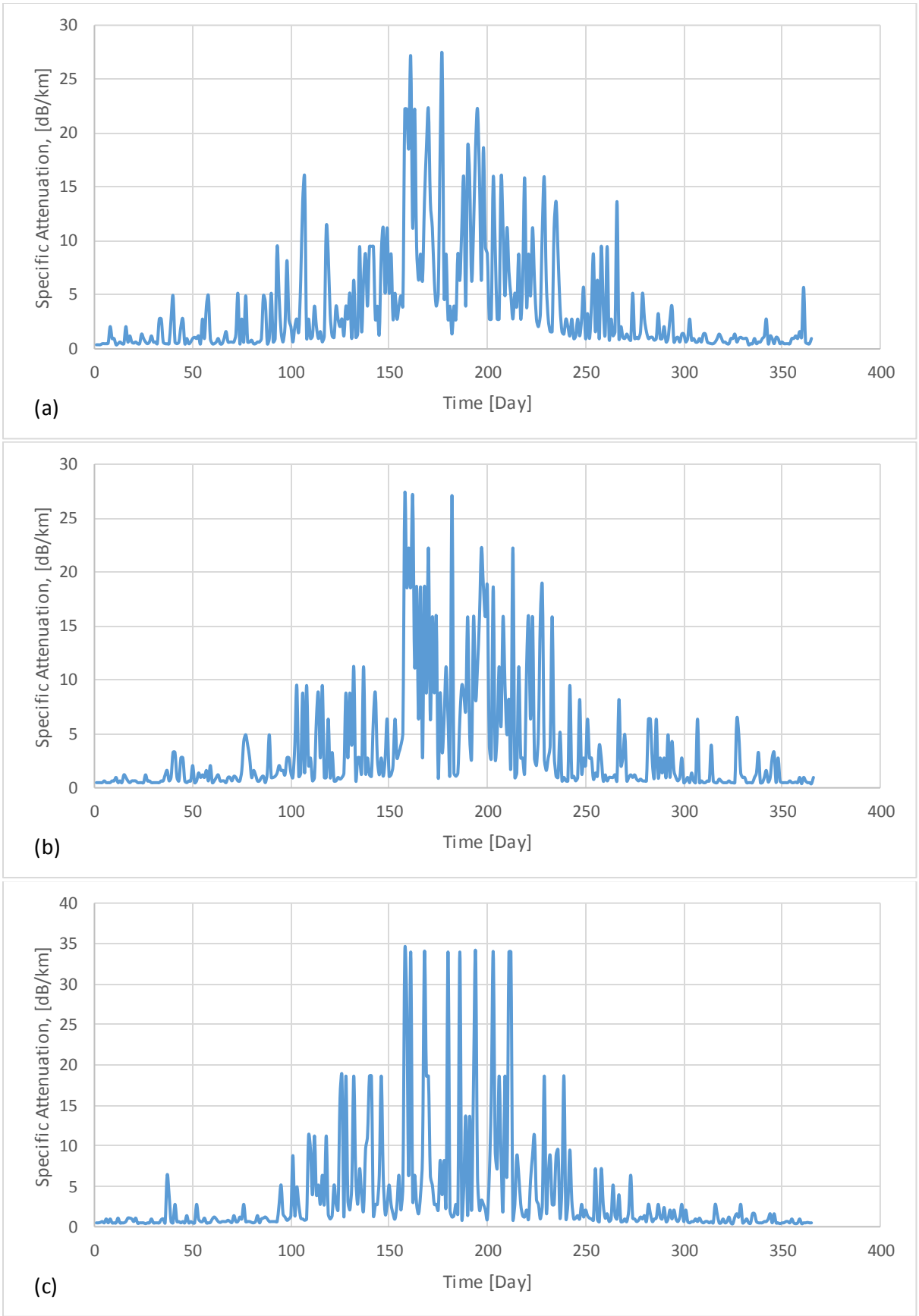

Figure 4.20: Typical time series display of the estimated specific attenuation at 850 nm using Kim model at 2 % transmittance threshold, at worst case conditions for Mafikeng over the years (a) 2011; (b) 2012 and (c) 2013.

Table 4.4: Descriptive statistics for the estimated specific attenuation (dB/km) data in synoptic interval scale over the entire period for all locations.

Summary Stat:2011-2013		***Durban***	***Cape Town***	***Umtata***	***Bloemfontein***	***Johannesburg***	***Mafikeng***
Descriptive Statistics							
Minimum	*Value (dB/km)*	0.32	0.17	0.32	0.14	0.24	0.24
	Atmospheric Condition	Very clear sky	Extremely clear sky	Very clear sky	Extremely clear sky	Very clear sky	Very clear sky
Maximum	*Value (dB/km)*	169.81	169.81	169.81	169.81	84.9	33.96
	Atmospheric Condition	Dense/Thick fog	Dense/Thick fog	Dense/Thick fog	Dense/Thick fog	Moderate fog	Light fog
Mode	*Value (dB/km)*	0.48	0.48	0.48	0.32	0.48	0.32
	Atmospheric Condition	Very clear sky	Very clear sky	Very clear sky	Very clear sky	Very clear sky	Very clear sky
Other Descriptive Statistics							
Mean		0.66	0.47	0.66	0.39	0.69	0.42
Range		0.32	0.19	0.32	0.14	0.24	0.24
Median		0.48	0.48	0.48	0.32	0.64	0.32
Standard Error		0.08	0.09	0.05	0.06	0.05	0.08
Standard Deviation		0.41	0.43	0.42	0.30	0.46	0.22
Sample Variance		0.17	0.19	0.18	0.09	0.21	0.05
Kurtosis		7.15	13.58	9.29	4.25	8.45	3.30
Skewness		4.61	4.37	2.05	2.03	3.94	2.34
Sum		2275.15	5725.27	2701.91	4636.85	3279.14	5938.64
Count		8768	8768	8768	8768	8768	8768

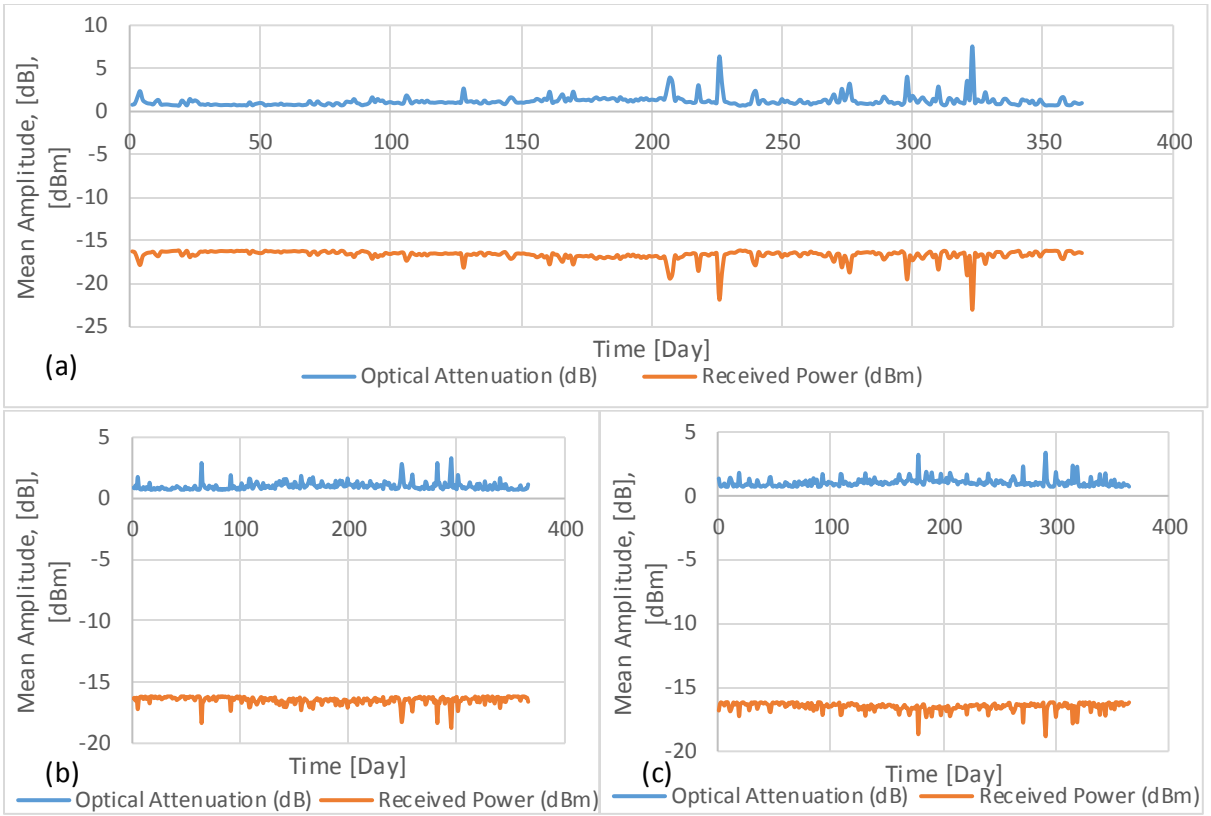

Figure 4.21: Typical time series display of the estimated daily mean optical attenuation and daily mean Received Power at an optical wavelength of 850 nm and optical link distance of 1.5 km for Durban over the years (a) 2011; (b) 2012 and (c) 2013.

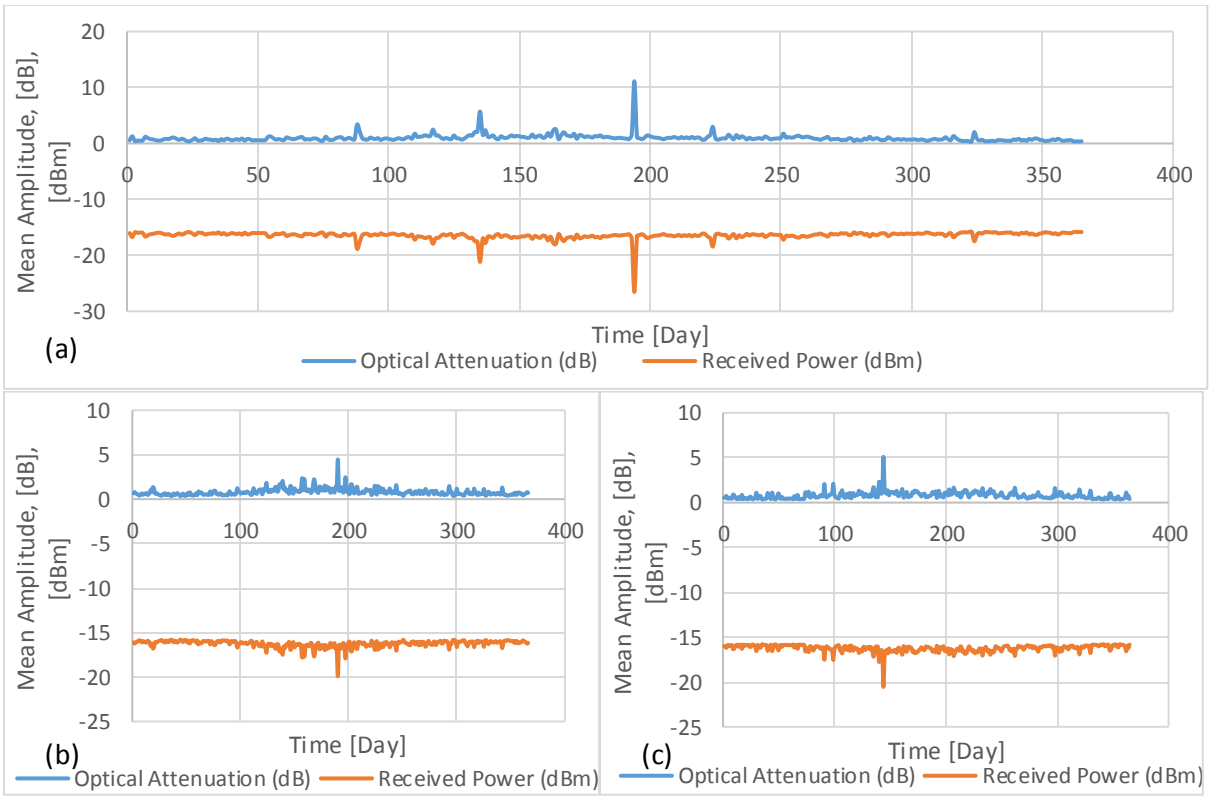

Figure 4.22: Typical time series display of the estimated daily mean optical attenuation and daily mean Received Power at an optical wavelength of 850 nm and optical link distance of 1.5 km for Cape Town over the years (a) 2011; (b) 2012 and (c) 2013.

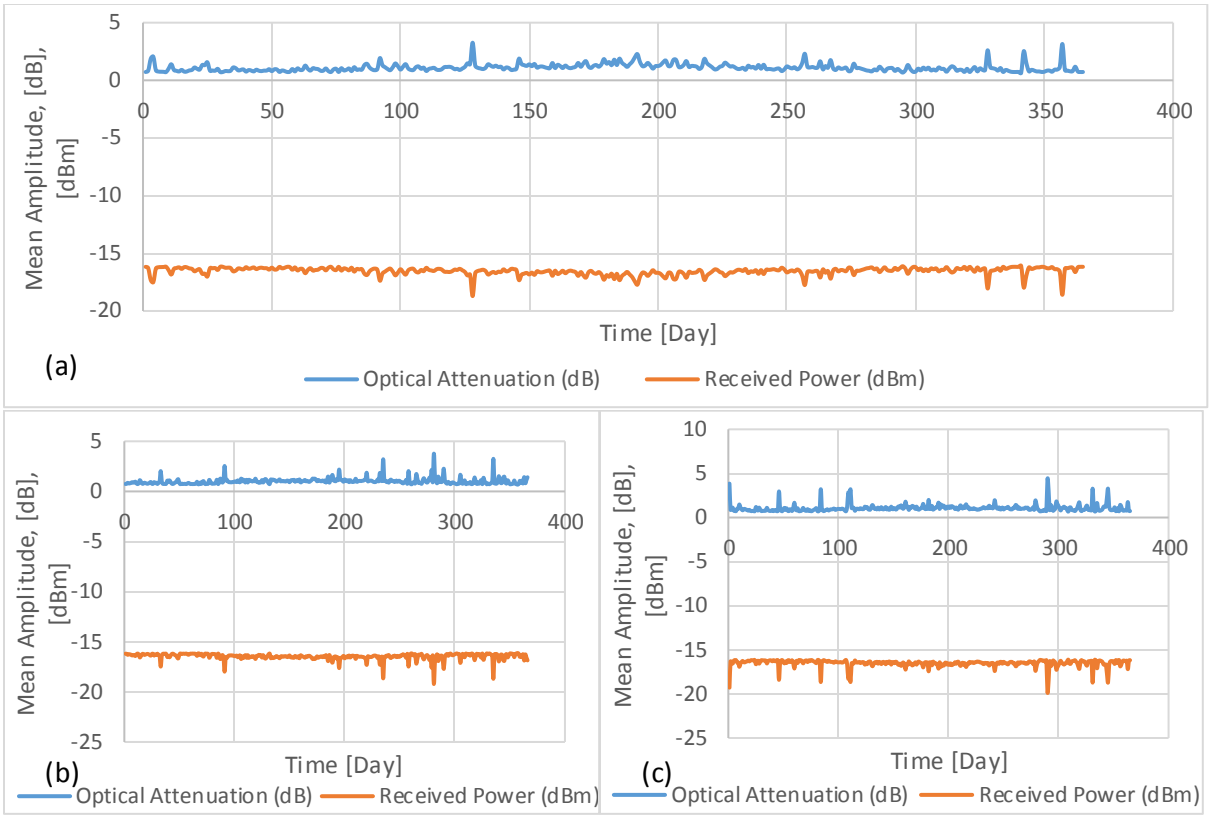

Figure 4.23: Typical time series display of the estimated daily mean optical attenuation and daily mean Received Power at an optical wavelength of 850 nm and optical link distance of 1.5 km for Umtata over the years (a) 2011; (b) 2012 and (c) 2013.

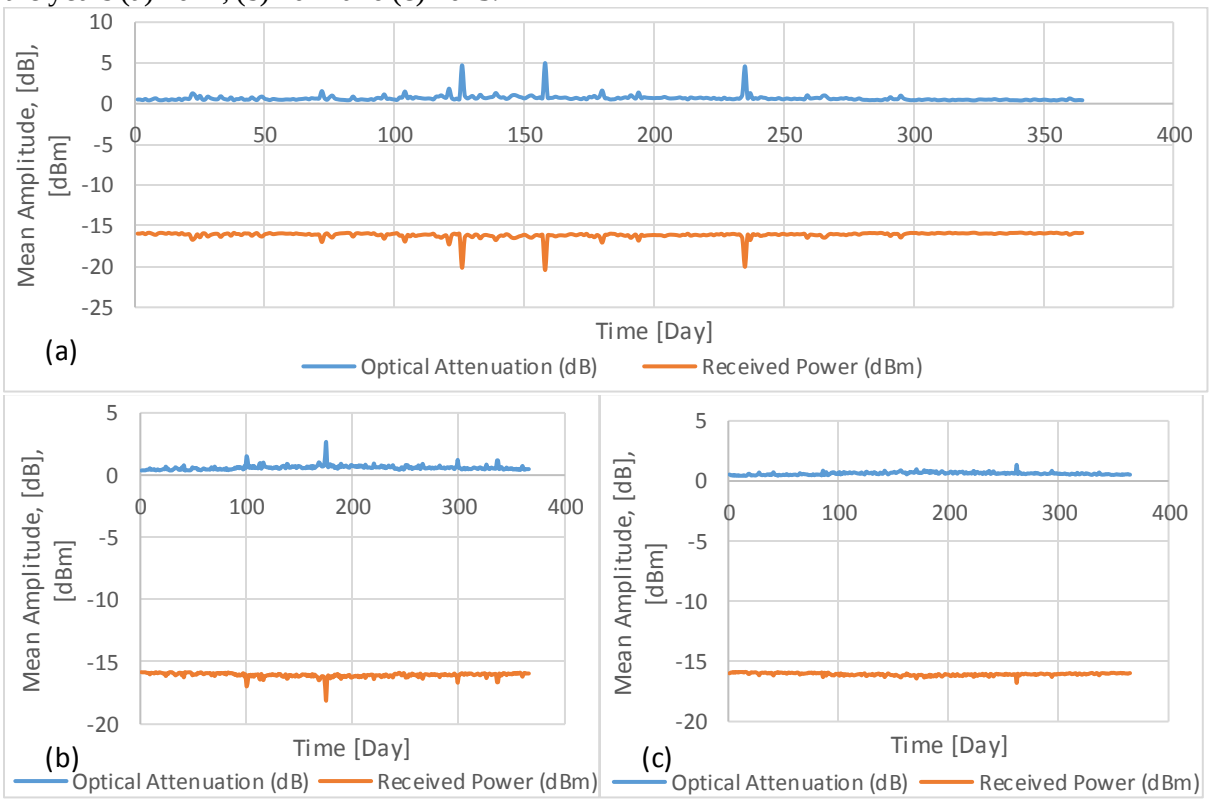

Figure 4.24: Typical time series display of the estimated daily mean optical attenuation and daily mean Received Power at an optical wavelength of 850 nm and optical link distance of 1.5 km for Bloemfontein over the years (a) 2011; (b) 2012 and (c) 2013.

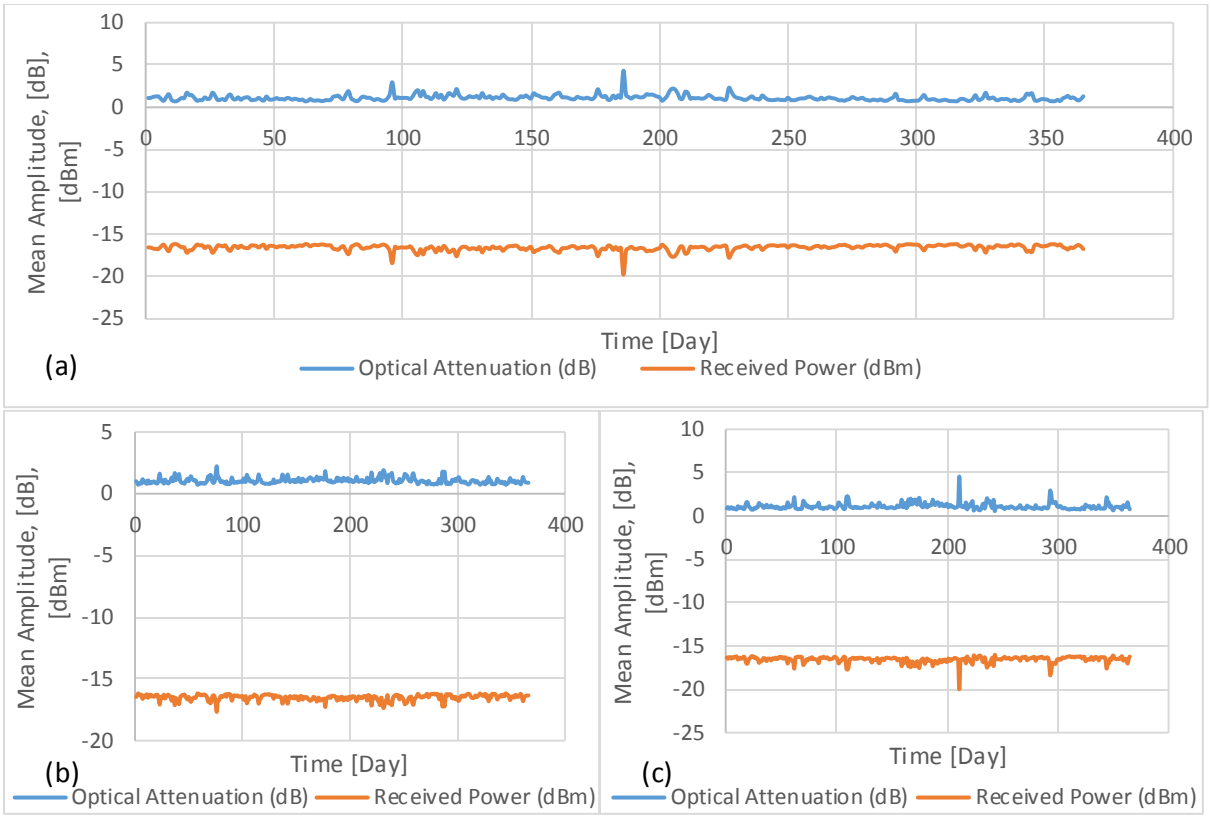

Figure 4.25: Typical time series display of the estimated daily mean optical attenuation and daily mean Received Power at an optical wavelength of 850 nm and optical link distance of 1.5 km for Johannesburg over the years (a) 2011; (b) 2012 and (c) 2013.

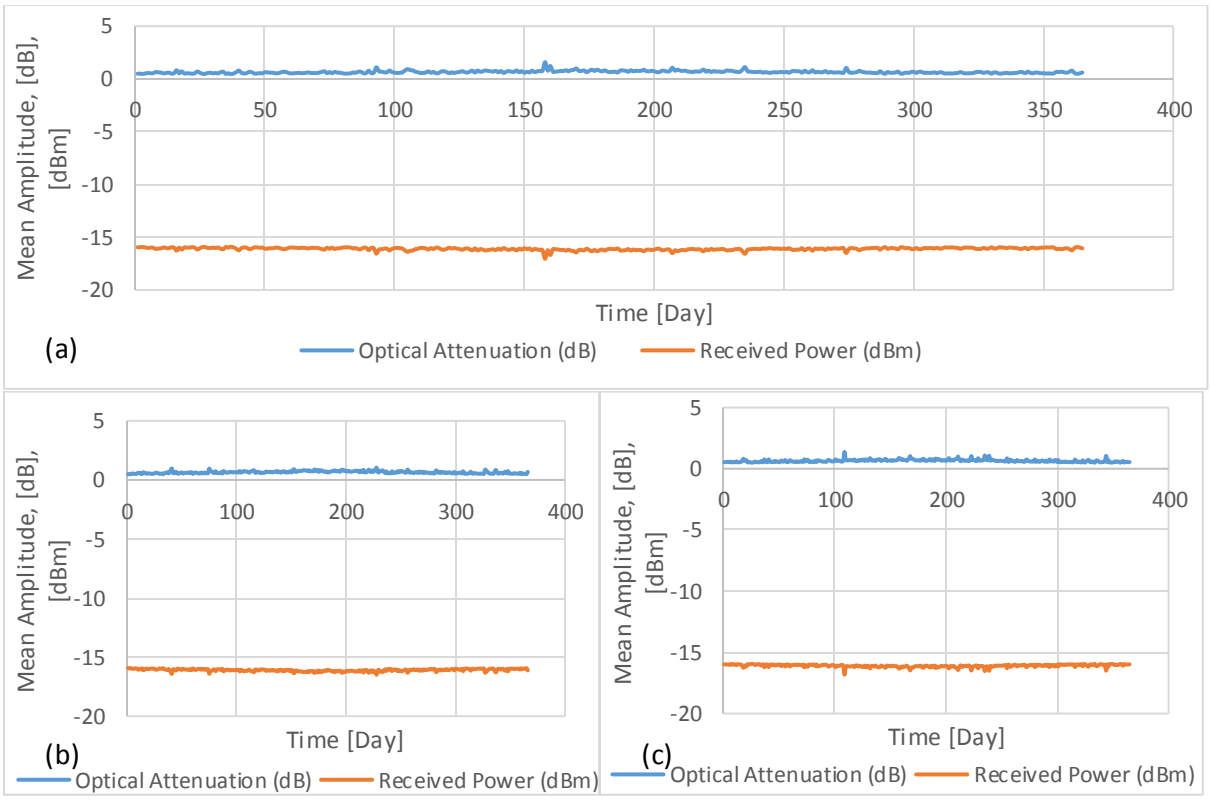

Figure 4.26: Typical time series display of the estimated daily mean optical attenuation and daily mean Received Power at an optical wavelength of 850 nm and optical link distance of 1.5 km for Mafikeng over the years (a) 2011; (b) 2012 and (c) 2013.

4.7.2 Impact of Low Visibility on the Received Optical Power over the FSO Link Design

The received optical power at the worst-case scenarios that involves the low visibility values was estimated for each of the locations using the optical attenuation at 1.5 km and operating wavelength of 850 nm. The receiver sensitivity of -38 dBm was used as a threshold to determine which points of interest would result into a link failure, due to the power limit of the specified receiver. This analysis was carried out using the daily minimum visibility values which can provide information on the daily status of the optical link. The time series analysis of the received optical power at the lowest daily visibility value over time were shown in Figures 4.27 to 4.32.

It was observed from the time series analysis of the received optical power over time that there are several instances of received optical power falling below the receiver sensitivity across all the locations and for the years under study. This implies, that there may be optical link failures at certain periods during each year and for each location. The results in this sub-section show that even at the non-coastal regions, there are periods that could pose a threat to the transmission of optical signals through the atmosphere within their vicinities at an operating wavelength of 850 nm and optical link distance of 1.5 km.

4.8 Atmospheric Stability Estimation from Optical Attenuation Observations

Before an FSO link can be deployed to a particular location, the effect of atmospheric stability needs to be examined. Based on the changes in specific attenuation, this work has been able to obtain the atmospheric stability, using the year 2011 as the case study. This is done to establish a maintainable FSO system. The authors in [19, 22, 96, 189,195, 197, 199, 200] noticed that for coastal locations (such as Nice) the variations in the computed attenuation changes can reach as high as $\pm 300\ dB/km$, and for continental locations (such as Graz) as low as $\pm 6\ dB/km$ was obtained, which means that the instabilities are lesser within the continental areas than in the coastal areas.

The estimated instabilities are shown in the time series plot in Figure 4.33 for the specific attenuation change. Therefore, it can be seen that all locations have considerable instability, excluding the city of Mafikeng with quite low instability. Durban and Cape Town (coastal areas) show a change (δ) which reaches to about $\pm 169\ dB/km$ on several occasions, and also Umtata (near-coastal area) had a change (δ) of about $\pm 169\ dB/km$ at several occasions, while both Bloemfontein and Johannesburg (non-coastal areas) had a change (δ) of up to $\pm 84\ dB/km$. But the changes in Mafikeng was much lower than the other locations with a change of about $\pm 26.5\ dB/km$. However, to determine the magnitude of the stability for each location, histograms can be used.

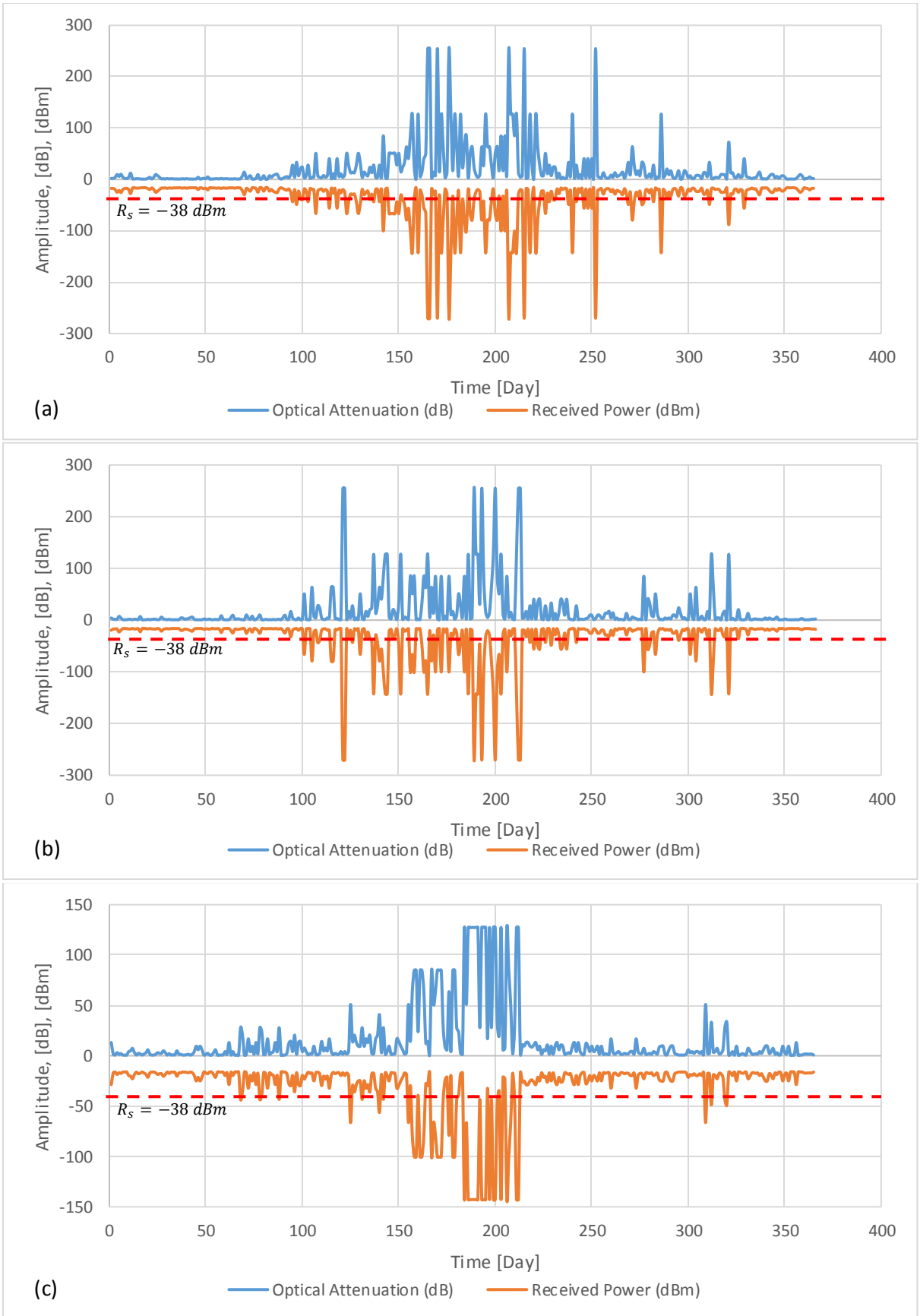

Figure 4.27: Typical time series display of the amplitude of the estimated optical attenuation and Received Power at an optical wavelength of 850 nm and optical link distance of 1.5 km for worst-case conditions for Durban over the years (a) 2011; (b) 2012 and (c) 2013.

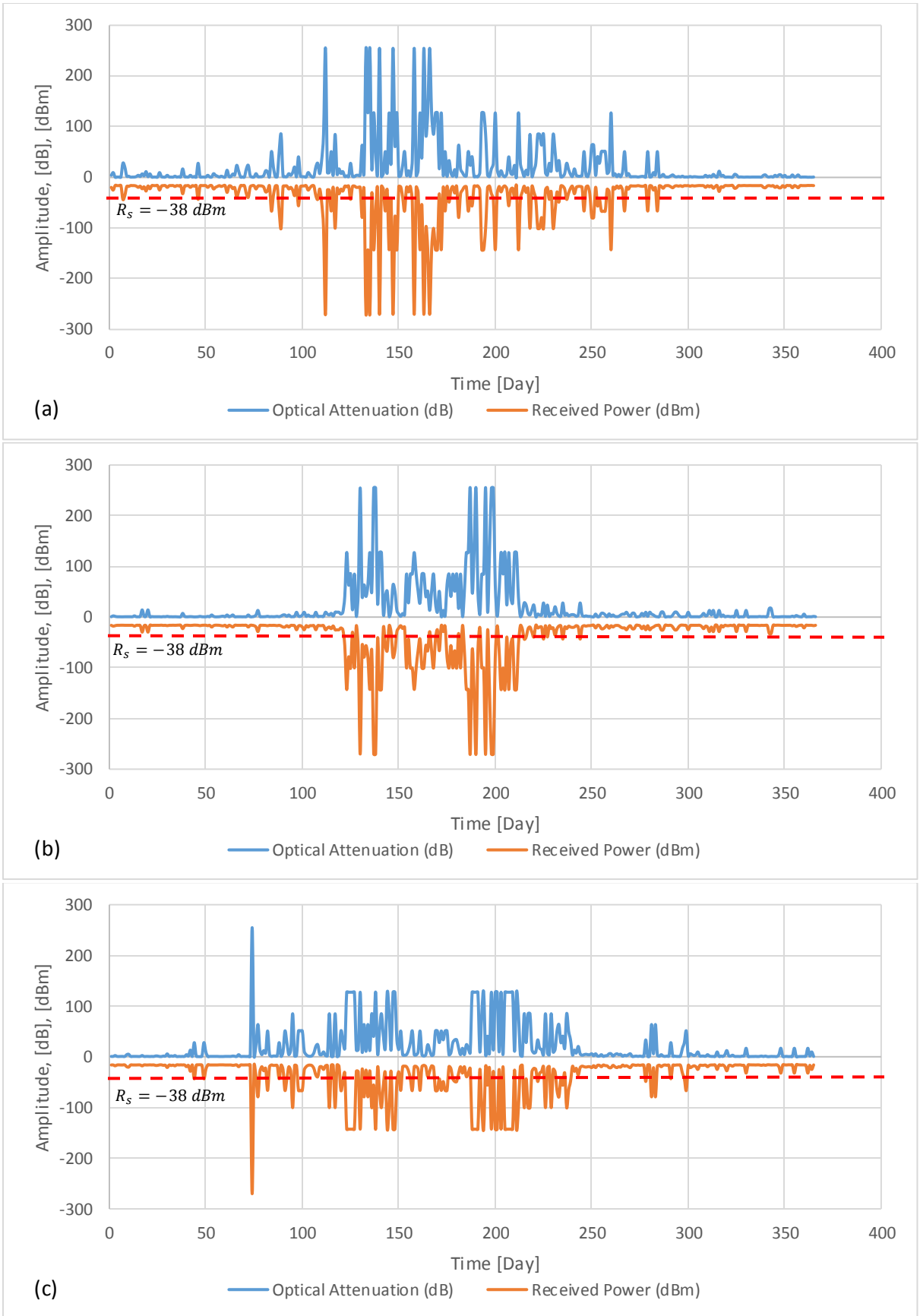

Figure 4.28: Typical time series display of the amplitude of the estimated optical attenuation and Received Power at an optical wavelength of 850 nm and optical link distance of 1.5 km for worst-case conditions for Cape Town over the years (a) 2011; (b) 2012 and (c) 2013.

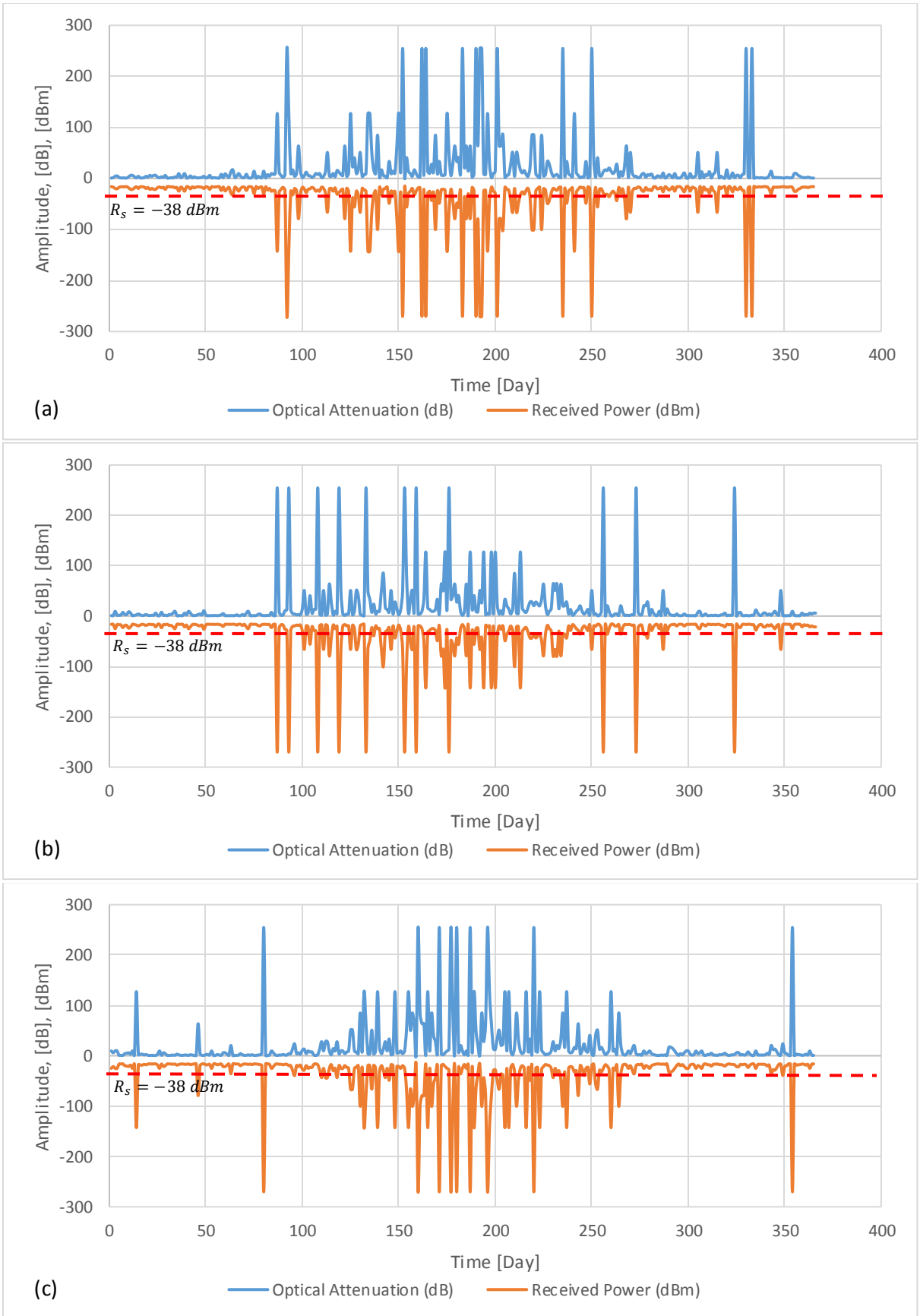

Figure 4.29: Typical time series display of the amplitude of the estimated optical attenuation and Received Power at an optical wavelength of 850 nm and optical link distance of 1.5 km for worst-case conditions for Umtata over the years (a) 2011; (b) 2012 and (c) 2013.

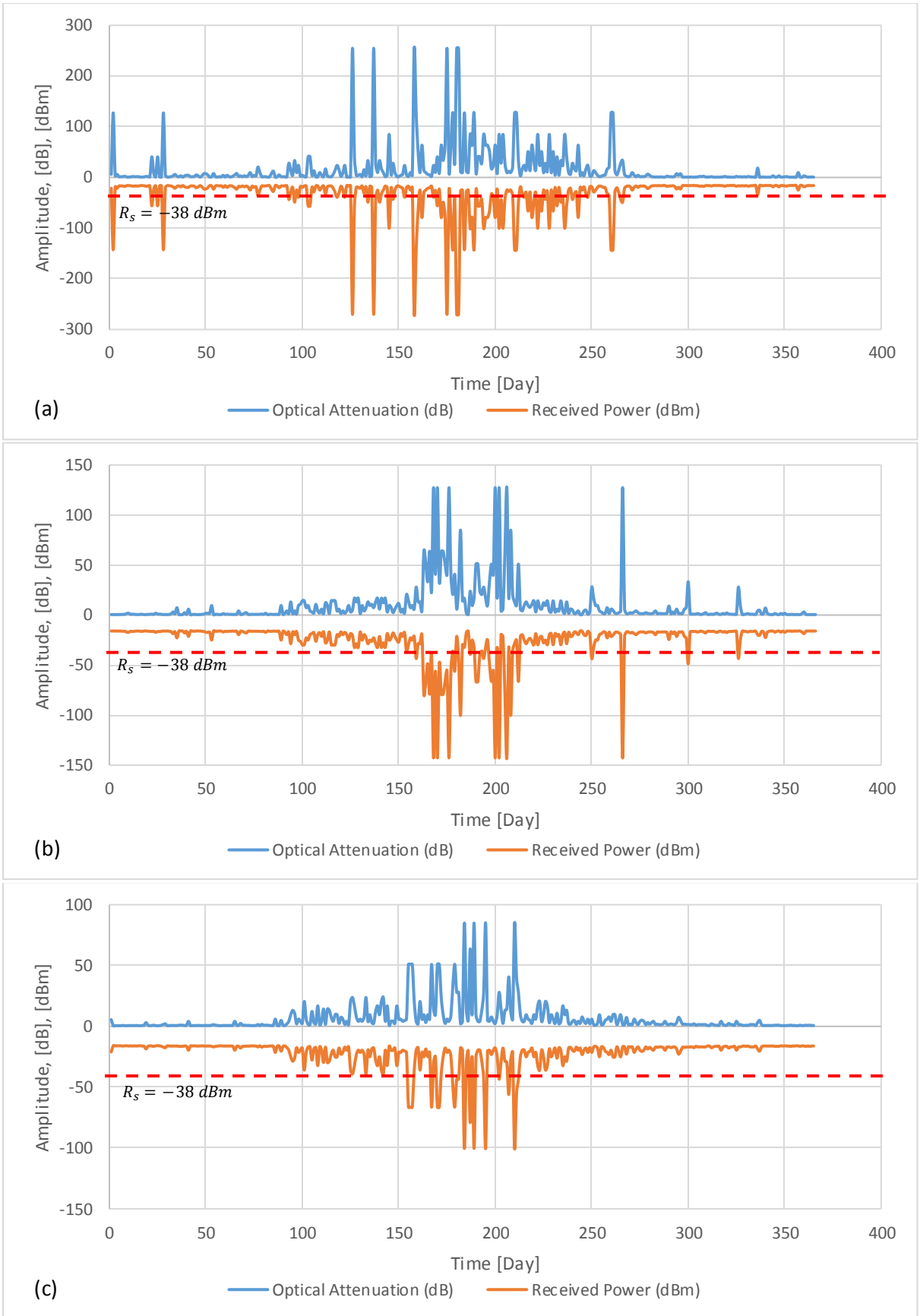

Figure 4.30: Typical time series display of the amplitude of the estimated optical attenuation and Received Power at an optical wavelength of 850 nm and optical link distance of 1.5 km for worst-case conditions for Bloemfontein over the years (a) 2011; (b) 2012 and (c) 2013.

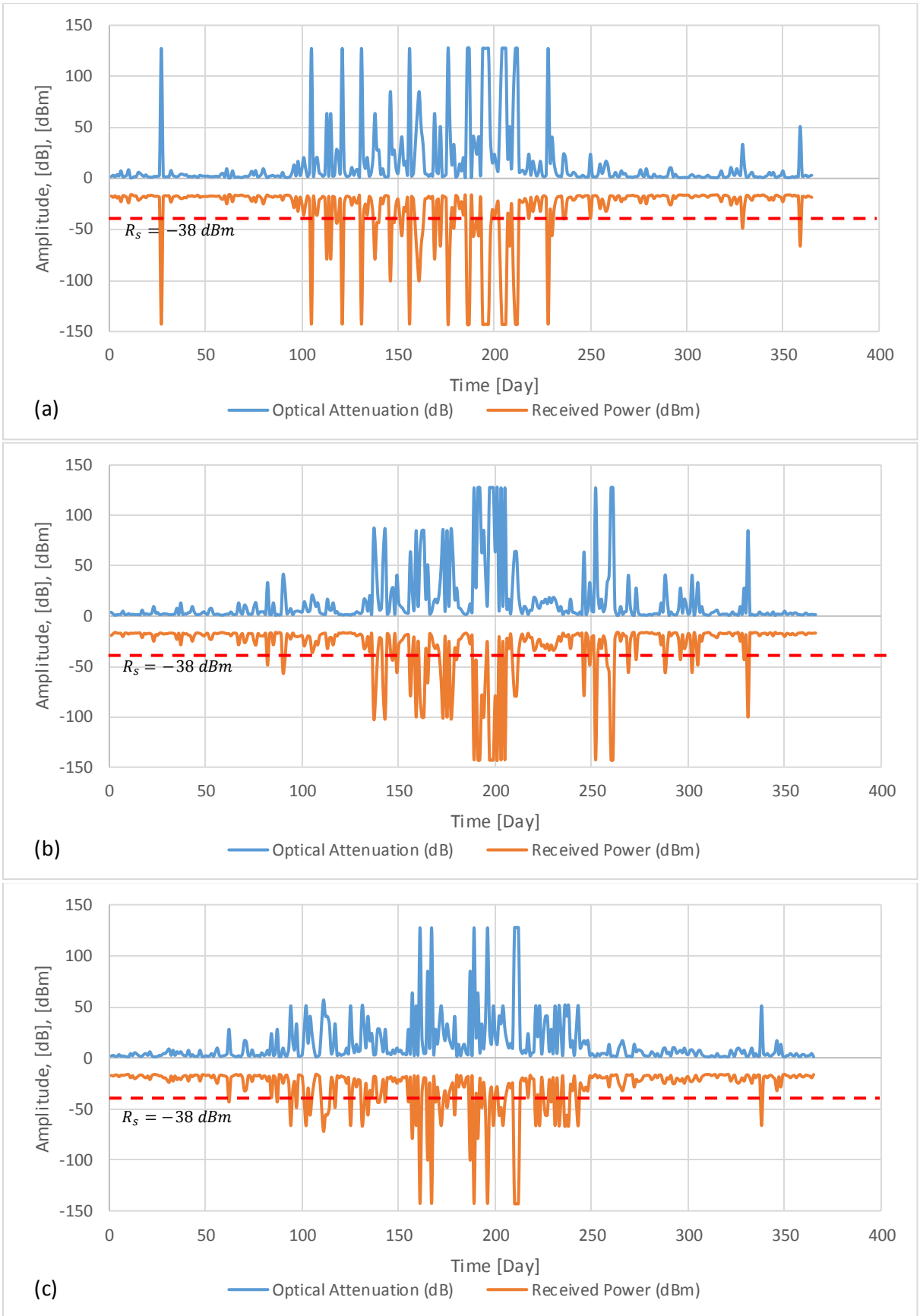

Figure 4.31: Typical time series display of the amplitude of the estimated optical attenuation and Received Power at an optical wavelength of 850 nm and optical link distance of 1.5 km for worst-case conditions for Johannesburg over the years (a) 2011; (b) 2012 and (c) 2013.

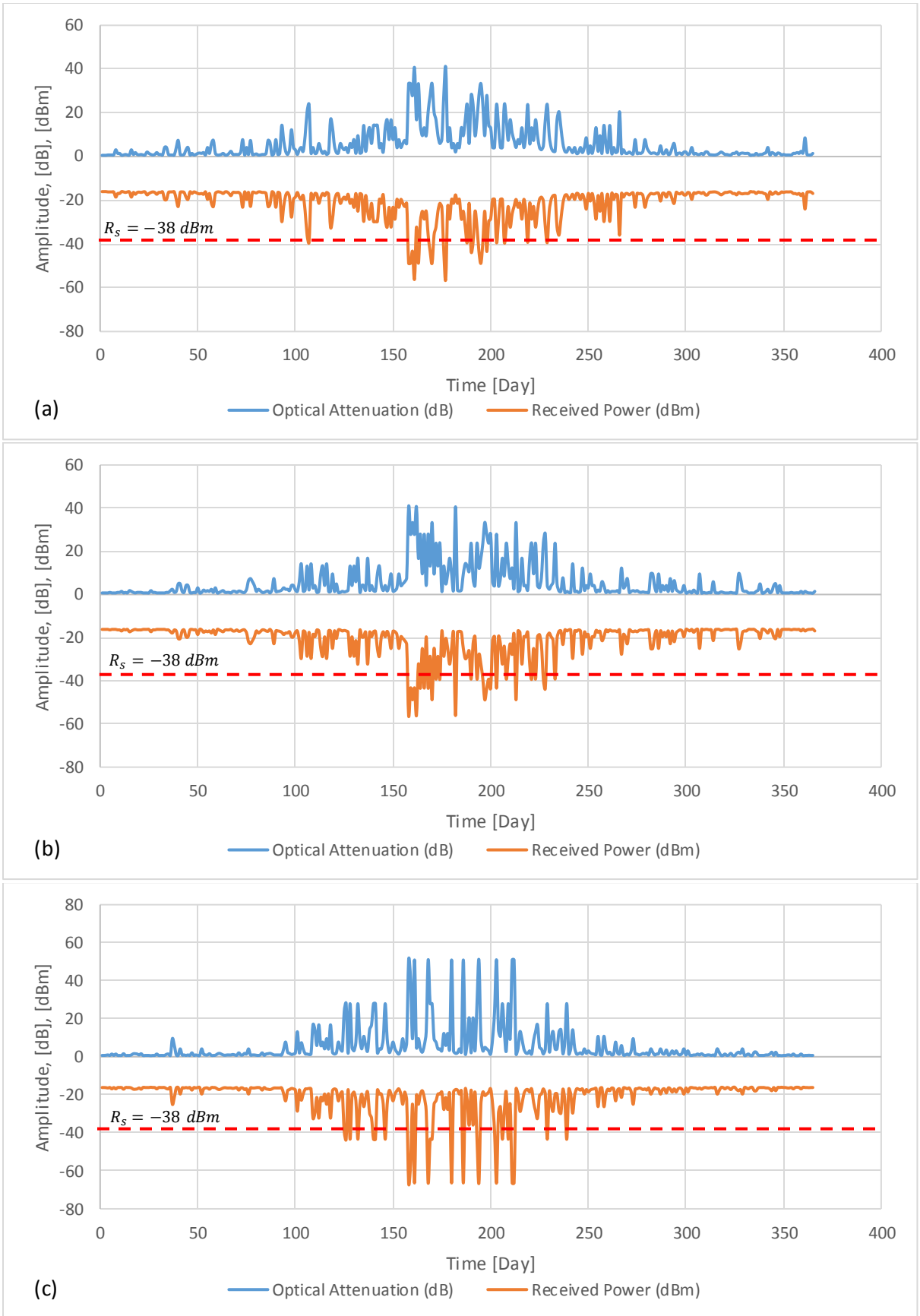

Figure 4.32: Typical time series display of the amplitude of the estimated optical attenuation and Received Power at an optical wavelength of 850 nm and optical link distance of 1.5 km for worst-case conditions for Mafikeng over the years (a) 2011; (b) 2012 and (c) 2013.

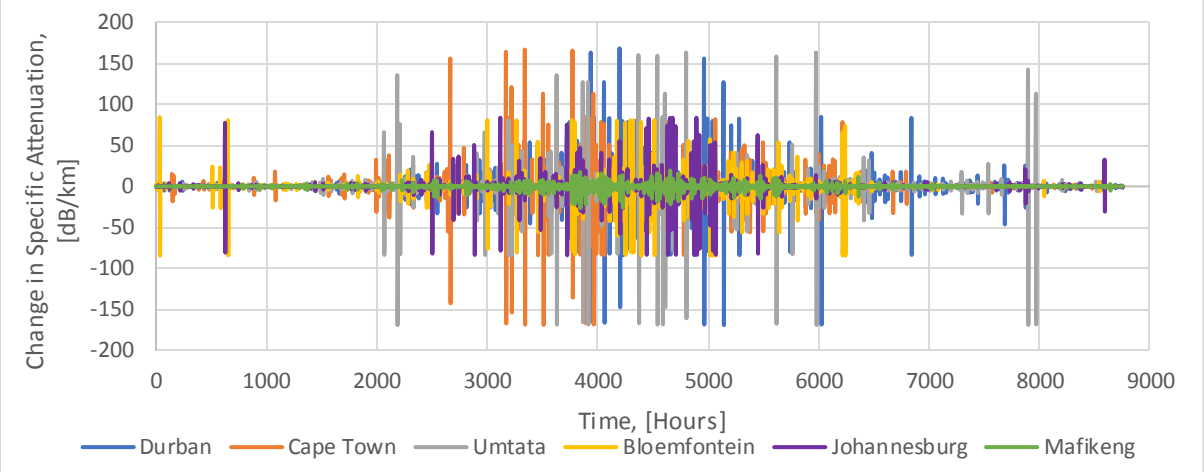

Figure 4.33: Changes in specific attenuation under diverse atmospheric conditions for all the locations over three-hour interval measurement scale for the year 2011.

4.9 FSO System Performance Analysis and Analytical Procedures under Various Atmospheric Conditions

4.9.1 Optical Link Performance Evaluation

In this sub-section, results for different performance metrics have been presented, in order to investigate the overall performance of FSO system deployed within South Africa. The FSO device parameters and their corresponding values presented in section 3.4 are considered in this performance analysis. Since the channel turbulence effect on FSO signal during foggy weather is weak and maybe negligible, then the main focus in this sub-section is to investigate the characteristic performance of the FSO communication system in foggy, hazy and cloudy weather conditions. The aim here is to determine the FSO system capability as well as limitations, through the parameters relating to the FSO transmitter and receiver as presented in the specifications of the FSO device.

4.9.1.1 Maximum Reachable Optical Link Length

The maximum reachable optical link length for the FSO system (described in Table 3.2) as a function of the visibility range with transmitted power $P_t = 40\ mW$, $R_s = -38\ dBm$ and at an optical wavelength of $\lambda = 850\ nm$ is presented in Figure 4.34. This optical link length was obtained using Equations (4.2) and (4.4), by varying the visibility range. It can be observed from this figure that maximum possible link length is very short for low visibility range, just as expected. It also reveals that as the visibility range increases or as the optical signal travels from Class 0 to a higher visibility class, then the maximum possible optical link distance also increases. For an optical signal propagating through free space with an FSO system given by the link specifications earlier provided, the maximum probable optical link length $L = 11\ km$ when the atmosphere is a class 6 category ($i.e.\ 10\ km < V < 20\ km$), $L = 8.3\ km$ for class 5 category ($i.e.\ 4\ km < V < 10\ km$), $L = 4.6\ km$ for class 4 category ($i.e.\ 2\ km < V < 4\ km$), $L = 2.8\ km$ for class 3 category ($i.e.\ 1\ km < V < 2\ km$), $L = 1.6\ km$ for

class 2 category ($i.e. 0.5\ km < V < 1\ km$), $L = 0.85\ km$ for class 1 category ($i.e. 0.2\ km < V < 0.5\ km$) and $L = 0.4\ km$ for class 0 category ($i.e. V = 0.2\ km$). To focus more on the predominant or most severe atmospheric conditions, the visibility classes 7 and 8 were omitted from the plot in Figure 4.34. Therefore, from the results it is obvious that for this given FSO system, the maximum possible link length for $V > 20\ km$ can be seen to be above 11 km.

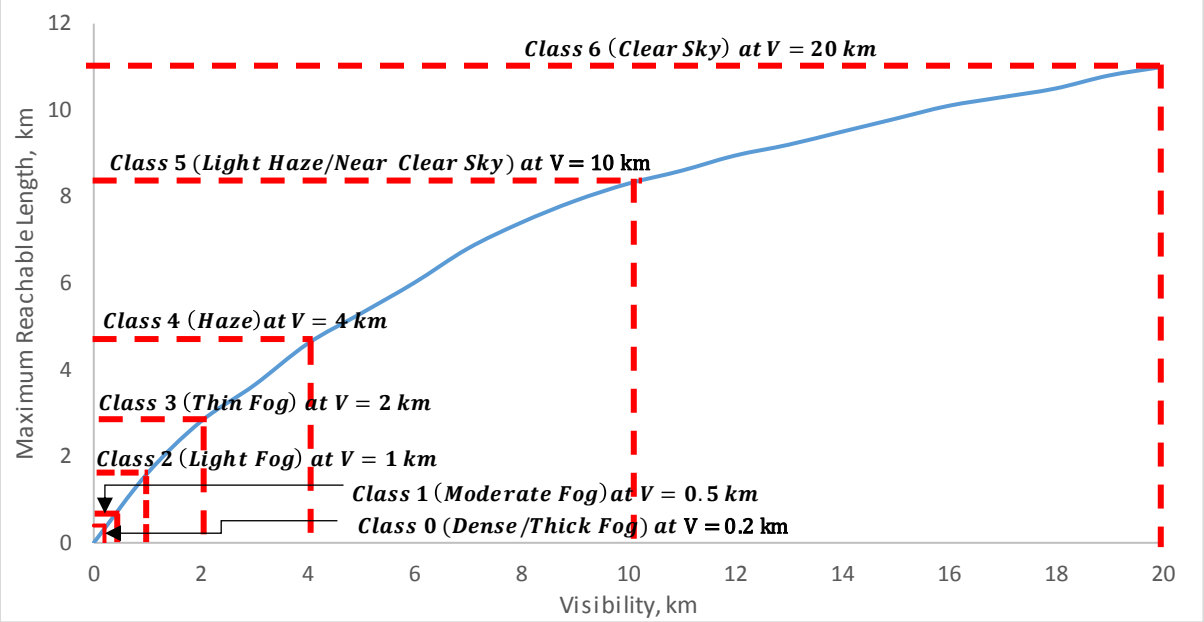

Figure 4.34: Maximum reachable link length for the FSO system against the visibility range with transmitted power $P_t = 40\ mW$, $R_s = -38\ dBm$ and at an optical wavelength of $\lambda = 850\ nm$.

4.9.1.2 Cellular Cell Size from Received Power and Optical Link Length

In order to improve mobile data coverage or to make allowances for any existing sophisticated generation network, the outdoor cells such as picocells and microcells which are small cell sites unlike the macro-cells are then set or designed for widespread deployment. With the intention of keeping up with the growing or incessant demand for large bandwidth by the end-users, these network cells have been introduced by the network operators. The size of these mobile communication network cells ranges from tens of meters to a few kilometres, whereas the macrocells are larger cells that are in the range of several kilometres (in particular, they are over 2 km cell dimension). However, due to the nature and severe consequences of the foggy or hazy weather during the transmission of optical signals, the picocells and microcells can be of great usefulness as a result of their limited short size without requiring any increase in the transmitted optical power, and therefore they will compensate for the impairments caused by fog or haze. Moreover, to compensate or cater for the high optical attenuation due to fog or haze conditions, arising from the higher frequencies (above 60 GHz bands), the size of the network cell will continue to reduce as the previous and the advancing mobile technology exploits higher frequencies [203]. This theoretical fact and the mobile cell analysis in this work have shown FSO communication system as a promising solution for backhaul applications in the current Fifth-Generation (5G) networks

and future generation networks. It is to be noted that the cell size reduction phenomenon in mobile communications has high impact power over the FSO system which compensates for severe conditions or the outdoor impairments (like fog, haze and snow). Therefore, FSO communication system can be employed as a typical backhaul solution in order to connect together these network cells (and with the backbone network), and as well as to connect the smaller indoor femtocells.

Figure 4.35 presents the received optical signal power under various atmospheric channels (foggy, hazy and cloudy channels) versus the optical link length. This result shows the performance of the FSO system used in this work under various units of cell sites (i.e., from small cell sites to very large cell sites) with transmitted optical power $P_t = 40\ dBm$, receiver sensitivity $R_s = -38\ dBm$ and optical wavelength $\lambda = 850\ nm$. The observations from the received optical power and link length reveals that the probable maximum optical link length (as shown in Table 4.5) is approximately $L_0 = 0.4\ km$ for an atmosphere of a class 0 regime $(i.e. V = 0.2\ km)$, $L_1 = 0.85\ km$ for class 1 regime $(i.e. V = 0.5\ km)$, $L_2 = 1.6\ km$ for class 2 regime $(i.e. V = 1\ km)$, $L_3 = 2.8\ km$ for class 3 regime $(i.e. V = 2\ km)$, $L_4 = 4.6\ km$ for class 4 regime $(i.e. V = 4\ km)$, $L_5 = 8.3\ km$ for class 5 regime $(i.e. V = 10\ km)$, $L_6 = 11\ km$ for class 6 regime $(i.e. V = 20\ km)$, $L_7 = 15.4\ km$ for class 7 regime $(i.e. V = 50\ km)$, and $L_8 = 17.4\ km$ for class 8 regime $(i.e. V = 100\ km)$.

For the selected FSO system provided in Table 3.2 to work for any of the cellular sites under various atmospheric conditions, the optical link length value obtained at $R_s = -38\ dBm$ for each of the visibility categories must fall within or above the size range of that cell site. It can be observed from the results that the FSO system can function well as a backhaul solution for picocells (typically ranging from $4 - 200\ m$), under all of the visibility classes without any problem, except that the optical link performance might drop for dense fog conditions. The result also shows that for the microcells (which typically ranges from $0.2 - 2\ km$ or sometimes it is said to range from $0.5 - 2\ km$), the FSO system can be employed as a backhaul solution under Class 0 (Dense/Thick fog) with optical link length $L \leq 0.4\ km$, Class 1 (Moderate fog) with $L \leq 0.85\ km$, Class 2 (Light fog) with $L \leq 1.6\ km$, Class 3 (Thin fog) with $L \leq 2.8\ km$, Class 4 (Haze) with $L \leq 4.6\ km$, Class 5 (Light Haze) with $L \leq 8.3\ km$, Class 6 (Clear sky) with $L \leq 11\ km$, Class 7 (Very clear sky) with $L \leq 15.4\ km$ and Class 8 (Extremely clear sky) with $L \leq 17.4\ km$. For macrocells (typically greater than $2\ km$), the FSO system can be applied as a backhaul solution under classes 4, 5, 6, 7 and 8 without any problem. However, for Classes 0, 1 and 2, this FSO system cannot support macrocells without having to increase the transmitted optical power, because the signal transmission cannot reach up to $2\ km$. Also, since the probable range of the optical link length under Class 3 is $1.6 < L_3 \leq 2.8\ km$, then the FSO link under Class 3 may sometimes not support macrocells, specifically when the length is reduced to less than $2\ km$.

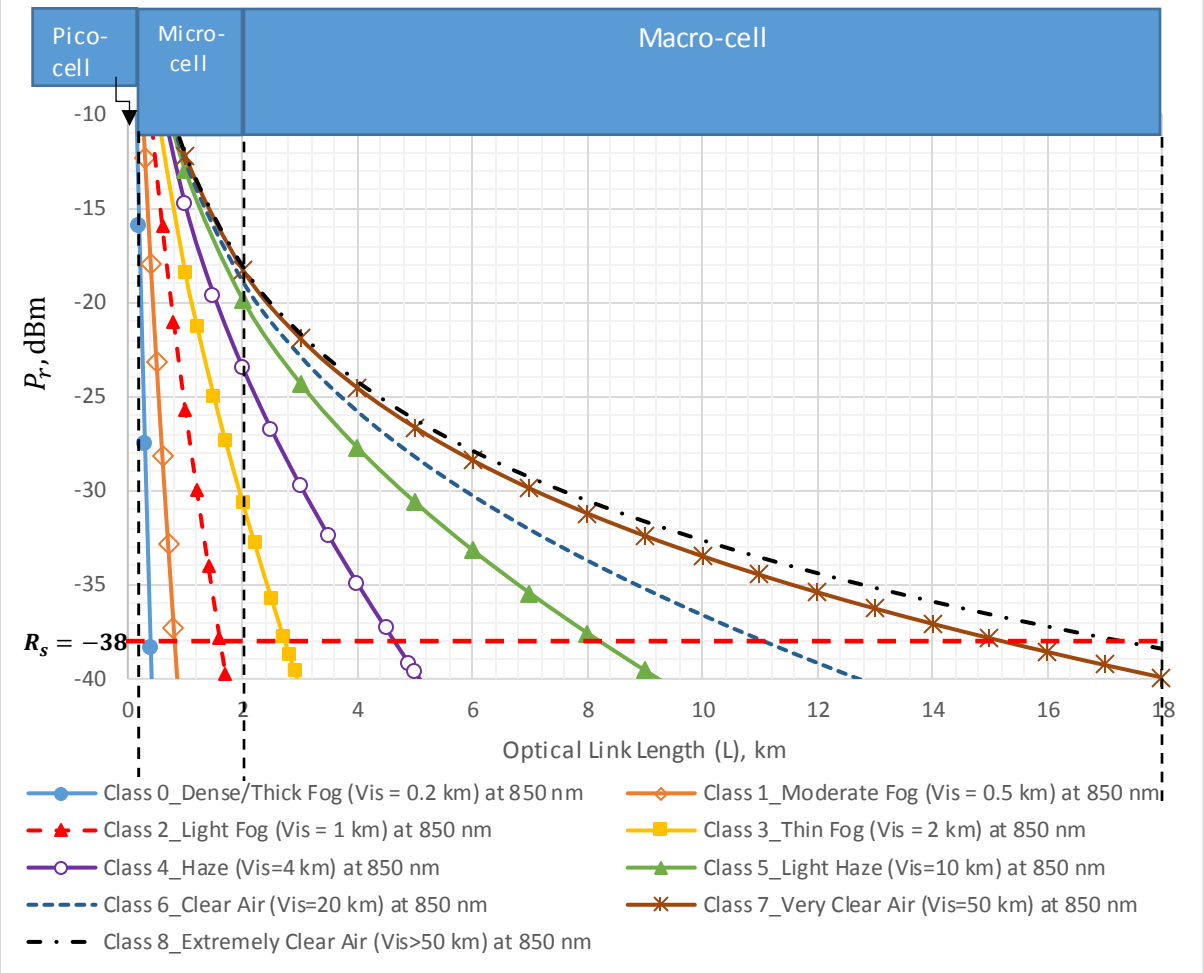

Figure 4.35: Received optical power versus the link range showing the performance of the FSO system under various units of cell sites with transmitted optical power $P_t = 40\ dBm$, receiver sensitivity $R_s = -38\ dBm$ and optical wavelength $\lambda = 850\ nm$.

Table 4.5: Maximum optical link length values for various atmospheric conditions at $P_t = 40\ dBm$, $R_s = -38\ dBm$ and $\lambda = 850\ nm$ for the FSO link specified in this research work.

Standard maximum optical path length for the FSO device in this work	**Visibility Classes**								
	Class 0 $L_0\ (km)$	**Class 1 $L_1\ (km)$**	**Class 2 $L_2\ (km)$**	**Class 3 $L_3\ (km)$**	**Class 4 $L_4\ (km)$**	**Class 5 $L_5\ (km)$**	**Class 6 $L_6\ (km)$**	**Class 7 $L_7\ (km)$**	**Class 8 $L_8\ (km)$**
	0.40	0.85	1.60	2.80	4.60	8.30	11.00	15.40	17.40

4.9.1.3 Received Power and Visibility Range

The results in Figure 4.36 show the optical link performance under various foggy channels as a function of the visibility range. The range of visibility as shown in Figure 4.36 is divided into four classes: Class 0 covers both dense fog (D) and thick fog (T), Class 1 or moderate fog (M), Class 2 or light fog (L) and Class 3 or thin fog (Th). The possibility of link failure occurrence is great when P_r drops to a value below the R_s (i.e., $P_r < R_s$). The performance of the FSO system with transmitted optical power $P_t = 40\ dBm$, $R_s = -38\ dBm$ and $\lambda = 850\ nm$, shows that the optical link length will reach $1\ km$, $1.5\ km$

and 2 km when the visibility (V) is greater or equal to 0.41 km, 0.93 km and 1.12 km respectively, according to R_s. This visibility values can be referred to as the cut-off visibility (V_c), suggesting when the link failure will take place, and in this case this corresponds to the Class 1 (moderate fog condition), Class 2 (light fog condition) and Class 3 (thin fog condition) regimes when the link lengths of 1 km, 1.5 km and 2 km respectively are achieved. This is synonymous with most FSO equipment operating under 1 W transmitted power.

Some of the ways to achieve a better link performance, so that the optical link designed for 1 km, 1.5 km and 2 km will respectively work under $V \ll 0.41\ km$, $V \ll 0.93\ km$ and $V \ll 1.12\ km$, while keeping most of the link specification parameters given in Table 3.2 unchanged, is by either increasing the transmitted power or optical wavelength to about 1550 nm, and by applying FSO/RF system which removes the effects of simultaneous link failure.

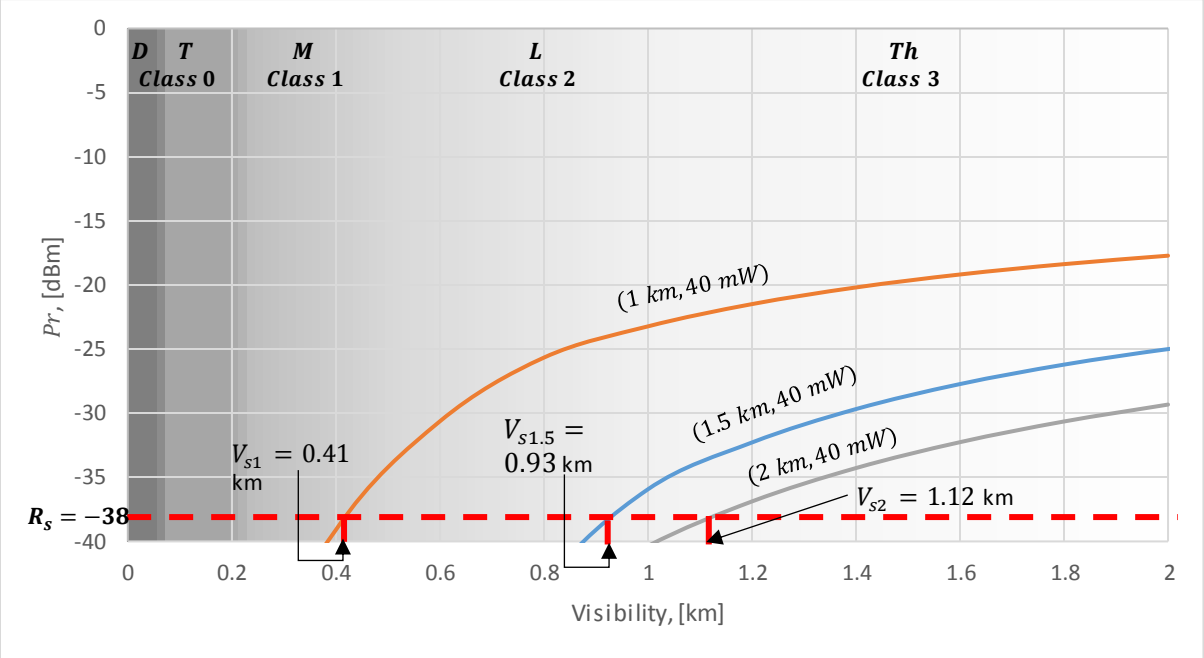

Figure 4.36: Performance of the FSO system under various foggy channels showing the received optical power versus visibility as a function of $P_t = 40\ mW$ and $\lambda = 850\ nm$, at $L = 1\ km$, 1.5 km and 2 km.

4.9.1.4 Signal-to-Noise Ratio of the FSO Link based on Visibility Range

To study the overall performance as well as the Bit-Error Rate (BER) and Average Channel Capacity (ACC) of a FSO system under various atmospheric conditions and optical link specifications, the Signal-to-Noise Ratio (SNR) must be determined. The SNR is one of the important metrics used to study the performance of FSO system as a function of the magnitude of the ratio of optical signal power to the noise power. However, the overall performance of any communication system is limited by the SNR. This SNR phenomenon is a function of the type of photodetector, that is, either PIN photo-diode

or Avalanche photo-diode (APD) used at the receiver end. In this work, the APD photodetector was used in the FSO receiver, and its SNR was obtained using [136]:

$$SNR = \frac{(R_s P_r M)^2}{2qBM^{x+2}(R_s P_r + I_D) + 2qI_L B + 4kTBF/R_{eq}}, \tag{4.7}$$

where M is the avalanche multiplication factor, q is the electron charge, B is the equivalent noise bandwidth, I_D is bulk dark current, I_L is the surface leakage current, k is he Boltzmann constant, T is the system temperature in kelvin, F is the noise figure and R_{eq} is the equivalent circuit resistance. The different components taken into consideration to determine the SNR are output photocurrent (which is a function of the received optical power), photo-detector responsivity, the shot noise and the thermal noise terms. Based on the parameters of the FSO device (such as the received power, Noise parameters, sensitivity of the receiver etc.) used in this work, the corresponding SNR limit to the receiver sensitivity was computed, and it was obtained as $SNR_s = 10.5\ dB$.

In this section, it will be great to investigate if there are instances or events where the SNR becomes insignificant during the year or over a particular period using the daily minimum visibility values (which shows the daily worst cases), and then to know how many of those instances exist. This examination will give an estimate that can provide the status of the optical link at the worst-case conditions of the day which is obtained from the minimum visibility value in each day.

The graphical results (based on the daily worst case scenarios) presented in Figure 4.37 show that there are several occasions within the day or year that resulted into the SNR falling below $10.5\ dB$ and even further resulting into a negative-SNR (NSNR), which implies that the noise power has become greater than the optical signal power at those periods. It should be therefore noted that most of those events are observed during the periods or seasons around the middle of the year. Therefore, since it has been confirmed that on the average this optical link will optimally perform well, but as a result of certain periodic harsh weather conditions (especially due to the occurrences of the LC of visibility), then the optical link will not be favourable at such instances which are just occasional. However, it will be important to find out how frequent these instances occurred or the live-span (either short-lived or long-lived) of those scenarios as analysed in the next sub-section.

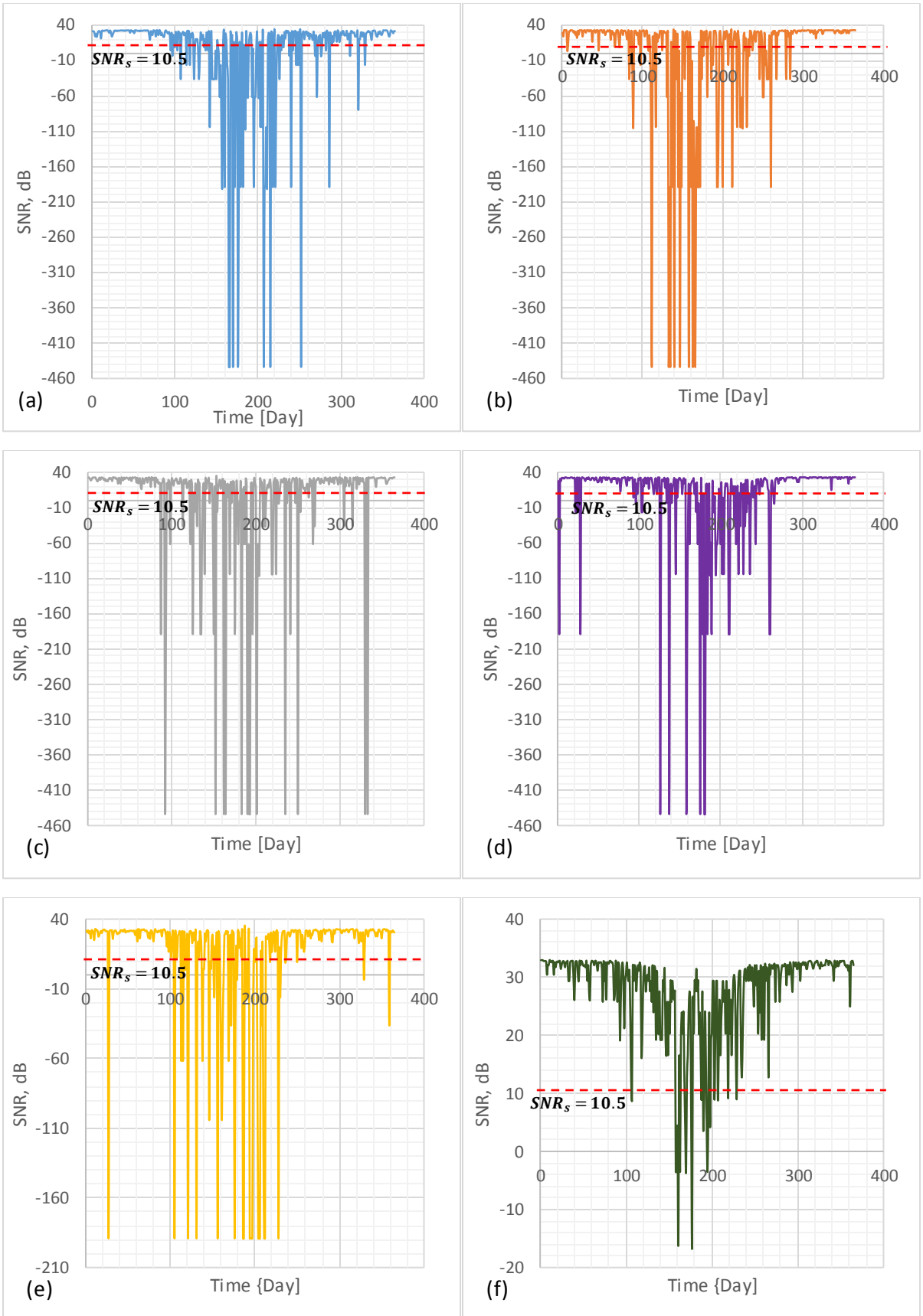

Figure 4.37: Typical time series display of the daily minimum SNR depending on the daily minimum visibility (at the daily worst case scenarios) and corresponding received power at 850 nm over the year 2011 for (a) Durban; (b) Cape Town; (c) Umtata; (d) Bloemfontein; (e) Johannesburg; (f) Mafikeng.

Thus, now that it is known that there could be outages at different periods within a year caused by the NSNR and also SNR values lower than 10.5 dB (i.e. $SNR < SNR_s$), then it is vital at this stage to investigate at what points in terms of visibility that there will be link failures. But before this can be achieved, the plot of a standard SNR curve must be made for this FSO system in order to determine the visibility limit that results into optical link failure. The plot in Figure 4.38 presents the SNR curves of the FSO system against visibility as a function of $P_t = 40\ mW$, $\lambda = 850\ nm$ and link distances $1\ km, 1.5\ km$ and $2\ km$. This figure shows that the overall performance of the FSO system using the APD photodetectors over the specified optical link distances and transmitted power is better when $V > V_{Class-1}\ (km)$, $V > V_{Class-2}\ (km)$ and $V \geq V_{Class-3}\ (km)$ for optical link distances $1\ km, 1.5\ km$ and $2\ km$ respectively, where $V_{Class-1}$, $V_{Class-2}$ and $V_{Class-3}$ indicate the viability range (in km) of Class-1, Class-2 and Class-3 respectively. The observed visibility limits corresponding to the SNR of the receiver sensitivity are $V_{s1} = 0.41\ km$, $V_{s1.5} = 0.93\ km$ and $V_{s2} = 1.12\ km$, which are the same with that observed in the last section. In conclusion, this section provides the link behaviour due to the SNR under various weather conditions. It was observed that at visibility values lower than $0.41\ km, 0.93\ km$ and $1.12\ km$ for $1\ km, 1.5\ km$ and $2\ km$ optical link distances respectively, various mitigation techniques (like spatial diversity) would be needed to boost the performance of the FSO system.

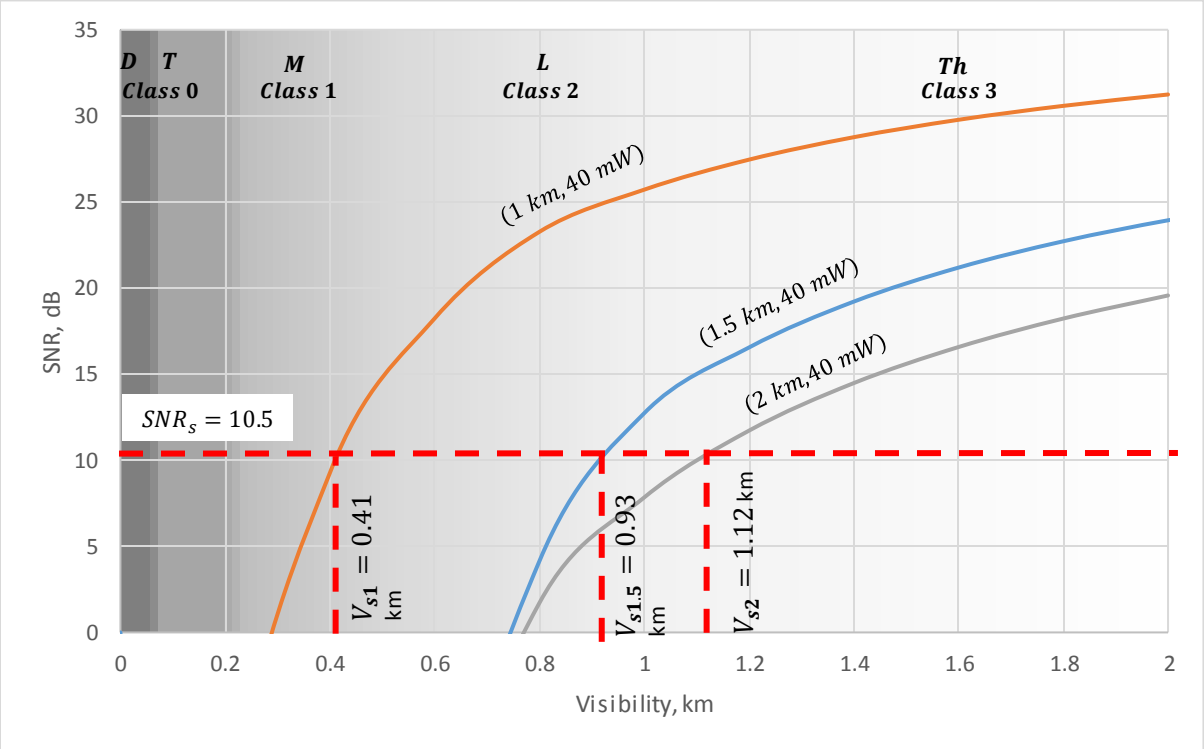

Figure 4.38: Performance of the FSO system under various foggy channels showing the Signal-to-Noise Ratio versus visibility as a function of $P_t = 40\ mW$ and $\lambda = 850\ nm$, at $L = 1\ km, 1.5\ km$ and $2\ km$.

4.9.1.5 Outage Probability of the Optical Link

The FSO link performance can be determined from the outage probability, whereby in this case, one of the key determining factors is the visibility range. In this work, a more thorough and accurate approach

has been used to calculate the outage probability for all the different locations covering three years visibility data.

Apart from investigating whether there are instances or events where the SNR becomes insignificant during the year or over a particular period using the daily minimum visibility values as discussed in the previous sub-section, it is also important to investigate further in order to know how many of those instances exist. This study will provide the optical link information and periodic status of the system, which can be used to determine the performance of the link. This has resulted into the determination of the percentage of time probability of link outage over the worst cases of each day using three hours interval time scale for each of the locations over the specified period. The frequency and percentage time probability of outage computations in Table 4.6 are based on the estimated SNR values observed to be below $SNR_s = 10.5\ dB$, which corresponds to receiver sensitivity $R_s = -38\ dBm$ or visibility threshold value of $V_s = 0.93\ km$. It was observed from the results in this table that the outage probability in percentage time over three hours interval resolutions can reach up to a maximum of ≈ 3.83%, 5.20%, 3.56%, 3.29%, 2.60% and 1.10% for Durban, Cape Town, Umtata, Bloemfontein, Johannesburg and Mafikeng, while it can only get to a minimum of ≈ 2.91%, 4.59%, 2,91%, 1.10%, 2.53% and 0.75% for Durban, Cape Town, Umtata, Bloemfontein, Johannesburg and Mafikeng. However, it should be noted that these values are only based on the impact of atmospheric conditions (especially visibility range) on the FSO system, ignoring the effects of atmospheric scintillation in terms of turbulence.

Table 4.6: Summary of the frequency and percentage time probability of optical link outage based on the observed optical attenuation at $SNR < 10.5\ dB$.

Year	**City**	**Class 0**		**Class 1**		**Class 2**		**Total**	
		Freq	***% Time probability of Outage***	***Freq***	***% Time probability of Outage***	***Freq***	***% Time probability of Outage***	***Freq***	***% Time probability of Outage***
2011	DBN	25	0.86	35	1.20	52	1.78	112	3.83
	CPT	29	0.99	60	2.05	45	1.54	134	4.59
	UMT	25	0.86	36	1.23	43	1.47	104	3.56
	BLFT	17	0.58	28	0.96	51	1.75	96	3.29
	JHB	19	0.65	22	0.75	35	1.20	76	2.60
	MFK	0	0	0	0	22	0.75	22	0.75
2012	DBN	22	0.75	33	1.13	40	1.37	95	3.25
	CPT	26	0.89	56	1.92	61	2.09	143	4.90
	UMT	20	0.69	33	1.13	32	1.10	85	2.91
	BLFT	8	0.27	13	0.45	21	0.72	42	1.44
	JHB	14	0.48	27	0.92	35	1.20	76	2.60
	MFK	0	0	0	0	30	1.03	30	1.03
2013	DBN	20	0.69	33	1.13	32	1.10	85	2.91
	CPT	28	0.96	67	2.29	57	1.95	152	5.20
	UMT	24	0.82	31	1.06	36	1.23	91	3.12
	BLFT	0	0	13	0.45	19	0.65	32	1.10
	JHB	8	0.27	24	0.82	42	1.44	74	2.53
	MFK	0	0	9	0.31	2	0.07	32	1.10

4.9.1.6 Link Availability of the FSO system

The optical link availability is one of the main factors of measuring the performance of the FSO link. It can be computed from the percentage of time of the visibility data over the entire period in the study. The link availability in this work is calculated using the percentage of time of the obtained visibility data, based on the various visibility classes for each of the six locations considered in this work. The first part of this analysis will consider the optical link availability as a function of percentage visibility under various visibility classes across the entire year, and the second part of the analysis will estimate the optical link availability based on the monthly percentage visibility under various visibility classes for each of the cities.

The visibility data to be used for each analysis is averaged over three hours interval time scale. The frequency of each visibility class is computed and then the percentage of time was calculated for each of the classes. The percentage of time of the various visibility class data over an entire year and on monthly basis for each of the locations and for the three successive years are presented in Tables 4.7, 4.8 and 4.9 respectively. The class visibility percentage across each year and month for each of the cities considered are determined by computing the given visibility over 2920 hours (for 2011 and 2013) and 2928 hours for 2012 (leap year). Using these data, the PDF of the visibility data for all the six cities can be calculated. Based on these PDF data, the CDF of the visibility data can be calculated for each city. The approach used for the computation of both the PDF and CDF of the visibility classes are given in section 3.9 (Equations (3.10) and (3.15)).

The relation for calculating the optical link availability (L_A) for a visibility V (km) can be defined as [200, 204]:

$$L_A = P_r[V \geq V_{min}(L)] = 1 - F[V_{min}(L)] \tag{4.8}$$

where $F[V = V_{min}(L)]$ represents the CDF of the visibility and this will be shown in the next chapter. The calculated PDF and CDF of each visibility class data are shown in Tables 4.7, 4.8 and 4.9. However, the main focus is the lower visibility classes, such as the foggy and hazy conditions which consists mostly of low visibility cases, since the optical link availability must be considered for worst case scenarios. In order to determine the FSO link availability data, the calculated CDF data (obtained from the PDF data) for each of the visibility classes and for each of the cities are needed.

The calculated optical link availability for the various visibility class data (in percentage) for all the locations over the three years 2011, 2012 and 2013 are shown in Tables 4.7, 4.8 and 4.9 respectively. Figure 4.39a presents the results of the link availability over the visibility class for different cities for the year 2011. This result shows that for the given optical link (with specified transmitted power, beam divergence, link distance and aperture area of the transmitter-receiver aperture areas), if the minimum visibility class is Class 0 (i.e. Dense and Thick fog), then the link availability will be 99.14% for

Durban, 99.01% for Cape Town, 99.14% for Umtata, 99.42% for Bloemfontein, 99.35% for Johannesburg and 100% for Mafikeng. Similarly, if the required minimum visibility range is Class 5, then the optical link availability is 59.42% for Durban, 70.17% for Cape Town, 62.47% for Umtata, 75.72% for Bloemfontein, 58.46% for Johannesburg and 78.94% for Mafikeng. Also, if the minimum visibility class required for the optical link is Class 6, then the link availability is 4.97% for Durban, 30.54% for Cape Town, 0.68% for Umtata, 56.82% for Bloemfontein, 0.55% for Johannesburg and 57.09% for Mafikeng.

The result in Figure 4.39b for the year 2012 shows that when visibility Class 2 is the minimum visibility (over a particular time), then the link availability will be 96.58% for Durban, 95.08% for Cape Town, 96.45% for Umtata, 98.29% for Bloemfontein, 97.30% for Johannesburg and 98.98% for Mafikeng. Likewise, when visibility Class 5 is the required minimum visibility range, then the link availability values will be 67.42% for Durban, 74.66% for Cape Town, 68.72% for Umtata, 80.94% for Bloemfontein, 59.60% for Johannesburg and 81. 73% for Mafikeng.

The result in Figure 4.39c for the year 2013 shows that when the required minimum visibility range is Class 2, then the link availability is 96.78% for Durban, 94.66% for Cape Town, 96.44% for Umtata, 98.66% for Bloemfontein, 97.16% for Johannesburg and 98.77% for Mafikeng. Similarly, if the minimum visibility range required for an optical link is Class 6, then the optical link availability is 0.41% for Durban, 43.49% for Cape Town, 0.51% for Umtata, 65.34% for Bloemfontein, 2.26% for Johannesburg and 59.59% for Mafikeng.

Based on the above results, the following observations were obtained:

i. It can be noticed from the optical link availability results that the same optical link cannot be proposed for the locations. The variations in the link availability value for each visibility class range is an indication that the optical link required for each station must be designed appropriately to suit the operation and factors of that particular site.
ii. The high percentage value recorded for the very low visibility classes suggests the low frequency of occurrence within those atmospheric conditions. However, this does not suggest that the optical link will perform perfectly well because there would still be instances where the link would fail due to the results obtained in the last sub-section about the outage probability which was obtained as a function of the receiver power limit and minimum required SNR.

In summary, this result shows that considering the whole period during a year when a certain visibility class is the required minimum visibility, then the link availability for the FSO system will depend on the equivalent percentage link availability.

Table 4.7: PDF, CDF and Link Availability values for the percentage visibility data under various atmospheric conditions (visibility classes) for different locations over the year 2011.

City		Visibility Class								
		C_0	C_1	C_2	C_3	C_4	C_5	C_6	C_7	C_8
2011										
DBN	**No of Hours**	25	35	55	83	224	763	1590	145	0
	%Time of Visibility	0.86	1.20	1.88	2.84	7.67	26.13	54.45	4.97	0.00
	PDF	0.009	0.012	0.019	0.028	0.077	0.261	0.545	0.050	0.000
	CDF [F(V)]	0.009	0.021	0.039	0.068	0.145	0.406	0.950	1.000	1.000
	%Link Availability	99.14	97.95	96.06	93.22	85.55	59.42	4.97	0.00	0.00
CPT	**No of Hours**	29	60	59	72	142	509	1157	892	0
	%Time of Visibility	0.99	2.05	2.02	2.47	4.86	17.43	39.62	30.55	0.00
	PDF	0.010	0.021	0.020	0.025	0.049	0.174	0.396	0.305	0.000
	CDF [F(V)]	0.010	0.030	0.051	0.075	0.124	0.298	0.695	1.000	1.000
	%Link Availability	99.01	96.95	94.93	92.47	87.60	70.17	30.55	0.00	0.00
UMT	**No of Hours**	25	36	46	116	183	690	1804	20	0
	%Time of Visibility	0.86	1.23	1.58	3.97	6.27	23.63	61.78	0.68	0.00
	PDF	0.009	0.012	0.016	0.040	0.063	0.236	0.618	0.007	0.000
	CDF [F(V)]	0.009	0.021	0.037	0.076	0.139	0.375	0.993	1.000	1.000
	%Link Availability	99.14	97.91	96.34	92.36	86.10	62.47	0.68	0.00	0.00
BLFT	**No of Hours**	17	28	58	87	137	382	552	1657	2
	%Time of Visibility	0.58	0.96	1.99	2.98	4.69	13.08	18.90	56.75	0.07
	PDF	0.006	0.010	0.020	0.030	0.047	0.131	0.189	0.567	0.001
	CDF [F(V)]	0.006	0.015	0.035	0.065	0.112	0.243	0.432	0.999	1.000
	%Link Availability	99.42	98.46	96.47	93.49	88.80	75.72	56.82	0.07	0.00
JHB	**No of Hours**	19	22	45	72	120	935	1691	16	0
	%Time of Visibility	0.65	0.75	1.54	2.47	4.11	32.02	57.91	0.55	0.00
	PDF	0.007	0.008	0.015	0.025	0.041	0.320	0.579	0.005	0.000
	CDF [F(V)]	0.007	0.014	0.029	0.054	0.095	0.415	0.995	1.000	1.000
	%Link Availability	99.35	98.60	97.05	94.59	90.48	58.46	0.55	0.00	0.00
MFK	**No of Hours**	0	0	31	68	121	395	638	1667	0
	%Time of Visibility	0.00	0.00	1.06	2.33	4.14	13.53	21.85	57.09	0.00
	PDF	0.000	0.000	0.011	0.023	0.041	0.135	0.218	0.571	0.000
	CDF [F(V)]	0.000	0.000	0.011	0.034	0.075	0.211	0.429	1.000	1.000
	%Link Availability	100.00	100.00	98.94	96.61	92.47	78.94	57.09	0.00	0.00

Table 4.8: PDF, CDF and Link Availability values for the percentage visibility data under various atmospheric conditions (visibility classes) for different locations over the year 2012.

City		Visibility Class								
		C_0	C_1	C_2	C_3	C_4	C_5	C_6	C_7	C_8
2012										
DBN	**No of Hours**	22	33	45	80	140	634	1943	31	0
	%Time of Visibility	0.75	1.13	1.54	2.73	4.78	21.65	66.36	1.06	0.00
	PDF	0.008	0.011	0.015	0.027	0.048	0.217	0.664	0.011	0.000
	CDF [F(V)]	0.008	0.019	0.034	0.061	0.109	0.326	0.989	1.000	1.000
	%Link Availability	99.25	98.12	96.58	93.85	89.07	67.42	1.06	0.00	0.00
CPT	**No of Hours**	26	56	62	63	129	406	932	1254	0
	%Time of Visibility	0.89	1.91	2.12	2.15	4.41	13.87	31.83	42.83	0.00
	PDF	0.009	0.019	0.021	0.022	0.044	0.139	0.318	0.428	0.000
	CDF [F(V)]	0.009	0.028	0.049	0.071	0.115	0.253	0.572	1.000	1.000
	%Link Availability	99.11	97.20	95.08	92.93	88.52	74.66	42.83	0.00	0.00
UMT	**No of Hours**	20	33	51	94	162	556	2006	6	0
	%Time of Visibility	0.68	1.13	1.74	3.21	5.53	18.99	68.51	0.20	0.00
	PDF	0.007	0.011	0.017	0.032	0.055	0.190	0.685	0.002	0.000
	CDF [F(V)]	0.007	0.018	0.036	0.068	0.123	0.313	0.998	1.000	1.000
	%Link Availability	99.32	98.19	96.45	93.24	87.70	68.72	0.20	0.00	0.00
BLFT	**No of Hours**	8	13	29	81	112	315	422	1943	5
	%Time of Visibility	0.27	0.44	0.99	2.77	3.83	10.76	14.41	66.36	0.17
	PDF	0.003	0.004	0.010	0.028	0.038	0.108	0.144	0.664	0.002
	CDF [F(V)]	0.003	0.007	0.017	0.045	0.083	0.191	0.335	0.998	1.000
	%Link Availability	99.73	99.28	98.29	95.53	91.70	80.94	66.53	0.17	0.00
JHB	**No of Hours**	14	27	38	72	120	912	1745	0	0
	%Time of Visibility	0.48	0.92	1.30	2.46	4.10	31.15	59.60	0.00	0.00
	PDF	0.005	0.009	0.013	0.025	0.041	0.311	0.596	0.000	0.000
	CDF [F(V)]	0.005	0.014	0.027	0.052	0.093	0.404	1.000	1.000	1.000
	%Link Availability	99.52	98.60	97.30	94.84	90.74	59.60	0.00	0.00	0.00
MFK	**No of Hours**	0	0	30	54	100	351	686	1707	0
	%Time of Visibility	0.00	0.00	1.02	1.84	3.42	11.99	23.43	58.30	0.00
	PDF	0.000	0.000	0.010	0.018	0.034	0.120	0.234	0.583	0.000
	CDF [F(V)]	0.000	0.000	0.010	0.029	0.063	0.183	0.417	1.000	1.000
	%Link Availability	100.00	100.00	98.98	97.13	93.72	81.73	58.30	0.00	0.00

Table 4.9: PDF, CDF and Link Availability values for the percentage visibility data under various atmospheric conditions (visibility classes) for different locations over the year 2013.

City		Visibility Class								
		C_0	C_1	C_2	C_3	C_4	C_5	C_6	C_7	C_8
2013										
DBN	**No of Hours**	20	33	41	98	164	682	1870	12	0
	%Time of Visibility	0.68	1.13	1.40	3.36	5.62	23.36	64.04	0.41	0.00
	PDF	0.007	0.011	0.014	0.034	0.056	0.234	0.640	0.004	0.000
	CDF [F(V)]	0.007	0.018	0.032	0.066	0.122	0.355	0.996	1.000	1.000
	%Link Availability	99.32	98.18	96.78	93.42	87.81	64.45	0.41	0.00	0.00
CPT	**No of Hours**	28	67	61	80	126	419	869	1270	0
	%Time of Visibility	0.96	2.29	2.09	2.74	4.32	14.35	29.76	43.49	0.00
	PDF	0.010	0.023	0.021	0.027	0.043	0.143	0.298	0.435	0.000
	CDF [F(V)]	0.010	0.033	0.053	0.081	0.124	0.267	0.565	1.000	1.000
	%Link Availability	99.04	96.75	94.66	91.92	87.60	73.25	43.49	0.00	0.00
UMT	**No of Hours**	24	31	49	120	170	604	1907	15	0
	%Time of Visibility	0.82	1.06	1.68	4.11	5.82	20.68	65.31	0.51	0.00
	PDF	0.008	0.011	0.017	0.041	0.058	0.207	0.653	0.005	0.000
	CDF [F(V)]	0.008	0.019	0.036	0.077	0.135	0.342	0.995	1.000	1.000
	%Link Availability	99.18	98.12	96.44	92.33	86.51	65.82	0.51	0.00	0.00
BLFT	**No of Hours**	0	13	26	61	116	308	488	1908	0
	%Time of Visibility	0.00	0.45	0.89	2.09	3.97	10.55	16.71	65.34	0.00
	PDF	0.000	0.004	0.009	0.021	0.040	0.105	0.167	0.653	0.000
	CDF [F(V)]	0.000	0.004	0.013	0.034	0.074	0.179	0.347	1.000	1.000
	%Link Availability	100.00	99.55	98.66	96.58	92.60	82.05	65.34	0.00	0.00
JHB	**No of Hours**	8	24	51	78	172	929	1592	66	0
	%Time of Visibility	0.27	0.82	1.75	2.67	5.89	31.82	54.52	2.26	0.00
	PDF	0.003	0.008	0.017	0.027	0.059	0.318	0.545	0.023	0.000
	CDF [F(V)]	0.003	0.011	0.028	0.055	0.114	0.432	0.977	1.000	1.000
	%Link Availability	99.73	98.90	97.16	94.49	88.60	56.78	2.26	0.00	0.00
MFK	**No of Hours**	0	9	27	52	89	324	679	1740	0
	%Time of Visibility	0.00	0.31	0.92	1.78	3.05	11.10	23.25	59.59	0.00
	PDF	0.000	0.003	0.009	0.018	0.030	0.111	0.233	0.596	0.000
	CDF [F(V)]	0.000	0.003	0.012	0.030	0.061	0.172	0.404	1.000	1.000
	%Link Availability	100.00	99.69	98.77	96.99	93.94	82.84	59.59	0.00	0.00

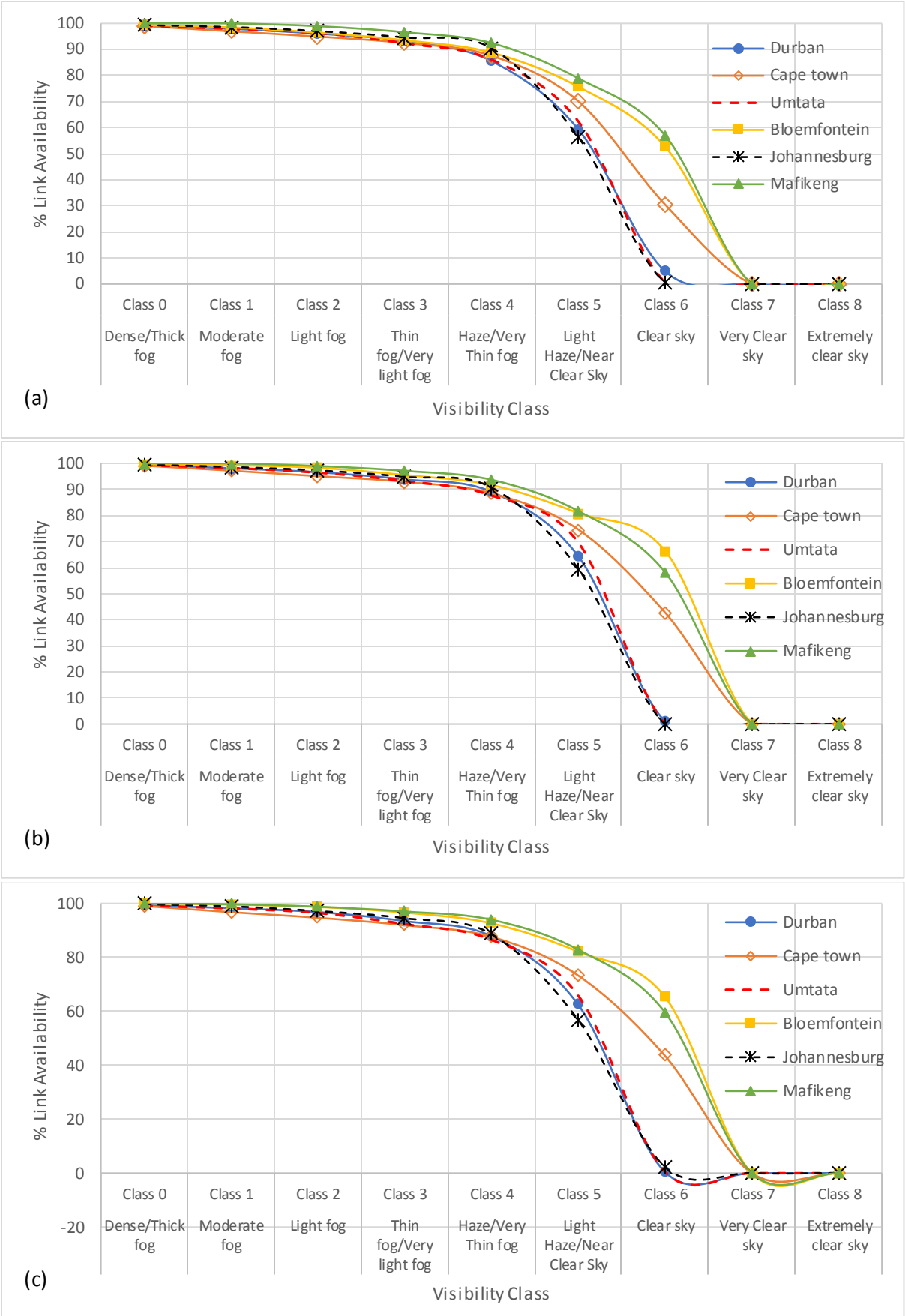

Figure 4.39: Link Availability values for the percentage visibility data under various atmospheric conditions (visibility classes) for different locations over the years (a) 2011; (b) 2012; (c) 2013.

4.9.2 Link Budget Derivation

The link margin is an important factor in the computation of the performance of FSO systems as discussed earlier in the literature review. The calculation of the link margin is required in order to design an appropriate FSO system, which depends on several parameters as well as the environment where the optical link is to be installed. The power link margin analysis in this sub-section is discussed using some typical link data such as transmitted optical power, antenna gain, geometrical attenuation, optical losses and sensitivity of the detector for various visibility conditions and at different optical wavelengths. In summary, the equation that defines the link margin (LM) is given as [5, 205, 206]:

$$LM = P_t - \alpha_{geo} - R_s - \alpha_{syst} \tag{4.9}$$

where P_t is the total power of the emitter (dBm), α_{geo} is the geometrical attenuation, R_s is the receiver sensitivity (dBm) and α_{syst} represents all other system dependent losses in dB. It should be noted that the system loss in a FSO system stated in the link margin equation can be as a result of imperfect lenses including other optical elements like couplers. However, all other system dependent losses term in the definition are ignored in this present analysis. Therefore, the equation of the link margin has been reduced to the following:

$$LM = P_t - \alpha_{geo} - R_s \tag{4.10}$$

$$\alpha_{geo} = -20 \log\left[\frac{D_r}{(D_t + \theta d)}\right] \tag{4.11}$$

As shown in the reduced equation, the LM now depends only on the transmitted optical power, geometrical attenuation and the receiver sensitivity. Based on the analysis in this work, the following data are assumed for the optical link in order to compute the LM: $P_t = 16\ dBm$ and $R_s = -38\ dBm$. While the geometric losses are the losses that arise from the spreading of the transmitted optical beam. Therefore, when the optical beam spreads to about a size which is comparatively larger than the dimension of the aperture of the receiver, then the overfill energy will be lost. In general, for a particular optical link distance, smaller transmit divergences or larger receive apertures induce lesser geometric loss. In the calculation of the link margin, the geometric losses may be computed using Equation (4.11), for a uniform transmit power distribution with a no obscured transmitter or receiver. The calculation of the geometric losses is a function of diameter of transmit aperture (D_t), diameter of receive aperture (D_r), optical link range (d) and the beam divergence (θ). From the link specifications, we have $D_t = 0.08\ m$, $D_r = 0.1524\ m$ and $\theta = 2.8\ mrad$. Considering these link parameters, the geometrical attenuation per km can be computed by substituting them into the Equation (4.11). For the FSO link deployed at any location to survive, the atmospheric optical attenuation must not exceed the calculated link margin, or else the link will fail. Using the link specifications for the FSO system given earlier in this work, the link margin and the atmospheric attenuation were calculated for different visibility values

representing various atmospheric conditions or visibility classes at wavelength of $850\,nm$ over the optical link length and are shown in Figure 4.40. Table 4.10 presents the optical path length data obtained from the relationship between the link margin and atmospheric attenuations for the various visibility classes (using their upper-class boundary limit) for the FSO system with known specifications. From the results, it was observed that the FSO link at $\lambda = 850\ nm$ is expected to fail at link length of about 0.40 km, 0.85 km, 1.60 km, 2.80 km, 4.60 km, 8.30 km, 11.00 km 15.40 km, and 17.40 km for visibility class values with upper boundaries of 0.20 km, 0.50 km, 1 km, 2 km, 4 km, 10 km, 20 km, 50 km and 100 km respectively. The link margin curve displayed in the plot reveals that it decreases with the increase in the optical link length as the geometrical loss increases with the link length. The other curves in this figure represents the optical attenuations for visibility conditions given by the upper boundaries of each of the visibility classes. Therefore, it should be noted that when the atmospheric attenuation curves cross the curve of the link margin, then it can be said that the link will fail.

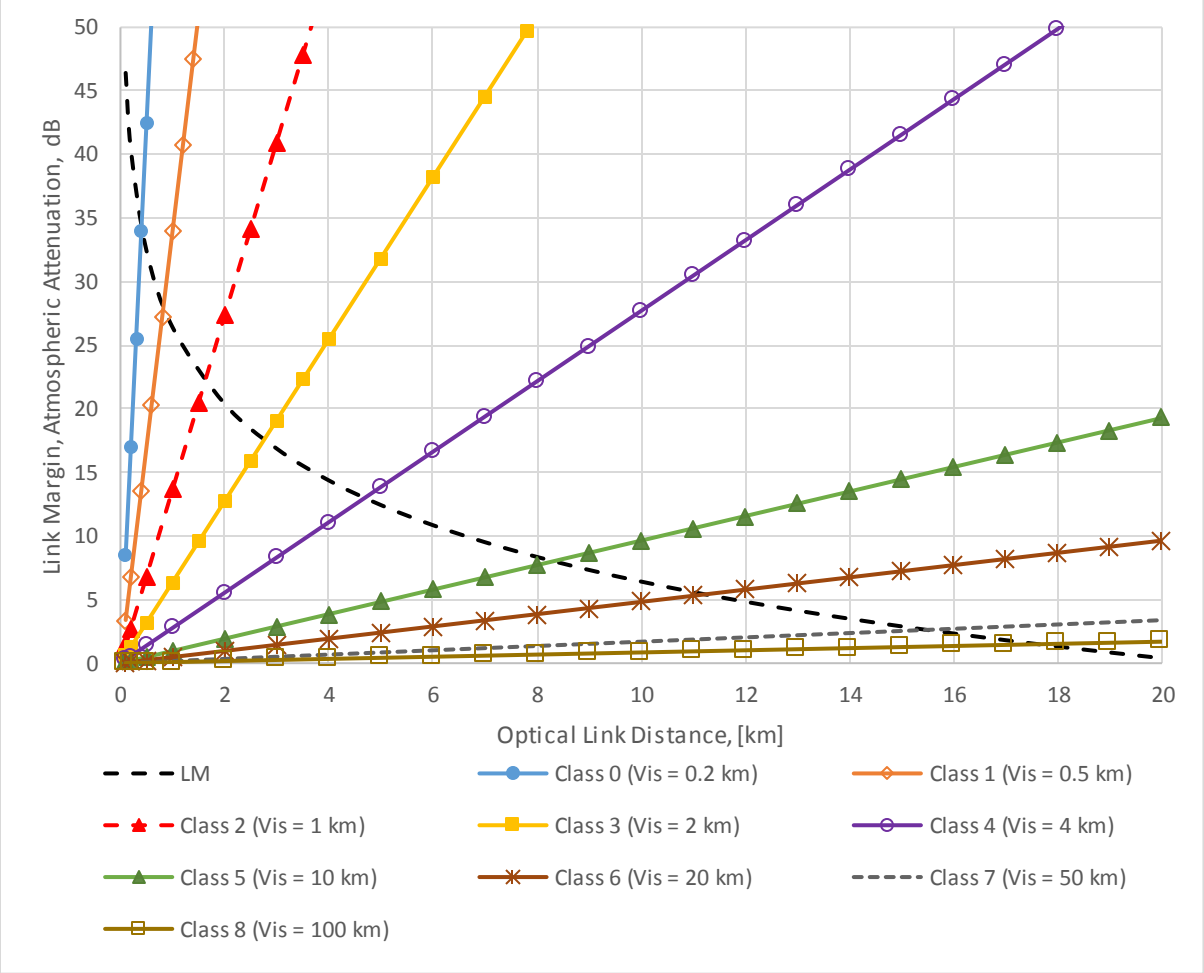

Figure 4.40: Link margin of the FSO system over the link range showing the performance of the FSO system with $P_t = 40\ dBm$, $R_s = -38\ dBm$ and at $\lambda = 850\ nm$, using the visibility of the Class boundary for each class range.

Table 4.10: Optical path length values obtained from the relationship between the link margin of the FSO system and various atmospheric conditions using $P_t = 40\ dBm$, $R_s = -38\ dBm$ and $\lambda = 850\ nm$.

Visibility Classes								
Class 0 $L_0\ (km)$	**Class 1** $L_1\ (km)$	**Class 2** $L_2\ (km)$	**Class 3** $L_3\ (km)$	**Class 4** $L_4\ (km)$	**Class 5** $L_5\ (km)$	**Class 6** $L_6\ (km)$	**Class 7** $L_7\ (km)$	**Class 8** $L_8\ (km)$
0.40	0.85	1.60	2.80	4.60	8.30	11.00	15.40	17.40

4.9.3 BER Performance Analysis of FSO link for South Africa

4.9.3.1 BER Performance for BPSK-SIM Modulation Scheme

The BER performance analysis was carried out for each of the months for all locations, using the monthly average optical attenuations and SNR. A comparison between the monthly BER performance against the optical distance are shown in this section. The BPSK-SIM modulation scheme was chosen as the initial modulation scheme due to its position in providing high power efficiency, and its BER is derived from [31]:

$$BER_{BPSK} = \frac{1}{2} erfc\left(\sqrt{SNR}\right) \tag{4.12}$$

Figure 4.41 illustrates the monthly BER performances of the optical link under various atmospheric conditions due to scattering for each of the locations over the year 2011. It is clearly shown from the plots that the distance between the transmitting laser and the receiving aperture are limited at very low BER of about 10^{-12} or less due to the increase in the exposure of the light wave to scattering.

According to these theoretical results, the worst months are mostly observed between May and August (which constitutes the autumn and winter months), while the most outstanding in this case are June and July. Nevertheless, at certain occasions, the attenuations during April and September also show considerable effects on the FSO system. For Durban over the year 2011, the average link distance L_{opt} (as shown in Figure 4.41a) during the very worst months are approximately 3.8 km, 1.8 km, 2.3 km and 3 km for May, June, July and August respectively at BER of 10^{-12}. Also, Cape Town has similar worst months with their average link distance given as 1.9 km, 1.9 km, 2.9 km and 3.0 km for May, June, July and August respectively, as shown in Figure 4.41b. In addition, the link distances for May, June, July and August are 3.0 km, 2.5 km, 1.95 km and 3.4 km respectively for Umtata for the same year. However, within the inlands such as Mafikeng (as shown in Figure 4.41f), the link distances are higher at BER of 10^{-12}, such that for the worst months of June and July the link distances reached up to 4.2 km and 4.8 km respectively. This shows that there is no need for any strong mitigation system for the FSO link within this city unlike in the maritime and near-maritime environments. This analysis suggests that in order to achieve a BER as low as 10^{-12}, the worst months especially June and July must be handled appropriately, by applying suitable mitigating techniques as described in Section 2.10.

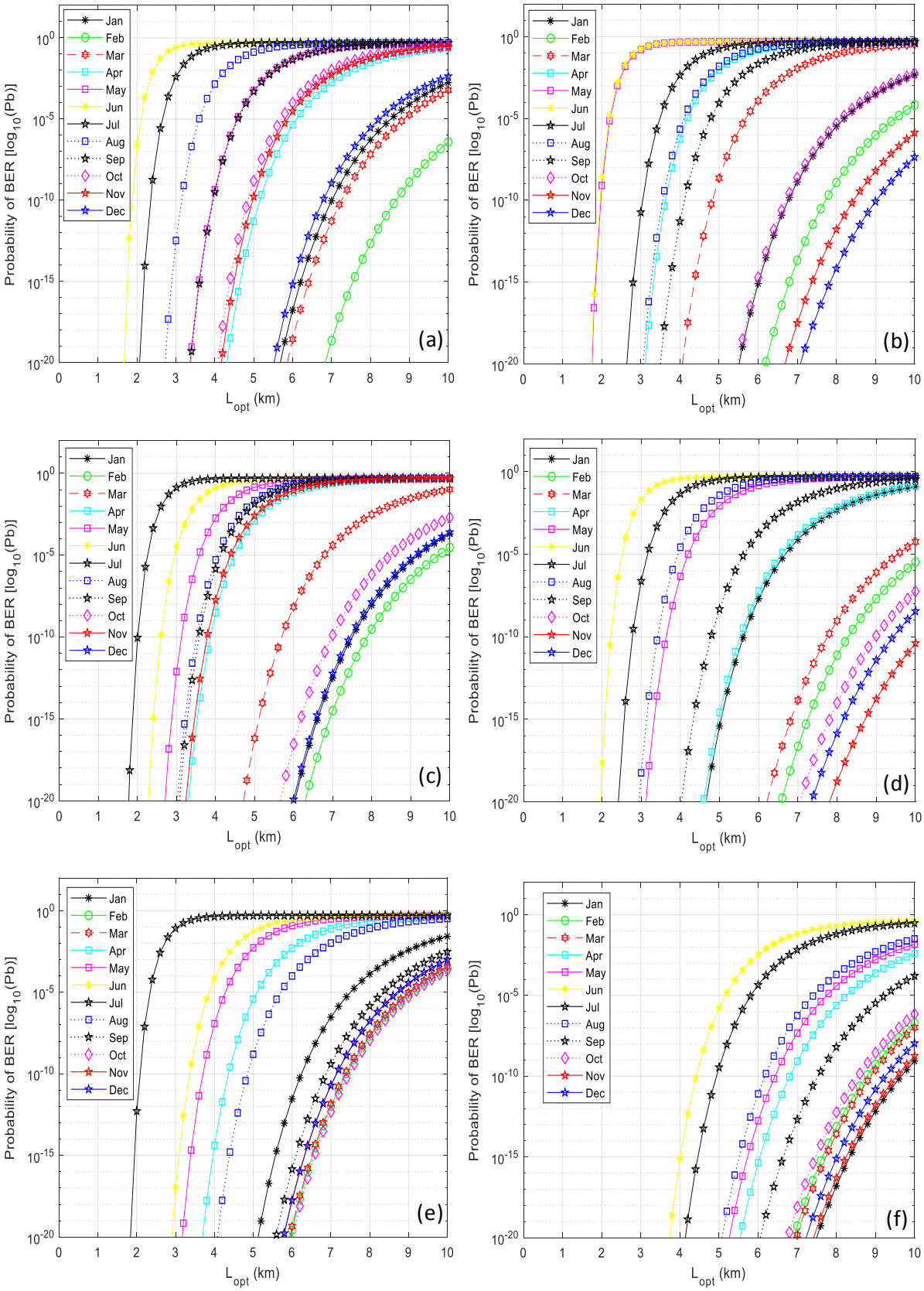

Figure 4.41: BER performance comparison of the FSO system during each month against the link distance under various atmospheric conditions due to scattering, using the monthly mean optical attenuation at 850 nm over the year 2011 for (a) Durban; (b) Cape Town; (c) Umtata; (d) Bloemfontein; (e) Johannesburg; (f) Mafikeng.

4.9.3.2 Mitigating the Effects of the Atmospheric Attenuation due to Scattering over FSO link

Power efficient mitigation techniques such as the Pulse Position Modulation (L-PPM) scheme is used in this analysis to reduce the effects of atmospheric attenuation due to scattering, and to increase the distance covered at BER of 10^{-12}. Therefore, this will improve the optimal performance of the FSO link within the locations considered in this study. The L-PPM (with L bits) was chosen since it is one of the best power efficient modulation schemes, and its theoretical BER equation is given as follows [52, 156]:

$$BER_{PPM} = \frac{1}{2} erfc\left(\frac{1}{2\sqrt{2}}\sqrt{SNR\frac{L}{2}\log_2 L}\right) \tag{4.13}$$

In overall, the atmospheric conditions dominant in June and July result into very great attenuation on the propagating optical signals at wavelength of $850\,nm$. This research has provided additional mitigation (other than just the PPM modulation enhancement) for those two months, by using a 4 × 4 MIMO spatial diversity technique with BPSK-SIM scheme. This is done to provide more improvement to the performance of the optical system to avoid link failure or outages. The block diagram of the MIMO system used in this work is shown in Figure 4.42.

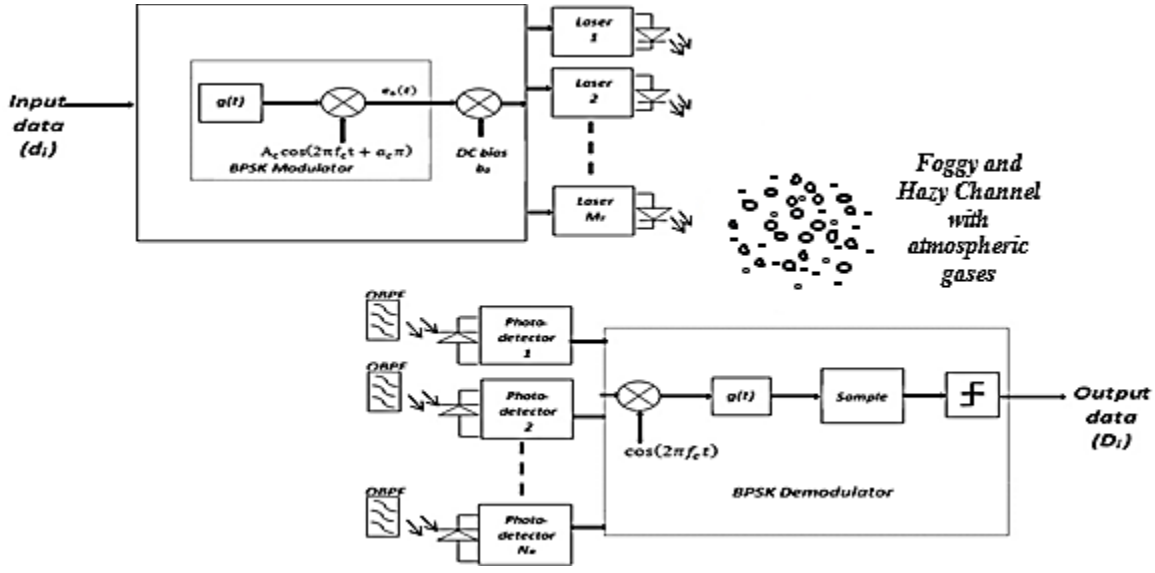

Figure 4.42: Block diagram of a MIMO FSO system with a BPSK-SIM scheme.

Figures 4.43 shows the BER performance comparison of SISO-BPSK, SISO-16-PPM and 4 × 4 MIMO-BPSK FSO systems during the worst months over the link distance for all the locations over the year 2011. To mitigate the effects of atmospheric attenuations, the PPM and 4 × 4 MIMO FSO systems were utilized, and it was noticed that these two methods were able to achieve the BER of 10^{-12} at higher distances than the BPSK modulation scheme. The results presented in this analysis shows improvements in the BER performance of the optical link based on the link distances in each of the locations, and the observed gain between the SISO-BPSK, SISO-PPM and the 4 × 4 MIMO-BPSK are shown in Table

4.11. It can be observed that the 4 × 4 MIMO improved the performance of the link with a gain of between 1.55 km and 5.45 km or more for both June and July, at BER of 10^{-12}, over all the locations.

In general, it was observed that the 4 × 4 MIMO system was a better improvement to the FSO system during the worst months over the 16-PPM scheme. Therefore, by applying any of 16-PPM or 4 × 4 MIMO spatial diversity technique to the FSO link within these locations will give good BER performance and power efficiencies. The 4 × 4 MIMO system was not necessary for Mafikeng during the month of July since it will give a result that does not include the BER of 10^{-12}.

Table 4.11: The average propagation distance and the estimated gain (in km) due to the improvement between the BPSK and the 4 × 4 MIMO FSO system at BER of 10^{-12}.

City	Average propagation distance (km)							
	June				July			
	BPSK	16PPM	4X4BPSK	Gain $_{BPSK\ -4X4BPSK}$	BPSK	16PPM	4X4BPSK	Gain $_{BPSK\ -4X4BPSK}$
Durban	1.85	2.20	3.40	1.55	2.30	2.80	4.40	2.10
Cape Town	1.90	2.30	3.60	1.70	2.90	3.70	6.00	3.10
Umtata	2.50	3.10	4.95	2.45	1.95	2.35	3.70	1.75
Bloemfontein	2.15	2.70	4.15	2.00	2.75	3.35	5.40	2.65
Johannesburg	3.25	4.10	6.85	3.60	2.00	2.45	3.80	1.80
Mafikeng	4.25	5.60	9.70	5.45	4.80	6.25	> 10.00	> 5.20

4.10 Summary

In this chapter, atmospheric attenuation due to scattering was investigated so as to test, validate, analyse and mitigate the impacts of fog, haze and clouds on FSO. Also, the system performance of free space optical link under the control of various atmospheric conditions were investigated and the necessary mitigating techniques were identified. The following deductions were obtained from this chapter:

(a) The minimum visibility value shown in the descriptive statistics of the visibility events obtained for each of the locations showed that there exist extreme fog conditions ranging from thick fog to light fog, such that most of the cities studied experiences thick fog. These minimum values were observed around the middle of the year which covers mostly the winter periods.

(b) The daily worst-case circumstances indicates that attenuation can sometimes get as high as 169. 81 dB/km or more, particularly in the maritime areas. Also, according to section 4.7.2, it was noticed that there will be several instances that the received optical power falls lower than receiver sensitivity of $-38\ dBm$.

(c) In section 4.9.1.4, the results of the SNR showed that there are several occasions within the day that resulted in the SNR falling below 10.5 dBm.

(d) According to section 4.9.1.6, the link availability shows that the same optical link can not be used for all the sites, hence, there is need to design appropriate link for individual sites.

(e) According to section 4.9.3, the 16PPM and 4X4 MIMO with BPSK schemes are appropriate mitigating techniques to achieve desirable results for all the locations studied.

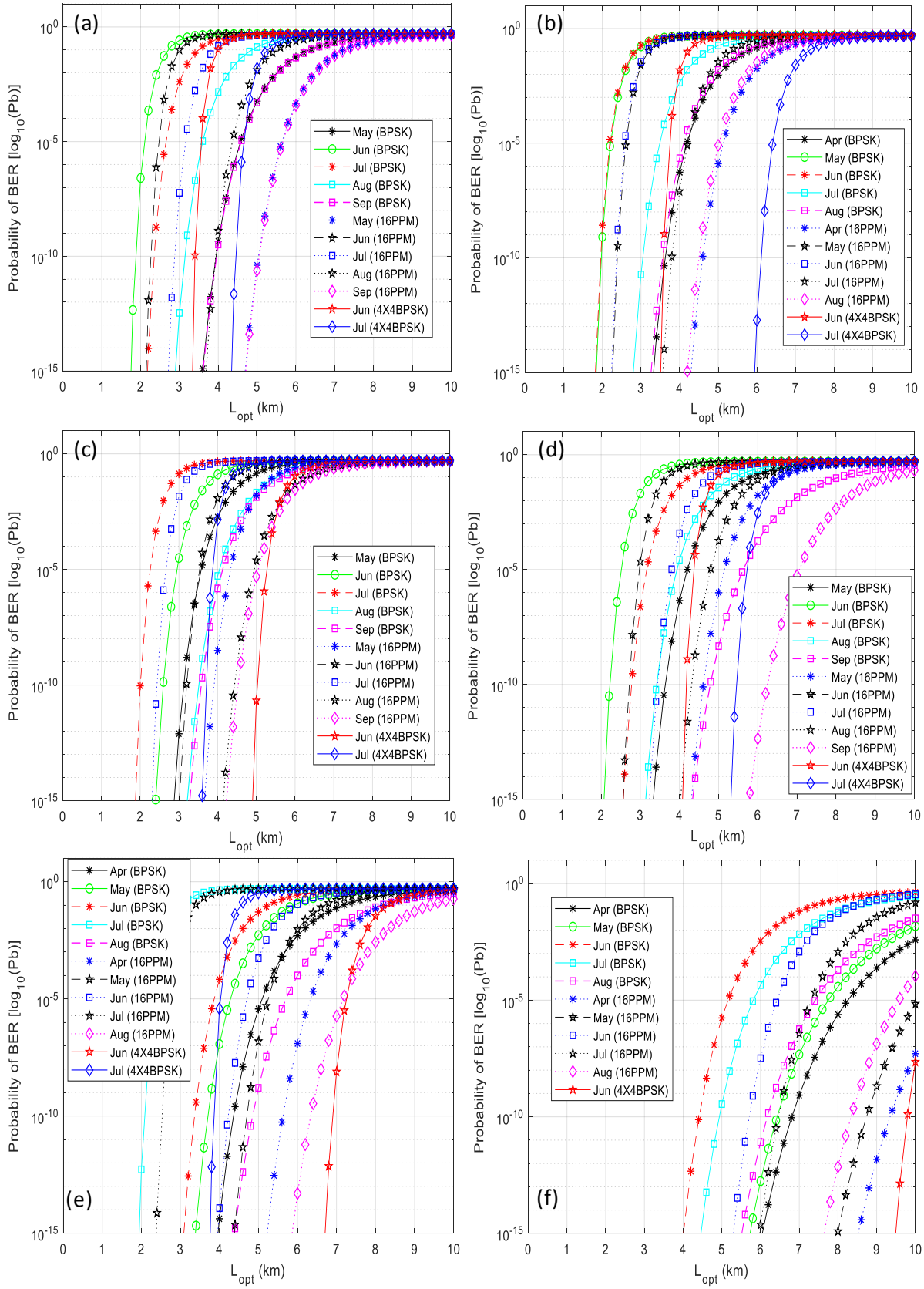

Figure 4.43: BER performance comparison of SISO-BPSK, SISO-16-PPM and 4 × 4 MIMO-BPSK FSO systems over link distance at 850 nm, during the worst months over the year 2011 for (a) Durban; (b) Cape Town; (c) Umtata; (d) Bloemfontein; (e) Johannesburg; (f) Mafikeng.

CHAPTER FIVE

Visibility Range Distribution and Optical Attenuation Modeling for Terrestrial Optical Link Design for South Africa

5.1 Introduction

The visibility range characterization earlier discussed in this thesis has provided estimations for the optical attenuations due to atmospheric scattering over FSO channels based on different atmospheric conditions or visibility classes. As a result of this characterization and estimations of the optical attenuations and received optical power, the visibility range distribution (VRD) and optical attenuation modeling for the optical link design in South Africa can be achieved using the climatic data for each of the considered locations over the three successive years (2011 – 2013).

This Chapter is focused on the statistical analysis and distribution modeling of the daily, monthly and seasonal variations of the optical attenuations under different atmospheric conditions that may be as a result of any of the four different climatic seasons in South Africa. In this analysis, three vital standard statistical quantities, that is, mean, standard deviation and median have been used to describe the monthly and seasonal variations and to adequately provide very important information on the variability, dispersion or location of the optical attenuation. In this chapter, the frequency of occurrence of the visibility range was examined first to understand the occurrence distribution of atmospheric events over the specified period, and then the statistical distribution for each visibility class was later studied. The seasonal and diurnal variations were also studied to determine the pattern of the optical attenuation across the locations considered, and this is accompanied by the various seasonal distributions. This was followed by the PDF modeling (with parametric distribution models) of the visibility range for all the locations, and the suitable models with their corresponding parameters were reported. Lastly, the optical attenuation modeling for various atmospheric conditions along the terrestrial FSO link was investigated using various CDF and CCDF models with curve fitting techniques.

5.2 Frequency of Occurrence of Visibility Range

5.2.1 Frequency of Occurrence of Visibility Range using Synoptic Data

Visibility range data of three hours (synoptic) measurement interval were collected for three successive years for each of the six locations considered in this study. The descriptive statistics of the monthly visibility data for all the three years are presented in Appendix II. Table 5.1 shows the number of visibility events for each given city and for the entire three years based on the respective visibility classes existing within each city. Also, the corresponding annual percentage value for each visibility class range are displayed. The 2-D Area plots shown in Figures 5.1 (a) – (f) present the typical discrete

sequence plots of the frequency of occurrence of the measured visibility range taken over a three-hour measurement interval data covering a successive period of three years for all the six cities considered in this study. According to the statistics in the table, there are quite a number of events with visibility below 1 km, which can be classified as the very worst-case periods for FSO links.

These results show several significant features, and it can be observed that:

1. The plotted frequency curves of the visibility range all have the same general behavior or pattern over each of the three years for all the six cities.
2. The frequency of occurrences of the lower visibilities decreased significantly in the continental environments when compared to the maritime environments, such that places like Mafikeng hardly even have events within the dense or thick fog conditions. Therefore, the frequency of occurrence of events with visibilities within the lower-class range (especially below 1 km corresponding to specific attenuation above 13.66 dB/km at 850 nm) also show a dependence on the location where the measurement was taken. In the course of the three-year period, there were 309, 448, 315, 192, 248 and 97 events equivalent to 3.52 %, 5.11 %, 3.59 %, 2.19 %, 2.83 % and 1.11 % of 3-Hour visibilities below 1 km (which is within the lower-class range) for Durban, Cape Town, Umtata, Bloemfontein, Johannesburg and Mafikeng respectively. The falling trend in frequency of occurrence of events with lower visibility values below 1 km is apparent in these statistics as the assessment is shifted from the maritime conditions to the continental conditions. This proposes that low visibility phenomenon is quite pronounced in the coastal regions than in the non-coastal region, and therefore merits more consideration during terrestrial FSO link budgeting within this coastal regions and Johannesburg inclusive. However, this is not to say that there are no occasional or perhaps regular and considerable optical attenuation at the non-coastal regions, such that the necessary measures and attention towards the non-coastal regions should be neglected. Therefore, as the visibility class range increases towards stronger visibilities, it is vital to note how higher visibilities or higher visibility classes continue to record higher events especially for the non-coastal areas. This observation which is more conspicuous in the non-coastal areas than in the coastal areas, buttresses the fact that there are high attenuations witnessed in the coastal areas.
3. All the visibility range measurements obtained for the cumulative years (2011-2013) within the maritime environments have modal visibility of 20 km, while the continental environments have their modal visibility as 30 km except for Johannesburg which also has 20 km modal visibility like that of the maritime environments. Therefore, since it can be noticed that the modal visibilities of coastal areas are significantly lower than that of non-coastal areas (except Johannesburg), this also buttresses the point that there are high attenuations witnessed in the coastal areas.

Therefore, based on the locations used in this study, it is obvious that strong atmospheric conditions such as fog are quite obvious in the maritime environments. Various investigations have reported that the fog droplet particles formed in the maritime environments are short-lived phenomena when compared to continental fog. The maritime fog particles tend to occur in clouds lasting only for a few hours at the most [22, 96, 189, 197-199]. As a result of the similarity observed in the shapes of the frequency curves, it can be suggested that one type or family of probability distribution function will be suitable to characterize or describe the distribution of the visibility range of all the cities considered in this study with some selection of the parameters of the distribution function.

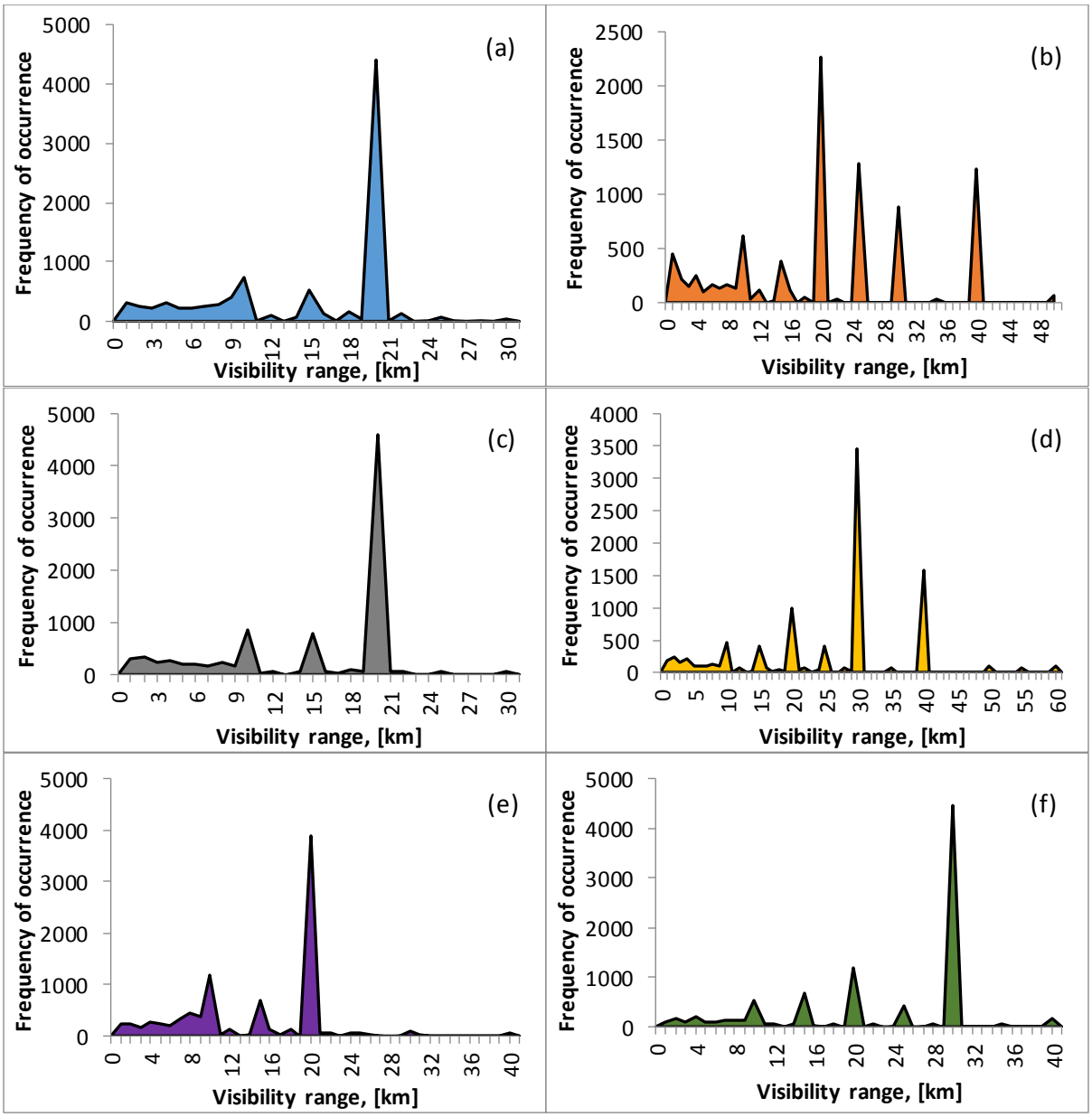

Figure 5.1: Frequency of occurrence of visibility range over the three years (2011-2013) for (a) Durban; (b) Cape Town; (c) Umtata; (d) Bloemfontein; (e) Johannesburg and (f) Mafikeng.

Table 5.1: Frequency and percentage of occurrence of visibility events over the cumulative years (2011-2013) for each of the location.

City		Visibility Class								
		Class 0	**Class 1**	**Class 2**	**Class 3**	**Class 4**	**Class 5**	**Class 6**	**Class 7**	**Class 8**
Durban	Number of Events	67	101	141	261	528	2079	5403	188	0
	Percentage of cumulative years (%)	0.76	1.15	1.61	2.98	6.02	23.71	61.62	2.14	0
Cape Town	Number of Events	83	183	182	215	397	1334	2958	3416	0
	Percentage of cumulative years (%)	0.95	2.09	2.08	2.45	4.53	15.21	33.74	38.96	0
Umtata	Number of Events	69	100	146	330	515	1850	5717	41	0
	Percentage of cumulative years (%)	0.79	1.14	1.67	3.76	5.87	21.10	65.20	0.47	0
Bloemfontein	Number of Events	25	54	113	229	365	1005	1462	5508	7
	Percentage of cumulative years (%)	0.29	0.62	1.29	2.61	4.16	11.46	16.67	62.82	0.08
Johannesburg	Number of Events	41	73	134	222	412	2776	5028	82	0
	Percentage of cumulative years (%)	0.47	0.83	1.53	2.53	4.70	31.66	57.34	0.94	0
Mafikeng	Number of Events	0	9	88	174	310	1070	2003	5114	0
	Percentage of cumulative years (%)	0.00	0.10	1.00	1.98	3.54	12.20	22.84	58.33	0

5.2.2 Frequency of Occurrence of Visibility Range based on Visibility Classes

The frequency of occurrence values obtained from the number of events of visibility based on the various visibility classes for each of the locations and for the three years in this study are presented in Figure 5.2. These results show the number of occurrences within each visibility class and a comparison between the occurrences of visibility and atmospheric conditions in each location for different years. It can be observed from these results that there are mainly two peaks in the regular pattern across the three years and these are Class 6 and Class 7. This can be used to classify all the locations into two, except Cape Town that was observed to spread across the two classes and does not clearly have a single peak all through the years. The explanation of the frequency of events have been separated into three major classes for clearer demonstration of the occurrences within the lower-class range which consist of fog conditions (especially below 1 km), the middle-class range of haze conditions and the upper-class range which is the clear air conditions. It also shows that there are lesser number of occurrences in the lower visibility classes and there are very high number of occurrences in the middle and upper visibility classes. Based on the frequency figures in Table 5.1, it is obvious that there are still a lot of events with visibility below 1 km (i.e., the very worst-case periods) for FSO links to contend with.

Considering the first three visibility classes across all the locations and over the year 2011 as shown in Figure 5.2a, these LVCs which are considered to be the worst-case classes have totals for their number of visibility events to be 115, 148, 107, 103, 86 and 31 for Durban, Cape Town, Umtata, Bloemfontein, Johannesburg and Mafikeng respectively. For 2012 as shown in Figure 5.2b, the totals of their number of visibility events are 100, 144, 104, 50, 79 and 30 for Durban, Cape Town, Umtata, Bloemfontein, Johannesburg and Mafikeng respectively. While for the year 2013 as shown in Figure 5.2c, the totals of their number of visibility events are 94, 156, 104, 39, 83 and 36 for Durban, Cape Town, Umtata, Bloemfontein, Johannesburg and Mafikeng respectively. Therefore, it is obvious from these results that the number of occurrences for the coastal areas clearly surpasses that of the non-coastal areas based on the worst-case classes. On the other hand, the non-coastal areas (especially Bloemfontein and Mafikeng) have peaks at Class 7 (i.e. very clear sky conditions), compared to coastal areas that have their peaks at Class 6 (i.e. clear sky), except for Cape Town in the years 2012 and 2013.

From the cumulative of all the years presented in Figure 5.2d, it can be observed that considering the first three classes (Class 0 to Class 2), which represent the dense/thick fog, moderate fog and light fog respectively, Cape Town has the highest number of occurrences with a total of 448 visibility events (with 83, 183 and 182 representing the three classes respectively). This is followed by the city of Umtata with a total of 315 (69, 100 and 146 events for the three classes respectively) and Durban with a total of 309 (67, 101 and 141 events for the three classes respectively), while the city of Mafikeng has the lowest total of about 97 (0, 9 and 88 events for the three classes respectively). The total of the visibility events within these three lower classes for the cities of Bloemfontein and Johannesburg are

192 and 248 respectively. This clearly shows that the coastal areas have very extensive occurrences for the lower visibility classes which will definitely result into greater risk of attenuation (as a result of more fog occurrences) on FSO links than the non-coastal areas.

From the results of the frequency of occurrences of the visibility range based on the various visibility classes, the following observations were deduced:

1. In general, it was observed in Figures 5.2a to 5.2d that the curves representing different locations show similarity in their pattern over all the years that were examined. This suggests that their distribution function may be quite similar, but with different distribution parameters due to the variation in their peaks.
2. From the results in Figures 5.2a to 5.2d, Durban, Umtata and Johannesburg, all regularly have their peaks at Class 6, while Bloemfontein and Mafikeng regularly have their peaks at Class 7. However, the city of Cape Town does not have a regular pattern for its peak, such that it had peaks at Class 6 in the year 2011 and then at Class 7 in the years 2012 and 2013. The unique characteristic of its randomness nature is that it widely spreads across several classes than the frequency of occurrence curves of the other cities.

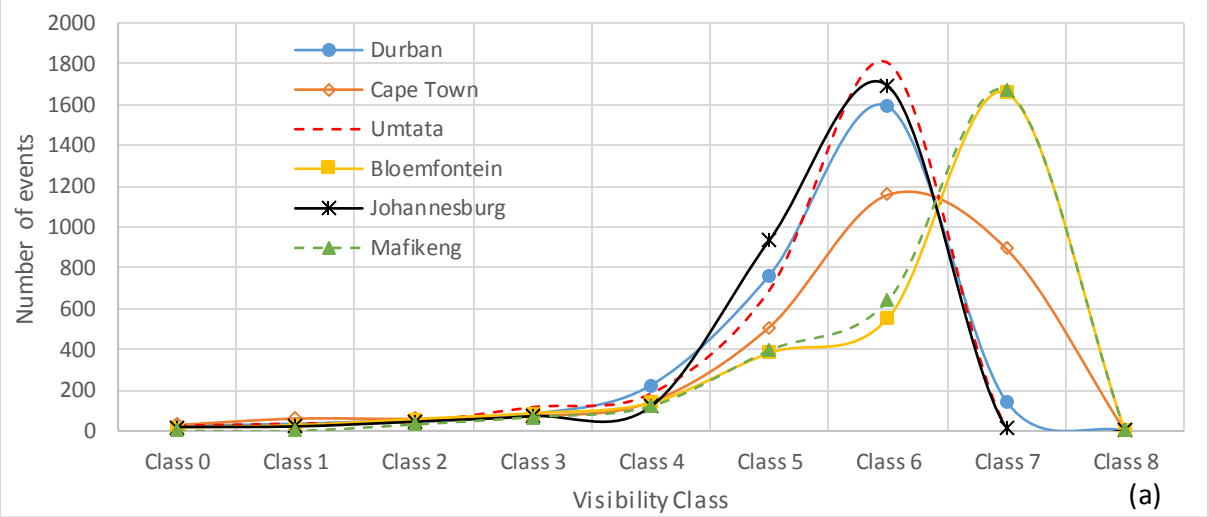

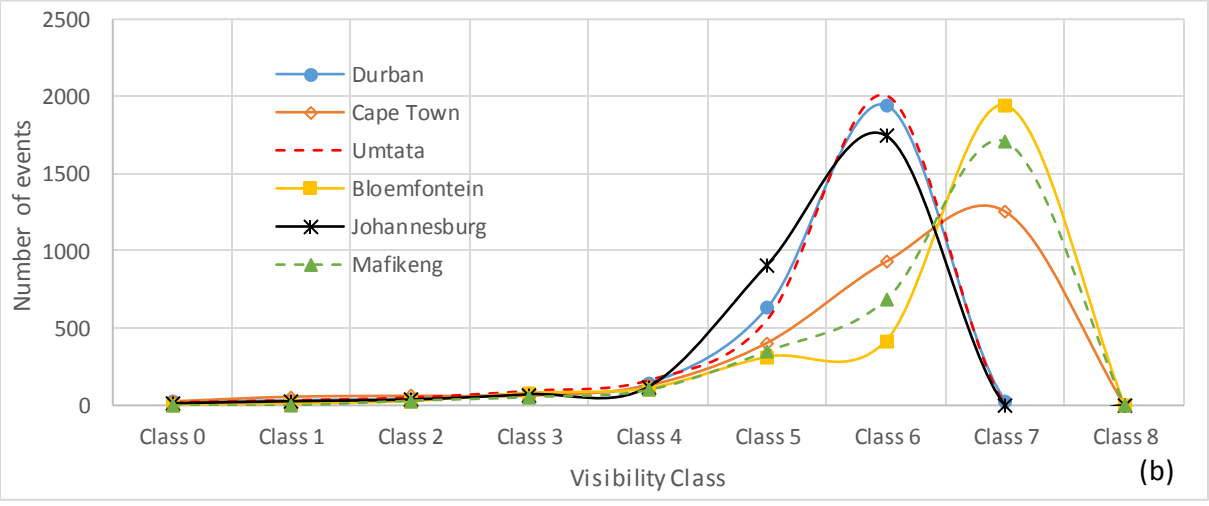

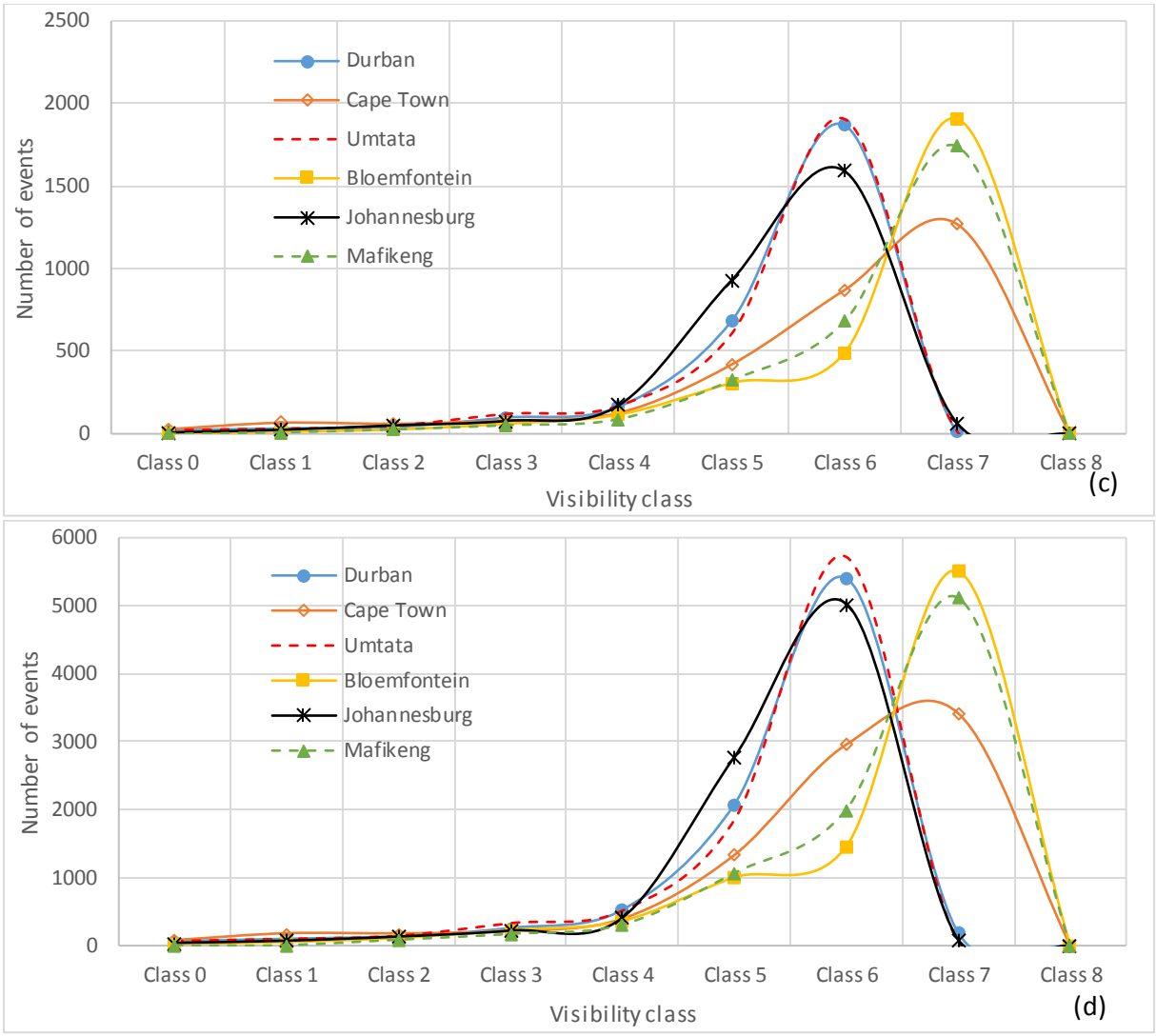

Figure 5.2: Frequency of occurrence based on different visibility classes for all the considered locations for the years (a) 2011; (b) 2012; (c) 2013 and (d) 2011-2013.

5.3 Monthly and Seasonal Variations of Optical Attenuation for South Africa

5.3.1 Seasonal Mean, Standard Deviation and Maximum of Specific Optical Attenuation

This part of the research work is focused on the statistical analyses of the seasonal and monthly variations, and trends of the optical attenuation due to different atmospheric conditions and seasons prevailing in South Africa. The optical attenuation obtained from the three-hour interval visibility range distributions are analyzed in terms of the mean, SD and maximum statistical descriptions, to describe the monthly and seasonal variations within the four different atmospheric seasons in Durban, Cape Town, Umtata, Bloemfontein, Johannesburg and Mafikeng, and are presented in Figures 5.3 to 5.5. These statistical distributions of the estimated optical attenuations are presented here in order to provide adequate responses to the serious problems arising from identifying the worst-case periods or seasons, locations, dispersion and magnitude. The monthly and seasonal variations of these statistical parameters for each of the cities considered are analyzed in order to get more insight about the relative magnitudes

of the optical attenuations (in particular, specific optical attenuations) obtained using the measured visibility range as well as their relative variability in each climatic season under different atmospheric conditions. These results will help to conveniently address various important FSO queries concerning which time or season as well as atmospheric condition(s) of the year within a specific location has on the average the largest optical attenuations resulting into the critical condition of the FSO channel (i.e., worst-case scenarios). Apart from this, it also gives response to queries bothering on which period or season of the year has the largest mean and variability or distribution of attenuation magnitudes, or in which season is the magnitude of optical attenuation within the atmosphere least predictable in the specified locations.

Figures 5.3 (a-c) show the plots of the monthly average specific optical attenuations for each of the three years and for all of the locations considered in this analysis, as a function of the month of year. These seasonal specific attenuation plots revealed that the trend of the monthly variations across all the cities considered is relatively comparable in each of the three years in this study. According to these results, a consistent monthly or seasonal periodicity of mean specific attenuation values for all the cities across the three years investigated in this study were noticed.

From Figure 5.3(a), it can be reported that for the year 2011 the peak monthly mean specific attenuation of approximately 9.52 dB/km was observed in the month of June and the minimum monthly mean specific attenuation of about 0.59 dB/km was observed in February for Durban. During the same year, the peak mean specific attenuation of approximately 9.91 dB/km was observed in the month of June and minimum mean specific attenuation of about 0.52 dB/km was observed in December for Cape Town. Also, the highest mean specific attenuation of approximately 8.85 dB/km was observed in the month of July and minimum mean specific attenuation of about 0.74 dB/km was observed in February for Umtata. For Bloemfontein, the peak mean specific attenuation of about 7.58 dB/km was observed in the month of June and minimum mean specific attenuation of about 0.37 dB/km was observed in November. The peak mean specific attenuation of approximately 8.40 dB/km was observed in the month of July and minimum mean specific attenuation of about 0.85 dB/km was detected in October for Johannesburg. Lastly, the peak mean specific attenuation of approximately 2.47 dB/km was noticed in the month of June and minimum mean specific attenuation of about 0.43 dB/km was observed in January for Mafikeng. Similarly, year 2012 and 2013 have similar results and trends to that obtained for year 2011.

In particular, the following observations are noticed as uppermost significance in this analysis:

1. In general, it was observed from all these monthly statistics and mean attenuation plots that the monthly mean specific attenuation values obtained within the winter months of June to August (especially June/July) were consistently far higher than the monthly mean values observed in the summer months of December to February across the three years and for all the locations

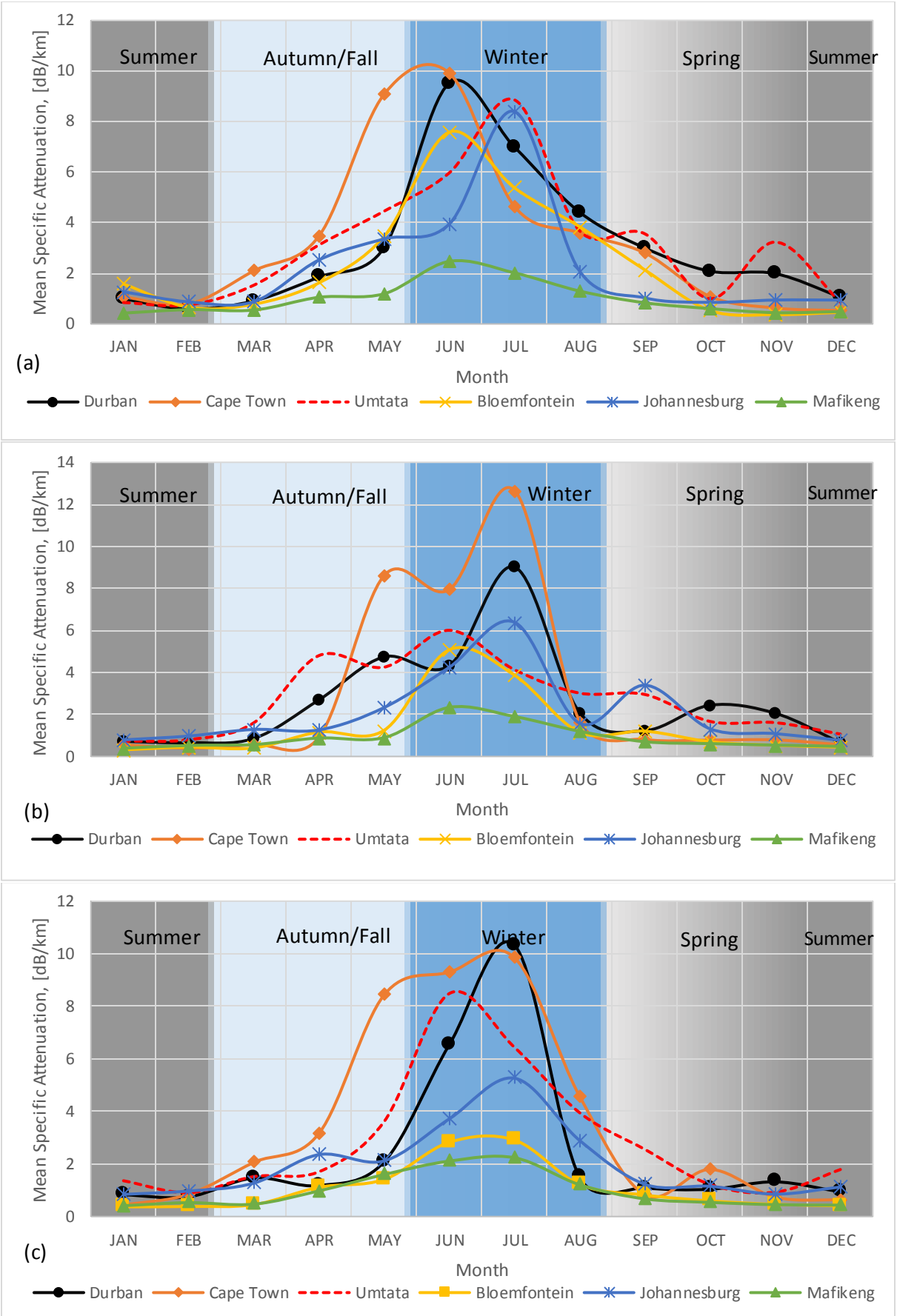

Figure 5.3: Monthly and seasonal periodicity of the mean specific attenuation for (a) 2011; (b) 2012 and (c) 2013, for all the locations considered in this study.

under study. Although, the monthly mean specific attenuation values observed in the winter seasons were consistently higher than the average values observed in the autumn/fall months of March to May (where May has the highest mean specific attenuation among them all) and far higher than in the spring months of September to November.

2. In this analysis, it was observed that the highest monthly mean specific attenuations across the entire period of study for the coastal areas reached as high as 10.32 dB/km in the month of June of 2013, 12.66 dB/km in June of 2012 and 8.85 dB/km in July of 2011 for Durban, Cape Town and Umtata respectively. Whereas, the highest monthly mean attenuations over the same period for the non-coastal areas were observed to be 7.58 dB/km in the month of June of 2011, 8.40 dB/km in July of 2011 and 2.47 dB/km in June of 2011 for Bloemfontein, Johannesburg and Mafikeng respectively. Comparing the peak and minimum monthly mean specific attenuations of the coastal and non-coastal environments shows that coastal areas including Johannesburg have the highest peak monthly mean specific attenuations all through the years and climatic seasons, while that of the non-coastal are lower all through the three years period under study. Though, all the locations (whether coastal or non-coastal) obviously have their monthly mean attenuation peaks (either large or small) during the winter season and a stable or almost constant value during the summer seasons across all the years. Thus, it can be deduced that the monthly influence of atmospheric conditions such as fog and haze within the coastal areas over the FSO channels within these regions should be taken very seriously. It can also be seen that the monthly effects of the non-coastal areas (especially in Bloemfontein and Johannesburg) are also considerable and should also not be ignored.
3. Across all the years and locations, the summer months or seasons show stable and very low monthly mean specific attenuations with maximum at 1.79 dB/km, such that most of the specific attenuations during this period for the coastal areas are below 1.40 dB/km (except in December 2013 where the value for Umtata was 1.79 dB/km), while most of those for the non-coastal areas are around or below 1.00 dB/km. This suggests that the summer months or seasons pose lesser threats to the terrestrial FSO link than the other seasons, whether it is located in the coastal or non-coastal area.
4. Also, it can be observed from the plots that towards the end of the summer periods there exist a starting point for a gradual rising of the monthly mean specific attenuation into the autumn periods, whereby the transition periods were observed from February to March. The features and properties of the autumn/fall months obviously show an inclining trend for a continuous rising of the monthly mean specific attenuation through the winter months which shows the peak of the specific attenuation which is short lived. The characteristics of the spring months or seasons apparently reveal a starting point for a continuous dipping of the monthly mean specific attenuation into the summer months which have constant lower mean specific

attenuation. Therefore, the characteristics of the months of May and June as transition months from autumn to winter seasons are likewise evident from the plots of the mean specific attenuation, as there appears to be consistent rise around May before a steady rising trend through the winter season which takes center stage. On the other hand, the features of August and September as transition months from winter to spring seasons are as well evident from the mean specific attenuation plots. There appears to be consistent dip around September before a little bulge (though not conspicuous in all the cities) in the middle of the spring periods. The characteristics of November and December as transition months from spring to summer seasons are equally significantly evident from the plots of the mean specific attenuation, as there appears to be a consistent drop in the mean specific attenuation after the observed bulge.

5. Therefore, according to the cities considered from the six different provinces which spread across the whole country, the season of the year across South Africa that on the average have the highest mean specific attenuation (which results to the worst-case scenarios with high light wave transmission risks) are the months of June, July and August indicating the winter season, whereas December, January and February which are the summer months have the lowest mean values of the specific attenuation across the three years used in this study.

Another statistical parameter computed and analyzed in this work is the standard deviation of the specific optical attenuation (σ_a) for each month of the three years and for all the locations. This statistical description provides the summary information about the dispersion of specific attenuation values in each month about its mean value as earlier explained. Figures 5.4 (a-c) which present the monthly periodicity of the standard deviation of specific attenuations for the three years and for all the locations, show similar observations to that of the mean specific attenuation. This means that it is in strong correspondence to that of its mean, and therefore buttresses the same points as were discussed and concluded above. Also, just like the inferences from the mean patterns, months or seasons experiencing high monthly mean specific attenuation values (i.e., the worst-case conditions) are also the same months having high variability and scattering, and are seen to be unstable as well as at high risk to the optical link. Although, those months with low values of monthly mean specific attenuations have SD values that are closely clustered around the mean and low impairments to the optical link.

Figure 5.5 shows the plot of the maximum specific attenuations for the three years and for all the locations, in terms of the months and seasons of the year. These results show that autumn, winter and spring (in particular, September and November) seasons are the most worst-case months and seasons with specific attenuation reaching as high or above 169.81 dB/km across all the entire three years (2011-2013). It should be noted that as a result of these results, we can have specific optical attenuations as high as 84.90 dB/km under the summer periods in all of the locations (either coastal or non-coastal). However, looking closely at the plot of the maximum attenuations, it can be generally noticed that it is the coastal areas that mostly have specific optical attenuations reaching about or above 169.81 dB/km

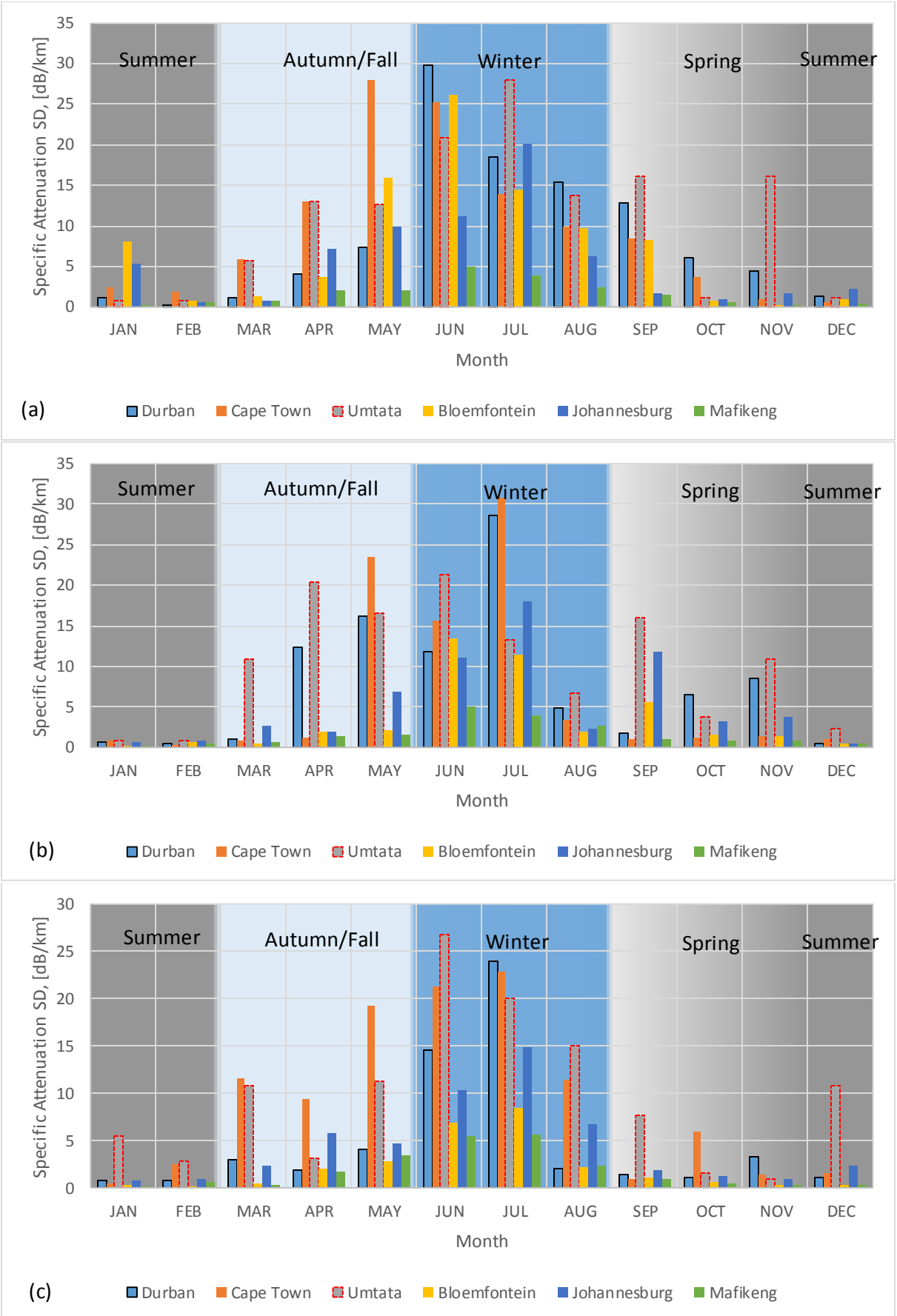

Figure 5.4: Monthly and seasonal periodicity of the standard deviation of the specific attenuation for (a) 2011; (b) 2012 and (c) 2013, for all the locations considered in this study.

within the worst-case months and seasons, with inclusion of Bloemfontein in May and June, while the results show that the maximum specific attenuations of non-coastal areas are generally about or below 84.90 dB/km across all the periods or seasons (except in Bloemfontein as discussed earlier).

Therefore, on an annual basis, it can be observed from these results that there exist a vivid monthly and seasonal variation of specific optical attenuation and its corresponding dispersion. It should be noted that the maximum specific optical attenuations for each of the locations can possibly go higher than 169.81 dB/km if a more lower measurement interval resolution was used (like 1-minute or 30-minute interval scale) or if a more sensitive visibility measuring device (that can measure visibility values within the tens of meters range) were used.

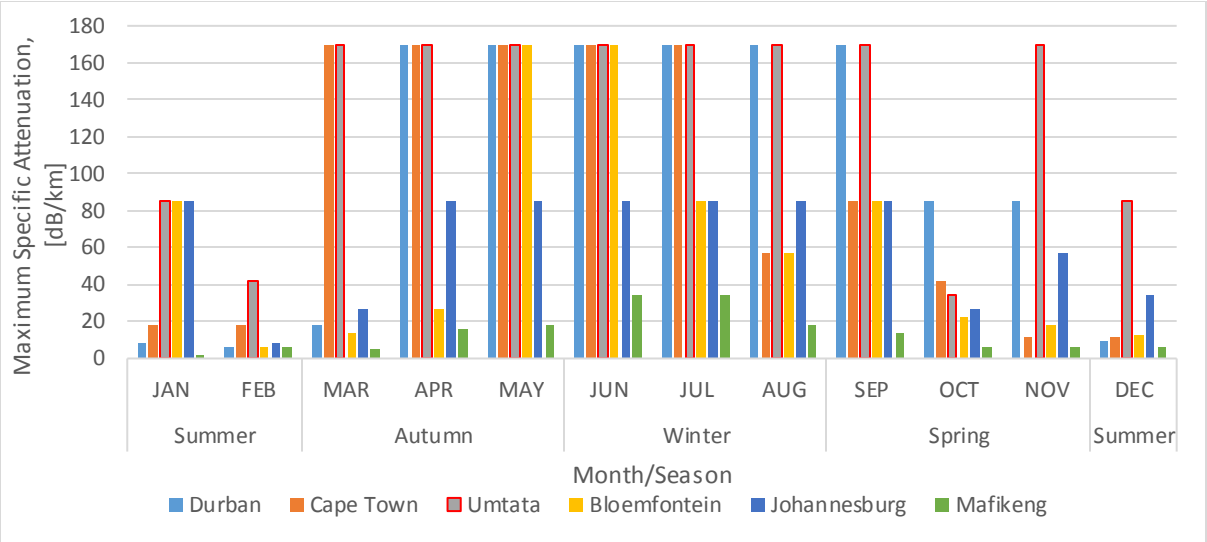

Figure 5.5: Monthly maximum specific attenuation over the entire period (2011-2013) for all the locations considered in this study.

5.3.2 Diurnal Variation of Atmospheric Optical Attenuation for South Africa

The diurnal variation of atmospheric optical attenuation is studied in this subsection, and its knowledge which is very important for FSO services within South Africa will definitely provide useful information on whether there exists any dependence of optical attenuation on the time or period of the day. Therefore, in the case where a suitable optical link design and optimal link performance system are required, this phenomenon will enable the atmospheric scattering (due to fog, haze and clouds) or turbulent (due to scintillations) periods to be taken into great consideration. In order to offer more information about the existence of any dependence of atmospheric attenuation on the time of the day, the three-hour resolution specific attenuation datasets were grouped and analysed based on the hour of the day, for each of the years and for each location. In this analysis, the overall diurnal mean, median and SD of the specific attenuations were examined in order to analyse its averages and variations.

Figures 5.6 and 5.7 which show the diurnal variations of the mean and median summarizes the magnitude and the middle value of attenuations, while Figure 5.8 which shows the diurnal variations of

the SD summarizes the variability of the attenuations in each three hours interval over each year and for each of the locations. Also, Figure 5.9 presents the diurnal variation of monthly mean specific attenuation for all the locations over the entire period. Due to the fact that the skewed frequency distribution condition (i.e., a situation where the specific attenuation datasets consist of very large and very small values) exist in this case, therefore the diurnal median was investigated.

In summary, the following observations were deduced from the obtained results:

1. It can be noticed from all the plots of the overall mean, median and SD of the diurnal variations of the specific attenuations that they all have similar patterns.
2. The attenuations between 9:00 am and 9:00 pm are observed to be mostly below $1\ dB/km$, while the attenuations between 12:00 am and 6:00 am are mostly above $1\ dB/km$ and reaching up to $13.39\ dB/km$ (especially, around 3:00 am for Umtata in the year 2011) according to the patterns of the diurnal mean specific attenuation. This means that the specific attenuation is noticed to be lowest during the day-time and extends partly into the early hours of the night-time, and it is highest during the night-time hours through the early morning hours for all the locations. This corresponds to why visibility is highest during the day.
3. Moreover, it was discovered from Figure 5.6 that during the day light hours of about 9:00 am in the morning the specific attenuation decreases steadily and thus attaining a minimum between 12:00 pm and 3:00 pm in the afternoon, and therefore rising gradually until the night-time of around 9:00 pm.
4. Also, the general level of the median specific attenuation is distinctively approximately constant during day-time hours.
5. According to the results of diurnal variation of standard deviation of specific attenuation shown in Figure 5.8, it was observed that during the day-time hours the specific attenuation is least variable and most variable at night and early morning. In general, the variability during the day-time was lower than $10\ dB/km$, while during the night-time hours the variability reached as high as approximately $31.01\ dB/km$ (as observed around 3:00 am in 2011 for Cape Town).

Therefore, on an annual basis, it can be observed from these results that there exist a clear diurnal variation of specific attenuation and its corresponding distribution spread. As a result of the fact that a three-hour interval scale was used in this work, the exact period at which the daily attenuation is highest or lowest for each day might not be visible on these plots, considering the time scales that are not appearing on the graphs. Although, a range can only be determined for this case. Based on the synoptic interval scale, it was generally observed that specific attenuation is highest between 9:00 pm and 9:00 am (though the graphs suggest that the possible exact time to achieve maximum attenuation is by 3:00 am) and lowest between 9:00 am and 9:00 pm. Therefore, it is estimated from the graphs that high attenuations will occur any time after 9:00 pm to any time before 9:00 am, but the exact time to

encounter the highest attenuation cannot be ascertained due to the time interval limitations. Similarly, the occurrences of the lower variable attenuations (as shown in Figure 5.8) are noticed from 9:00 am to 9:00 pm, and as observed from the synoptic graphs, the most dispersed is around 3:00 am. But when the interval scale limitation is circumvented, high dispersion may take place any time after 9:00 pm to any time before 9:00 am.

Also, it was deduced from Figures 5.9 (a-f) that the diurnal variation of monthly mean specific attenuation for all the locations over the entire period, all have the same pattern which is likewise similar to the plots in Figures 5.6, 5.7 and 5.8. In general, it can be said that the months of April, May, June, July and August (which mostly constitutes the winter and autumn seasons) show very high monthly mean specific attenuations during the early hours of the morning and at night (i.e., after 9:00 pm to before 9:00 am corresponding to the 'peak hours'). During these months, in the coastal locations, the average attenuations span from 6.75 dB/km to 43.53 dB/km at 3:00 am, while in the inland locations it varies from 3.34 dB/km to 33.57 dB/km around the same time. This reveals that at 3:00 am in South Africa, the atmospheric attenuation can get as high as 43.53 dB/km, and consequently resulting into havoc to the transmission of optical signals through the atmosphere. Consequently, this will then need strict mitigating actions to avoid any challenges on the functions and performances of the optical link. However, during the peak hours, the mean values are quite lower in the spring season than in the winter and autumn periods, and during the summer months the values are continuously minimal or even during the less peak hours (which is from 9:00 am to before 9:00 pm) and are very low during the peak hours.

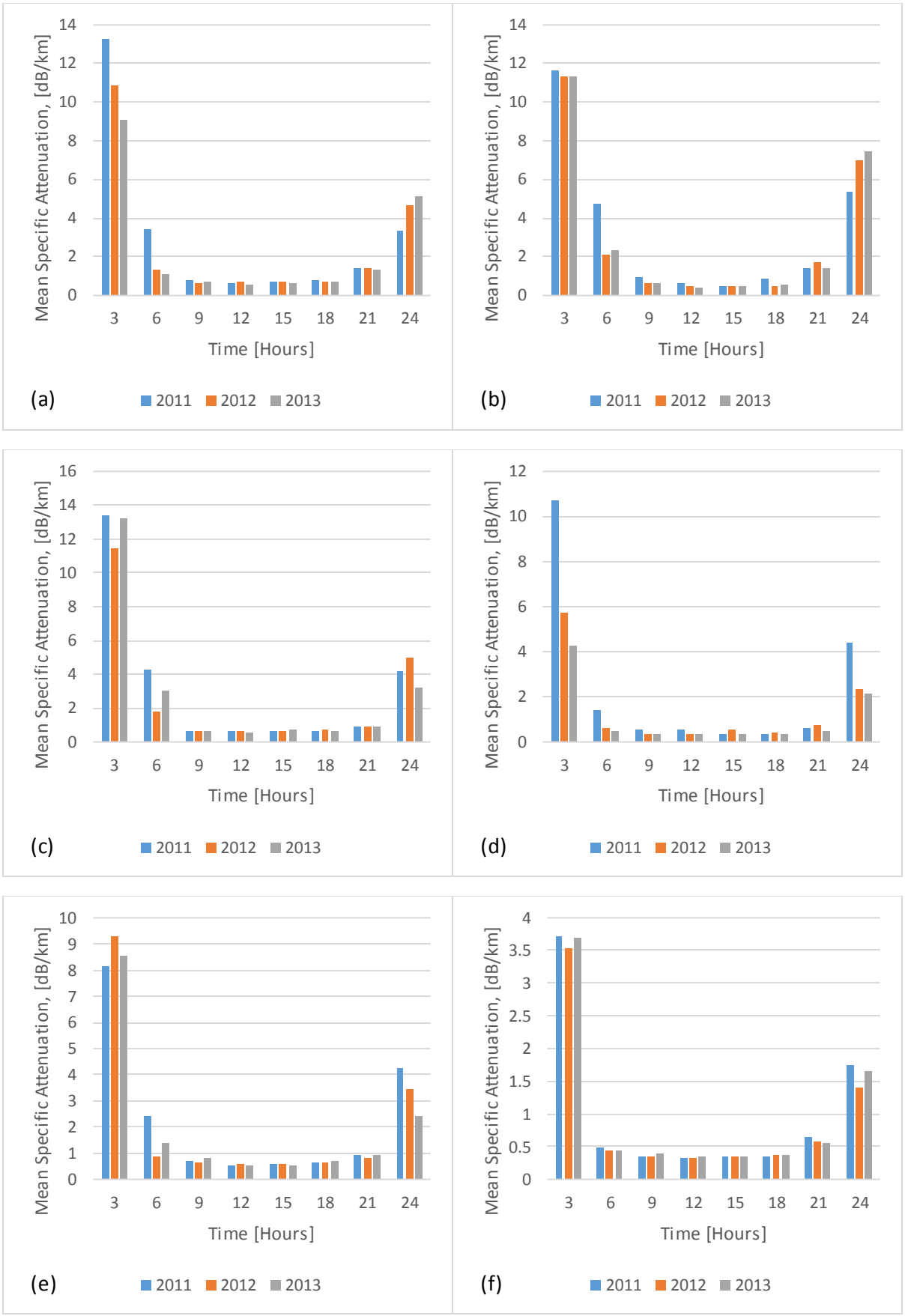

Figure 5.6: Diurnal variation of annual mean specific attenuation for (a) Durban; (b) Cape Town; (c) Umtata; (d) Bloemfontein; (e) Johannesburg and (f) Mafikeng, for the years 2011 to 2013.

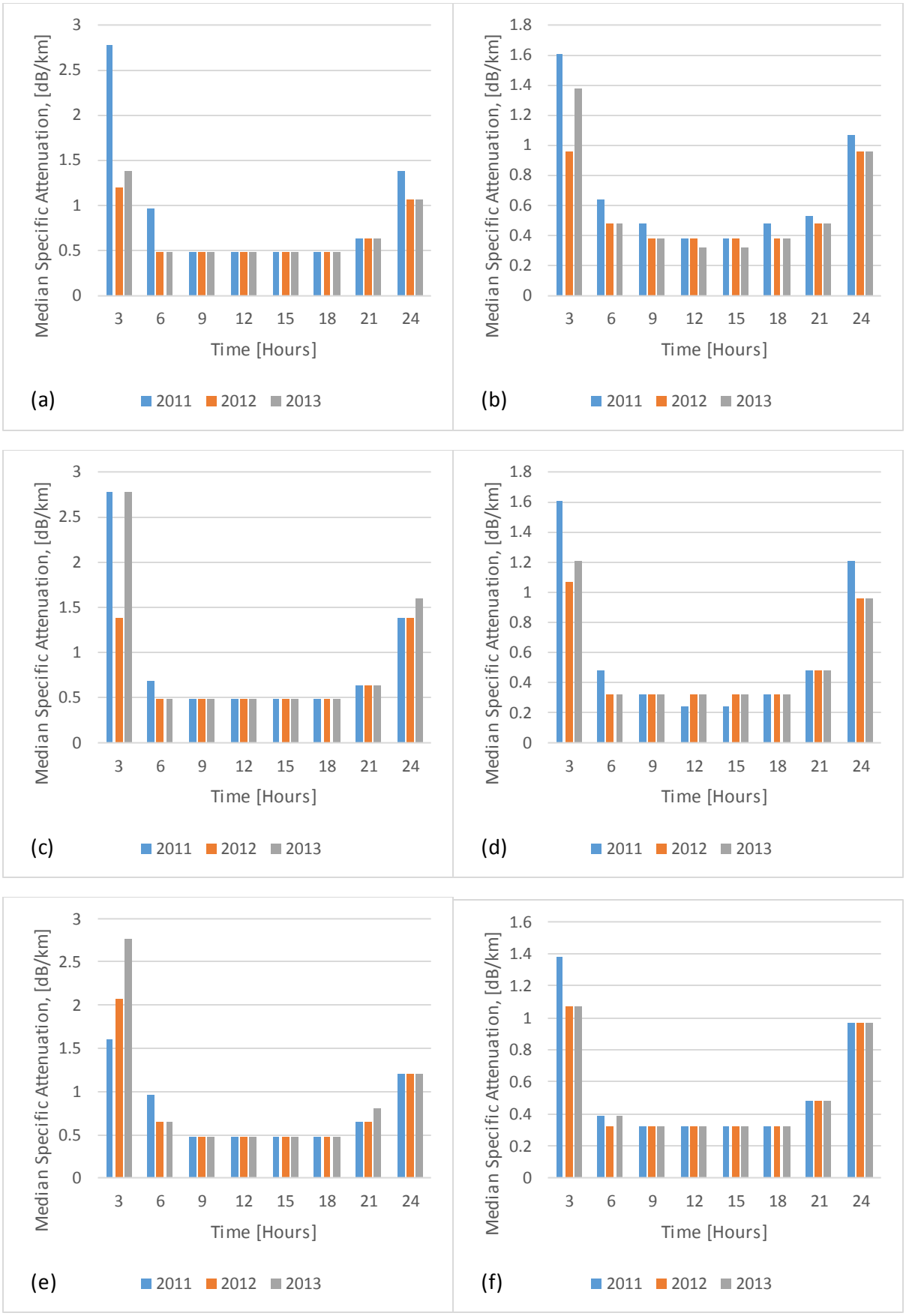

Figure 5.7: Diurnal variation of annual median of specific attenuation for (a) Durban; (b) Cape Town; (c) Umtata; (d) Bloemfontein; (e) Johannesburg and (f) Mafikeng, for the years 2011 to 2013.

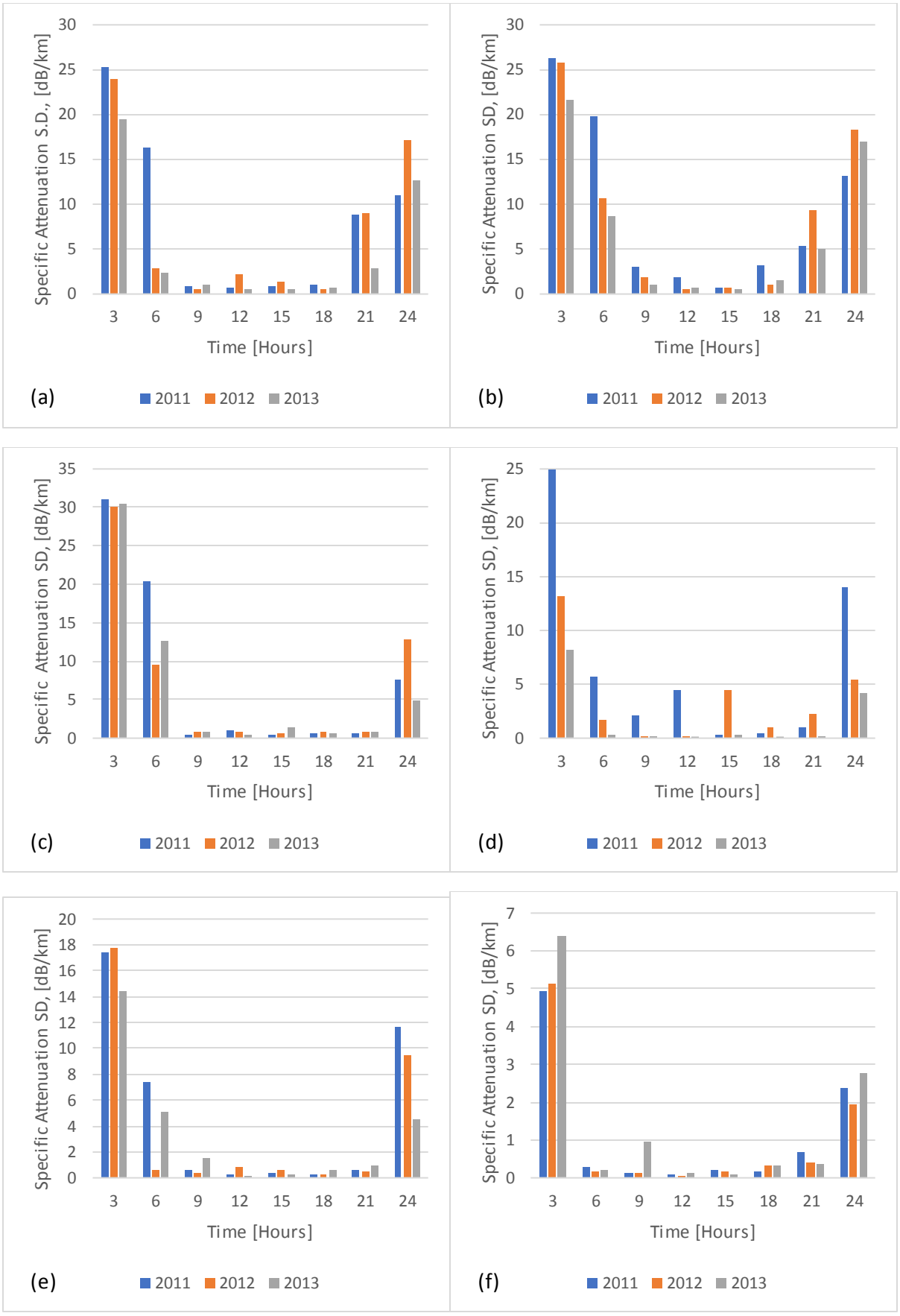

Figure 5.8: Diurnal variation of standard deviation of specific attenuation for (a) Durban; (b) Cape Town; (c) Umtata; (d) Bloemfontein; (e) Johannesburg and (f) Mafikeng, for the years 2011 to 2013.

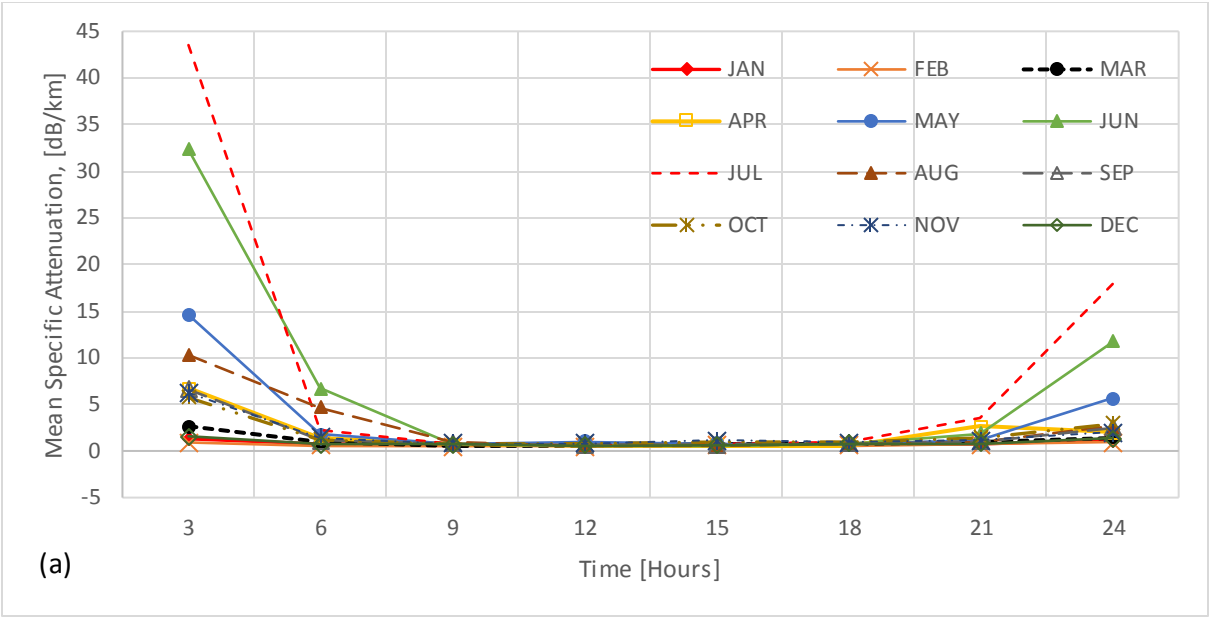
Mean Specific Attenuation, [dB/km]
45
40
35
30
25
20
15
10
5
0
-5
3
6
9
12
15
18
21
24
Time [Hours]
JAN
FEB
MAR
APR
MAY
JUN
JUL
AUG
SEP
OCT
NOV
DEC

(a)

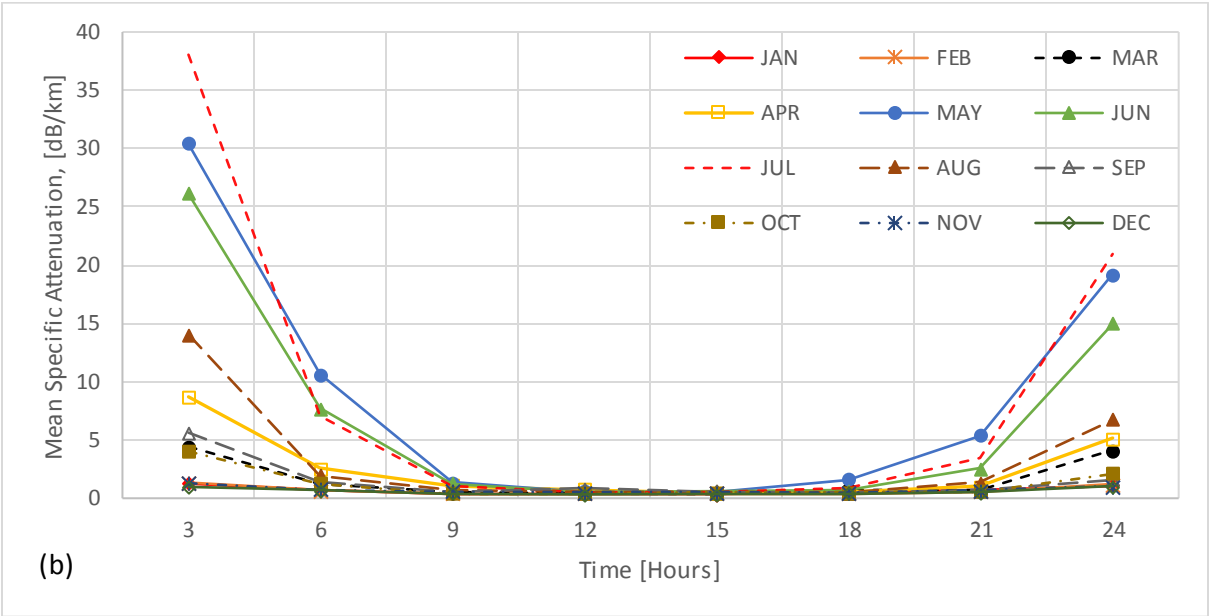
Mean Specific Attenuation, [dB/km]
40
35
30
25
20
15
10
5
0
3
6
9
12
15
18
21
24
Time [Hours]
JAN
FEB
MAR
APR
MAY
JUN
JUL
AUG
SEP
OCT
NOV
DEC

(b)

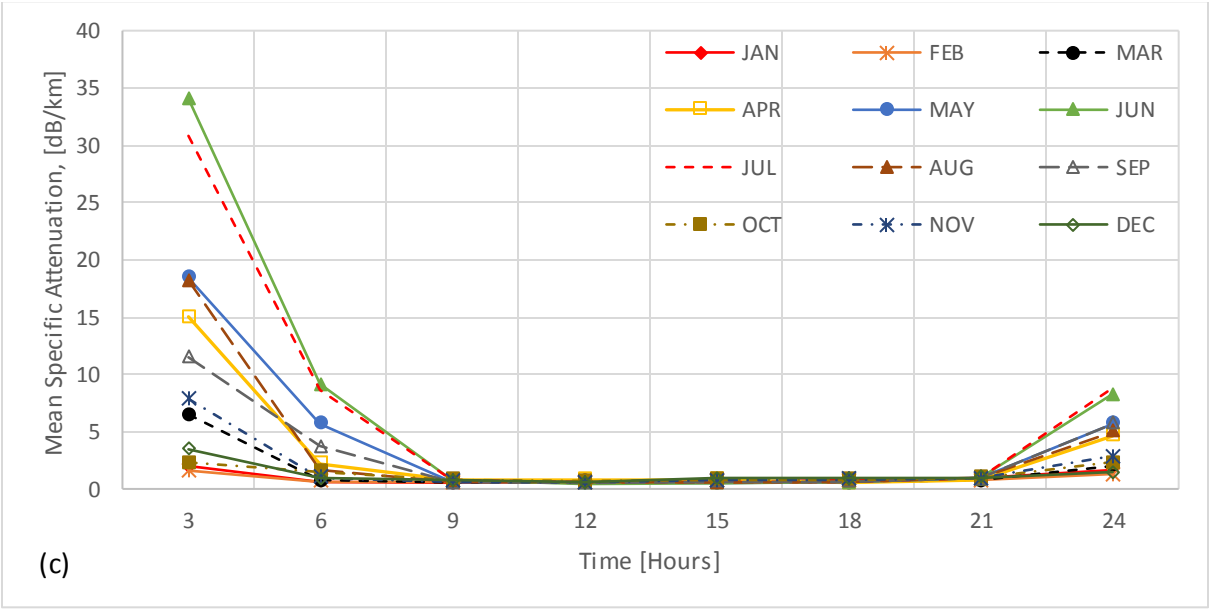
Mean Specific Attenuation, [dB/km]
40
35
30
25
20
15
10
5
0
3
6
9
12
15
18
21
24
Time [Hours]
JAN
FEB
MAR
APR
MAY
JUN
JUL
AUG
SEP
OCT
NOV
DEC

(c)

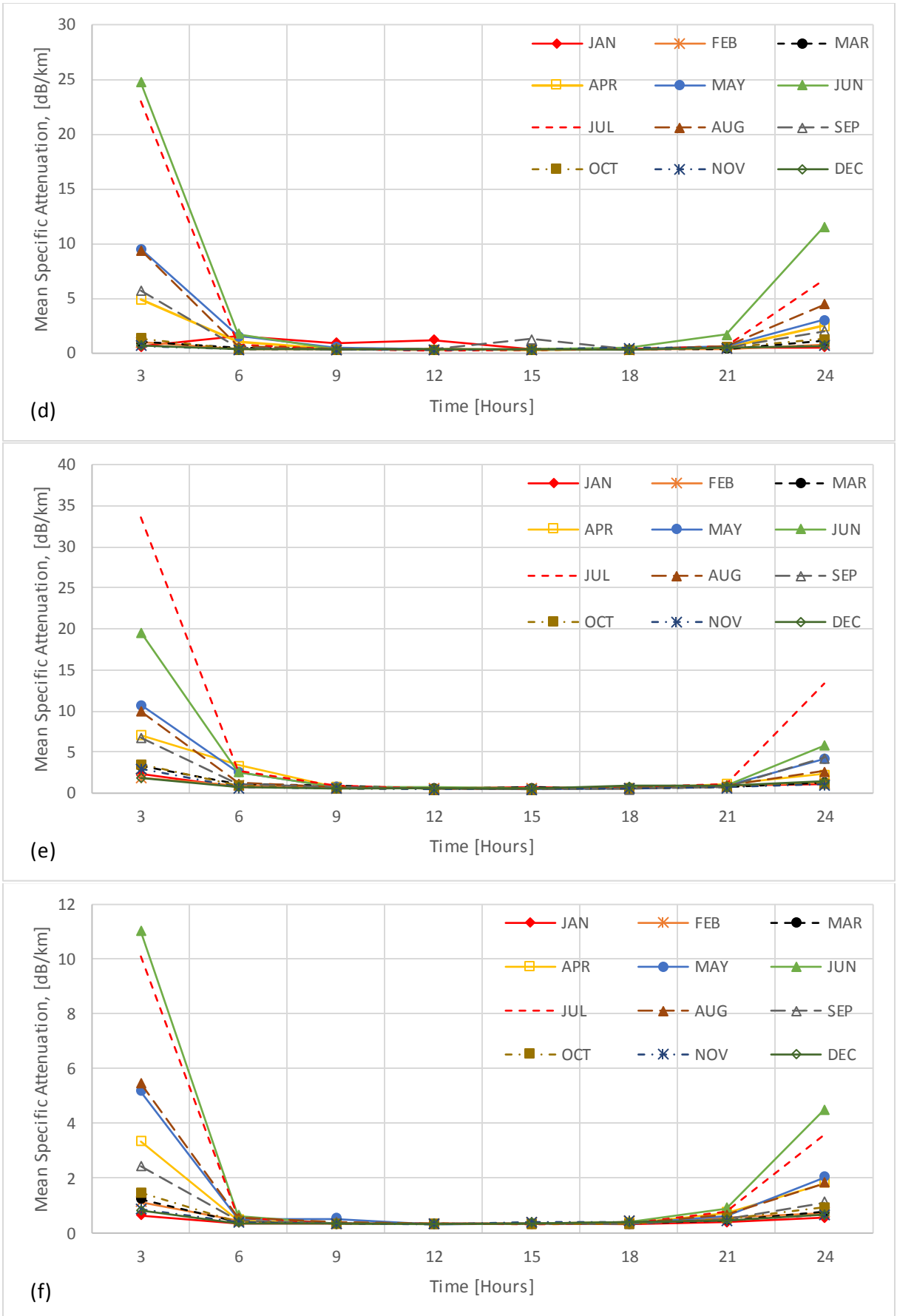

Figure 5.9: Diurnal variation of monthly mean specific attenuation for (a) Durban; (b) Cape Town; (c) Umtata; (d) Bloemfontein; (e) Johannesburg and (f) Mafikeng, over the years 2011 to 2013.

5.4 Visibility Range Distribution Modeling for Various Atmospheric Conditions using Climatic Data for South Africa

The Visibility Range Distribution (VRD) is a way of describing the distributions of the visibility values obtained at a particular location using a suitable distribution model. This can be achieved by determining the PDF of the visibility variable. This section has investigated in detail the VRD of various locations within South Africa for a successive period of three years (2011 to 2013), and the most suitable PDF model has been proposed which can be used for various analysis concerning optical or radio communications, as well as for research works concerning fields related to weather factors.

5.4.1 Probability Density Function of Visibility Range (with Parametric Modeling)

In the case of a random variable like visibility range, V, the Probability Density Function (PDF) phenomenon of this variable is a positive function which provides detailed description or pattern of the relative distribution of the visibility data. Therefore, according to Equation (3.10) the PDF of a density function V is described as any function that can satisfy the equation given by:

$$C \int_{V_{min}}^{V_{max}} p(V)dV = 1, \tag{5.1}$$

where the parameter C is a constant that makes the equation true and must be determined before the probability function $p(V)$ can be converted into a PDF through normalization.

The PDF of visibility range in this analysis was determined for all the locations considered over the entire period in this study through a three-stage process (as earlier discussed in Chapter three) which are smoothing, likelihood estimation and normalization using *Mathwave (Easyfit)* and Mathworks (*Matlab)* applications. The measured visibility PDFs were computed manually using *Excel* application while the distribution fits and curve fittings were achieved through the use of both *Mathwave (Easyfit)* and *Matlab* applications.

In the case of Durban, which is located in the eastern coast of South Africa, Layioye et al. (2017) [3] postulated that the most suitable visibility PDF describing the visibility events of this location is the three-parameter Weibull distribution fit. This investigation reported the results of both the initial and optimized estimates of three-parameter Weibull (W3P) and Log-Pearson Type-3 (LP3) probability distribution models. The results of both PDF models were compared and were also compared to that of the Kernel density estimates (in particular, the tri-weight model) in terms of both Integral Square Error (ISE) and RMSE estimations. Though, the extent of research in their work was limited to a period of one-year data and few distribution fits. However, before now the VRD for the geographical location in this study (i.e., South Africa) has not been adequately investigated and appropriate distribution fits have not been postulated.

Therefore, in order to perform a more thorough examination of the VRD over all the locations and to make a proper generalization of the PDF for each location and for the entire region, this analysis went beyond considering the W3P and LP3 PDFs by engaging more probability distribution models. The synoptic visibility range measurements for each of the six locations were considered on an annual basis and were fitted to different PDF models to determine the best distribution model. Each of these visibility datasets were all subjected to about 60 different PDF models, where the best six models were selected and plotted accordingly to show comparisons between their features. The results are shown in Tables 5.2 to 5.7 along with their distribution parameters and error estimations for all of the six locations over the three successive years. It should be noted that for each location, environment (either maritime or continental) or general distribution, the mean SSE, mean RMSE and mean R^2 values were used to propose the most suitable distribution fit for all the measured visibility data set analysed in this work.

Figures 5.10 to 5.15 show the annual measured PDF of visibility range fitted to various PDFs for all the locations over all the years in this study and based on the suitable top six PDFs for each visibility data set. Also, the distribution parameters of all the selected PDFs comprising any or all of the shape parameter(s), scale parameter, location parameter, relative parameter, and their respective error and regression estimations are presented in Tables 5.2 to 5.7 for all the locations and covering a period of three years. Thus, among all the tested PDFs and based on the annual PDF analysis, the Generalized Pareto (GP) model with overall mean values of 0.0108, 0.0271 and 0.5974 for SSE, RMSE and R^2 was observed to be the most suitable for characterizing or modelling the PDF of the visibility range within the respective locations and also in general for South Africa, based on its overall lowest mean SSE and RMSE values, and highest mean R^2 value. It can be noticed from the shape of the PDF curves for all the locations and for all the years under study that very low visibility range values are rarely occurring when compared to the higher visibility range values. However, it should be noted that the generalization of the goodness of fit of the PDF models for describing the PDF of the measured visibility range is based on only the six locations considered over the years 2011-2013.

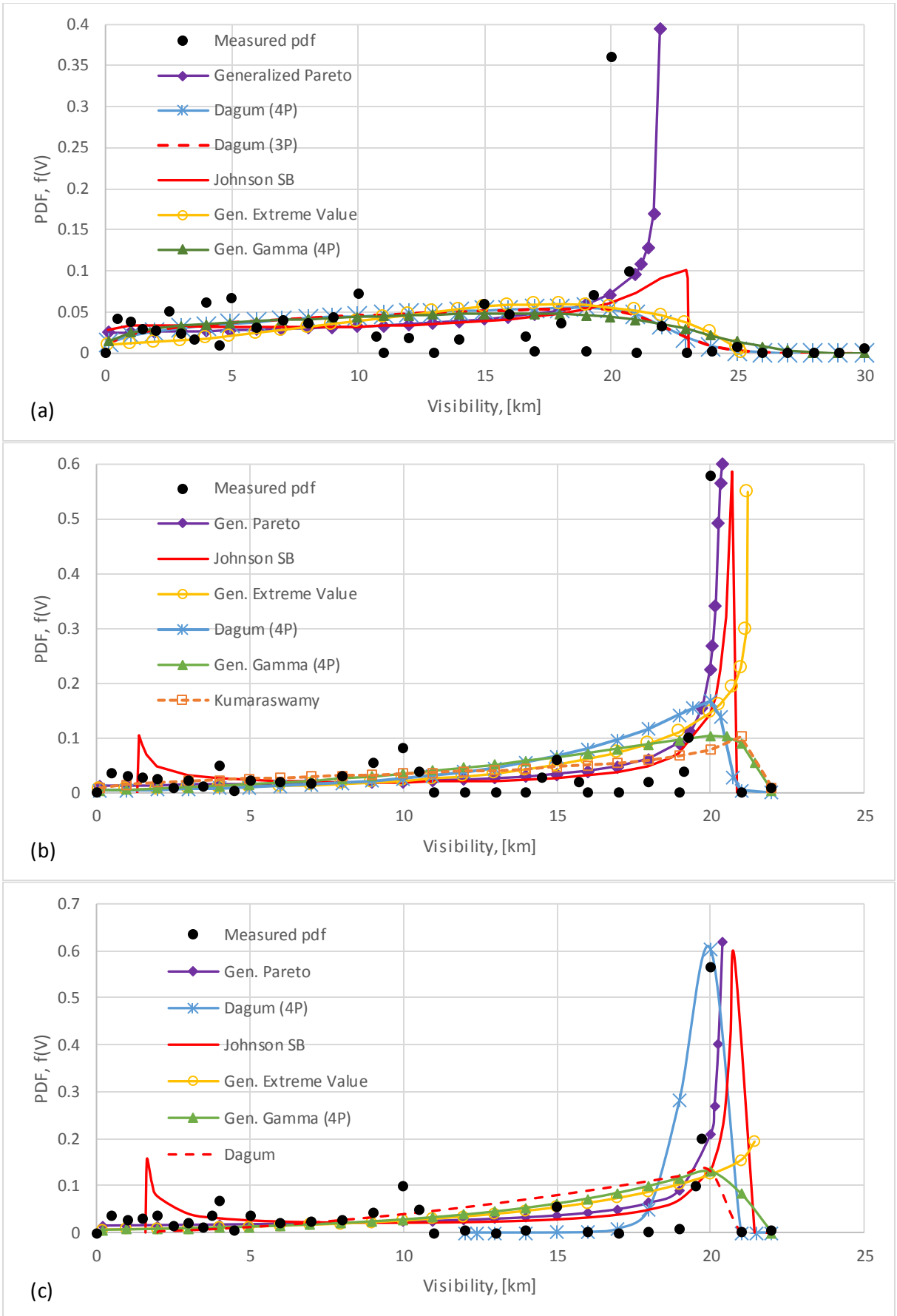

Figure 5.10: Annual measured PDF of visibility range fitted to various PDFs for Durban over the years (a) 2011; (b) 2012; (c) 2013.

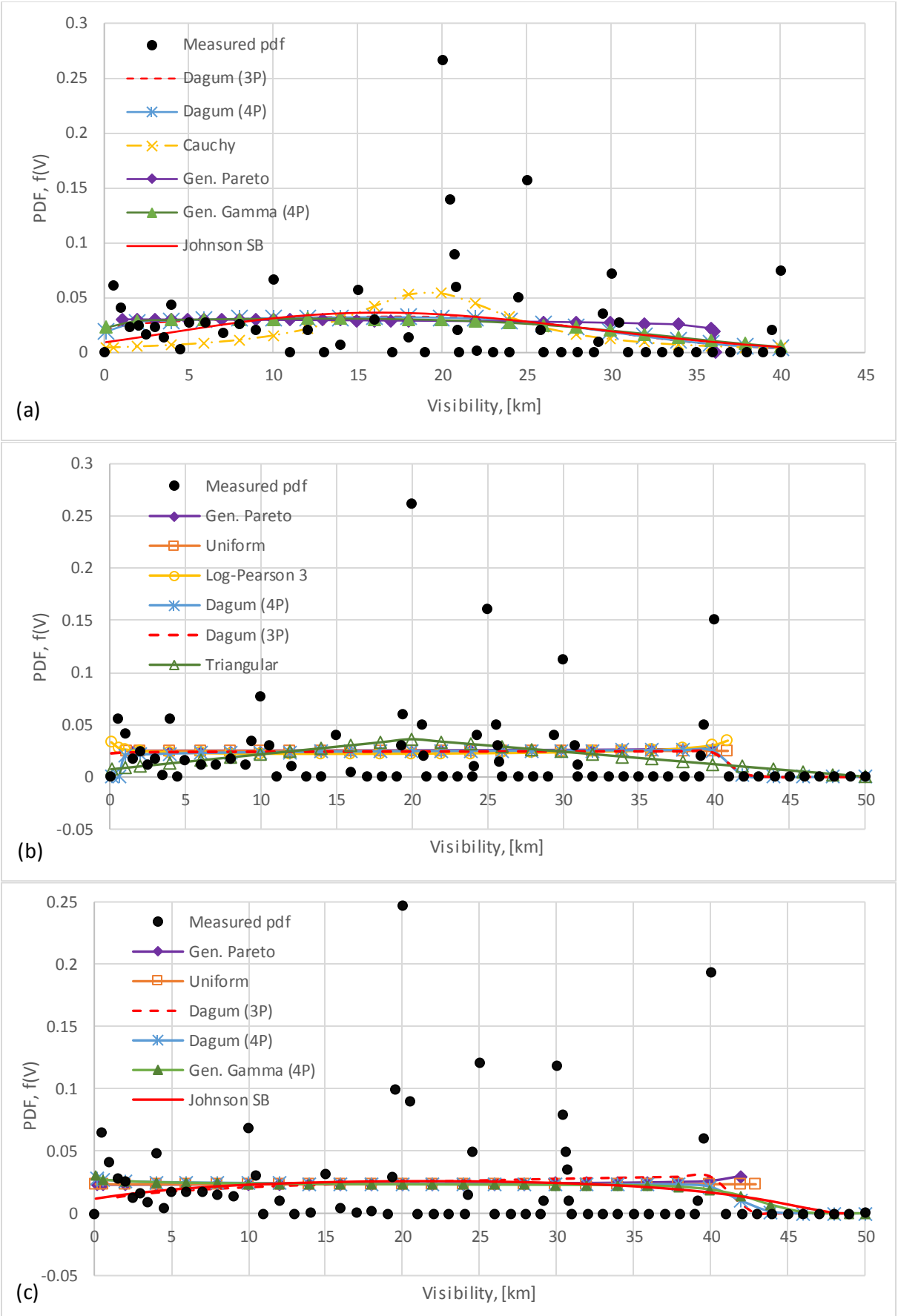

Figure 5.11: Annual measured PDF of visibility range fitted to various PDFs for Cape Town over the years (a) 2011; (b) 2012; (c) 2013.

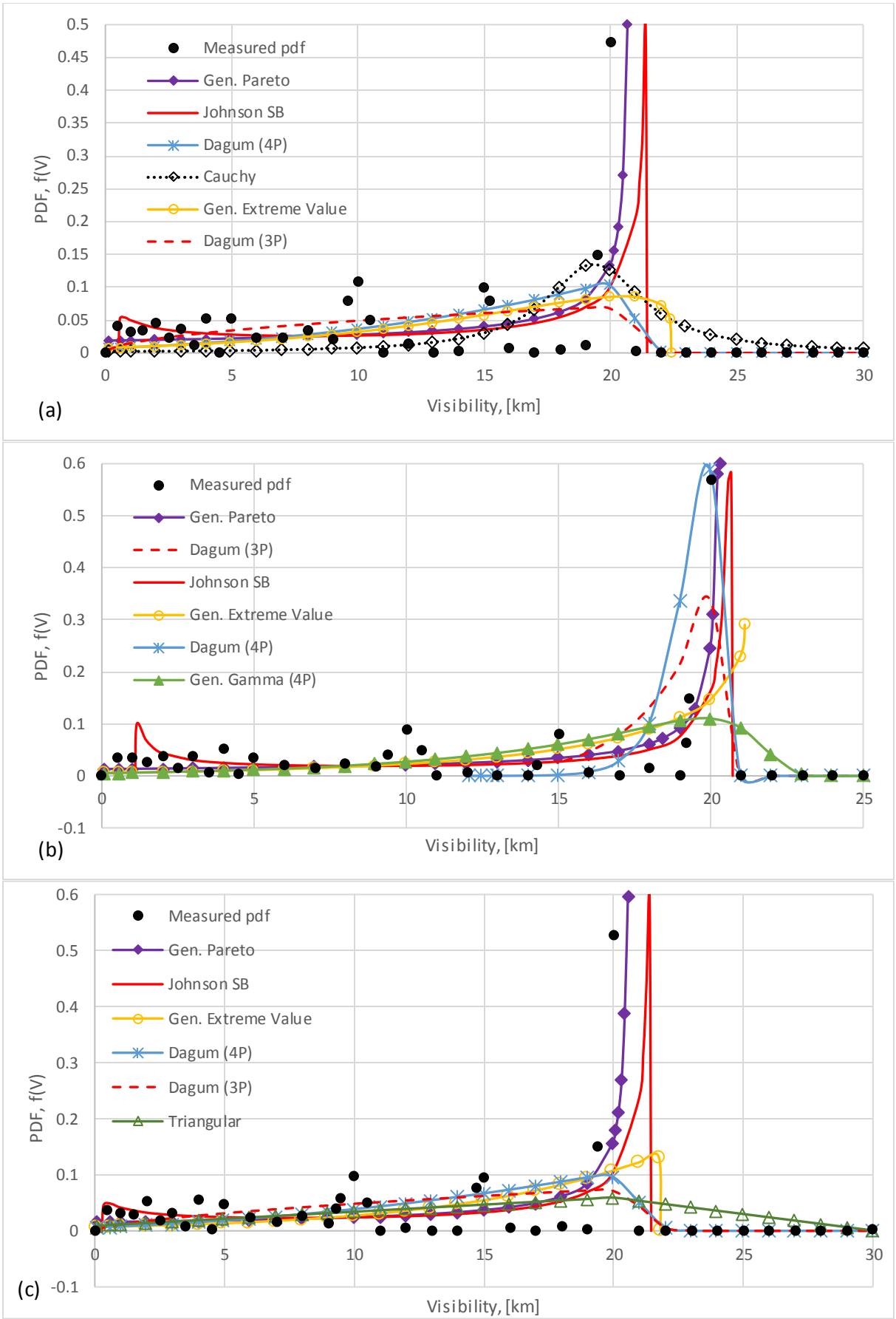

Figure 5.12: Annual measured PDF of visibility range fitted to various PDFs for Umtata over the years (a) 2011; (b) 2012; (c) 2013.

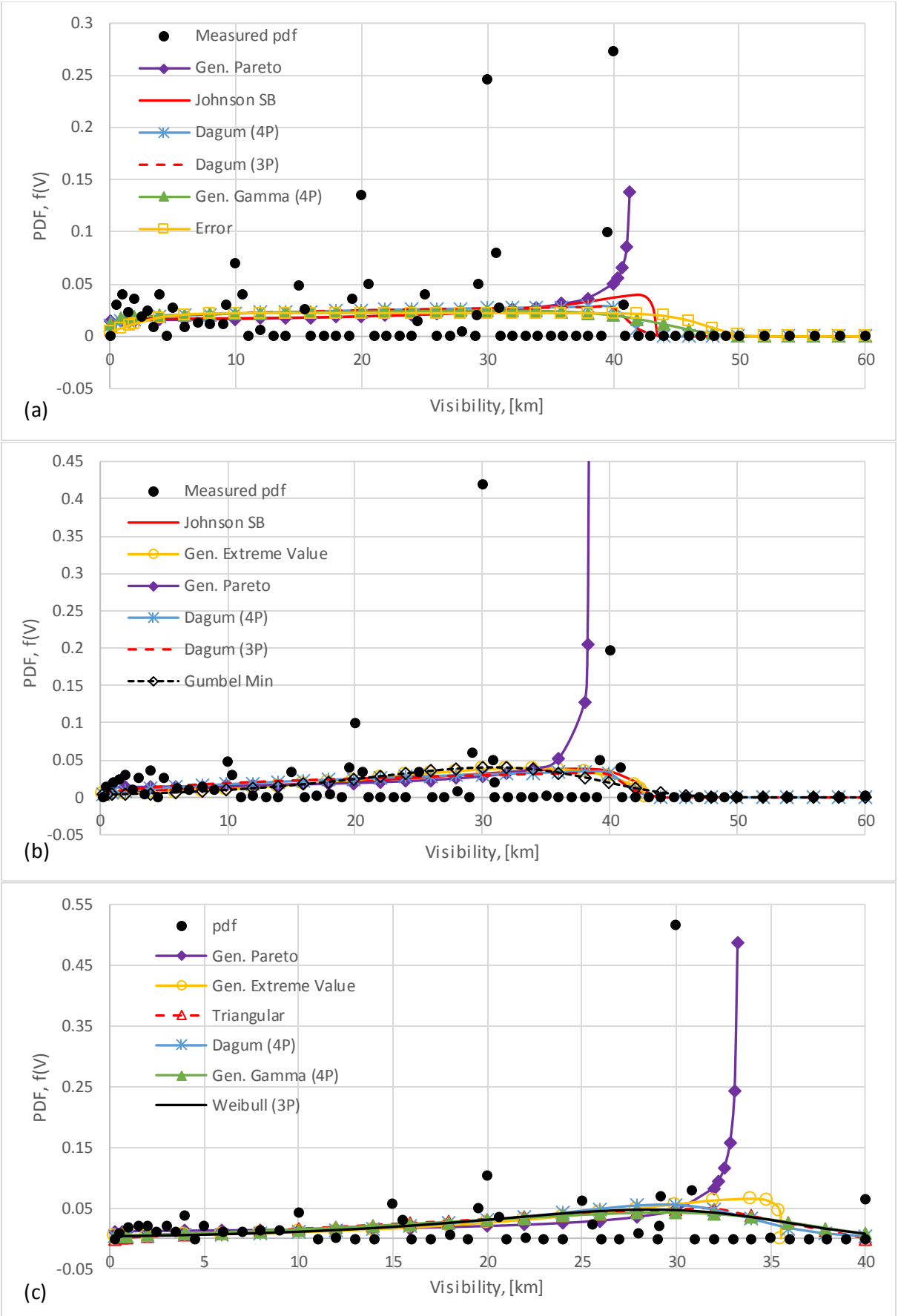

Figure 5.13: Annual measured PDF of visibility range fitted to various PDFs for Bloemfontein over the years (a) 2011; (b) 2012; (c) 2013.

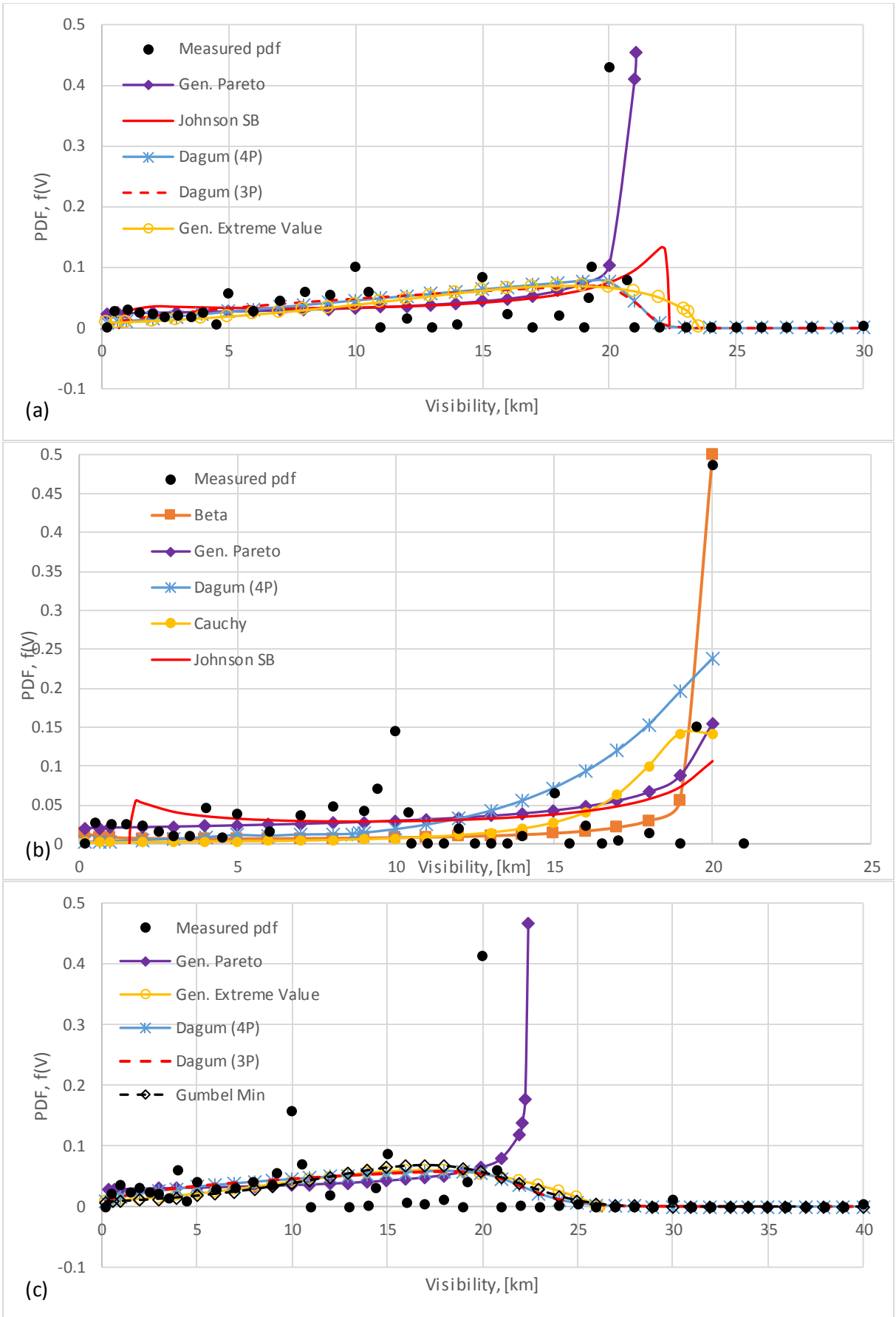

Figure 5.14: Annual measured PDF of visibility range fitted to various PDFs for Johannesburg over the years (a) 2011; (b) 2012; (c) 2013.

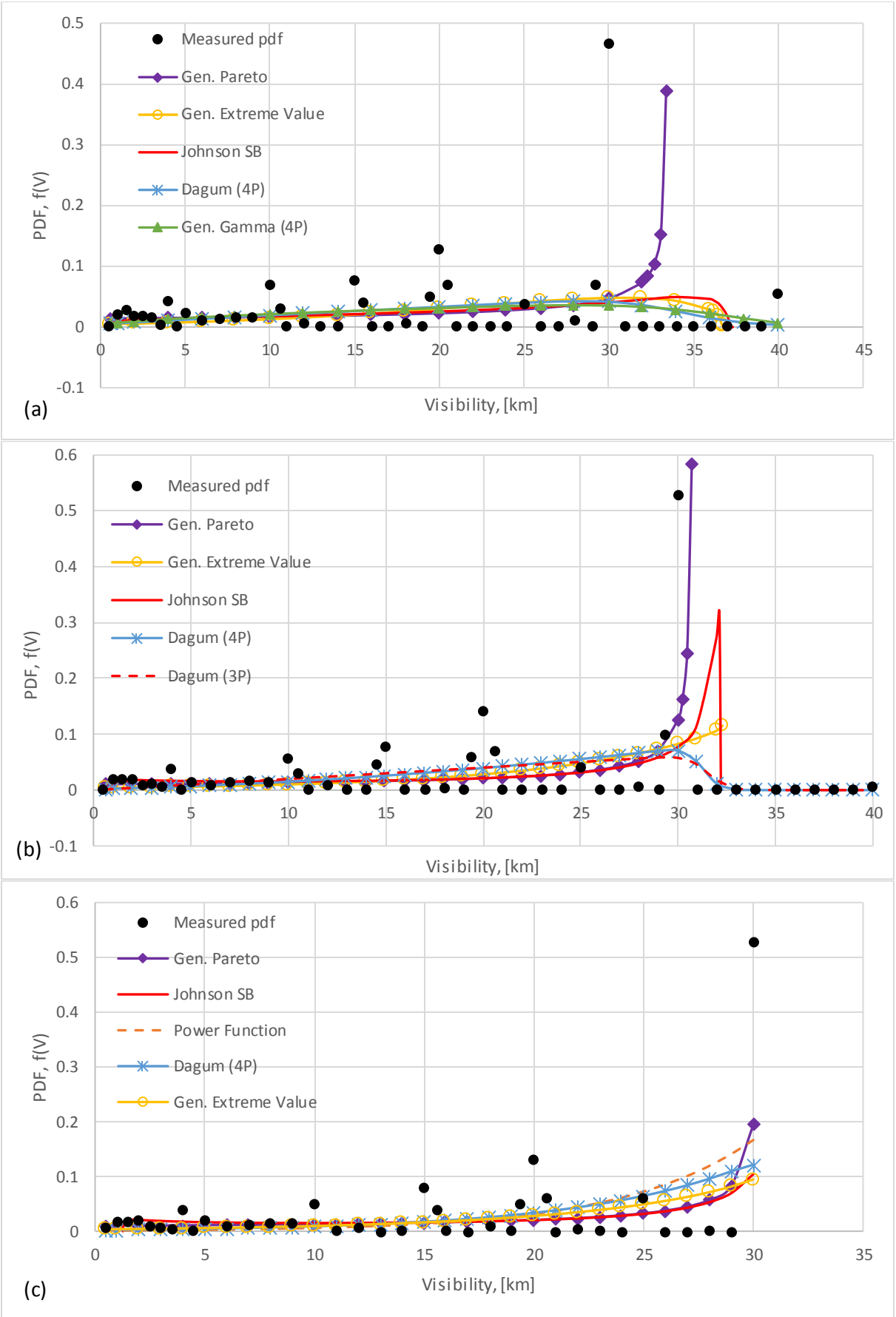

Figure 5.15: Annual measured PDF of visibility range fitted to various PDFs for Mafikeng over the years (a) 2011; (b) 2012; (c) 2013.

5.4.2 Overview of various Probability Density Function Models

This sub-section describes the most common probability distribution models that made top six in each of the locations. The distribution parameters of these PDFs were obtained experimentally using the measured visibility histograms. It should be noted that most of these distribution parameters (for instance, shape, scale and location parameters) for each of the PDF models are obtained in terms of the mean μ_v and standard deviation σ_v of the measured visibility range, V.

i. Generalized Pareto:

The Generalized Pareto (GP) distribution is a three-parameter distribution model, which provides the characteristics of the visibility variable to be described. The PDF of the GP distribution employed in this work is given by [207]:

$$f_V(V) = \begin{cases} \frac{1}{\sigma}\left(1 + k\frac{(V-\mu)}{\sigma}\right)^{-1-1/k} & k \neq 0 \\ \frac{1}{\sigma}\exp\left(-\frac{(V-\mu)}{\sigma}\right) & k = 0 \end{cases} \tag{5.2}$$

where the distribution parameter σ denotes the continuous scale parameter ($\sigma > 0$), k represents the continuous shape parameter and μ is the continuous location parameter. The domain of these distribution parameters is given by:

$$\mu \leq V < +\infty \qquad for\ k \geq 0 \tag{5.3}$$

$$\mu \leq V \leq \mu - \sigma/k \qquad for\ k < 0 \tag{5.4}$$

ii. Johnson SB Distribution:

Unlike the GP distribution model, the Johnson SB (JSB) distribution model is a four-parameter distribution model and another parameter z (relative parameter) which gives the relationship between the visibility variable V and other distribution parameters. The PDF of the JSB distribution used in this analysis is given by [208]:

$$f_V(V) = \frac{\delta}{\lambda\sqrt{2\pi}z(1-z)}\exp\left(-\frac{1}{2}\left(\gamma + \delta\ln\left(\frac{z}{(1-z)}\right)\right)^2\right), \tag{5.5}$$

and the domain of these distribution parameters is given as:

$$\xi \leq V \leq \xi + \lambda, \tag{5.6}$$

where the distribution parameter δ is the continuous shape parameter ($\delta > 0$), γ is also a continuous shape parameter, λ is the continuous scale parameter ($\lambda > 0$), ξ is the continuous location parameter and the variable z is given as $z \equiv {}^{V-\xi}/_{\lambda}$.

iii. Four-Parameter Dagum (Dagum 4P) Distribution:

The PDF of the Dagum 4P distribution can be computed from the following equation [208]:

$$f_V(V) = \frac{\alpha k \left(\frac{V-\gamma}{\beta}\right)^{\alpha k-1}}{\beta\left(1+\left(\frac{V-\gamma}{\beta}\right)^{\alpha}\right)^{k+1}}, \tag{5.7}$$

where the distribution parameters α and k represent the continuous shape parameters with $\alpha > 0$ and $k > 0$, β denotes the continuous scale parameter $\beta > 0$ and γ denotes the continuous location parameter. The distribution domain of this PDF is given as:

$$\gamma \leq V < +\infty \tag{5.8}$$

iv. Three-Parameter Dagum (Dagum 3P) Distribution:

This PDF model is also referred to as Dagum distribution and its PDF can be calculated from the following equation [208]:

$$f_V(V) = \frac{\alpha k \left(\frac{V}{\beta}\right)^{\alpha k-1}}{\beta\left(1+\left(\frac{V}{\beta}\right)^{\alpha}\right)^{k+1}}, \tag{5.9}$$

where the description of the parameters α, k and β remain the same as stated under Dagum 4P distribution, while in this case $\gamma \equiv 0$ yields the Dagum 3P distribution.

v. Generalized Extreme Value (GEV) Distribution:

The GEV PDF is also a three-parameter distribution model which is given by [208]:

$$f_V(V) = \begin{cases} \frac{1}{\sigma}\exp\left(-(1+kz)^{-1/k}\right)(1+kz)^{-1-1/k} & k \neq 0 \\ \frac{1}{\sigma}\exp(-z-\exp(-z)) & k = 0 \end{cases} \tag{5.10}$$

The domain of this distribution is given as:

$$1 + k\frac{(V-\mu)}{\sigma} > 0 \qquad for\ k \neq 0, \tag{5.11}$$

$$-\infty < V < +\infty \qquad for\ k = 0, \tag{5.12}$$

where the parameter σ represents the continuous scale parameter ($\sigma > 0$), k is the continuous shape parameter and the μ is the continuous location parameter, while the relation parameter $z \equiv {}^{V-\mu}/_{\sigma}$.

vi. Four-Parameter Generalized Gamma Distribution:

The Four-Parameter Generalized Gamma (Gen. Gamma 4P) distribution as the name implies is a four-parameter distribution model and its PDF is given by [209]:

$$f_V(V) = \frac{k(V-\gamma)^{k\alpha-1}}{\beta^{k\alpha}\Gamma(\alpha)} \exp\left(-\left((V-\gamma)/\beta\right)^k\right) \tag{5.13}$$

where the parameter k and α are the continuous shape parameters with $k > 0$ and $\alpha > 0$, β denotes the continuous scale parameter $\beta > 0$ and γ denotes the continuous location parameter. The domain of this distribution model is given as:

$$\gamma \leq V < +\infty \tag{5.14}$$

Table 5.2: Distribution parameters and fit statistics for various PDFs for the visibility range distribution of Durban for the years 2011 to 2013.

City	Year	Distribution		Distribution Parameters	Error and Regression Estimations		
			Rank		SSE	RMSE	R^2
Durban	2011	Gen. Pareto	1	*k=-1.7683 σ=40.875 μ=-1.1602*	0.1620	0.0329	0.4408
		Dagum 4P	2	*k=0.0524 α=25.668 β=22.49 γ=-0.1650*	0.2140	0.0377	0.2514
		Dagum 3P	3	*k=0.0511 α=25.395 β=22.361*	0.2150	0.0379	0.2463
		Johnson SB	4	*γ=-0.3151 δ=0.5178 λ=23.36 ξ=-0.2534*	0.2290	0.0391	0.2355
		GEV	5	*k=-0.5970 σ=7.7284 μ=12.222*	0.2350	0.0395	0.1933
		G. Gamma 4P	6	*k=9.2006 α=0.1348 β=24.23 γ=0.0037*	0.2360	0.0396	0.1743
	2012	Gen. Pareto	1	*k=-3.5869 σ=84.897 μ=-3.2871*	0.1100	0.0316	0.8417
		Johnson SB	2	*γ=-0.6346 δ=0.3049 λ=19.47 ξ=1.3609*	0.2680	0.0494	0.6148
		GEV	3	*k=-1.1616 σ=6.4466 μ=15.663*	0.3360	0.0553	0.5160
		Dagum 4P	4	*k=0.02562 α=1.1020E+6 β=1.4959E+5 γ=-1.4957E+5*	0.3610	0.0573	0.4798
		G. Gamma 4P	5	*k=75.973 α=0.0454 β=29.19 γ=-7.6623*	0.4940	0.0670	0.2885
		Kumaraswamy	6	*α_1=1.2929 α_2=0.6421 a=-0.0605 b=22.000*	0.5220	0.0689	0.2534
	2013	Gen. Pareto	1	k=-3.1976 σ=75.429 μ=-3.1681	0.1440	0.0362	0.7899
		Dagum 4P	2	k=0.0223 α=2158.9 β=28.799 γ=-8.7426	0.1970	0.0424	0.7726
		Johnson SB	3	γ=-0.5440 δ=0.2971 λ=19.225 ξ=1.6317	0.3090	0.0530	0.5491
		GEV	4	k=-1.0562 σ=6.8623 μ=14.964	0.4130	0.0613	0.3966
		G. Gamma 4P	5	k=6564.6 α=0.0598 β=2473.4 γ=-2452.3	0.4290	0.0625	0.3732
		Dagum 3P	6	k=0.0090 α=305.52 β=20.324	0.4970	0.0672	0.2817

Table 5.3: Distribution parameters and fit statistics for various PDFs for the visibility range distribution of Cape Town for the years 2011 to 2013.

City	Year	Distribution		Distribution Parameters	Error and Regression Estimations		
			Rank		SSE	RMSE	R^2
Cape Town	2011	Dagum 3P	1	*k=0.15153 α=7.3249 β=31.246*	0.0300	0.0174	0.4674
		Dagum 4P	2	*k=0.1454 α=7.3892 β=31.451 γ=0.0857*	0.0300	0.0174	0.4642
		Cauchy	3	*σ=5.7952 μ=19.157*	0.0320	0.0179	0.4602
		Gen. Pareto	4	*k=-0.9410 σ=32.985 μ=1.0568*	0.0310	0.0175	0.4594
		G. Gamma 4P	5	*k=4.6397 α=0.2244 β=35.112 γ=0.0943*	0.0310	0.0175	0.4564
		Johnson SB	6	*γ=0.6333 δ=1.7619λ=80.199 ξ=-15.404*	0.0310	0.0175	0.4535
	2012	Gen. Pareto	1	*k=-1.0224 σ=39.714 μ=1.4407*	0.0370	0.0168	0.6531
		Uniform	2	*a=1.0600 b=41.095*	0.0370	0.0168	0.6335
		Log-Pearson3	3	*α=0.8652 β=-1.1481 γ=3.7252*	0.0370	0.0168	0.6150
		Dagum 4P	4	*k=0.0087 α=121.62 β=40.997 γ=0.0720*	0.0370	0.0168	0.5748
		Dagum 3P	5	*k=0.0106 α=95.735 β=41.165*	0.0370	0.0169	0.5714
		Triangular	6	*m=20.00 a=-4.9831 b=50.25*	0.0370	0.0170	0.5639
	2013	Gen. Pareto	1	*k=-1.0428 σ=43.596 μ=0.176*	0.0360	0.0166	0.6279
		Uniform	2	*a=0.0659 b=42.968*	0.0370	0.0168	0.6060
		Dagum 3P	3	*k=0.0060 α=209.38 β=41.723*	0.0370	0.0169	0.5645
		Dagum 4P	4	*k=0.0175 α=55.075 β=41.689 γ=0.1000*	0.0370	0.0170	0.5605
		G. Gamma 4P	5	*k=20.711 α=0.0462 β=43.517 γ=0.0485*	0.0390	0.0173	0.5332
		Johnson SB	6	*γ=-6.1612E-4 δ=0.8774 λ=54.284 ξ=-5.6326*	0.0410	0.0177	0.4937

Table 5.4: Distribution parameters and fit statistics for various PDFs for the visibility range distribution of Umtata for the years 2011 to 2013.

City	Year	Distribution		Distribution Parameters	Error and Regression Estimations		
			Rank		SSE	RMSE	R^2
Umtata	2011	Gen. Pareto	1	*k=-2.4742 σ=56.929 μ=-2.2833*	0.1940	0.0360	0.6450
		Johnson SB	2	*γ=-0.4667 δ=0.39816 λ=20.91 ξ=0.52466*	0.2650	0.0421	0.5096
		Dagum 4P	3	*k=0.0361 α=115.92 β=35.586 γ=-14.665*	0.3410	0.0477	0.3629
		Cauchy	4	*σ=2.3478 μ=19.359*	0.3430	0.0478	0.3607
		GEV	5	*k=-0.8400 σ=7.3948 μ=13.598*	0.4150	0.0526	0.2516
		Dagum 3P	6	*k=0.02392 α=63.508 β=21.048*	0.4120	0.0524	0.2304
	2012	Gen. Pareto	1	*k=-3.5872 σ=86.315 μ=-3.7417*	0.0750	0.0241	0.8948
		Dagum 3P	2	*k=0.0044 α=2252.7 β=20.767*	0.2370	0.0427	0.7623
		Johnson SB	3	*γ=-0.63361 δ=0.2975 λ=19.553 ξ=1.1412*	0.1970	0.0390	0.7191
		GEV	4	*k=-1.1617 σ=6.5533 μ=15.523*	0.3120	0.0490	0.5576
		Dagum 4P	5	*k=0.0165 α=1559.6β=22.063 γ=-2.0058*	0.6710	0.0719	0.3495
		G. Gamma 4P	6	*k=195.54 α=0.1483 β=184.11 γ=-162.48*	0.4620	0.0596	0.3417
	2013	Gen. Pareto	1	*k=-2.9589 σ=69.929 μ=-3.0408*	0.1870	0.0353	0.7099
		Johnson SB	2	*γ=-0.5562 δ=0.3811 λ=21.091 ξ=0.3156*	0.3180	0.0461	0.5000
		GEV	3	*k=-0.9880 σ=7.1338 μ=14.587*	0.3670	0.0495	0.4306
		Dagum 4P	4	*k=0.0408 α=78.103 β=28.564 γ=-7.6234*	0.4300	0.0536	0.3213
		Dagum 3P	5	*k=0.0279 α=58.197 β=21.094*	0.4930	0.0573	0.2229
		Triangular	6	*m=20.00 a=-3.5497 b=30.114*	0.5390	0.0599	0.1506

Table 5.5: Distribution parameters and fit statistics for various PDFs for the visibility range distribution of Bloemfontein for the years 2011 to 2013.

City	Year	Distribution		Distribution Parameters	Error and Regression Estimations		
			Rank		SSE	RMSE	R^2
Bloemfontein	2011	Gen. Pareto	1	*k=-1.5517 σ=67.118 μ=-1.8624*	0.0350	0.0154	0.5482
		Johnson SB	2	*γ=-0.3043 δ=0.5813 λ=46.014 ξ=-2.5056*	0.0410	0.0166	0.4583
		Dagum 4P	3	*k=0.0135 α=88.618 β=41.514 γ=-0.0777*	0.0490	0.0181	0.3119
		Dagum 3P	4	*k=0.0134 α=87.972 β=41.447*	0.0490	0.0181	0.3100
		G. Gamma 4P	5	*k=12.442 α=0.089 β=44.767 γ=0.0684*	0.0550	0.0192	0.2257
		Error	6	*k=11.553 σ=13.157 μ=24.441*	0.0560	0.0194	0.2052
	2012	Johnson SB	1	*γ=-0.7026 δ=0.8074 λ=52.734 ξ=-9.3355*	0.0790	0.0230	0.3313
		GEV	2	*k=-0.66312 σ=12.614 μ=23.705*	0.0800	0.0232	0.3207
		Gen. Pareto	3	*k=-1.95 σ=73.689 μ=0.5863*	0.0970	0.0255	0.2744
		Dagum 4P	4	*k=0.0211 α=72.383 β=42.198 γ=-0.9342*	0.0820	0.0234	0.2589
		Dagum 3P	5	*k=0.02056 α=68.007 β=41.36*	0.0830	0.0235	0.2480
		Gumbel Min	6	*σ=9.1361 μ=30.839*	0.0840	0.0237	0.2412
	2013	Gen. Pareto	1	*k=-2.6104 σ=87.695 μ=-0.2671*	0.0340	0.0185	0.7305
		GEV	2	*k=-0.88301 σ=10.63 μ=23.493*	0.0720	0.0269	0.4322
		Triangular	3	*m=31.767 a=0.24 b=40.0*	0.0970	0.0312	0.2312
		Dagum 4P	4	*k=0.1848 α=36.839β=77.068 γ=-43.92*	0.1040	0.0323	0.1768
		G. Gamma 4P	5	*k=10.716 α=0.2486 β=44.66 γ=-8.2011*	0.1090	0.0330	0.1398
		Weibull (3P)	6	*α=2.3962E+7 β=1.8699E+8 γ=-1.8699E+8*	0.1100	0.0332	0.1318

Table 5.6: Distribution parameters and fit statistics for various PDFs for the visibility range distribution of Johannesburg for the years 2011 to 2013.

City	Year	Distribution		Distribution Parameters	Error and Regression Estimations		
			Rank		SSE	RMSE	R^2
Johannesburg	2011	Gen. Pareto	1	*k=-1.959 σ=41.948 μ=-0.34841*	0.1980	0.0363	0.5578
		Johnson SB	2	*γ=-0.3579 δ=0.5089 λ=21.625 ξ=0.7169*	0.2410	0.0401	0.4812
		Dagum 4P	3	*k=0.0344 α=56.756 β=22.861 γ=-1.8117*	0.3000	0.0447	0.3051
		Dagum 3P	4	*k=0.0313 α=49.991 β=21.146*	0.3130	0.0457	0.2757
		GEV	5	*k=-0.6663 σ=7.1458 μ=12.784*	0.3490	0.0483	0.2170
		Log-Pearson 3	6	*α=0.8356 β=-0.9028 γ=3.1684*	0.3580	0.0489	0.1899
	2012	Beta	1	*α_1=0.7437 α_2=0.0719 a=0.0962 b=20.0*	0.1600	0.0400	0.6706
		Gen. Pareto	2	*k=-2.3666 σ=50.434 μ=-0.7038*	0.1790	0.0423	0.6277
		Dagum 4P	3	*k=0.0045 α=4156.0 β=72.993 γ=-52.941*	0.3660	0.0605	0.4903
		Cauchy	4	*σ=2.122 μ=19.478*	0.2930	0.0541	0.4233
		Johnson SB	5	*γ=-0.4440 δ=0.4115 λ=19.748 ξ=1.6175*	0.2850	0.0534	0.4104
		Kumaraswamy	6	*α_1=1.8473 α_2=0.7254 a=0.1988 b=20.0*	0.2880	0.0536	0.4040
	2013	Gen. Pareto	1	*k=-1.5933 σ=35.143 μ=0.3566*	0.0250	0.0158	0.8129
		GEV	2	*k=-0.5308 σ=7.3262 μ=12.357*	0.0480	0.0219	0.6185
		Dagum 4P	3	*k=0.0799 α=18.557 β=22.38 γ=-0.1806*	0.0400	0.0200	0.6169
		Dagum 3P	4	*k=0.0785 α=18.335 β=22.238*	0.0410	0.0202	0.6102
		Gumbel Min	5	*σ=5.3855 μ=17.017*	0.0480	0.0219	0.5401
		Log-Pearson 3	6	*α=1.0979 β=-0.7729 γ=3.2653*	0.0620	0.0250	0.5059

Table 5.7: Distribution parameters and fit statistics for various PDFs for the visibility range distribution of Mafikeng for the years 2011 to 2013.

City	Year	Distribution	Rank	Distribution Parameters	Error and Regression Estimations		
					SSE	RMSE	R^2
Mafikeng	2011	Gen. Pareto	1	*k=-2.1404 σ=72.167 μ=-0.27176*	0.0350	0.0187	0.6586
		GEV	2	*k=-0.7296 σ=11.155 μ=21.403*	0.0850	0.0292	0.1677
		Johnson SB	3	*γ=-0.5545 δ=0.6755 λ=40.679 ξ=-3.4302*	0.0870	0.0295	0.1534
		Dagum 4P	4	*k=0.1108 α=17.604 β=37.005 γ=-2.7665*	0.0880	0.0297	0.1319
		G. Gamma 4P	5	*k=10.001 α=0.1586 β=38.049 γ=-0.6263*	0.0890	0.0298	0.1269
		Dagum 3P	6	*k=0.0971 α=16.205 β=34.77*	0.0890	0.0298	0.1250
	2012	Gen. Pareto	1	*k=-3.0693 σ=100.06 μ=-1.8523*	0.0400	0.0199	0.7260
		GEV	2	*k=-1.0199 σ=9.6774 μ=22.818*	0.0570	0.0239	0.6246
		Johnson SB	3	*γ=-0.6561 δ=0.4392 λ=31.253 ξ=0.8855*	0.0860	0.0294	0.4857
		Dagum 4P	4	*k=0.0344 α=84.12 β=36.432 γ=-5.1984*	0.1080	0.0329	0.2342
		Dagum 3P	5	*k=0.0338 α=59.534 β=31.512*	0.1160	0.0341	0.1721
		Triangular	6	*m=30.0 a=-2.5053 b=40.242*	0.1190	0.0346	0.1465
	2013	Gen. Pareto	1	*k=-3.2604 σ=106.07 μ=-2.1215*	0.1300	0.0294	0.7912
		Johnson SB	2	*γ=-0.6894 δ=0.4065 λ=30.132 ξ=1.2866*	0.3340	0.0472	0.4674
		Power Function	3	*α=1.0808E+8 a=-6.4901E+8 b=30.0*	0.3560	0.0487	0.4316
		Dagum 4P	4	*k=0.0141 α=1.1667E+8 β=1.2568E+7 γ=-1.2568E+7*	0.3940	0.0513	0.3661
		GEV	5	*k=-1.0737 σ=9.3681 μ=23.067*	0.4080	0.0521	0.3475
		G. Gamma 4P	6	*k=4.6299E+8 α=0.0502 β=1.8517E+8 γ=-1.8517E+8*	0.4260	0.0533	0.3144

5.5 Visibility based Optical Attenuation Modeling under various Atmospheric Conditions along Terrestrial FSO Link for South Africa: using Cumulative Distribution Function

The optical attenuation of FSO systems due to various atmospheric conditions (such as fog, haze, mist, snow, rain and clouds) is dependent on the visibility range at a particular time and place, which results into impairments and then limits the operation and performance of the FSO system. This visibility range is a random phenomenon which is a factor of the magnitude of the various atmospheric conditions within the surrounding considered. Therefore, with the knowledge of the visibility phenomenon (such as its effects), visibility information, distribution and its variations, an optical attenuation profile (time series or frequency series) can be investigated based on the visibility range characterization. In this work (particularly in Chapter 4), the specific and optical attenuations were estimated based on the information obtained for the visibility range of six different locations across South Africa over the years 2011-2013. The optical attenuations were calculated for an optical link transmitting optical signal at a wavelength of 850 nm and at a link distance of 1.5 km. This work has been able to perform a thorough analysis on optical attenuation due to various atmospheric conditions along the terrestrial FSO channel and thus optical attenuation modelling using the cumulative distribution function have been achieved for each of the locations considered.

Based on the measured visibility phenomenon, the optical attenuations are most effectively presented in terms of cumulative distributions on either monthly, seasonally or yearly frequency. Using the cumulative distribution technique, the contribution of the impairments (relating to the optical attenuation phenomenon) to the optical link failure can be estimated. Likewise, this cumulative distribution can be used to determine the margins which is to be embedded into the FSO system to achieve the required performance against certain impairments imposed by the optical attenuation phenomenon. Interestingly, the most important deduction from the CCDF curves is the optical attenuation estimate equivalent to the $0.01\ \%$ of time as recommended by the ITU-R for effective and reliable optical system performance. This theory technically means that the optical link outage must not exceed the time equivalence of 52.56 minutes of an average year. According to section 3.9.3, the CCDF of the optical attenuation range defines the percentage of time that the attenuation variable (α) exceeds a specified amount (which is most often taken as $0.01\ \%$). Therefore, according to equation (3.16), the CCDF $(F(\alpha))$ of the optical attenuation (α) gives the percentage of time that α exceeds a specific level, which can be determined using the equation [182, 185]:

$$F(\alpha) = 100 \cdot C \int_{\alpha_{min}}^{\alpha} P(\alpha) d\alpha. \tag{5.15}$$

This CCDF equation can be used to find the distribution function of the specific attenuation data in dB/km.

The measured CCDF curves for the optical (at $850\ nm$ and $1.5\ km$ distance) and specific attenuations for each of the locations in this study over the years 2011-2013, are presented in Figures 5.16 (a) – (f). From these plots, the similarity in the cumulative distribution curves is very vivid, especially at low attenuations. It is necessary to observe the value of the time exceedance at strong attenuations above $13.66\ dB/km$ corresponding to visibility above 1 km, which is observed in this work and seen in other literatures as a very critical level where severe impairments can cause damage to the optical link network and may even result to total or partial link failure or outage. It was observed across all the locations and years investigated that strong attenuation values above $13.66\ dB/km$ (which is within the lower visibility class range) are the barely occurring attenuation events to the link compared to the whole distribution, while lower attenuations are the most frequently occurring attenuation events, accounting for more than $90\ \%$ of the measurement duration annually. Also, it was observed that at lower attenuations all the curves for each location over all the years follow the same trend. Another significant observation is the fact that there are varying attenuation peaks noticed among the distribution curves for each location, such that the peak of the CCDF curves of the optical attenuation (at 850 nm and 1.5 km distance) for Durban, Cape Town and Umtata over all the considered years reached as high as $254.71\ dB$ (except in year 2013 for Durban which was lower with about $127.36\ dB$). Whereas, the peaks of the optical attenuation curves for Johannesburg were at $127.36\ dB$ for all the years, and for Bloemfontein the peak varied all through the three successive years reaching highest in 2011 with about

254.71 dB and lower in both 2012 and 2013 with approximately 127.36 dB and 84.90 dB respectively, and lastly that of Mafikeng were much lower than the peaks of all the other cities with years 2011 and 2012 having about 40.64 dB, and year 2013 has a little higher value of about 50.94 dB.

There is a great distinction noticed between the coastal or near-coastal areas which were all within the range 127.36 dB to 254.71 dB and the non-coastal areas which were mostly lower than 127.36 dB, except in year 2011 for Bloemfontein. Therefore, these results show that it can vary in magnitude based on location. This indicates that the distribution and presence of optical attenuation depends on the location as have been observed here and in several sections of this thesis. Again, it can be deduced that since all the curves for all the locations and years show appreciable resemblance in the trend of yearly distribution, indicating that there is a likelihood of using similar distribution model for their characterization. At this point it is important to investigate the optical attenuation values corresponding to 0.01 % of time recommended by ITU-R for achieving an effective system performance with 99.99 % optical link availability. This indicates that the optical link outage must not surpass the equivalence of about 52.56 minutes of an average year. The respective overall average values (shown in Table 5.8) of the specific attenuation and optical attenuation (at 850 nm and 1.5 km link distance) at the exceedance window of 0.01 %, over all the years for each of the locations are 56.82 dB/km and 85.23 dB, 58.45 dB/km and 87.67 dB, 52.84 dB/km and 79.26 dB, 28.05 dB/km and 42.07 dB, 40.77 dB/km and 61.16 dB, and 15.24 dB/km and 22.287 dB for Durban, Cape Town, Umtata, Bloemfontein, Johannesburg and Mafikeng respectively. Therefore, to meet the ITU-R recommendation, the specific attenuation or optical attenuation values (as the case may be) that exceeded the 0.01 % standard performance window for all the years (2011-2013) and for the stations studied will serve as additional fade margin that must be allowed for attenuation on the terrestrial FSO links across all the locations considered in South Africa.

In addition, attempt was made to obtain the CDF $P(\alpha)$ of the specific attenuations and then fit the obtained CDF curves to a series of distribution models. This CDF data for the specific attenuation in terms of the PDF $p(\alpha)$ were derived using the following syntax [182, 185]:

$$P(\alpha) = 100 \cdot C \int_{\alpha}^{\alpha_{max}} p(\alpha)\, d\alpha. \tag{5.16}$$

The appropriate model for the CDF was developed using the combined specific attenuation data of the years 2011 and 2012, whereas the data for 2013 was used for its validation. This developed distribution model estimates the attenuation as a function of its percentage exceedance. Figures 5.17 (a) – (l) presents the distribution fit of the specific attenuation CDF (both in % scale and Log % scale) to various curve fitting distribution models for the respective locations. After the comparison of the error and coefficient of determination values for all the tested distribution models, the two-part general exponential model was better in describing the distribution by slightly having a lower RMSE than the

two-part Gaussian model which has close values to it. This distribution model evaluates the percentage of time each value of specific attenuation is exceeded for an average year. The equation of the two-part exponential model is given as [208]:

$$\alpha = a * \exp(b * p) + c * \exp(d * p), \quad (5.17)$$

where the coefficients a, b, c and d are constants and the parameter p is the percentage time exceeded.

The results showed that there is a good relationship between the CDF curves of the specific attenuation and validation data and also with the line of best fit (except for Johannesburg where its validation data didn't agree at higher attenuation values). The obtained distribution parameters with the corresponding coefficient values of the two-part exponential model, including the parameters of the goodness of fit and goodness of validation are all shown in Table 5.9. The analysis for each location produced good SSE and RMSE values that are adequately low and very high R^2 values, which are indications that the model for representing the obtained CDFs of the attenuation over all the locations under study is a good distribution model. The high R^2 and adjusted R^2 estimates of about 0.8766 and 0.8727, 0.8765 and 0.8726, 0.8761 and 0.8723, 0.8764 and 0.8726, 0.9578 and 0.9565, and 0.9851 and 0.9846 were obtained respectively for Durban, Cape Town, Umtata, Bloemfontein, Johannesburg and Mafikeng. This indicates that the two-part exponential model is outstanding among several other models that were investigated for characterizing attenuation CDF over all the six locations representing South Africa, and maybe over South Africa in general.

The specific attenuation values obtained for the different percentages of time exceeded using the developed model are shown in Table 5.10. The accuracy of the developed Exponential type-2 model for representing the optical attenuation of FSO links within these locations is shown by the exceedance of 0.01 % allowance, whose mean estimates from the CDF curves are reported to range from $13.25\ dB$ to $69.35\ dB$ for all the locations. However, comparing the attenuation results obtained for the exceedance of 0.01 % window from the CDF curves and that estimated by the Exponential type-2 model, it can be noticed that there a few of underestimations and overestimations, but the general performance yields a very suitable report of the developed model accuracy.

5.6 Summary

In summary,

(a) based on the monthly and seasonal dependence, the maritime environments have higher mean specific attenuation values than the continental environments.

(b) in general, the seasonal mean analysis showed that the mean attenuation values obtained in the winter season (especially June/July) were consistently far higher than the mean values observed in the other seasons, across the three successive years investigated in this study.

(c) Finally, visibility based optical attenuation model under various atmospheric conditions over a terrestrial FSO link for South Africa was proposed, using the Exponential type-2 model.

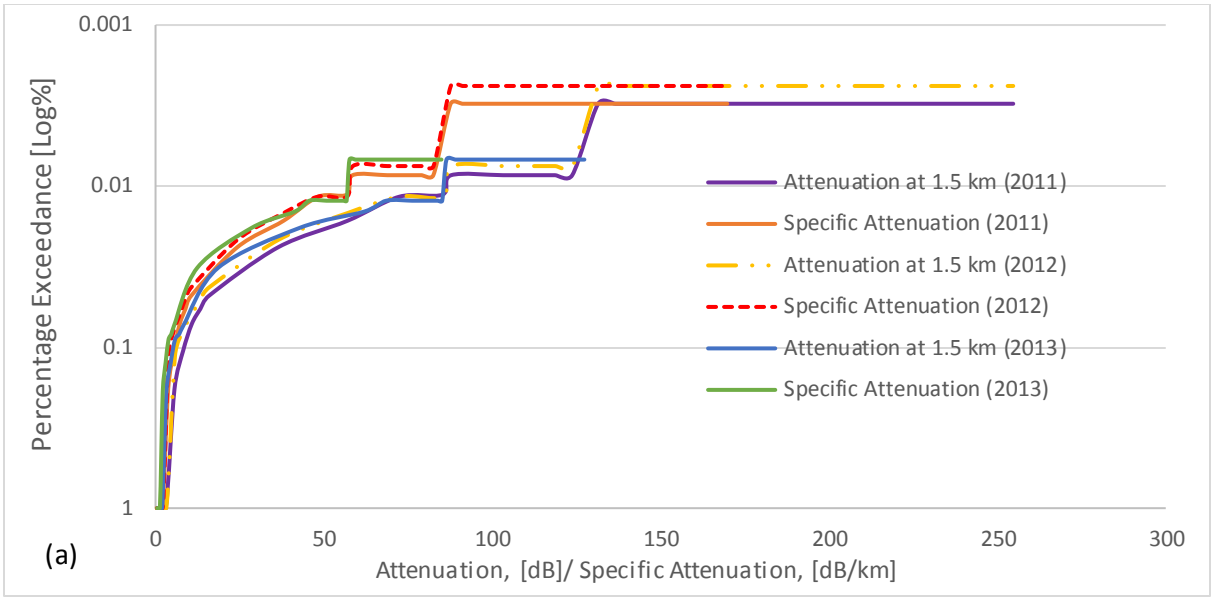
0.001
0.01
0.1
1
Percentage Exceedance [Log%]
0
50
100
150
200
250
300
Attenuation, [dB]/ Specific Attenuation, [dB/km]
Attenuation at 1.5 km (2011)
Specific Attenuation (2011)
Attenuation at 1.5 km (2012)
Specific Attenuation (2012)
Attenuation at 1.5 km (2013)
Specific Attenuation (2013)
(a)

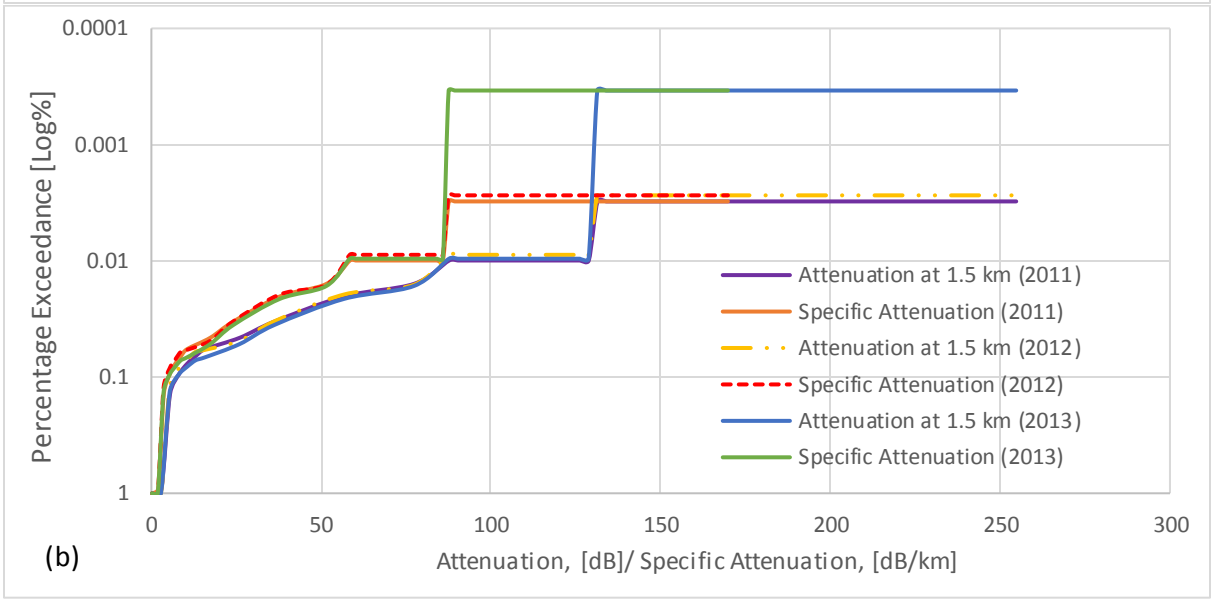
0.0001
0.001
0.01
0.1
1
Percentage Exceedance [Log%]
0
50
100
150
200
250
300
Attenuation, [dB]/ Specific Attenuation, [dB/km]
Attenuation at 1.5 km (2011)
Specific Attenuation (2011)
Attenuation at 1.5 km (2012)
Specific Attenuation (2012)
Attenuation at 1.5 km (2013)
Specific Attenuation (2013)
(b)

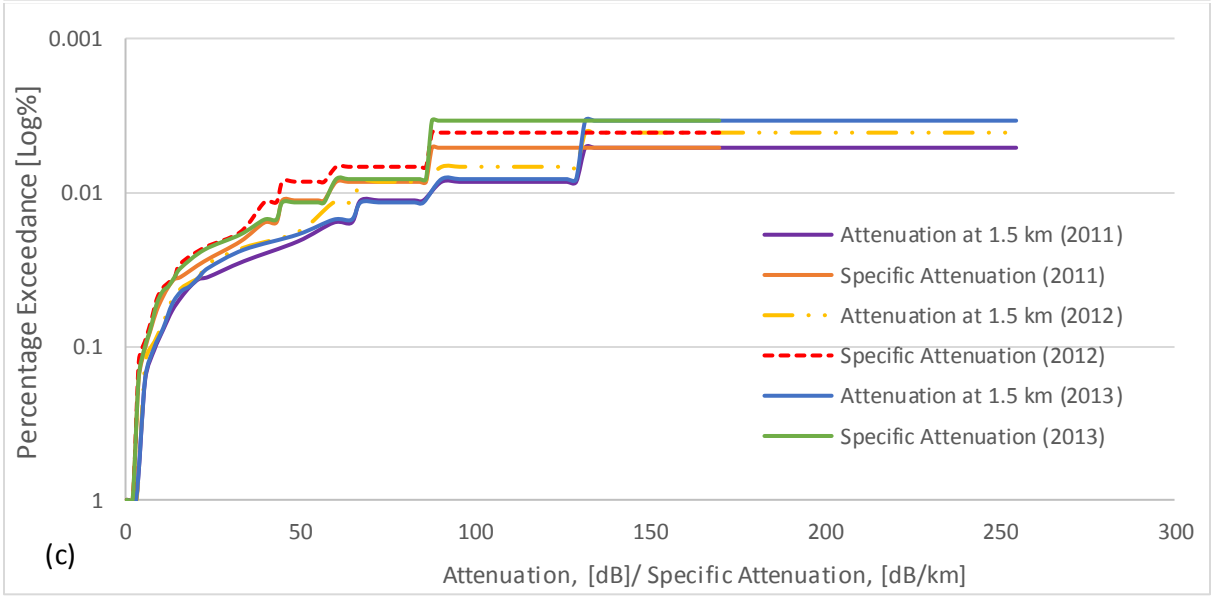
0.001
0.01
0.1
1
Percentage Exceedance [Log%]
0
50
100
150
200
250
300
Attenuation, [dB]/ Specific Attenuation, [dB/km]
Attenuation at 1.5 km (2011)
Specific Attenuation (2011)
Attenuation at 1.5 km (2012)
Specific Attenuation (2012)
Attenuation at 1.5 km (2013)
Specific Attenuation (2013)
(c)

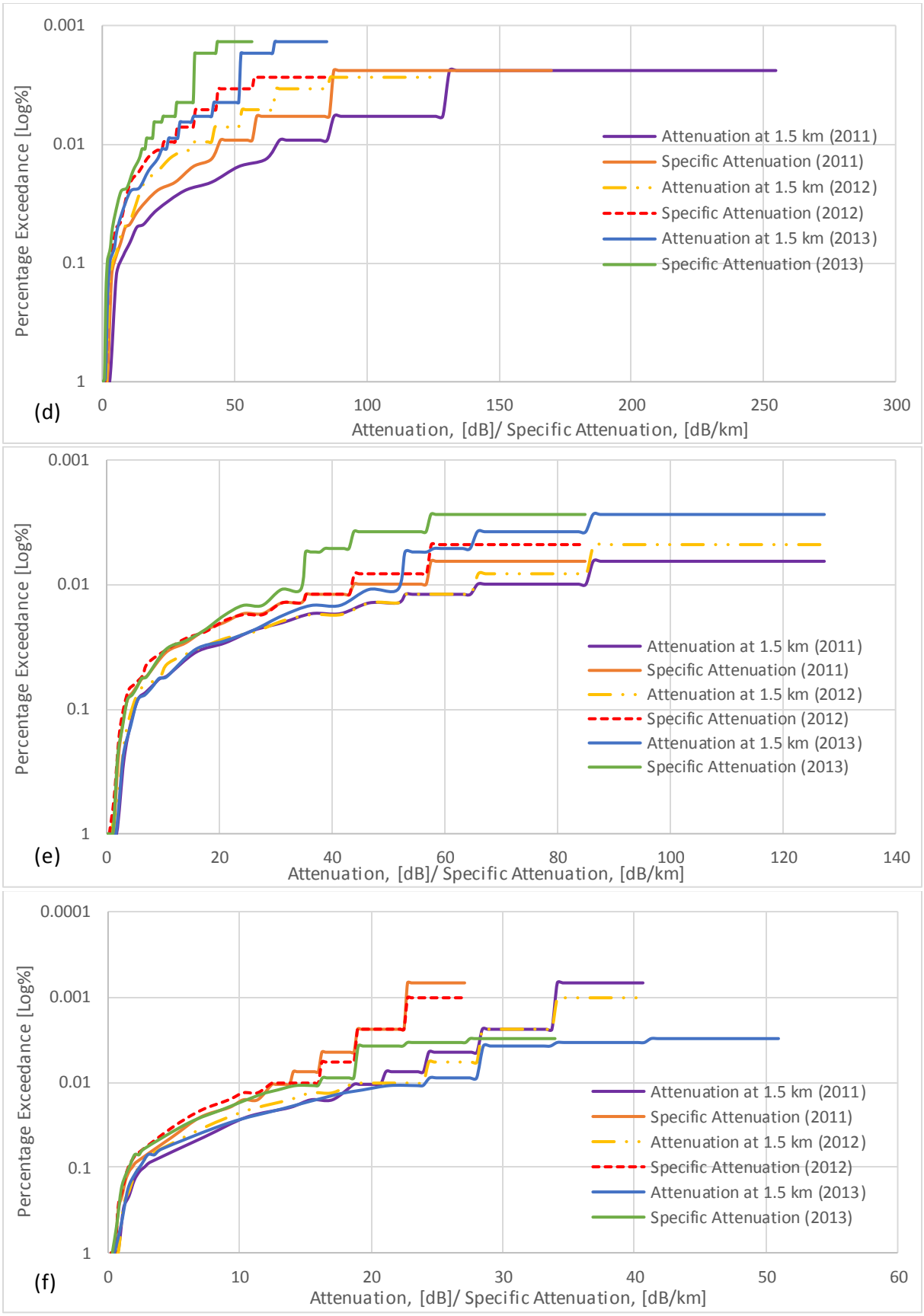

Figure 5.16: Annual cumulative distribution curves for optical attenuation (at 850 nm and 1.5 km distance) and specific attenuation over the years 2011-2013 for (a) Durban; (b) Cape Town; (c) Umtata; (d) Bloemfontein; (e) Johannesburg and (f) Mafikeng.

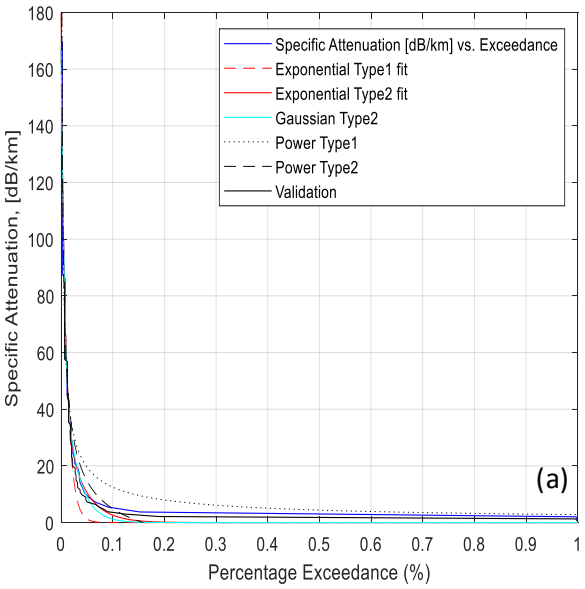
Specific Attenuation [dB/km] vs. Exceedance
Exponential Type1 fit
Exponential Type2 fit
Gaussian Type2
Power Type1
Power Type2
Validation
Specific Attenuation, [dB/km]
Percentage Exceedance (%)
(a)

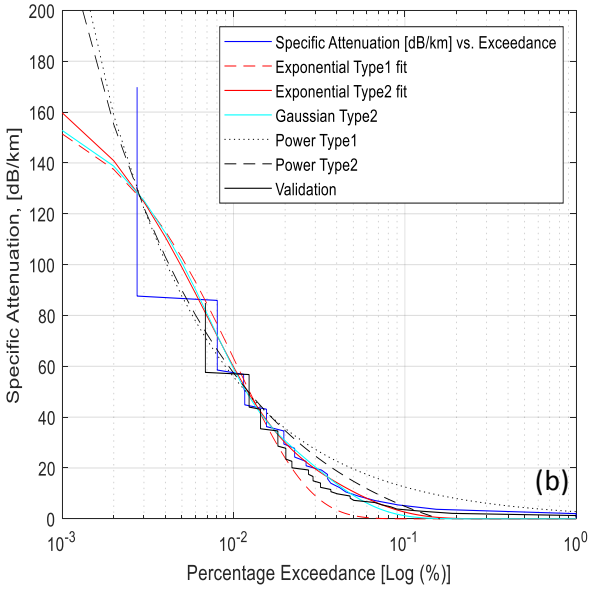
Specific Attenuation [dB/km] vs. Exceedance
Exponential Type1 fit
Exponential Type2 fit
Gaussian Type2
Power Type1
Power Type2
Validation
Specific Attenuation, [dB/km]
Percentage Exceedance [Log (%)]
(b)

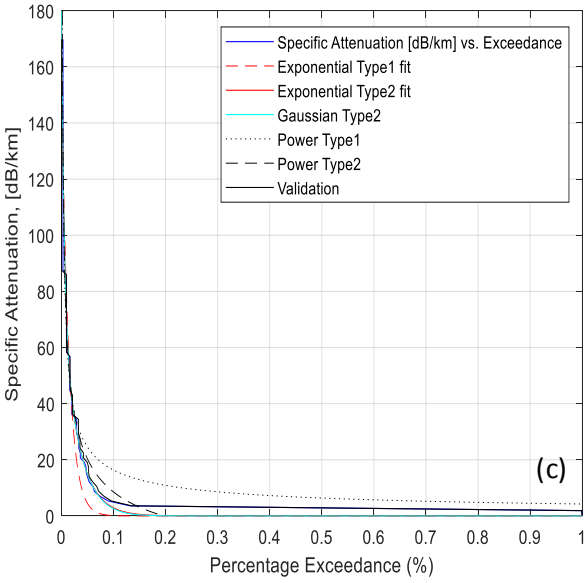
Specific Attenuation [dB/km] vs. Exceedance
Exponential Type1 fit
Exponential Type2 fit
Gaussian Type2
Power Type1
Power Type2
Validation
Specific Attenuation, [dB/km]
Percentage Exceedance (%)
(c)

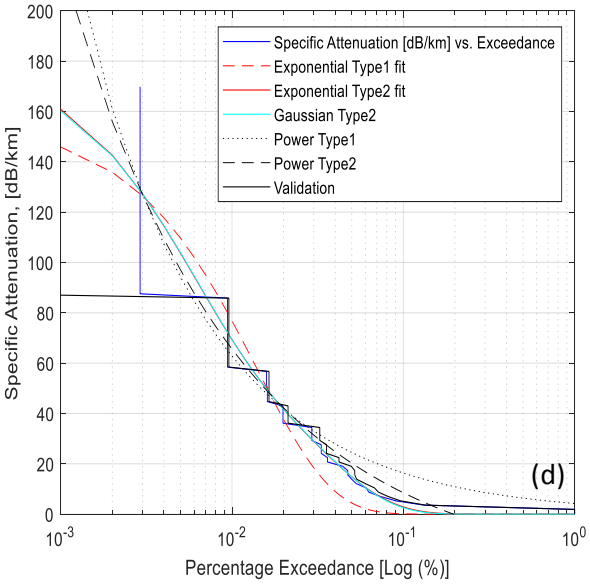
Specific Attenuation [dB/km] vs. Exceedance
Exponential Type1 fit
Exponential Type2 fit
Gaussian Type2
Power Type1
Power Type2
Validation
Specific Attenuation, [dB/km]
Percentage Exceedance [Log (%)]
(d)

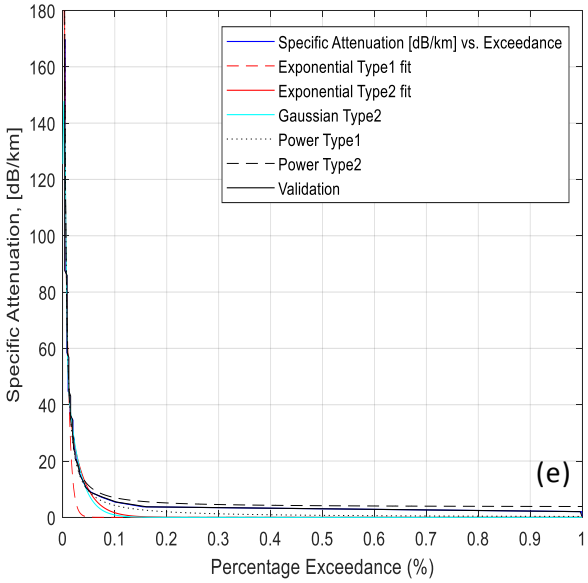
Specific Attenuation [dB/km] vs. Exceedance
Exponential Type1 fit
Exponential Type2 fit
Gaussian Type2
Power Type1
Power Type2
Validation
Specific Attenuation, [dB/km]
Percentage Exceedance (%)
(e)

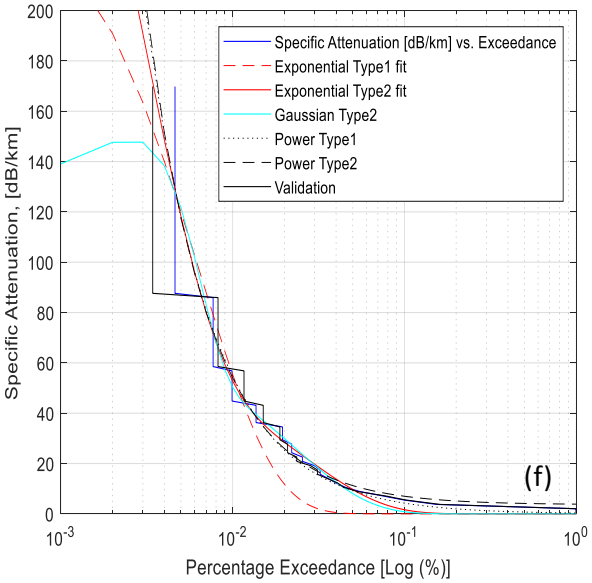
Specific Attenuation [dB/km] vs. Exceedance
Exponential Type1 fit
Exponential Type2 fit
Gaussian Type2
Power Type1
Power Type2
Validation
Specific Attenuation, [dB/km]
Percentage Exceedance [Log (%)]
(f)

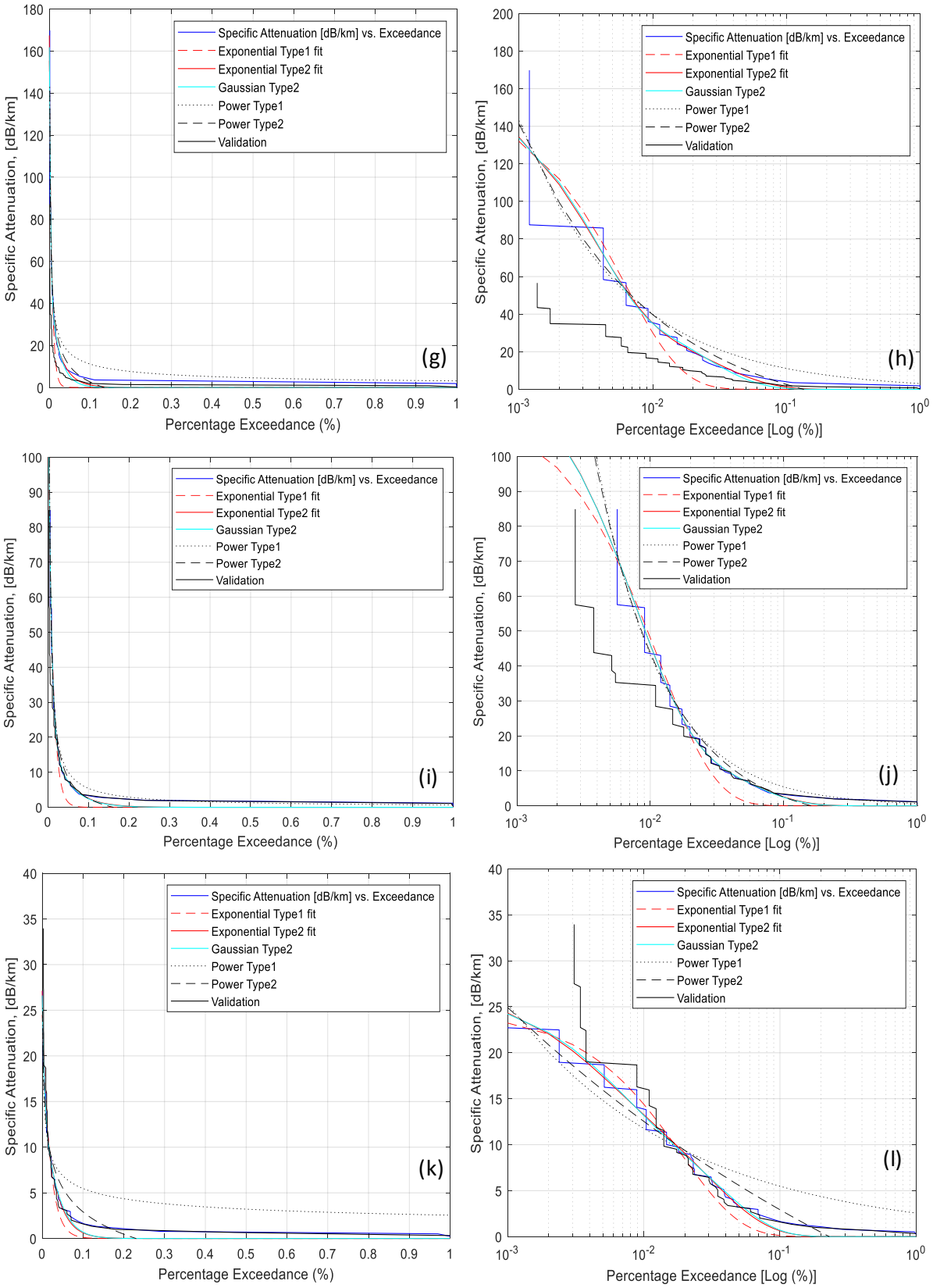

Figure 5.17: Performance evaluation and model validation for various models of Specific attenuation for (a) Durban [in % (scale)]; (b) Durban [in Log%]; (c) Cape Town [in %]; (d) Cape Town [in Log%]; (e) Umtata [in %]; (f) Umtata [in Log%]; (g) Bloemfontein [in %]; (h) Bloemfontein [in Log%]; (i) Johannesburg [in %]; (j) Johannesburg [in Log%]; (k) Mafikeng [in %]; (l) Mafikeng [in Log%], using years 2011 and 2012 as actual cumulative distribution curve and 2013 for validation.

Table 5.8: Specific attenuation and Optical attenuation (at 850 nm and 1.5 km link distance) values at 0.01 % exceedance window obtained from the CDF curves for each location over the three years.

	2011		2012		2013		Overall Mean	
City	Specific Att. [dB/km]	Optical Att. [dB]	Specific Att. [dB/km]	Optical Att. [dB]	Specific Att. [dB/km]	Optical Att. [dB]	Specific Att. [dB/km]	Optical Att. [dB]
Durban	56.817	85.225	56.895	85.342	56.749	85.123	56.820	85.230
Cape Town	58.476	87.714	58.429	87.643	58.429	87.643	58.445	87.667
Umtata	56.817	85.225	44.880	67.320	56.817	85.225	52.838	79.257
Bloemfontein	44.700	67.050	23.258	34.887	16.182	24.272	28.047	42.070
Johannesburg	43.894	65.841	43.972	65.958	34.448	51.672	40.771	61.157
Mafikeng	13.804	20.706	15.974	23.961	15.952	23.928	15.243	22.865

Table 5.9: Distribution parameters and fit statistics for Exponential Type 2 model of specific attenuation for different locations over the entire period under study.

General Optical Attenuation (due to visibility) Model: Exponential Type 2 (Exp2) $\alpha = a * \exp(b * p) + c * \exp(d * p)$ Coefficients (with 95% confidence bounds):						
Coefficients	Durban	Cape Town	Umtata	Bloemfontein	Johannesburg	Mafikeng
a	138.80	76.900	57.070	127.80	113.50	9.6170
b	-162.70	-32.900	-35.450	-286.80	-134.00	-263.10
c	42.950	105.90	122.70	39.680	20.170	17.500
d	-27.910	-202.30	-282.20	-35.070	-20.680	-33.160
Goodness of fit:						
SSE	0.3014	0.3022	0.3025	0.3024	0.2567	0.0913
R^2	0.8766	0.8765	0.8761	0.8764	0.9578	0.9851
Adjusted R^2	0.8727	0.8726	0.8723	0.8726	0.9565	0.9846
RMSE	0.0177	0.0177	0.0178	0.0177	0.0052	0.0010
Goodness of Validation						
SSE	0.6231	0.1346	0.1201	0.2573	0.6073	0.2998
RMSE	0.0795	0.0367	0.0347	0.0507	0.0246	0.0055

Table 5.10: Specific attenuation modelling from two-part general exponential model over selected percentage exceedance values for different locations.

General Optical Attenuation (due to visibility) Model: Exponential Type 2 (Exp2) $\boldsymbol{\alpha = a * \exp(b * p) + c * \exp(d * p)}$						
Percentage Exceedance (p)	Durban	Cape Town	Umtata	Bloemfontein	Johannesburg	Mafikeng
			dB/km			
0.1	2.64	2.86	1.65	1.19	2.55	0.64
0.01	59.77	69.35	47.34	35.20	46.12	13.25
0.001	159.73	160.92	147.61	134.25	119.02	24.32
0.0001	179.39	180.43	176.15	163.73	132.12	26.81

CHAPTER SIX

Time Series Prediction and Modeling of Visibility with Artificial Neural Network Technique using Meteorological Data for South Africa

6.1 Introduction

Weather forecasting is a system that depicts the atmospheric conditions predicted for a particular length of time and location, supplemented by many statistical and empirical methods [210]. This phenomenon can significantly impact several life and global human activities like wireless communications (particularly, FSO transmission system), atmospheric change, air traffic control, public health and safety, and agriculture. In FSO technology, weather prediction has become an interesting matter, based on its great applications. As a matter of fact, one of the most vital meteorological data for FSO is visibility. There are several meteorological parameters (temperature (T), relative humidity (RH), wind speed (WS), pressure (P)) studied in this work that can strongly impact the range of visibility and its trends (daily or seasonal), and then considerably affect the optical link performance. Visibility degradation because of various suspended atmospheric particles like fog, haze, clouds, water vapor and gases, is one of the greatest indicators of high atmospheric attenuation along the FSO path, and as earlier reported in Chapters 4 and 5 of this dissertation, it was observed that it is the main concern in the marine or near-coastal environments. This indicates that measurement and study of certain variables like visibility as well as other climatic observables, are important to ensure a condition where there are low or no atmospheric attenuations. The significance of predicting or measuring visibility for FSO transmission technology are many, which includes delivering sufficient statistics to the FSO engineers and technicians so as to advise and design suitable FSO links and then produce appropriate attenuation mitigating measures.

Time series can generally be described as an organized order of different measurements for a particular event at a specific period that apparently disagrees with any discrete pattern, model or law. Furthermore, a question that still needs great consideration is how to realize an enhanced as well as more correct prediction time series with good efficiency. To tackle this subject, many scholars have recommended several time series predicting methods, such as Artificial Neural Network (ANN), Simple Moving Average (SMA), Multi-variant Regression Analysis (MRA), Auto-Regressive Integrated Moving Average (ARIMA), etc. [211-213].

The main goal of this study is to predict visibility, and therefore to demonstrate the distinction between the relationships of different climatic data (like RH, T, P and WS) to the visibility range through Artificial Intelligence (AI) techniques, particularly the ANN architecture, over FSO channels for the year 2013 for six different regions within South Africa. The goal isn't to find the optimal ANN technique or architecture; rather, it is to illustrate how each or all the meteorological variables relate to the

observed visibility range. Because of its simplicity and flexibility, the Feedforward backdrop propagation neural network (FF-BPNN) was chosen as the network type, with the "Levenberg-Marquardt (LM)" as the training algorithm (which suggests that the option "trainlm" was naturally selected as the training function), "LearnGDM" as the adaption learning function, and "TANSIG" as the transfer function. The above-mentioned meteorological factors were employed as independent variables, whereas visibility was used as the dependent variable. The respective connections between the numerous independent factors and the dependent variable were initially determined using Single-Variable Regression Analysis (SVRA) before the ANN method was used. The RMSE, Mean Bias Error (MBE), and coefficient of determination (R^2) are the performance metrics for the ANN approach in this study.

6.2 Past Works on the Relationship between Visibility and various Meteorological Variables

The transmission of optical signals through the atmosphere for OWC system is among the numerous operations that are impacted negatively by the occurrence of low visibility values or foggy weather within the atmosphere. Therefore, this drastic visibility condition significantly impacts FSO activities within the period considered, most importantly resulting into extremely low atmospheric attenuation [213 - 215].

It has been established in the literature review that visibility depends on the conditions of various atmospheric variables (most importantly, relative humidity and temperature). Several studies have disclosed that there is a relationship between low visibility and high RH. Based on the results presented by Usman *et al.* [216], it was revealed that there is a linear relationship between visibility range and RH, and T respectively, using a 5-year data of monthly-mean visibility. Using data obtained in the extratropical stratiform clouds, Boudala and Isaac [217] in their work suggested that during the winter period of the years 2005-2007, visibility showed substantial relationship with snowfall rate, and weaker relationship with both RH and T, while it showed weakest relationship with WS.

6.3 Past Works on the Prediction of Visibility in terms of Atmospheric Variables using ANN

Artificial Intelligence (AI) techniques have been discussed in several literatures over the years, based on their effective application in solving complicated weather problems. Lopez *et al.* [218] estimated visibility by means of the ANN technique using meteorological and radiometric parameters collected in Huelva (southern Spain). The results from their work showed that the relationships were non-linear and an improvement was observed when the numerous input data involving RH, T, P, WS, precipitable water (PW), diffuse horizontal irradiance and direct normal irradiance were analysed simultaneously. In 2015, Chaudhuri *et al.* [219], used ANN to predict fog occurrences at some airfields, and it was revealed that fog prediction at airports is quite a hard and weighty task, despite the incessant developments in many numerical weather prediction models. Nevertheless, these scholars used a multi-layer perception neural network (MLPNN) type to improve those models, and it was discovered that

there was a considerable drop in the estimated errors. As a result, the learning model for forecasting the likelihood of fog on airports has been enhanced and modified.

6.4 ANN Architecture Description and its Applications

When determining a parametric relationship between various atmospheric variables (i.e., between dependent and independent atmospheric variables), complexities or inaccuracies are frequently encountered, particularly when standard statistical techniques (SST) are utilized to predict specific weather variables (in this case, visibility and extinction coefficient). Thus, a sophisticated and unusual AI tool like the ANN or Fuzzy logic may be used to tackle challenges that arise as a result of linking dependent and independent atmospheric factors, such as visibility and any or all of RH, T, P, and WS. As a result, when examining the link between visibility and other atmospheric inputs, the SST has not been able to eliminate these problems.

The ANN is a modeling tool that may be used to anticipate a variety of activities, such as atmospheric occurrences, that have non-linear relationships and are difficult to predict using traditional statistical or numerical methods [213, 220]. The overall concept of a common ANN approach is shown in Figure 6.1. The ANNs are nodal networks that are trained by utilizing a large number of entries originating from the system's internal or external situations. These resulting entries are then multiplied by weights that are assigned at random (as shown in Figure 6.1). This training procedure continues across all the segments of the network, until the neural network achieves an anticipated error that is within the intended limit. Otherwise, this process continues to do fresh calculations using the backpropagation approach for error correction of incoming data [213, 220].

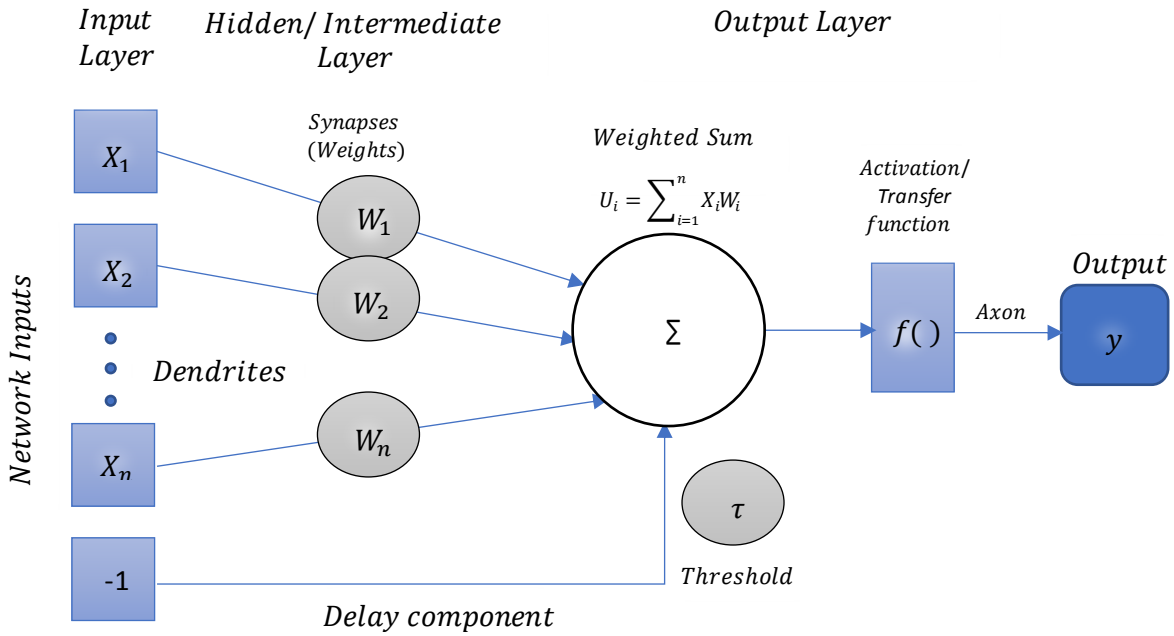

Figure 6.1: Schematic diagram of the model of a typical Artificial Neural Network.

The network training procedure produces the desired output value, which is then tested and validated using known values. In general, a greater percentage of the input data (about 3/4) is used for training, while the remaining 1/4 is used for network testing and validation.

6.5 Meteorological Materials and Methods

6.5.1 Site Study and Description of Meteorological Data

The areas under study in this section of the research work include all the sites described in Table 3.1, which consists of coastal, near-coastal and non-coastal environments. The climatic dataset utilized in this analysis comprises of synoptically averaged values of relative humidity, temperature, pressure, wind speed, and visibility acquired from the SAWS and NCIE/NOAA databases. The measurement period is from 1st January 2013 to 31st December 2013.

6.5.2 General Methodology

In this work, visibility dependence on different atmospheric parameters was studied, in order to improve the design of the FSO link as well as the operations of the FSO technology. As stated earlier in this thesis, that the occurrences with severe visibility impairments during fog events greatly and negatively affect the surface operations of the FSO system. Therefore, since there are limited or no adequate work on predicting both the visibility and the optical attenuations for FSO applications with respect to various meteorological factors and variables, unlike the numerous research works done on aerodrome visibility and atmospheric variables, the results and models resulting from this work is to help improve the FSO link design. For proper FSO design and operation, the visibility outcome of a particular region at some given period or season needs to be monitored, which is often not performed at all sites as a result of certain complexities. In addition, these generated models can be used by other numerous areas of applications, which require visibility data to fill gaps in various phenomena like in time series measurement. Using the ANN architecture and one year data of temporal series of the atmospheric variables mentioned earlier, this research work has been able to propose an AI technique intended to forecast visibility. These climatic data were employed to train the MPLNN architecture with a backpropagation error correction method, with the intention of predicting visibility for different provinces within South Africa.

Nevertheless, a multivariate analytical analysis that uses the normal statistical techniques may not be able to provide adequate solution to this relationship due to its complexity. Therefore, this research work used the ANN method to provide a better relationship between the visibility range and the atmospheric variables. A fitting relationship between V and different parameters of the atmosphere were obtained using the ANN approach. It was possible to design a suitable ANN model to achieve the visibility parametrization based on a certain number of input variables, by using a computer simulation tool (that is, MATLAB software). This model was activated according to a uniformly random distribution approach, such that the entire set of data were categorized into three subsets in order to train, validate and test the obtained ANN models. Consequently, for each location considered, the sets

of data for training, validation and testing consist of 75%, 15% and 15% of the whole one-year climatic data values respectively, which also matches to 2044, 438 and 438 samples of each atmospheric variable respectively. Moreover, the "nnstart" application tool accessible in the MATLAB software, can be used to accomplish this neural network model as well as the random distribution of data.

6.5.3 ANN Approach and Methodology to Predict Visibility

6.5.3.1 Feed-Forward Neural Network

A Feed-forward Neural Network (FFNN) is a type of ANN technique which can be referred to as a multilayer perceptron (MLP) network, with one directional flow system starting from the input to the output, through a series of network layers. The FFNN model can approximate any function specified by f', such that $y = f'(X)$ maps an input (X) to an output (y). Thus, it can be used to obtain the values of the parameter (μ) that results into the best function approximation, by mapping $y = f(X;\mu)$. It should be noted that the ANN improves its network by learning from the environment [221-223].

A simple arrangement of the multi-layer FFNN model used in this work is provided in Figure 6.2 [247]. In order to predict visibility under the ANN technique, the Back Propagation Neural Network (BPNN) method was applied in a feed-forward system. Mostly, this type of network architecture of the feed-forward primarily involves three layers, that is independent, hidden and dependent layers, along with the appropriate weights (w) and biases or disturbances (b).

Figure 6.2 gives the typical MLP neural network architecture (specifically, a FF-BPNN model) with three layers. The hyperbolic tangent transform is selected as the non-linear activation function for the intermediate network layer (symbolised by h), while the identity function is chosen as the activation function for the dependent or output network layer (signified by o). However, a non-linear mapping (shown as series of lines in Figure 6.2) is created from an input vector $\{x_1, x_2, \dots, x_{N_i}\}$ with N_i input variables (representing the existing meteorological variables) to the output (that is visibility (V)), and the generated model is given as [218, 220]:

$$V = \sum_{j=1}^{N_h} w_j^o \, tanh\left(\sum_{i=1}^{N_i+1} w_{ij}^h x_1\right) + w_{N_h+1}^o , \tag{6.1}$$

where the variables i and j represent the varying inputs and the iteration variable (which depends on the number of hidden neurons) respectively, the parameter N_h are the number of hidden neurons, w_{ij}^h denoted the weights relating the input layer to the hidden layers and w_j^o are the weights connecting the hidden layers to the output layers.

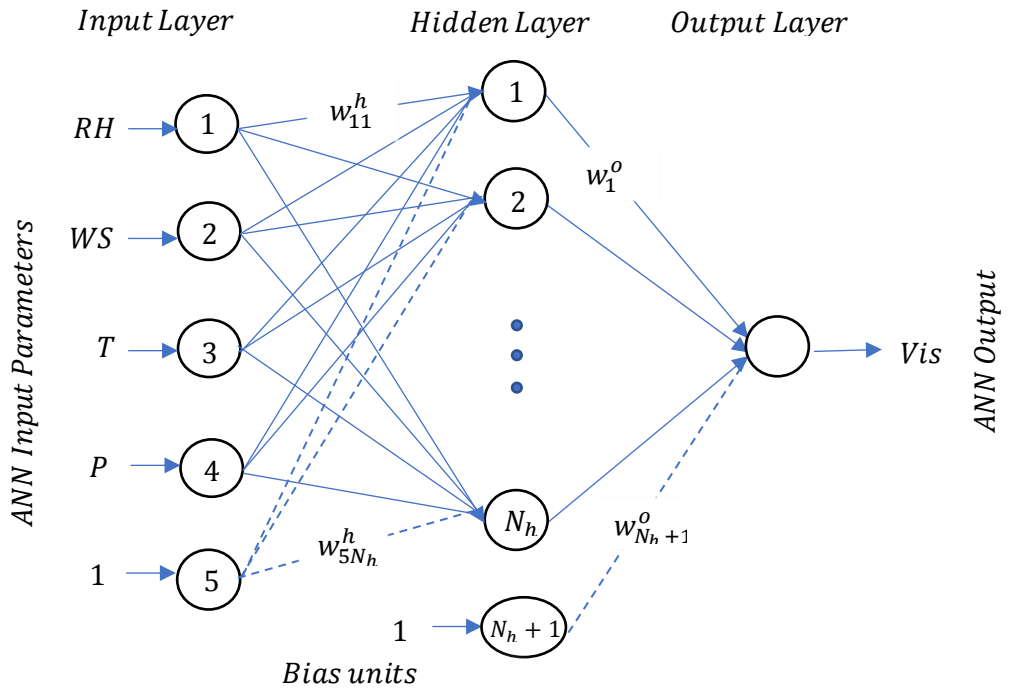

Figure 6.2: A typical Multi-layer Feed-Forward Neural Network.

6.5.3.2 Selection and Allocation of the ANN model parameters

In this research study, the employed ANNs are constructed through a blend of custom-designed MATLAB functions, particularly the neural network dynamic time series and neural network fitting application tools. In this case, the number of independent and dependent variables determines the number of both input and output neurons respectively. There are some important points to note; that the N_h choice for this ANN model is usually vital as well as the fact that the number of intermediate neurons is generally chosen randomly. Therefore, the minimum amount of neurons such that the performance assessed on the validation dataset becomes acceptable, practically determines the optimum N_h value.

Using a synoptic data consisting of four atmospheric variables over a period of one year (corresponding to 2920 data points) were trained, tested and validated by the FF-BPNN model. An efficient ANN architecture was generated from the several input data for the estimation of visibility. Iterations were accomplished according to the number of hidden layers and the properties of the layers (like number of neurons and the transfer function of each of the hidden layers) chosen for this work. Since the primary goal of this study is to demonstrate the functional dependence of visibility on various meteorological factors rather than to distinguish between various ANN predictive model configurations, certain neural network structures and parameters have been chosen and presented in Table 6.1. As a result, the number of iterations required by the ANN model was calculated using the model parameters shown in Table 6.1. In addition, MATLAB-ANN application tools were utilized to construct the neural network system in this study, where the input data from the six sites was processed and used for the proposed ANN model's training, validation, and testing.

Table 6.1: ANN properties with their corresponding functions and values.

ANN Properties	Functions and Values
Network Type	Feed-forward Back Propagation Neural Network
Training Method	Gauss-Newton based Lavenberg-Marquartd
Training Function	TRAINLM
Adaptive Learning Function	LEARNGDM
Number of Layers	2
Number of Neurons	15
Transfer Function	TANSIG

6.6 Accuracy Measures

Therefore, a visibility estimate was generated every three hours using the created ANN-Visibility model, while the error or accuracy analysis (in terms of R^2, RMSE and MBE) were produced from the evaluation of the measured visibility with the predicted visibility in km. Error measurements were determined for all the input cases formulated for all the stations considered in this work. Due to the difficulties in deciding if the computed value of R^2 is considered significant, the value must be taken as either very weak or strong if $R^2 < 0.3$ or $R^2 > 0.7$ respectively, while it is weak or moderate if $0.3 < R^2 < 0.5$ or $0.5 < R^2 < 0.7$ respectively [178, 225].

6.7 Analysis and Results of the Dependence of Visibility on various Meteorological Variables

In this section, the SST was first employed then followed by the ANN method, to examine the effects of several atmospheric variables (independent observables) on visibility.

6.7.1 Standard Statistical Techniques

This method involves carrying out regression on V against various meteorological variables. Non-linear functional relationships between visibility and the various meteorological variables were obtained by using the SST on synoptic datasets over the year 2013 for all the locations under study. The type of curve fitting and error results (in terms of R^2) of these non-linear regression fits are presented in Table 6.2.

According to the coefficient of determination, the statistical results of the SST performances provided in Table 6.2 for different input variables, showed that there is moderately strong relationship between V and RH, whereas there are weak dependences of V on both T and WS for all of the cities considered. Therefore, visibility variability explained by RH ranges from $\approx 25\,\% - 36\,\%$, and that of T, WS and P ranges from $\approx 12\,\% - 15\,\%$, $\approx 9\,\% - 18\,\%$ and $\approx 2\,\% - 7\,\%$ respectively over the different locations considered. In other words, the mean R^2 value defined by RH, T, P and WS for all the stations are 0.3043, 0.1283, 0.0443 and 0.1306 respectively. These results show that the functional dependence of visibility in South Africa is strongest on relative humidity and weakest on pressure. In addition, these

mean visibility variabilities defined by T and WS indicates that they both contribute fairly to the fluctuations in visibility within these regions. Therefore, using the SST, the functional dependence of visibility on the climatic parameters have been determined, and the outcome revealed that relationship between them lack good correlation.

Table 6.2: Curve fitting and error estimation results of the SST performances using various meteorological variables for each of the locations.

City	Input Variable	Type of Fit	R^2
Durban	RH	Poly2	0.3017
	T	Poly2	0.1169
	P	Exp1	0.0356
	WS	Poly2	0.1091
Cape Town	RH	Poly2	0.3618
	T	Poly2	0.1515
	P	Poly2	0.0234
	WS	Poly2	0.1509
Umtata	RH	Poly2	0.3475
	T	Poly2	0.1213
	P	Poly2	0.0574
	WS	Poly2	0.0937
Bloemfontein	RH	Poly2	0.2513
	T	Poly2	0.1305
	P	Poly2	0.0349
	WS	Poly2	0.1786
Johannesburg	RH	Poly2	0.3072
	T	Poly2	0.1219
	P	Poly2	0.0489
	WS	Poly2	0.1122
Mafikeng	RH	Poly2	0.2565
	T	Poly2	0.1309
	P	Poly2	0.0658
	WS	Poly2	0.1391

6.7.2 Artificial Neural Network Technique

In this section, the ANN technique was utilized for the prediction of visibility through datasets of various meteorological variables. Based on the earlier discussed literatures, it is plausible to obtain a more accurate result between V and the other weather parameters, using the ANN method.

As presented in Table 6.3, the four input variables used in data training and prediction of visibility were classified into five different input cases, which comprises one or more input variables at a time. The input Case-1 which is referred to as the base case consist of only RH, whereas the input Case-5 consists

of all the variables, and it is referred to as the saturated case. According to the findings of the SST, which reported that the RH was the most significant meteorological parameter, therefore RH was chosen as the base case for the ANN input configurations. The WS and T were then taken as the next significant input variables due to their almost equal mean error estimates, while P is considered as the least significant. The input time series were loaded with respect to the trend of the input cases and the visibility time series were loaded as the target time series. As earlier discussed, the ANN technique can only be executed by assigning a certain portion of the respective input data to the training, validating and testing modes. Each of the input data were divided as follows: 70 % for training the network, 15 % for validation and 15 % for testing.

6.7.2.1 ANN simulation procedure and analysis

The simulation of the ANN model using the Neural Network time series application tool (in particular, the Nonlinear Autoregressive network with External (Exogenous) input (NARX) model) in MATLAB was attained using the following steps:

a. Use the input case with all the parameters to select the proper number of hidden neurons N_h and hidden layers. To select the best value for N_h, a range of values from $N_h = 2$ to $N_h = 40$ were tried, and the appropriate value was identified.

b. The obtained values of $N_h = 15$ and $h = 2$ (from (a)) were used as pre-set values to train, validate and test all the input cases specified in Table 6.3.

c. Perform ten trainings for each input case and calculate average, to remove over or under estimation.

d. Use forward adding method to add more input data and then select best input case with lowest error.

e. The average of all the error metrics were calculated and recorded in Table 6.4.

6.7.2.2 ANN prediction results and discussion

The results of the network training, validation, testing and prediction using 75 %, 15 %, 15 % and 100 % of the entire data respectively are presented in Figures 6.3 to 6.8, for all the cities. In these plots, the R values and the generated equations of the estimated visibility obtained from the ANN model are also presented. For each of these plots, coloured lines signify the final outcomes of the network training, validation, testing and forecasting, whereas the dotted lines show the anticipated visibility outcome. The regression results presented only show the output of the input Case-5 analysis which contains all the input variables and these figures also show the plots with maximum R^2 among the 10 different trainings performed for each input Case-5.

The results of the network training for Durban, Cape Town, Umtata, Bloemfontein, Johannesburg and Mafikeng showed quite reasonable reliability of around 83.60 %, 86.83 %, 84.38 %, 80.81 %, 84.33 % and 80.30 % respectively. Also, the results of the network validation for Durban, Cape Town, Umtata, Bloemfontein, Johannesburg and Mafikeng showed acceptable reliability of about 81.03 %, 82.45 %, 80.13 %, 80.88 %, 79.83 % and 81.65 % respectively. The statistical results of the error estimations of the proposed ANN model used to determine the predicted visibility from various atmospheric data over the year 2013 for all the locations are shown in Table 6.3.

The performances of the ANN models were observed for all input cases based on the averages of R^2, RMSE, and MBE, and their SDs. As the number of input increases, the results show clear significant improvement in the estimated visibility, when compared to the base case consisting of only the RH. It can also be observed that all the input variables together seem to show some good correlation with visibility, which indicates that all these parameters yield an extra visibility variability.

Table 6.3 shows that the average R^2 for Durban, Cape Town, Umtata, Bloemfontein, Johannesburg and Mafikeng all improved from 0.5156 to 0.6701, 0.5368 to 0.7002, 0.5191 to 0.6612, 0.4955 to 0.6322, 0.5073 to 0.6658 and 0.4798 to 0.6235 respectively, while the mean RMSE actually drop from 38.56 % to 31.97 %, 36.62 % to 29.42 %, 39.71 % to 32.55 %, 40.05 % to 34.13 %, 39.11 % to 32.92 % and 41.09 % to 35.67 % respectively. The average bias in the predicted visibility is estimated by the MBE, which indicates when the obtained visibility data have been either over-estimated or under-estimated. The values of the MBE (in %) gotten from the ANN model for all the input cases are presented in Table 6.3, where its values for the input Case-5 are $-0.22 \pm 0.12, -0.15 \pm 0.10, -0.25 \pm 0.25, -0.30 \pm 0.35, -0.35 \pm 0.25$ and -0.32 ± 0.26 for Durban, Cape Town, Umtata, Bloemfontein, Johannesburg and Mafikeng respectively. Therefore, the consequences of the average prediction accuracy plainly illustrates that the produced ANN models did not over-estimate the predicted visibility, because values of the MBE are lower than zero.

It was inferred from the outcomes presented in Tables 6.2 and 6.3 that the mean R^2 when only the RH datasets were utilized to forecast visibility for Durban, Cape Town, Umtata, Bloemfontein, Johannesburg and Mafikeng, improved from 0.3017 to 0.5156, 0.3618 to 0.5368, 0.3475 to 0.5191, 0.2513 to 0.4955, 0.3072 to 0.5073 and 0.2565 to 0.4798 respectively. Therefore, for all the considered locations, the results of the ANN models performed better and therefore it is superior when compared with the SST for predicting visibility.

Using the climatological data that contains relative humidity, temperature, pressure and wind speed for each of the sites considered, the model equation of the proposed ANN for the visibility range in km is expressed as follows:

$$V_p = \alpha V_m + \beta, \tag{6.2}$$

where V_p represents the predicted visibility, V_m denotes the observed visibility, and α and β are two different constants that are functions of RH, T, WS and P. The parameters of the generated model for all of the stations under study, are shown in Table 6.4.

The time series analysis plots that represent the everyday development of the measured and ANN predicted visibilities, and the estimated (using KIM model) and ANN predicted average specific attenuations due to various meteorological data for Durban, Cape Town, Umtata, Bloemfontein, Johannesburg and Mafikeng over the year 2013 are provided in Figures 6.9 (a) to (f). Based on these representations, this research has been able to recreate the daily tours on visibility and average specific attenuation using the ANN method for each of the cities considered. It was observed that the predicted specific attenuation as a result of various atmospheric variables is in good accordance with estimated specific attenuation based on the observed visibility in terms of shape and magnitude.

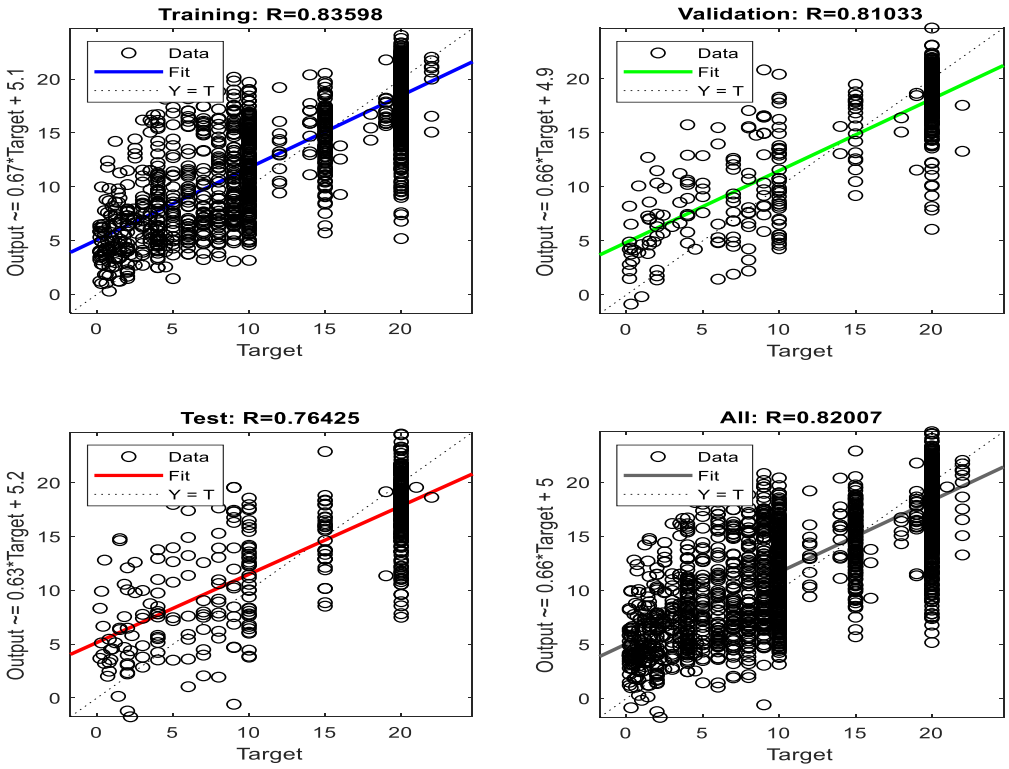

Figure 6.3: Regression plots of the ANN model (a) training; (b) validation; (c) testing and (d) prediction of visibility over the year 2013 for Durban using the multilayer perceptron network with feedback backpropagation algorithm.

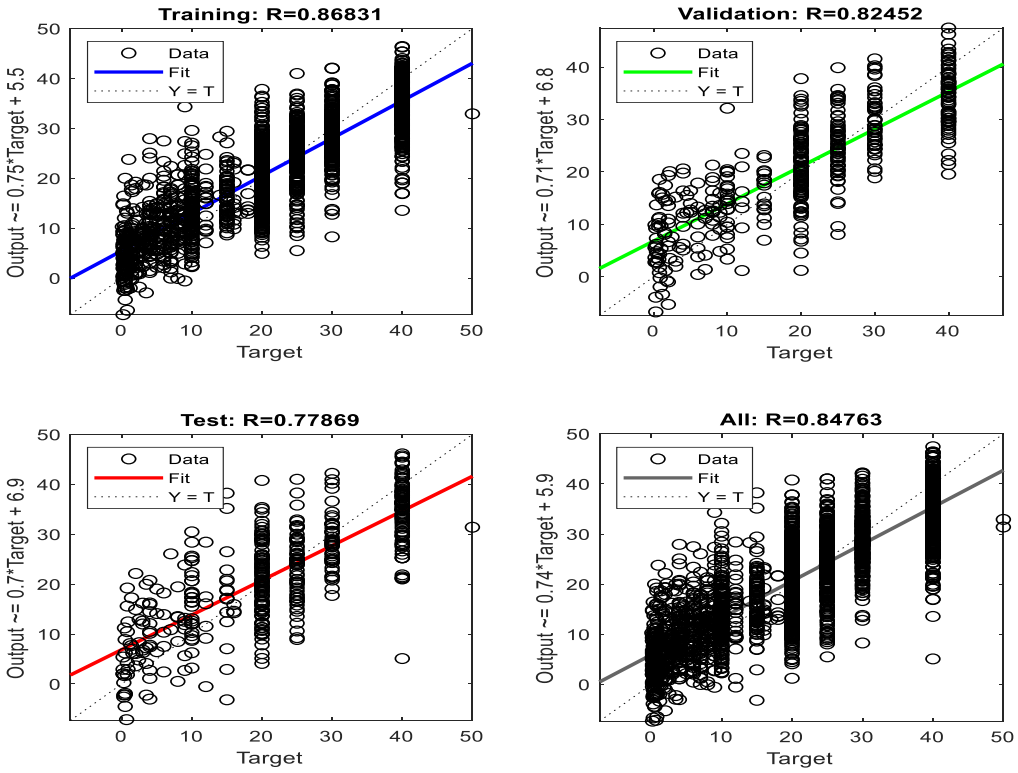

Figure 6.4: Regression plots of the ANN model (a) training; (b) validation; (c) testing and (d) prediction of visibility over the year 2013 for Cape Town using the multilayer perceptron network with feedback backpropagation algorithm.

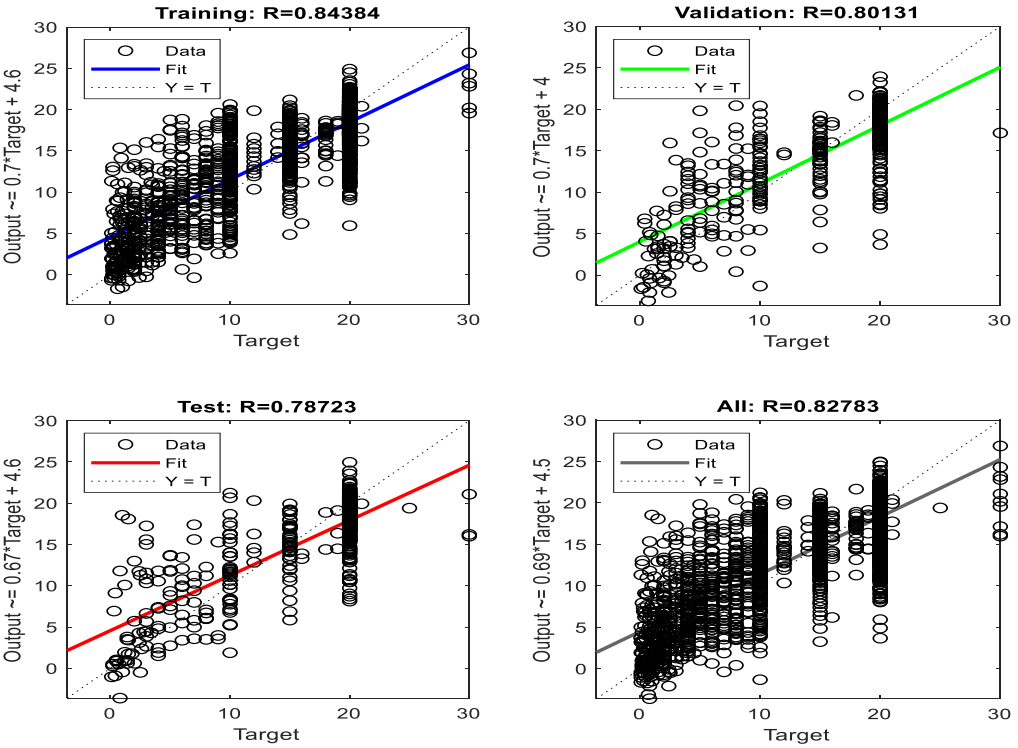

Figure 6.5: Regression plots of the ANN model (a) training; (b) validation; (c) testing and (d) prediction of visibility over the year 2013 for Umtata using the multilayer perceptron network with feedback backpropagation algorithm.

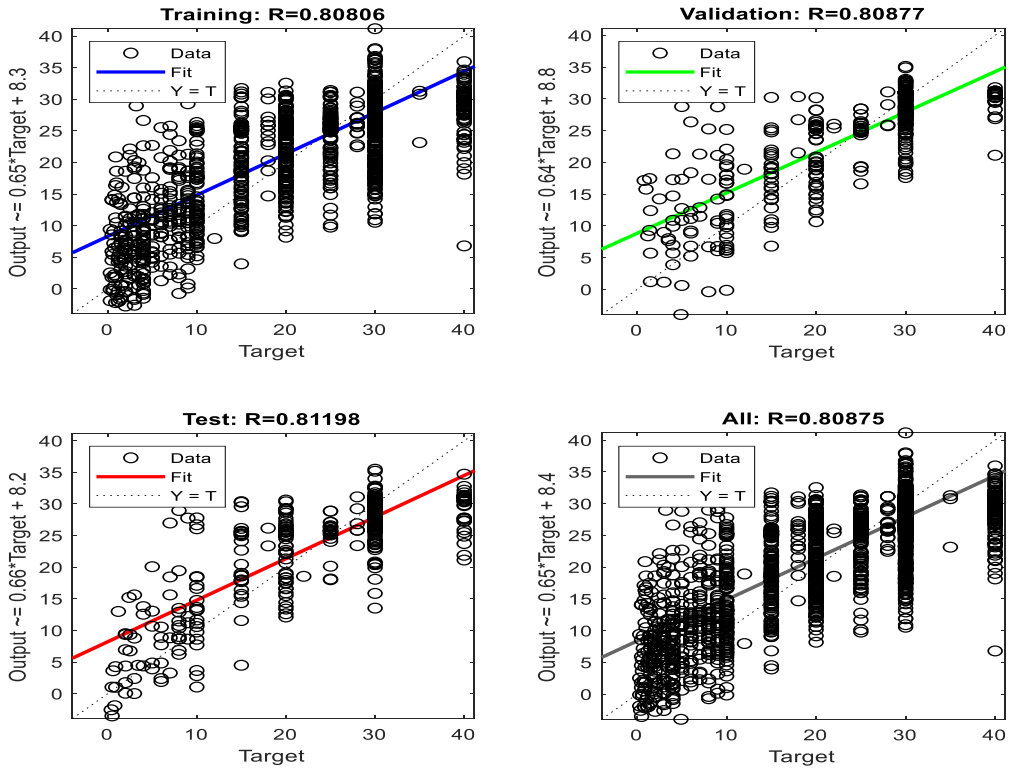

Figure 6.6: Regression plots of the ANN model (a) training; (b) validation; (c) testing and (d) prediction of visibility over the year 2013 for Bloemfontein using the multilayer perceptron network with feedback backpropagation algorithm.

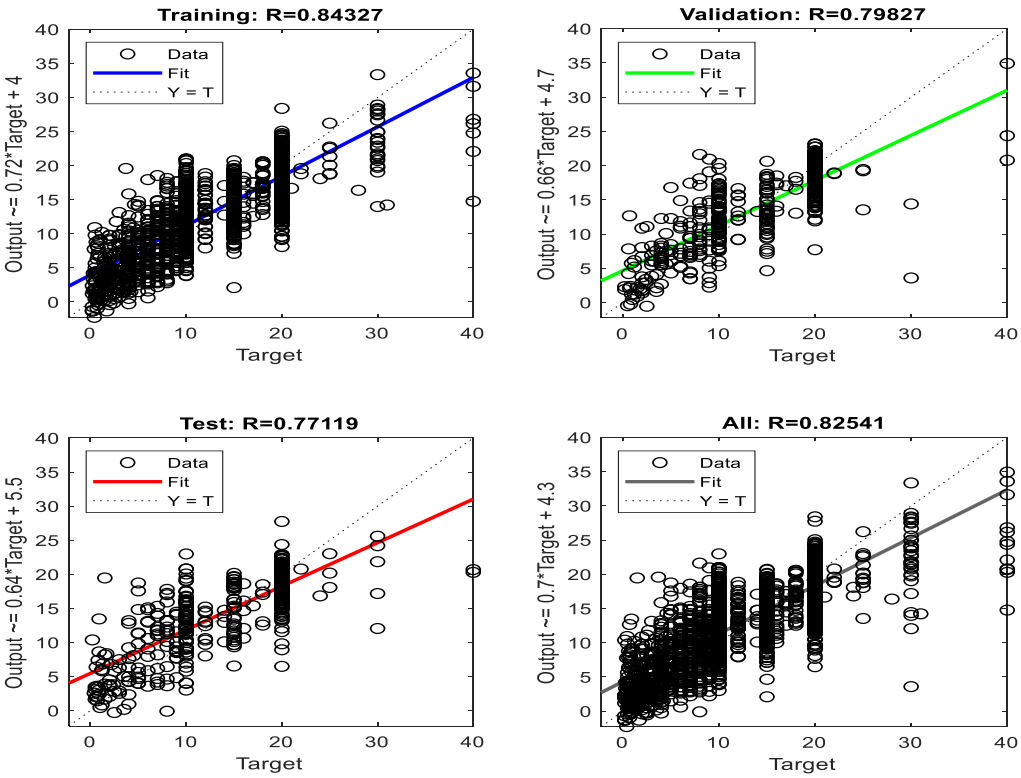

Figure 6.7: Regression plots of the ANN model (a) training; (b) validation; (c) testing and (d) prediction of visibility over the year 2013 for Johannesburg using the multilayer perceptron network with feedback backpropagation algorithm.

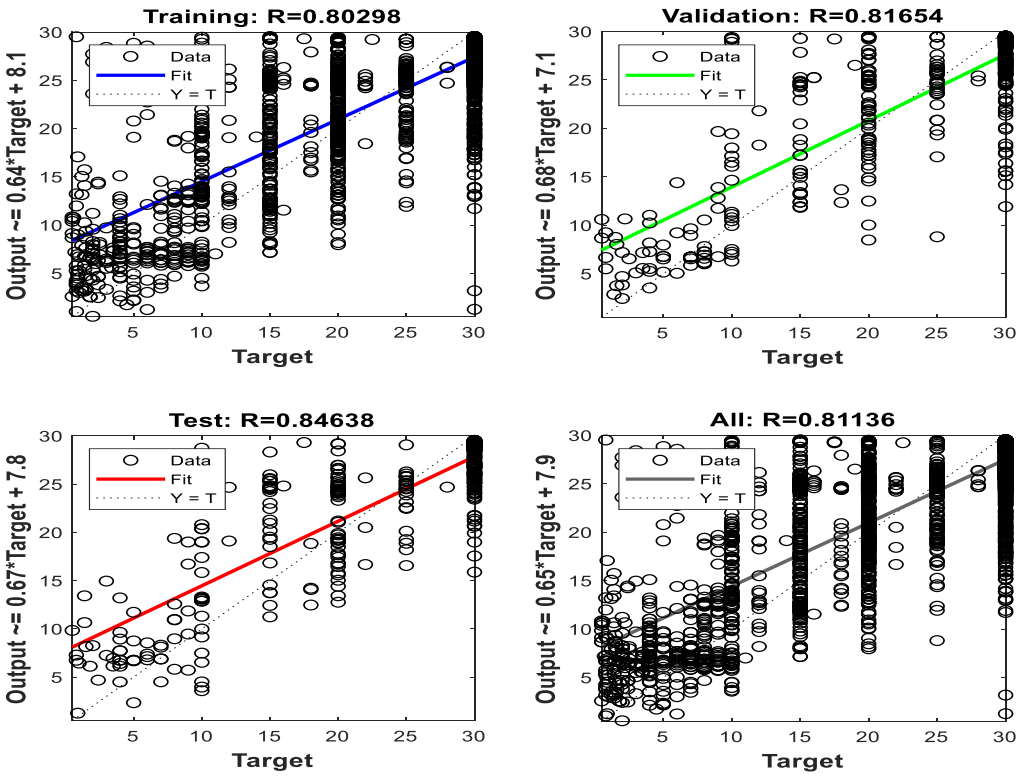

Figure 6.8: Regression plots of the ANN model (a) training; (b) validation; (c) testing and (d) prediction of visibility over the year 2013 for Mafikeng using the multilayer perceptron network with feedback backpropagation algorithm.

Table 6.3: Statistical results of the performances of the ANN models using different input configurations.

Durban				
Input Case	Input Variables	Mean R^2	Mean RMSE (%)	Mean MBE (%)
Case -1	RH	0.5156	38.56±0.25	-0.32±0.11
Case -2	RH, WS	0.6065	35.48±0.24	-0.35±0.10
Case -3	RH, T, P	0.6219	33.82±0.45	-0.50±0.35
Case -4	RH, WS, P	0.6450	33.01±0.68	-0.20±0.30
Case -5	RH, T, P, WS (All Variables)	0.6701	31.97±0.88	-0.22±0.12
Cape Town				
Input Case	Input Variables	Mean R^2	Mean RMSE (%)	Mean MBE (%)
Case -1	RH	0.5368	36.62±0.15	-0.25±0.12
Case -2	RH, WS	0.6335	33.59±0.22	-0.10±0.25
Case -3	RH, T, P	0.6573	32.76±0.55	-0.34±0.30
Case -4	RH, WS, P	0.6760	31.45±0.76	-0.20±0.13
Case -5	RH, T, P, WS (All Variables)	0.7002	29.42±0.92	-0.15±0.10
Umtata				
Input Case	Input Variables	Mean R^2	Mean RMSE (%)	Mean MBE (%)
Case -1	RH	0.5191	39.71±0.17	-0.34±0.22
Case -2	RH, WS	0.5964	37.02±0.28	-0.20±0.10
Case -3	RH, T, P	0.6178	35.77±0.43	-0.41±0.32
Case -4	RH, WS, P	0.6384	34.32±0.65	-0.55±0.25
Case -5	RH, T, P, WS (All Variables)	0.6612	32.55±0.75	-0.25±0.25
Bloemfontein				
Input Case	Input Variables	Mean R^2	Mean RMSE (%)	Mean MBE (%)
Case -1	RH	0.4955	40.05±0.27	-0.20±0.33
Case -2	RH, WS	0.5792	37.88±0.34	-0.44±0.29
Case -3	RH, T, P	0.5912	36.85±0.39	-0.56±0.30
Case -4	RH, WS, P	0.6001	36.01±0.58	-0.25±0.31
Case -5	RH, T, P, WS (All Variables)	0.6322	34.13±0.76	-0.30±0.35
Johannesburg				
Input Case	Input Variables	Mean R^2	Mean RMSE (%)	Mean MBE (%)
Case -1	RH	0.5073	39.11±0.14	-0.32±0.26
Case -2	RH, WS	0.5899	36.89±0.33	-0.48±0.30
Case -3	RH, T, P	0.6132	35.66±0.42	-0.50±0.32
Case -4	RH, WS, P	0.6221	35.13±0.56	-0.24±0.10
Case -5	RH, T, P, WS (All Variables)	0.6658	32.92±0.69	-0.35±0.25
Mafikeng				
Input Case	Input Variables	Mean R^2	Mean RMSE (%)	Mean MBE (%)
Case -1	RH	0.4798	41.09±0.29	-0.46±0.20
Case -2	RH, WS	0.5714	39.68±0.32	-0.33±0.23
Case -3	RH, T, P	0.5955	37.03±0.48	-0.40±0.15
Case -4	RH, WS, P	0.6011	36.23±0.64	-0.34±0.30
Case -5	RH, T, P, WS (All Variables)	0.6235	35.67±0.83	-0.32±0.26

Table 6.4: Generated model equation and parameters for visibility using meteorological parameters based on input Case-5.

Generated Model Equation for Visibility: $V_p = \alpha V_m + \beta$		
City	$\alpha\ (km)$	$\beta\ (km)$
Durban	0.66	5.0
Cape Town	0.74	5.9
Umtata	0.69	4.5
Bloemfontein	0.65	8.4
Johannesburg	0.70	4.3
Mafikeng	0.65	7.9

6.8 Summary

In summary, based on the above results and the daily mean values of the predicted visibility for the various cities using the SST and ANN methods, it is observed that:

i. The maximum reliability obtained for the predicted visibility as a function of all the four climatic variables when the ANN method was used are 82.01 %, 84.76 %, 82.78 %, 80.88 %, 82.54 % and 81.14 % for Durban, Cape Town, Umtata, Bloemfontein, Johannesburg and Mafikeng respectively. These results showed good performance and the developed ANN model proved it is reliable in predicting non-linear relationship between visibility and other weather parameters. Therefore, this can give important details about the present or future to the relevant people who deal with profiling and forecasting of visibility such as the FSO personnel for optical link design and civilian or military personnel for flight activity planning.

ii. It should be noted that the prediction accuracy increased when T, P and WS were added to the base case.

iii. The ANN performed better than the SST with a variation of about 21.39 %, 17.50 %, 17.16 %, 24.42 %, 20.01 % and 22.33 % for Durban, Cape Town, Umtata, Bloemfontein, Johannesburg and Mafikeng respectively.

iv. Therefore, it is recommended that other atmospheric parameters (such as solar radiation components) should be included in the research so as enhance the visibility prediction results.

v. In conclusion, this analysis has shown that the complete weather condition of a particular place in terms of the atmospheric temperature, pressure, relative humidity and wind speed are a determining factor of the possible atmospheric optical attenuation on the FSO link within that location. The result has shown that there is a direct relationship between all these atmospheric variables and the optical attenuations (based on visibility) obtained during the propagation of optical beam within the free space. Therefore, the conditions of these variables at every point in time determines the behaviour of the optical link.

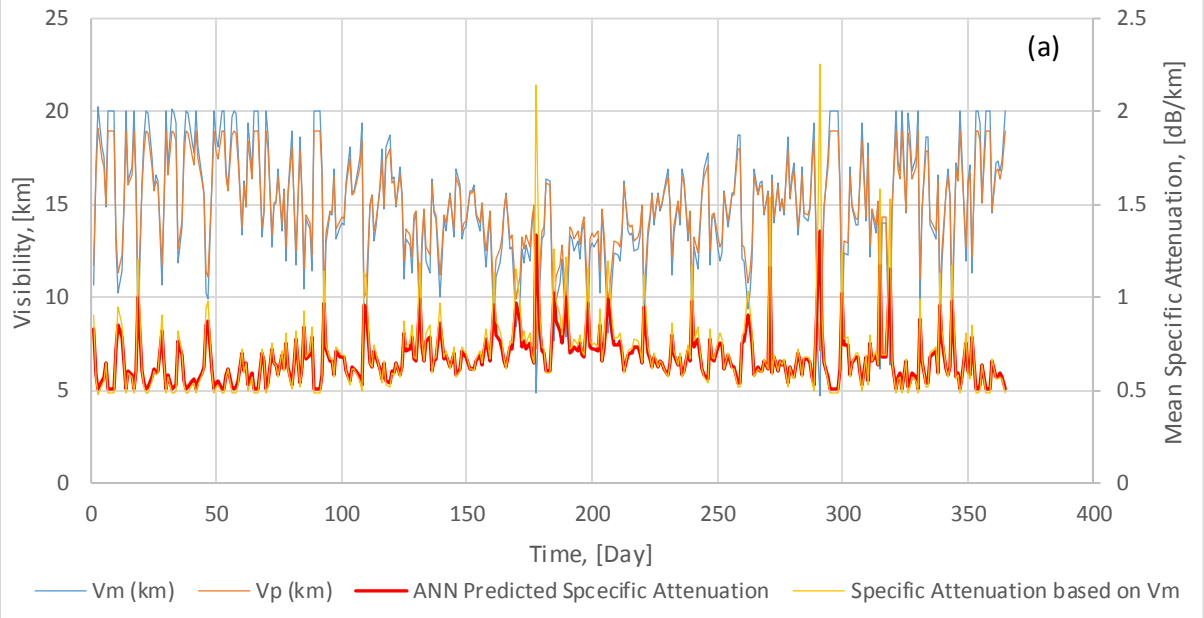
(a)
Visibility, [km]
Mean Specific Attenuation, [dB/km]
Time, [Day]
Vm (km)
Vp (km)
ANN Predicted Spcecific Attenuation
Specific Attenuation based on Vm

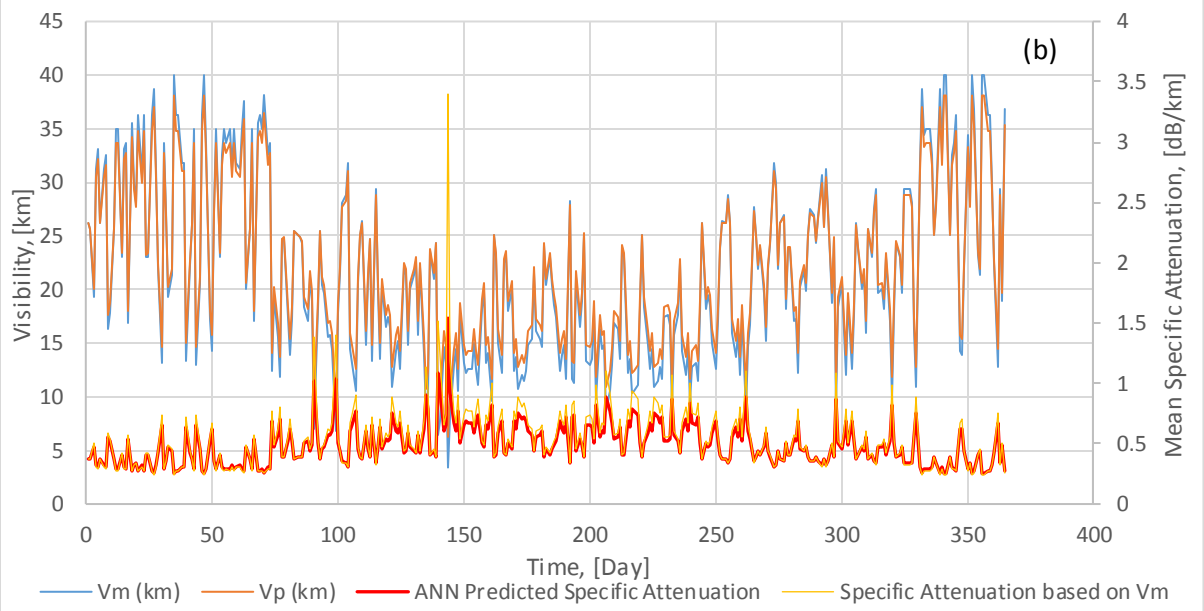
(b)
Visibility, [km]
Mean Specific Attenuation, [dB/km]
Time, [Day]
Vm (km)
Vp (km)
ANN Predicted Specific Attenuation
Specific Attenuation based on Vm

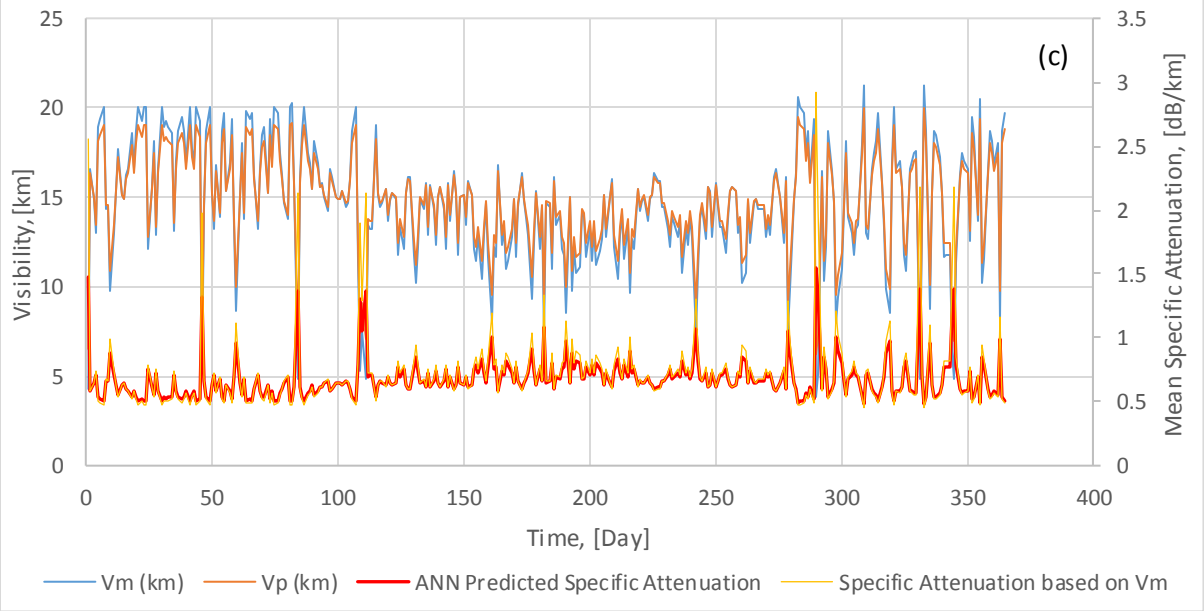
(c)
Visibility, [km]
Mean Specific Attenuation, [dB/km]
Time, [Day]
Vm (km)
Vp (km)
ANN Predicted Specific Attenuation
Specific Attenuation based on Vm

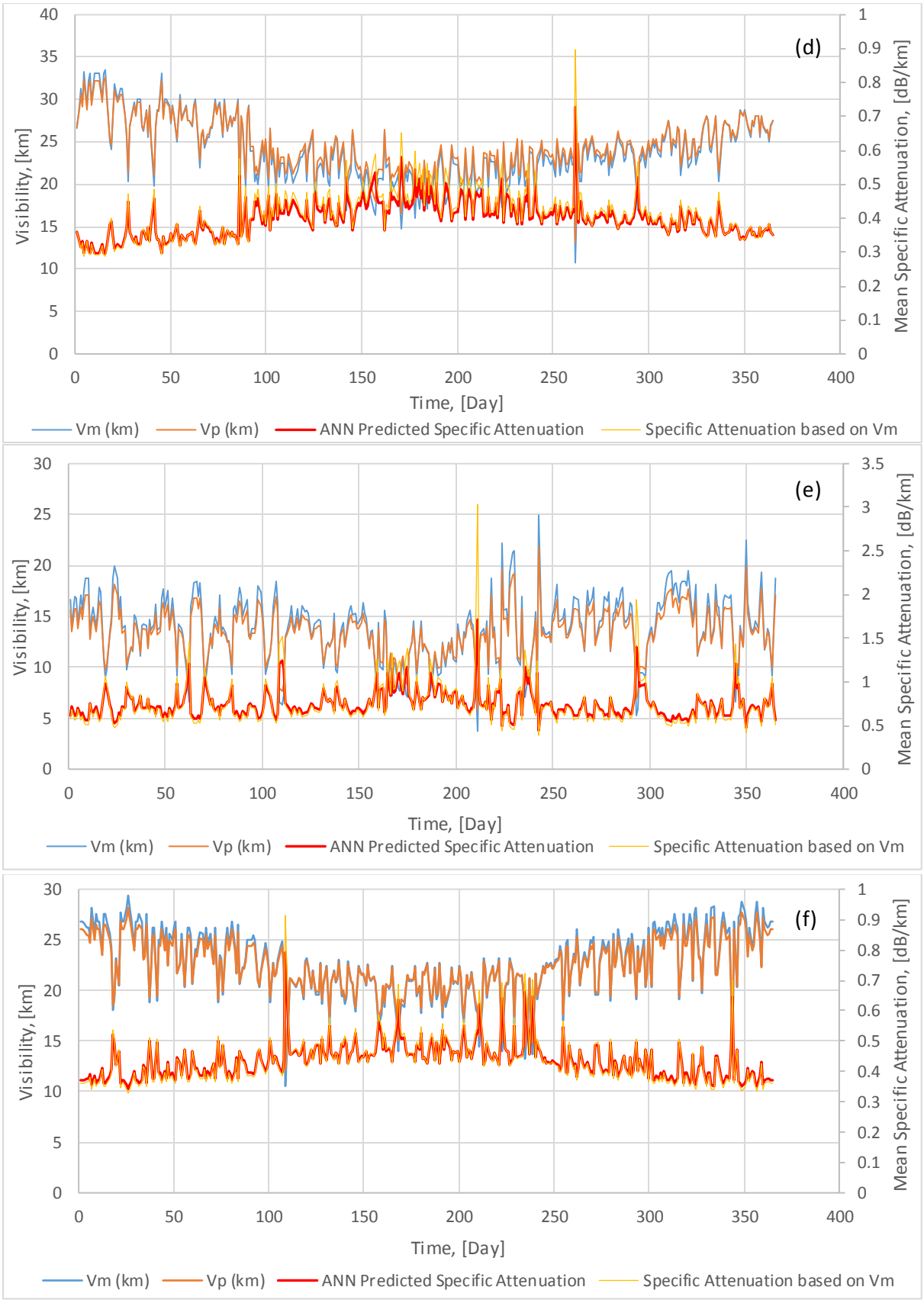

Figure 6.9: Time series analysis profile of the measured visibility, ANN predicted visibility, estimated specific attenuation using Kim model and the predicted specific attenuation using the generated ANN models with all the meteorological variables (in terms of daily mean) over the year 2013 for (a) Durban; (b) Cape Town; (c) Umtata; (d) Bloemfontein; (e) Johannesburg and (f) Mafikeng.

CHAPTER SEVEN

Characterization and Modeling of Atmospheric Turbulence Level based on C_n^2 and Scintillation Index using Climatic Data for South Africa

7.1 Introduction

In OWC system, laser beam propagation is mostly influenced by various atmospheric phenomena occurring within the atmosphere, for instance, molecular scattering and absorption, and atmospheric turbulence. However, with the expectation of Free Space Optics (FSO), both molecular scattering as well as atmospheric turbulence are to be greatly considered as a result of the insignificant effects of the molecular absorption mechanism obtained at certain optical wavelengths. The most significant atmospheric turbulence effects on a propagating laser beam are considered as follows: redistribution of the intensity (power) within the laser beam wave, beam broadening, phase front distortion (beam bending) and beam wander. The temporary redistribution of the optical intensity within the laser beam, which is referred to as scintillation, is as a result of chaotic flow changes of air within a particular region of the atmosphere as well as due to the thermal gradients along the optical signal propagating path, resulting from the fluctuations in the temperature and pressure of the atmosphere as well as air density. The air masses (which are typically called zones or three-dimensional eddies) of numerous sizes and varying densities serves as focal points or lenses scattering light off its intended optical path. Subsequently, parts of the transmitted light will propagate in diverse directions and then recombine, which reduces the power of the received signal [3, 15, 23, 24, 26, 31, 226].

One of the sections of this research work will investigate the use of a heuristic theory of scintillation, on the model of real FSO system and with the purpose of estimating the impact of scintillation over the operation of optical links located in various sites within South Africa. This heuristic theory of scintillation applied in this work was developed by the US Research Army Laboratory. In this case, the computation assumption is that there exist a laser beam having an ideal Gaussian intensity profile and travelling along a horizontal pathway through a turbulent atmosphere.

7.2 Characterization and Modeling of Atmospheric Optical Turbulence

7.2.1 Theory and Overview of Turbulent Energy flow based on Kolmogorov Theory

Atmospheric Turbulence is a phenomenon which is formed as a result of an induced kinetic energy resulting from the random movement of air masses within the atmosphere due to either convection process or wind shear, which are purely meteorological events [227]. In the initial step of this process, the created energy permits the formation of turbulent three-dimensional eddies with characteristic sizes extending from a few tens of meters up to a few hundreds of meters. These turbulent eddies produced are referred to as the turbulence outer-scale and denoted by L_0. Afterwards, this energy is transmitted

to other new eddies of decreasing proportions, until it reaches the viscosity regime, that is when it is totally dissipated. Therefore, this viscosity regime implies that it has attained the characteristic sizes of the order of the milli-meter, which is commonly referred to as the inner-scale and denoted by l_0. In the literature of atmospheric optical turbulence, this division process is recognized as the energy cascade theory, according to Richardson's theory presented in [228]. Richardson, in 1922, revealed that the atmospheric turbulence which occurs in the inertial subrange shown in Figure 7.1 is a decay process whereby the larger eddies break down into smaller ones during heat dissipation. The inertial subrange according to the Kolmogorov theory, separates the dissipation region from the input region [227-229].

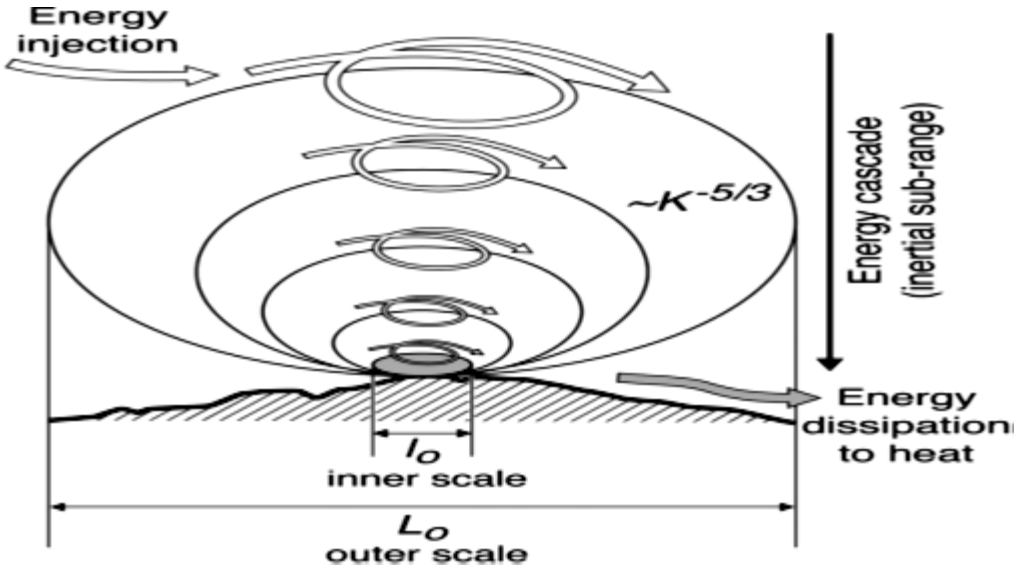

Figure 7.1: Schematic presentation of the turbulent energy cascade process [227].

7.2.2 Statistical Description of Atmospheric Turbulence

The physical source and characteristics of the optical impacts of atmospheric turbulence (optical turbulence) is observed in the random fluctuations of the refractive index. The energy origin for optical turbulence is gotten from larger scale wind shear or convection [227]. With the aid of statistics, the mathematical description of atmospheric turbulence and its properties can be appropriately achieved. Considering this fact, the structure function of wind velocity ($D_V(r)$) between two given points (r_1 and r_2), for a homogenous medium is expressed in terms of the inertial sub-range by [100, 227, 229, 230]:

$$\begin{aligned} D_V(r) &= \langle [V(r_1) - V(r_2)]^2 \rangle \\ &= \langle [V(r_1 + r) - V(r_1)]^2 \rangle \\ &= C_V^2 \, r^{2/3}, \qquad l_0 < r < L_0 \,, \end{aligned} \tag{7.1}$$

where $\langle \cdot \rangle$ represents the mean operator and C_V^2 denotes the structure constant of wind velocity signifying the strength of the atmospheric turbulence. This treatment was also applied on the fluctuations of temperature and index of refraction (n), such that within the optical range, it can be given as [227]:

$$n - 1 \cong 79 \times 10^{-6} \frac{P}{T}, \tag{7.2}$$

where the parameter *P* represents the pressure and *T* is temperature.

Thus, using the following expression, the refractive index structure function of air can be obtained [100, 229, 231]:

$$D_n\big(n(r)\big) = \langle [n(r) - n(r_1 + r)]^2 \rangle \; = \; C_n^2 \, r^{2/3}, \qquad l_0 < r < L_0 \,, \tag{7.3}$$

where the strength of the atmospheric turbulence is indicated by C_n^2 which is known as the Refractive Index Structure Parameter (RISP), and its dimensions are measured in $m^{-2/3}$.

To characterize random as well as ergodic processes occurring in the eddy division process, the power spectrum tool can be used. Therefore, the power spectral density based on the inertial sub-range is [24, 100, 230]:

$$\Phi_n(k) = 0.033 C_n^2 \kappa^{-11/3} \,, \quad \frac{1}{L_0} \ll \kappa \ll \frac{1}{l_0} \,. \tag{7.4}$$

This expression of the power spectral density ($\Phi_n(k)$) defines the Kolmogorov power law spectrum. Though this equation is only valid theoretically over the inertial domain, however it can as well be extended to all wave numbers (κ) if a negligibly small inner-scale ($l_0 = 0$) and an infinite outer-scale ($L_0 = \infty$) is assumed. But if this is extended into the dissipation range ($\kappa > 1/l_0$), therefore this needs to be modified. The modification was given by Tatarski spectrum as [100, 230, 232]:

$$\Phi_n(k) = 0.033 C_n^2 \kappa^{-11/3} \exp\left(-\frac{\kappa^2}{\kappa_m^2}\right), \quad \kappa \gg \frac{1}{L_0}, \qquad \kappa_m = \frac{5.92}{l_0}. \tag{7.5}$$

7.2.3 Statistical Treatment of the Propagation of Optical Waves in Free Space

7.2.3.1 Reduced Wave Equation or Method of Analysis

In many FSO propagation applications, the received optical signal can be characterized as a function of statistical moments of the random optical field $U(r, L)$, such that the parameter r denotes a vector in the plane of the receiver transverse to the propagation axis and the variable *L* represents the propagation length along the positive z-axis. Therefore, if the effect of polarization is ignored, the following reduced wave equation shows the random optical field propagation [100, 105, 227, 229, 233]:

$$\nabla^2 U(r) + \; k^2 n r^2 U r = 0, \tag{7.6}$$

where the parameter n is the random refractive index and the other parameters remains as earlier defined. To solve this expression, one of the easiest methods is Rytov approximation [229, 233]. Also, for the terrestrial FSO system considered in this research work, the optical signal was taken as a plane wave, whereby this assumption simplifies further the propagation modelling of the random optical field.

7.2.3.2 Rytov Approximations

Rytov approximation defines a propagating optical field at a distance L from a transmitter as follows [105, 230, 233, 234]:

$$U(r,L) = U_0(r,L)e^{\Psi_1(r,L)+\Psi_2(r,L)+\cdots}, \tag{7.7}$$

where $U_0(r,L)$ represents the received wave field and $\Psi(r,L)$ represents the overall complex phase perturbation of the field as a result of random inhomogeneities along the path of propagation. The first-order statistical moment of this optical propagating field relates to the mean field which defines the coherent component of the optical wave, and this is given by [105, 233, 234]:

$$\langle U(r,L)\rangle = U_0(r,L)\langle e^{\Psi(r,L)}\rangle. \tag{7.8}$$

Furthermore, the second-order moment which is often referred to as the Mutual Coherence Function (MCF) can be described by the average given as:

$$\Gamma_2(r_1,r_2,L) = \langle U(r_1,L)U^*(r_2,L)\rangle. \tag{7.9}$$

Assuming an incident plane wave (that is, an infinite wave model without a phase curvature) propagates through an atmosphere of weak fluctuations, then the following expression can be obtained from Eqn. 7.9 [105, 233]:

$$\Gamma_2(\rho,L) = \exp\left\{-4\pi^2k^2L\int_0^\infty \kappa\Phi_n(\kappa)[1-J_0(\kappa\rho)]d\kappa\right\}. \tag{7.10}$$

The MCF can also be defined as follows, when considering a simple Kolmogorov turbulence spectrum model [105, 229, 233]:

$$\begin{aligned}\Gamma_2(\rho,L) &= \exp\left[-\left(\frac{1.22(\sigma_R^2)^{6/5}k\rho^2}{L}\right)^{5/6}\right] \\ &= \exp\left(-1.46C_n^2k^2L\rho^{5/3}\right), \quad l_0 \ll \rho \ll L_0\,.\end{aligned} \tag{7.11}$$

7.2.4 Atmospheric Turbulence and Optical Scintillation Modeling

7.2.4.1 Statistical Analysis of the Scintillation Theory

Scintillation theory involves formulating a general expression of the fourth-order cross-coherence function to describe the beam of the optical field propagating a specific path length, and this can be expressed as [100, 234-236]:

$$\Gamma_4(r_1,r_2,r_3,r_4,L) = \langle U(r_1,L)U^*(r_2,L)U(r_3,L)U^*(r_4,L)\rangle\,. \tag{7.12}$$

As depicted above, the fourth-order statistical quantities of the optical field must be taking into account in order to derive statistical expressions for index of scintillation. Using this expression, and by setting

$r_1 = r_2 = r_3 = r_4 = r$, we can derive a relationship for the second-order moment of the irradiance as follows [100, 234-236]:

$$\langle I^2(r,L)\rangle = \Gamma_4(r,r,r,r,L)\,. \tag{7.13}$$

Thus, the scintillation index (σ_I^2) can be derived by first estimating the covariance function of irradiance defined by a two-point statistic model which relies upon Γ_2 and Γ_4 [100, 234-236].

$$\mathrm{B}_I(r_1,r_2,L) = \frac{\Gamma_4(r_1,r_2,r_3,r_4,L)}{\Gamma_2(r_1,r_1,L)\Gamma_2(r_2,r_2,L)} - 1\,. \tag{7.14}$$

Thus, the σ_I^2 is just the covariance function of the irradiance determined for $r_1 = r_2 = r$, and it is defined as:

$$\sigma_I^2(r,L) = \frac{\langle I^2(r,L)\rangle}{\langle I(r,L)\rangle^2} - 1\,. \tag{7.15}$$

The normalized variance of the intensity fluctuations can be used to calculate the intensity fluctuations of the optical signal received. The normalized variance of the intensity fluctuation of the optical wave, commonly known as scintillation index is expressed as follows [12, 23, 24, 237]:

$$\sigma_I^2 = \frac{\langle I^2\rangle - \langle I\rangle^2}{\langle I\rangle^2} = \frac{\langle I^2\rangle}{\langle I\rangle^2} - 1\,, \tag{7.16}$$

where the variable parameter I stands for the irradiance or intensity of the optical beam at some point within the detector plane and the angle brackets ($\langle\,\rangle$) signifies an ensemble average.

In other terms, the scintillation index which indicates the strength of the irradiance fluctuations, can also be defined as the variance of log-amplitude (σ_x^2), and it is given in the form [12, 23, 24]:

$$\sigma_I^2 \approx 4\sigma_x^2\,, for\ \sigma_x^2 \ll 1. \tag{7.17}$$

In addition, it is to be noted that σ_I^2 is a function of the RISP which is denoted by C_n^2 ($m^{-2/3}$). The strength of the atmospheric turbulence within the free space can be determined by using this structure parameter. Obviously, it has been ascertained that RISP varies with certain factors such as the altitude, time of the day (specifically day or night) as well as the geographical location.

In cases of near-ground or surface layer horizontal link which is considered in this research work, the C_n^2 value according to certain literatures and models (such as the Hufnagel-Valley model) is assumed to be nearly constant and its typical estimate for weak atmospheric turbulence is around $10^{-17}\ m^{-3/2}$ and in the strong atmospheric turbulence case it can be up to $10^{-13}\ m^{-3/2}$ or even much more. As a matter of fact, other literatures and models such as the ARML model that considers atmospheric parameters to determine the C_n^2 values, shows that these values may not necessarily be constant or near constant all through the time at a particular height. However, it is agreed that the value of C_n^2 is a function of height, and it is shown in this work that there could be a little variance in the C_n^2 profile value between time of the day and night. This work has shown that when the atmospheric parameters

as well as the height of a location are considered in order to determine the strength of the atmospheric turbulence, a more reliable value of the C_n^2 profile can be obtained rather than just considering the altitude. Also, when there is a drastic change in weather condition of a certain place, the values of C_n^2 are not always constant.

Numerous empirical models of the RISP have been proposed by several researchers in this research field in order to estimate the profile of atmospheric turbulence. These models are dependent on experimental measurements obtained at different times of the day, geographical locations, wind speed, atmospheric conditions, terrain or topological type, and so on [238, 239]. Presented in the later part of this chapter are some of the generally used atmospheric turbulence profile models.

The intensity of the irradiance fluctuation at the photodetector resulting from scintillation is described by various distributions as shown in Table 7.1.

Table 7.1: Various atmospheric turbulence regimes and their corresponding probability distribution statistics [152, 240-244].

Atmospheric Turbulence Regime	Weak	Moderate to Strong	Strong	All turbulence regimes (Weak to Strong)
Probability Distribution Statistics	Log-normal [152]	Negative exponential [152] Double-Weibull [243]	K distribution [240]	Gamma-Gamma [241, 242] I-K [240] Double Generalized Gamma [244]

7.2.4.2 Atmospheric Turbulence Models for Estimating Optical Attenuation

The optical attenuation due to atmospheric turbulence can be depicted by several atmospheric turbulence models, such as the Rytov approximation and the Andrew's method.

7.2.4.2.1 Modeling based on Rytov Approximation

This method of approximation gives a connection between C_n^2 and Rytov variance or relative variance of optical intensity ($\sigma_{I,rel}^2$) as follows [24, 29, 237, 245]:

$$\sigma_{I,rel}^2 = 0.5\, C_n^2\, k^{7/6} L^{11/6}\,, \tag{7.18}$$

where k denotes the wave number and it is given as $k = {}^{2\pi}/_{\lambda}$, and L is the optical link distance. However, this relationship is only valid for spherical waves and also for $\sigma_{I,rel}^2 < 1$, while for the plane waves, the Rytov variance is given as [24, 29, 237, 245]:

$$\sigma_{I,rel}^2 = 1.23\, C_n^2\, k^{7/6} L^{11/6}\,. \tag{7.19}$$

The Rytov approximation model can be used to estimate the scintillation variance (σ_χ^2) which is given as [24, 29, 237, 245]:

$$\sigma_\chi^2 = 23.17\, C_n^2\, k^{7/6}\, L^{11/6}\,. \tag{7.20}$$

Thus, attenuation due to atmospheric turbulence (α_{Rytov}) is given as [246, 247]:

$$\alpha_{Rytov} = 2\sqrt{\sigma_\chi^2} = 2\sqrt{23.17\ C_n^2\ k^{7/6}\ L^{11/6}}\,. \tag{7.21}$$

Hence, unlike the Andrew's method, it can be observed from the expression of the α_{Rytov}, that the Rytov approximation approach is not a function of the receiver optical lens diameter D_{REC}.

Scintillation index in case of weak atmospheric turbulence for both plane and spherical waves are given as follows:

$$\sigma_I^2 = \ \sigma_R^2 = 1.23 C_n^2 k^{7/6} L^{11/6} \ \ for\ plane\ wave, \tag{7.22}$$

$$\sigma_I^2 = \ 0.4\sigma_R^2 = 0.5 C_n^2 k^{7/6} L^{11/6} \ \ for\ spherical\ wave, \tag{7.23}$$

where σ_R^2 is the Rytov variance, k denotes the optical wave number and it is expressed as $2\pi/\lambda$, and L denotes the optical link distance. It is obvious from the two expressions given by Eqns. 7.22 and 7.23, that the irradiance fluctuations will decrease at longer wavelength in the case of weak atmospheric turbulence for a given optical link distance. On the other hand, for strong atmospheric turbulence, the index of scintillation is expressed as:

$$\sigma_I^2 = 1 + \frac{0.86}{\sigma_R^{4/5}}\,, \sigma_R^2 \gg 1 \ \ for\ plane\ wave, \tag{7.24}$$

$$\sigma_I^2 = 1 + \frac{2.73}{\sigma_R^{4/5}}\,, \sigma_R^2 \gg 1\ for\ spherical\ wave, \tag{7.25}$$

Since the scintillation index can be used to characterize the irradiance fluctuation of the optical beam, and it shows the strength of the atmospheric turbulence. For a plane wave, the scintillation index is (directly) proportional and inversely proportional to the Rytov variance for weak and strong fluctuations respectively [23].

7.2.4.2.2 Andrew's Method

The theoretical mean variance of optical intensity obtained from the turbulence analysis performed by L. C. Andrews is given as [245, 247]:

$$\bar{\sigma}_I^2(D_{REC}) \approx exp\left[\frac{0.49\ \beta_0^2}{\left(1 + 0.18d^2 + 0.56\beta_0^{12/5}\right)^{7/5}} + \frac{0.51\beta_0^2\ \left(1 + 0.69\ \beta_0^{12/5}\right)^{-5/6}}{1 + 0.9\ d^2 + 0.62\ d^2\beta_0^{12/5}}\right] - 1, \tag{7.26}$$

where β_0^2 is the Rytov variance, and the optical parameter d depends on the wavelength λ, link distance L, and also on the diameter of the receiver aperture D_{REC}. The optical parameter d is given as:

$$d = \sqrt{\frac{2\pi}{4\,\lambda\,L} \cdot {D_{REC}}^2}\,. \tag{7.27}$$

Since the Andrew's method considers the size of the receiver aperture in its analysis, therefore this implies that the most significant asset of this method is the aperture averaging technique. As a result of this, in comparison with other existing approaches, it can be noticed that the atmospheric turbulence attenuation obtained using this method is lower [24]. Thus, the expression for the atmospheric turbulence attenuation obtained in dB is given as [247]:

$$\alpha_{Andrew} = 10\,log\left(1 - \sqrt{\bar{\sigma}_I^2\,(D_{REC})}\right). \tag{7.28}$$

7.2.4.2.3 Modified Rytov Theory for Gaussian Beam

The modified Rytov theory gives a suitable scintillation index model that can be used for all the different atmospheric turbulence regimes, whereby the intensity (I) is expressed as a modulation process [23, 237, 248] given as:

$$I = xy \tag{7.29}$$

where x and y are statistical random variables representing the effects of small- and large-scale eddies. The scintillation index in the Rytov theory was obtained from the log-intensity of the optical wave. If $\langle x\rangle = \langle y\rangle = \langle I\rangle = 1$ and $\langle I^2\rangle = \langle x^2\rangle\langle y^2\rangle$, and applying eqns. 7.16 and 7.29, then the scintillation index can be derived as [23, 24]:

$$\sigma_I^2 = (1+\sigma_x^2)\left(1+\sigma_y^2\right) - 1 = \exp\left(\sigma_{\ln x}^2 + \sigma_{\ln y}^2\right) - 1, \tag{7.30}$$

where the normalized variances are denoted by σ_x^2 and σ_y^2, while $\sigma_{\ln x}^2$ and $\sigma_{\ln y}^2$ represents the log-irradiance variances of the small- and large-scale turbulent eddies (i.e., x and y) [24].

7.3 Atmospheric Attenuation in Free Space Optics Channel

7.3.1 Optical Attenuation due to Atmospheric Turbulence Channel

In general, scintillation can be described as arbitrary variations over the strength of the received field which occurs from erratic changes along the transmission path. Therefore, the random variation of a propagating optical signal through the free space, resulting from fluctuations of the index of refraction along the optical path is simply referred to as scintillation in OWC system [3, 23].

7.3.1.1 Fluctuations of Optical Signal

As power from the sun strikes the atmosphere, different temperatures are produced from numerous distinctive cells, leading to differences in the index of refraction, and optical turbulences are produced during the propagation of light signal through the free space, as shown in Figure 7.2. The amplitude of the signal at the receiver changes because of the created optical turbulence based on the changes in the

air refractive index. Therefore, the index of refraction can be obtained from humidity, temperature, pressure and wavelength of the light signal [3, 23, 24, 226], which is one of the objectives of this work.

The expression describing the atmosphere's index of refraction structure function is given by [246]:

$$\langle [n(A,t) - n(B,t)]^2 \rangle = \begin{cases} C_n^2 \cdot r^{\frac{2}{3}} & l_o \ll r \ll L_o \\ C_n^2 \cdot l_o^{-4/3} \cdot r^2 & r \ll L_o \end{cases} \quad (7.31)$$

where n specifies the optical function of the refractive index, the parameters A and B are the spatial points, t is the time in secs, and the other parameters have already been defined.

These changes in n causes atmospheric turbulences that brings about scintillation. The atmospheric turbulences are classified into different turbulence regimes based on their strengths, and these are given in Table 7.2, with their respective C_n^2 [246]. During FSO transmission, the effect of scintillation is observed fluctuations in the received optical power. Therefore, the variation in the amplitude is related to the various turbulence regimes at specific time and can be calculated using some turbulence models.

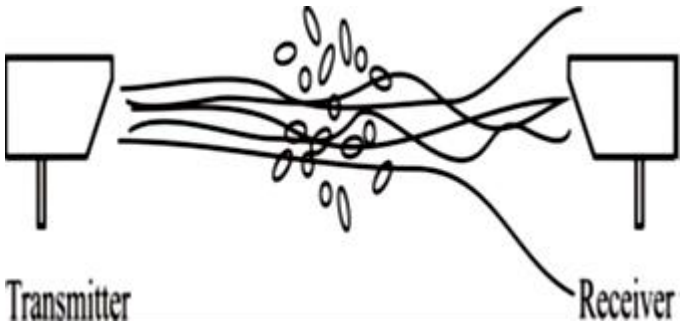

Figure 7.2: Diagram showing the scintillation effects on the propagated optical wave [246].

Table 7.2: Table showing the various atmospheric turbulence regimes and their corresponding C_n^2 and Rytov ranges.

Atmospheric Turbulence Regime	$C_n^2\ m^{-2/3}$	**Scintillation Index,** σ_I^2
Weak	$< 10^{-17}$	$\sigma_I^2 < 1$
Moderate	$10^{-16}\ to\ 10^{-15}$	$1 \leq \sigma_I^2 < 3$
Strong	$10^{-14}\ to\ 10^{-13}$	$\sigma_I^2 \geq 3$

7.3.2 Characteristic Scale Sizes of Atmospheric Turbulence

As earlier discussed, the normalized irradiance fluctuations obtained at the receiving aperture defines scintillation and this is as a result of a randomly varying index of refraction along the propagation path within the atmosphere. Turbulence cells commonly known as the three-dimensional eddies are formed by air packets having constant refractive index. The produced eddies range in scale size from the small scale (l_o) to the large scale (L_o) of turbulence as shown in Figure 7.3, which are also respectively referred to as the inner and outer characteristic scales of atmospheric turbulence. The inner- and outer-

scales of turbulence diffract and refract the optical wave respectively. Therefore, the two likely processes that contributes to scintillation are refractive and diffractive processes taking place in the atmosphere, which are based on the relationships between the characteristic scales and spatial coherence radius (ρ_o), Fresnel zone ($(L/k)^{-1/2}$) and scattering disk ($L/k\rho_o$) [23, 246].

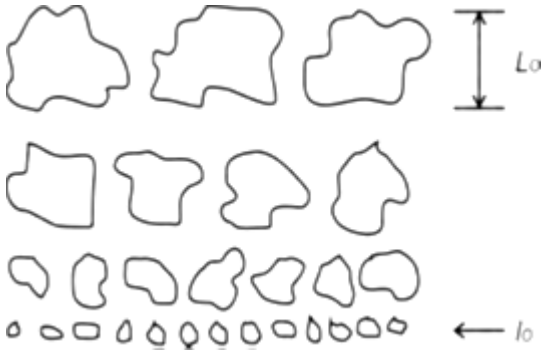

Figure 7.3: Inner and Outer scales of the turbulent cells [246].

At the moment, several height-dependent outer characteristic scale ($L_0(h)$) models exist, such as the model proposed by Tatarski in [230] for low altitudes of about 1 m more or less, which is given as [230, 249]:

$$L_0(h) = \begin{cases} 0.4 & h \leq 1\ m, \\ 0.4h & h > 1\ m. \end{cases} \tag{7.32}$$

7.4 Modeling of the Refractive Index Structure Parameter

7.4.1 Overview of Refractive Index Structure Parameter

The RISP of the atmosphere, often denoted by C_n^2, can be described as the measure of the intensity or strength of the optical turbulence occurring within the atmosphere. Several models by different researchers have been developed to estimate the magnitude of the atmospheric turbulence at different levels of the atmosphere as a function of height and the exerting forces within the free space. Moreover, various models that predict this atmospheric turbulence parameter exist at many levels or degree of complexity. These turbulence models are based on theoretical or empirical developments. Likewise, they can be presented under a purely analytical form, either closed or not, otherwise presented as a numerical model which requires input parameters for computation.

Among various weather variables, the RISP is dependent mainly on the altitude, geographical location, time of day and so on. In ideal cases, geographical locations exist with distinct features and characteristics, for instance, different locations may possess different characteristics of temperature distribution that are reflected on the estimates assumed by the RISP. Below the tropopause atmospheric layer, the greatest obtainable temperature gradients, corresponding to the values of greatest atmospheric pressure and air density are achieved close to the ground (at sea-level), where thus the largest estimate of the RISP value is expected. Small RISP values result as the height increases which leads to a decrease

in the gradient of the temperature and atmospheric pressure as well as the air density, until the tropopause where strong wind shear takes place, thereby producing anew the RISP.

Also, when the temperature dynamics is considered during the day, closer to the earth surface, it should be expected that the atmospheric turbulence is stronger around the noon-time. On the other hand, at dawn and sunset, as a result of a form of thermal equilibrium along the vertical profile of the atmosphere, it is expected that refractive index structure constant should have lower values [132, 232, 250]. According to the study carried out in [232], showing the diumal analysis chart (presented in Figure 7.4) of the fifteen-minute average measured values of C_n^2 for a cloudless day at a height of 9 m over dry soil within the desert region. It was reported that a well-developed diurnal cycle, with an obvious peak point during the day-time were visible. This suggests that the optical turbulence within the atmosphere is strongest near the earth surface in the day-time. However, on average at night, it was observed to be near constant, while near sunrise and sunset it appeared to be minimum resulting into the neutral atmospheric condition. It was also reported that the day-time behavior of the C_n^2 profile is as a result of solar irradiance. The most stable atmospheric conditions are observed at the neutral events which is obtained when there is an equality between the soil and air temperatures. The night-time fluctuations were described as difficult to characterize from location to location, and these data are said to be more variable. This is due to the existence of a strong surface temperature inversion, which makes the surface to cool by radiation and then becomes colder than the air.

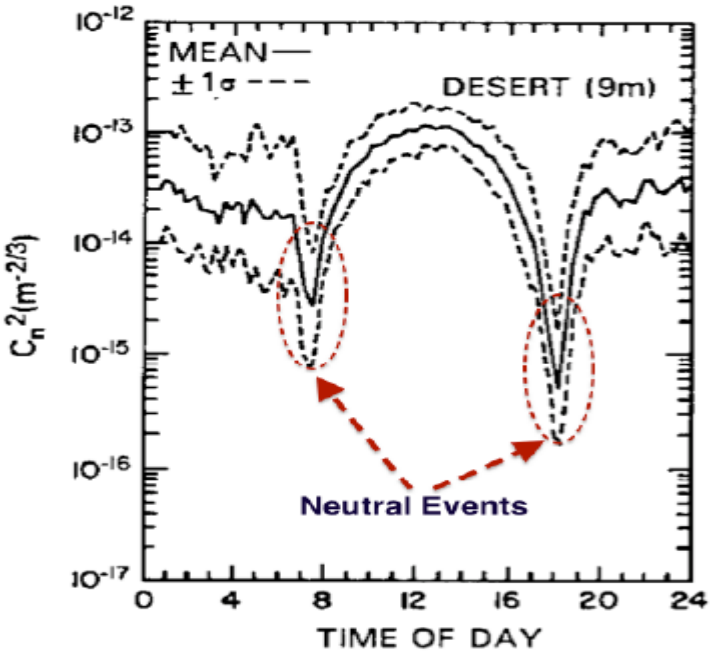

Figure 7.4: Fifteen-minute average C_n^2 measurements and $\pm SD$ plotted over a 24 hrs period [232].

While in the case of directional positioning structure, the RISP along the horizontal path may be considered "constant" at a particular time, and a slant or inclined path indicates that the C_n^2 varies as a

result of different atmospheric temperature gradient, atmospheric pressure and density of air along the altitude.

7.4.2 Refractive Index Structure Parameter (C_n^2) Models

The determination of the RISP profile with altitude is very cumbersome due to the fact that empirical data are not readily available as well as the point that it is difficult to properly capture its variations measured usually with any of radiosondes, Radar, SCIDAR (SCIntillation Detection And Ranging), SODAR (Sonic Detection And Ranging) and SLODAR (SLOpe Detection And Ranging). But since the 1970s, lots of models have been formulated by different researchers in the field, in order to describe such profiles. Majority of these initial C_n^2 models such as the Submarine Laser Communications (SLC), AFGL Critical Laser Enhancing Atmospheric Research (AFGL CLEAR(s)) and AFGL Air Force's Maui Optical Station (AFGL AMOS) [250, 251] were established for specific locations and (micro)-climates complicating their generalization [250]. These classification of C_n^2 models are typically considered as 'non-parametric models', that is, they rely only upon the height and represent average profiles (without stratification) that are generally highly location-dependent. Whereas, 'parametric models' were established with the aim of including the location-dependence, the stratification and the meteorological parameters. The inclusion of the stratification allows typical profiles to illustrate RISP varying in layers of thickness of about hundreds of meters. Besides, as a result of differing atmospheric dynamical turbulence regimes, the refractive index structure constant ranges from $10^{-13}\ m^{-2/3}$ near the earth's surface to about $10^{-20}\ m^{-2/3}$ in the upper atmosphere. Thus, majority of the developed C_n^2 models at the moment describe either the free atmosphere or the boundary layer, the latter being the most complex to model because its depth is continuously changing and it is highly location-dependent in terms of solar radiation, humidity, peculiar wind profile, soil roughness among many others.

The summary of the bibliographic work associated with the modelling of the refractive index structure constant profiles undertaken during this research work is presented in this section of this thesis. Also, to the best of my knowledge, the referencing process of many of the existing index of refraction structure constant models has been done as extensively as possible. Some of these existing models are the common models, for example, the famous Hufnagel-Valley (HV) model (with its derivatives) [252-254], the Greenwood model [255] and the SLC Day model [250]. Likewise, the more recent as well as less popular RISP models, for instance, the Hufnagel/Andrews/Philips (HAP) model [251, 256], the PAMELA model [257], and the US Army Research Lab (ARL) model [251] are also discussed in detail. The latter model is of great importance, and it is the model used in this research work to determine the level of atmospheric turbulence in terms of C_n^2 for surface layer turbulence.

However, when the performance evaluation of a ground-to-satellite OWC system is to be adequately achieved, the RISP may not be the only fundamental parameter of interest. There are other parameters which are likewise of primary relevance such as the characteristic scales of turbulence, that is, the inner-

scale l_0 and the outer-scale L_0. These dynamic parameters become more important when for example, it is necessary to evaluate the performance of adaptive optics as well as focal-plane statistics because they constitute fundamental parameters for the estimation of the turbulence spectrum to be utilized. Thus, subsequent part of this section, is devoted to deliver a synthesis of the RISP models and the means of measurements existing of the inner-scale and outer-scale characteristic lengths.

7.4.3 Parametric Models

This type of models relies on more than only the height in describing the evolution of the refractive index structure constant. Among all the models discussed in this section, the Hufnagel-Valley model, the Hufnagel/Andrews/Philips (HAP) model as well as the ARL model demonstrate C_n^2 profiles ranging from surface layer to the upper atmosphere. Nevertheless, the latter presents the combination of the effects of each layer (i.e., surface layer, boundary layer and the upper troposphere), but it is one of the very few models that properly describe the profile of C_n^2 for the surface layer. It is reliant upon a very large dataset of meteorological input parameters such as, atmospheric temperature, atmospheric pressure, relative humidity, wind speed and direction and so on. The Hufnagel-Valley and Hufnagel/Andrews/Philips (HAP) models have their limitations when used to estimate RISP in the surface layer. The Aeronomy Laboratory Model (NOAA) and the AFGL Radiosonde Models apply only to the free atmosphere, though they present high resolution C_n^2 profiles because they are based on thermosonde measurements. Then, the next two models which are the PAMELA model and Sado-Kopeika model only potentially defines the RISP within the Boundary Layer (BL), however very accurately. Also, they are both dependent on a large set of weather input data, for instance, atmospheric temperature, wind speed and wind direction, solar flux, relative humidity, and so on. A brief summary and description of each of the parametric models are presented in Table 7.3. However, the US Army Research Laboratory model was selected for this work among all the other models due to its suitability in estimating the RISP for the surface layer, and it is described in detail in the following sub-sections.

7.4.3.1 US Army Research Laboratory (US-ARL) Model

The US Army Research Laboratory (US-ARL) Model is a more recent C_n^2 model proposed by Tostfed in 2006. This model comprises of a single expression which combines the influences of each atmospheric layer from the ground level (surface layer) to the upper troposphere. Different C_n^2 profile models that described diverse portions of the atmosphere, such as the surface layer, boundary layer and the upper troposphere, were well unified together into a single-equation model. In order to compute the refractive index structure constant using this approach, there are certain required inputs to the C_n^2 model which includes: surface meteorological measurements of atmospheric temperature, atmospheric pressure, wind speed, relative humidity, the time of day, an initial estimate of the present C_n^2 turbulence strength, and cloud cover fraction. In addition, the model also necessitates information about the log-normal distribution of the strength of the turbulence. The reason for this is that the log-mean C_n^2 is

obviously not the same or equivalent to the average C_n^2. However, the two expressions are somehow related through the form of log-normal distribution. Then, in order to obtain the mean C_n^2 based on log-mean statistics which results from parametric models (for example, the AFGL AMOS and CLEAR I which have been described earlier in this thesis), the variance of this distribution is needed.

Thus, the final profile model derived as a result of the combination contains features that adjust for arbitrary surface measured atmospheric turbulence levels and stability. The profile model describing the surface layer is integrated into a BL model which is presented in [258]. Therefore, a similarity theory was consistently applied with the (modified) CLEAR I model, in order to connect the BL interface to the upper troposphere.

7.4.3.2 Surface Layer Model

The surface layer profile model which is used for determining the C_n^2 and atmospheric turbulence strength in this research work directly makes use of the fundamental results of the Monin-Obhukov Similarity Theory, popularly known as 'MOST' [259]. This fundamental findings of MOST, depends on the following equations proposed by Wyngaard in [260]:

$$C_n^2 \propto h^{-\frac{2}{3}} \left[1 - 7\frac{h}{L_{ob}}\right]^{-\frac{2}{3}} \quad in\ unstable\ conditions\ where\ (L_{ob} < 0) \tag{7.33a}$$

$$C_n^2 \propto h^{-\frac{2}{3}} \left[1 + 2.4\left(\frac{h}{L_{ob}}\right)^{-\frac{2}{3}}\right] \quad in\ stable\ conditions\ where\ (L_{ob} > 0). \tag{7.33b}$$

As the MOST approach uses dimensional analysis as well as physical modeling to obtain dominant length scales, it typically produces a characteristic scaling length within the ground layer (that is, the Monin-Obhukov length, L_{ob} or sometimes called the inertial subrange) that describes the dynamic process of heat and momentum transfer between the earth surface and the atmosphere. As discussed earlier, in theory, it is expected that the parameter C_n^2 should follow $h^{-4/3}$ power-law, while under stable conditions (or at night) and under neutral conditions, a power-law of $h^{-2/3}$ altitude-dependence is anticipated.

The major challenge in the C_n^2 profile modeling of the surface layer is actually to obtain the Monin-Obhukov length, L_{ob}, and not even the determination of the altitude-dependence given for example in Eqns. 7.33a and 7.33b. In order to achieve this objective, the similarity theory has to be applied, which implies that the profiles of the atmospheric temperature and wind close to the surface are assumed to be similar under comparable stability conditions. The determination of three stability-dependent quantities (that is, the Monin-Obhukov length (L_{ob}) itself, the scaling potential temperature (θ_*), and the friction velocity (u_*)) are of utmost interest in this modeling, because they parameterize the vertical

structures of the wind speed and atmospheric temperature in the surface layer. Thus, the three quantities are related through the expression given by [259, 260]:

$$L_{ob} = \frac{u_*^2 \theta}{k^2 g \theta_*}\,, \tag{7.34}$$

where θ represents the potential temperature at a reference height (h_r), $k = 0.4$ represents the dimensionless von Karman's constant, and g denotes the gravity acceleration.

The friction velocity as a function of the stability-dependent diabatic influence is given by:

$$u_* = \frac{ku}{\ln(h_r/h_0) - \Psi(L_{ob})}, \tag{7.35}$$

where u denotes the wind speed ($in\ m/s$) at the reference height h_r, h_0 is the surface roughness height, and the function Ψ represents the stability-dependent diabatic influence function of wind velocity, which is given as:

$$\Psi = \Psi_i\left(\frac{h_r}{L_{ob}}\right) + \Psi_i\left(\frac{h_0}{L_{ob}}\right). \tag{7.36}$$

Due to the diurnal nature of the day, this function can be sub-divided into unstable and stable turbulence conditions. For the unstable conditions, the following expression is valid:

$$\Psi_i\left(\frac{h}{L_{ob}}\right) = 2\ln\left(\frac{1+x}{2}\right) + \ln\left(\frac{1+x^2}{2}\right) - 2\tan^{-1}(x) + \frac{\pi}{2} \tag{7.37}$$

where

$$x = \left(1 - \frac{16h}{L_{ob}}\right)^{1/4}, \tag{7.38}$$

and for the case of stable conditions:

$$\Psi_i\left(\frac{h}{L_{ob}}\right) = -17\left[1 - exp\left(-0.29\,\frac{h}{L_{ob}}\right)\right]. \tag{7.39}$$

The scaling potential temperature is defined by:

$$\theta_* = \frac{\theta - \theta_0}{\ln(h_r/h_0) - \Psi_h(L_{ob})}, \tag{7.40}$$

where θ_0 represents the atmospheric temperature at the height h_0 and Ψ_h defines the diabatic influence function of temperature.

By substituting Eqns. 7.35 and 7.40 into Eqn. 7.34, the characteristic scaling length, L_{ob}, can be computed using measurements of u, θ and θ_0. But typically, the parameter θ_0 is not easy to predict due

to the fact that it does not take place at a specific surface level. On the other hand, it represents the corresponding effects of the surface temperatures of the bare ground (soil, sand, and stones) and foliage (leaf, Stem and twig) surfaces. In addition, the challenge of observationally estimating the Monin-Obhukov length L_{ob} is as well related to taking measurements of the atmospheric temperature and the wind speed (at different levels of the atmosphere). This is generally complex to practically accomplish in the field, and ordinarily, no one actually takes measurements of meteorological parameters at more than one atmospheric level in a particular location. However, in order to proffer solutions to ease this difficulty, Tofsted et al suggested an iterative scheme which resulted into the refining of the Monin-Obhukov length, and this helped to circumvent the measurements issue [259].

7.4.3.3 The L_{ob} Iterative Process

The proposed iterative process directly requires about four parameters as inputs (that is, the atmospheric temperature T, atmospheric pressure P, wind speed u, and the initial value of C_n^2), all observed at the same reference height h_r. Moreover, if the diurnal condition of the day is to be taken into account, then the daytime and nighttime conditions is also needed in this computation, as well as the location's roughness height (h_r). However, among other parameters that are indirectly required is the relative humidity, which is a measured meteorological parameter needed to determine the virtual potential temperature, by first obtaining the either the wet (moist) or dry adiabatic lapse rate (as discussed earlier in this report). Also, since the initial C_n^2 value as requested is not a readily available parameter or easily measured quantity, it is suggested that any of the available C_n^2 profile model which is height-dependent can be used (such as the HV model, HAP model, e.t.c.). In this research work, the HV model was used to obtain the initial C_n^2 value. The flow diagram illustrating this L_{ob} iterative process is presented in Figure 7.5. Firstly, to determine the initial L_{ob} using this iterative scheme, we have to find an algorithm that will associate it to the four input parameters (i.e., T, P, u, and C_n^2). The first three parameters need to be measured at a specific height of reference h_r, and the initial C_n^2 must also be estimated at this height. By considering the expression for the refractive index structure function C_T^2 as [260]:

$$C_T^2 = T_*^2 h^{-2/3}\, 4.9 \times \begin{cases} \left[1 - 7.0\left(\frac{h}{L_{ob}}\right)\right]^{-2/3}, & L_{ob} < 0 \\ 1 + 2.4\left(\frac{h}{L_{ob}}\right)^{2/3}, & L_{ob} > 0 \end{cases} \tag{7.41}$$

as well as considering the following mean to convert C_T^2 to C_n^2 [260]:

$$C_n^2 = C_T^2 \frac{A^2 P^2}{T^4} \tag{7.42}$$

where the constant $A = 79 \times 10^{-6}\ K/mb$, is a standard ratio of the atmospheric temperature to the pressure. Thus, an initial guess of the Monin-Obhukov length (L_{ob}), can be determined by eliminating C_T^2 from Eqn. 7.41 for the neutral atmospheric conditions, which results into:

$$L_{ob} \sim \pi_s \frac{ku^2}{g[\ln(h_r/h_0)]^2} \frac{AP}{T} \frac{1}{\sqrt{C_n^2 h_r^{1/3}}} \sqrt{4.9} \tag{7.43}$$

where π_s is the stability determination factor, which can be predicted by applying local sunrise/sunset times and offsets in order to estimate neutral event transitions. The values of this factor are $\pi_s = \pm 1$, whereby $\pi_s = -1$ represents the daytime (i.e., unstable atmospheric conditions) and $\pi_s = +1$ represents the nighttime (i.e., stable atmospheric conditions). Together with the T, P, u, and C_n^2 values obtained at h_r, the determined initial L_{ob} is utilized in the estimation of the temperature (T_*) and wind velocity (u_*) functions. Hence, the new L_{ob} estimate is finally calculated by:

$$L_{ob} = \frac{u_*^2 T}{kgT_*}. \tag{7.44}$$

It should be noted that this iterative process typically stabilizes in less than ten steps.

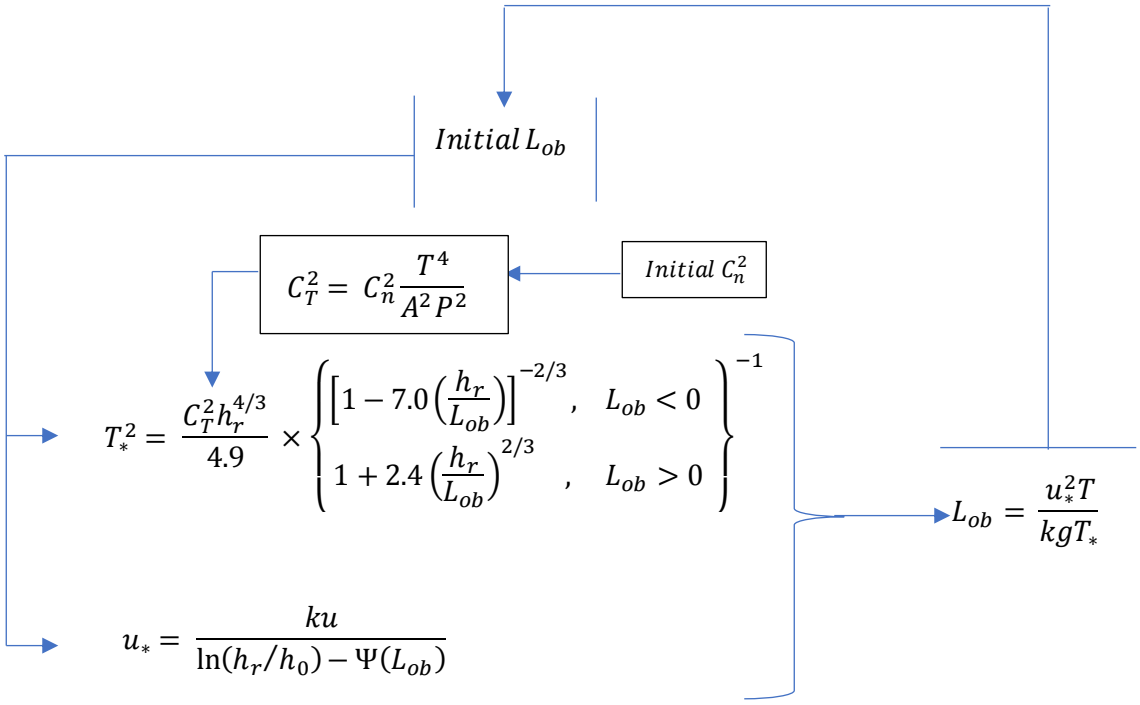

Figure 7.5: Flow diagram illustrating the iterative process of the L_{ob}.

Table 7.3: Parametric models for estimating C_n^2 and their corresponding expressions and description.

Parametric Models				
Model	Expression	Input Parameters	Brief Description (Physical implication and limitations)	References
Hufnagel(H) Model	$C_n^2(h) = A\left[2.2\times\ 10^{-53}h^{10}\left(\frac{v}{27}\right)^2 e^{-\frac{h}{1000}} + 1\times 10^{-16}e^{-\frac{h}{1500}}\right]$ where wind speed (v^2): $v^2 = \left(\frac{1}{15\times10^3}\right)\int_{5\times10^3}^{20\times10^3} v_{wind}^2\ (h)\,dh$ and $A = e \simeq 2.7$ models the fine structure of the atmospheric turbulence in terms of altitude (h) as well as time	A and v	Proposed by Hufnagel in 1974. Physical Implication: The physical implication of this H model is that the wind velocity controls the atmospheric turbulence strength at high heights and its temporal spectrum by means of the factor v^2. Limitation: The original Hufnagel(H) model is constituted by two components, which are an exponentially decreasing RISP value through the troposphere with a $1/e$ scale altitude of about 1.5 km as well as a peak at the troposphere around 10 km, which is scaled by the velocity factor v^2. Also, this model is appropriate for an altitude ranging from 3 km to 24 km.	[250-252, 254]
Hufnagel-Valley (HV) Model	$C_n^2(h) = 0.00594\left(v/27\right)^2(10^{-5}h)^{10}\ e^{\frac{-h}{1000}} + 2.7\times\ 10^{-16}\ e^{\frac{-h}{1500}} + Ae^{\frac{-h}{100}}$ where $A = C_n^2(0)$ is defined as a nominal ground-level value of the RISp (C_n^2) and v represents the high altitude rms wind speed and it is assumed as 21 m/s or for strong wind conditions it is 57 m/s or obtained by applying the Bufton wind speed model: $v = \left[\frac{1}{15\times10^3}\int_{5\times10^3}^{20\times10^3}\left(v_s h + v_g + v_T\, e^{-\left(\frac{h\sin(\alpha)-H_T}{L_T}\right)^2}\right)^2\right]^{1/2}$ where the velocity factors v_s, v_g and v_T respectively denotes the beam slew rate, ground wind speed and wind velocity at the tropopause. Also, the parameter α denotes the zenith angle of observation, and H_T and L_T are both the tropopause height as well as the thickness of the tropopause layer respectively	A and v	However, when considering altitudes below 3 km, there exist large local and diurnal variations of atmospheric turbulence created mostly by the convection from solar heating. In 1980, Valley proposed the inclusion of the term describing the boundary layer of around 1 km, whereby the last exponential term in the expression accounts for the BL correction. Therefore, this suggests that this model is not suitable for the surface layer, but only for the free atmosphere and mid-latitude regions.	[250, 252-254]

Hufnagel/Andrews/Philips (HAP) Model	$C_n^2(h) = M\left[0.00594\left({}^{v}/_{27}\right)^2(10^{-5}(h+h_s))^{10}\, e^{\frac{-(h+h_s)}{1000}} + 2.7\times\ 10^{-16}\, e^{\frac{-(h+h_s)}{1500}}\right] + C_n^2(h_0)\left(\frac{h_0}{h}\right)^p$ where M, h_s, h_0, are the random background turbulence determined at heights generally above 1 km, height of ground above sea level, instrument height above the earth surface, whereby $h > h_0$ and the constant $C_n^2(h_0)$ indicates the average RISP at h_0. The parameter p denotes the power-law relationship parameter which depends on the Temporal Hour (TH) of the day. $p = \begin{cases} -0.11(12-TH)^2 + 1.83(12-TH) - 6.22, & 0.75 < TH < 3.5 \\ 1.45 - 0.02(TH-6)^2, & 3.5 < TH < 8.5 \\ -0.048(TH)^2 + 0.68(TH) - 1.06, & 8.5 < TH < 11.25 \end{cases}$ $TH = \frac{TIME\ -SUNRISE}{TP}; \quad TP = \frac{SUNSET\ -SUNRISE}{12}$	M, h_s, h_0, $C_n^2(h_0)$ and p	The HV model lacks credibility for daytime conditions (this is supported by kaimal et al. [258) and it does not provide an accurate description of the atmospheric turbulences' behavior of the lowest layers of the atmosphere, though it is applied to the whole atmosphere. Therefore, this latest HAP model (2012) was proposed for stable (nighttime), unstable (daytime) and neutral (i.e., near sunrise and sunset) conditions. Additionally, it should be known that the stable turbulence conditions may well take place in the daytime, as soon as when there is 'warm-air over cold ground', such as a snow-covered terrain. In [258], the comparison of four HAP profiles was shown and it indicated that the night-time has lower turbulence strength.	[251-254, 256]
Aeronomy Laboratory Model (NOAA) (Free atmosphere only)	$C_n^2 = 2.8M^2L^{4/3}$ $M = -77.6\times 10^{-6}\,\frac{P}{T}\,\frac{N^2}{g}\left[1 + 15500\,\frac{q}{T} - 7750\,\frac{\frac{\acute{q}}{T}}{N^2/g}\right]$ $C_n^2 = 2.8M_0^2\int_{L_{min}}^{L_{max}} dLp_L L^{4/3}\int_0^{\infty} dSp_S\int_{-\infty}^{S^2R_{ic}} dN^2 p_N(N^2)^2$ $M_0 = -77.6\times 10^{-6}\frac{P}{T}\frac{1}{g}$ where P, T and g denotes the atmospheric pressure measured in $mbar$, atmospheric temperature in units of Kelvin, and acceleration due to gravity in m/s^2 respectively. S, N^2 and $\acute{q}$ are wind shear, mean stability value and gradient of humidity of the virtual atmosphere respectively. Also, p_L, p_S, p_N respectively represents the probability densities for the outer-scale of the layer, the wind shear and the Brunt-Vaisala frequency.	Mean values of T, P, S, N^2 and $\acute{q}$	This model started with the Tatarskii derivation [100], where C_n^2 is provided for a thin-turbulent layer (by assuming the turbulence is homogenous and isotropic). This was provided in terms of M (vertical gradient of generalized potential refractive index for the turbulent layer and L is the outer scale length. In 1978, VanZandt et. al. proposed the NOAA model for estimating the mean values of the refractive index structure constant, only for the free atmosphere, using standard radiosonde measurements.	[100, 261]
AFGL Radiosonde Model (Free atmosphere only)	$C_n^2(h) = 2.8(0.1)^{4/3}M(h)^2 10^{Y(h)}$ $Y = 1.64 + 42.0S_{raw} \quad Troposphere$ $Y = 0.51 + 50.0S_{raw} \quad Stratosphere$	T, P and S_{raw} directly from radiosondes	This model also used a similar starting point (i.e., Tatarskii expression) like that of the NOAA, but it is given anewhere. A new expression for M is presented/defined in terms of T, P, ${}^{dT}/_{dh}$ (temperature gradient)	[262]

			and γ (the dry adiabatic lapse rate of $9.8 \times 10^3 K/m$).	
Sadot and Kopeika Models (Boundary Layer only)	$C_n^2 = A_1 W + B_1 T + C_1 RHA_1 + C_1 RH^2 + C_2 RH^3 + D_1 WS + D_2 WS^2 + D_3 WS^3 + E_1 flux + F_1 TCSA + F_2 TCSA^2 + G$ where $W, T, RH, WS, flux$ and $TCSA$ are temporal hour weight, temperature, relative humidity, wind speed, solar flux and total cross-sectional area of particles per cubic meter.	$W, T, RH, WS, flux$ and $TCSA$	In 1992, Sadot and Kopeika proposed a model for C_n^2 using macroscale meteorological measurements. However, this model has limitations of only applicable to boundary layers, requires uncommon input parameters and it does not give an actual profile.	[263]
PAMELA (Boundary Layer only)	$C_n^2 = \frac{bK_h}{\epsilon^{1/3}}\left(\frac{\partial n}{\partial h}\right)^2$ $\frac{\partial n}{\partial h} \cong \frac{(-77.6 \times 10^{-6} Pa) T_* \Phi_h \left(\frac{h}{L}\right)}{k_v h T^2}$ where K_h, k_v, L and Φ_h are turbulent exchange coeff., von Karman's constant, Monin-Obukhov length and temp. gradient	Lat, Long, data, time, % cloud cover, terrain type, T, P and WS	This is developed for the surface boundary layer up to several hundreds of meters. It requires a large set of input parameters such as latitude, longitude, data, time of day, percent cloud, terrain type (roughness), and others like T, P and wind speed	[257, 264]
US Army Research Laboratory (US-ARL) Model	Surface Layer Model: Discussed in detail in section 7.4.3.2		The US Army Research Laboratory (US-ARL) Model is a more recent C_n^2 model proposed by Tostfed in 2006. It combines three aspects: surface layer, boundary layer and the upper troposphere. However, each of them was proposed individually. **For Boundary layers:** The research work proposed by Kukharets and Tsvang in [235] inspired the profile established by Tofsted et al., which they altered based on the data presented by Kunkel et. al. [237] describing desert regions. Tofsted et al. gave the final formulation of the BL model. **For Upper Troposphere:** Tofsted et al. took into account primarily two non-parametric models (i.e., CLEAR I and AFGL AMOS) in order to develop a model for the upper atmosphere (above 10 km) C_n^2 structure. The ARL model describing the C_n^2 profiles for the daytime (blue line) and nighttime (green line) conditions are shown in Fig. 7.6.	[251, 260]
	Boundary Layer Model: $X_K(h) = \log_{10}(C_T^2) = \log_{10}(C_{TS}^2) + 0.775 \exp\left[-\frac{(h-0.95h_i)^2}{2\left(\frac{h_i}{7}\right)^2}\right] + \left[\frac{1}{3} + \frac{4}{3}\log_{10}\left(\frac{h}{h_i}\right)\right]\sigma\left[\frac{h_i - h}{h_i/8}\right]$ where C_{TS}^2 represents the refractive index structure function of the surface layer and h_i indicates the height of the elevated inversion base.	C_n^2		[232, 250, 251]
	Troposphere Model: $N_{m\_u}(h) = N_{mid}\sigma\left[\frac{h-7.8}{2.4}\right] + N_{upper}(h)\sigma\left[\frac{7.8-h}{2.4}\right] - 1.3\sigma\left[\frac{h-9.2}{1.6}\right]\sigma\left[\frac{9.2-h}{1.6}\right]$ Where $N_{mid} = -16.23$ and N_{upper} is a function of height.			[251]

The chart showing the ARL model describing the C_n^2 profiles covering the whole atmosphere for the daytime and nighttime conditions is presented in Figure 7.6.

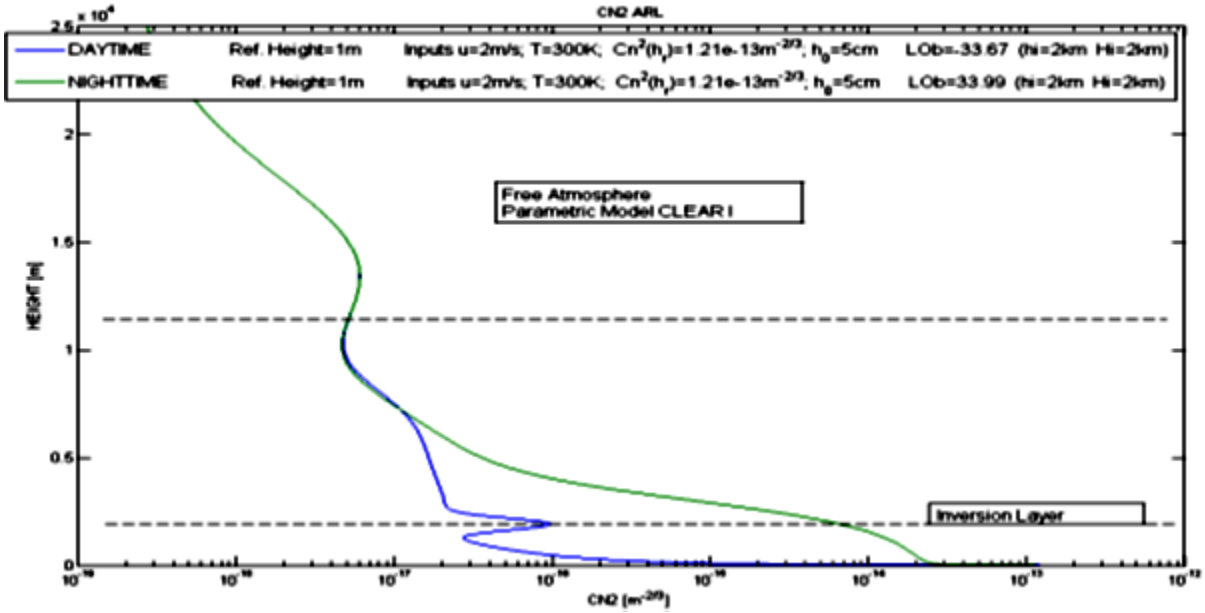

Figure 7.6: ARL model describing the C_n^2 profiles covering the whole atmosphere for the daytime (blue line) and nighttime (green line) conditions [264].

7.5 Thermodynamic Properties of the Turbulent Atmosphere

7.5.1 Reynolds Number

The Reynolds number serves as criterion that can be employed in order to determine if a specific flow at a particular time is said to be laminar (non-turbulent) or turbulent. This number can be defined as a dimensionless quantity which is the ratio between the inertial and viscous forces. Therefore, this quantity which is used to characterize the nature of a particular flow is also considered as the most significant dimensionless number in fluid dynamics theory. The conversion of a given flow or entity from a laminar condition to a turbulent state can take place when the Reynolds number of the flow exceeds a certain critical value. The Reynolds number can be expressed as [265, 266]:

$$R_e = \frac{VL_0}{\nu}, \tag{7.45}$$

where V represents the wind speed in m/s, the parameter L_0 is the characteristic outer-scale length, and constant parameter ν is the kinematic viscosity which is given as $\nu = 1.1 \times 10^{-5}\, m^2/s$.

In the case of the atmosphere, the critical Reynolds number denoted by $R_{e_{cr}}$ is given to be around 10^6 to 10^7. Moreover, this characteristic outer-scale size L_0, is determined as a function of altitude of a particular location and its derivation has been earlier discussed in detail. But the involvement of this criteria as a condition in this research work is as a measure of completeness to determine if a given atmospheric measurement is turbulent or not, rather than applied as a conclusive method [265, 266].

7.5.2 Richardson Number

The first facts to be established in this research work is determining which atmospheric measurements are turbulent before the C_n^2 is computed. This is done initially in order not to risk the inclusion of non-turbulent or laminar atmospheric measurements in a theory which is particularly for turbulence only. After this is accomplished, then the status of the turbulence can be determined based on whether the atmospheric measurement is either stable or unstable. Therefore, in order to achieve this, the R_i has to be computed per data points. It should also be noted that this calculation can be used to determine how turbulent an atmospheric layer is at a particular time. In other words, this computation simply defines the measurement of the degree of atmospheric turbulence within the atmosphere at a particular time. The Richardson number which is defined as a stability criterion for the natural growth of small-scale waves in a stably stratified atmosphere with vertical wind shear gives the ratio between the work done against gravity as a result of the vertical motions in the waves to the kinetic energy available in the shear flow, and it is given by [142, 267]:

$$R_i = \frac{|g| \cdot (\Delta T_v + \gamma_a \cdot \Delta z) \cdot \Delta z}{T_v \cdot [(\Delta U)^2 + (\Delta V)^2]} \tag{7.46}$$

where the parameter g denotes the acceleration due to gravity (in m/s^2), T_v is the potential or virtual temperature, γ_a denotes the adiabatic lapse rate of decrease of temperature which is given as $\gamma_a = 0.0098\ K/m$, z is the height above the ground surface, and both ΔU and ΔV are components of the wind.

Therefore, the lower the calculated magnitude of this R_i, the less stable the flow will be. However, the most frequently utilized value of the Richardson number that determines the shear-induced turbulence is between 0.15 and 0.5, but most often the critical Richardson value is set at about $R_{i_{cr}} = 0.25$. Although, according to Wallace in 1977, as soon as the turbulence is established in a shear layer, it would be continuous for as long as $R_i < 1.0$. The effect of applying any of $R_{i_{cr}} = 0.25$ or $R_{i_{cr}} = 0.5$ as the critical value of the Richardson number has been estimated and the results shows that there exist no direct obvious differences between the two estimates [267].

Therefore, the three stability criteria based on R_i considered in this work are described as follows: sub-critical condition which is divided into two categories, one suggests that when $R_i \leq 0.25$ the flow (at that data point) is unstable, while $R_i > 0.25$ indicates that the flow is stable. The second category suggests that when $R_i \leq 0.5$ the flow is unstable, while $R_i > 0.5$ indicates that the flow is stable. The critical condition indicates that when $R_i < 1$ the flow is unstable, while $R_i \geq 1$ indicates that the flow is stable. The super-critical condition indicates that when $R_i < 10$ the flow is unstable, while $R_i \geq 10$ indicates that the flow is stable. However, the super-critical is meant for highly sensitive systems and not often recommended for atmospheric conditions. In this work, the criteria used for R_i over all the data points are the critical condition.

7.5.3 Potential Temperature Gradient

It was pointed out by Tatarski in [100, 230], that the temperature T cannot be described as a conservative passive additive, as a result a pseudo-potential temperature was given to appropriately describe the effects of temperature. As a result of several heat exchanges taking place due to irregular eddy movements, a pseudo-potential temperature is necessary instead of the actual temperature. In such cases, the adiabatic lapse rate should be considered. The pseudo-potential temperature (H) is given as:

$$H = T + \gamma_a z, \tag{7.47}$$

where the adiabatic lapse rate, $\gamma_a = g/C_p$; g is the gravitational acceleration in m/s^2, and C_p is the heat capacity at constant pressure. Thus, a potential temperature gradient $\partial H/\partial Z$ was obtained from Equation (7.47). The wet adiabatic lapse rate, γ_a was also calculated for each of the data points by first calculating the water vapour at every hour and then used to determine both H and its corresponding gradient $\partial H/\partial Z$.

7.6 Methodology and Step-by-Step approach of deriving C_n^2

To calculate the C_n^2 parameter so as to generate a general atmospheric turbulence profile for South Africa or location-based profile for each location considered, it is essential to first identify the turbulent data points within the whole data sets available. This procedure can be achieved through the computation of both the Reynolds (R_e) and Richardson (R_i) numbers for each data point at the antenna height (h). Also, required to be calculated at these points are the potential temperature (H) and its corresponding gradient ($\partial H/\partial Z$), which is a function of the adiabatic lapse rate (either wet or dry), water vapour, specific humidity, specific heat at constant pressure etc.

The US-ARL model to be used in this work requires two complete meteorological data sets measured at two different heights along a vertical profile within a particular location. These heights are referred to as reference height (h_r) and antenna height ($h = 10\ m$). The reference height for each location vary depending on the altitude above sea level of that location (see Table 3.1 for a complete altitude description for all locations), while the same antenna height was used for all locations. In this study, the roughness height (which is as a result of vegetation at that location) of $h_0 = 2\ m$ was used for Durban, Cape Town, Bloemfontein and Johannesburg, due to the fact that the average height of the vegetation within this region is between 1 and $2m$. However, $h_0 = 1\ m$ was used for Umtata and Mafikeng because they are less developed or populated and do not have as much industrialization or urbanization like the aforementioned cities. Two other important parameters that must be determined before the derivation of the final C_n^2 are the initial C_n^2 from the Hufnagel-Valley model at the reference height and the initial Monin-Obukov length L_{ob} using the Monin-Obukhov Similarity Theory (MOST) based on the inertial sub-range between h_r and h_0.

In this analysis, it was ensured that the antenna height h (which is the altitude level where the C_n^2 estimates are to be observed for each location) is placed in between the h_r and h_0, which forms the inertial sub-range, consisting of the constantly moving turbulent eddies or air masses. As the air-masses move, there is an exchange of heat, which then results into the adiabatic lapse rate of decrease in temperature, and irregular variations in the temperature and pressure. The refractive index structure function C_T^2 is derived for all the data points, however it is only used to calculate C_n^2 in those that are identified as turbulent (that is, when estimated R_e is within the critical value $R_{e_{Cr}}$). There are other parameters (apart from R_e and R_i numbers) such as the potential temperature gradient or the thermodynamic property that can be used as additional criteria to determine either the level of turbulence of each data point or the frequency of data points that are turbulent.

In summary, after the data collection and processing, the following step-wise approach was applied to each atmospheric data set for each location over the three successive years (2013-2015)

a. Compute the Reynolds (R_e) number for all the data points in each data set for all the locations at the antenna height (h) using the wind speed at that height. This computation is done over the entire hourly measured data set for all the six cities considered. Then extract the data points that satisfy $R_e \gg R_{e_{cr}}$ (where $R_{e_{cr}}$ is around $10^6\ to\ 10^7$) as turbulent data points. This result can be used to determine which data points are laminar or turbulent.
b. Calculate the potential temperature gradient or thermodynamic stability for each of the selected hourly data points, for further investigation of the existence of atmospheric turbulence. In this work, we used only the potential temperature gradient as an additional measure.
c. Derive the Richardson (R_i) number for all the hourly data points for each location at the antenna heights involving h_r, by using the difference of their potential temperatures, the difference of the two heights (i.e., h and h_r), the adiabatic lapse rate and the components of the wind at that altitude range. The obtained R_i is then compared with the various criteria of the critical Richardson number $R_{i_{cr}}$ (which is any of critical, sub-critical and super-critical criteria) so as to determine the frequency of atmospheric turbulence in each category, based on $R_i < R_{i_{cr}}$. Therefore, as a result of this classification, the turbulent data set can be grouped based on their level of stability.
d. Compute the initial C_n^2 using the Hufnagel-Valley model at the reference height (h_r) and the initial Monin-Obukov length L_{ob} using the MOST model based on the inertial sub-range between h_r and h_0.
e. Estimate the refractive index structure function C_T^2 for all the data points for all the stations covering the three years in this study.
f. Furthermore, generate data sub-set for each location under study based on the criteria $R_e \geq R_{e_{Cr}}$ and $R_i < R_{i_{Cr}}$, such that the resultants will only comprise of hourly measurements where the data points are turbulent or chaotic.

g. Calculate the RISP (C_n^2) using the obtained C_T^2 for all the turbulent (stable, unstable or neutral) data points in each data set for all the locations and for all the years.

The observation which involves determining whether a certain meteorological measurement of a particular location is turbulent or not, has been included more as a measure of completeness than as a conclusive approach. The flow chart presented in Figure 7.7 is provided to help understand the step-wise approach.

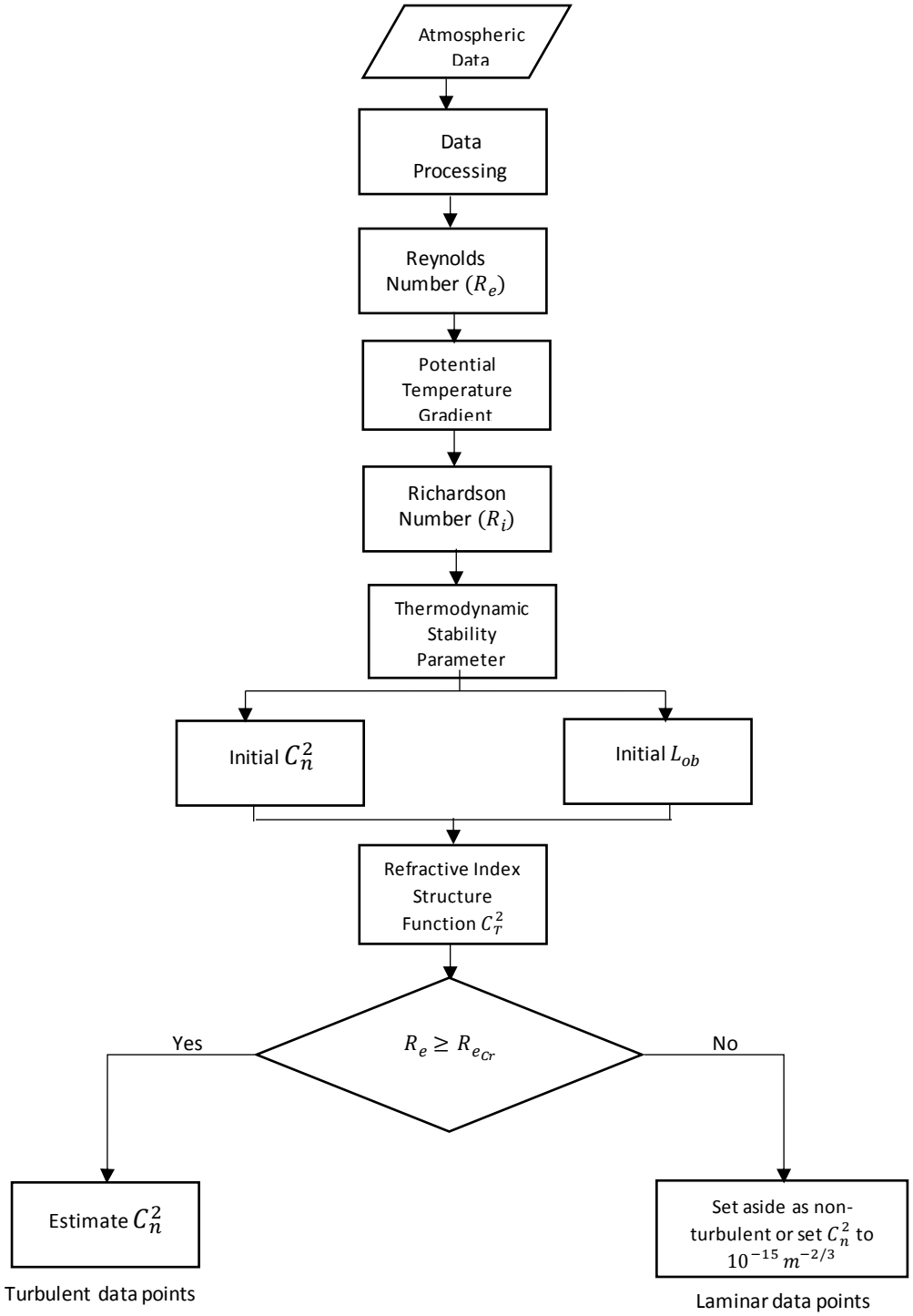

Figure 7.7: Flow Chart representation of the methodology and step-by-step approach of determining C_n^2.

7.7 Estimation of Atmospheric Turbulence in terms of Refractive Index Structure Parameter

Several authors have applied a number of techniques to estimate atmospheric turbulence as a function of C_T^2 and RISP (C_n^2). The techniques used to obtain the vertical profiles of C_n^2 can be classified into parametric and non-parametric analyses as earlier discussed and are mostly dependent on measurements of meteorological variables obtained from the radar, thermosondes and radiosondes, whereas only a few can use earth surface measurements to properly estimate the surface layer profile. These instruments can be employed to carry out real-time measurements of C_n^2, but are mostly limited to space observations. Most authors publish the C_n^2 measurements in form of averages (such as diurnal, monthly or seasonal means), with little or no information of the time series profile or the probability distributions of the measurements. Therefore, such data is not easy to utilize in any communication application that needs statistical information, like the optical- or radio-wave propagation, whereby the probability of outage of the system needs to be estimated.

In this work, one of the main interests is to determine the hourly time and frequency series profiles of the C_n^2 parameter, for further research on scintillation and atmospheric turbulence. The US-ARL model is ideally suited for this work, because it does not only use the height and wind speed in the estimation of the C_n^2 parameter, but it also uses most meteorological variables of interest (such as temperature, pressure, humidity and wind speed, as well as water vapour) across two different altitudes, i.e. the reference and antenna heights. Therefore, the occurrence or evidence of turbulent layers within the specified location are necessary to determine C_n^2. Meteorological data from six different stations relating to six different provinces within South Africa have been used in this work over three successive years, and their locations spread out latitudinally. Since the aim of this work is to characterize the constant parameter C_n^2 for different climatic types within South Africa, these locations were chosen at certain latitudes that range from the most available northern part to the most available southern part of SA. The climatic data were obtained from the archives of the SAWS and the NOAA/NCIE databases, and were used for measurements at h_r and h respectively. The data sets available from these organizations cover a wide range of years, but just a subset of these data (2013 to 2015) was selected based on the completeness of the data.

The statistical description of the estimated hourly C_n^2 profile at an antenna height $h = 10\ m$ is presented in Table 7.4, and it covers all the common statistical quantities for all the locations over the three successive years under study. The minimum and maximum values of the obtained C_n^2 for each location at this height shows that the atmospheric turbulence stability level in these areas (including coastal, near coastal and non-coastal) are within the strong turbulence regime, that is between $10^{-14}\ m^{-2/3}$ and $10^{-13}\ m^{-2/3}$. It can be observed from these results that the coastal and near-coastal areas of Durban, Cape Town and Umtata have higher average of the maximum C_n^2 values of about $3.37 \times 10^{-13}\ m^{-2/3}$,

$4.11 \times 10^{-13}\ m^{-2/3}$ and $2.88 \times 10^{-13}\ m^{-2/3}$ respectively over the three years (2013-2015), while the non-coastal environs of Bloemfontein and Mafikeng have relatively lesser values of $2.43 \times 10^{-13}\ m^{-2/3}$ and $2.40 \times 10^{-13}\ m^{-2/3}$ respectively over the three years under study. Whereas, for the city of Johannesburg which is also seen as an inland area but on a much higher altitude, has the lowest overall maximum C_n^2 value of around $1.79 \times 10^{-13}\ m^{-2/3}$. It should be noted that these maximum values are expected to occur during the day-time, since the diurnal chat in Figure 7.4 showed that during the day time the atmospheric turbulence strength is expected to be higher and unstable and then lower and stable during the night, while it is lowest or neutral during two unique periods within a day.

However, all their cumulative minimum values over the three years, which is expected to have occurred within the night time or as a result of stable turbulence are around the range of $2.76 \times 10^{-14}\ m^{-2/3}$ and $4.11 \times 10^{-14}\ m^{-2/3}$, whereby Johannesburg is observed to have the lowest and Cape Town has the highest of these cumulative minimum values. Thus, these are assumed to be the most stable and unstable turbulent atmospheres respectively during night-time among all the locations under study.

Moreover, the overall SD values of the estimated C_n^2 over all the locations are approximately $1.05 \times 10^{-13}\ m^{-2/3}$, $1.26 \times 10^{-13}\ m^{-2/3}$, $8.14 \times 10^{-14}\ m^{-2/3}$, $7.67 \times 10^{-14}\ m^{-2/3}$, $3.99 \times 10^{-14}\ m^{-2/3}$ and $5.86 \times 10^{-14}\ m^{-2/3}$ over the three years (2013-2015) for Durban, Cape Town, Umtata, Bloemfontein, Johannesburg and Mafikeng respectively. The SD results show that the locations with the higher magnitudes of atmospheric turbulence have the higher deviations respectively, with Cape Town showing that its atmosphere is the most unstable.

7.8 Time Series Profiling of the Refractive Index Structure Parameter

The typical day- and night-time series profiles of the estimated C_n^2 phenomenon for all the locations over the three successive years are presented in Figures 7.8 and 7.9 respectively. These time series profiles for C_n^2 at height $h = 10\ m$ were computed using hourly meteorological data of a period of three years and over the four seasons observed in South Africa. In the day-time, the observed Atmospheric Turbulence Level (thereafter, ATL) in terms of C_n^2 as presented in Figure 7.8 showed that it is generally unstable with high magnitude of chaos noticed at frequent periods, which suggests that the turbulence around this time of the day is long-lived. It can also be deduced that the periodicity of the turbulence form groups at the mean point. Though, these observations were only based on physical inspection, and they are not obvious deductions from the plots since there are no much differences in the obtained ATL across the whole periods, which is a consequence of the scale. Therefore, to properly view the pattern more obviously we may have to zoom in to the time series or probably use a wider scale.

Table 7.4: Statistical description of the estimated C_n^2 for all the locations and over each of the years in this study.

	Durban			*Cape Town*			*Umtata*		
Statistical Description	*2013*	*2014*	*2015*	*2013*	*2014*	*2015*	*2013*	*2014*	*2015*
Mean	1.58E-13	1.57E-13	1.59E-13	1.88E-13	1.87E-13	1.87E-13	1.25E-13	1.22E-13	1.17E-13
Standard Error	1.14E-15	1.12E-15	1.16E-15	1.35E-15	1.38E-15	1.35E-15	9.13E-16	8.93E-16	8.36E-16
Median	1.91E-13	1.96E-13	1.94E-13	2.28E-13	2.34E-13	2.27E-13	1.44E-13	1.36E-13	1.32E-13
Mode	4.40E-14	1.91E-13	4.34E-14	5.42E-14	5.40E-14	5.00E-14	2.19E-13	2.31E-13	3.53E-14
Standard Deviation	1.06E-13	1.01E-13	1.07E-13	1.25E-13	1.28E-13	1.26E-13	8.43E-14	8.24E-14	7.74E-14
Sample Variance	1.12E-26	1.02E-26	1.13E-26	1.55E-26	1.64E-26	1.59E-26	7.10E-27	6.80E-27	5.99E-27
Kurtosis	-1.7494	-1.7637	-1.7379	-1.7573	-1.8168	-1.7988	-1.6194	-1.5707	-1.5744
Skewness	0.0343	-0.0681	0.0239	0.0035	-0.0059	0.0038	0.1517	0.1860	0.1676
Range	3.08E-13	2.89E-13	3.04E-13	3.67E-13	3.81E-13	3.62E-13	2.54E-13	2.62E-13	2.48E-13
Minimum	3.59E-14	3.58E-14	3.94E-14	4.14E-14	4.01E-14	4.18E-14	3.33E-14	3.34E-14	3.27E-14
Maximum	3.44E-13	3.25E-13	3.43E-13	4.08E-13	4.21E-13	4.04E-13	2.87E-13	2.95E-13	2.81E-13
Sum	1.36E-09	1.27E-09	1.34E-09	1.60E-09	1.62E-09	1.63E-09	1.06E-09	1.04E-09	1.00E-09
Count	8612	8107	8419	8522	8628	8708	8520	8518	8564
	Bloemfontein			*Johannesburg*			*Mafikeng*		
Statistical Description	*2013*	*2014*	*2015*	*2013*	*2014*	*2015*	*2013*	*2014*	*2015*
Mean	1.10E-13	1.18E-13	1.21E-13	8.58E-14	8.70E-14	8.70E-14	1.01E-13	9.80E-14	1.01E-13
Standard Error	7.37E-16	8.50E-16	8.78E-16	4.45E-16	4.24E-16	4.21E-16	6.23E-16	6.27E-16	6.41E-16
Median	1.20E-13	1.30E-13	1.35E-13	1.00E-13	9.87E-14	9.70E-14	1.05E-13	1.02E-13	1.06E-13
Mode	3.85E-14	3.63E-14	2.17E-13	1.08E-13	4.00E-14	3.20E-14	3.64E-14	1.75E-13	3.20E-14
Standard Deviation	6.86E-14	7.94E-14	8.21E-14	4.15E-14	3.93E-14	3.89E-14	5.80E-14	5.80E-14	5.97E-14
Sample Variance	4.70E-27	6.30E-27	6.74E-27	1.72E-27	1.54E-27	1.51E-27	3.37E-27	3.36E-27	3.56E-27
Kurtosis	-1.5668	-1.6572	-1.6781	-1.5833	-1.5492	-1.4281	-1.1823	-1.2595	-1.2381
Skewness	0.1922	0.1488	0.1309	0.0480	0.0723	0.1257	0.3445	0.3332	0.3308
Range	1.96E-13	2.25E-13	2.18E-13	1.56E-13	1.44E-13	1.54E-13	2.11E-13	2.05E-13	2.15E-13
Minimum	3.57E-14	2.15E-14	3.35E-14	1.49E-14	3.45E-14	3.34E-14	3.00E-14	2.93E-14	3.00E-14
Maximum	2.32E-13	2.46E-13	2.52E-13	1.71E-13	1.79E-13	1.87E-13	2.41E-13	2.34E-13	2.45E-13
Sum	9.52E-10	1.03E-09	1.06E-09	7.44E-10	7.45E-10	7.42E-10	8.75E-10	8.38E-10	8.79E-10
Count	8663	8735	8745	8669	8565	8528	8685	8551	8657

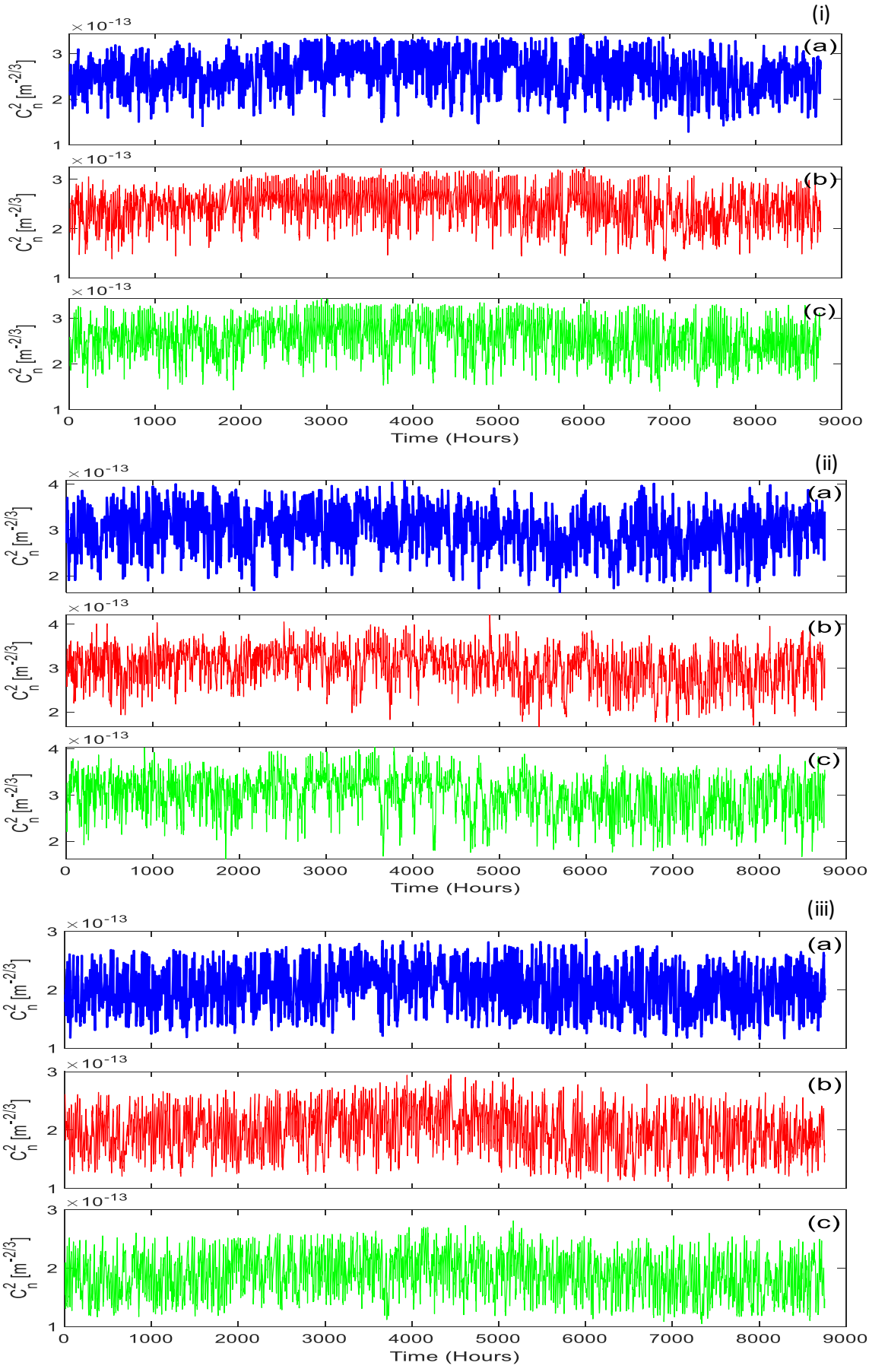
(i)
(a)
(b)
(c)
(ii)
(a)
(b)
(c)
(iii)
(a)
(b)
(c)
$\times 10^{-13}$
$C_n^2 [m^{-2/3}]$
Time (Hours)
0
1000
2000
3000
4000
5000
6000
7000
8000
9000

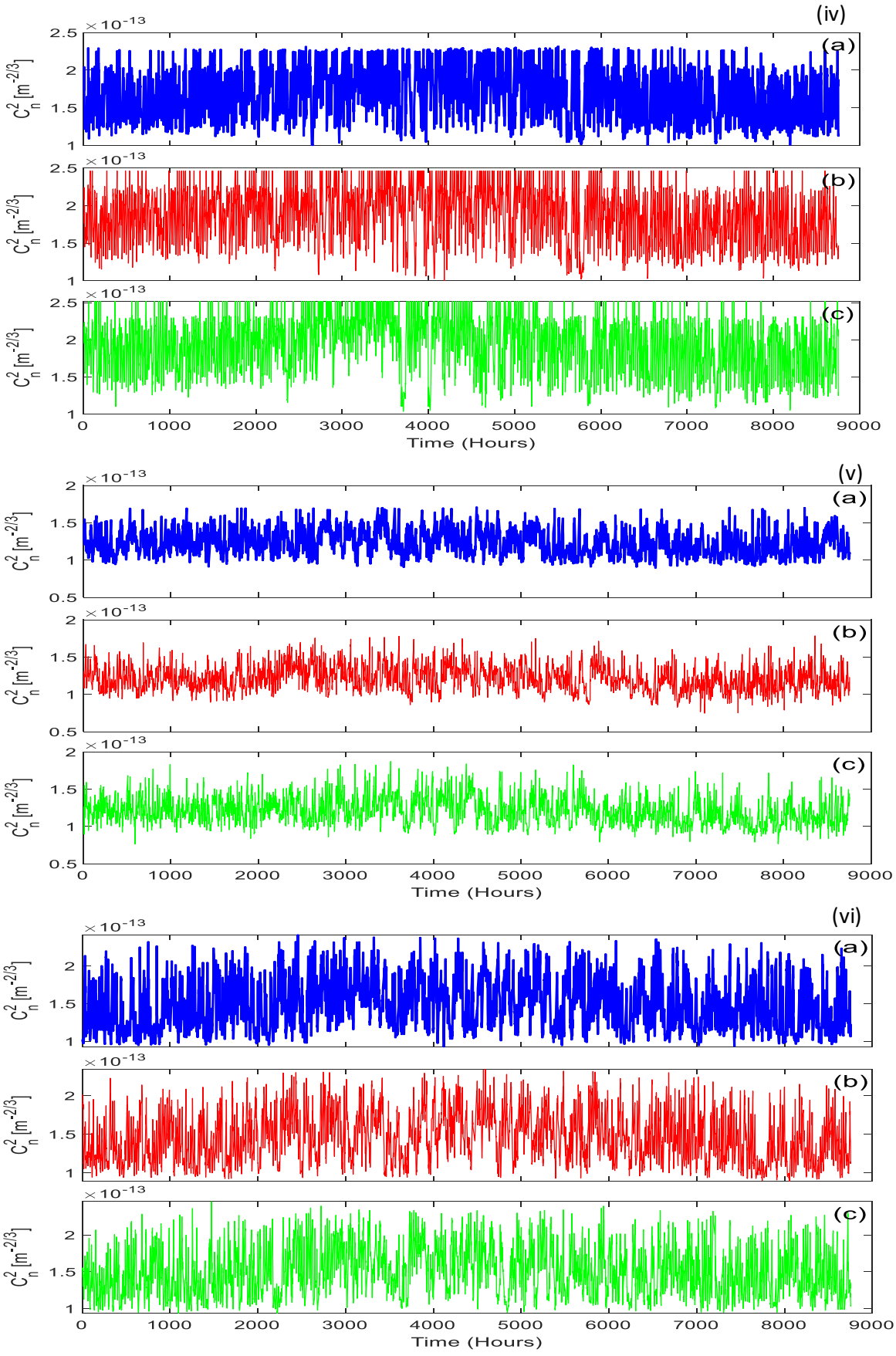

Figure 7.8: Day time series profile of the estimated C_n^2 for (i) Durban; (ii) Cape Town; (iii) Umtata; (iv) Bloemfontein; (v) Johannesburg and (vi) Mafikeng and over each of the years (a) 2013; (b) 2014 and (c) 2015.

The ATL observed in terms of C_n^2 during the night-time as presented in Figure 7.9 showed that it is generally stable with little chaos noticed at sporadic periods, which suggests that the turbulence around this time of the day is short-lived. It can also be deduced that the periodicity of the turbulence does not form groups at the mean point, unlike what is obtained around the day-time periods. This observation is quite expected due to the fact that at the ground level the values are expected to be close at night (as discussed in section 7.4.1).

In order to really explain the uniqueness or variations of this atmospheric turbulence phenomenon in terms of the C_n^2 profile, standard or advanced statistical (for instance mean, SD, frequency of occurrence etc.) techniques are required, which is the focus of the subsequent sub-sections in this Chapter.

In summary, the following observations were deduced from the presented results:

a. The thermodynamic behavior and the ATL are generally unstable during the day, while it is generally stable during the night.
b. The level of atmospheric stability and the trend observed during the day showed that turbulence is generally unstable with significant amount of turbulence within the atmosphere at long moments which shows that the perturbation is long-lived around this time of the day, while it is generally stable at night with little chaos noticed at sporadic periods, which suggests that the turbulence around this time of the day is short-term.
c. The periodicity of the turbulence observed during the night-time do not cluster around the mean unlike that of the day-time, which results into a general serenity at the night time.

7.9 Frequency Series Profiling of the Refractive Index Structure Parameter

The frequency series profile of the estimated C_n^2 has been presented in form of histograms showing the number of occurrences of both daytime and night-time in one plot. Figure 7.10 presents the typical frequency series analysis of the C_n^2 profile over the six locations and for the three-year period covering all the four climatic seasons available in South Africa. One of the very obvious observations in these histogram plots is the symmetrical shape showing the differences between the day-time and the night-time in terms of the C_n^2 magnitude as well as its corresponding number of events.

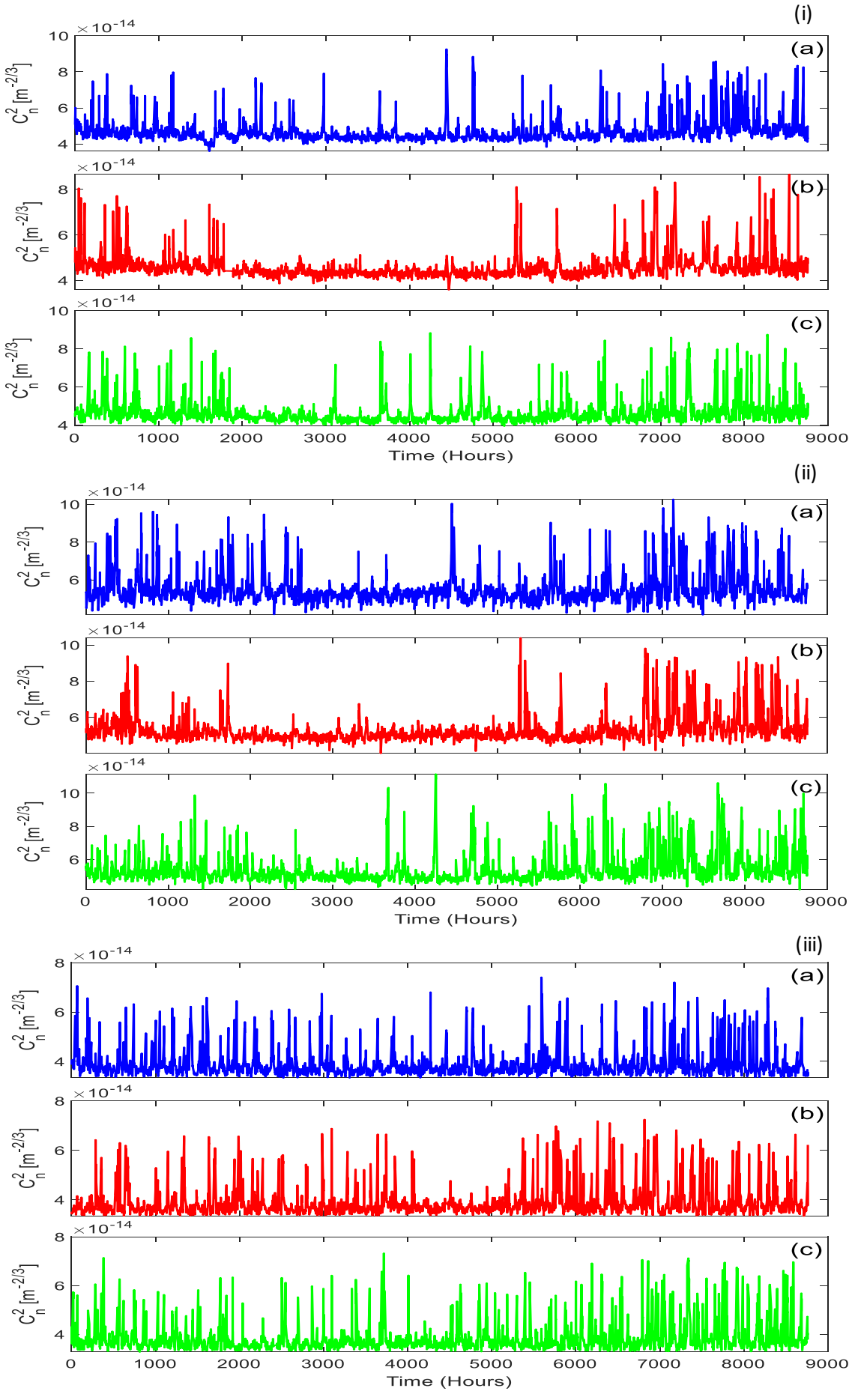
(i)
(a)
(b)
(c)
$\times 10^{-14}$
C_n^2 [$m^{-2/3}$]
Time (Hours)
(ii)
(a)
(b)
(c)
$\times 10^{-14}$
C_n^2 [$m^{-2/3}$]
Time (Hours)
(iii)
(a)
(b)
(c)
$\times 10^{-14}$
C_n^2 [$m^{-2/3}$]
Time (Hours)

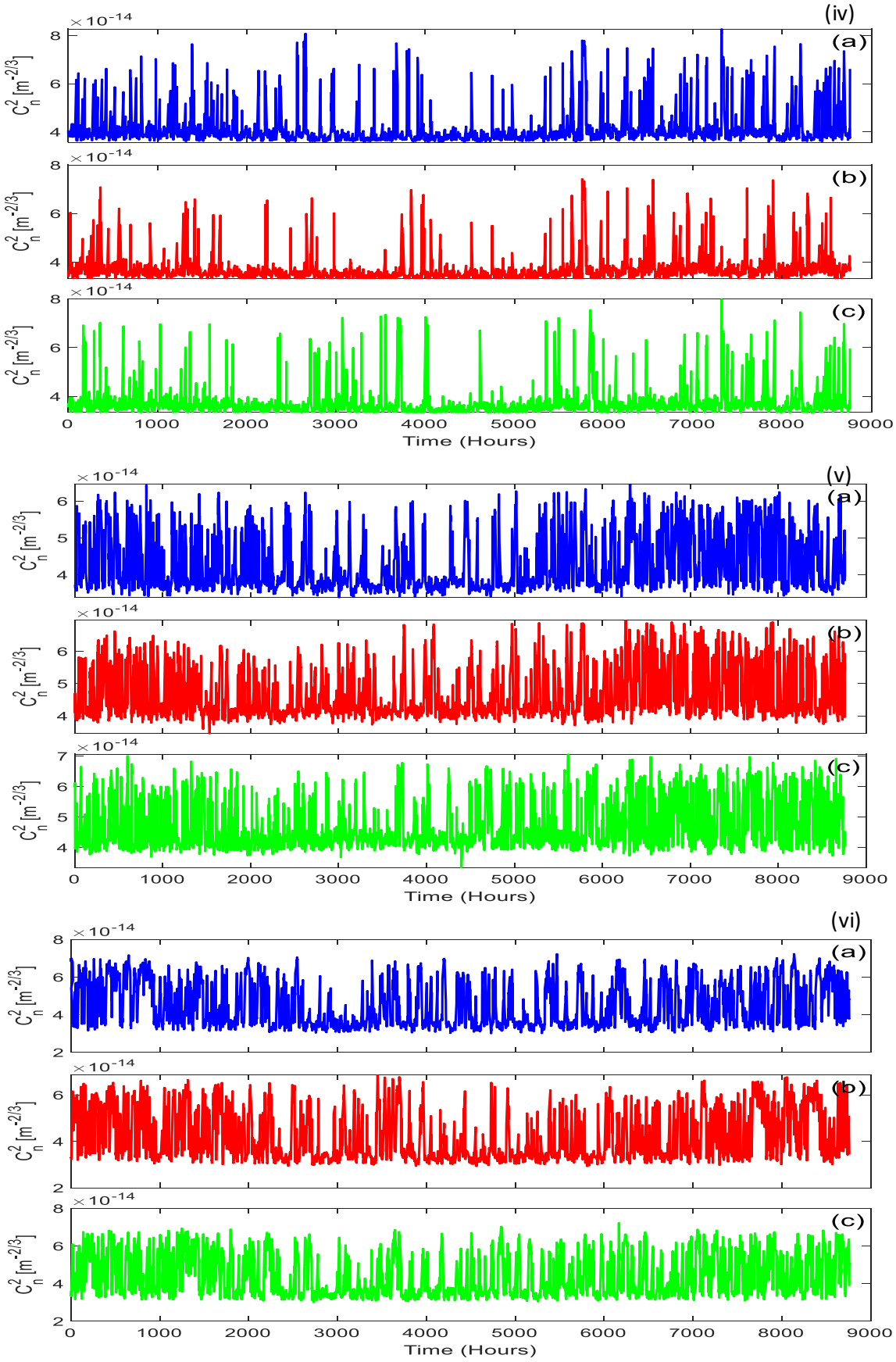

Figure 7.9: Night-time series profile of the estimated C_n^2 for (i) Durban; (ii) Cape Town; (iii) Umtata; (iv) Bloemfontein; (v) Johannesburg and (vi) Mafikeng and over each of the years (a) 2013; (b) 2014 and (c) 2015.

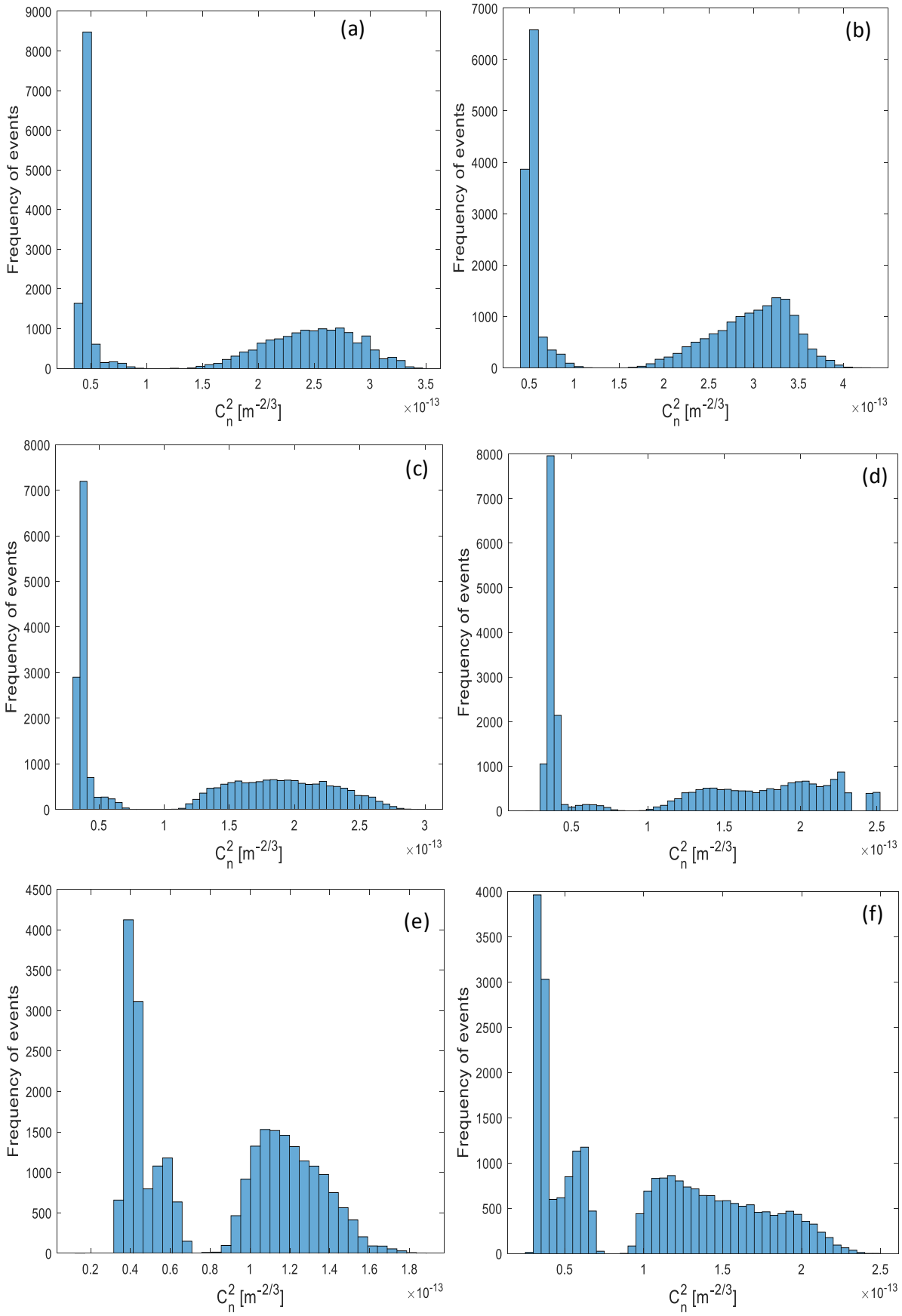

Figure 7.10: Typical frequency series profiles plotted using histograms over the cumulative years (2013-2015) for (a) Durban; (b) Cape Town; (c) Umtata; (d) Bloemfontein; (e) Johannesburg and (f) Mafikeng.

From the histogram plot for Durban which is provided in Figure 7.10 (a), it was noticed that during the day the most frequent range of C_n^2 is within the range $2.65 \times 10^{-13}\ m^{-2/3}$ and $2.75 \times 10^{-13}\ m^{-2/3}$, which suggest the modal C_n^2 is given as $2.70 \times 10^{-13}\ m^{-2/3}$, and the most frequent range of C_n^2 phenomenon at night is from $4.0 \times 10^{-14}\ m^{-2/3}$ to $5.0 \times 10^{-14}\ m^{-2/3}$ such that the modal C_n^2 is given as $4.50 \times 10^{-14}\ m^{-2/3}$. Similarly, from the other histogram plots available in Figures 10 (b) to (f) for Cape Town, Umtata, Bloemfontein, Johannesburg and Mafikeng respectively, the modal C_n^2 is obtained as $3.25 \times 10^{-13}\ m^{-2/3}$, $2.30 \times 10^{-13}\ m^{-2/3}$, $2.275 \times 10^{-13}\ m^{-2/3}$, $1.075 \times 10^{-13}\ m^{-2/3}$ and $1.175 \times 10^{-13}\ m^{-2/3}$ respectively, while at night the modal C_n^2 values are $5.50 \times 10^{-14}\ m^{-2/3}$, $3.75 \times 10^{-14}\ m^{-2/3}$, $3.625 \times 10^{-14}\ m^{-2/3}$, $4.25 \times 10^{-14}\ m^{-2/3}$ and $3.25 \times 10^{-14}\ m^{-2/3}$ respectively. These results show that the highest modal C_n^2 occurred in Cape Town for both day and night times, followed by Durban and Umtata. This suggests that the coastal and near-coastal areas often exhibit high ATL. For the non-coastal areas such as Bloemfontein, Johannesburg and Mafikeng the level of atmospheric turbulence given by the modal C_n^2 are relatively lower than that of the coastal areas. However, the modal C_n^2 for Johannesburg show a distinction such that it was the lowest during the day-time but was considerably high during the night time.

7.10 Monthly Mean and Standard Deviation of C_n^2 over South Africa

This section shows the monthly mean and SD of the estimated day and night C_n^2 data for the collective years from 2013 to 2015 for South Africa. From these monthly results, more insight into the relative magnitudes and variability of scintillation in each month and season will be presented. Therefore, issues such as which period on the average has the largest turbulence or the period with the largest dispersion of turbulence magnitude will be answered. Figure 7.11 presents the monthly average C_n^2 for both the daytime and night time data for all the locations over the three successive years. These plots show that, apart from a small and irregular increase of the cumulative mean of the turbulence strength, the trend of the monthly variations is quite similar for all the locations considered in the entire period. Based on these results, the maximum mean C_n^2 values of $1.77 \times 10^{-13}\ m^{-2/3}$, $1.98 \times 10^{-13}\ m^{-2/3}$ and $1.46 \times 10^{-13}\ m^{-2/3}$ were all observed in February for Durban, Cape Town and Umtata respectively, $1.27 \times 10^{-13}\ m^{-2/3}$ and $8.91 \times 10^{-14}\ m^{-2/3}$ were observed in December for Bloemfontein and Johannesburg respectively, and $1.05 \times 10^{-13}\ m^{-2/3}$ was observed in January for Mafikeng. While the lowest mean C_n^2 values of $1.52 \times 10^{-13}\ m^{-2/3}$, $1.78 \times 10^{-13}\ m^{-2/3}$ and $1.15 \times 10^{-13}\ m^{-2/3}$ were observed in June for Durban, Cape Town and Umtata respectively, and $1.08 \times 10^{-13}\ m^{-2/3}$, $8.36 \times 10^{-14}\ m^{-2/3}$ and $9.55 \times 10^{-14}\ m^{-2/3}$ were noticed in July for Bloemfontein, Johannesburg and Mafikeng respectively. These results show that the summer and autumn seasons have higher ATL, where January, February and December have the highest mean C_n^2 across all the locations under study. Also, the comparison of the monthly averages revealed that more atmospheric turbulence was observed in the coastal areas than in the non-coastal areas.

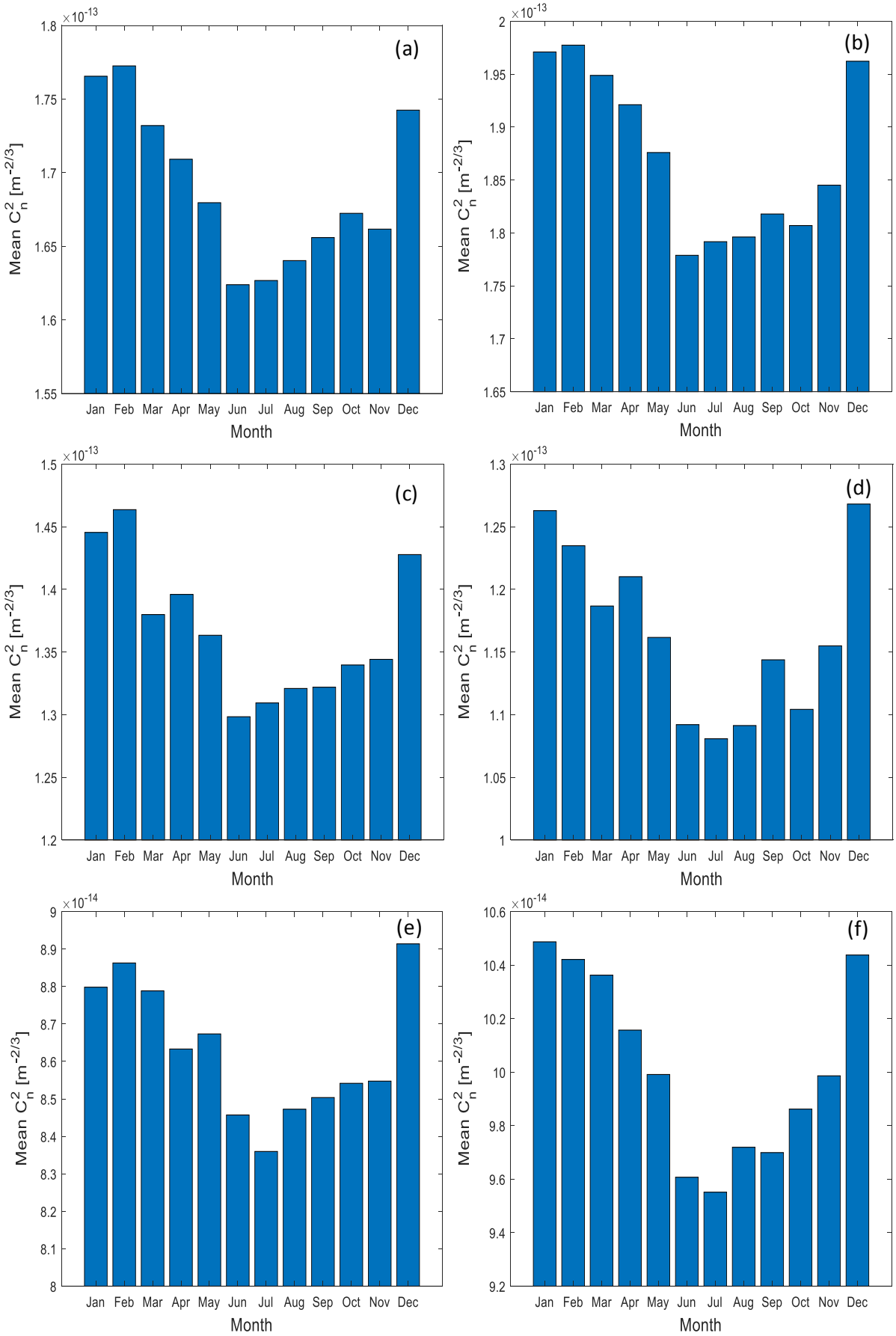

Figure 7.11: Monthly cumulative mean C_n^2 for both day and night times for (a) Durban; (b) Cape Town; (c) Umtata; (d) Bloemfontein; (e) Johannesburg and (f) Mafikeng over the entire period under study.

The monthly SD of the ATL for each of the locations over the entire three years in this analysis were calculated and presented in Figure 7.12. This explains the summary about the dispersion of the estimates of the C_n^2 for each month about its average value across all the four seasons in South Africa. The dispersion results of the C_n^2 as presented in Figure 7.12 showed that the monthly or seasonal variability of the SD of C_n^2 is in strong correspondence to that of its mean. That is, the months or periods having high mean values of ATL are the ones undergoing high variations, whereas the months with low C_n^2 values have turbulence values that are more closely gathered around the average value. In conclusion, the following observations were deduced:

a. The high mean C_n^2 values were observed mostly in the summer months (i.e., January, February and December) which are the peak periods of the wet season and partly between March and May. Thus, it is generally high all through the summer and autumn periods, but less considerable during the winter and spring seasons. This is consistent with the fact that there are high scintillations expected in the wet or rainy seasons compared to the dry seasons.
b. A consistency in the monthly periodicity of mean turbulence was noticed in all the locations.
c. Therefore, the time within the year that have high turbulence strength in terms of overall mean value are the months of February and December, while the least mean C_n^2 values were observed in June and July.
d. The seasonal pattern of the mean C_n^2 is noticed to be consistent with what has been discussed earlier in this thesis, and this is due to the dependence of the ATL on various meteorological variables.
e. The coastal and near-coastal areas experienced higher magnitudes as well as variability than the non-coastal areas as indicated by the plot of the mean and standard deviations.

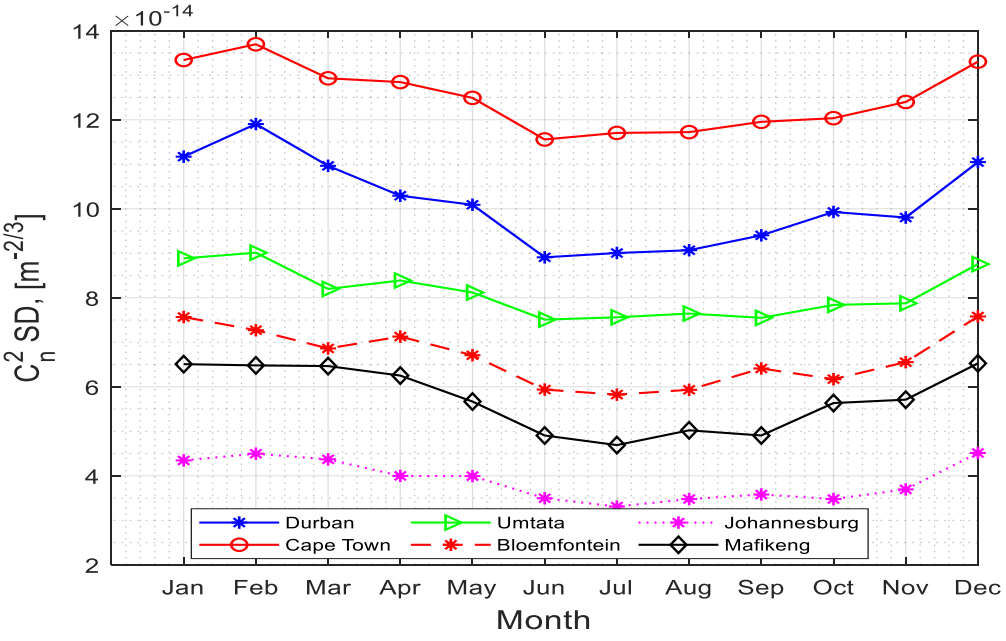

Figure 7.12: Monthly standard deviation of C_n^2 for all the locations over the entire period under study (2013-2015).

7.11 Scintillation Index Variability Curve and its influence on FSO

This section shows the scintillation index (SI) variability curve and its resulting effects over an FSO link at various distances for the respective locations and across the three years under study. These analyses help to address two important questions bothering on how much of atmospheric turbulence affects the optical link at certain optical wavelength over different link distances and also to determine which location might pose greater threat to the implementation of optical communication system.

Figure 7.13 presents the cumulative scintillation index variation over various optical link ranges for an FSO link operating at 850 nm wavelength at the considered locations for the entire period of three years (2013-2015). The specific SI (i.e., scintillation index at optical link distance of 1 km) for Durban ranged between 0.26 dB and 0.78 dB, but revolves around the mean value of 0.59 dB. Likewise, the specific SI range for Cape Town, Umtata, Bloemfontein, Johannesburg and Mafikeng are respectively between 0.29 dB and 0.85 dB, 0.20 dB and 0.68 dB, 0.20 dB and 0.66 dB, 0.23 dB and 0.51 dB, and 0.21 dB and 0.59 dB, whereas their respective mean SI at 1 km are 0.65 dB, 0.49 dB 0.48 dB, 0.38 dB and 0.43 dB.

Since the specific SI of both Durban and Cape Town (which are coastal areas) can get as high as 0.78 dB and 0.85 dB respectively at optical link distance of 1 km, with equivalent mean SI estimate of about 0.59 dB and 0.65 dB, then it can be concluded that there will be considerable atmospheric attenuation due to scintillation over the 850 nm optical link placed at these two locations than at Bloemfontein, Johannesburg and Mafikeng (which are non-coastal areas).

7.12 Monthly Mean and Standard Deviation of Atmospheric Attenuation based on Scintillation

The mean and the standard deviation of the atmospheric attenuation due to scintillation for all the locations over the three years in this study are presented in Figures 7.14 and 7.15 respectively. The location as well as variability of the optical attenuation are summarized in these charts for each of the months and seasons. The relative magnitudes and variability of attenuation in each month and season were observed from the monthly variations presented. Figures 7.14 (a) and (b) show the mean of the specific attenuation for an optical link operating at 850 nm and 1550 nm respectively for each of the locations. Therefore, in general, it was observed that the months of January, February and December have on the average the highest peaks across all the locations considered, with other surrounding months (such as March, April and May) also showing considerable attenuation. At 850 nm wavelength, the mean attenuation values for Durban, Cape Town, Umtata, Bloemfontein, Johannesburg and Mafikeng reached as high as 23.15 dB/km in February, 24.45 dB/km in February, 21.04 dB/km in February, 19.58 dB/km in December, 16.42 dB/km in December, and 17.81 dB/km in January respectively.

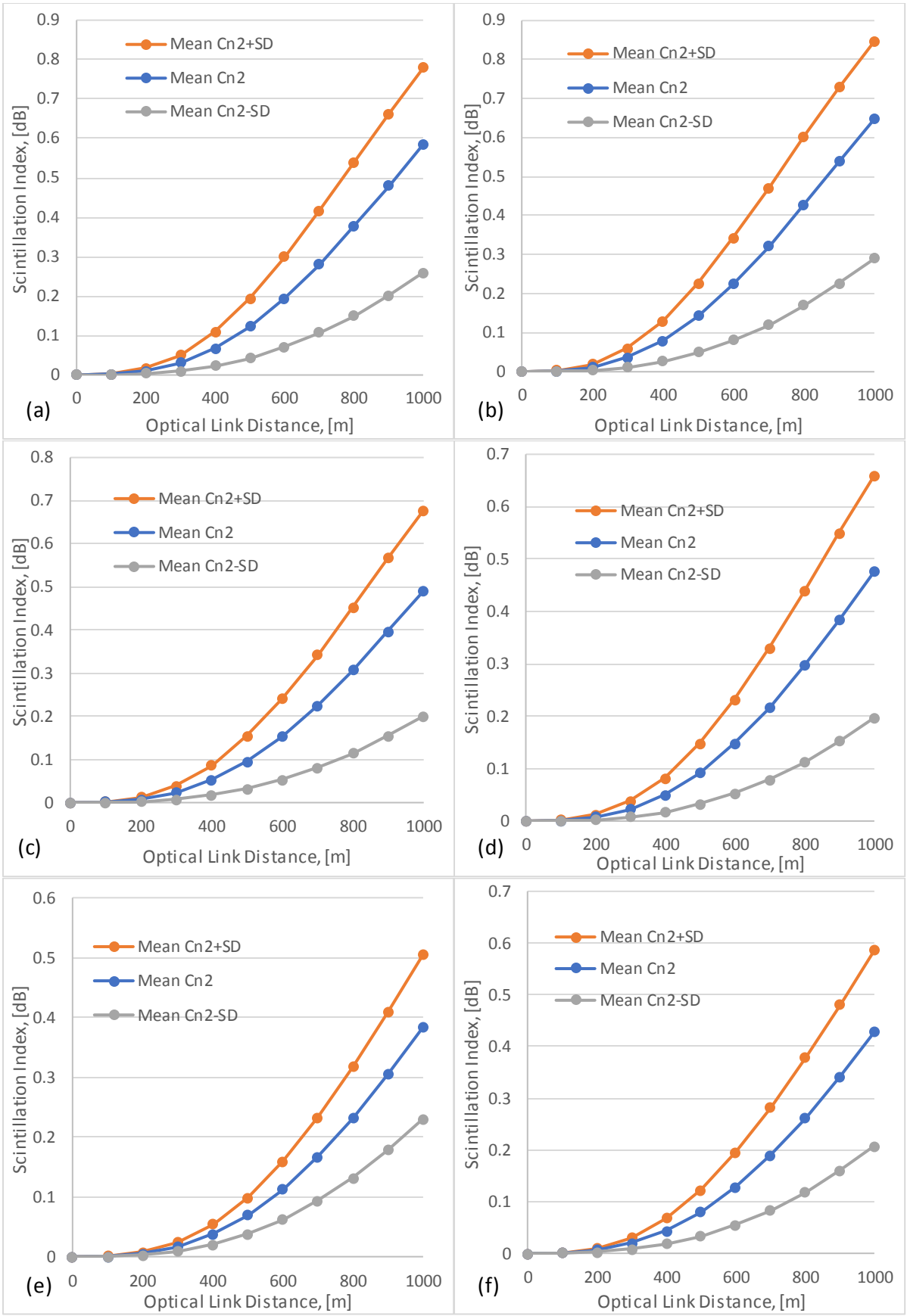

Figure 7.13: Cumulative scintillation index curve against the optical link distance for 850 *nm* FSO links at (a) Durban; (b) Cape Town; (c) Umtata; (d) Bloemfontein; (e) Johannesburg and (f) Mafikeng over the entire period under study.

Whereas, for 1550 nm wavelength, the mean attenuation values for Durban, Cape Town, Umtata, Bloemfontein, Johannesburg and Mafikeng reached as high as 16.31 dB/km in February, 17.22 dB/km in February, 14.82 dB/km in February, 13.79 dB/km in December, 11.56 dB/km in December, and 12.54 dB/km in January respectively. This obviously shows that the attenuation obtained from the 1550 nm FSO link is much lower than that of the 850 nm optical link as expected. Therefore, it can be concluded that for the deployment of optical links within South Africa, an FSO device with 1550 nm wavelength is required. Also, from these results it was observed that the attenuation trend for each of the locations are similar and it can be concluded that there exists a consistency in the monthly periodicity of the mean attenuation. Another obvious consideration is that the mean attenuation values of the coastal and near-coastal areas are relatively higher than that of the non-coastal areas, indicating that more attention is needed in these regions. In general, from these results the summer and autumn months have been observed to likely have the highest effects of atmospheric attenuation on the propagating optical signals, whereby this is lower in the winter and spring months. The plots for the standard deviation of the atmospheric attenuation due to scintillation at optical wavelengths of 850 nm and 1550 nm are presented in Figures 7.15 (a) and (b) respectively. These results reveal the period of the year that has the highest dispersion of attenuation magnitudes. It was observed that the monthly trends of the standard deviation are in strong accordance with that of the mean attenuation. Therefore, it can be said that the months having large mean atmospheric attenuation values are also the months having high variability.

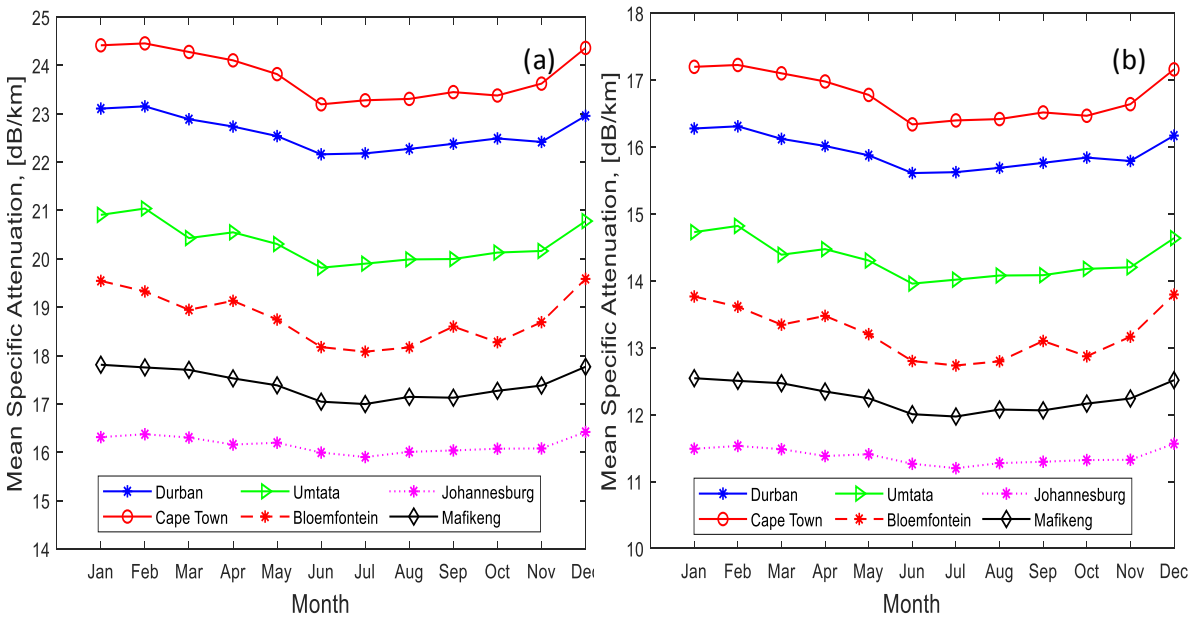

Figure 7.14: Monthly mean specific attenuation due to atmospheric scintillation for South Africa over the entire period under study for optical links at (a) 850 nm and (b) 1550 nm wavelengths.

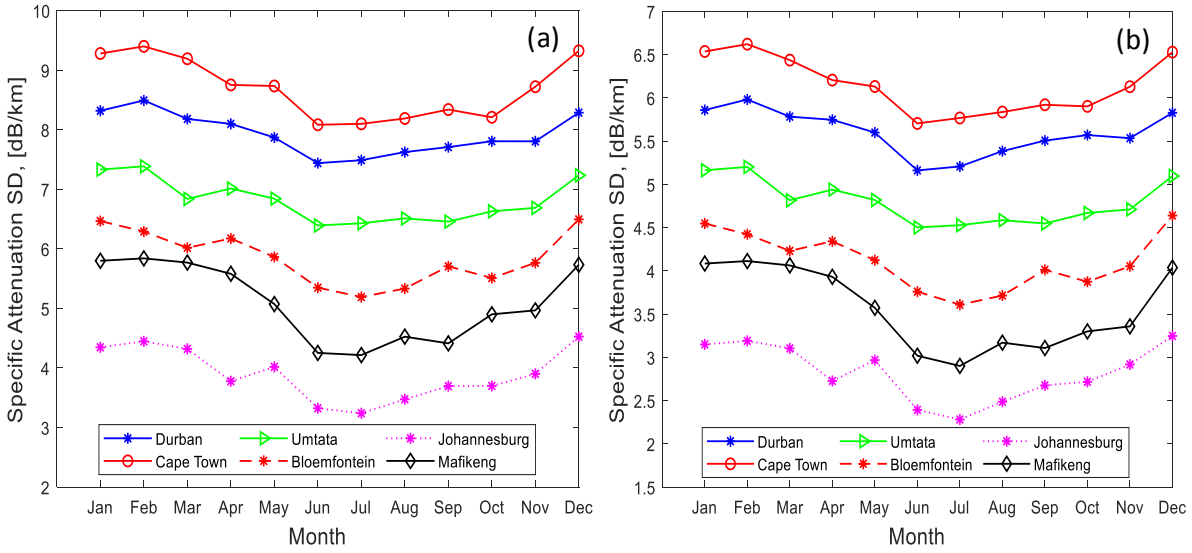

Figure 7.15: Monthly standard deviation of specific attenuation due to atmospheric scintillation for South Africa over the entire period under study for optical links at (a) 850 nm and (b) 1550 nm wavelengths.

7.13 Cumulative Distribution of the Optical Attenuation due to Atmospheric Turbulence for South Africa

The Cumulative Distributions (CDs) of three-year hourly atmospheric attenuation due to scintillation for various climatic regions in South Africa are estimated according to Equation (3.14) and plotted in Figure 7.16. This cumulative distribution is based on percentages of time and various meteorological variables. This analysis is carried out for six locations within South Africa and over the period of three years. At a time percentage of 0.01 %, the attenuations recorded for year 2013 are 32.47 dB, 35.38 dB, 29.65 dB, 26.65 dB, 22.92 dB and 27.02 dB for Durban, Cape Town, Umtata, Bloemfontein, Johannesburg and Mafikeng respectively. For the year 2014, at the same time percentage the attenuations are 31.34 dB, 35.70 dB, 30.07 dB, 27.29 dB, 23.24 dB and 26.61 dB for Durban, Cape Town, Umtata, Bloemfontein, Johannesburg and Mafikeng respectively. Also, for the year 2015 the attenuation values at the time percentage of 0.01 % are 32.22 dB, 35.17 dB, 29.16 dB, 27.77 dB, 23.94 dB and 27.24 dB for Durban, Cape Town, Umtata, Bloemfontein, Johannesburg and Mafikeng respectively. Figure 7.17 shows the performance evaluation and model validation for various distribution models of optical attenuation due to atmospheric turbulence for South Africa. These plots were achieved by using the years 2013 and 2014 as the actual data, while 2015 was used as the validation data.

In this work, an attenuation model was developed in terms of the percentage exceedance. To confirm the most suitable fit distribution to best describe each of these locations, the coefficient of determination was used as shown in Table 7.5. This table presents the best fit distribution that describes the attenuation due to atmospheric scintillation for South Africa. Among several distribution fits that were applied to the CDF curves of the attenuations, the best three have been shown in Table 7.5 (a) and their respective overall averages of R^2 were computed across all the locations to determine the most suitable. The

overall average R^2 values of the respective distribution fits, shows that the two-term Sum of Sine (SOS) model has the highest mean R^2. At time percentage of 0.01 %, the two-term SOS model is considered as the best with very low relative errors of about 2.08 %, 2.20 %, 1.58 %, 1.32 %, 0.98 % and 0.75 % for Durban, Cape Town, Umtata, Bloemfontein, Johannesburg and Mafikeng respectively.

Therefore, the two-term SOS model is recommended for the distribution of the optical attenuation due to scintillation in South Africa and probably the surrounding islands with a simple general expression which is given by:

$$\alpha = \ a1 * \sin(b1 * p + c1) + a2 * \sin(b2 * p + c2), \tag{7.48}$$

where its distribution parameters as well as the error estimations are provided in Table 7.5 (b). Also, Table 7.5 (c) presents the attenuation values of each of these locations at various time percentages. The attenuation values at 0.01 % time exceedance window presented in the table can be found to be similar to those given above which are obtained from Figure 7.16.

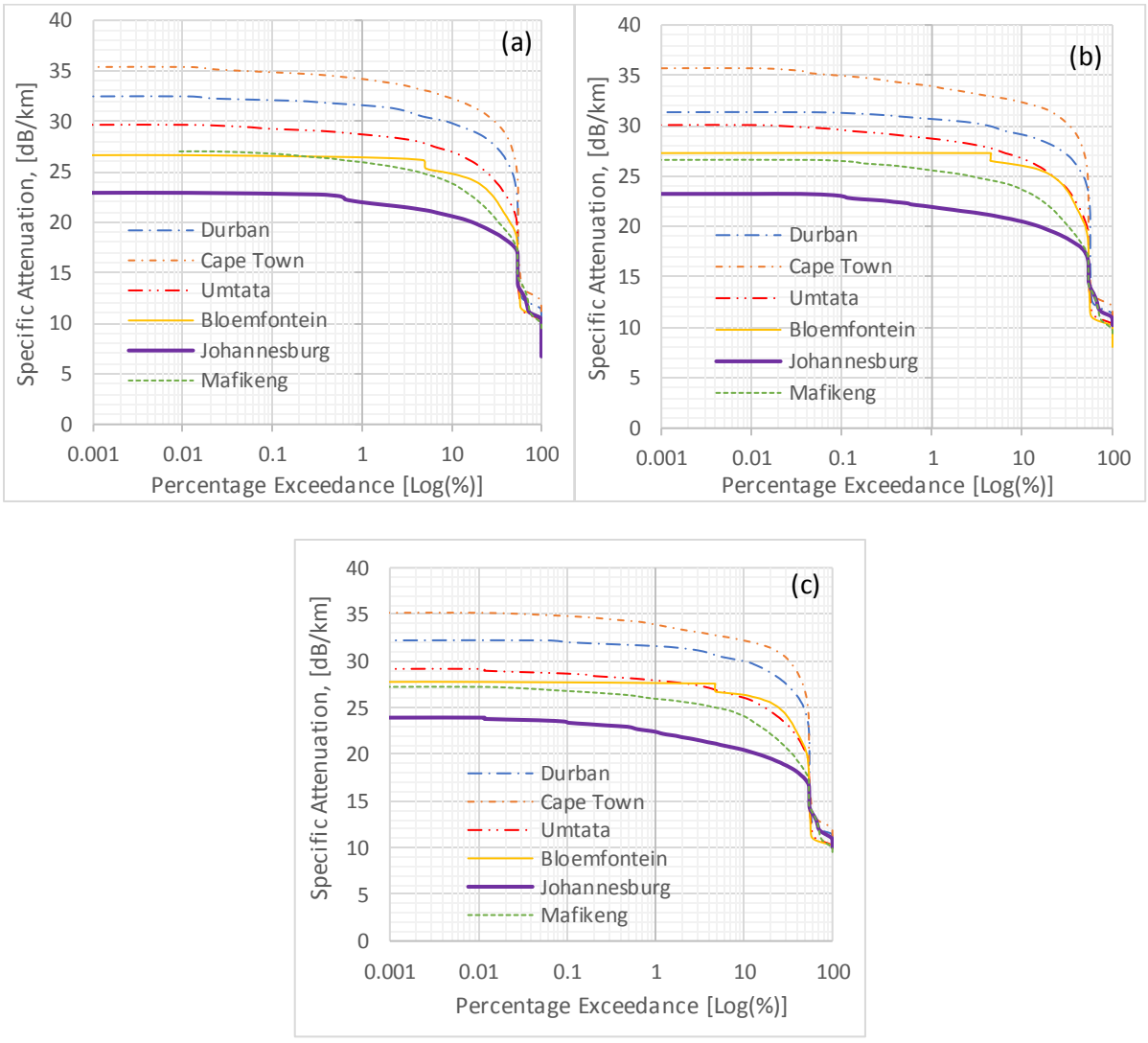

Figure 7.16: Cumulative distribution of optical attenuation due to scintillation for South Africa for (a) 2013; (b) 2014 and (c) 2015.

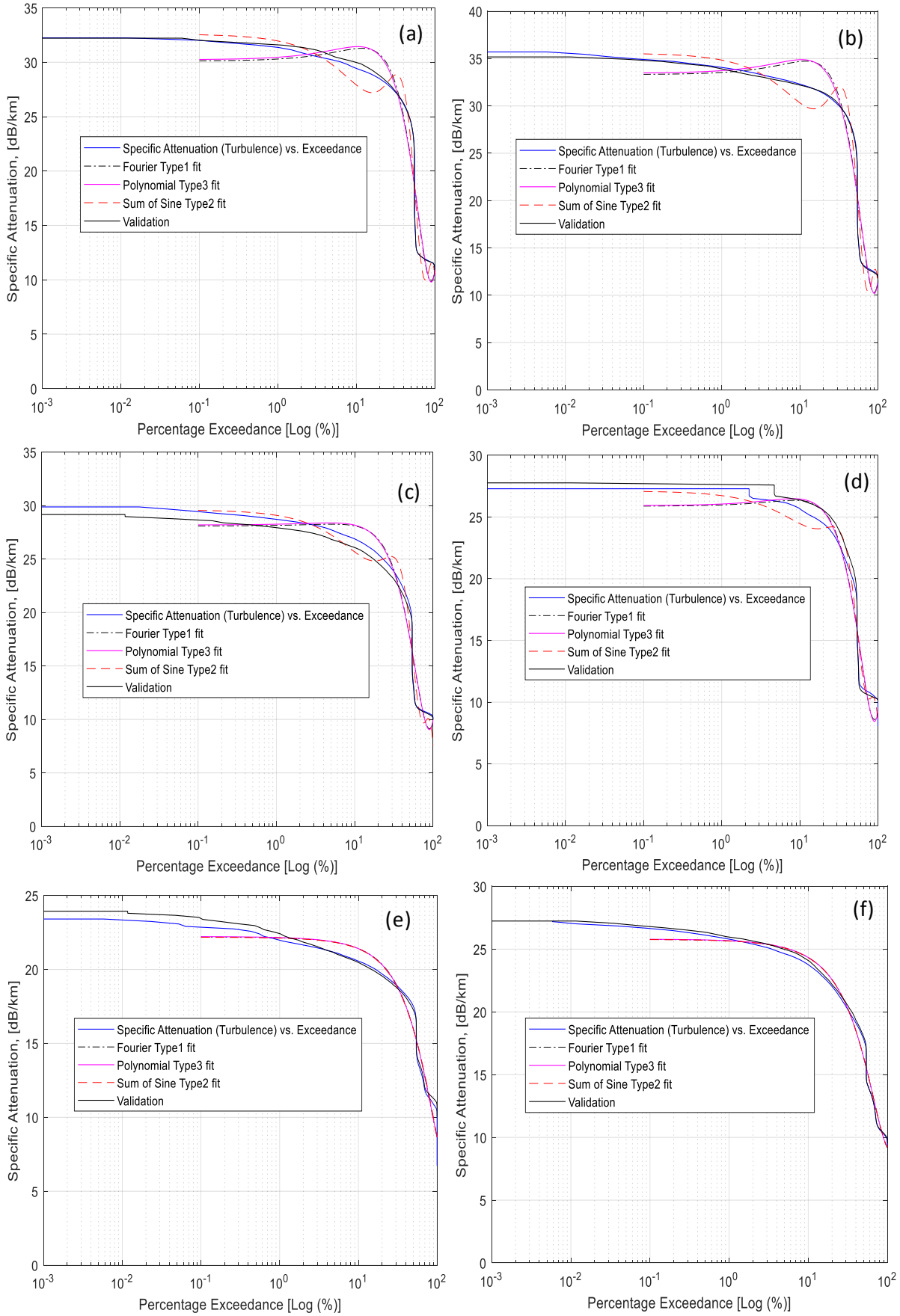

Figure 7.17: Performance evaluation and model validation for various distribution models of optical attenuation due to atmospheric turbulence for (a) Durban; (b) Cape Town; (c) Umtata; (d) Bloemfontein; (e) Johannesburg and (f) Mafikeng, over the entire period under study.

Table 7.5: (a) Comparison of coefficient of determination (R^2) obtained for the various models for different locations; (b) Distribution parameters and fit statistics for the Sum of Sine model of optical attenuation; (c) Percentage exceedance of optical attenuation modelled from Sum of Sine model for different locations.

(a)

Model	**Durban**	**Cape Town**	**Umtata**	**Bloemfontein**	**Johannesburg**	**Mafikeng**	**Mean R^2**
Fourier (1st Order)	0.8581	0.8651	0.9024	0.9363	0.9637	0.9806	0.9177
Polynomial (3rd Order)	0.8541	0.8605	0.9008	0.9343	0.9635	0.9808	0.9157
Sum of Sine (Two-terms)	0.9017	0.9136	0.9314	0.9488	0.9627	0.9806	0.9398

(b)

General Optical Attenuation Model (due to scintillation): Sum of Sine Type 2 (Sin2) $\alpha = a1 * \sin(b1 * p + c1) + a2 * \sin(b2 * p + c2)$ Coefficients (with 95% confidence bounds):						
Coefficients	Durban	Cape Town	Umtata	Bloemfontein	Johannesburg	Mafikeng
$a1$	492.70	416.60	861.80	969.20	44.570	39.750
$b1$	0.0005835	0.0007794	0.0003045	0.0002365	0.01637	0.001128
$c1$	3.0710	3.0490	3.1050	3.1120	0.8939	0.4320
$a2$	4.2030	5.0280	2.9280	2.4450	28.280	12.110
$b2$	0.1049	0.1056	0.1088	0.1044	0.0204	0.0208
$c2$	3.7450	3.7760	3.7190	4.0460	3.6020	2.2880
Goodness of fit:						
SSE	0.4101	0.4608	0.2362	0.1658	0.0917	0.0527
R^2	0.9017	0.9136	0.9314	0.9488	0.9627	0.9806
Adjusted R^2	0.8966	0.9091	0.9278	0.9461	0.9608	0.9796
RMSE	0.0208	0.0220	0.0158	0.0132	0.0098	0.0075
Goodness of Validation						
SSE	0.4259	0.4165	0.2163	0.2892	0.0975	0.0625
RMSE	0.0205	0.0202	0.0146	0.0168	0.0098	0.0079

(c)

General Optical Attenuation Model: Sum of Sine Type 2 (Sin2) $\alpha = a1 * \sin(b1 * p + c1) + a2 * \sin(b2 * p + c2)$						
Percentage Exceedance (p)	Durban α (dB/km)	Cape Town α (dB/km)	Umtata α (dB/km)	Bloemfontein α (dB/km)	Johannesburg α (dB/km)	Mafikeng α (dB/km)
75	9.7894	10.3747	9.9960	9.9327	12.1418	11.7798
50	22.1710	24.1410	19.1823	17.6061	15.9606	16.4128
10	27.6948	30.2927	25.9910	24.1130	21.3935	24.3362
1	31.7311	34.8053	29.4111	26.3789	22.1165	25.6428
0.1	32.3023	35.4640	29.8774	26.7165	22.1721	25.7570
0.01	32.3606	35.5314	29.9250	26.7512	22.1775	25.7683
0.001	32.3665	35.5382	29.9297	26.7547	22.1780	25.7694
0.0001	32.3671	35.5388	29.9302	26.7551	22.1781	25.7695

7.14 Summary

In summary, based on the above results and the hourly mean values of the predicted C_n^2 (obtained from various meteorological parameters), scintillation index and optical attenuations for the various cities using the MOST approach, US-ARL model and the Rytov approximation method, it is observed that:

i. The minimum and maximum values of the obtained C_n^2 for each location shows that the ATL in these areas (including coastal, near coastal and non-coastal) are within the strong turbulence regime, that is between $10^{-14}\, m^{-2/3}$ and $10^{-13}\, m^{-2/3}$. It can be observed from these results that the coastal and near-coastal areas of Durban, Cape Town and Umtata have higher average of the maximum C_n^2 values of about $3.37 \times 10^{-13}\, m^{-2/3}$, $4.11 \times 10^{-13}\, m^{-2/3}$ and $2.88 \times 10^{-13}\, m^{-2/3}$ respectively over the three years (2013-2015), while the non-coastal environs of Bloemfontein, Johannesburg and Mafikeng have relatively lesser values of $2.43 \times 10^{-13}\, m^{-2/3}$, $1.79 \times 10^{-13}\, m^{-2/3}$ and $2.40 \times 10^{-13}\, m^{-2/3}$ respectively.

ii. The SD results for the obtained C_n^2 show that the locations with the higher magnitudes of atmospheric turbulence have the higher deviations respectively, with the coastal areas showing that their atmospheres are the most unstable.

iii. In the day-time, the observed ATL in terms of C_n^2 as presented in Figure 7.8 showed that it is generally unstable with high magnitude of chaos noticed at frequent periods, which suggests that the turbulence around this time of the day is long-lived, while that of the night-time is short-lived, since it is generally stable with little chaos noticed at sporadic periods.

iv. The coastal and near-coastal areas experienced higher magnitudes of C_n^2 and atmospheric attenuation, as well as variability than the non-coastal areas as indicated by the plot of the mean and standard deviations, indicating that more attention is needed in those regions.

v. The results also show that the summer and autumn seasons have higher ATL, where January, February and December have the highest mean C_n^2 across all the locations under study, while the ATL of the winter and spring seasons have lower magnitudes.

vi. In conclusion, based on the estimated attenuations due to scintillation, it was observed that the months of January, February and December have on the average the highest peaks across all the locations, with other surrounding months (such as March, April and May) also showing considerable attenuations. In general, from these results the summer and autumn months have the highest effects of atmospheric attenuation, whereby this is lower in winter and spring months.

vii. In addition, an attenuation model was developed in terms of the percentage exceedance using the ccdf approach. Therefore, the two-term SOS model was recommended for the distribution of the optical attenuation due to scintillation in South Africa.

CHAPTER EIGHT

Conclusion and Recommendations for Future Work

8.1 Introduction

A detailed investigation of atmospheric impairments (such as scattering and scintillations) over a FSO communication link using climatic data for South Africa has been presented in this work, based on the analysis of various meteorological variable measurements on terrestrial path over various locations within South Africa for a period of three successive years (January 2011 to December 2013 for scattering analysis and January 2013 to December 2015 for scintillation analysis). The atmospheric scattering and scintillations were quantified by the atmospheric transmittance, fog and haze attenuations, refractive index structure parameter, scintillation intensity, Rytov variance (log-amplitude variance), and so on.

Due to the usual severe earth's surface layer or tropospheric propagation conditions which exist in many locations around the world, leading to constraints on the terrestrial (FSO) transmission systems operating in the visible or near infra-red bands, accurate propagation predictions are very essential. Under-prediction and over-prediction of an optical propagation effect may result into a FSO communication system that is undependable and costly over-design of the system respectively. However, due to the occurrences of fog, haze, dust, rain, snow, clouds, and the irregular fluctuations in the temperature and pressure resulting to variations in the refractive index of air within the surface layer, severe propagation effects may occasionally occur in each of those conditions, as a result of scattering and scintillation. In spite of all the aforementioned benefits of the FSO communication system in this dissertation, the limitations and impairments imposed by its atmospheric channel such as fog, haze, snow, rain, mist, cloud and scintillation decrease the FSO system performance and link availability, and this results into a particular need for accurate optical propagation predictions. Therefore, this research work has addressed the complications of this technology by achieving the characterization and modelling of the atmospheric attenuations of this FSO channel (due to both scattering and turbulence), which is the main aim of this research work. This analysis will enhance the robustness and global acceptability of the optical link when it is deployed to areas of severe weather conditions.

8.2 Conclusion

Based on the results obtained in chapters four, five, six and seven, the following conclusions have been drawn:

8.2.1 Chapter 4 - Estimation of Fog and Cloud Attenuations from Visibility Range Characterization for FSO Link Design Using Climatic Data for South Africa.

In this Chapter, an evaluation of the various fog attenuation models used to estimate the atmospheric optical attenuation due to scattering were applied, over the visibility range characterization for South

Africa. This characterization ranging from $V = 0\ km$ to $V = 100\ km$, is based on the International Visibility Code (IVC). However, the visibility range characterization used in this work (as shown in Table 3.3) is a slight modification to the usual IVC. Therefore, this study proposes this new visibility range characterization which covers the whole visibility spectrum and presented each atmospheric condition in form of class codes (i.e., Class-0 to Class-8) and sub-class codes (or groups) (i.e., Low, Middle and High visibility class ranges).

The obtained atmospheric transmittance pattern and magnitudes revealed that in general, the daily mean atmospheric transmittance is observed to have more lower values mostly in the maritime and near-maritime environments (such as Durban, Cape Town and Umtata) including Johannesburg than in the non-coastal environments, and this results into high atmospheric attenuation of light wave. The low transmittance values, high instabilities and the over-saturation in the atmospheres of the maritime locations suggests that if optical signals are transmitted through this type of atmosphere, then more photons of the optical signal will be highly scattered due to the atmospheric conditions in these locations.

A comparison of the estimated daily specific optical attenuation at different optical wavelengths obtained using different fog attenuation models were presented. In general, based on the daily mean specific attenuation values and visibility values, the maritime locations (especially Cape Town and Durban) show characteristics of an atmosphere with higher risk to transmission of optical signal than the non-coastal environs during the period under study. Umtata, Bloemfontein and Johannesburg showed considerable qualities of an atmosphere that can cause from high to moderately high risk to FSO. Whereas, the lowest risk to FSO transmission system within the entire period was observed in Mafikeng.

The influence of the worst-case conditions in terms of the predicted specific attenuations over the FSO link design for South Africa, showed how much effects should be expected on a regular basis and the extent at which the optical signals can be attenuated within each of the locations considered. This study can enable an adequate mitigation technique to be chosen for each location based on their environmental factors and optical attenuation trend. The results showed that (within the entire period of study) the maximum expected specific attenuation can reach as high as 169.81 dB/km (corresponding to 0.1 km visibility) on several occasions in the coastal and near-coastal areas. Whereas, for the non-coastal regions, their maximum expected specific attenuation within a day are quite lower than that of the coastal areas, except for Bloemfontein in the year 2011 which had few days with 169.81 dB/km. However, it was observed that the maximum expected specific attenuation for Mafikeng (which is around 35 dB/km) was far lower than that of the other cities.

The estimated received optical power and the SNR both showed similar observations to the inferences from the expected specific attenuations. The comparison between the received optical power and the

selected receiver sensitivity, and that between the SNR and selected receiver sensitivity both showed that there are several events or data points where there might be link failure or total outage. This is because those situations had received optical power below the receiver sensitivity of -38 dBm and SNR above the equivalent receiver sensitivity of 10.5 dBm.

Lastly in this Chapter, the FSO system performance analyses were performed under various atmospheric conditions within South Africa, and this showed that the atmospheres over each of the cities will cause considerable risk to FSO. From the performance analysis, it is obvious that a better optical link device with better specifications (such as the transmitter power, operating wavelength, antenna diameter and so on) than what is presented in Table 3.2 is required in each of these cities, unless a proper mitigating technique is employed. The BER performance analysis and attenuation mitigation were achieved for the FSO system for each of the locations and presented in Chapter 4. The mitigation techniques such as spatial diversity (4 × 4 MIMO) and modulation schemes (BPSK and L-PPM) were applied to reduce the level of optical attenuation on the FSO link. Therefore, with the applied mitigating techniques in this research work, there were outstanding improvements that were achieved on the FSO system.

8.2.2 Chapter 5 - Visibility Range Distribution and Optical Attenuation Modeling for Terrestrial Optical Link Design for South Africa.

In this Chapter, the visibility range distribution modelling and the optical attenuation modelling due to atmospheric scattering for various atmospheric conditions were achieved. The similarity observed in the shapes of the frequency curves, suggests that one type or family of probability distribution function will be suitable to characterize or describe the distribution of the visibility range of all the cities considered in this study, but with different distribution parameters due to the variation in their peaks.

Based on the monthly and seasonal dependence of visibility and optical attenuation due to scattering for South Africa which showed that in general, the maritime environments have lower mean visibility values and higher mean specific attenuation values than the continental environments, except for the case of Johannesburg which may be as a result of its unique topology or climatic conditions. In general, the seasonal mean analysis showed that the mean visibility range and mean attenuation values obtained in the winter season from June to August (especially June/July) were consistently far lower and higher respectively than the mean values observed in the other seasons (most especially the summer season of December to February), across the three successive years investigated in this study. Similarly, the standard deviation of the optical attenuations follows the same trend with that of the mean. Also, based on the diurnal mean and median pattems, visibility is noticed to be lowest at night-time (in particular during 12:00 am and 3:00 am), and it is highest during the day-time hours (especially during 12:00 pm and 3:00 pm) for all the locations. Whereas, the opposite is the case for the diurnal pattern of the mean and median specific attenuation.

A proposed general PDF model for the Visibility Range Distribution (VRD) using climatic data for South Africa was discussed, and comparison of the proposed model with several other distribution models were presented. The estimates of each location-based model were combined to produce the proposed general model. This model consists of regional-based parameters so as to characterize the visibility range distribution for the specific location. The resulting probability distribution of the collected visibility range is fitted with different distribution fits such as Generalized Pareto, Dagum (4P), Dagum (3P), Johnson SB, Generalized Extreme Value, Generalized Gamma (4P), Kumaraswamy, and so on. The performances of these fits were optimized using the MLE approach and the results showed great improvement. Therefore, the Generalized Pareto distribution model performed relative better than its counterparts, and should be adopted for South Africa and possibly its surrounding islands and countries.

Finally in this chapter, the visibility based optical attenuation modeling under various atmospheric conditions over a terrestrial FSO link for South Africa was proposed. This general model was developed for the cumulative distribution of optical attenuation due to atmospheric scattering for South Africa. Several models including first-order exponential, second-order exponential, two-parameter Gaussian, first-order and second-order power fits were compared with the CDF curves. The accuracy of the developed exponential type-2 model for representing the optical attenuations of FSO links within these locations is shown by the percentage exceedance allowance. However, comparing the attenuation results obtained for the exceedance of 0.01 % window from the CDF curves and that estimated by the exponential type-2 model, it can be noticed that there a few underestimations and overestimations, but the general performance yields a very suitable report of the developed model accuracy.

8.2.3 Chapter 6 - Time Series Prediction and Modeling of Visibility with Artificial Neural Network Technique using Meteorological Data for South Africa

The purpose of this Chapter was to model the characteristics of the time series of visibility values with Artificial Neural Network (ANN) technique using meteorological data for South Africa. The set of meteorological variables expended in this work are atmospheric temperature, pressure, relative humidity and wind speed. From the results presented in Chapter six, the RMSE values were observed to be lower and R^2 values were observed to be higher for the input cases with combination of all atmospheric parameters, when compared to the other input cases for all the locations presented.

After the proposed neural networks have undergone training, validation and testing procedures, then the calculated visibility results showed a maximum reliability of about 82.01 %, 84.76 %, 82.78 %, 80.88 %, 82.54 % and 81.14 %, achieved when all of the meteorological data were considered for Durban, Cape Town, Umtata, Bloemfontein, Johannesburg and Mafikeng respectively. According to these results, the neural network with input data X_i and output data V attained satisfactory reliability results by going through the network evaluation. Therefore, these reliability results prove that the

developed ANN model has the ability to learn, and the evaluation results are satisfactory, which will provide useful information to those who engage in visibility profiling and forecasting such as the FSO personnel for planning and designing an optical link with very low attenuation risk and the civilian or military personnel for the planning of flight activities. Also, this serves as an effective and robust tool or model, which enables these officials to develop and maintain a strategic plan for the future years, with quite reliable and significant predictions on the sole basis of historical data of average reliability of about 83 % for all the stations considered. In summary, this analysis has shown that the complete weather condition of a particular place in terms of the atmospheric temperature, pressure, relative humidity and wind speed are a determining factor of the possible atmospheric optical attenuation on the FSO link within that location. The result has shown that there is a direct relationship between all these atmospheric variables and the optical attenuations (based on visibility) obtained during the propagation of optical beam within the free space. Therefore, the conditions of these variables at every point in time determines the behaviour of the optical link.

8.2.4 Chapter 7 - Characterization and Modeling of Atmospheric Turbulence Level based on C_n^2 and Scintillation Index Using Climatic Data for South Africa.

The purpose of this chapter is to characterize and model the atmospheric turbulence over a FSO link based on C_n^2 and scintillation index using climatic data for South Africa. The motivation for this Chapter was as a result of the fact that there has been very limited research works that considers the estimation of C_n^2 using climatic data and then finding its equivalent atmospheric optical attenuation due to scintillation. The surface layer model developed by the US Army Research Laboratory used in this work to compute C_n^2 directly makes use of the Monin-Obhukov Similarity Theory (MOST). The US-ARL model is ideally suited for this work, because it does not only use the height and wind speed in the estimation of the C_n^2 parameter unlike most other models, but it also uses most meteorological variables of interest (such as temperature, pressure, humidity and wind speed as well as water vapour) across two different altitudes (reference and antenna heights).

In general, the estimated results of C_n^2 for all the considered locations showed that the thermodynamic behavior of the turbulent eddies in the atmosphere and the ATL are generally unstable during the day, while it is generally stable during the night. The level of atmospheric stability and the trend observed during the day showed that there is significant amount of turbulence within the atmosphere at long moments which shows that the perturbation is long-lived around this time of the day, while it is generally stable at night with little chaos noticed at sporadic periods, which suggests that the turbulence around this time of the day is short-termed.

Several statistical analyses (such as frequency series profiling, monthly mean and standard deviation) were carried out over the estimated C_n^2, and the following were observed:

- The results showed similar trends across all the years and all the locations, with a general rise in ATL (in terms of the mean C_n^2 and optical attenuation) around the end and beginning of each year, spanning through the whole of the summer season and across the autumn season. Whereas there was a general drop in ATL around the middle part of the year, spanning across the whole of the winter season and through the spring season.
- The results show that the highest modal C_n^2 occurred in Cape Town for both day and night times, followed by Durban, which are both coastal areas. This suggests that the coastal areas often exhibit high ATL. For the inlands such as Bloemfontein, Johannesburg and Mafikeng, the level of atmospheric turbulence given by the modal C_n^2 is relatively lower than that of the coastal areas.
- These results show that the summer and autumn seasons have higher ATL, where January, February and December have the highest mean C_n^2 values across all the locations under study. Also, the comparison of the monthly averages revealed that more atmospheric turbulence was observed in each month in the coastal and near-coastal areas than in the non-coastal areas.
- The higher magnitudes and variabilities of both C_n^2 and optical attenuation experienced in the coastal and near-coastal areas, can also be due to the fact that these areas are on a much lower lowland than the inland areas (as indicated in Table 3.1). This agrees with several theories which suggests that there exists high turbulence at heights close to the ground level.

The study proposes a model for the cumulative distribution of the optical attenuation based on scintillation for South Africa. Several models including one-term Fourier, third-order polynomial and two-term Sum of Sine fits were compared with the measured CDF curves. Therefore, based on the error estimates computed, the two-term Sum of Sine distribution model performed relative better than its counterparts, and should be adopted for South Africa and possibly its surrounding islands and countries.

8.3 Recommendations for Future Work

8.3.1 Measurement Campaign

According to the analyses and observations in this work, the need for a proper estimation of the effects of visibility range and microphysics of fog and haze requires equipment that is capable of detecting or measuring both spatial and real-time events at optimum resolutions, as well as to measure very low visibility range values (i.e., less than 100 m). The investigations done in this dissertation has been limited to archived data and hourly visibility data that does not include the dense fog range (i.e., $0 < V < 0.1\ km$), because of unavailability of real-time data, and costly purchase and installation of highly sensitive and wider range visibilimeter device.

It is known that the measurement of atmospheric turbulence is quite difficult and cumbersome, and as a result it is not readily available. Also, the most common and easiest approach of calculating the C_n^2 is

by using only the altitude and wind speed (especially by HV and HAP models). However, they are still not considered as accurate for surface layer turbulence estimations. Therefore, the need for proper spatial and real-time measurements of the atmospheric turbulence strength in terms of refractive index structure parameter is very essential, to perfectly predict a more accurate scintillation distribution, and this will serve as a validation model for the estimated C_n^2 obtained in this work using atmospheric parameters.

8.3.2 Modeling and Simulation

In order to improve the work done on the modelling of the visibility and optical attenuation due to both scattering and turbulence, there is need to further widen the study in this area by examining the possibility of modelling the visibility and optical attenuation using different estimator approaches such as the Kernel Density Estimator (KDE) and Method of Moments (MOM). Also, further improvements can be done on the visibility range characterization and modelling by using different types of atmospheric conditions (like fog, haze and clear air types) as well as visibility classes as proposed in Table 3.3. This implies that, the variability characteristics of the visibility range distribution can be evaluated using various atmospheric classifications of fog, haze and clear air such as the atmospheric conditions described by each visibility class (i.e., from Class-0 to Class-8).

The variability characteristics of time series prediction of visibility range which was achieved in this work by the ANN method using various meteorological variables (such as temperature, relative humidity, wind speed and pressure) can also be evaluated and enhanced by the inclusion of other atmospheric components such as the solar radiation related components (for instance, direct and indirect solar irradiance) and gas related atmospheric components.

8.3.3 Applications

According to the overall results obtained in this research work due to the effects of atmospheric scattering and scintillation, the results can be extended to cover various research topics such as the ones mentioned as follows:

- Effects of microphysical characteristics of fog in terrestrial optical links.
- Evaluation of fog particle drop size distribution using statistical distribution and estimator methods for Southern Africa.
- Development of different models or techniques to mitigate against optical signal loss as a result of fog and scintillation at frequencies above 193 THz.
- Modeling and parameterization of turbulence power distribution using different turbulent characteristic scales.
- Parameterization of fog particle drop size distribution using different drop-size characterizations.

References

[1] Andrews L., (2005), "Free-space laser propagation: atmospheric effects," in *2005 Digest of the LEOS Summer Topical Meetings, Newport Beach, California, USA*, pp. 3–4.

[2] Henniger H. and Wilfert O., (2010), "An introduction to free-space optical communications," *Journal of Radio Engineering*, Vol. 19, No. 2, pp. 203-212.

[3] Layioye O. A., Afullo T. J. O. and Owolawi P. A., (2017), "Performance analysis of FSO communication systems with higher-order spatial diversity schemes using BPSK-SIM over log-normal atmospheric channels," *Journal of Communications*, Vol. 12, No. 6, pp. 312-327, doi: https://doi.org/10.12720/jcm.12.6.312-327.

[4] Gagliardi R. and Karp S., (1995), "Optical Communications", *2nd ed. New York, NY: Wiley*.

[5] Bloom S., Korevaar E., Schuster J. and Willebrand H., (2003), "Understanding the performance of free-space optics," *Journal of Optical Networking*, Vol. 2, No. 6, pp. 178-200.

[6] Majumdar A. K., (2015), "Advanced Free Space optics (FSO): A Systems Approach," *Springer, New York*.

[7] Heatley D., Wisely D., Neild I., and Cochrane P., (1998), "Optical wireless: The story so far," *IEEE Communications Magazine,/Comm. Mag.*, Vol. 36, No. 12, pp. 72–74, 79-82.

[8] Goodwin F. E., (1970), "A review of operational laser communication systems," *Proceedings of IEEE*, Vol. 58, pp.1746-1752.

[9] Juarez J., Dwivedi A., Mammons A., Jones S., Weerackody V., and Nichols R., (2006), "Free-space optical communications for next-generation military networks," *IEEE Communications Magazine*, Vol. 44, No. 11, pp. 46–51.

[10] Hochfelder D., (2015), "Alexander graham bell," *Encyclopaedia Britannica*, 17th Jan. 2019, [Online], Retrieved from: https://www.britannica.com/biography/Alexander-Graham-Bell, Accessed on: 15th Jun. 2019.

[11] Hutt D. L., Snell k. J. and Belanger P. A., (1993), "Alexander graham bell's photophone," *Tech Report: Optics & Photonics News*.

[12] Kaushal H. and Kaddoum G., (2015), "Free space optical communication: challenges and mitigation techniques," *Wireless Information Networks and Systems (WINSYS), Proceedings of the 2010 International Conference on*, pp. 1-6.

[13] Hecht J., (2005), "Beam: the race to make the laser," *Tech Report: Optics & Photonics News*.

[14] Treacy E. A., (2020), "NEC corporation", *Encyclopedia Britannica*, 25th Apr. 2020, [Online], Retrieved from: https://www.britannica.com/topic/NEC-Corporation, Accessed on: 30th Sept. 2020.

[15] Chan V. W. S., (2006), "Free-space optical communications," *J. Lightwave Tech.*, Vol. 24, No. 12, pp. 4750-4762.

[16] Majumdar A. K. and Ricklin J. C., (2008), "Free-Space Laser Communications: Principles and Advances", *Springer, New York*.

[17] Bloom S. and Hartley W., (2002), "The last-mile solution: hybrid FSO radio," in *Whitepaper, AirFiber Inc*.

[18] Acampora A., (2002), "Last mile by laser," *Scientific American*, vol. 287, no. 1, pp. 32–37.

[19] Khan M. S., Muhammad S. S., Awan M. S., Leitgeb E., Grabner M. and Kvicera V., (2011), "Validating relationship between aerosol's liquid water content and optical attenuation for terrestrial FSO links," *11th International Conference on Telecommunications – ConTel 2011, Graz, Austria*, ISBN: 978-953-184-152-8, pp. 195-198.

[20] Gebhart M., Leitgeb E., Muhammad S. S. et al., (2005), "Measurement of light attenuation in dense fog conditions for optical wireless links," *In SPIE Proceedings, Optics and Photonics Symposium, San Diego (USA)*, Vol. 5891/589, pp. 58910K1-12.

[21] Muhammad S. S., Flecker B., Leitgeb E. and Gebhart M., (2007), "Characterization of fog attenuation for terrestrial FSO links," *Optical Engineering*, Vol. 46, No. 6, p. 066001.

[22] Awan M. S., Csugai-Horvath L., Muhammad S. S., Leitgeb E., Nadeem F. and Khan M. S., (2009), "Characterization of fog and snow attenuations for free-space optical propagation," *Journal of Communications*, Vol. 4, No. 8, pp. 533-545.

[23] Andrews L., Phillips R., and Hopen C., (2001), "Laser Beam Scintillation with Applications", *Bellingham, WA: SPIE Press*.

[24] Andrews L. and Phillips R., (2005), "Laser Beam Propagation through Random Media", *Bellingham, WA: SPIE Press*.

[25] Layioye O. A., Afullo T. J. O. and Owolawi P. A., (2017): Visibility Range Distribution Modeling for FSO link design in South Africa: Durban as case Study. *2017 Progress in Electromagnetics Research Symposium – Fall, (PIERS- FALL), Singapore*, pp. 2732-2741. doi: 10.1109/piers-fall.2017.8293601.

[26] Zhu X. and Kahn J., (2002), "Free-space optical communication through atmospheric turbulence channels," *IEEE Transactions on Communications*, vol. 50, no. 8, pp. 1293–1300.

[27] Kiasaleh K., (2002), "Performance analysis of free-space on-off-keying optical communication systems impaired by turbulence," in *Proceedings of SPIE 4635, SPIE Free-Space Laser Communication Technologies XIV*, G. S. Mecherle, Ed., vol. 4635, no. 1. San Jose, CA, USA: SPIE, pp. 150–161. [Online]. Available: http://www.link.aip.org/link/?PSI/4635/150/1.

[28] Li J. and Uysal M., (2003), "Optical wireless communications: system model, capacity and coding," in *2003 IEEE 58th Vehicular Technology Conference, 2003. VTC 2003-Fall*, Vol. 1, Orlando, Florida, USA, pp. 168–172.

[29] Layioye O. A., Afullo T. J. O. and Owolawi P. A., (2016), "Calculations of the influence of diverse atmospheric turbulence conditions on Free Space Optical Communication system using BPSK-SIM over the Gamma-Gamma Model," *In the Proceedings of Southern Africa Telecommunication Networks and Applications Conference, SATNAC 2016, Cape Town, South Africa*. pp. 362-367.

[30] Nebuloni R. and Capsoni C., (2008), "Laser attenuation by falling snow," *In Proceedings of IEEE CSNDSP, Graz (Austria)*, pp. 265-269.

[31] Popoola W. O., Ghassemlooy Z., Allen J. I. H., Leitgeb E., and Gao S., (2008), "Free-space optical communication employing subcarrier modulation and spatial diversity in atmospheric turbulence channel," *Journal of Optoelectronics, IET,* vol. 2, pp. 16-23.

[32] Alkholidi A. and Altowij K., (2012), "Effect of Clear Atmospheric Turbulence on Quality of Free Space Optical Communications in Western Asia," *Optical Communications Systems, Dr. Narottam Das (Ed.)*, ISBN: 978-953-51-0170-3, *InTech*, [Online]. Available at: http://www.intechopen.com/books/optical-communicationssystems/effect-of-clear-atmospheric-turbulence-on-quality-of-free-space-optical-communications-in-yemen.

[33] Achour M., (2002), "Simulating Atmospheric Free-Space Optical Propagation part I, Haze, Fog and Low Clouds, Rainfall Attenuation", *Optical Wireless Communications*, Proceedings of SPIE.

[34] Jassim M. and Kodeary A. K., (2013), "Experimental Study of the influence of aerosol particles on link range of Free Space Laser communication system in Iraq, *Journal of Applied Electromagnetism*, Vol. 15, No. 2, pp. 28-33.

[35] Layioye O. A., Afullo T. J. O. and Owolawi P. A., (2016b): Variation of Altitude on the Variance of Angle of Arrival Fluctuations for Beam Propagation in Free Space Optical Communications. *In Proceedings of International Conference on Advances in Computing and Communication Engineering (ICACCE – IEEE 2016), Durban, South Africa*. Pp. 117-122. doi: 10.1109/icacce.2016.8073734.

[36] Rouissat M., Borsali, M. and Chikh-Bled E., (2012), "Free Space Optical Channel Characterization and Modeling with Focus on Algeria Weather Conditions," *I. J. Computer Network and Information Security*, Vol. 4, No. 3, pp. 17-23.

[37] Naimullah B., Hitam S., Shah N., Othman M. and Anas S., (2007), "Analysis of the Effect of Haze on Free Space Optical Communication in the Malaysian Environment", *IEEE*.

[38] Lee I. E., Ghassemlooy Z., Ng W. P. and Rajbhandari S., (2011), "Fundamental Analysis of Hybrid Free Space Optical and Radio Frequency Communication Systems", ISBN:978-1-902560-25, PGNet.

[39] Stotts, L., Foshee, J., Stadler, B., Young, D., Cherry, P., McIntire, W., Northcott, M., Kolodzy, P., Andrews, L., Phillips, R. and Pike, A., (2009), "Hybrid Optical RF Communications," *Proceedings of the IEEE*, Vol. 97, No. 6, pp.1109-1127.

[40] Kim I. I. and Korevaar E., (2001), "Availability of free space optics (FSO) and hybrid FSO/RF systems", in *Proc. SPIE, Optical Wireless Communications IV*, Vol. 4530, Denver, CO, USA, pp. 84-95.

[41] Derenick J., Thorne C. and Spletzer J., (2005), "On the development of a hybrid free-space optic/radio frequency (FSO/RF) mobile ad-hoc network," *In 2005 IEEE/RSJ International Conference on Intelligent Robots and Systems, (IROS 2005)*, pp. 3990-3996.

[42] Tapse H. and Borah D. K., (2009), "Hybrid optical/RF channels: characterization and performance study using low density parity check codes", *IEEE Trans. Commun.*, Vol. 57, No. 11, pp. 3288-3297.

[43] He B. and Schober R., (2009), "Bit-interleaved coded modulation for hybrid RF/FSO systems", *IEEE Trans. Commun.*, Vol. 57, No. 12, pp. 3753-3763.

[44] Navidpour S. M., Uysal M. and Kavehrad M., (2007), "BER Performance of Free-Space Optical Transmission with Spatial Diversity", *IEEE Transactions on Wireless Communications*, Vol. 6, No. 8, pp. 2813-2819.

[45] Nistazakis H., Tsiftsis T., and Tombras G., (2009), "Performance analysis of freespace optical communication systems over atmospheric turbulence channels," *Communications, IET*, vol. 3, pp. 1402-1409.

[46] Uysal M., Navidpour S. M. and Li J., (2004), "Error rate performance of coded freespace optical links over strong turbulence channels," *Communications Letters, IEEE*, vol. 8, pp. 635-637.

[47] Phillips R. L. and Andrews L. C., (1982), "Universal statistical model for irradiance fluctuations in a turbulent medium," *Journal of the Optical Society of America*, vol. 72, no. 7, pp. 864–870. [Online]. Available at: http://www.opticsinfobase.org/abstract.cfm?URI=josa-72-7-864.

[48] Xu G., Zhang X., Wei J. and Fu X., (2003), "Influence of atmospheric turbulence on FSO link performance," in *Proceedings of SPIE*, pp. 816-823.

[49] Hill R. J. and Frehlich R. G., (1997), "Probability distribution of irradiance for the onset of strong scintillation," *Journal of the Optical Society of America A*, vol. 14, no. 7, pp. 1530–1540. [Online]. Available at: http://josaa.osa.org/abstract.cfm?URI=josaa-14-7-1530.

[50] Al-Habash M. A., Andrews L. C. and Phillips R. L., (2001), "Mathematical model for the irradiance probability density function of a laser beam propagating through turbulent media," *Optical Engineering*, vol. 40, no. 8, pp. 1554–1562. [Online]. Available at: http://link.aip.org/link/?JOE/40/1554/1.

[51] Chen C., Yang H., Fan J., Feng X., Han C. and Ding Y., (2009), "Model for Outage Probability of Free-space Optical Links with Spatial Diversity through Atmospheric Turbulence", *Second International Conference on Information and Computing Science*, pp. 209-211.

[52] Letzepis N., Guillen A. and Fabregas I., (2009), "Outage Probability of the Gaussian MIMO Free-Space Optical Channel with PPM", *IEEE Transactions on Communications*, Vol. 57, No. 12, pp. 3682-3690.

[53] Yuksel H., Milner S. and Davis C., (2005), "Aperture averaging for optimizing receiver design and system performance on free-space optical communication links," *Journal of Optical Networking*, vol. 4, pp. 462-475.

[54] Xu F., Khalighi A., Causse P. and Bourennane S., (2009), "Channel coding and time-diversity for optical wireless links", *Optics Express*, Vol. 17, No. 2, pp. 872-887.

[55] Wang Z. X., Zhong W. D., Fu S. N. and Lin C., (2009), "Performance comparison of different modulation formats over free-space optical (FSO) turbulence links with space diversity reception technique", *IEEE Photonics Journal*, Vol. 1, No. 6, pp. 277-285.

[56] Nadeem F., Flecker B., Leitgeb E., Khan M., Awan M. and Javornik T., (2008), "Comparing the fog effects on hybrid network using optical wireless and GHz links," in *Communication Systems, Networks and Digital Signal Processing, 2008. CNSDSP 2008. 6th International Symposium on*, pp. 278-282.

[57] Kvicera V., Grabner M., and Fiser O., (2008), "Visibility and attenuation due to hydrometeors at 850 nm measured on an 850 m path," in *Communication Systems, Networks and Digital Signal Processing, CNSDSP, 6th International Symposium on*, 2008, pp. 270-272.

[58] Zhao Z. and Liao R., (2010), "Effects of beam wander on free-space optical communications through turbulent atmosphere," in *Proceedings of SPIE 7685-19, SPIE Defense, Security, and Sensing*, L. M. W. Thomas and E. J. Spillar, Eds., Vol. 7685, No. 1. Orlando, Florida, USA: SPIE, Apr. 5-9, 2010. Available at: http://www.link.aip.org/link/?PSI/7685/76850K/1.

[59] Chen C.-C., Ansari H., and Lesh J. R., (1993), "Precision beam pointing for laser communication system using a ccd-based tracker," in *Proceeding of SPIE 1949, SPIE Space Guidance, Control, and Tracking*, Vol. 1949, No. 1, pp. 15–24. Available at: http://www.link.aip.org/link/?PSI/1949/15/1.

[60] Dunphy J. R. and Kerr J. R., (1974), "Atmospheric beam-wander cancellation by a fast-tracking transmitter," *Journal of the Optical Society of America*, Vol. 64, No. 7, pp. 1015–1016. Available at: http://www.opticsinfobase.org/abstract.cfm?URI=josa-64-7-1015.

[61] Hansel G. and Kube E., (2003), "Simulation in the Design Process of Free Space Optical Transmission Systems", Proc. 6th Workshop, *Optics in Computing Technology*, Paderborn (Germany), pp. 45-53.

[62] Tsiftsis T. A., Sandalidis H. G., Karagiannidis G. K. and Uysal M., (2009), "Optical Wireless Links with Spatial Diversity over Strong Atmospheric Turbulence Channels", IEEE Transactions on wireless Communication, Vol. 8, No. 2, pp. 951-957.

[63] Popoola W. O., Ghassemlooy Z., Haasl H., Leitgeb E. and Ahmadi V., (2011), "Error performance of terrestrial free space optical links with subcarrier time diversity", *IET Communication*, Vol. 6, Issue-5 pp. 1-8.

[64] Khalighi M. A., Schwartz N., Aitamer N. and Bourennane S., (2009), "Fading Reduction by Aperture Averaging and Spatial Diversity in Optical Wireless Systems," *J. Opt. Commun. Netw.*, Vol. 1, No. 6, pp. 580-593.

[65] Barua B., (2011), "Comparison the Performance of Free-Space Optical Communication with OOK and BPSK Modulation under Atmospheric Turbulence", *International Journal of Engineering Science and Technology (IJEST)*, Vol. 3 No. 5, pp.4391-4399.

[66] Faridzadeh M., Gholami A., Ghassemlooy Z. and Rajbhandari S., (2011), "Hybrid PPMBPSK subcarrier intensity modulation for free space optical communications", *Proc. IEEE, 16th European Conf. on Netw. and Opt. Comm., (Newcastle-Upon-Tyne)*, pp. 36–39.

[67] Parry G. and Pusey P. N., (1979), "K distributions in atmospheric propagation of laser light," *Journal of the Optical Society of America*, vol. 69, no. 5, pp. 796–798. Available at: http://www.opticsinfobase.org/abstract.cfm?URI=josa-69-5-796.

[68] Bouchet O., Sizun H., Boisrobert C., Fornel F. D. and Favennec P., (2006), "Free-space optics, propagation and communication," 1st Ed., ed. *London, UK: Wiley, ISTE*.

[69] Killinger D., (2002), "Free space optics for laser communications through the air," *Optics and Photonics News*, Vol. 13, pp. 36 – 42.

[70] McKendry, I. G., (1994), "Synoptic circulation and summertime ground level ozone concentrations at Vancouver, British Columbia," *J. Appl. Meteor.*, Vol. 33, pp. 627–641.

[71] Moulin, C., and Coauthors, (1998), "Satellite climatology of African dust transport in the Mediterranean atmosphere," *J. Geophys. Res.*, Vol. 103, No. 13, pp. 137–144.

[72] Shwarzhoff, P. J., and Reid, P. D., (2000) "Classification of meteorological patterns associated with the ozone categories in Kelowna, British Columbia," *J. Appl. Meteor.*, Vol. 39, pp. 384–398.

[73] Yarnal, B., Comrie, A., Frakes, B. and Brown, D. P., (2001), "Developments and prospects in synoptic climatology," *Int. J. Climatol.*, Vol. 21, pp. 1923–1950.

[74] Lee D. O., (1990), "The influence of wind direction, circulation type and air pollution emissions on summer visibility trends in southern England," *Atmos. Environ.*, Vol. 24A, pp. 195–201.

[75] Kulmala, M., and Coauthors, (2000), "Characterization of atmospheric trace gas and aerosol concentrations at forest sites in southern and northern Finland using back trajectories," *Monogr. Boreal Environ. Res.*, Vol. 5, pp. 315–336.

[76] Sloane, C. S., (1982), "Visibility trends—I. Methods of analysis," *Atmos. Environ.*, Vol. 16, pp. 41–51.

[77] Szymber, R. J., and Sellers, W. D., (1985), "Atmospheric turbidity at Tucson, Arizona, 1956–1983: Variations and their causes," *J. Climate Appl. Meteor.*, Vol. 24, pp. 725–734.

[78] Vinzani, P. G., and Lamb, P. J., (1985), "Temporal and spatial visibility variations in the Illinois vicinity during 1949–1980," *J. Climate Appl. Meteor.*, Vol. 24, pp. 435–451.

[79] Tombach I., (2000), Welcome to a Special Issue from the Specialty Conference on Visual Air Quality, Aerosols, and Global Radiation Balance, *Journal of the Air & Waste Management Association*, Vol. 50, Issue-5, pp. 647-907, Published online: 27th December 2011, doi: 10.1080/10473289.2000.10464112.

[80] Horvath, H., (1981), "Atmospheric visibility," *Atmos. Environ.*, Vol. 15, pp. 1785–1796.

[81] Vislocky, R. L. and Fritsch, J. M., (1997), "An automated, observations-based system for shortterm prediction of ceiling and visibility," *Wea. Forecasting*. Vol. 12, No. 1, pp. 31–43.

[82] Scherrer, S. C., & Appenzeller, C. (2014). Fog and low stratus over the Swiss Plateau - a climatological study. *International Journal of Climatology*, *34*(3), 678–686.

[83] Giulianelli, L., Gilardoni, S., Tarozzi, L., Rinaldi, M., Decesari, S., Carbone, C., … Fuzzi, S. (2014). Fog occurrence and chemical composition in the Po valley over the last twenty years. *Atmospheric Environment*, *98*, 394–401.

[84] Glickman, T. S., & Zenk, W. (2000). Glossary of meteorology.

[85] Hautière, N., Tarel, J.-P., Lavenant, J., & Aubert, D. (2006). Automatic fog detection and estimation of visibility distance through use of an onboard camera. *Machine Vision and Applications*, *17*(1), 8–20. https://doi.org/10.1007/s00138-005-0011-1.

[86] Hautiere, N., Labayrade, R., & Aubert, D. (2006). Estimation of the visibility distance by stereovision: A generic approach. *IEICE Transactions on Information and Systems*, *E89-D*(7), 2084–2091. https://doi.org/10.1093/ietisy/e89-d.7.2084.

[87] Horvath, H., & Noll, K. E. (1969). The relationship between atmospheric light scattering coefficient and visibility. *Atmospheric Environment (1967)*, *3*(5), 543–550.

[88] Kunkel, B. A. (1984). Parameterization of droplet terminal velocity and extinction coefficient in fog models. *Journal of Climate and Applied Meteorology*, *23*(1), 34–41.

[89] Li, C., & Peng, P. (2012). Visibility measurement using multi-angle forward scattering by liquid droplets. *Measurement Science and Technology*, *23*(10), 105802.

[90] Dumont, E. (2002). *Caractérisation, modélisation et simulation des effets visuels du brouillard pour l'usager de la route*. Université René Descartes-Paris V.

[91] Rogers, R., & Yau, M. K. (1996). *A short course in cloud physics*. Elsevier.

[92] Mazoyer, M. (2016). *Impact du processus d'activation sur les propriétés microphysiques des brouillards et sur leur cycle de vie*.

[93] Dupont, J.-C., Haeffelin, M., Protat, A., Bouniol, D., Boyouk, N., & Morille, Y. (2012). Stratus–fog formation and dissipation: a 6-day case study. *Boundary-Layer Meteorology*, Vol. *143*, *No*. 1, pp. 207–225.

[94] Gultepe, I., Müller, M. D. & Boybeyi, Z. (2006). "A new visibility parameterization for warm-fog applications in numerical weather prediction models," *Journal of Applied Meteorology and Climatology*, *45*(11), pp. 1469–1480.

[95] Kim I., Mcarthur B. and Korevaar E., (2001), "Comparison of laser beam propagation at 785 nm and 1550 nm in fog and haze for optical wireless communications," *Proceedings of SPIE*, Vol. 214/4214, pp. 38-45/26-37.

[96] Awan M. S., Nebuloni R., Capsoni C., Csugai-Horvath L., Muhammad S. S., Leitgeb E., Nadeem F. and Khan M. S., (2010), "Prediction of drop size distribution parameters for optical wireless communications through moderate continental fog," *International Journal of Satellite Communications and Networking*, Vol. 29, No. 1, pp. 97-116.

[97] Grabner M. and Kvicera V., (2011), "The wavelength dependent model of extinction in fog and haze for free space optical communication," *Optics Express*, Vol. 19, No. 4, pp. 3379-3386.

[98] Schowengerdt R. A., (2007), "Optical radiation Models", in *Remote Sensing, 3rd ed., Academic Press*, ISBN: 9780123694072, pp. 45-XIII, https://doi.org/10.1016/B978-012369407-2/50005-X.

[99] Malm W. C., (2016), "How the transfer of Light (Radiation) through the atmosphere affects visibility", *Elsevier*, ISBN: 9780128044506, pp. 73-92, doi: https://doi.org/10.1016/B978-0-12-8044506.00003-6.

[100] Tatarski V. I., (1961), The effect of the turbulent atmosphere on wave propagation, *Keter Press, Jerusalem*.

[101] Hinder R. A. (1970), "Observations of atmospheric turbulence with a radio telescope at 5 GHz," *Nature*, 225(5233), p 614.

[102] Vilar E. and Haddon J., (1984), "Measurement and modeling of scintillation intensity to estimate turbulence parameters in an earth-space path," *IEEE Transactions on Antennas and Propagation*, 32(4), pp. 340-346.

[103] Vilar E., Lo P., Haddon J. and Moulsley T. J., (1985), "Measurement and modeling of amplitude and phase scintillations in an earth-space ," *Journal of the Institution of Electronic and Radio Engineers*, 55(3), pp. 87-96.

[104] Karasawa Y., Yamada M. and Allnutt J. E., (1988), "A new prediction method for tropospheric scintillation on earth-space paths," *IEEE Transactions on Antennas and Propagation*, 36(11), pp. 1608-1614.

[105] Ishimaru A., (1978), "Wave propagation and scattering in random media," *Academic Press, New York*, Vol. 2, pp. 336-393.

[106] Cang J. and Liu X., (2011), "Scintillation index and performance analysis of wireless optical links over non-Kolmogorov weak turbulence based on generalized atmospheric spectral model," *Optics Express*, Vol. 19, No. 20, pp. 19067 – 19077.

[107] CCIR, (1986), "Effects of tropospheric refraction on radiowave propagation," CCIR SG-5, Rep. 781-2, ITU, Geneva.

[108] Ochs G. R., (1989), "Measurement of refractive-index structure parameter by incoherent aperture scintillation techniques," *Proc. SPIE* **1115**, pp. 107– 115.

[109] d'Auria G., Marzano F. S., and Merlo U., (1991), "Statistical estimation of mean refractive-index structure constant in clear air," in *Proc. of 7th Int. Conf. Antennas and Propagation, ICAP '91*, 15–18 April 1991, IEEE, Vol. 1, pp. 177–180.

[110] Rasouli S. and Tavassoly M., (2006), "Measurement of the refractive-index structure constant, C_n^2, and its profile in the ground level atmosphere by moire technique," *Proc. SPIE* **6364**, 63640G.

[111] Prokes A., (2009), "Atmospheric effects on availability of free space optics systems," *Optical Engineering*, Vol. 48, No. 6, pp. 066001 – 066010.

[112] Karasawa Y., Yasukawa K. and Yamada M., (1988), "Tropospheric scintillation in the 14/11-GHz bands on earth-space paths with low elevation angles," IEEE *Transactions on Antennas and Propagation*, Vol. 36, No. 4, pp. 563-569.

[113] Crane R. K., (1976), "Low elevation angle measurement limitations imposed by the troposphere: an analysis of scintillation observations made at Haystack and Millstone," (No. TR-518), *Massachusetts Inst. Of Tech., Lexington Lincoln Lab*.

[114] Mayer C. E., Jaeger B. E., Crane R. K. and Wang X., (1997), "Ka-band scintillations: measurements and model predictions," *Proceedings of IEEE*, 85(6), 936-945.

[115] Priyadarshi S., (2015), "Ionospheric scintillation modelling for high-and mid-latitude using B-spline technique," *Astrophys Space Sci.*, Vol. 359, No. 12, pp. 1-8, doi: 10.1007/s10509-015-2461-x.

[116] Ahmed W. A., Wu F., Agbaje G. I., Ednofri E., Marlia D. and Zhao Y., (2017), "Seasonal ionospheric scintillation analysis during increasing solar activity at mid-latitude," *Proc. SPIE 10425, Optics in Atmospheric Propagation and Adaptive Systems XX*, Vol. 10425, pp. 104250A-1 to 10425A-13, doi: 10.1117/12.2278224.

[117] Sahithi K., Sridhar M., Kotamraju S. K., Sri Kavya K. Ch., Sivavaraprasad G., Ratnam D. V. and Deepthi Ch., (2019), "Characteristics of ionospheric scintillation climatology over Indian low-latitude region during the 24th solar maximum period," *Geodesy and Geodynamics*, Vol. 10, pp. 110-117, doi: 10.1016/j.geog.2018.11.006.

[118] Thompson M. C., Wood L. E., James H. B. and Smith D., (1975), "Phase and amplitude scintillations in the 10 to 40 GHz band," *IEEE Transaction on Antennas and Propagation*, Vol. 23, No. 6, pp. 792-797.

[119] Yokoi H., Yamada M. and Satoh T., (1970), "Atmospheric attenuation and scintillation of microwaves from outer space," *Astron. Soc., Japan*, pp. 511-524.

[120] Haidara F. M., Bostian C. W. and Pratt T., (1994), "Measurements of tropospheric scintillations on a 14 degree path at 12, 20 and 30 GHz," *AIAA*-94, pp. 921-931.

[121] Ortgies G., (1993), "Frequency dependence of slant-path amplitude scintillations," *Electronics Letters*, Vol. 29, pp. 2219-2220.

[122] Banjo O. P. and Vilar E., (1987), "The dependence of slant path amplitude scintillations on various meteorological parameters," *ICAP '87 5th Int. Conf. on Antennas and Propagation, IEE London*, Vol. 2, pp. 277-280.

[123] Guenther B. D., (2005), "Diffraction: Fresnel diffraction," *Encyclopedia of Modern optics, Elsevier*, pp. 257-270, ISBN: 9780123693952, doi: https://doi.org/10.1016/B0-12-369395-0/00696-5.

[124] Bouchet O., (2013), "Wireless optical communications", *Wiley*, ISBN: 978-1-118-56327-4.

[125] Hemmati H., (2009), "Near-Earth laser communications," *Taylor & Francis*, 1st Edition, ISBN: 978-1-315-22142-7, doi: https://doi.org/10.1201/9781420015447.

[126] Martini R. and Whittaker E., (2005), "Quantum cascade laser-based free space optical communications," *Journal of Optical and Fiber Communications Research*, Vol. 2, pp. 279-292.

[127] Baier S., (2012), "What is Full Spectrum Lighting?", Lumenistics website, [Online], Available at: http://lumenistics.com/what-is-full-spectrum-lighting/, Accessed on January 17, 2018.

[128] Franz J. H., Jain V. K. and Jain V. K., (2000), *Optical Communications: Components and Systems: Analysis, Design, Optimization, Application*. CRC press.

[129] Hall M. P. and Barclay L. W., (1989), "Radio-wave propagation," NASA STI/Recon. Technical Report A, 90, 45603.

[130] Lutgens F. K. Tarbuck E. J. and Tusa D., (1995), "The atmosphere", 9th ed. *Prentice Hall*.

[131] Karp S., Gagliardi R. M., Moran S. E. and Stotts L. B., (1988), "Optical Channels: fibers, clouds, water and the atmosphere", *Plenum Press, New York*.

[132] Ricklin J. C., Hammel S. M., Eaton F. D. and Lachinova S. L., (2006), "Atmospheric channel effects on free-space laser communication," *Journal of Optical and Fiber Communications Research*, vol. 3, pp. 111-158.

[133] Ijaz M., Ghassemlooy Z., Le Minh H., Rajbhandari S. and Perez J., (2012), "Analysis of fog and smoke attenuation in a free space optical communication link under controlled laboratory conditions," in *Optical Wireless Communications (IWOW), International Workshop on*, pp. 1-3.

[134] Jia Z., Zhu Q. and Ao F., (2006), "Atmospheric attenuation analysis in the FSO link," in *Communication Technology, ICCT'06. International Conference on*, pp. 1-4.

[135] Rockwell D. A. and Mecherle G. S., (2001), "Wavelength selection for optical wireless communications systems," *Optical Wireless Communications IV, in Proc. SPIE*, pp. 27-35.

[136] Alkholidi, A. G. and Altowij, K. S., (2014), "Free Space Optical Communications — Theory and Practices", in M. Khatib (ed.), Contemporary Issues in Wireless Communications, *IntechOpen, London*, doi: 10.5772/58884.

[137] Gudimetla V., Holmes R. B., Smith C. and Needham G., (2012), "Analytical expressions for the log-amplitude correlation function of a plane wave through anisotropic atmospheric refractive turbulence," *JOSA A*, vol. 29, pp. 832-841.

[138] Takashi S., Morio T. and Hideki T., (2012), "Fading simulator for satellite-to-ground optical communication," *Journal of the National Institute of Information and Communications Technology*, vol. 59, pp. 95-102.

[139] Sofieva V., Dalaudier F. and Vernin J., (2013), "Using stellar scintillation for studies of turbulence in the Earth's atmosphere," *Philosophical Transactions of the Royal Society A: Mathematical, Physical and Engineering Sciences*, vol. 371.

[140] Kim I. I., McArthur B. and Korevaar E., (2000), "Comparison of laser beam propagation at 785 nm and 850 nm in fog and haze for optical wireless communications," *Proc. SPIE, Opt. wireless comm. III*, vol. 4214, pp. 26–37.

[141] Awan M. S., Brandl P., Leitgeb E., Nadeem F., Plank T. and Capsoni C., (2009), "Results of an optical wireless ground link experiment in continental fog and dry snow conditions," *in 10th Int. Conf. on Telecom. (CONTEL-2009), (Zagreb)*, pp. 45–49.

[142] Wallace J. M. and Hobbs P. V., (1977), "Atmospheric Science: An Introductory Survey", *Academic Press, San Diego*, pp. 437-439.

[143] Willebrand H. and Ghuman B. S., (2002), "Free space optics: enabling optical connectivity in today's networks," *Sams Publishing, London*.

[144] Mahalati R. N. and Kahn J. M., (2012), "Effect of fog on free-space optical links employing imaging receivers," *Opt. Exp.*, vol. 20, no. 2, pp. 1649–661.

[145] Chen C. C., (1975), “Attenuation of electromagnetic radiation by haze, fog, cloud and rain,” Tech. Report: R-1694-PR, United States of Air Force Project Rand.

[146] Suriza A. Z., Rafiqul I. M., Wajdi A. K. and Naji A. W., (2013), “Proposed parameters of specific rain attenuation prediction for free space optics link operating in tropical region,” *J. of Atmosp. and Solar-Terres. Phys.*, vol. 94, pp. 93–99.

[147] Vavoulas A., Sandalidis H. G. and Varoutas D., (2012), “Weather effects on FSO network connectivity,” *J. Opt. Comm. and Net.*, vol. 4, no. 10, pp. 734–740.

[148] ITU-R P.1814, (2007), “Prediction methods required for the design of terrestrial free-space optical links,” Recommendation ITU-R P.1814, Geneva (Switzerland): International Telecommunication Union

[149] Crane R. K. and Robinson P. C., (1997), “ACTS propagation experiment: rain-rate distribution observations and prediction model comparisons,” *Proc. IEEE*, vol. 86, no. 6, pp. 946–958.

[150] Ijaz M., Ghassemlooy Z., Pesek J., Fiser O., Le Minh H. and Bentley E., (2013), "Modeling of Fog and Smoke Attenuation in Free Space Optical Communications Link under Controlled Laboratory Conditions," *Lightwave Technology, Journal of*, vol. PP, pp. 1-1.

[151] Awwad O., Al-Fuqaha A., Khan B. and Brahim G. B., (2012), “Topology control schema for better qos in hybrid RF/FSO mesh networks,” *Communications, IEEE Transactions on*, Vol. 60, pp. 1398-1406.

[152] Libich J., Mudroch M., Dvorak P. and Zvanovec S., (2012), “Performance analysis of hybrid FSO/RF link,” *in Antennas and Propagation (EUCAP), 6th European Conference on*, pp. 1235-1238.

[153] Vishnevskii V., Semenova O. and Sharov S. Y., (2013), “Modeling and analysis of a hybrid communication channel based on free-space optical and radio-frequency technologies,” *Automation and Remote Control*, Vol. 74, pp. 521-528.

[154] Leitgeb E., Plank T., Awan M. S., Brandl P., Popoola W., Ghassemlooy Z., Ozek F. and Wittig M., (2010), "Analysis and evaluation of optimum wavelengths for free-space optical transceivers," *Transparent Optical Networks (ICTON),12th International Conference on*, pp. 1-7.

[155] Hranilovic S., (2005), “Wireless Optical Communication Systems”, *Springer, New York*.

[156] Faridzadeh M., Gholami A., Ghassemlooy Z. and Rajbhandari S., (2011), “Hybrid PPMBPSK subcarrier intensity modulation for free space optical communications”, *Proc. IEEE, 16th European Conf. on Netw. and Opt. Comm., (Newcastle-Upon-Tyne)*, pp. 36–39.

[157] Barry J. R., Kahn J. M., Krause W. J., Lee E. A. and Messerschmitt D. G., (1993), "Simulation of multipath impulse response for indoor wireless optical channels," *Selected Areas in Communications, IEEE Journal on*, Vol. 11, pp. 367-379.

[158] Wu G., Zhang Y. A., Yuan X. G., Zhang J. N., Zhang M. L. and Li Y. P., (2013), "Design and Realization of 10Gbps DPSK System for Free Space Optical Communication," *Applied Mechanics and Materials*, Vol. 263, pp. 1150-1155.

[159] Selvi M. and Murugesan K., (2012) "The performance of orthogonal frequency division multiplexing in the weak turbulence regime of free space optics communication systems," *Journal of Optics*, Vol. 14, p. 125401.

[160] Barros D. J., Wilson S. K. and Kahn J. M., (2012), "Comparison of Orthogonal Frequency-Division Multiplexing and Pulse-Amplitude Modulation in Indoor Optical Wireless Links," *Communications, IEEE Transactions on*, Vol. 60, pp. 153-163.

[161] Awan M. S., Leitgeb E., Nadeem F., Khan M. S. and Capsoni C., (2009), "Weather Effects Impact on the Optical Pulse Propagation in Free Space," in *Vehicular Technology Conference, VTC Spring, IEEE 69th*, pp. 1-5.

[162] Awan M. S., Leitgeb E., Capsoni C., Nebuloni R., Nadeem F. and Khan M. S., (2008), "Attenuation analysis for optical wireless link measurements under moderate continental fog conditions at milan and graz," in *Vehicular Technology Conference, 2008. VTC 2008-Fall. IEEE 68th*, pp. 1-5.

[163] Van der Walt A. J. and Fitchett J. M., (2020), “Statistical classification of South African seasonal divisions on the basis of daily temperature data,” *S. Afr. J. Sci.*, Vol. 116, No. 9/10, pp. 1-15, doi: 10.17159/sajs.2020/7614.

[164] Mabin A. S., Nel A., Hall M., Thompson L. M., Cobbing J. R. D., Bundy C. J., Vigne R., Lowe C. C. and Gordon D. F., (2021), "South Africa," *Encyclopedia Britannica*, Revised on: 20 June 2021, Retrieved from: https://www.britannica.com/place/South-Africa, Accessed on: 22 June 2021.

[165] Knight J. and Rogerson C.M., (2019), "The Geography of South Africa," *Springer: Cham, Switzerland*, ISBN: 978-3-319-94974, pp. 7-26, doi: 10.1007/978-3-319-94974.

[166] Government Communications (GCIS), (2016), "South Africa yearbook 2015/2016", *Government communications, Pretoria*, 23rd ed.

[167] Statistics South Africa, (2012), "Census 2011 Statistical Release," *Statistics South Africa, Pretoria*, Report No.: P0301.4, pp. 9, 14-15, Available on: www.statssa.gov.za.

[168] Statistics South Africa, (2012), "Census 2011: Census in Brief," *Statistics South Africa, Pretoria*, Report No.: 03-01-41, ISBN: 978-0-62-41388-5, pp. 9, 18-19, Available on: www.statssa.gov.za.

[169] McCarthy T. and Rubidge B., (2005), "The story of earth and life," *Struik Publishers, Cape Town*, pp. 263, 267–268.

[170] Encyclopædia Britannica, (1975), "Micropaedia," *Helen Hemingway Benton Publishers, Chicago*, Vol. III, p. 655.

[171] Beck H.E., Zimmermann N. E., McVicar T. R., Vergopolan N., Berg A., and Wood E. F., (2018), "Present and future Köppen-Geiger climate classification maps at 1-km resolution," *Nature Scientific Data*, Retrieved from https://commons.wikimedia.org/w/index.php?curid=74674206, Accessed on: 22 June 2021. DOI:10.1038/sdata.2018.214.

[172] Karl T. R., Jones P. D., Knight R,. Kukla G., Plummer N., et al., (1993), "Asymmetric trends of daily maximum and minimum temperature," *Bull Am Meteorol. Soc.*, Vol. 74, No. 6, pp. 1007-1023, doi: 10.1175/1520-0477(1933)074<1007.

[173] Klopper E., Landman W. A. and Van Heerden J., (1998), "The predictability of seasonal maximum temperature in South Africa," *Int. J. Climatol.*, Vol. 18, No. 7, pp. 741-758, doi: 10.10029(sici)1097-0088(19980615)18:7<747.

[174] Kruger A. C. and Nxumalo M., (2017), "Surface temperature trends from homogenized time series in South Africa: 1931-2015," *Int. J. Climatol.*, Vol. 27, No. 5, pp. 1-52, doi: 10.1002/joc.4851.

[175] Owolawi, P. A., (2010), Characteristics of rain at microwave and millimeter bands for terrestrial and satellite links attenuation in South Africa and surrounding islands, PhD thesis, University of KwaZulu-Natal, Durban, South Africa, [Online], Available at: http://citeseerx.ist.psu.edu/viewdoc/download?doi=10.1.1.969.7527&rep=rep1&type=pdf, Accessed on: 7th March 2017.

[176] ITU-R P.1817-1, (2012), "*Propagation data required for the design of terrestrial free-space optical links*," Recommendation ITU-R P.1817-1, Geneva (Switzerland): International Telecommunication Union.

[177] Pal R., (2017), "Predictive Modeling of Drug Sensitivity," *Academic Press, Elsevier*, ISBN: 9780128052747, pp. 83-107, doi:10.1016/B978-0-12-8052747.00004-X.

[178] Moore D. S., Notz W. I. and Flinger M. A., (2013), "The basic practice of statistics", 6th Edition, *New York, NY: W. H. Freeman and Company*, p 138.

[179] Henseler J., Ringle C. and Sinkovics R., (2009), "The use of partial least squares path modelling in international marketing," *Advances in International Marketing (AIM)*, Vol. 20, pp 277-320.

[180] Kato T., (2016), "Integration of Distributed Energy Resources in Power Systems, *Academic Press, Elsevier*, ISBN: 9780128032121, pp. 77-108, doi: 10.1016/B978-0-12-8032121.00004-0.

[181] Odic, D., Im, H. Y., Eisinger, R., Ly, R., Halberda, J., (2016), "PsiMLE: A maximum-likelihood estimation approach to estimating psychophysical scaling and variability more reliably, efficiently, and flexibly," *Behavior Research Methods*, Vol. 48, No. 2, pp. 445–462. doi:10.3758/s13428-015-0600-5. ISSN 1554-3528. PMID 25987306.

[182] Arora, J. S. (2012). "Introduction to Optimum Design: Additional Topics on Optimum Design", *Elsevier*, pp. 731–784. ISBN: 9780123813756, doi:10.1016/b978-0-12-381375-6.00029-2. https://doi.org/10.1016/B978-0-12-381375-6.00029-2.

[183] Ross, S. (2013). "Elements of Probability", *Simulation, Elsevier*, pp. 5–38, ISBN 9780124158252, https://doi.org/10.1016/B978-0-12-415825-2.00002-4.

[184] Feller, W., (1991), "An Introduction to Probability Theory and its Applications", *John Wiley & Sons*, New York, Vol. 1, 3rd Edition, ISBN: 978-0-471-25708-0.

[185] Gabbiani, F. & Cox, S. J., (2010). "Probability and Random Variables. Mathematics for Neuroscientists", *Academic Press. Elsevier*, pp. 155–173, ISBN 9780123748829, https://doi.org/10.1016/B978-0-12-374882-9.00011-3.

[186] Kamalakis T., Sphicopolous T., Muhammad S. S. and Leitgeb E., (2006), "Estimation of the power scintillation probability density function in free space optical links by use of multi canonical Monte Carlo sampling," *Optics Letters*, Vol. 31, No. 21, pp. 3077-3079.

[187] Gultepe I. and Isaac G. A., (2001), "Scale effects on averaging of cloud droplet and aerosol number concentrations observations and models," *Journal of Climatology*, pp. 507-525.

[188] Al-Naboulsi M., Defornel F., Sizun H., Muhammad S. S., et al., (2008), "Measured and predicted light attenuations in dense coastal upslope fog at 650, 850 and 950 nm for free space optical applications," *Optical Engineering*, Vol, 47, No. 3, p 036001.

[189] Muhammad S. S., Awan M. S. and Rehman A., (2010), "PDF estimation and liquid water content based modeling for fog in terrestrial FSO links," *Radioengineering*, Vol. 19, No. 2, pp. 228-236.

[190] Muhammad S. S., Kohldorfer P. and Leitgeb E., (2005), "Channel modeling for terrestrial free space optical links," *In Proceedings of IEEE International Conference on Transparent Optical Networks, Barcelona (Spain)*, Vol. 1, pp. 407-410.

[191] Kruse P. W., (1962), "Elements of infrared technology: Generation, Transmission and Detection", *New York: J. Wiley and Sons*.

[192] Tomasi C. and Tampieri F., (1976), "Features of the proportionality coefficient in the relationship between visibility and liquid water content in haze and fog," *Atmosphere*, Vol. 14, No. 2, pp. 61-76.

[193] Shettle E. P., (1989), "Models of aerosols, clouds and precipitation for atmospheric propagation studies," *AGARD Conference Proceedings*, Vol. 454, No. 15. Pp. 1-13.

[194] Achour M., (2002), "Simulating atmospheric free-space optical propagation: II, haze. Fog and low cloud attenuations," *Proceedings of SPIE*, Vol. 4873, pp. 1-12.

[195] Nadeem F. and Leitgeb E., (2010), "Dense maritime fog attenuation from measured visibility data," Radioengineering, Vol. 19, No. 2, pp. 223-227.

[196] Gebhart M., Leitgeb E., Al Naboulsi M. and Sizun H., (2004), "Measurements of light attenuation at different wavelengths in dense fog conditions for FSO applications," COST 270 Short Term Scientific Mission 7 Report.

[197] Awan M. S, Leitgeb E., Muhammad S. S., Marzuki, Nadeem F., Khan M. S. and Capsoni C., (2008), "Distribution function for continental and maritime fog environments for optical wireless communication," *CSNDSP 2008, In Proceedings, IEEE*, pp. 260-264.

[198] Nadeem F., Leitgeb E., Awan M. S. and Kandus G., (2009), "Comparison of different models for prediction of attenuation from visibility data," *IWSSC, IEEE*.

[199] Nadeem F., Javornik T., Leitgeb E., Kvicera V. and Kandus G., (2010), "Continental fog attenuation empirical relationship from measured visibility data," *Radioengineering*, Vol. 19, No. 4, pp. 596-600.

[200] Khan M. S., Muhammad S. S., Awan M. S., Kvicera V., Grabner M. and Leitgeb E., (2012), "Further results on fog modeling for terrestrial free-space optical links," *Optical Engineering*, Vol. 51, No. 3, pp. 031207-1 – 031207-8.

[201] Al-Naboulsi M., Sizun H. and Defornel F., (2004), "Fog attenuation prediction for optical and infrared waves," *Optical Engineering*, Vol. 43, No. 2, pp. 319-329.

[202] ITU-R, (2013), "*Handbook on Radiometeorology*," Radiocommunication Bureau, Geneva (Switzerland): International Telecommunication Union, pp. 166-169, https://www.itu.int/dms_pub/itu-r/opb/hdb/R-HDB-26-2013-OAS-PDF-E.pdf.

[203] Achour M., (2003), "Free-space optics wavelength selection: 10 μm versus shorter wavelengths," *Journal of Optical Networking*, Vol. 2, No. 6, pp. 127-143, https://doi.org/10.1364/JON.2000127.

[204] Popoola W. O., Ghassemlooy Z., Awan M. S. and Leitgeb E., (2009), "Atmospheric effects on terrestrial free space optical communication link," *ECAI 2009 – 3rd International Conference*, pp. 17-23.

[205] Hamat F. H., Sahmah A., Supaat M. and Mahad F. D., (2010), "Simulation of FSO Transmission at Petaling Jaya due to Attenuations Effect," *ELEKTRIKA*, Vol. 12, No. 1, pp. 30-34.

[206] Virk A. K., Malhotra J. S., and Pahuja S., (2012), "Link Margin Optimization of Free Space Optical Link under the Impact of Varying Meteorological Conditions," *International Journal of Engineering Science and Technology (IJEST)"*, Vol. 4 No.3, ISSN: 0975-5462, pp. 20-25.

[207] Krishna H. and Pundir P.S., (2009), "Discrete Burr and discrete Pareto distributions," *Stat. Methodol.* Vol. 6, pp. 177–188.

[208] Chakraborty S., (2015), "Generating discrete analogues of continuous probability distributions-A survey of methods and constructions," *J Stat Distrib App*, Vol. 2, No. 6, pp. 1-30, https://doi.org/10.1186/s40488-015-0028-6.

[209] Chakraborty S., (2015), "A new discrete distribution related to generalized gamma distribution and its properties," *Commun. Stat. Theory. Methods*. Vol. 44, No. 8, pp. 1691–1705, doi:10.1080/03610926.2013.781635.

[210] Cahir, J. J., (2019), "weather forecasting". *Encyclopedia Britannica*, 17th January 2019, Available at: https://www.britannica.com/science/weather-forecasting, Accessed on 6th December 2021.

[211] Zhao J., Mo H. and Deng Y., (2020), "An Efficient Network Method for Time Series Forecasting Based on the DC Algorithm and Visibility Relation," *IEEE Access*, Vol. 8, pp. 7598-7608, doi: 10.1109/ACCESS.2020.2964067.

[212] Salman A. G. and Kanigoro B., (2021), "Visibility Forecasting Using Autoregressive Integrated Moving Average (ARIMA) Models," Procedia Computer Science, Elsevier B. V., Vol. 179, pp. 252-259, doi: 10.1016/j.procs.2021.01.004.

[213] Colabone R. O., Ferrari A. L., Vecchia F. A. S. and Tech A. R. B., (2015), "Application of Artificial Neural Network for Fog Forecast," *J. Aerosp. Technol. Manag*,. Sao Jose dos Campos, Vol. 7, No. 2, pp. 240-246, Apr.-Jun., 2015, doi: 10.5028/jatm.v7i2.446.

[214] Gultepe, I., Tardif, R., Michaelides, S.C., Cermak, J., Bott, A., Bendix, J., Müller, M.D., Pagowski, M., Hansen, B., Ellrod, G., Jacobs, W., Toth, G., Cober, S.G., (2007), "Fog research: a review of past achievements and future perspectives", In Fog and Boundary Layer Clouds: Fog Visibility and Forecasting, *Pure and Applied Geophysics, Springer*, Vol. 167. Issue 6-7, pp. 1121–1159, doi: 10.1007/s00024-007-0211-x.

[215] Fabbian D., de Dear R. and Lellyett S., (2007), "Application of Artificial Neural Network Forecasts to Predict Fog at Canberra International Airport," *Weather and Forecasting*, Vol. 22, No. 2, pp. 372-381, doi: 10.1175/WAF980.1.

[216] Usman A., Olaore K. O. and Ismaila G. S., (2013), "Estimating Visibility using some Meteorological Data at Sokoto, Nigeria," *International Journal of Basic and Applied Science*, Vol. 1, No. 4, pp. 810-815.

[217] Boudala F. S. and Isaac G. A., (2009), "Parametrization of Visibility in Snow: Application in Numerical Weather Prediction Models," *J. Geophys Res.*, Vol. 114, D19202, doi: 10.1029/2008JD011130.

[218] Lopez G., Bosch J. L., Pulido-Calco I. and Gueymard C. A., (2017), "Visibility Estimates from Atmospheric and Radiometric Variables using Artificial Neural Networks," *WIT Transactions on Ecology and The Environment, WIT Press*, Vol. 211, pp. 129-136, doi: 10.2495/AIR170131.

[219] Chaudhuri S., Sarkar L., Das D. and Goswami S., (2015), "Multilayer Perceptron Model for Nowcasting Visibility from Surface Observations: Results and Sensitivity to Dissimilar Station Altitudes," *Pure and Applied Geophysics*, doi: 10.1007/s00024-015-1065-2. Retrieved in May 13, 2015, from http://link.springer.com/article/10.1007%2Fs00024-015-1065-2*ashtag*page-2.

[220] Russel S. J. and Norvig P., (2009), "Artificial Intelligence: A Modern Approach", Third Edition, *Prentice Hall*, pp. 727-737.

[221] Dixon M. F., Halperin I. and Bilokon P., (2020), "Feedforward Neural Networks," *In Machine Learning in Finance, Springer, Cham*, pp. 111-166, doi: 10.1007/978-3-030-41068-1_4.

[222] Lavine B. K. and Blank T. R., (2009), "Feed-Forward Neural Network", *Comprehensive Chemometrics, Elsevier*, Vol. 3, pp. 571-586, ISBN: 9780444527011, doi: 10.1016/B978-044452701-1.00026-0.

[223] Schmidhuber J., (2005), "Deep learning in neural networks: An Overview," *Neural Networks, Elsevier*, Vol. 61, pp. 85-117, doi: 10.1016/j.neunet.2014.09.003.

[224] Goodfellow I., Bengio Y. and Courville A., (2016), "Deep Learning", *MIT Press*, pp. 164-172, Retrieved from: http://www.deeplearningbook.org.

[225] Henseler J., Ringle C. and Sinkovics R., (2009), "The use of partial least squares path modelling in international marketing," *Advances in International Marketing (AIM)*, Vol. 20, pp 277-320.

[226] Andrews, L. C. and Phillips, R. L., (2002), "Impact of scintillation on laser communication systems: recent advances in modeling," *Proc. SPIE* 4489, pp. 23–34.

[227] Cherubini T. and Businger S., (2013), "Another look at the refractive index structure function," *J. of Applied Meteorology and Climatology*, Vol. 52, pp. 498-506, doi: 10.1175/JAMC-D-11-0263.1.

[228] Richardson L. F., (1922), Weather Prediction by Numerical Process, *Cambridge Mathematical library*.

[229] Kolmogorov A. N., (1941), "Local structure of turbulence in an incompressible viscous fluid at very large Reynolds numbers," *C. R. (Dokl.) Acad. Sci., URSS*, Vol. 30, pp. 301-305.

[230] Tatarski V. I., (1967), "Wave propagation in a turbulent medium", *Dover Publications, New York*.

[231] Roddier F., (1981), "The effect of atmospheric turbulence in optical astronomy," *Prog. Opt.*, Vol. 19, pp. 281-377.

[232] Walters D. L. and Kunkel K. E., "Atmospheric modulation transfer function for desert and mountain locations: the atmospheric effects on r_0," *J. Opt. Soc. Am.*, Vol. 71, pp. 397–405, 1981.

[233] Grabner M. and Kvicera V., (2012), "Measurement of the structure constant of refractivity at optical wavelengths using a scintillometer," *Radioengineering*, Vol. 21, No. 1, pp. 455-458.

[234] Yeh K.C. and Liu C. H., (1982), "Radio wave scintillations in the ionosphere," *Proc. IEEE*. Vol. 70, No. 4 pp. 324-360.

[235] Yeh, K.C., and Liu C. H., (1979), "Ionospheric effects on radio communication and ranging pulses," *IEEE Trans. Antennas and Prop. AP-27*, pp. 747-751.

[236] Wernik A. W., Alfonsi L. and Materassi M., (2004), "Ionospheric irregularities, scintillation and its effects on systems," *Acta Geophysica Polonica*, Vol. 52, No. 2, pp. 237-249.

[237] Prokes A., (2009), "Modeling of atmospheric turbulence effect on terrestrial FSO link," *Radio Engineering*, Vol. 18, No. 1, pp. 42-47.

[238] Oh E. S., Ricklin J. C., Gilbreath G. C., Vallestero N. J. and Eaton F. D., (2004), "Optical turbulence model for laser propagation and imaging applications," *Proc. SPIE, Free Space Laser Comm. and Active Laser Illumina. III*, Vol. 5106, pp. 25-32.

[239] Andrews L. C., (1992), "An analytical model for the refractive index power spectrum and its application to optical scintillations in the atmosphere," *J. Mod. Opt.*, Vol. 39, pp. 1849–1853.

[240] Parikh J. and Jain V. K., (2011), "Study on statistical models of atmospheric channel for FSO communication link," *in Nirma University Int. Conf. on Eng.-(NUiCONE)*, pp. 1-7.

[241] Sandalidis H. G., (2010), "Performance analysis of a laser ground-station-to-satellite link with modulated gamma-distributed irradiance fluctuations," *J. Opt. Comm. and Net.*, Vol. 2, No. 11, pp. 938-943.

[242] Park J., Lee E. and Yoon G., (2011), "Average bit-error rate of the Alamouti scheme in gamma-gamma fading channels," *IEEE Photon. Tech. Lett.*, Vol. 23, No. 4, pp. 269-271.

[243] Chatzidiamantis N. D., Sandalidis H. G., Karagiannidis G. and Kotsopoulos S. A., (2010), "New results on turbulence modeling for free-space optical systems," *Proc. IEEE, Int. Conf. on Tele. Comm.*, pp. 487-492.

[244] Kashani M. A., Uysal M. and Kavehrad M., (2015), *A novel statistics channel model for turbulence-induced fading in free-space optical systems*, PhD thesis, Cornell University.

[245] Andrews L. C., (2004), "Field guide to atmospheric optics," Washington, SPIE Press.

[246] Vitásek J, Látal J, Hejduk S, Bocheza J, Koudelka P, Skapa J, Šiška P, Vašinek V., (2011), "Atmospheric turbulences in free space optics channel," *In 34th International Conference on Telecommunications and Signal Processing (TSP) 2011, IEEE*, pp. 104-107.

[247] Dordova L. and Wilfert O., (2011), "Calculation and comparison of turbulence attenuation by different methods," *Radioengineering*, [online], ISSN: 1210-2512, pp. 162-167, Available from: www.<http://www.radioeng.cz/fulltexts/2010/10_01_162_167.pdf>, Accessed on: 15th January 2019.

[248] Korotkova O., Andrews L. C. and Phillips R. L., (2004), "Model for a partially coherent Gaussian beam in atmospheric turbulence with application in Lasercom," *Opt. Eng.*, Vol. 43, No. 2, pp. 330–341.

[249] Lukin V., (2002), "Atmospheric turbulence parameter measurements," *Astronomical Society of the Pacific Conference Series*, Vol. 266, pp. 18-27.

[250] Murphy E. A., Brown J. H., Good R. E., Beland R. R. and Dewan E. M., (1988), "Atmospheric models of optical turbulence," *SPIE*.

[251] Obrien S. G., Tofsted D. H. and Vaucher G. T., (2006), "An atmospheric turbulence profile model for use in army wargaming applications," *in Technical report, Army Re-search Laboratory*.

[252] Hufnagel R. E., (1974), "Variations of atmospheric turbulence," *in Digest of topical meeting on optical propagation through turbulence, Optical Society of America, Washington, D.C.*, p. WA1.

[253] Valley C., (1980), "Isoplanatic degradation of tilt correction and short-term imaging systems," *Opt. Soc. of Am.*, Vol. 19, No. 4.

[254] Hufnagel R. E., (1974), "Propagation through atmospheric turbulence," *In The Infrared Hand-book*, chapter 6, USGPO.

[255] Greenwood D. P., (1977), "Bandwidth specification for adaptive optics systems," *Optical Society of America*, Vol. 67, No. 3.

[256] Crabbs R., Wayne D., Leclerc T., Andrews L. C., Phillips R. L. and Sauer P., (2012), "Creating a cn2 profile as a function of altitude using scintillation measurements along a slant path," *Proc. of SPIE*.

[257] Eaton F., Gilbreath C., Doss-Hammel S., Moore C., Murphy J., Oh J. H., Oh M. S. and Ricklin J. C., (2004), "Estimating optical turbulence using the pamela model," *Proc. of SPIE*.

[258] Haugen-O D. A., Cote R., Kaimal J. C., Wyngaard J. C. and Izumi Y., (1976), "Turbulence structure in the convective boundary layer," *Journal of the Atmospheric Sciences*.

[259] Monin A. S. and Obukhov A. M., (1954), "Basic law of turbulent mixing near the ground," *Trans. Geophys. Inst. Akad. Nauk USSR*, Vol. 24, pp. 163-187.

[260] Wyngaard J. C., (1973), "On Surface Layer Turbulence," *in Workshop on Microceteorology, American Meteorological society*.

[261] Oh E., Doss-Hammel S., Eaton F., Oh Y. H. and Ricklin J. C., (2004), "Estimating optical turbulence effects on free space laser communication: modeling and measurements at arl s alot facility," *Proc. of SPIE*.

[262] Warnock J. M. and VanZandt T. E., (1985), "A statistical model to estimate the refractivity turbulence structure constant cn2 in the free atmosphere," *Technical report, National Oceanic and Atmospheric Administration*.

[263] Beland R., Dewan E. M., Good R. E. and Brown J., (1993), "A model for cn2 (optical turbulence) profiles using radiosonde data," Technical report, Phillips Laboratory Directorate of Geophysics US Air Force, Hanscom Air Force Base, MA 01731-3010.

[264] Kopeika N. S., Bendersky S. and Blaunstein N., (2004), "Atmospheric optical turbulence overland in middle east coastal environments: prediction modeling and measurements," Optical society of America, Vol. 43, No. 20.

[265] Reynolds O., (1883), "An experimental investigation of the circumstances which determine whether the motion of water shall be direct or sinuous, and the law of resistance in parallel channels," *Philosophical Transactions of the Royal Society of London*, Vol. 174, pp. 935-982, Retrieved from: https://royalsocietypublishing.org/ , Accessed on: 24th July 2021.

[266] Yousefi K. and Razeghi A., (2018), "Determination of the critical Reynolds number for flow over symmetric NACA airfoils," *2018 AIAA Aerospace Science Meeting, American Institute of Aeronautics and Astronautics*, pp. 1-11, doi: 10.2514/6.2018-0818.

[267] Galperin B., Sukoriansky S. and Anderson P. S., (2007), "On the critical Richardson number in stab ly stratified turbulence," *Atmospheric Science Letters, in Wiley Inter Science*, Vol. 8, pp. 65-69.

APPENDIX

Appendix I: Descriptive statistics for the daily specific attenuation (dB/km) data for each of the locations.

Summary Stat-2011	DBN	CPT	UMT	BLFT	JHB	MFK
Mean	0.678	0.515	0.637	0.370	0.680	0.369
Standard Error	0.032	0.026	0.044	0.057	0.015	0.008
Median	0.667	0.539	0.627	0.366	0.671	0.359
Mode	0.508	0.428	0.482	0.321	0.482	0.351
Standard Deviation	0.381	0.474	0.389	0.191	0.424	0.123
Sample Variance	0.145	0.225	0.151	0.037	0.180	0.015
Kurtosis	9.582	14.048	10.269	26.048	12.039	27.538
Skewness	6.042	4.765	5.769	9.363	8.615	9.577
Range	0.457	0.252	0.545	0.283	0.631	0.369
Minimum	0.404	0.241	0.429	0.257	0.482	0.275
Maximum	4.389	7.408	2.176	3.323	2.230	1.086
Sum	3189.825	3839.994	3528.325	5511.025	4179.388	5534.025
Count	365	365	365	365	365	365

Summary Stat-2012	DBN	CPT	UMT	BLFT	JHB	MFK
Mean	0.600	0.391	0.589	0.334	0.638	0.378
Standard Error	0.029	0.043	0.068	0.081	0.074	0.047
Median	0.584	0.406	0.559	0.328	0.625	0.367
Mode	0.482	0.406	0.498	0.309	0.532	0.351
Standard Deviation	0.389	0.409	0.362	0.060	0.254	0.041
Sample Variance	0.151	0.167	0.131	0.004	0.060	0.002
Kurtosis	10.671	15.651	7.939	16.997	8.073	16.863
Skewness	6.166	8.248	3.032	8.220	1.215	6.004
Range	0.632	0.315	0.569	0.291	0.768	0.502
Minimum	0.470	0.241	0.454	0.249	0.482	0.291
Maximum	1.935	1.022	2.514	1.782	1.296	0.692
Sum	3881.950	4026.825	3989.400	6570.590	3533.550	6329.888
Count	366	366	366	366	366	366

Summary Stat-2013	DBN	CPT	UMT	BLFT	JHB	MFK
Mean	0.597	0.387	0.597	0.362	0.628	0.378
Standard Error	0.048	0.043	0.037	0.068	0.807	0.054
Median	0.584	0.396	0.576	0.354	0.622	0.367
Mode	0.482	0.266	0.514	0.343	0.551	0.335
Standard Deviation	0.457	0.500	0.435	0.166	0.338	0.147
Sample Variance	0.209	0.250	0.189	0.028	0.114	0.022
Kurtosis	13.098	19.015	10.900	19.345	9.250	19.496
Skewness	9.496	6.883	3.329	8.215	5.655	6.095
Range	0.610	0.263	0.531	0.562	0.245	0.525
Minimum	0.470	0.241	0.441	0.286	0.219	0.321
Maximum	2.254	3.399	3.045	0.581	2.230	0.828
Sum	3898.813	5091.563	3894.025	6735.588	3606.694	6309.313
Count	365	365	365	365	365	365

Appendix II: Descriptive Statistics for Monthly Cumulative Visibility Range over the years 2011-2013.

Durban	**JAN**	**FEB**	**MAR**	**APR**	**MAY**	**JUN**	**JUL**	**AUG**	**SEP**	**OCT**	**NOV**	**DEC**
Number of Samples	744	680	744	720	744	720	744	744	720	744	720	744
Mean	16.305	17.962	16.455	14.486	13.514	12.094	11.641	13.783	13.914	13.796	14.481	16.280
Median	20	20	20	20	15	14	12	15	16	18	20	20
Mode	20	20	20	20	20	20	20	20	20	20	20	20
Standard Deviation	5.783	4.541	5.978	6.584	7.038	7.292	7.374	7.258	6.665	6.959	6.852	6.008
Sample Variance	33.445	20.619	35.736	43.346	49.528	53.173	54.382	52.681	44.422	48.426	46.957	36.097
Range	20.5	23	21.2	21.9	21.9	21.9	21.9	29.9	24.9	24.8	29.8	28.6
Minimum	1.5	2	0.8	0.1	0.1	0.1	0.1	0.1	0.1	0.2	0.2	1.4
Maximum	22	25	22	22	22	22	22	30	25	25	30	30
Cape Town	**JAN**	**FEB**	**MAR**	**APR**	**MAY**	**JUN**	**JUL**	**AUG**	**SEP**	**OCT**	**NOV**	**DEC**
Number of Samples	744	680	744	720	744	720	744	744	720	744	720	744
Mean	25.154	26.748	22.404	18.190	13.884	13.385	15.170	15.702	18.929	21.793	24.132	27.459
Median	25	25	20	20	14	12	15	15	20	20	25	25
Mode	20	40	20	20	20	20	20	20	20	20	20	40
Standard Deviation	10.048	10.463	10.967	11.124	10.431	10.085	11.086	10.282	10.348	10.205	10.633	10.386
Sample Variance	100.956	109.466	120.285	123.750	108.805	101.713	122.900	105.723	107.076	104.138	113.052	107.866
Range	49.2	39.2	39.9	39.9	39.9	39.9	39.9	39.7	39.8	39.6	38.8	48.8
Minimum	0.8	0.8	0.1	0.1	0.1	0.1	0.1	0.3	0.2	0.4	1.2	1.2
Maximum	50	40	40	40	40	40	40	40	40	40	40	50
Umtata	**JAN**	**FEB**	**MAR**	**APR**	**MAY**	**JUN**	**JUL**	**AUG**	**SEP**	**OCT**	**NOV**	**DEC**
Number of Samples	744	680	744	720	744	720	744	744	720	744	720	744
Mean	16.442	16.982	16.214	14.070	13.575	12.701	12.003	13.047	14.033	14.797	15.618	15.868
Median	20	20	20	20	17.5	15	10	15	15	20	20	20
Mode	20	20	20	20	20	20	20	20	20	20	20	20
Standard Deviation	5.693	5.152	5.855	7.062	7.363	7.519	7.167	7.030	6.846	6.485	6.227	6.258
Sample Variance	32.407	26.545	34.282	49.878	54.217	56.534	51.368	49.422	46.866	42.061	38.771	39.157
Range	24.8	20.6	20.9	29.9	19.9	20.9	20.9	19.9	29.9	29.5	29.9	29.9
Minimum	0.2	0.4	0.1	0.1	0.1	0.1	0.1	0.1	0.1	0.5	0.1	0.1
Maximum	25	21	21	30	20	21	21	20	30	30	30	30

Appendix II Continuation

Bloemfontein	**JAN**	**FEB**	**MAR**	**APR**	**MAY**	**JUN**	**JUL**	**AUG**	**SEP**	**OCT**	**NOV**	**DEC**
Number of Samples	744	680	744	720	744	720	744	744	720	744	720	744
Mean	29.912	28.254	27.473	21.949	21.011	19.739	20.767	22.098	23.316	25.347	27.539	28.831
Median	30	30	30	25	25	20	20	30	30	30	30	30
Mode	40	30	30	30	30	30	30	30	30	30	30	30
Standard Deviation	9.820	10.271	10.091	12.108	12.422	13.253	13.102	13.014	11.985	10.368	8.726	8.200
Sample Variance	96.429	105.492	101.820	146.614	154.304	175.646	171.674	169.355	143.631	107.494	76.148	67.245
Range	39.8	38	39	39.4	39.9	39.9	39.8	59.7	59.8	39.3	39.2	58.9
Minimum	0.2	2	1	0.6	0.1	0.1	0.2	0.3	0.2	0.7	0.8	1.1
Maximum	40	40	40	40	40	40	40	60	60	40	40	60
Johannesburg	**JAN**	**FEB**	**MAR**	**APR**	**MAY**	**JUN**	**JUL**	**AUG**	**SEP**	**OCT**	**NOV**	**DEC**
Number of Samples	744	680	744	720	744	720	744	744	720	744	720	744
Mean	14.825	14.068	14.518	13.341	13.427	12.100	12.034	13.178	14.532	14.835	16.167	15.037
Median	19	15	18	15	15	10	10	10	16	18	20	18
Mode	20	20	20	20	20	20	20	20	20	20	20	20
Standard Deviation	5.752	5.868	6.097	6.781	6.963	6.925	7.587	7.723	6.291	6.099	5.557	6.100
Sample Variance	33.089	34.430	37.176	45.980	48.483	47.950	57.555	59.644	39.576	37.199	30.881	37.206
Range	29.8	18.5	19.4	19.8	19.8	24.8	29.8	39.8	27.8	29.4	19.7	39.5
Minimum	0.2	1.5	0.6	0.2	0.2	0.2	0.2	0.2	0.2	0.6	0.3	0.5
Maximum	30	20	20	20	20	25	30	40	28	30	20	40
Mafikeng	**JAN**	**FEB**	**MAR**	**APR**	**MAY**	**JUN**	**JUL**	**AUG**	**SEP**	**OCT**	**NOV**	**DEC**
Number of Samples	744	680	744	720	744	720	744	744	720	744	720	744
Mean	26.159	24.509	24.023	21.664	21.182	19.055	19.613	20.345	22.345	23.575	25.369	25.114
Median	30	30	30	30	26.5	20	20	20	30	30	30	30
Mode	30	30	30	30	30	30	30	30	30	30	30	30
Standard Deviation	6.637	8.217	8.086	10.206	10.986	11.579	11.383	10.409	9.301	8.877	7.301	7.173
Sample Variance	44.047	67.514	65.391	104.162	120.692	134.082	129.576	108.350	86.516	78.797	53.304	51.455
Range	35	38	37.6	39.1	39.2	39.5	39.5	39.2	29	38	38	37.8
Minimum	5	2	2.4	0.9	0.8	0.5	0.5	0.8	1	2	2	2.2
Maximum	40	40	40	40	40	40	40	40	30	40	40	40